

Hamzah Asyrani Sulaiman

Mohd Azlishah Othman

Mohamad Zoinol Abidin Abd. Aziz

Mohd Fareq Abd Malek

Editors

Theory and Applications of Applied Electromagnetics

APPEIC 2014

Lecture Notes in Electrical Engineering

Volume 344

Board of Series editors

Leopoldo Angrisani, Napoli, Italy
Marco Arteaga, Coyoacán, México
Samarjit Chakraborty, München, Germany
Jiming Chen, Hangzhou, P.R. China
Tan Kay Chen, Singapore, Singapore
Rüdiger Dillmann, Karlsruhe, Germany
Haibin Duan, Beijing, China
Gianluigi Ferrari, Parma, Italy
Manuel Ferre, Madrid, Spain
Sandra Hirche, München, Germany
Faryar Jabbari, Irvine, USA
Janusz Kacprzyk, Warsaw, Poland
Alaa Khamis, New Cairo City, Egypt
Torsten Kroeger, Stanford, USA
Tan Cher Ming, Singapore, Singapore
Wolfgang Minker, Ulm, Germany
Pradeep Misra, Dayton, USA
Sebastian Möller, Berlin, Germany
Subhas Mukhopadhyay, Palmerston, New Zealand
Cun-Zheng Ning, Tempe, USA
Toyoaki Nishida, Sakyo-ku, Japan
Bijaya Ketan Panigrahi, New Delhi, India
Federica Pascucci, Roma, Italy
Tariq Samad, Minneapolis, USA
Gan Woon Seng, Nanyang Avenue, Singapore
Germano Veiga, Porto, Portugal
Haitao Wu, Beijing, China
Junjie James Zhang, Charlotte, USA

About this Series

“Lecture Notes in Electrical Engineering (LNEE)” is a book series which reports the latest research and developments in Electrical Engineering, namely:

- Communication, Networks, and Information Theory
- Computer Engineering
- Signal, Image, Speech and Information Processing
- Circuits and Systems
- Bioengineering

LNEE publishes authored monographs and contributed volumes which present cutting edge research information as well as new perspectives on classical fields, while maintaining Springer’s high standards of academic excellence. Also considered for publication are lecture materials, proceedings, and other related materials of exceptionally high quality and interest. The subject matter should be original and timely, reporting the latest research and developments in all areas of electrical engineering.

The audience for the books in LNEE consists of advanced level students, researchers, and industry professionals working at the forefront of their fields. Much like Springer’s other Lecture Notes series, LNEE will be distributed through Springer’s print and electronic publishing channels.

More information about this series at <http://www.springer.com/series/7818>

Hamzah Asyrani Sulaiman
Mohd Azlishah Othman
Mohamad Zoinol Abidin Abd. Aziz
Mohd Fareq Abd Malek
Editors

Theory and Applications of Applied Electromagnetics

APPEIC 2014

 Springer

Editors

Hamzah Asyrani Sulaiman
Universiti Teknikal Malaysia Melaka
Melaka
Malaysia

Mohamad Zoinol Abidin Abd. Aziz
Universiti Teknikal Malaysia Melaka
Melaka
Malaysia

Mohd Azlishah Othman
Universiti Teknikal Malaysia Melaka
Melaka
Malaysia

Mohd Fareq Abd Malek
Universiti Malaysia Perlis
Arau
Malaysia

ISSN 1876-1100

ISSN 1876-1119 (electronic)

Lecture Notes in Electrical Engineering

ISBN 978-3-319-17268-2

ISBN 978-3-319-17269-9 (eBook)

DOI 10.1007/978-3-319-17269-9

Library of Congress Control Number: 2015936294

Springer Cham Heidelberg New York Dordrecht London

© Springer International Publishing Switzerland 2015

This work is subject to copyright. All rights are reserved by the Publisher, whether the whole or part of the material is concerned, specifically the rights of translation, reprinting, reuse of illustrations, recitation, broadcasting, reproduction on microfilms or in any other physical way, and transmission or information storage and retrieval, electronic adaptation, computer software, or by similar or dissimilar methodology now known or hereafter developed.

The use of general descriptive names, registered names, trademarks, service marks, etc. in this publication does not imply, even in the absence of a specific statement, that such names are exempt from the relevant protective laws and regulations and therefore free for general use.

The publisher, the authors and the editors are safe to assume that the advice and information in this book are believed to be true and accurate at the date of publication. Neither the publisher nor the authors or the editors give a warranty, express or implied, with respect to the material contained herein or for any errors or omissions that may have been made.

Printed on acid-free paper

Springer International Publishing AG Switzerland is part of Springer Science+Business Media
(www.springer.com)

Preface

The first Applied Electromagnetic International Conference (APPEIC 2014) was held in the beautiful city of Bandung, Indonesia, during December 16–18, 2014. APPEIC 2014 focused on scientific theories and applications of applied electromagnetic in electronics, communications and computer technology. This international level conference aimed to be more specific in the development and cutting-edge technology related to Applied Electromagnetics. A total of 104 submissions were received from 11 countries such as Malaysia, India, Indonesia, China, Pakistan, Iran, Thailand, Tanzania, United Kingdom, Tunisia and USA. The conference provides a platform where researchers, professionals, academicians and industries share and generate a forum for the latest embedded technologies.

APPEIC 2014 was handled by the Malaysia Technical Scientist Association (MALTESAS) registered with Registrar of Society together with institution of Universiti Malaysia Perlis (UNIMAP). The collaboration was unique in getting participants from the public and private sectors, local and foreign universities, research institute, stakeholders and various industries from all over the region in the field of applied electromagnetic. Associate Prof. Chuwong Phongcharoenpanich delivered the keynote speech entitled ‘Antenna Design for Radio Frequency Identification (RFID) Systems’ where he described the latest technology on antenna design techniques. Professor Ng Kwan Hoong from Universiti Malaysia delivered an interesting topic entitled ‘A Review on the Biological Effects of Radiofrequency Electromagnetic Fields’ where he described the effects of using electromagnetics on human bodies and so on.

The articles in the book were peer reviewed by experts in applied electromagnetics and cover a wide range of applied electromagnetics scientific theories and applications. It should be able to provide industrialists, academia and as well as researchers in this field of applied electromagnetics on the latest technology and development.

The editors acknowledge the Narujaya Enterprise, Malaysia Technical Scientist Association (MALTESAS) and Universiti Malaysia Perlis for organizing and sponsoring this very successful conference.

Hamzah Asyrani Sulaiman
Mohd Azlishah Othman
Mohamad Zoinol Abidin Abd. Aziz
Mohd Fareq Abd Malek

Contents

| | |
|--|----|
| Cluster-Based Spectrum Sensing Scheme in Heterogeneous Network | 1 |
| Mohammad Kamrul Hasan, Ahmad Fadzil Ismail, Aisha-Hassan Abdalla, H.A.M. Ramli, Shayla Islam, Wahidah Hashim and Khairayu Badron | |
| Classification of Precipitation Types Detected in Malaysia | 13 |
| Khairayu Badron, Ahmad Fadzil Ismail, Aniliza Asnawi, Mimi Aminah Wan Nordin, A.H.M. Zahirul Alam and Sheroz Khan | |
| Two Small Antenna Designs for Ultra-Wideband Wireless Systems | 23 |
| Rashid A. Fayadh, Mohd Fareq Abd Malek, Hilal Adnan Fadhil, Ahmad Zaidi Abdullah, Nur Sabrina Md Noorpi, Nurhakimah Mohd Mokhtar and Mohd Asri Jusoh | |
| Strength Pareto Evolutionary Algorithm 2 in Optimizing Ninth Order Multiple Feedback Chebyshev Low Pass Filter | 31 |
| Wei Jer Lim, Asral Bahari Jambek, Siew Chin Neoh, Mohd Fareq Malek, Ahmad Zaidi Abdullah, Nur Sabrina Md Noorpi, Nurhakimah Mohd Mokhtar and Mohd Asri Jusoh | |
| Composites Based on Rice Husk Ash/Polyester for Use as Microwave Absorber | 41 |
| Yeng Seng Lee, Fareq Malek, Ee Meng Cheng, Wei Wen Liu, Fwen Hoon Wee, Muhammad Nadeem Iqbal, Liyana Zahid, Farah Abdullah, Ahmad Zaidi Abdullah, Nur Sabrina Noorpi, Nurhakimah Mohd Mokhtar and Mohd Asri Jusoh | |

| | |
|---|-----|
| Analysis of EEG Signals for Detection of Epileptic Seizure Using Hybrid Feature Set | 49 |
| Ammama Furrukh Gill, Syeda Alishbah Fatima, M. Usman Akram, Sajid Gul Khawaja and Saqib Ejaz Awan | |
| CPW Circular Patch Antenna for Ground Penetrating Radar Applications | 59 |
| M.N.A. Karim, M.F.A. Malek, M.F. Jamlos, A.Z. Abdullah, N.S. Md Noorpi, N.M. Mokhtar and M.A. Jusoh | |
| Investigation of MultiSlot and Stacked Layer on Dual Band Printed Dipole Antenna | 69 |
| Mohamad Hafize Ramli, Mohamad Zoinol Abidin Abd. Aziz, Mohd Azlishah Othman, Badrul Hisham Ahmad, Mohd Kadim Suaidi and Abdul Halim Dahalan | |
| A Numerical Study on MM-NEMO Scheme: Impact of Rising Number of Mobile Routers and Cell Residence Time | 77 |
| Shayla Islam, Aisha Hasan A. Hashim, Mohamed Hadi Habaebi, Wan H. Hassan, Suhaimi A. Latif, Mohammad Kamrul Hasan and H.A.M. Ramli | |
| Design Strategy for Optimum Planar Square Loop FSS with Different Dielectric Substrates | 87 |
| F.C. Seman and N.K. Khalid | |
| Estimations of Fade Margin for the New Malaysian MEASAT-3B Ku-Band Link | 95 |
| Khairayu Badron, Ahmad Fadzil Ismail, Ani Liza Asnawi, Norun Farihah Abdul Malek, Suriza Zainal Abidin and Md. Rafiqul Islam | |
| Improve the Performance of Cooperative Spectrum Sensing Using Hopping Sequence Scheme | 105 |
| Ammar Abdul-Hamed Khader, Mainuddin Mainuddin and Mirza Tariq Beg | |
| Investigation of Rice Husk/CNTs Composites Performance in Microwave Properties | 119 |
| Yeng Seng Lee, Fareq Malek, Ee Meng Cheng, Wei Wen Liu, Fwen Hoon Wee, Muhammad Nadeem Iqbal, Liyana Zahid, Been Seok Yew, Ahmad Zaidi Abdullah, Nur Sabrina Noorpi, Nurhakimah Mohd Mokhtar and Mohd Asri Jusoh | |

Development of Spectrum Management Tool for Malaysia Using Open-Source GIS Software 127
 Mohamad Afif Saman, Ahmad Fadzil Ismail, Khairayu Badron, Huda Adibah Mohd Ramli, Wahidah Hashim and Ahmad Nasruddin 'Atiqullah Fakrullah

Monopole Ellipse Antenna for Ultra-Wideband Applications 137
 M.C. Lim, S.K.A. Rahim, M.I. Sabran and A.A. Eteng

Synthesis of a Biasing Circuit for a Reconfigurable WiMAX Antenna (RWA) at 2.3 GHz. 145
 Muzammil Jusoh, Mohammad Ramlee Kamarudin, Mohamad Rubel Basar, Soh Ping Jack, Thennarasan Sabapathy and Ku Nurul Fazira Ku Azir

Design of Bandpass Filter Based on Metamaterial Concepts 155
 Ahmed Hameed Reja, Syed Naseem Ahmad and Asaad A.M. Al-Salih

A Comparative Study of Electromagnetic Absorption of PIFA and Helical Antenna in the Human Head 167
 M.I. Hossain, M.R.I. Faruque and M.T. Islam

Assessment of Conversion Methods to Acquire 1-Minute Integration Time Rain Intensity Statistic. 175
 Muhamad Haziq Khairolanuar, Ahmad Fadzil Ismail, Ahmad Zamani Jusoh, Nuurul Huda Mohd Sobli and Khairayu Badron

Analysis of Permanent Magnet Brushless AC Motor Using Two Dimensional Fourier Transform-Parseval's Theorem. 185
 Ankita Dwivedi, S.K. Singh and R.K. Srivastava

Dual Band Stacked Artificial Magnetic Conductor with Dipole Antenna 197
 R. Dewan, M.K.A. Rahim, M.R. Hamid, N.A. Samsuri, M.F.M. Yusoff, B.D. Bala and M.E. Jalil

Performance of Sugarcane Bagasse and Rubber Tire Dust Microwave Absorber in Ku Band Frequency 207
 Liyana Zahid, Mohd Fareq Abd Malek, Cheng Ee Meng, Liu Wei Wen, Lee Yeng Seng, Ahmad Zaidi Abdullah, Nur Sabrina Md Noorpi, Nurhakimah Mohd Mokhtar and Mohd Asri Jusoh

| | |
|--|-----|
| Multi-resonator Using Complementary Split Ring Resonator for Chip-Less RFID Application | 215 |
| Mohd Ezwan Bin Jalil, Mohammad Kamal A. Rahim, Noor Asmawati Samsuri and Raimi Dewan | |
| Energy Detection Spectrum Sensing Measurement Using GNU Radio and USRP B200 at Wi-Fi Frequency | 223 |
| K.H. Yusof, M.K.A. Rahim, K.M. Yusof and M.E. Jalil | |
| Double Layer Polarization Insensitive Metamaterial Absorber with Dual Resonances | 231 |
| Osman Ayop, Mohamad Kamal A. Rahim, Noor Asniza Murad and Noor Asmawati Samsuri | |
| A Low Profile Dual-Mode Reconfigurable Antenna Design | 239 |
| Thennarasan Sabapathy, Muzammil Jusoh, R. Badlishah Ahmad and Muhammad Ramlee Kamarudin | |
| Fade Margin Estimation Technique Using Radar Data for Satellite Link | 247 |
| Khairayu Badron, Ahmad Fadzil Ismail, Mimi Aminah Wan Nordin, Farah Nadia Mohd Isa and Aniliza Asnawi | |
| Circular Polarization Textile Antenna for GPS Application | 255 |
| Shakhirul Mat Salleh, Muzammil Jusoh, Abdul Hafiizh Ismail, Mohd Najib Mohd Yasin, Muhammad Ramlee Kamarudin and Roshayati Yahya | |
| Power Management in LTE Femtocell Networks | 265 |
| Jing Huey Lim, R. Badlishah Ahmad, Muzammil Jusoh and Thennarasan Sabapathy | |
| Design and Analysis of a Circular Ring Patch Antenna Array for UHF Applications | 275 |
| Usama Ahmed Adem, Ajmal Hussain Shah, Chandrasekharan Nataraj, Sathish Kumar and Sheroz Khan | |
| Broadband Triangle Shape Printed Antenna for Mobile Wireless Communication | 287 |
| T. Alam, M.R.I. Faruque and M.T. Islam | |
| Parametric Analysis of a Low Profile UWB Trapezoidal Antenna for Ultra Wireless Communication System | 295 |
| Noor Z.A. Naharuddin and Nurul H. Noordin | |

Investigation of Inverted Suspended Rectangular Patch Circular Polarized Antenna 305
 K.S. Phoo, M.Z.A. Abd. Aziz, B.H. Ahmad, M.A. Othman, M.K. Suaidi and F. Abd. Malek

Dual-Band Copper Rod Monopole Antenna for Wireless Communication System 313
 Abdul Halim Dahalan, Mohamad Hafize Ramli, Mohamad Zoinol Abidin Abd. Aziz, Mohd Azlishah Othman, Badrul Hisham Ahmad and Mohd Kadim Suaidi

Investigation of the Shape of SRR Slot and Hybrid Material on Wideband Monopole Antenna 321
 T.K. Ong, B.H. Ahmad, M.Z.A. Abd. Aziz, M.A. Othman, M.K. Suaidi and F. Abd. Malek

Analytical Study of Energy Absorption in Human Body Due to Bendable Behaviour of Textile Antenna 329
 N.A. Elias, N.A. Samsuri and M.K.A. Rahim

A Comparative Study on Polarization Reconfigurable Circular Patch Antenna. 339
 Mohamed Nasrun Osman, Mohamad Kamal A. Rahim, Mohd Fairus Mohd Yusoff, Mohamad Rijal Hamid, Huda A. Majid, Mohd Ezwan Jalil and Khairul Hilmi Yusof

Design Annular Ring with Slots 4 GHz for Satellite Downlink Communication 349
 Saidatul Adawiyah Amiruddin, Mohd Azlishah Othman, Muhammad Ramlee Kamarudin, Mohamad Harris Misran and Mohamad Zoinol Abidin Abd. Aziz

2 × 1 Circular Array Patch Antennas with Double Circular Slots for WLAN Application 359
 Nik Muhammad Farid Nik Mohd Salleh, Mohd Fareq Abd Malek, Nornikman Hassan, Amier Hafizun Ab Rashid, Mohamad Zoinol Abidin Abd. Aziz, Mohd Khairulezmi Che Seman, Nornabila Md Nor, Saidatul Adawiyah Amiruddin, Badrul Hisham Ahmad, Ahmad Zaidi Abdullah and Nur Sabrina Md Noorpi

Circular Polarized Patch Antenna for 1.8 and 2.4 GHz Applications 367
Muhammad Syafiq Noor Azizi, Mohd Fareq Abd Malek,
Nornikman Hassan, Mohamad Zoinol Abidin Abd. Aziz,
Mohd Khairy Ismail, Nur Azimah Basir, Muhamad Faisal Iswandi,
Nurul Norhasmazuani, Badrul Hisham Ahmad,
Nurhakimah Mohd Mukhtar and Mohd Asri Jusoh

Short-Term Non-ionizing 2.45 GHz WBAN RF Exposure Does not Affect Human Physiological Measures and Cognitive Performance Exposed by Wearable Textile Monopole Antenna 375
Hasliza A. Rahim, Fareq Malek, Ping Jack Soh,
Fairul Afzal Ahmad Fuad, Che Muhammad Nor Che Isa,
Nurbaizatul Badrul Hisham, Noor Anida Abu Talib
and Farrah Salwani Abdullah

Specifically Designed Tag Antenna Based on I-Loop Structure for UHF RFID Applications 383
Tajchai Pumpoung, Pitchanun Wongsiritorn,
Chuwong Phongcharoenpanich and Sompol Kosulvit

Cluster-Based Spectrum Sensing Scheme in Heterogeneous Network

Mohammad Kamrul Hasan, Ahmad Fadzil Ismail,
Aisha-Hassan Abdalla, H.A.M. Ramli, Shayla Islam,
Wahidah Hashim and Khairayu Badron

Abstract In OFDM based Heterogeneous Networks (HetNet) deploying femto-cells (HeNodeBs) causes inter-cell interference in uplink as well as downlink. Spectrum allocation is one of the technique as many researcher identified. However, using frequency reuse/cognitive system for dynamic spectrum reallocation is also a challenging issues. Therefore, this paper focuses on unused spectrum sensing (SS) through proposing cluster-based spectrum sensing for OFDM based two-tier HetNets. The proposed SS scheme adopted the basic model of energy detector and compared with cooperative spectrum sensing scheme. In the proposed scheme, the energy detection model is extended into multiple channel detection model. To detect spectrums from nearby macrocell (macro-eNodeB) HeNodeBs are grouped into cluster. A cluster formation algorithm is also proposed in where, cluster head (CH) and signaling node (SN) will detect implies the multi-channel SS technique. The simulation results demonstrate that the proposed scheme can improve the

M.K. Hasan (✉) · A.F. Ismail · A.-H. Abdalla
H.A.M. Ramli · S. Islam · K. Badron
Department of Electrical and Computer Engineering, Faculty of Engineering,
International Islamic University, Kuala Lumpur, Malaysia
e-mail: hasankamrul@ieee.org

A.F. Ismail
e-mail: af_ismail@iium.edu.my

A.-H. Abdalla
e-mail: aisha@iium.edu.my

H.A.M. Ramli
e-mail: hadibahmr@iium.edu.my

S. Islam
e-mail: iium19612@hotmail.com

K. Badron
e-mail: Khairayu@iium.edu.my

W. Hashim
College of Information Technology, Universiti Tenaga Nasional, Selangor, Malaysia
e-mail: wahidah@uniten.edu.my

spectrum detection with minimum error. The performance of the proposed scheme is evaluated in Monte Carlo simulation validate the scheme performance.

Keywords Spectrum sensing · OFDM · Heterogeneous network · ED

1 Introduction

Nowadays, heterogeneous wireless networks deployed due to increasing the number of access technologies, aggregate bandwidth demand as well as coverage extension. Therefore, telecom industries faces more challenges in terms of interference [1], and spectrum scarcity [2–12] Spectrum allocation is one of the current challenges since it regulated by static allocation. Consequently, it is necessity to find out the idle spectrums to reassign. Recently, Cognitive Enabled Radio (CER) techniques are promising in HetNet. CER facilitates much higher spectrum efficiency by the dynamic spectrum access [2]. In HetNet, a CER base stations like HeNodeB performs as a secondary (SU) base station (BS) which is sanctioned to reuse the spectrum bands only, avoiding the source primary (licensed) users' (PUs) interference that entails continuous spectrum sensing (SS). Consequently, it becomes a significant concern to detect the presence of primary signals consistently and promptly [3, 4]. However, it is important to guide the SS capability through developing such mechanism of SUs which will not have any impact on the PUs normal communication [3–5]. A cooperative based sensing is presented with an intention to decrease the probability of interference to legacy systems [6]. Nevertheless, it is observed that the techniques are founded on validity and consistency of sensing, and control channel also. Indecisiveness about noise and interference imposes obligatory limits while realizing the cooperative sensing. Moreover, a centralized signaling center is essential which have coherence with its architecture. Authors in [7] have proposed cooperative energy detection (ED) through identical gain fusion owing to its low complexity. Enhancing ED for cooperative SS is through the extension of various numbers of antennas, and also with different sampling rate. To detect the spectrum, an adaptive SNR based SS algorithm was proposed with a hybrid approach of cyclostationary detection and ED [8]. The principles of this algorithm are OR functions. Authors have proposed resource allocation in OFDM-based HetNets with SS, to maximize the capacity, minimize the sensing errors, and formulate the subcarrier as well as power allocation problems through linear programming [9]. Utilization of idle OFDM sub carrier spectrums is the optimum choice to sense. Authors in [10] have improved the ED through applying the multiple antenna to detect the spectrum and reducing the errors.

In this paper, SS techniques are investigated to sort out the current challenges. Finally, to meet up the solution, a cluster based SS scheme is proposed, aided by the

threshold optimization over ED. The performance analysis is carried out through Monte Carlo simulation in order to validate the effectiveness.

The rest of the paper is organized as follows: Sect. 2 started with the general system model and problem formulation. Section 3 carried out the proposed scheme, in Sect. 4 represents the numerical results with the analysis, and followed by conclusion in Sect. 5.

2 System Model and Prior Solutions

The spectrums of OFDM based two-tier HetNets are laid in both time domain and frequency domain. Here, the received signals which are sampled at sampling frequency (f_s). The general model for SS can be expressed in Eq. (1) [10, 11].

$$Y_i(n) = \begin{cases} \theta_i(n) & \text{Active PU}(\sigma_0^2); \quad H_0 \\ F_i S_i(n) + \theta_i(n) & \text{Inactive PU}(\sigma_S^2); \quad H_1 \end{cases} \quad (1)$$

where, $Y_i(t)$ represents the observed signal from PU transmitter, F_i denoted as Rayleigh fading channel gain, $\theta_i(n)$ denoted the Additive White Gaussian Noise (AWGN) which is autonomous and likely spreading random procedure through mean zero and variance as $E[|\theta_i(n)|^2] = \sigma_0^2$. Therefore, for the energy detector the general output decision matrix can be expressed as in Eq. (2) [10, 11].

$$M = \sum_{n=0}^r |Y(n)|^2 \quad (2)$$

In where, r is the size of observation vector. The decision on the occupancy of a band can be obtained by comparing M with a fixed threshold λ which will be accomplished on the basis of above two hypothesis testing. For the probability statistics, false alarm probability P_f and the probability of detection P_d is expressed in Eqs. (3) and (4) respectively [11, 13]. Where, $\sigma_S^2/\sigma_0^2 = \rho$ represents the SNR and τ used for sensing slot received through SUs (HeNodeBs). Where, $\mathbb{Q}(\cdot)$ is standard AWGN function, represented as $\mathbb{Q}(x) = \frac{1}{\sqrt{2\pi}} \int_x^\infty \exp\left(-\frac{t^2}{2}\right) dt$ [8, 10, 11].

$$P_f = \left[\mathbb{Q} \left\{ \left(\frac{\lambda}{\sigma_0^2} - 1 \right) \sqrt{\tau f_s} \right\} \right] \quad (3)$$

$$P_d = \left[\mathbb{Q} \left\{ \left(\frac{\lambda}{\sigma_0^2} - \rho - 1 \right) \sqrt{\frac{\tau f_s}{2\rho + 1}} \right\} \right] \quad (4)$$

Therefore, the desired $\overline{P_d}$ as in Eq. (5), and P_f is determined in Eq. (6) [11]. Thereby, the number of error rate will be equal to the P_f and the P_d , so that the P_{md} has represented as in Eq. (7) [10, 11].

$$\left[\left\{ \left(\frac{\lambda}{\sigma_0^2} - \rho - 1 \right) \sqrt{\frac{\tau f_s}{2\rho + 1}} \right\} \right] = \mathbb{Q}^{-1}(\overline{P_d}) \quad (5)$$

$$P_f = \mathbb{Q} \left(\sqrt{2\rho + 1} \mathbb{Q}^{-1}(\overline{P_d}) + \sqrt{\tau f_s \rho} \right) \quad (6)$$

$$P_{md} = P_f + (1 - P_d) \quad (7)$$

However, due to the effects on multipath as well as shadowing possessions throughout SS. Uncertainty continues if SUs are unable sense the PU signals owing to a hurdle otherwise deep fade consequences, at that juncture the probability of interference to PU will be increase.

3 Proposed Spectrum Sensing Model

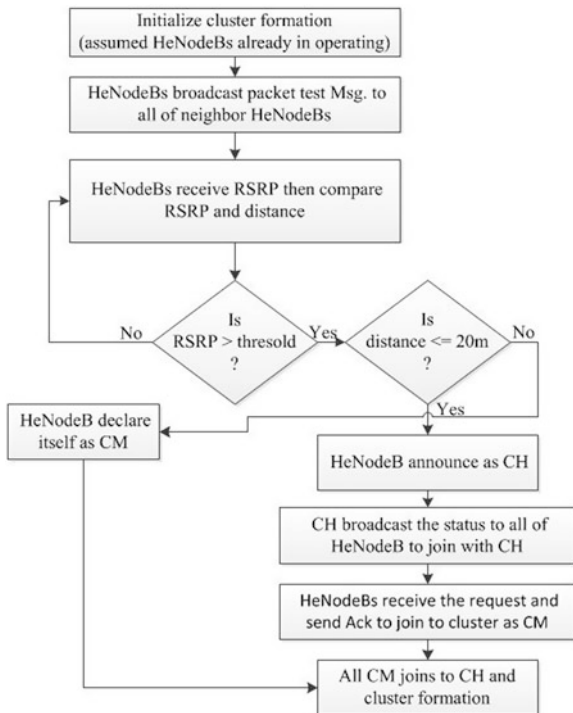
The proposed scheme is classified into two sections: cluster formation and spectrum sensing with threshold optimization.

3.1 Cluster Based Formation

For each of the cluster, there will be a cluster-head (CH), signaling node (SN) and rest of all will play as cluster-member (CM) (Fig. 1). The cluster will be formed considering the underlay SUs. The details procedure is depicted as in Fig. 2.

3.2 Selection of Signaling Node and SS with Reporting

For signaling Node (SN) the details of algorithms' flowchart is enacted in Fig. 3. In order to more accurate quantizing sensing data and disabling the influence of noise variance at SU, the energy of the received signals will be acknowledge through SUs receivers to SN. The local test statistic with reporting errors which can be represented in extended Eq. (9) from ED [5, 10]. In terms of quantization as well as decoding errors, the acknowledge information is corresponding to the k th SUs at the SN is presented in Eq. (8).

Fig. 1 Proposed CH selection algorithm

$$\mathfrak{R}_k = \frac{1}{M_k N_k \sigma_{\theta,k}^2} \sum_{n=1}^N Y(n)^2 + R'_k, \quad k = 1, 2, 3, \dots, K \quad (8)$$

If the acknowledged information statistics exceed of the threshold (λ) with reporting decision $\tilde{\mathfrak{R}}_{SN}$ and without decision $\hat{\mathfrak{R}}$ which can be expressed as in Eq. (9). Where, L is the average reporting bits.

$$\tilde{\mathfrak{R}}_{SN} = \begin{cases} \mathfrak{R}_k < \lambda & \hat{\mathfrak{R}} & L = 0 \\ \mathfrak{R}_k \geq \lambda & \tilde{\mathfrak{R}}_{SN} & 1 \leq L \leq M_k \end{cases} \quad (9)$$

Therefore, in the independent channel of M_k for $M_k N_k$ can be expressed with the \mathfrak{R}_k in Eq. (10), where, ρ is the SNR of the k th SU.

$$\mathfrak{R}_k \sim \begin{cases} T\left(1, \frac{1}{M_k N_k} + \sigma_{\theta,k}^2\right), & H_0 \\ T\left(\rho + 1, \frac{1}{M_k N_k} + \sigma_{\theta,k}^2\right), & H_1 \end{cases} \quad (10)$$

Fig. 2 Proposed SN algorithm

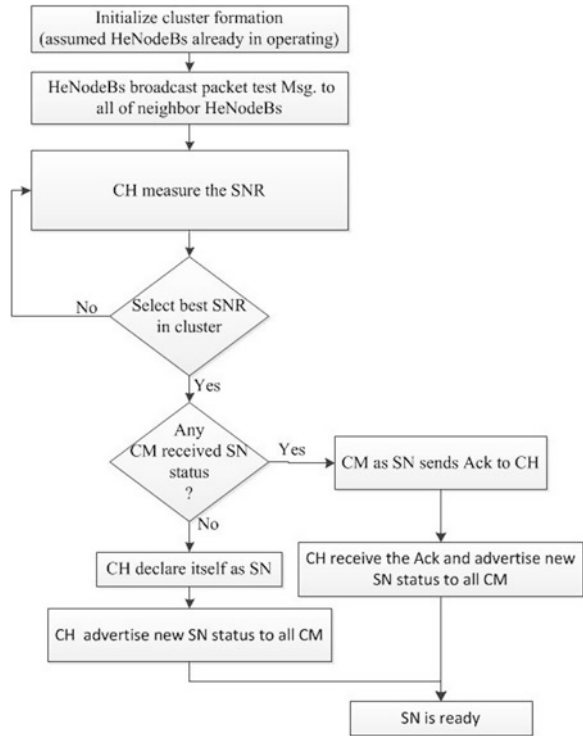
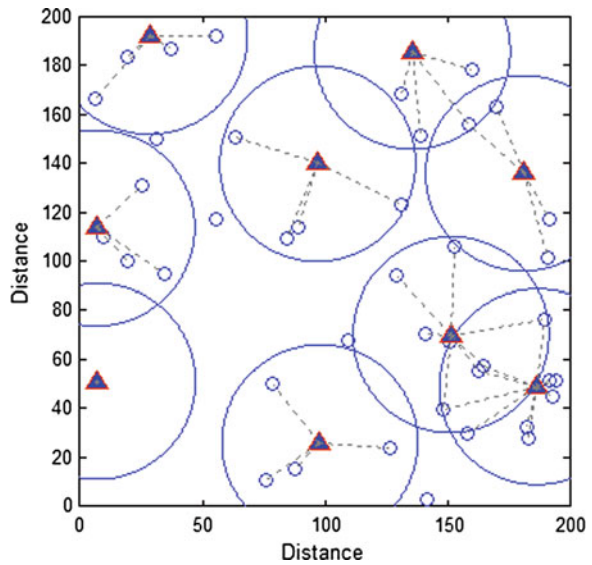


Fig. 3 Representation of cluster formation



Taking consideration of Neyman-Pearson theorem established P_f and P_d can be illustrate the proposed schemes test hypothesis with reporting which is expressed as in Eq. (11) test statistics, Eq. (12) for P_f as well as Eq. (13) for P_d . Where, Q function is followed from Eq. (5).

$$T_{CSS} = \sum_{k=1}^K \frac{\rho_k M_k N_k (1 - M_k N_k \sigma_{\theta,k}^2)}{(1 + M_k N_k \sigma_{\theta,k}^2) (1 + 2\rho_k + \rho_k)} \quad (11)$$

$$Z_{f,CSAS}^{SC} = 1 - \prod_{k=1}^K \left(1 - Q \left(\frac{\lambda - 1}{\sqrt{M_k N_k + \sigma_{\theta,k}^2}} \right) \right) \quad (12)$$

$$Z_{d,CSS}^{SC} = 1 - \prod_{k=1}^K \left(1 - Q \left(\frac{\lambda - 1 - \sigma_{\theta,k}^2}{\sqrt{\frac{1+2\sigma_{\theta,k}^2}{M_k N_k} + \sigma_{\theta,k}^2}} \right) \right) \quad (13)$$

However, the detection may still suffer with error rate, so that the proposed scheme needs to optimize the detection threshold. Subsequently the association of the total error rate for imperfect reporting channel between the *HeNodeB*i and *SN*. Aimed at those noisy channels, channel error probability of r' is considered, which is expressed in Eqs. (14) and (15) using Eqs. (12) and (13).

$$Z_{f,prop}^{SC} = 1 - \prod_{i=1}^K r' \left(1 - Q \left(\frac{\lambda - 1}{\sqrt{L_k N_k + \sigma_{\theta,k}^2}} \right) \right) \quad (14)$$

$$Z_{d,prop}^{SC} = 1 - \prod_{i=1}^K r' \left(1 - Q \left(\frac{\lambda - 1 - \sigma_{\theta,k}^2}{\sqrt{\frac{1+2\sigma_{\theta,k}^2}{L_k N_k} + \sigma_{\theta,k}^2}} \right) \right) \quad (15)$$

Accordingly, the total error rate the optimization for the value of Y , λ and K , can be express using the function as $G(Y, \lambda, K)$ obtained through totaling $Z_{f,prop}^{SC}$ and $Z_{d,prop}^{SC}$ which indicates the total error rate of this scheme and is double the probability of bit error. The value of Y , λ and K , can be found by first order partial derivative concerning of $Y(Y = M_k N_k \sigma_{\theta,k}^2)$, with a fixed repetition manner; is formalizes in Eq. (16).

$$G(Y, \lambda, K) \triangleq Z_{f,prop}^{SC} + Z_{d,prop}^{SC} \quad (16)$$

In the same way, the value of K is the optimized significance of λ . Therefore, the optimized threshold δ_{val} of i th HeNodeBs for the assumed value of J , and λ can be written in Eq. (17).

$$\Delta G(Y\lambda, O) = G(Y, \lambda, K + 1) - G(Y, \lambda, K) = 0 \quad (17)$$

Using Eqs. (14), (15) and (17), the value of δ_{val}^* can be expressed as in Eq. (18), also subsequently $f_1\left(r', Z_{f,\text{prop}}^{\text{SC}}, Z_{d,\text{prop}}^{\text{SC}}\right)$ and $f_2\left(Y, Z_{f,\text{prop}}^{\text{SC}}, Z_{d,\text{prop}}^{\text{SC}}\right)$ is clarified in Eq. (19).

$$\delta_{\text{val}}^* = \left\lceil \frac{\ln f_2\left(r', Z_{f,\text{prop}}^{\text{SC}}, Z_{d,\text{prop}}^{\text{SC}}\right)}{\ln f_1\left(Y, Z_{f,\text{prop}}^{\text{SC}}, Z_{d,\text{prop}}^{\text{SC}}\right)} \right\rceil \quad (18)$$

$$f_1\left(r', Z_{f,\text{prop}}^{\text{SC}}, Z_{d,\text{prop}}^{\text{SC}}\right) = \frac{Z_{d,\text{prop}}^{\text{SC}}(1-r) + Y(1 - Z_{d,\text{prop}}^{\text{SC}})}{(1 - Z_{f,\text{prop}}^{\text{SC}})(1 - Y) + YZ_{f,\text{prop}}^{\text{SC}}}$$

and,

$$f_2\left(Y, Z_{f,\text{prop}}^{\text{SC}}, Z_{d,\text{prop}}^{\text{SC}}\right) = \frac{2YZ_{f,\text{prop}}^{\text{SC}} - Y - Z_{f,\text{prop}}^{\text{SC}}}{Z_{d,\text{prop}}^{\text{SC}} - 2Y + Y - 1} \quad (19)$$

where, $\lceil \cdot \rceil$ represents the ceiling function. The parameters of r' , K , and λ for optimizing the threshold is designed for the reason of minimizing total error rate of the proposed multi-channel SS scheme.

4 Simulation Setup and Result Analysis

The cluster scenario is simulated using proposed cluster formation algorithm. The number of HeNodeBs (SUs) are randomly distributed, the area of the locations can be varied. The channel is well-thought-out with physical path loss model for indoor and outdoor conditions [14, 15]. In terms of estimating the variance of reporting errors by the Y factors. Considering SUs devices $M = 4$ antennas, while the transmitter transmits self-governing BPSK signals. The number of samples is considered here is 8, this is because of more samples stands supportive to expand the sensing enactment.

The cluster formation is represented in Fig. 4. The “blue delta” symbol is representing the CH and “small circle” presents the CM. The SN is fully random which is depends on the algorithm. Based on algorithm (Fig. 5) SN can be selected. The proposed scheme is compared with the cooperative SS [11]. In Fig. 5 demonstrates

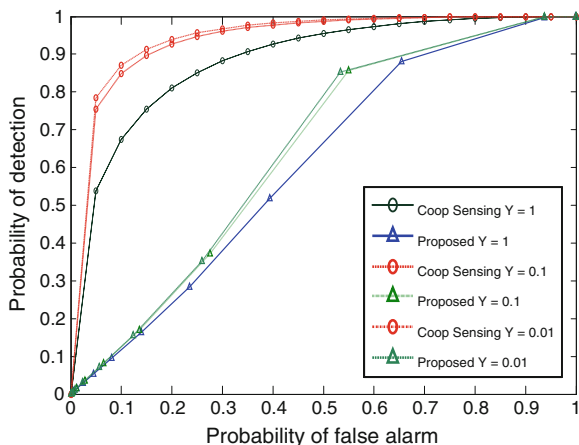


Fig. 4 A receiver operating characteristic (ROC) through recording errors during SS

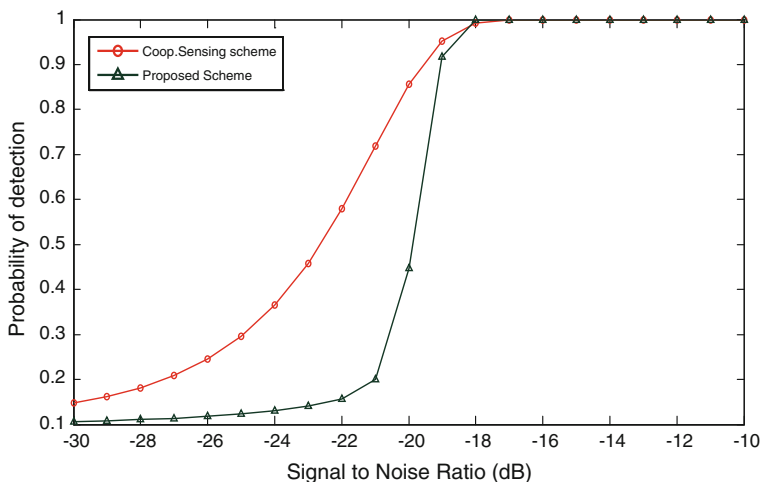


Fig. 5 Probability of distribution over SNR

the receiver operating characteristic (ROC) through recording errors for HetNet concerning with $Y = 1$, $Y = 0.01$ as well as $Y = 0.01$, correspondingly. It is also demonstrated that, the ROC performance reduces if Y increases reporting errors also increases. The simulation time has been observed 0.55 s.

The detection enactment is compared in Fig. 6 for HetNet with respect to different SNR. In addition, the number of receiver is employed as the proposed scheme specified. For ROC reporting, the Monte Carlo simulation elapsed time was taken 0.12 s.

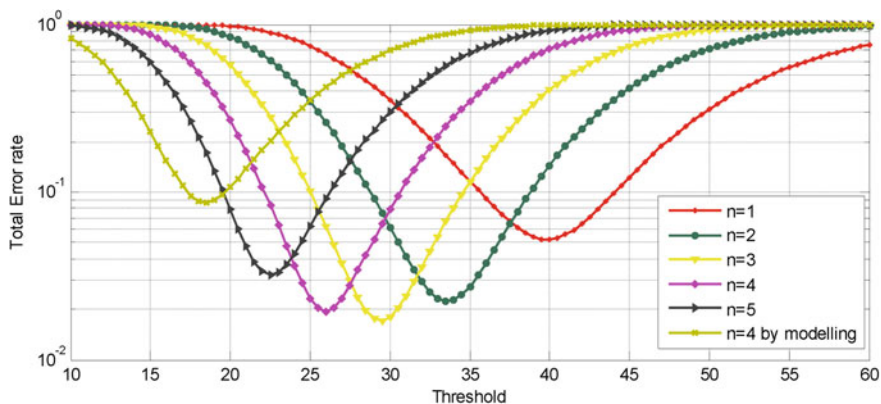


Fig. 6 Total error versus threshold

Figure 6 shows the total error over threshold, representing the 5 number of samples. It can be seen that, when $N = 5$ the total error is minimum while $Y' = 0.001$ through the proposed CSS scheme.

5 Conclusion

To detect the idle spectrums in the licensed macro-eNB (PU) with minimum tolerance of fading effects CSS performs better than cooperative SS. A cluster with SN algorithm also introduced which imposes to the detecting spectrums in HetNet. The simulation results have emphasized the improvement of the desired improvement. Furthermore, a number of previous works investigated as well. The future study aiming to develop a novel algorithm to improve the detection and resource sharing.

Acknowledgments A special thanks to government of Malaysia, through Ministry of Education for the education sponsorship, and thanks to Research Management Center (RMC), International Islamic University Malaysia (IIUM).

References

1. Hasan, M.K., Ismail, A.F., Abdalla, A.H., Abdullah, K., Ramli, H.A.M.: Performance Analysis of Interference Coordination Techniques in Heterogeneous Network. *Res. J. Appl. Sci. Eng. Technol.* **7**(8), 1536–1550 (2014). doi:11178-RJASET-DOI
2. Choi, Y., Lee, Y., Cioffi, J.M.: Optimization of cooperative inter-operability in heterogeneous networks with cognitive ability. *IEEE Commun. Lett.* **15**(11), 1178–1180 (2011)
3. Miao, J., Hu, Z., Yang, K., Wang, C., Tian, H.: Joint power and bandwidth allocation algorithm with QoS support in heterogeneous wireless networks. *IEEE Commun. Lett.* **16**(4), 479–481 (2012)

4. Ismail, M., Zhuang, W.: Decentralized radio resource allocation for single-network and multi-homing services in cooperative heterogeneous wireless access medium. *IEEE Trans. Wirel. Commun.* **11**(11), 4085–4095 (2012)
5. Choi, Y., Kim, H., Han, S.W., Han, Y.: Joint resource allocation for parallel multi-radio access in heterogeneous wireless networks. *IEEE Trans. Wirel. Commun.* **9**(11), 3324–3329 (2010)
6. Chen, X., BIE, Z.S., WU, W.L.: Detection efficiency of cooperative spectrum sensing in cognitive radio network. *J. China Univ. Posts Telecommun.* **15**(3), 1–7 (2008)
7. Zeng, Y., Liang, Y.C., Zheng, S., Peh, E.C.Y.: Optimal cooperative sensing and its robustness to decoding errors. In: 2011 IEEE International Conference on Communications (ICC), pp. 1–5. IEEE (2011, June)
8. Ejaz, W., Hasan, N.U., Kim, H.S.: SNR-based adaptive spectrum sensing for cognitive radio networks. *Int. J. Innov. Comput. Inf. Control.* **8**(9), 6095–6106 (2012)
9. Chen, F., Xu, W., Guo, Y., Lin, J., Chen, M.: Resource allocation in OFDM-based heterogeneous cognitive radio networks with imperfect spectrum sensing and guaranteed QoS. In: 2013 8th International ICST Conference on Communications and Networking in China (CHINACOM), pp. 46–51. IEEE (2013, August)
10. Singh, A., Bhatnagar, M.R., Mallik, R.K.: Cooperative spectrum sensing in multiple antenna based cognitive radio network using an improved energy detector. *IEEE Commun. Lett.* **16**(1), 64–67 (2012)
11. Mokhtar, R., Noordin, N., Ali, B.M., Ramli, A., Abdalla, Y.: Cooperative spectrum sensing with distributed detection threshold. In: 2010 Second International Conference on Network Applications Protocols and Services (NETAPPS), pp. 176–181. IEEE (2010, September)
12. Aravind, K.N., Arun, P.S., Santhoshkumar, K., Sathiesh, L.K., Ka, N.: optimization of threshold for energy based spectrum sensing using differential evolution. In: *Wireless Engineering and Technology* (2011)
13. Zhao, H., Gao, H., Liang, X., Mu, X.: Joint design of spectrum sensing and data transmission for cognitive radio networks. In 2013 6th International Conference on Biomedical Engineering and Informatics (BMEI), pp. 792–796. IEEE (2013, December)
14. Han-Shin, J., Cheol, M., June M., Jong-Gwan, Y.: Interference mitigation using uplink power control for two-tier femtocell networks. *IEEE Trans. Wirel. Commun.* **8**(10) (2009)
15. Report ITU-R P.1238.: Propagation data and prediction methods for the planning of indoor radio communications systems and radio local area networks in the frequency range of 900 MHz to 100 GHz (2009)

Classification of Precipitation Types Detected in Malaysia

**Khairayu Badron, Ahmad Fadzil Ismail, Aniliza Asnawi,
Mimi Aminah Wan Nordin, A.H.M. Zahirul Alam and Sheroz Khan**

Abstract The occurrences of precipitation, also commonly known as rain, in the form of “convective” and “stratiform” have been identified to exist worldwide. In this study, radar return echo or known as reflectivity have been exploited in the process of classifying the type of rain endured. The Malaysian meteorology radar data is used in this investigation. It is possible to discriminate the types of rain experienced in such tropical environment by observing the vertical characteristics of the rain structure. Heavy rain in tropical region profoundly affect microwave and milimetre wave signals, causing interference on transmission and signal fading. Required fade margin for wireless system largely depends on the type of rain. Information relating to the two most prevalent types of rain are critical for the system engineers and researchers in their endeavour to improve the reliability of communication links. This paper highlights the quantification of percentage occurrences over 1 year period of 2009.

K. Badron (✉) · A.F. Ismail · A. Asnawi · M.A.W. Nordin · A.H.M. Zahirul Alam · S. Khan
Faculty of Engineering, International Islamic University Malaysia,
Jln Gombak, 50310 Kuala Lumpur, Malaysia
e-mail: khairayu@iium.edu.my

A.F. Ismail
e-mail: af_ismail@iium.edu.my

A. Asnawi
e-mail: aniliza@iium.edu.my

M.A.W. Nordin
e-mail: mimie@iium.edu.my

A.H.M. Zahirul Alam
e-mail: zahirulalam@iium.edu.my

S. Khan
e-mail: sheroz@iium.edu.my

1 Introduction

According to the literatures [1, 2] precipitation that occurs all over the world may be grouped into four different types. However, precipitation events are generally classified in only two broad classes namely “convective” and “stratiform”. “Convective” type typically involves a very intense and relatively short-lived precipitation with variable rain heights that might go up to more than 13 km [3]. Convective rain is being characterised by severe rainfall that occurs for duration of limited periods and typically covers a small or localised area. “Stratiform” rain on the other hand can be characterised by medium and low rate events that occurs for a longer period of time. This type of rain comprises a very well developed “melting layer” at a constant height. The melting layers are the transition regions between snow and rain. They usually start at the 0 °C and finish a few degrees above 0 °C where the entire snow particles melted and become raindrops.

A radar system is an ideal tool for studying the climate conditions in the tropics. This is one of the feasible techniques of collecting data that will furnish information pertaining to both horizontal and vertical structure of rain. It is also practical for studying rain scatter and signal interference [4]. The evaluation of rain events using radar data is realistic. This is due to the fact that there are large numbers of space-based and ground-based radar around. There are two types of radar display namely the constant altitude plan position indicator (CAPPI) and the range height indicator (RHI). The types of precipitation can be classified from the analysis carried out upon the RHI scans. The vertical variability of the rain at instantaneous time can be observed from RHI views. From the RHI raster scan, the reflectivity values, precipitation rain height and the rain cell size can be ascertained. Rain attenuates wireless communication link both terrestrial and satellite links especially for those with operating frequency higher than 10 GHz. The access attenuation of a radio wave due to precipitation is formed from two components. The components are described as absorption and scattering. The relative importance of scattering and absorption is a function of the complex refraction of the absorbing/scattering particle. The complex index of refraction itself is a function of signal wavelength, temperature, and the size of the particle, relative to the wavelength of the radio wave. It is important to examine the variation of the scattering and/or absorption contributions to extinction, for water spheres of various radii.

2 Classification of Rain Types

Among previously proposed method to classify whether the precipitation is stratiform is by establishing existence of melting layers in radar reflectivity display [5, 6]. If there is no indication of melting layer the rain will be usually of convective type. The melting layer is associated with cumulus–scale convection in unstable air. During convective events, the bright band is entirely absent because of convective

Table 1 Criteria to differentiate rain types using radar data [5–9]

| Stratiform | Convective |
|--|---|
| 1. Reflectivity ranges (2–37 dBz) | 1. Reflectivity ranges >38 dBz) |
| 2. Rainfall intensity values (0–9.9 mm/h) | 2. Rainfall intensity values (>10 mm/h) |
| 3. Clear melting height | 3. No melting height |
| 4. Rain height between 4 and 5 km | 4. Rain height >6 km |
| 5. Slow differences in vertical profile | 5. Rapid increase in vertical profile |
| 6. Bright band height for each bin has to be approximated within the same height of the neighboring bins | 6. Bright band height for each bin is extremely different with the neighboring bins |
| 7. Low values of reflectivity gradient | 7. High values of reflectivity gradient |

overturning. In this investigation, precipitation is classified as convective or stratiform from the inspection upon the radar reflectivity. The inspection involved determination of melting layer signature up to 15 km height. The two rain types (convective and stratiform) can also be determined from their reflectivity values displayed on the radar scan. The convective rain type region can be modeled as an area with high reflectivity compared to its surrounding area. Steiner et al. [2] proposed this technique to distinguish the convective rain region from stratiform rain region using reflectivity values at certain height from ground. Previous studies [5–9] also utilised similar rain classification technique for investigation in Bangalore, India, Milan, Italy and Changi, Singapore. Table 1 shows the criteria used to differentiate the stratiform and convective rain types based on the RHI radar views.

3 System Configuration and Measurement Setup

3.1 Description of the Radar System

The Malaysian Meteorology Department (MMD) installed a fixed Terminal Doppler Radar (TDR) at the Bukit Tampoi, Sepang, Selangor (2° 51' 0"N/101° 40' 0.0114"E). The 8.5 m diameter parabolic reflector antenna operates at 2.8 GHz S-band frequency. It is a single polarisation system capable of measuring and recording reflectivity (Z), linear depolarisation ratio (LDR), radial velocity and velocity spectral width at 3 μ s sampling rate. The radar antenna rotates at the speed of 2 revolution per minute (RPM) with pulse repetition frequency (PRF) equals to 300 Hz for scanning elevation angles of less than 5°. The radar will rotate at faster speed of 4 revolution per minute (RPM) with PRF equals to 1000 Hz for angles of elevation between 5° and 40°. The radar bin size is 238.3 \times 23.8 m square. Figure 1 shows the radar system being covered by a 12 m radome. Such system can be utilized in the process to obtain information regarding the vertical structure of precipitation in tropical climate [10, 11]. The radar can detect precipitation up to

Fig. 1 Meteorological Radar

240 km from its station. The location of interest for the precipitation types analysis is carried out for area within the vicinity of Cyberjaya (2.945262°/101.667976°) where MEASAT ground stations are located. It is hoped that the findings are able to facilitate the greater understanding of millimetre wave propagation characteristics.

4 Correlation of Rainfall Rate with Reflectivity and Attenuation

Rain types can be determined from the rainfall rate values as highlighted in Table 1. Rainfall rate can be estimated using radar reflectivity values. The technique exploits the pre-determined rainfall rate versus reflectivity relationship (R - Z relationship) to convert radar reflectivity measurements to rainfall rates. Over the years, several different R - Z relationships have been developed and proposed [12, 13]. These are mostly empirical models that were developed using collocated rainfall rate measurements equipment (rain gauge) and radars. There has been significant variability in the suggested models for estimating the rainfall rate from radar reflectivity measurements [14]. It has been discussed that the models may be site-specific and that they do not apply universally to different locations around the world [15, 16]. In addition, the models after all, might be dependent on the type of rainfall, which commonly accepted to deviate considerably as from one specific region of the world to another. The rainfall rate, R is inferred from the value of the measured reflectivity according to the formulation;

$$R = \sqrt[|b|]{\frac{Z}{a}} \quad (1)$$

where $a = 200$ and $b = 1.6$ are the values proposed by Marshal Palmer [17].

The reflectivity Z can be expressed on a logarithmic scale in unit dBZ, which can be calculated from (1):

$$dBZ = 10 \log Z \tag{2}$$

5 Result and Discussion

The preliminary stage of the research only involve the investigations of the first 3 criterion identified in Table 1 shown in Fig. 7 is one of the RHI scans that portray the vertical variation of rain where the radar reflectivity values can be analyzed. The raw values of radar reflectivity can be converted to rainfall rate according to (1). For example the RHI stratiform event on 26/12/2009 in Fig. 2 can be read as 34 dBZ or equal to 0.35 mm/hr at that particular bin marked as square in the figure.

Figures 3 and 4 shows convective and stratiform events time series derived from radar data. It has been identified during the convective rain event the rainfall rate is higher than 10 mm/h. Figures 5 and 6 shows the same time interval showing the values in radar reflectivity, dBZ. The convective event ranges more than 37 dBz.

The radar data can then classified into two groups. Figure 7 below depict displays of Z vertical scan recorded on selected days during stratiform events within the period of campaign. It is apparent in the presented figures, that each exhibits clear melting height of approximately 6.5 km with approximate layer thickness between 200 and 500 m. Examples of convective events can be observed in labelled as in Fig. 8. Even though the reflectivity measurements do not exhibit existence of a

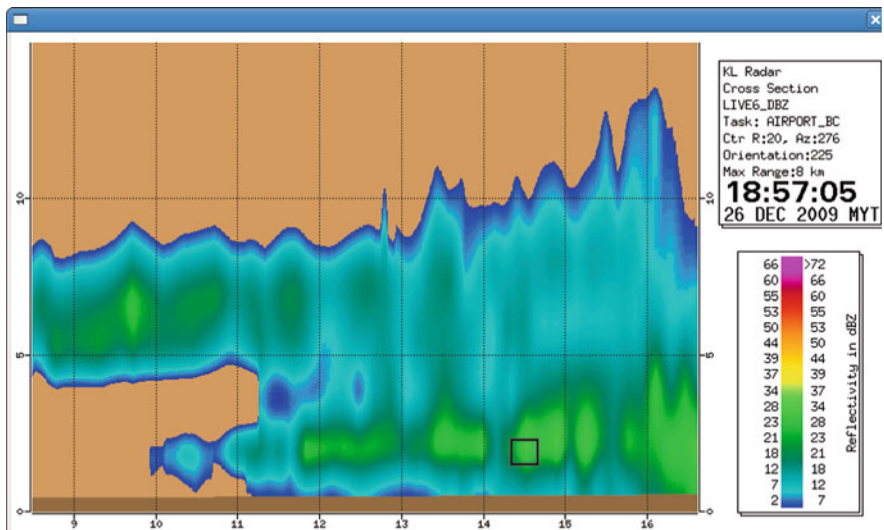


Fig. 2 RHI scan example that will be converted to reflectivity values

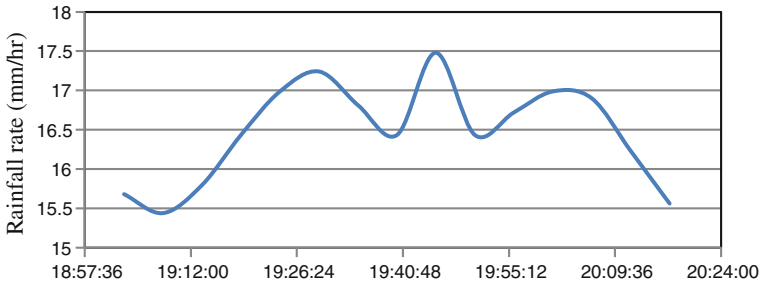


Fig. 3 Convective rain events on 12/08/2009 (Rainfall rates Values)

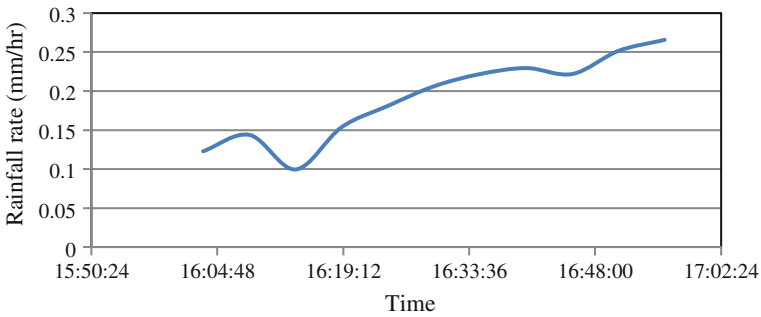


Fig. 4 Stratiform events on 28/8/2009 (Rainfall rates Values)

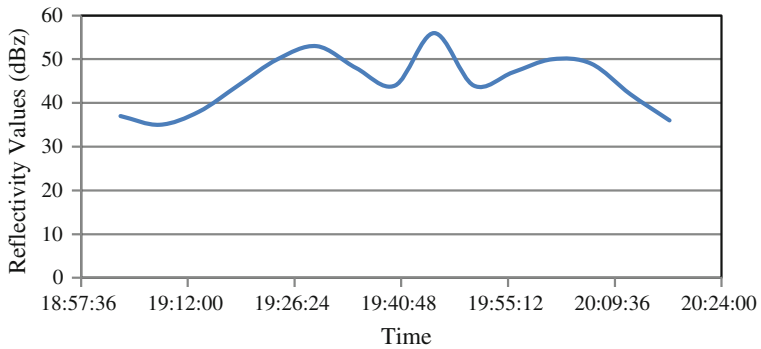


Fig. 5 Convective rain events on 12/08/2009 (Reflectivity Values)

melting layer, such enhancement can be seen in the cross-polar reflectivity that indicative of the melting process.

Based on the 1 year data, the radar scans were inspected and rain events are identified and recorded. Table 2 shows the number of occurrences of stratiform and

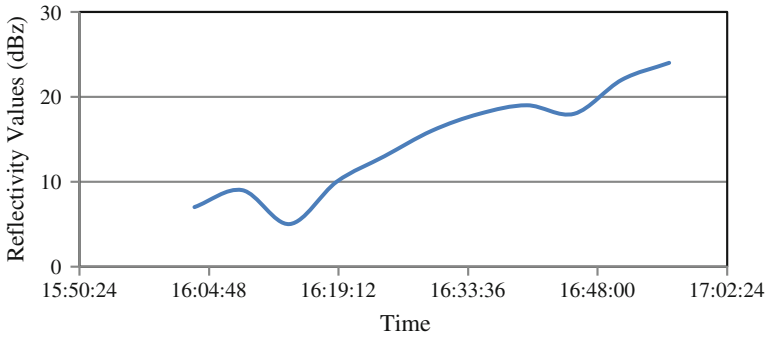


Fig. 6 Stratiform events on 28/8/2009 (Reflectivity Values)

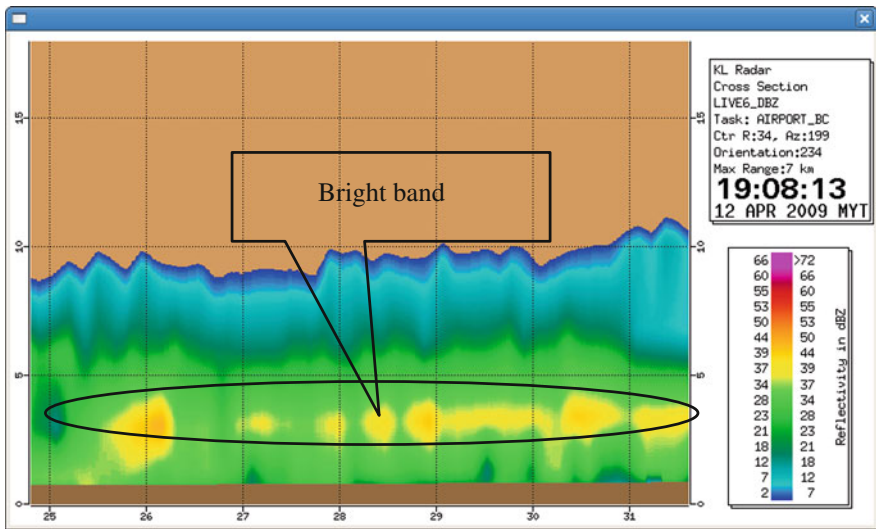


Fig. 7 Stratiform events on 19/08/2009

convective events identified from the radar data in the year 2009. It appears that in 2009 the numbers of occurrences of the two types are about equal. This might signify typical characteristics of tropical country such as Malaysia. Meanwhile in temperate region convective rain are rare occurrences.

The tropical region are having dense rainfall rate and mostly convective compared to temperate region. The satellite links with operating frequency higher than 10 GHz will definitely experience severe attenuation if proper fade countermeasure is not being implemented. Engineers and researchers should take account these behavior in order to overcome such disadvantages and would be able to serve the communication services with better prediction.

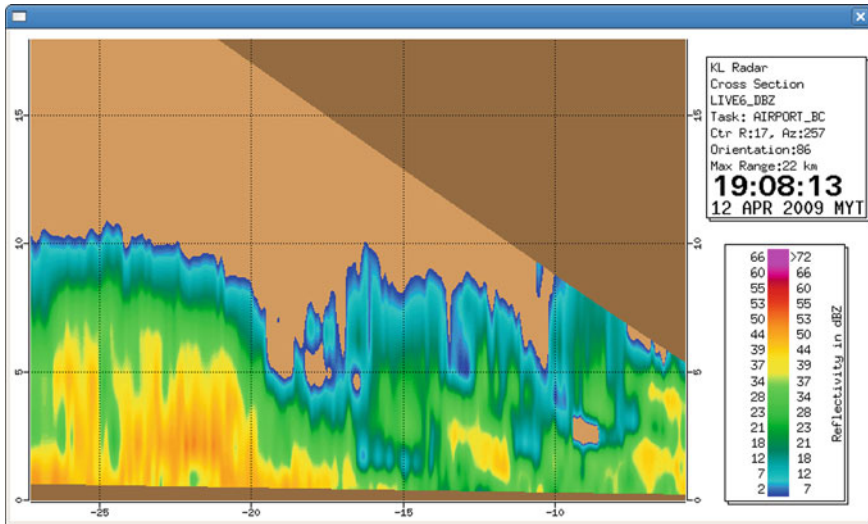


Fig. 8 Convective events on 19/08/2009

Table 2 Rain types based on radar data

| Number of events | Stratiform events | Convective events |
|------------------|-------------------|-------------------|
| 486 | 226 | 220 |
| 100 % | 54.7 % | 45.3 % |

6 Conclusion

High reflectivity values, high rainfall rates and non existence of melting height often associated with the characteristics of convective precipitation. Low reflectivity values and lower rain rates on average reflect characteristics of stratiform precipitation. The presence of a bright band typically indicates stratiform region. In the future, satellite link margin would be best predicted if the characteristics of the rain can be studied profoundly at each location.

References

1. International Communication Union (ITU): Radiocommunication Beureau: Handbook on Radiometeorology, Geneva (1976)
2. Ulbrich, C.W., Atlas, D.: On the separation of tropical convective and stratiform rains. J. Appl. Meteor. **41**, 188–195 (2002)
3. Zafar, B.J.: Classification of Precipitation Type from Space Borne Precipitation Radar Data and 2D Wavelet Analysis, vol. 00, no. V, pp. 3570–3573, 2004

4. Al, H.E.T.: Separation of convective and stratiform precipitation using microwave brightness temperature, pp. 1195–1213 (1999)
5. Das, S., Ashish, K., Maitra, A.: Classification of Convective and Stratiform Types of Rain and their Characteristics Features at a Tropical Location, pp. 0–3 (2009)
6. Steiner, M.R., Houze Jr, R.A., Yuter, S.E.: Climatological characterization of three-dimensional storm structure from operational radar and rain gauge data. *J. Appl. Meteorol* **34**, 1978–2007 (1995)
7. Matricciani, E.: From Radar Measurements Useful to Design Satellite Communication Systems for Mobile Terminals. *IEEE Trans Veh Technol* **49**(5), 1534–1546 (2000)
8. *Progr Electromagn Res B* **32**, 107–127 (2011)
9. Badron, K., Ismail, A. F., Ramli, H.A.M.: Evaluation of RazakSAT 's S-band Link Signal Measurement with the Radar Derived Rain Attenuation, pp. 1–3 (2013)
10. Eastment, J.D., Ladd, D. N., Thurai, M.: Rain Radar measurements in Papua New Guinea and Their Implications for Slant Path Propagation, pp. 1–6, 1996
11. Luini, L., Jeannin, N.: Use of weather radar data for site diversity predictions and impact of rain field advection. In: 2008 4th Advanced Satellite Mobile Systems, pp. 116–121 (2008)
12. Matrosov, S.Y., Clark, K.A., Kingsmill, D.E.: A polarimetric radar approach to identify rain, melting-layer, and snow regions for applying corrections to vertical profiles of reflectivity. *J. Appl. Meteorol. Climatol.* **46**(2), 154–166 (2007)
13. Bech, J., Magaldi, A., Codina, B., Lorente, J. : Effects of Anomalous Propagation Conditions on Weather Radar Observations (2008)
14. Akimoto, M., Watanabe, K.: Study on rain attenuation considering rainfall-intensity dependent spatial correlation characteristics. In: IEEE Global Telecommunications Conference 2004. GLOBECOM '04., vol. 5, pp. 2864–2868 (2004)
15. Khamis, N.H., Din, J., Rahman, T.A.: Rainfall Rate from Meteorological Radar Data for Microwave Applications in Malaysia, pp. 1008–1010
16. Marshall, J.S., Palmer, W.K.: The distribution of raindrops with size. *J. Atmos. Sci.* **5**(4), 165–166 (1948)
17. Olsen, R.L., David, V.R., Daniel, B.H.: The aRb Relation in the Calculation of Rain Attenuation. *IEEE Trans Antenna Propag* **AP-26**(2), 318–329 (1978)

Two Small Antenna Designs for Ultra-Wideband Wireless Systems

**Rashid A. Fayadh, Mohd Fareq Abd Malek, Hilal Adnan Fadhil,
Ahmad Zaidi Abdullah, Nur Sabrina Md Noorpi,
Nurhakimah Mohd Mokhtar and Mohd Asri Jusoh**

Abstract This chapter focuses on designing small antennas used by Ultra Wideband (UWB) wireless systems. The study has been taken from the conventional rectangular manuscript patch antenna to miniaturize the size of used antenna to be more suitable for future 5G system applications. These applications are dealing with high data transmission rates over a very large spread spectrum frequency (3.1–10.6 GHz), so that, many challenges are provided in the antenna design. The main objective of this research is to design, and analyze two small manuscript patch antennas to satisfy UWB technology requirements. Several techniques were used to optimize the UWB bandwidth performance such as radiator dimensions, planar ground plane, and unprinted gaps between ground plane and radiators. Therefore, this work introduces two designs of microstrip-fed, small, and low profile which are called ax-shaped and socket-shaped patch antennas. It has

R.A. Fayadh · H.A. Fadhil
School of Computer and Communication Engineering, University Malaysia Perlis
(UniMAP), 02600 Arau, Perlis, Malaysia
e-mail: rashidfayadh47@gmail.com

H.A. Fadhil
e-mail: hilaladnan@unimap.edu.my

M.F.A. Malek (✉)
College of Electrical and Electronic Technical Engineering,
Middle Technical University, Baghdad, Iraq
e-mail: mfareq@unimap.edu.my

A.Z. Abdullah · N.S.M. Noorpi · N.M. Mokhtar · M.A. Jusoh
School of Electrical System Engineering, University Malaysia Perlis (UniMAP),
02600 Arau, Perlis, Malaysia
e-mail: zaidiabdullah@unimap.edu.my

N.S.M. Noorpi
e-mail: nursabrina@unimap.edu.my

N.M. Mokhtar
e-mail: nurhakimah@unimap.edu.my

M.A. Jusoh
e-mail: asrijusoh@unimap.edu.my

been demonstrated numerically that the proposed antennas are suitable for UWB systems. They can provide satisfactory frequency domain performance (less than -10 dB return loss), including ultra-wide bandwidth with nearly omni-directional radiation patterns, and relatively good current density over the radiator parts of the proposed antenna designs.

1 Introduction

The wireless communication technology is very important in our daily lives and the people around the world use to have this technology especially in cellular phones and medical sensors. The wireless systems give us more freedom without geographical limitations. In 2002 the Federal Communications Commission (FCC) has been licensed the UWB frequency range (3.1–10.6 GHz) [1]. Then, it had a good attention in researches with considering as a promising technology. Because of low UWB transmission power (-41.3 dBm/MHz), the wireless system elements such as antenna need to be very sensitive in implementation [2]. A train of narrow pulses (less than 1 ns pulse duration) in the transmission and reception scenarios forced us to look for high sensitive antenna. This antenna is very important element for improving the UWB systems through daily several applications. In addition, lightweight, small size, low cost, and high performance are required in designing of wireless antennas. To achieve the previous requirements, microstrip planar antennas can be designed to radiate electromagnetic energy [3].

During the literature review, there are several published UWB antennas such as large monopole microstrip antenna of 40×38 mm² dimensions [4] use RF-4 substrate material and non uniform matching antenna of 30×35 mm² dimensions using FR-4 epoxy substrate material [5]. Also another two antenna schemes were implemented in [6] of 45×25 mm² dimensions and in [7] of 40×35 mm² dimensions to satisfy the operating frequency range. In addition, to these designs, slotted ground plane of manuscript planar antennas as deployed in [8] or rigged ground plane in [9] or U slot in the radiator as in [10] were implemented to cover the required band by maintain several resonance frequencies.

In this work, small size antenna designs with planar ground plane were proposed and curved edges of the patch are fed by microstrip feed line. These designs were used to achieve the frequency range of UWB to cover most of its applications. For organization of this work, Sect. 2 shows the configuration of designs and parametric study of antenna parameters. Section 3 detailed the CST simulation results for return loss with discussions for both designs. Section 4 presents current density on the radiators and omni-directional radiation patterns, while Sect. 5 concentrates with conclusions.

2 The Configuration of the Proposed Antenna Designs

The UWB wireless communication systems operate with train of very short pulses spread over the whole bandwidth which are suitable with high bit rate transmission [11, 12]. The propagation power is very low (-41.3 dBm/MHz) that leads to use sensitive and high gain antenna. The antenna should be designed to cover the UWB bandwidth and the antenna design based on developing the conventional rectangular patch antenna. Figure 1 shows the design elements which are including the antenna parameters and the steps of the proposed design methodology. First, the substrate material was chosen to be Taconic TLY-5 with relative dielectric constant (ϵ_r) of 2.2, loss tangent of 0.0009, and dimensions of $30 \times 28 \times 1.575 \text{ mm}^3$ for designs, ax-shaped patch antenna and socket-shaped patch antenna. Second, the radiated shape (patch of $14 \times 16 \text{ mm}^2$) in Fig. 1a was selected to be two sided ax-shaped to extend the operating frequency range that can exhibit the UWB characteristics. In addition, the radiated shape with same dimensions in Fig. 1b was proposed to be socket shape to increase the surface current density at the edges. Third, microstrip transmission feed line was used in both antennas to feed the radiating areas with dimensions of $12 \times 4.8 \text{ mm}^2$ and $12 \times 5 \text{ mm}^2$. Forth, the ground planes on the back sides of the substrate material were proposed to be planar ground plane of 11.25 mm with gap of 0.75 mm for ax-shaped and of 11.75 mm with gap of 0.25 mm between the radiators and ground planes. Next, the parameter was used to optimize the impedance matching bandwidth is the feed gap height; also this parameter introduces the effects of changing the gap dimensions on radiation pattern characteristics.

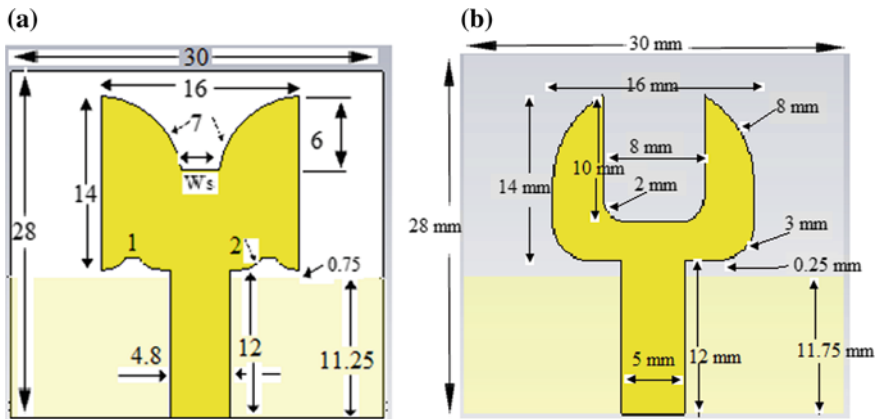


Fig. 1 The geometry of the proposed two antennas: a Ax-shaped patch, b socket-shaped patch

3 CST Simulation Results and Discussions

By using the CST microwave studio software, the simulation process was run to introduce the matching impedance bandwidth all over the UWB frequency range. The under -10 dB return loss curves are shown in Fig. 2 for two antenna designs. Ax-shaped antenna covers frequency range from 3.5 to 11.2 GHz, while socket-shaped antenna covers frequency range from 3.6 to 13.8 GHz. The coverage of both designs indicates that more than 90 % of incident power can be radiated by using these designs. The size of the conventional rectangular antenna substrate is reduced to be more suitable for future small UWB wireless systems. These reducing antenna sizes are maintained with improved antenna performance by keeping the radiation of desired signals over the UWB frequency range. To optimize the antenna performance, parametric study of feed gap was carried out to get the optimal gap depth in two designs. In Fig. 3, the study of feed gap depth is represented for socket-shaped antenna to show the suitable depth which is 1 mm to cover all UWB frequency range. In addition, the same parametric study was done for ax-shaped design as shown in Fig. 4 to get the optimal gap depth after adjusting the feed gap to 0.5 mm with high impedance matching can be achieved. From these figures, the effects of the feed gap between the radiator and the upper edge of the partial ground plane are affecting the entire frequency band but with higher sensitivity at high frequencies. Therefore, the feed gap is very crucial for the impedance matching since it can reduce the coupling between the currents at the bottom outer edge of the patch and the top edge of the ground plane. The feed gap thus has to be precisely tuned to achieve the desirable impedance matching. This tuning is noticed that when the feed gap is getting smaller as 1 mm in socket-shaped and 0.5 mm in ax-shaped patch antennas.

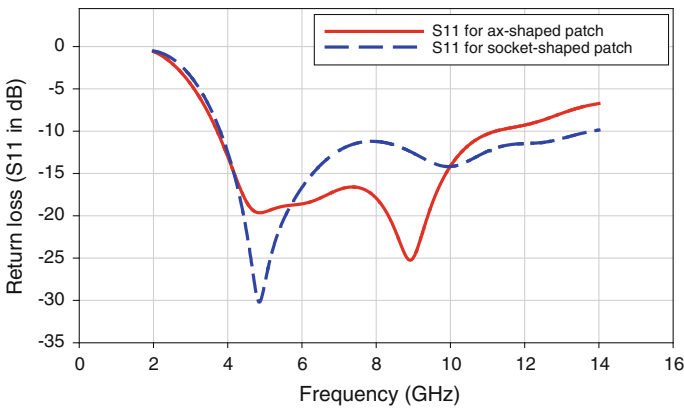


Fig. 2 Comparison between simulated S_{11} for ax-shaped and socket-shaped patch antennas

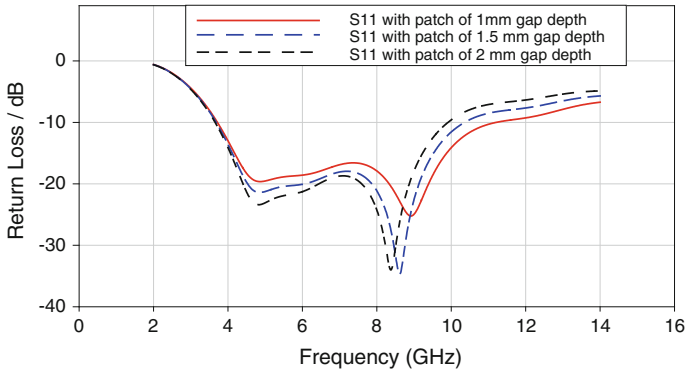


Fig. 3 The effects of feed gap depth on bandwidth for socket-shaped patch antenna

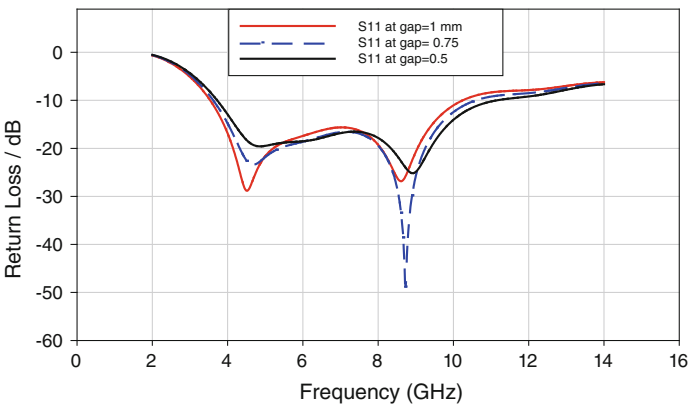


Fig. 4 The effects of feed gap depth on bandwidth for ax-shaped patch antenna

4 Current Density and Radiation Pattern for Two Designs

The simulated current densities of the proposed geometries are shown in Fig. 5a and b at frequency of 10 GHz. It is absorbed that the most of current field is concentrated near the slots of low patch edge and on the other radiated area; the current is distributed in different densities. The maximum surface current density is 15.6 A/m² for Ax-shaped patch and 11 A/m² for socket-shaped patch. The current density is mainly concentrated on the bottom portion and the edges of the patch with low current density toward the patch center.

For Ax-shaped antenna design, Fig. 6a shows the two dimensional simulated radiation patterns were taken at resonant frequency of 5 GHz in E-plane and H-plane when Phi = 90° and Theta = 90°. Figure 6b shows the radiation patterns in

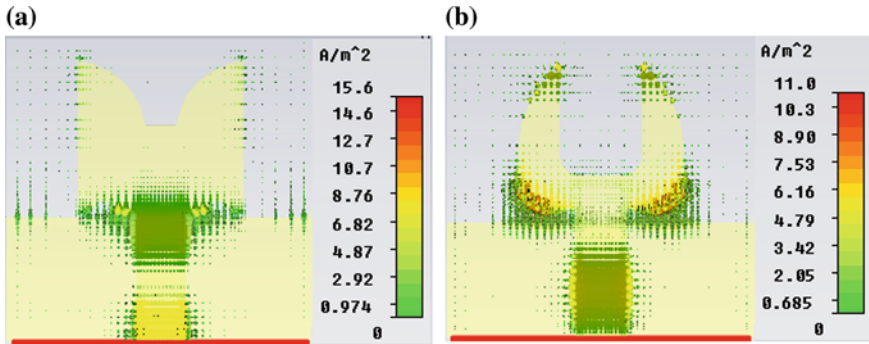


Fig. 5 Surface current density at frequency of 10 GHz for **a** ax-shaped patch and **b** socket-shaped patch

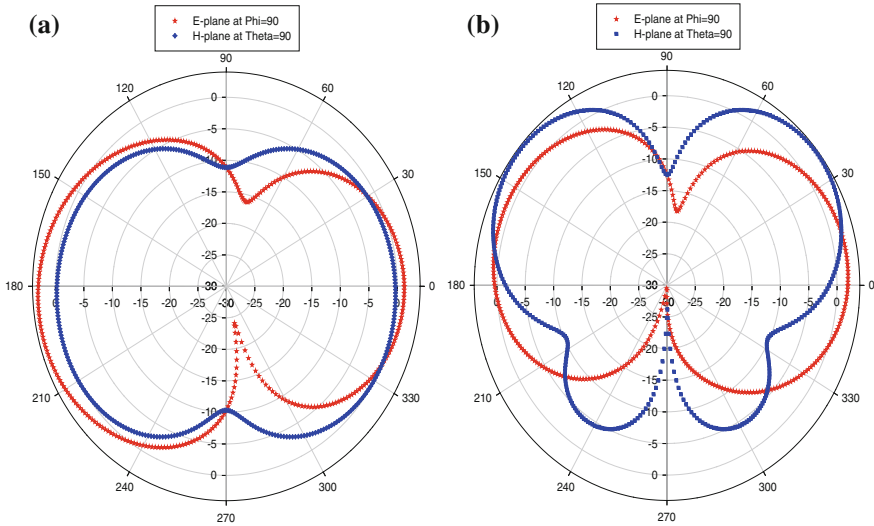


Fig. 6 Simulated radiation patterns for ax-shaped patch antenna in E-plane and H-plane at resonant frequencies of **a** 5 GHz, and **b** 9 GHz

E-plane and H-plane when $\Phi = 90^\circ$ and $\Theta = 90^\circ$ at resonance frequency of 9 GHz. While the simulated radiation patterns for socket-shaped antenna design are illustrated in Fig. 7a in H-plane and E-plane with $\Phi = 90^\circ$ and $\Theta = 90^\circ$ at resonant frequency of 5 GHz and are illustrated in Fig. 7b at resonant frequency of 9 GHz. However, the behavior and analysis of these radiation patterns shows that the proposed microstrip antennas are characterized by omni-directional radiation patterns in both planes across UWB bandwidth.

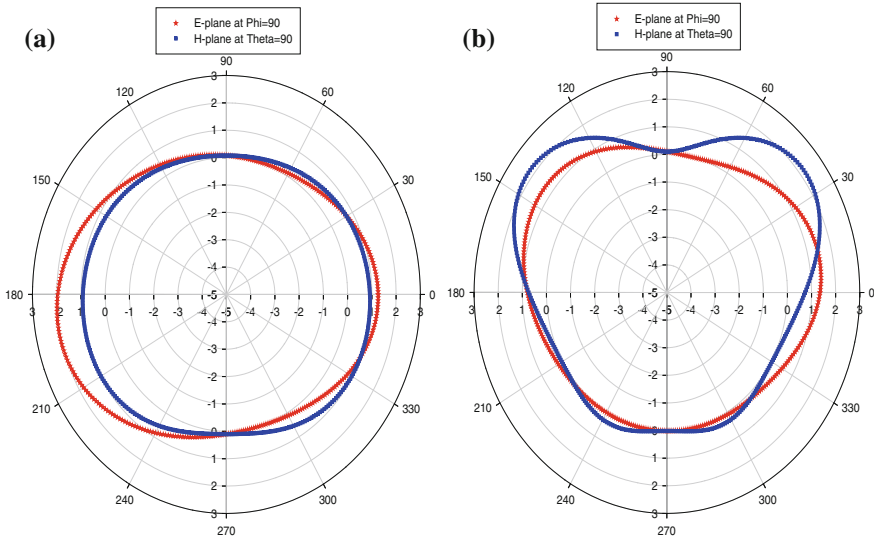


Fig. 7 Simulated radiation patterns for socket-shaped patch antenna in E-plane and H-plane at resonant frequencies of **a** 5 GHz, and **b** 9 GHz

5 Conclusions

In this work, two small and low-profile manuscript-fed simulated UWB antenna designs are studied and analyzed to satisfy UWB wireless technology requirements. The proposed antenna designs are covering the bandwidth of 7.5 GHz which are desired for UWB applications such as in indoor and outdoor propagation. These antennas are namely: the ax-shaped patch antenna and socket-shaped patch antenna. They are designed using different techniques to enhance the bandwidth in order to satisfy UWB frequency range. These techniques are: planar ground plane, adjust the gap between radiator and ground plane, and cutting notches in the radiating element. Cutting notches are used to miniaturize the size of printed patch. From the simulated results, ax-shaped antenna operates over a fractional bandwidth of 110 % and socket-shaped antenna operates over a fractional bandwidth of 138 %. In addition, the simulated radiations patterns are omni-directional to make both designs are suitable for indoor transmission and reception techniques.

References

1. Federal Communications Commission (FCC): Revision of Part 15 of the Commission's rules regarding ultra-wideband transmission systems. FCC first report and order 02-48 (2002)
2. Dotto, K.: Development of a novel ultra-wideband antenna and prototype scanner for detection and location of voids in wood. PHD thesis, The University of British Columbia (2005)

3. Bataller, M., Fabres, M., Daviu, E., Nogueira, A.: Overview of planar monopole antennas for UWB applications. In: Proceeding of EUCAP 2006, November (2006)
4. Tilanthe, P., Sharma, P.C., Bandopadhyay, T.K.: A Monopole microstrip antenna with enhanced dual band rejection for UWB applications. *Prog. Electromagn. Res. B* **38**, 315–331 (2012)
5. Hayouni, M., El Oualkadi, A., Choubani, F., Vuong, T.H., David, J.: Antenna ultra wideband enhancement by non-uniform matching. *Prog. Electromagn. Res. Lett.* **31**, 121–129 (2012)
6. Karmarkar, A., Verma, S., Pal, M., Ghatak, R.: An ultra wideband monopole antenna with multiple fractal slots with dual band rejection characteristics. *Prog. Electromagn. Res. C* **31**, 185–197 (2012)
7. Kasi, B., Chakrabarty, C.K.: Ultra-Wideband antenna array design for target detection. *Prog. Electromagn. Res. C* **25**, 67–78 (2012)
8. Sim, C.Y.D., Chung, W.T., Lee, C.H.: Compact slot antenna for UWB applications. In: *Antenna and Wireless Propagation Letters*, pp. 62–66 (2010)
9. Lin, C.C., Chuang, H.R.: A 3–12 GHz UWB planar triangular monopole antenna with ridged ground-plane. *Prog. Electromagn. Res.* **83**, 307–321 (2008)
10. Sze, J.Y., Wong, K.L.: Bandwidth enhancement of a microstripline-fed printed wide slot antenna. In: *IEEE Transactions and Propagation*, pp. 1020–1024 (2011, July)
11. Jia, Lu, Shu Lin, Yu., Tian, Liwen Jing, Liu, Mengqian, Zhao, Zhihua: The simulation and experiment of a UWB printed dipole antenna. *Prog. Electromagn. Res. Lett.* **36**, 21–30 (2013)
12. Srifi, M.N.: *Ultra Wideband Communications: Novel Trends-Antennas and Propagation*, Chapter 10, *Ultra-Wideband Printed Antennas Design*. ISBN:978-953-307-452-8, pp. 196–215 (2011)

Strength Pareto Evolutionary Algorithm 2 in Optimizing Ninth Order Multiple Feedback Chebyshev Low Pass Filter

**Wei Jer Lim, Asral Bahari Jambek, Siew Chin Neoh,
Mohd Fareq Malek, Ahmad Zaidi Abdullah, Nur Sabrina Md Noorpi,
Nurhakimah Mohd Mokhtar and Mohd Asri Jusoh**

Abstract Circuit design optimization has become a common research to reduce the manpower and computational resource required for circuit design industries. Despite the involvement of multiple design objectives, higher order circuit designs are often more complicated and difficult to be optimized using conventional circuit tuning method. This paper proposed Strength Pareto Evolutionary Algorithm 2 (SPEA2) to optimize a ninth order multiple feedback Chebyshev low pass filter. This research aims to search the best trade-off solution that could minimize the passband ripple, maximize the gain and achieve the targeted cutoff frequency.

W.J. Lim (✉) · A.B. Jambek
School of Microelectronic Engineering, Universiti Malaysia Perlis, Kampus Alam,
Pauh Putra, 02600 Arau, Perlis, Malaysia
e-mail: limweijer1987@gmail.com

A.B. Jambek
e-mail: asral@unimap.edu.my

M.F. Malek · A.Z. Abdullah · N.S.M. Noorpi · N.M. Mokhtar · M.A. Jusoh
School of Electrical System Engineering, Universiti Malaysia Perlis, Kampus Alam,
Pauh Putra, 02600 Arau, Perlis, Malaysia
e-mail: mfareq@unimap.edu.my

A.Z. Abdullah
e-mail: zaidiabdullah@unimap.edu.my

N.S.M. Noorpi
e-mail: nursabrina@unimap.edu.my

N.M. Mokhtar
e-mail: nurhakimah@unimap.edu.my

M.A. Jusoh
e-mail: asrijusoh@unimap.edu.my

S.C. Neoh
Faculty of Engineering and Environment, Computational Intelligence Research Group,
Department of Computing Science and Digital Technologies, University of Northumbria,
Newcastle, NE1 8ST, UK
e-mail: siew.neoh@northumbria.ac.uk

The NGSPICE circuit simulator is interacted with SPEA2 algorithm to perform the circuit optimization. The results obtained show the reliability of the algorithm in achieving the required optimization objectives.

1 Introduction

Multi-Objective Evolutionary Algorithms (MOEAs) become a popular research in electronic and circuit optimization since the last decade [1–7]. The implementation of MOEA in RF design has been conducted by Huang in [1] whereas a vector Tabu search algorithm has been proposed to produce a good distribution of the Pareto solutions in antenna array by Kashfi et al. [3]. Besides that, multi-objective genetic algorithm (MOGA) has been developed to optimize the soft error tolerance of the standard cell circuit by Song et al. [4].

Active filters are widely used in the area of instrumentation, communication and automatic control [8]. The design of a higher order filter often involves large number of components. Meanwhile, according to [9], the higher order filter has a performance approaching ideal filter. As a result, the design of a higher order filter is tedious and challenging. In this research, we develop a SPEA2-based filter optimizer to assist the time consuming circuit tuning process of a ninth order multiple feedback Chebyshev low pass filter.

2 Ninth Order Multiple Feedback Chebyshev Low Pass Filter

Multiple feedback low pass filter is widely used in electronic systems, such as electronic devices, telecommunications, medical instruments and etc. The function of filter design in this application is to filter out the unwanted noise and get the clear information from the signal received.

Ninth order multiple feedback Chebyshev filter shown in Fig. 1 is designed by cascading resistor-capacitor filter with five selected AD797 operational amplifiers from spice library. The complexity of circuit design is directly proportional to the order of the filter. The higher the order of the filter, the more the parameters required to be optimized. Resistors and capacitors are components that will affect the performance of the filter, thus, optimum parameter setting of these components is vital to achieve the design objectives such as gain, cutoff frequency and passband ripple. Table 1 depicts the design objectives/specifications for the ninth order multiple feedback Chebyshev low pass filter. The resistors and capacitors in the filter are to be optimized within the feasible range of values listed in Table 2.

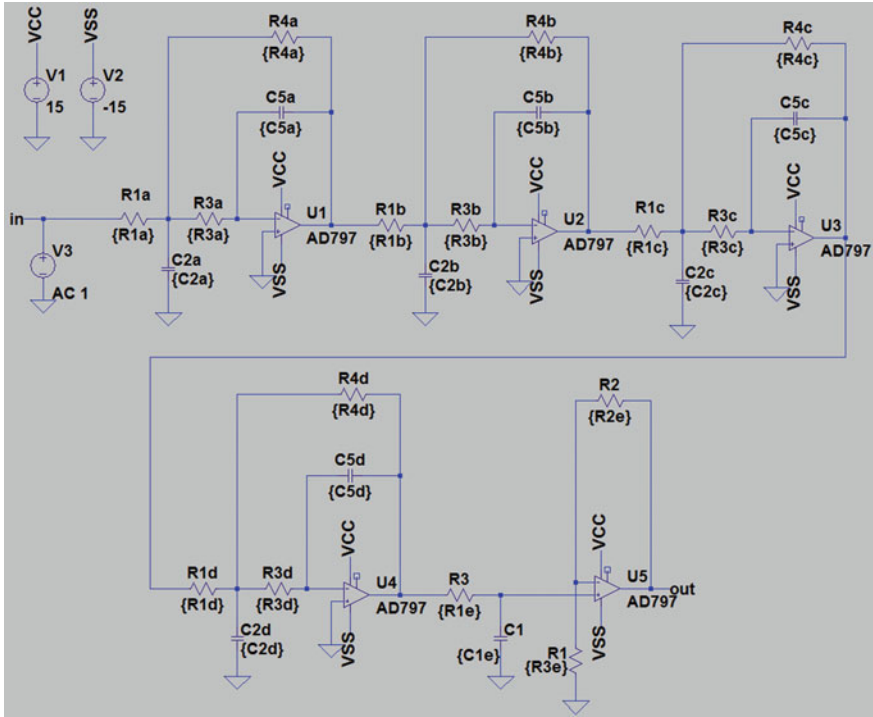


Fig. 1 Schematic of ninth order multiple feedback Chebyshev low pass filter

Table 1 Design specifications for ninth order multiple feedback Chebyshev low pass filter

| Objective | Lower | Upper |
|-----------------------|-------|-------|
| Gain (dB) | 25.37 | 26.67 |
| Passband Ripple (dB) | 0 | 1 |
| Cutoff frequency (Hz) | 975 | 1025 |

3 Strength Pareto Evolutionary Algorithm 2 (SPEA2)

SPEA2 [10] is an improved version of SPEA [10] in terms of archive truncation methods for solution preservation. The algorithm increases the precision during the searching process by using nearest neighbor density estimation technique and also the domination counter as the fitness assignment scheme. Pseudo code of SPEA2 is shown in Fig. 2.

In this research, SPEA2 is started with a random initialization of a population of possible solutions, P_t , with size of M , and empty set of archive, Z_t , with size N , whereby t represents the generation number. We then compute fitness values for

Table 2 Input parameters specification

| Input parameter | Lower limit | Upper limit | Input parameter | Lower limit | Upper limit |
|-----------------|-------------|-------------|-----------------|-------------|-------------|
| C2a | 400n | 443n | R3c | 9 k | 11 k |
| R1a | 17 k | 29 k | R4c | 14 k | 16 k |
| R3a | 19 k | 21 k | C2d | 53n | 65n |
| R4a | 29 k | 32 k | R1d | 19 k | 22 k |
| C2b | 341n | 417n | R3d | 25 k | 27 k |
| R1b | 6 k | 8 k | R4d | 38 k | 40 k |
| R3b | 7 k | 9 k | R1e | 226 k | 277 k |
| R4b | 11 k | 13 k | R2e | 1.5 k | 1.7 k |
| C2c | 165n | 201n | R3e | 1.9 k | 2.1 k |
| R1c | 8 k | 10 k | | | |

```

Procedure of SPEA2
Initialize : Generate population,  $P_t$  and empty external
set (archive),  $Z_t$ ;  $Z_t=0$  and  $t=0$ 
for  $t=1$  to  $g$  do
    Fitness assignment on each individual in  $P_t$  and  $Z_t$ 
    Copy all individual nondominated individual to  $Z_{t+1}$ ;
    If the capacity of  $Z_{t+1}$  exceeded  $N$  then use truncation
operator to remove elements from  $Z_{t+1}$ .
    If  $Z_{t+1}$  not exceeded the capacity then the dominated
individual will be sorted and filled to  $Z_{t+1}$ .
    Perform binary tournament selection to fill the mating
pool, apply crossover and mutation to the mating pool.
end for
end SPEA2

```

Fig. 2 SPEA2 pseudo code

candidate solutions in both P_t and Z_t according to the fitness assignment method shown in Sect. 3.1. Based on the Pareto dominance concept given in [12], all nondominated vectors are moved to a new archive, Z_{t+1} . In this operation, there are two possible situations: (i) if the number of solutions in Z_{t+1} is more than N then truncation operator [11] will remove the vectors; (ii) if number of Z_{t+1} is less than N , then the empty space in Z_{t+1} will be filled with dominated vectors using environmental selection given in Sect. 3.2. Subsequently, the mating pool is filled with solutions that are selected from P_t by binary tournament selection and gone through the process of crossover and mutation. The offspring population is formed after execution of genetic operators. Optimization is then continued from generation to generation until the required filter specifications or the maximum generation

number is achieved. At the end of optimization, the best set of nondominated solutions is obtained as the best Pareto optimal front and the best proposed solution of SPEA2 is selected from these set of solutions by comparing its close proximity towards the filter design objectives in Table 1.

3.1 Fitness Assignment

SPEA2 [11] calculates the fitness value according to Eq. (1) where the total fitness value of an individual or candidate solution is equal to the summation of density, $D(i)$ and raw fitness value, $R(i)$

$$F(i) = R(i) + D(i) \quad (1)$$

Density is defined in Eq. (2) where σ_i is the density estimator of individual i to nearest neighbor and $k = \sqrt{N + \bar{N}}$ where k is equal to the square root of the sample [11].

$$D(i) = \frac{1}{\sigma_i^k + 2} \quad (2)$$

Pareto dominance concept [12] is applied to all the individual in the population and archive. Raw fitness calculates the number of dominator, from both archive, Z_t and population, P_t as Eq. (3). Note that the value of raw fitness is to be minimized where $R(i) = 0$ will be assigned to nondominated solutions.

$$R(i) = \sum_{j \in P_t + \bar{P}_t, j > i} S(j) \quad (3)$$

3.2 Environmental Selection

Environmental selection is the archive update operation of SPEA2. The selection of the individual is conducted according to Eq. (4) in which solutions with fitness value lower than 1 are selected into archive of next generation, Z_{t+1} .

$$Z_{t+1} = \{i | i \in P_t + Z_t \wedge F(i) < 1\} \quad (4)$$

Table 3 SPEA2 parameters setting

| Parameter | Value |
|------------------------|-----------------------------|
| Population size, M | 20 |
| Archive size, N | 100 |
| Number evaluation, g | 500 |
| Crossover operator | SBX crossover |
| Crossover probability | 0.8 |
| Mutation operator | Polynomial mutation |
| Mutation probability | 20 |
| Selection operator | Binary tournament selection |

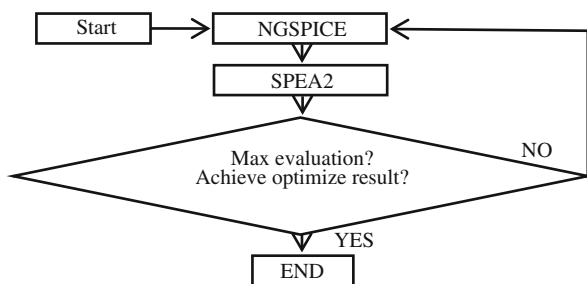
There is a situation when the archive is not fully contain with the nondominated individual, then the dominated individual is inserted to the archive until the archive achieves the size of N .

3.3 SPEA2 Evolutionary Parameter Setting

The proposed SPEA2 adopts the optimization setting listed in Table 3 where population size of 20 and archive size of 100 are used with maximum 500 evaluations. Genetic operators chosen for this optimization are SBX crossover [13], polynomial mutation [14] and binary tournament selection.

In this research, the filter performance is simulated using the NGSPICE circuit simulator. The developed SPEA2 optimizer is interacted with NGSPICE to optimize the circuit performance interactively as shown in Fig. 3. First, the population of possible filter design setting will undergo the NGSPICE simulation. Then the performance obtained from the simulation is fed to the proposed SPEA2 for evolutionary optimization (Fig. 2) whereby the fitness assignment, environmental selection and genetic operator will be executed to produce offspring to the next generation. This optimization process is repeated until the required specifications are achieved or maximum number of evaluation is reached.

Fig. 3 Flow of SPEA2 optimization



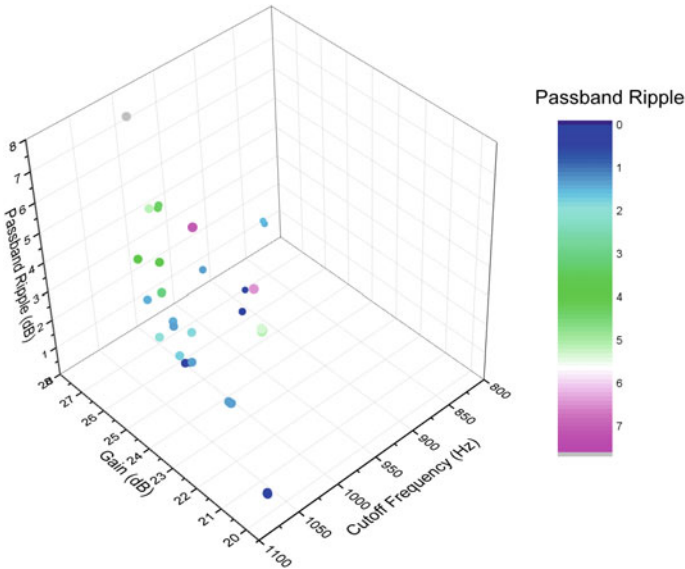


Fig. 4 Suggested solutions scattered in the design objective space

4 Results and Discussion

Based on the model in Fig. 3, the solutions that produce the best tradeoff among all design objectives are obtained. These solutions are visualized in a Pareto plot as illustrated in Fig. 4. We chose the best point from the solutions suggested by SPEA2 which fulfills the objective specifications. The dark blue color dots are the solutions that achieved the passband ripple requirement (0–1 dB). In order to choose as the best solution, the other two objectives, gain (25.37–26.67 dB) and cutoff frequency (975–1025 Hz) must achieve. Thus, the dot scattered in the region/specification range given in Table 1 has been spotted and the output performance and suggested design variable of the best spotted solution is depicted in Tables 4 and 5 respectively.

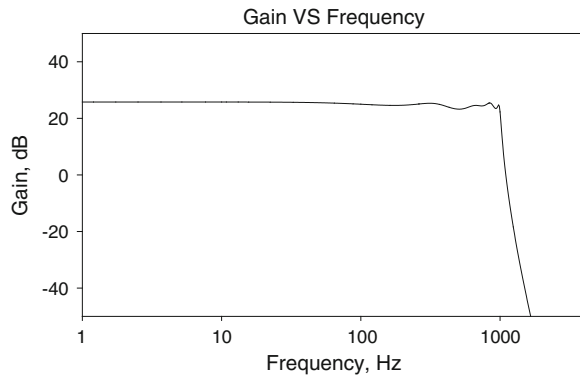
The characteristic of the optimized solution is shown in the bode plot graph in Fig. 5. The bode plot that shows the low pass filter characteristic illustrates the output gain of 25.78 dB, the passband ripple of 0.085 dB with the cutoff frequency at 1000.78 Hz.

Table 4 Suggested design variables

| Input parameter | Value | Input parameter | Value |
|-----------------|---------|-----------------|----------|
| C2a | 427.94n | R3c | 9.56 k |
| R1a | 18.46 k | R4c | 15.93 k |
| R3a | 19.16 k | C2d | 63.38n |
| R4a | 31.52 k | R1d | 21.52 k |
| C2b | 378.35n | R3d | 26.74 k |
| R1b | 7.40 k | R4d | 38.97 k |
| R3b | 7.21 k | R1e | 271.89 k |
| R4b | 12.49 k | R2e | 1.68 k |
| C2c | 185.30n | R3e | 1.90 k |
| R1c | 8.04 k | | |

Table 5 Optimized output performance

| Objective | Optimized result |
|-----------------------|------------------|
| Gain (dB) | 25.78 |
| Passband ripple (dB) | 0.085 |
| Cutoff frequency (Hz) | 1000.78 |

Fig. 5 Simulation of the suggested optimized result

5 Conclusions

In this paper, SPEA2 is interacted with the NGSPICE circuit simulator to optimize the ninth order multiple feedback Chebyshev low pass filter. Despite the complexity of higher order filter, the proposed SPEA2-NGSPICE model is capable to obtain the required design specifications. Overall, 19 decision variables are involved and three design objectives are to be achieved in the experiment. The proposed SPEA2 is shown to perform well and managed to obtain output gain of 25.78 dB, passband ripple of 0.085 dB, and cutoff frequency of 1000.78 Hz which is within the feasible region of specification requirements. Thus, SPEA2 is a potential tool to assist circuit design tuning and further exploration on MOEAs-based circuit optimization is possible in future.

References

1. Huang, W.-T., et al.: Multiobjective evolutionary approach to silicon solar cell design optimization. In: 2013 5th Asia Symposium on Quality Electronic Design (ASQED) (2013)
2. Kashfi, F., Hatami, S., Pedram, M.: Multi-objective optimization techniques for VLSI circuits. In: 2011 12th International Symposium on Quality Electronic Design (ISQED) (2011)
3. Ho, S.L., Shiyou, Y.: Multiobjective synthesis of antenna arrays using a vector tabu search algorithm. *IEEE Antenna Wirel. Propag. Lett.* **8**, 947–950 (2009)
4. Song, W., Multiobjective memetic algorithm and its application in robust airfoil shape optimization. In: Goh, C.-K., Ong, Y.-S., Tan, K. (eds.) *Multi-Objective Memetic Algorithms*, pp. 389–402. Springer Berlin Heidelberg (2009)
5. Liyi, X., Weiguang, S., Zhigang, M.: Soft error optimization of standard cell circuits based on gate sizing and multi-objective genetic algorithm. In: Design Automation Conference, 2009. DAC '09. 46th ACM/IEEE (2009)
6. Michal, J., Dobes, J.: Electronic circuit design using multiobjective optimization. In: 50th Midwest Symposium on Circuits and Systems, 2007. MWSCAS (2007)
7. Sag, T., Cunkas, M.: Multiobjective genetic estimation to induction motor parameters. In: International Aegean Conference on Electrical Machines and Power Electronics, 2007. ACEMP '07 (2007)
8. Pirajanchai, V., Benjankaprasert, C., Janchitrapongvej, K.: Active low pass notch filter using multielectrode distributed RC circuit. In: 2010 7th International Symposium on Communication Systems Networks and Digital Signal Processing (CSNDSP) (2010)
9. Su, K.L.: *Analog Filters*. Springer, New York (1996)
10. Zitzler, E., Thiele, L.: Multiobjective evolutionary algorithms: a comparative case study and the strength Pareto approach. *IEEE Trans. Evol. Comput.* **3**(4), 257–271 (1999)
11. Zitzler, E., Laumanns, M., Thiele, L.: SPEA2: Improving the strength Pareto evolutionary algorithm. Eidgenössische Technische Hochschule Zürich (ETH), Institut für Technische Informatik und Kommunikationsnetze (TIK) (2001)
12. Deb, K.: Introduction to evolutionary multiobjective optimization. In: Branke, J. et al. (eds.) *Multiobjective Optimization*, pp. 59–96. Springer, Berlin (2008)
13. Deb, K., et al.: A fast and elitist multiobjective genetic algorithm: NSGA-II. *IEEE Trans. Evol. Comput.* **6**(2), 182–197 (2002)
14. Agrawal, R.B., Deb, K., Agrawal, R.B.: Simulated binary crossover for continuous search space (1994)

Composites Based on Rice Husk Ash/Polyester for Use as Microwave Absorber

Yeng Seng Lee, Fareq Malek, Ee Meng Cheng, Wei Wen Liu, Fwen Hoon Wee, Muhammad Nadeem Iqbal, Liyana Zahid, Farah Abdullah, Ahmad Zaidi Abdullah, Nur Sabrina Noorpi, Nurhakimah Mohd Mokhtar and Mohd Asri Jusoh

Abstract This paper is to study the dielectric properties and microwave absorption of rice husk ash/polyester (RHAP) composites. The RHAP composites prepared with different weight ratio (40–80 wt. %) of rice husk ash (RHA) loading into polyester was fabricated. A rectangular waveguide transmission line method was used to measure the dielectric properties of the RHAP composites. The RHAP samples were designed and simulated with different thickness and percentage of RHA loading by using Computer Simulation Technology Microwave Studio (CST-MWS) software. The materials, their dielectrics properties measurement and

Y.S. Lee (✉) · F.H. Wee · M.N. Iqbal · L. Zahid
School of Computer and Communication Engineering, Universiti Malaysia Perlis (UniMAP),
Pauh Putra Campus, 02600 Arau, Perlis, Malaysia
e-mail: leeyengseng@gmail.com

F.H. Wee
e-mail: weefwenhoon@gmail.com

M.N. Iqbal
e-mail: mr.nadeemiqbal@gmail.com

L. Zahid
e-mail: liyanazahid@gmail.com

F. Malek · F. Abdullah · A.Z. Abdullah · N.S. Noorpi · N.M. Mokhtar · M.A. Jusoh
School of Electrical Systems Engineering, Universiti Malaysia Perlis (UniMAP), Pauh Putra
Campus, 02600 Arau, Perlis, Malaysia
e-mail: mfareq@unimap.edu.my

F. Abdullah
e-mail: farrahsalwani@unimap.edu.my

A.Z. Abdullah
e-mail: zaidiabdullah@unimap.edu.my

N.S. Noorpi
e-mail: nursabrina@unimap.edu.my

N.M. Mokhtar
e-mail: nurhakimah@unimap.edu.my

microwave absorption result over 12.4–18 GHz (Ku-Band) frequency range are discussed. The dielectric properties of composites increase with increasing loading the RA wt%. The RHAP sample with different thickness was investigated in Ku-Band. The microwave absorption was up to 99.84 %, using 80 % loading of RHA with thickness 15 mm at 13.81 GHz, and showing the RHAP composites is applicable as microwave absorber.

1 Introduction

Microwave absorbers typically consist of unique materials with their properties which absorb electromagnetic (EM) waves. To design of microwave absorber requires specific materials properties, such as dielectric and magnetic properties [1, 2]. The effectiveness of the microwave absorber depends on the dielectric and/or magnetic materials loading in the composite. Recent years, agriculture wastes materials have been reuse as microwave absorbing composites include oil palm, sugar bagasse, rubber tire dust, and rice husk [3–5]. RHA is an industrial waste obtained after burning the rice husks in furnace, open air or as fuel generate energy. RHA has been used in adsorbent application for oils and chemicals [6].

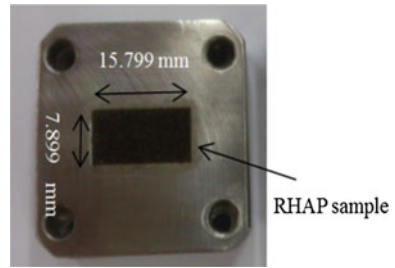
In this paper, a type of RHA as loading in polyester resin for application as microwave was investigated. The RHA-polyester (RHAP) composites of different weight ratio of RHA loading are described. Dielectric properties and microwave absorption of the composites have been evaluated. The RHA/polyester (RHAP) was composites with difference loading of RHA from 40 to 80 wt. % of weight ratio. The dielectric properties ($\epsilon_r = \epsilon_r' - j\epsilon_r''$) of RHAP samples are measured and investigated in Ku-band. The ϵ_r is called dielectric constant where is describes the ability of a material to store electromagnetic wave, whereas the loss factor, ϵ_r'' is describes the ability of a material convert the electromagnetic wave into heat and dissipated [7, 8].

M.A. Jusoh
e-mail: asrijusoh@unimap.edu.my

E.M. Cheng
School of Mechatronic Engineering, Universiti Malaysia Perlis (UniMAP), Pauh Putra
Campus, 02600 Arau, Perlis, Malaysia
e-mail: emcheng@unimap.edu.my

W.W. Liu
Institute of Nano Electronic Engineering (INEE), Universiti Malaysia Perlis (UniMAP),
01000 Kangar, Perlis, Malaysia
e-mail: emcheng@unimap.edu.my

Fig. 1 WR-62 sample holder with RHAP sample



2 Sample Preparations

To form the composites, raw RHA were mixed with polyester and methyl-ketone-polymer (MEKP). The RHAP composite were filled into waveguide sample holder to form into rectangular shape for WR-62 waveguide. Figure 1 shows the fabricated sample filled into WR-62 waveguide sample holder to conduct measurement. The size of the RHAP samples was fabricated in $15.799 \times 7.899 \times 5 \text{ mm}^3$.

3 Experimental

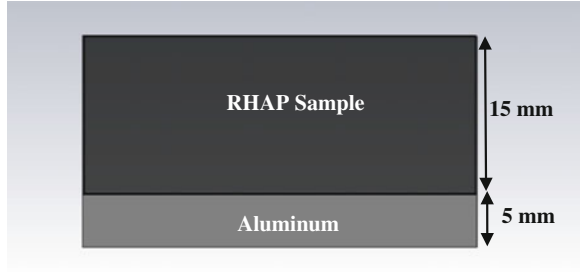
3.1 Dielectric Properties Measurement

Rectangular waveguide transmission line technique was used to measure the dielectric of RHAP samples. In this measurement, the calibration technique TRL (through-reflect-line) applied is to minimize the residual errors of the measurements. The Agilent 85071E software is to measure the dielectric properties from transmission and reflection coefficient [9]. A pair of coaxial cable was connected to Agilent E8362B performance network analyzer and the coaxial cables were connected to the two waveguide. The sample holder was place between the two waveguide adaptors.

3.2 Simulation

The size RHAP samples were designed to be $300 \times 300 \text{ mm}^2$ (length \times width) to evaluate the microwave absorption. To define the dielectric properties of the material in the CST simulation, the dielectric properties of RHAP samples were obtained from the dielectric properties measurement. RHAP sample with 80 % RHA loading was tested with different thickness of 5, 10, 15, and 20 mm. The size of aluminum plate was designed $300 \times 300 \times 5 \text{ mm}^3$ (length \times width \times thickness)

Fig. 2 RHAP flat absorber with aluminum backed plate



was used as metal back plate which placed at bottom of the RHAP flat absorber shown in Fig. 2. The purpose of the aluminum plate is to reflect back EM waves where the EM waves could not penetrate through the aluminum plate. The RHAP samples were simulated in normal incidence plane wave with different thickness and various weight ratio of RHA loading by using Computer Simulation Technology Microwave Studio (CST-MWS).

The reflection loss RL_{dB} of the sample was calculated in decibel by using Eq. (1) [10]:

$$RL_{dB} = 20 \log \frac{RL_{Sample}}{RL_{ref}} \quad (1)$$

RL_{sample} is referring to reflection loss of the samples with the metal back plate. RL_{ref} is the reflection loss (RL) of the aluminum as the reference, fully reflected ($RL_{ref} \approx 0$ dB). The formula to calculate the percentage of microwave absorption can refer to Eq. (2) [11];

$$\text{Absorption, \%} = [1 - RL_{linear}] \times 100 \% \quad (2)$$

Where RL_{linear} is the RL expressed in linear form.

4 Results and Discussion

4.1 Dielectric Properties

The measured dielectric properties of RHAP composites versus frequency were shown in Fig. 3a, b. From the results, the dielectric constant (ϵ_r') and loss factor, (ϵ_r'') of the composites increased with increasing RHA loading in the composites over the measured frequency region.

The 50 % RHA loading has the lowest average values of $\epsilon_r' = 3.62$ and $\epsilon_r'' = 0.24$ compare with 60, 70, and 80 % RHA loading. For 60 % RHA loading, average values of ϵ_r' and ϵ_r'' are 3.89 and 0.30 respectively. Figure 3a, b clearly shows that

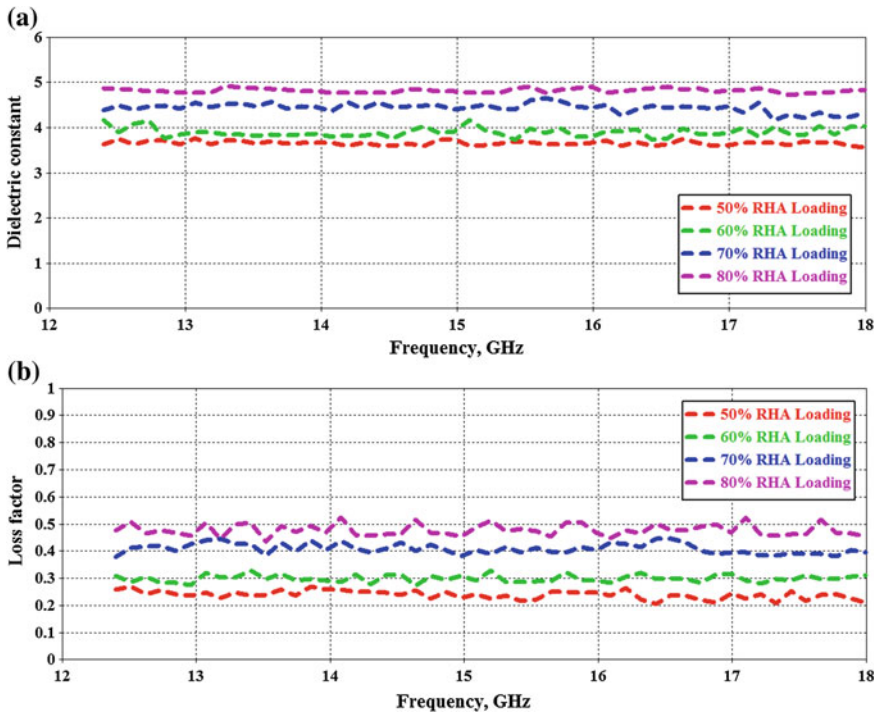


Fig. 3 a Dielectric constant and b loss factor of RHAP samples with 50–80 wt% RHA loading

Table 1 Average values of ϵ_r' , ϵ_r'' of the different RHA with 5 mm thickness

| RHA Loading (%) | (Average values) | |
|-----------------|---------------------------------------|--------------------------------|
| | Dielectric constant (ϵ_r') | Loss factor (ϵ_r'') |
| 50 | 3.62 | 0.24 |
| 60 | 3.89 | 0.30 |
| 70 | 4.43 | 0.41 |
| 80 | 4.80 | 0.47 |

the RHA loading increase to 70 %, the average values of dielectric constant and loss factor also increased by 0.54 and 0.11 compared to 60 % RHA loading. The 80 % RHA loading has the highest average values of $\epsilon_r' = 4.80$ and $\epsilon_r'' = 0.47$. From the analysis show increasing the weight ratio of RHA loading in the composites can enhance dielectric properties of the RHAP composites. Table 1 shows the average values of dielectric constant and loss factor of the different RHA loading over 12.4–18 GHz frequency range.

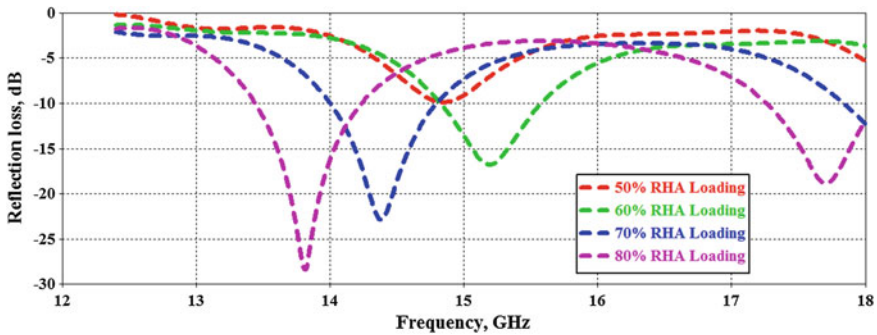


Fig. 4 Reflection loss with different wt% RHA loading

Table 2 Performance of different RHAP samples with thickness 15 mm

| RHA Loading (%) | Frequency (GHz) | Minimum peak (dB) | Absorption (%) |
|-----------------|-----------------|-------------------|----------------|
| 50 | 14.85 | -9.9 | 89.76 |
| 60 | 15.20 | -16.8 | 97.92 |
| 70 | 14.38 | -22.9 | 99.48 |
| 80 | 13.81 | -28.4 | 99.84 |

4.2 Reflection Loss and Microwave Absorption

The plane wave for evaluate RHAP samples performance were carried out in the time domain solver using CST Microwave studio. The reflection loss with different wt% (50, 60, 70, and 80 %) of RHA loading was simulated and evaluated. The reflection loss of different RHA loading in the composites was shown in Fig. 4.

Figure 4 shows the 80 % RHA loading with 15 mm thickness has two minimum RL peak < -10 dB; first peak = -28.4 dB at 13.81 GHz and second peak = -18.82 dB at 17.72 GHz. For 70 % RHA loading, the RL < -20 dB is over 14.29–14.46 GHz. Besides, the 60 % RHA loading only have the RL < -10 dB (>90 % absorption) between 14.82 and 15.60 GHz bandwidth. The 50 % RHA loading do not has microwave absorption more than 90 % with thickness 15 mm, but it has the maximum absorption 89.76 % at 14.85 GHz. The results clearly show that the minimum peak of RL was shift to lower frequency with increasing the wt% RHA loading. The RL and microwave absorption with 15 mm thickness of different RHAP samples were shown in Table 2.

Figure 5 shows the reflection loss determined in the single layer of 80 % RHA loading samples with different thickness (5, 10, 15, and 20 mm). The 80 % RHA loading samples were simulated with different thickness.

From the results, the reflection loss minimum peak value and bandwidth change with the different thickness of 80 % RHA loading. The minimum absorption with

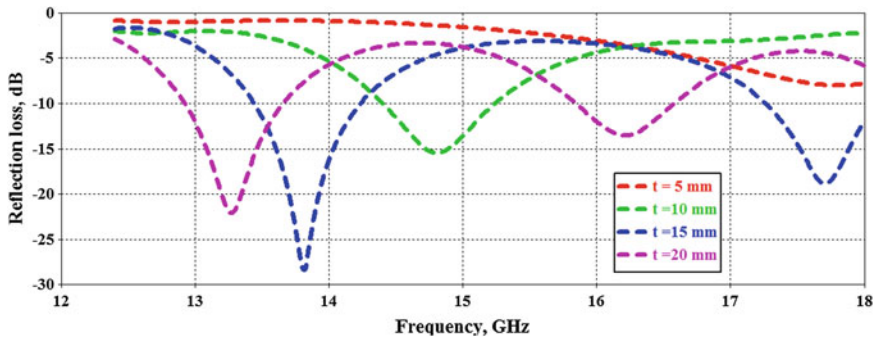


Fig. 5 Reflection loss of 80 % RHA loading samples with thickness (5, 10, 15, and 20 mm)

Table 3 Microwave absorption of 80 % RHA loading with different thickness

| Thickness (t) (mm) | Frequency (GHz) | Minimum peak (dB) | Absorption (%) |
|--------------------|-----------------|-------------------|----------------|
| 5 | 14.85 | -9.9 | 89.76 |
| 10 | 15.20 | -16.8 | 97.92 |
| 15 | 14.38 | -22.9 | 99.48 |
| 20 | 13.81 | -28.4 | 99.84 |

different thickness of 80 % RHA loading was showed in Table 3. When increased the thickness of the 80 % RHA loading, the minimum peak was shift to lower frequency. Different thickness of the 80 % RHA loading has different microwave absorption more than 90–99 % at certain frequency. For thickness 15 and 20 mm, both of the thicknesses have two minimum peaks. The happen due to the quarter wavelength and impedance matching.

5 Conclusions

In this paper, the rice husk ash (RHA) have found considerable as microwave absorber due to their carbon content and dielectric properties. RHAP samples with different weight ratio (50, 60, 70, 80 wt. %) of RHA were fabricated and simulated. The dielectric properties of RHAP samples were measured with rectangular waveguide transmission technique support by Agilent 85071E software in 12.4–GHz. Single layer microwave absorber with backed by aluminum plate was simulated and designed in CST-MWS. This work clearly shows that the values of dielectric constant and loss factor increase by increasing the loading of RHA into the composites. The reflection loss of 80 % RHA shows good absorption with -28.4 dB (99.84 %) at 13.81 GHz and 90 % absorption (RL < -10 dB) at 13.44–14.23 GHz and 17.28–18 GHz of frequency bandwidth. The results of

reflection loss show RHAP composite can absorb microwave in frequency range 12.4–18 GHz. The reflection loss and absorption results show that the RHAP composites are suitable apply as microwave absorber.

References

1. Abbas, S., Mahesh Chandra, M., Verma, A., Chatterjee, R., Goel, T.C.: Complex permittivity and microwave absorption properties of a composite dielectric absorber. *Compos. A Appl. Sci. Manuf.* **37**, 2148–2154 (2006)
2. Yu, X., Lin, G., Zhang, D., He, H.: An optimizing method for design of microwave absorbing materials. *Mater. Des.* **27**, 700–705 (2006)
3. Nornikman, H., Malek, M.F.B.A., Ahmed, M., Wee, F.H., Soh, P.J., Azremi, A., Ghani, S.A., Hasnain, A., Taib, M.N.: Setup and results of pyramidal microwave absorbers using rice husks. *Prog. Electromagn. Res.* **111**, 141–161 (2011)
4. Nornikman, H., Malek, M.F.B.A., Soh, P.J., Azremi, A.A.H., Wee, F.H., Hasnain, A.: Parametric study of pyramidal microwave absorber using rice husk. *Prog. Electromagn. Res.* **104**, 145–166 (2010)
5. Zahid, L., Nornikman, M.F.B.A.M.H., Mohd Affendi, N.A., Ali, A., Hussin, N., Ahmad, B. H., Abdul Aziz, M.Z.A.: Development of pyramidal microwave absorber using sugar cane bagasse (scb). *Prog. Electromagn. Res.* **137**, 687–702 (2013)
6. Foo, K., Hameed, B.: Utilization of rice husk ash as novel adsorbent: a judicious recycling of the colloidal agricultural waste. *Adv. Colloid Interface Sci.* **152**, 39–47 (2009)
7. Lee, Y.S., Cheng, E.M., Liu, W.W., You, K.Y., Iqbal, M.N., Wee, F.H., Khor, S.F., Zahid, L., Haji Abd Malek, M.F.B.: Experimental determination of the performance of rice husk-carbon nanotube composites for absorbing microwave signals in the frequency range of 12.4–18 GHz. *Prog. Electromagn. Res.* **140**, 795–812 (2013)
8. Oyharçabal, M., Olinga, T., Foulc, M.P., Lacomme, S., Gontier, E., Vigneras, V.: Influence of the morphology of polyaniline on the microwave absorption properties of epoxy polyaniline composites. *Compos. Sci. Technol.* **74**, 107–112 (2013)
9. Agilent Technical Overview.: Agilent Technical Overview. Agilent 85071E Materials Measurement Software. Agilent literature number 5988-9472EN (2012)
10. Dai, Y., Sun, M., Liu, C., Li, Z.: Electromagnetic wave absorbing characteristics of carbon black cement-based composites. *Cement Concr. Compos.* **32**, 508–513 (2010)
11. Wang, Z., Zhao, G.-L.: Microwave Absorption properties of carbon nanotubes-epoxy composites in a frequency range of 2–20 GHz. *Open J. Compos. Mater.* **3**, 17 (2013)

Analysis of EEG Signals for Detection of Epileptic Seizure Using Hybrid Feature Set

Ammama Furrukh Gill, Syeda Alishbah Fatima, M. Usman Akram, Sajid Gul Khawaja and Saqib Ejaz Awan

Abstract Epileptic Seizures occur as a result of certain electrical action in the brain. This makes the patient behave abnormally for a limited amount of time. The electrical activity can be measured with the help electrodes attached to different areas of the scalp to capture the EEG signals. Usually, the signals from the aforementioned device are interpreted by the specialists who specialize in this very thing but their detection is susceptible to errors which prove fatal in some cases. This paper provides an automated system which will detect epileptic seizure without involving an expert opinion. The proposed system goes through a four step process i.e. pre-processing, where the data is organized to suit the system processing and noise is removed. Then temporal and spectral feature extraction is performed. The system then applies the feature selection procedure to extract best set of features which are finally passed to the next phase for classification of EEG signals as normal or abnormal. The suggested system is established on a publicly open dataset and provides an average accuracy of 86.93 %.

A.F. Gill (✉) · S.A. Fatima · M. Usman Akram · S.G. Khawaja · S.E. Awan
College of Electrical and Mechanical Engineering, National University of Sciences
and Technology, Rawalpindi, Pakistan
e-mail: ammamagill@live.com

S.A. Fatima
e-mail: syeda.alishbah@gmail.com

M. Usman Akram
e-mail: usmakram@gmail.com

S.G. Khawaja
e-mail: sajid.gul.2009@gmail.com

S.E. Awan
e-mail: saqib.ejaz@yahoo.com

1 Introduction

Human brain continuously generates electrical signals which are transmitted afterwards to different parts of the body in order to achieve several physical, semi-physical and non-physical activities [1]. These electrical signals are prone to multiple disorders which then leads to various human impairments. Epilepsy is ranked as the second most widespread neurological disorder of the human brain after stroke, nearly affecting 1 % of the world’s total population [1]. Many irregular discharges of neurons are observed in the brain structures due to this disorder. These discharges arise either during the seizures (referred as the ictal periods) or between the two consecutive seizures (referred as the inter-ictal periods) [2]. The electroencephalogram (EEG) signals are recorded with the help of the electrodes pasted at dissimilar but definite positions over the patient’s scalp. This is done to capture information regarding a number of physiological states of the brain as well as body. These signals are first recorded and then scrutinized for any anomaly that may take place in the brain. Seizures either appear as spikes or sharp waves in the EEG readings. The epileptic seizures are detected as partial seizures or widespread seizures. Partial seizures are the seizures where the disorder is detected in only a small number of channels of the EEG recordings while in widespread seizures, the disorder is observed in all the channels. [3] Conventionally epileptic seizures were determined by regularly checking the EEG recordings, which was both tiresome and consumed a lot of time. Also it was exposed to a lot of errors. Diagnostic systems, these days, are equipped with capabilities of automatic recognition of epileptic seizure since they seek the help of computer hence really helpful. Figure 1 shows an EEG signal for all the 23 channel inputs.

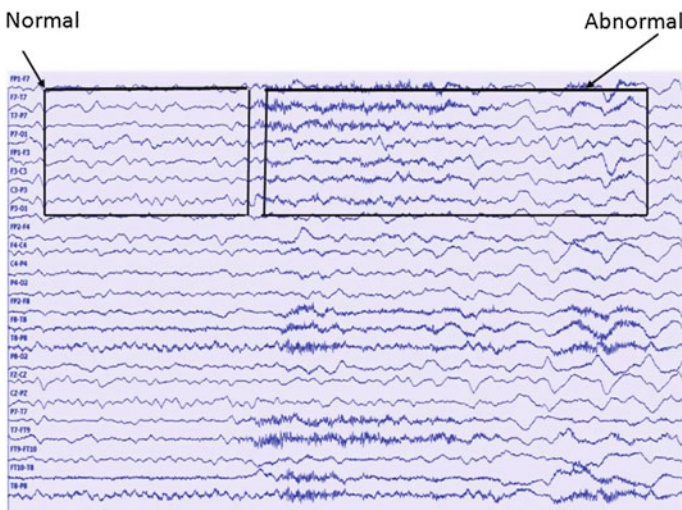


Fig. 1 EEG signal showing part of normal and abnormal waveforms

A variety of methods have been projected for recognition of epileptic seizures. In [4], the authors proposed a multiple stage fuzzy algorithm for the recognition of epileptic seizures. Average amplitude, entropy, rhythmicity (coefficient of variation of amplitude) and dominant frequency are the features used to implement the proposed technique. To combine all the features, a flexible fuzzy sub-system was formulated, the output of this sub-system was used in a threshold procedure to control the final result. iEEG datasets collected out of Freiburg Seizure Prediction EEG (FSPEEG) database were used to test the planned system, which returned an average detection latency of 15.8 s and a false recognition rate of 0.26 per h.

Sharanreddy et al. [5], presented a novel technique, combining multi-wavelet transform, feed forward artificial neural network and enhanced approximate entropy, to facilitate signal classification for epilepsy seizure detection. EEG signal was first converted from the EDF (European Data Format) to ASCII (American Standard Code for Information Interchange) format, which was then provided as input to MWT (Multi-Wavelet Transform). Irregularities were then determined in the brain signal, using IApE (Improved Approximate Entropy Method). IApE was then trained using a feed forward neural network (FFNN). CHB-MIT Scalp EEG Database was used as the testing database. Approximate accuracy of 90 % was achieved. Yet another technique for the automated detection of seizures was given in [6]. It covered two statistical features: skewness and kurtosis, and normalized coefficient of variation (NCOV): a feature from the wavelet background and a meek linear classifier. The proposed scheme was tested, using data for 10 patients, from the CHB-MIT scalp EEG database. An average latency of 3.2 s was detected, with a mean false recognition rate of 1.1 (per hour).

In [7], Ali Shoeb et al. assessed a machine learning approach to produce classifiers with reference to the patients. The features in this study include rhythmic activity, channel identity and a non-EEG feature (such as ECG) to establish the final output. The approach was tested on the CHB-MIT database and yielded a median false recognition rate of 2 false detections per 24 h.

This article consists of four sections. Section 2 describes an overview and details regarding all the steps of the recommended system. The results are presented in Sect. 3. Section 4 carries the conclusions.

2 Proposed System

The recommended system comprises of 4 steps including the preprocessing, feature extraction followed by feature selection and classification. In the preprocessing phase, the data from the CHB-MIT Scalp EEG database is arranged in a manner suitable for the further processing. This arranged data is then divided into multiple blocks with 1000 samples in each block. Various temporal and spectral domain features are extracted from the data to form a hybrid feature set. Rank sum tests are then applied to figure out the best and most discriminating features. Then these

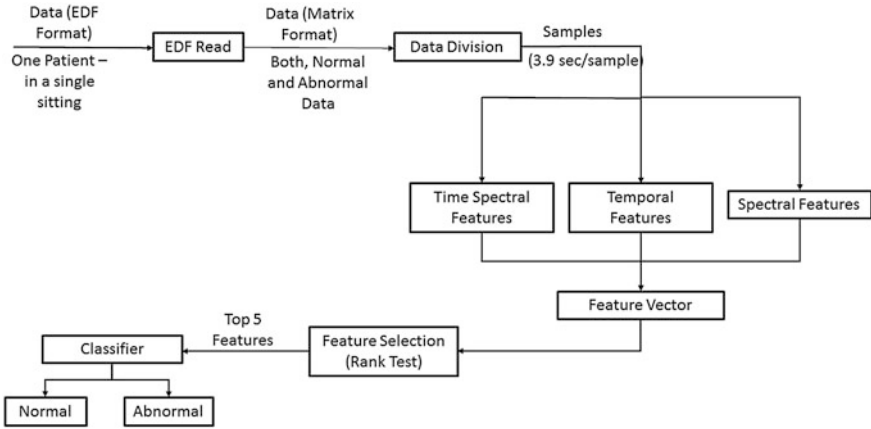


Fig. 2 Flow diagram of proposed system

features are fed to a classifier for the recognition of epileptic seizures. Figure 2 shows the flow diagram representing the recommended system.

2.1 Preprocessing

The dataset contained the CHB—MIT Scalp EEG data in European Data Format (EDF) [8]. This format is often used for multi-channel physical and biological signals. The data is collected from multiple channels for a lengthy timed durations, may be over 60 min, for most of the cases of a single sitting. The preprocessing step removes the noise present in the signal and arranges the data to further processing. The de-noised data is then divided into chunks one thousand samples, 3.9 s long in time. Then the patient summary is reviewed les that contain information regarding the events occurred during that particular EEG sitting of the respective patient. The blocks of data containing seizures are labelled abnormal while the ones which do not possess seizure information are labelled as normal.

2.2 Feature Extraction

The proposed system consists of a hybrid feature set which is a combination of multiple time domain, spectral domain and time spectral features. The details of features are

- Temporal -Domain Features
 1. Entropy (f_1) is calculated a first feature which is calculated in time domain to capture the variation in signal due to presence of seizure [9].

2. Mean (f_2) represents the average value of all samples present in selected window.
 3. Harmonic Mean (f_3) is third feature calculated in time domain to suppress the effect of large values [10].
 4. Range (f_4) is calculated to have an idea about the difference between maximum and minimum values.
 5. Inter Quartile Range (f_5) [11] is calculated as a feature to have good idea about the range even in the presence of outliers as it only considers the difference between first and third quintiles.
 6. Mean Absolute Deviation (f_6) [12] is the average distance of all samples from data mean present in the window.
 7. Moment (f_7) calculates the central moment of the signals under study.
 8. Skewness (f_8) [13] is calculated to have an idea about the distribution of sample along overall mean.
 9. Kurtosis (f_9) [14] determines if the data, under study, is tall and thin or short and squat when compared to the normal distribution.
 10. Percentile (f_{10}) indicates the value below which a given percentage of values in a group of values fall.
 11. Gradient (f_{11}) points towards the greatest rate of increase in the under study data points.
- Time—Spectral Features
 1. Wavelet Transform [15] is the type of a time-frequency transform which follows the basic idea of changes in time-extension without altering its overall shape. The wavelet decomposition vector (f_{12}) and the book keeping vectors (f_{13}) are formed by choosing the appropriate basis functions. A multi-level one dimensional wavelet decomposition is performed using ‘db1’ as the shape of the wave to work upon.
 - Spectral—Domain Features
 1. Wavelet Energy [15] calculates the energy for a 1-D wavelet packet decomposition. The percentage of energy which corresponds to the approximation (f_{14}) and the percentage of energy corresponding to the details (f_{15}) of the outputs of the wavelet transform feature are calculated to comprehend the energy details of the wavelet decomposition, calculated prior to this. Pseudo spectrum [16] refers to a set that contains the spectrum of the operators and the numbers which are almost Eigen values.
 2. The pseudo spectrum estimate (f_{16}) of the input data and the normalized frequencies (f_{17}), where the estimate is calculated, are found. These values are calculated by using the correlation matrix of the data under study and utilizing its Eigen vector estimates.
 3. Fast Approximate Entropy (f_{18}) [9] calculates the amount of irregularity over the time-series of a given data set.

Table 1 Feature selection based on rank tests

| Wilcoxon Test | | | Ansari Bradley Test | | |
|---------------|------------------|-------|---------------------|------------------|-------|
| Features | P Value | Score | Features | P Value | Score |
| f18 | <10 ⁶ | 5.47 | f7 | <10 ⁶ | 5.02 |
| f16 | <10 ⁶ | 6.67 | f3 | <10 ⁶ | 5.86 |
| f12 | <10 ⁶ | 9.27 | f9 | <10 ⁶ | 6.13 |
| f1 | <10 ⁶ | 9.4 | f18 | <10 ⁶ | 7.05 |
| f3 | <10 ⁶ | 10.04 | f14 | <10 ⁶ | 11.8 |
| f10 | <10 ⁶ | 10.38 | f15 | <10 ⁶ | 11.8 |
| f11 | <10 ⁶ | 12.06 | f4 | <10 ⁶ | 22.58 |
| f6 | <10 ⁶ | 12.24 | f16 | <10 ⁶ | 23.02 |
| f5 | <10 ⁶ | 15.4 | f1 | <10 ⁶ | 24.9 |
| f7 | <10 ⁶ | 18.56 | f12 | <10 ⁶ | 26.21 |
| f2 | 0.0000261 | 3.94 | f5 | <10 ⁶ | 27.15 |
| f4 | 0.0000804 | 4.2 | f8 | 0.0000472 | 4.07 |
| f8 | 0.0000864 | 3.33 | f10 | 0.011 | 2.54 |
| f9 | 0.0238 | 2.26 | f6 | 0.025 | 2.24 |
| f14 | 0.62 | 0.5 | f2 | 0.67 | 0.43 |
| f15 | 0.62 | 0.5 | f11 | 0.8747 | 0.16 |
| f17 | 0.9 | 0.2 | f13 | 0.89 | 0.11 |
| f13 | 0.95 | 0.15 | f17 | 0.91 | 0.06 |

2.3 Feature Selection

The feature selection process extracts those features which possess the maximum discriminating power out of the set of available features. This process increases the quality of the proposed mechanism. In this workout, we carried out two types of statistical tests: Wilcoxon signed—rank test [17] and the Ansari-Bradley test [18]. Table 1 depicts the results of Rank Sum tests over all features. Best five features based on lowest P value and best scores in both rank tests are selected. Final feature vector consists of entropy (f_1), central moment (f_7), wavelet de-composition vector (f_{12}), pseudo spectrum estimate (f_{16}) and fast approximate entropy (f_{18}).

2.4 Classification

Gaussian mixture models (GMM) were used to classify the data in this paper. This technique is based on Bayesian decision rule [19]. Seventy percent of the whole dataset constitutes the training data, with two class labels $X_1 = \text{Abnormal}$ and $X_2 = \text{Normal}$. The GMM parameters are optimized using Expectation Maximization (EM). It uses an iterative procedure to find optimal values for each parameter [21].

3 Experimental Results

A publicly available EEG signal database for seizure detection is used for proper evaluation of proposed system. The CHB–MIT Scalp EEG database [7] served as the dataset for all the experimentation purposes and the data is sampled at a frequency of 256 Hz. The dataset consists of data from 12 patients suffering from different levels of seizure. In order to perform experiments properly, the data is broken into small segments of 1000 samples which is roughly of 3.90 s length. To avoid biasness in training and cross validation phase, equal number of normal and seizure samples are used for training.

Different confusion matrix based performance parameters are calculated for proper evaluation of proposed system. Equations 1–3 show the relations for these parameters such as sensitivity (TPR), specificity (TNR) and overall accuracy (Acc). These parameters were calculated using Eqs. 1–3 respectively.

$$\text{TPR} = \frac{\text{TP}}{(\text{TP} + \text{FN})} \quad (1)$$

$$\text{TNR} = \frac{\text{TN}}{(\text{TN} + \text{FP})} \quad (2)$$

$$\text{Acc} = \frac{\text{TP} + \text{TN}}{(\text{TP} + \text{TN} + \text{FN} + \text{FP})} \quad (3)$$

where

- TP are correctly classified seizure segments out of all segments;
- TN are correctly classified normal segments out of all segments;

Table 2 Performance evaluation results of proposed system

| Patient | Accuracy | Sensitivity | Specificity |
|----------|----------|-------------|-------------|
| 1 | 95.3 | 94.1 | 95.7 |
| 2 | 93.4 | 93.9 | 93.1 |
| 3 | 90.1 | 88.3 | 92.3 |
| 4 | 80.1 | 79.9 | 80.7 |
| 5 | 99.6 | 99.9 | 99.3 |
| 6 | 87.3 | 86.8 | 88.9 |
| 7 | 90.4 | 91.3 | 89.3 |
| 8 | 79.5 | 77.2 | 82.3 |
| 9 | 95.7 | 94.3 | 95.9 |
| 10 | 75.9 | 75.3 | 76.3 |
| 11 | 79.2 | 78.7 | 80.1 |
| 12 | 76.7 | 75.4 | 77.1 |
| Averaged | 86.93 | 86.26 | 87.58 |

- FP are those segments which are wrongly classified as seizure however they actually belong to normal class;
- FN are those segments which are wrongly classified as normal however they actually belong to seizure class;

The evaluation results of our system for each patient are given in Table 2. It shows that proposed system detects seizure with good accuracy but with exception for those patients who have mild level of seizure.

4 Conclusion

Digital Signal Processing techniques have always proven to be very crucial to the automation of seizure detection. Research institutes have worked exhaustively to come up with methodologies targeting this domain. The proposed system presents a novel technique that focuses on automating seizure detection, under-going four distinct steps: Preprocessing, feature extraction, feature selection and classification. Average values of sensitivity, specificity and accuracy are 86.26, 87.58 and 86.93 % respectively as obtained with this technique. The proposed system has been shown valid since it has automatically detected a number of seizures in the dataset.

References

1. Alexandros, T.T.: Epileptic seizure detection in EEGs using time-frequency analysis. *IEEE Trans. Inf. Technol. Biomed.* **13**(5), 703–710 (2009)
2. Exarchos, T.P., Tzallas, A.T., Fotiadis, D.I., Konitsiotis, S., Giannopoulos, S.: EEG transient event detection and classification using association rules. *IEEE Trans. Inf. Technol. Biomed.* **10**(3), 451–457 (2006)
3. Gotman, J.: Automatic detection of seizures and spikes. *J. Clin. Neurophysiol.* **16**(2), 130–140 (1999)
4. Rabbi, A.F., Fazel-Rezai, R.: A fuzzy logic system for seizure onset detection in intracranial EEG. *Comput. Intell. Neurosc.* **2012**, Article ID 705140, 12 pp (2012). doi:[10.1155/2012/705140](https://doi.org/10.1155/2012/705140)
5. Sharanreddy, M.A., Kulkarni, P.K.: EEG Signal classification for epilepsy seizure detection using improved approximate entropy. *Int. J. Public Health Sci. (IJPHS)* **2**(1), 23–32 (2013). ISSN: 2252–8806
6. Khan, Y.U., Farooq, O., Sharma, P.: Automatic detection of seizure onset in pediatric EEG. *Int. J. Embed. Syst. Appl. (IJESA)* **2**(3), 81–89 16 pp (2012)
7. Shoeb, A.H., Guttag, J.V.: Application of machine learning to epileptic seizure detection. In: *Proceedings of the 27th International Conference on Machine Learning (ICML-10)*, pp. 975–982 (2010)
8. Kemp, B., Varri^b, A., Rosa^c, A.C., Nielsen^d, K.D., Gade, J.: A simple format for exchange of digitized polygraphic recordings. *Electroencephalogr. Clin. Neurophysiol.* **82**, 391–393 (1992)
9. Kannathal, N., Choo, M.L., Acharya, U.R., Sadasivan, P.K.: Entropies for detection of epilepsy in EEG. *Comput. Methods Prog. Biomed.* **80**, 187–194 (2005)

10. Mitchell, Douglas W.: More on spreads and non-arithmetic means. *The Mathematical Gazette* **88**, 142–144 (2004)
11. Upton, G., Cook, I.: *Understanding Statistics*. Oxford University Press, Oxford, p. 55 (1996)
12. Kader, G.: Means and MADS. *Math. Teach. Middle Sch.* **4**(6), 398–403 (March 1999). Retrieved 20 Feb 2013
13. Dean, S., Illowsky, B.: *Descriptive Statistics: Skewness and the Mean, Median, and Mode*
14. Ballanda, Kevin P., MacGillivray, H.L.: Kurtosis: A Critical Review. *Am. Stat. (American Statistical Association)* **42**(2), 111–119 (1988)
15. Adeli, H., Zhou, Z., Dadmehr, N.: Analysis of EEG records in an epileptic patient using wavelet transform. *J. Neurosci. Methods* **123**, 69–87 (2003)
16. Marple, S.L.: *Digital Spectral Analysis*. Prentice-Hall, Englewood Cliffs, pp. 373–378 (1987)
17. Lowry, R.: *Concepts and Applications of Inferential Statistics*. Retrieved 24 March 2011
18. Bauer, D.F.: Constructing confidence sets using rank statistics. *J. Am. Stat. Assoc.* **67**, 687–690 (1972)
19. Akram, M.U., Tariq, A., Anjum, M.A., Javed, Y.: Automated detection of exudates in colored retinal images for diagnosis of diabetic retinopathy. *Appl. Opt.* **51**(20)
20. Theodoridis, S., Koutroumbas, K.: *Pattern Recognition*, 1st edn. Academic, New York (1999)
21. Duda, R.O., Hart, P.E., Stork, D.G.: *Pattern Classification*. Wiley, New York (2001)

CPW Circular Patch Antenna for Ground Penetrating Radar Applications

M.N.A. Karim, M.F.A. Malek, M.F. Jamlos, A.Z. Abdullah,
N.S. Md Noorpi, N.M. Mokhtar and M.A. Jusoh

Abstract A Co-planar Waveguide (CPW) Circular patch antenna for Ground Penetrating Radar (GPR) applications is presented in this paper. The antenna is designed on Rogers substrate RO 3010 with dielectric constant of 10.2 with a thickness, $h = 1.22$ mm and tangent loss = 0.0022 operates from 1.1 to 5.5 GHz with the overall size is 140 mm \times 140 mm. CPW was used as an input method for the antenna with 50 Ω impedance matching and Computer Simulation Technology (CST 2013) has been used as simulation tools to observe the antenna performances. In order to produce antenna with high gain performance, a reflector is located at the back of the antenna. The antenna parameters such as simulated return loss, gain, radiation pattern and current distribution of the antenna is presented.

M.N.A. Karim (✉) · M.F.A. Malek · M.F. Jamlos
School of Computer and Communication Engineering, Universiti Malaysia Perlis,
Pauh Putra, 02600 Arau, Perlis, Malaysia
e-mail: nazri1601@yahoo.com

M.F.A. Malek
e-mail: mfareq@unimap.edu.my

M.F. Jamlos
e-mail: faizaljamlos@unimap.edu.my

M.N.A. Karim · M.F.A. Malek · A.Z. Abdullah
N.S. Md Noorpi · N.M. Mokhtar · M.A. Jusoh
School of Electrical System Engineering, Universiti Malaysia Perlis, Pauh Putra,
02600 Arau, Perlis, Malaysia
e-mail: zaidiabdullah@unimap.edu.my

N.S. Md Noorpi
e-mail: nursabrina@unimap.edu.my

N.M. Mokhtar
e-mail: nurhakimah@unimap.edu.my

M.A. Jusoh
e-mail: asrijusoh@unimap.edu.my

1 Introduction

Ground Penetrating Radar (GPR) is one of the radar application which transmits a radio wave signal, typically from tens of MHz to some GHz frequency range. The main task of GPR is to map structures and features buried in the ground. The GPR system can work at different frequencies depending on the required resolution and depths detection, which can be used for different applications such as detecting buried objects likes pipes, underground cables, land mines, gold and metal rod inside concrete wall, archaeological digs, etc. In other words, the term ground in GPR does not necessarily means soil, but it could be concrete, wood or any non-metallic materials (man-made structures).

The concept of applying radio wave to the internal structure of the ground is not a new concept. This works have been applied to map the thickness of ice sheets in the Arctic and Antarctic and sound the glaciers. However, in the early 1970s, peoples start using GPR to the non-ice environments [1–3].

GPR is basically working with the same principle with classical radar or space radar. However, GPR works in more complicated scenario as compared to free space radar. This is because in GPR enviroment, GPR signal has to travel throughout the medium which can have losses and exhibit dependent electromagnetic properties, thus introducing dispersive effects [4].

In GPR system, the needs for good penetrating depth and fine resolution are always enticing researcher to develop a good transmitter and receiver system. One of the important components of this system is the antenna which has good features such as high gain, wide-bandwidth, compact in size, good matching and directional radiation pattern. There are many GPR antennas have been developed over the past few years and the most popular are the horn antenna, bow-tie and monopole antenna. Out of these antennas options, planar antenna are the most preferred one since it is easy to integrate with other GPR components.

In this paper, the Co-Planar Waveguide (CPW) Circular patch structure is presented. The proposed antenna is designed on Rogers substrate RO 3010 ($\epsilon_r = 10.2$ and tangent loss = 0.0022). It features wide operational bandwidth covering across 1.1–5.5 GHz frequency band. By having this feature, the antenna is suitable for GPR system for buried objects detection including the measurement of thickness pavement and the detection of steel rod inside concrete wall, pipeline, archaeologies and etc. The design methodology of circular patch antenna with CPW as the feeding line method is elaborated in this paper. The simulated results, such as, return loss, gain, radiation pattern and current distribution of the proposed antenna are presented.

1.1 Ground Penetrating Radar

In a GPR system, there are few types of radar architecture which are commonly used such as mono-static, bi-static and multi-static architecture. In mono-static radar architecture, the transmitting and receiving radar pulse signal are accomplished by

a single antenna. In turn, two separated antennas are required in bi-static radar architecture, with one antenna used for transmitting and one antenna used for receiving. In a multi-static radar system, the transmitting signal is performed by a single antenna while multiple receiving antennas in an array configuration are required for the receiving part [5, 6]. Each of these architectures has their own advantages and disadvantages. In a nutshell, there are many factors or parameters has to be considered in a GPR system which bring many researchers to get involved in this area. Nowadays, GPR is being used in various areas, such locating buried utilities, searching for buried object, forensic investigation and etc. Thus different specification of GPR may be considered for different applications.

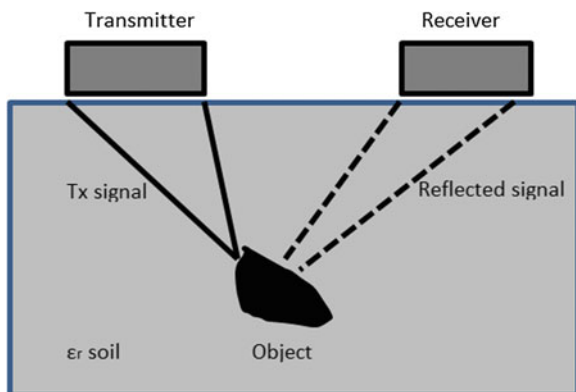
Many people think GPR performance is only limited by the instrumentation. This is true in some cases, but another factor such as the depth of penetration is primarily governed material itself. Lossy materials will limit the penetration depth. The selection of the operating frequency, transmitted power and the gain of the antenna, may affect the GPR performance. Lower frequencies will improve the depth of penetration because attenuation primarily increases with frequency. However, lowering the frequency results in loss of resolution and it is not suitable for imaging system. The basic GPR working principal will be elaborated in Sect. 1.2 and the antenna design methodology will be discussed in Sect. 2.

1.2 GPR Working Principles

Figure 1 shows the bi-static radar architecture to detect buried objects under the earth’s surface.

Basically, the working principle of a GPR similar to a space radar as mentioned in the previous section, but in GPR, it involves materials that introduce signal loss and clutter. GPR uses radio frequency signal that emits by a transmitter. The signal propagates through a host materials and hit an object, reflection occurred and the

Fig. 1 GPR principal for Bi-static radar architecture



reflected signal is captured by a receiver. The image will be plotted based on the received signal in the receiver. In lossy host materials, the signal can penetrate to a limited depth before being absorbed by the materials. Therefore, penetration is always an issue for lossy materials.

2 The Antenna Design Methodology

The design for circular patch antennas can be found in various antenna design handbook and papers [5–7] and the designed structure is accomplished using commercial electromagnetic software Computer Simulation Technology (CST 2013). The antenna is designed using Rogers substrate RO 3010 which has a thickness, $h = 1.22$ mm, $\epsilon_r = 10.2$ and tangent loss = 0.0022. The initial dimension of the radius of the circular patch antenna, a is calculated using expression (1) and (2) [7].

$$a = \frac{F}{\left\{ 1 + \frac{2h}{\pi\epsilon_r F} \left[\ln\left(\frac{\pi F}{2h}\right) + 1.7726 \right] \right\}^{\frac{1}{2}}} \quad (1)$$

where,

$$F = \frac{8.791 \times 10^9}{f_r \sqrt{\epsilon_r}} \quad (2)$$

In expression (1) and (2), one has to note that, the resonant frequency, f_r must be in Hz and thickness of the substrate, h must be in cm. In this expression, the fringing fields effect is neglected. In usual case, fringing fields make the size of patch electrically large. By considering the fringing fields effect, expression (3) is used to determine the effective radius, a_e of the circular patch antenna.

$$a_e = a \left\{ 1 + \frac{2h}{\pi a \epsilon_r} \left[\ln\left(\frac{\pi a}{2h}\right) + 1.7726 \right] \right\}^{\frac{1}{2}} \quad (3)$$

The coplanar waveguide technique (CPW) is chosen as the feeding method of the proposed antenna. Easy in fabrication and less complex impedance matching are the advantages of this feeding technique. These are some of the reasons why CPW feeding method is mostly preferred mainly in the design of planar antennas [8].

The design structure of the proposed antenna is depicted in Fig. 2.

Because of the used of high dielectric constant substrate, the overall dimension of the patch is very small which is 140×140 mm². To achieve high gain antenna and directional radiation pattern, the reflector is located 60 mm away from patch antenna. The radius, r for the circular patch is 27.5 mm with the length, l_2 CPW is 22 mm. The gap for the CPW feed slot is 1.0 mm. The overall optimized dimensions of the proposed antenna are shown in Table 1.

Fig. 2 Proposed antenna structure

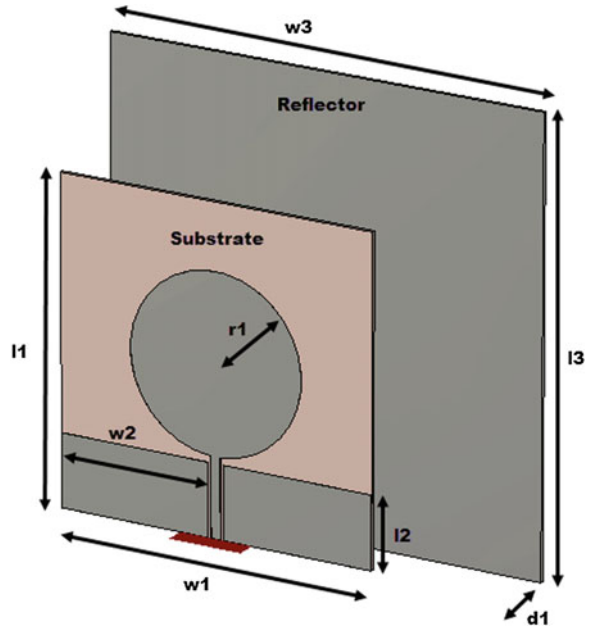


Table 1 Dimensions of proposed antenna

| Antenna parameters | Size (mm) |
|--|-----------|
| Width substrate, w_1 | 100 |
| Length substrate, l_1 | 100 |
| Length ground plane, l_2 | 22 |
| Width of ground plane, w_2 | 47.5 |
| Length of the reflector, l_3 | 140 |
| The width of the reflector, w_3 | 140 |
| Radius patch, r_1 | 27.5 |
| Gap between patch and reflector, d_1 | 60 |

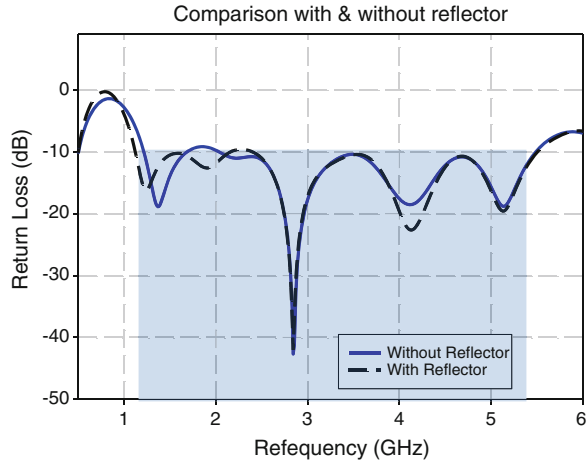
3 Result and Discussion

In this section, the simulated results of reflection coefficient, radiation pattern, gain and the effect of the reflector are discussed. Current distribution on the CPW circular patch antenna is also presented in this section.

3.1 Simulated Reflection Coefficient

The simulated reflection coefficient of the proposed antenna with reflector and without reflector are shown in Fig. 3. By considering return loss better than 10 dB,

Fig. 3 Simulated reflection coefficient (dB) of the proposed antenna



the operational bandwidth of the antenna covers from 1.2 to 5.5 GHz without the presence of the reflector. When the reflector is placed behind the antenna, the operational bandwidth increased about 0.1 GHz at the lower frequency, which results to 1.1–5.5 GHz operational bandwidth. The proposed antenna in this paper has fulfill one of the requirement of the GPR antenna, which require a wide operational bandwidth. As explained in Sect. 1, wider bandwidth is demanded because of the need of higher resolution when plotting the image. As a results, the proposed antenna is suitable for GPR application such as to detect object inside concrete wall, to detect pavement thickness, forensic investigations, archaeologies etc. At present, researcher in various research fields are still looking for the best transmitter such as antenna part and good processing part (depending on their application) for image processing.

3.2 Radiation Pattern and Gain

The simulated 3D far-field radiation pattern for the proposed antenna are depicted in Fig. 4. Three different frequencies such as at 1.5, 2.0 and 2.5 GHz has been selected and analysed in this paper. Figure 4a, b shows the comparison radiation pattern of the proposed antenna at 1.5 GHz for with and without reflector. As can be seen in Fig. 4a, the antenna radiates omnidirectional with gain 2.25 dB. When the reflector is placed at the back of the antenna, the gain is increased to 4.3 dB and the radiation pattern is more directive. From this finding, it can be concluded that by placing the reflector at the back of the antenna, the antenna performance improved in terms of gain and radiation pattern as well as the bandwidth as discussed in Sect. 3.1. As illustrated in Fig. 4b, c, the gain increase from 2.5 to 5.5 dB and the pattern is still directive toward the front antenna. However, the radiation pattern split into two

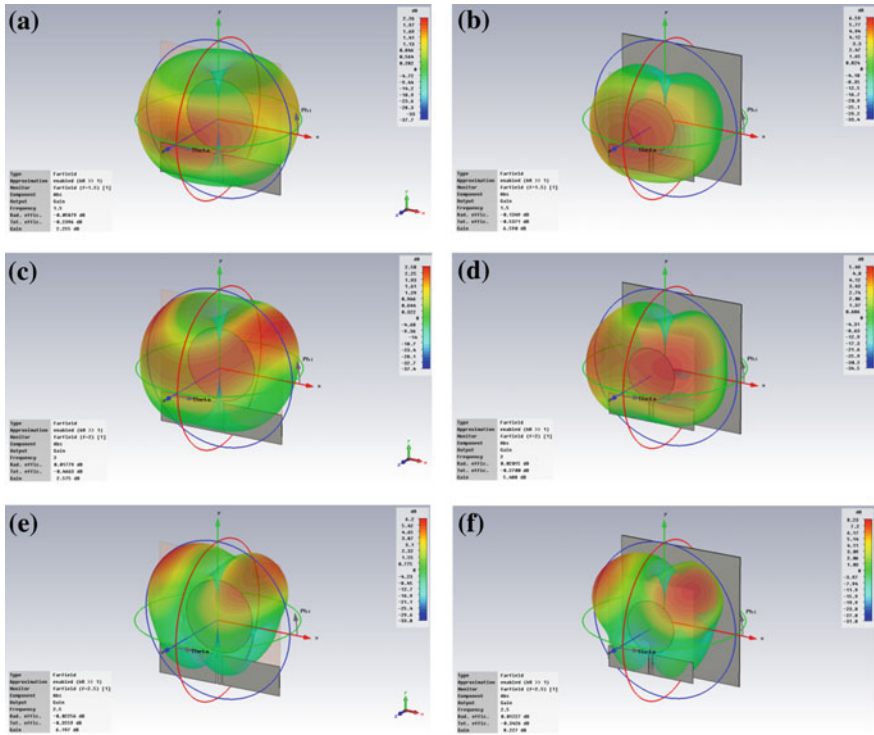


Fig. 4 Simulated Radiation Pattern. **a** Radiation pattern at 1.5 GHz without reflector. **b** Radiation pattern at 1.5 GHz with reflector. **c** Radiation pattern at 2.0 GHz without reflector. **d** Radiation pattern at 2.0 GHz with reflector. **e** Radiation pattern at 2.5 GHz without reflector. **f** Radiation pattern at 2.5 GHz with reflector

main directives at frequency 2.5 GHz for both with reflector and without reflector as depicted in Fig. 4e, f. The gain of the proposed antenna for 1.5 GHz until 5.5 GHz is tabulated in Table 2.

Table 2 shows the gain in dB for the CPW circular patch antenna from 1.5 to 5.5 GHz. According to the results, it clearly shows that the gain is increased when the reflector is located to the antenna. The peak gain occurs at frequency 4.5 GHz, which is about 9.24 dB with a reflector and the gain of the antenna is maintained across the frequencies 2.5–4.0 GHz where the value is about 8.0 dB.

3.3 Current Distribution

The current distribution of the proposed antenna is shown in Fig. 5. Current distribution normally gives an insight view the physical behaviour of the antenna. For consistent observation, the current distribution of CPW circular patch antenna with

Table 2 Simulated gain of CPW Circular patch antenna for with and without reflector

| Frequency (GHz) | Gain (dB) | |
|-----------------|-------------------|----------------|
| | Without reflector | With reflector |
| 1.5 | 2.55 | 6.59 |
| 2.0 | 2.57 | 5.48 |
| 2.5 | 6.19 | 8.23 |
| 3.0 | 6.12 | 8.76 |
| 3.5 | 6.05 | 8.16 |
| 4.0 | 6.91 | 8.70 |
| 4.5 | 6.96 | 9.24 |
| 5.0 | 5.50 | 6.54 |
| 5.5 | 6.47 | 7.31 |

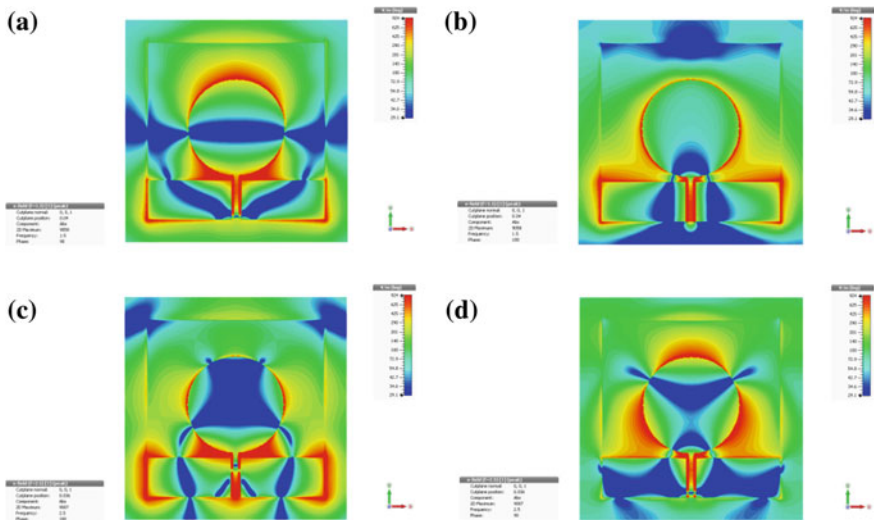


Fig. 5 Current distribution at 1.5–2.5 GHz. **a** Current distribution at 1.5 GHz (0/180°). **b** Current distribution at 1.5 GHz (90/270°). **c** Current distribution at 2.5 GHz (0/180°). **d** Current distribution at 2.5 GHz (90/270°)

reflector is demonstrated at phase 0/180° and 90/270° for both 1.5 and 2.5 GHz respectively. Figure 5a, b shows a top view of the current distribution for the proposed antenna at 1.5 GHz (0/180°). As can be seen, the red colour on the patch antenna indicates strong current density the blue colour present less density. The current distribution only can be viewed in the simulation tools and it is importance, particularly to analyse the performance of the antenna when different types of materials are considered.

4 Conclusion

In conclusion, the coplanar waveguide (CPW) circular patch antenna for Ground Penetrating Radar (GPR) applications has been designed using Rogers RO3010 operates from 1.1 to 5.5 GHz is presented in this paper. The investigation of the antenna has been extended by adding a metallic reflector at the back of the antenna and the performances of the antenna are observed. The performance of the antenna in term of return loss, radiation pattern, gain and current distribution has been discussed and analysed. The reflector helps the antenna to be more directive and increase gain from 2.25 to 6.59 dB at 1.5 GHz, 6.12–8.76 dB at and 6.96–9.24 dB at 4.5 GHz. These are significant benefits of the proposed antenna which make it suitable for GPR applications, especially when wide bandwidth and high resolution is considered.

References

1. Li, M., Luk, K.M.: A low-profile wideband planar antenna. *IEEE Trans. Antennas Propag.* **61**, 4411–4418 (2013)
2. Rufus, E., Alex Z.C.: Microwave imaging system for the detection of buried objects using UWB antenna—an experimental study. In: *PIERS*, pp. 786–788 (2012)
3. Daniels, D.J.: *Ground Penetrating Radar*, 2nd edn. The Institute of Electrical Engineers, London (2004)
4. Soldovieri, F., Solimene, R.: Ground penetrating radar subsurface imaging of buried objects. www.intechopen.com (2010)
5. Karim, M.N.A., Malek, M.F.A., Jamlos, M.F., et al.: Design of ground penetrating radar antenna for buried object detection. *IEEE Int. RF Microw. Conf.* **2013**, 253–257 (2013). doi:[10.1109/RFM.2013.6757260](https://doi.org/10.1109/RFM.2013.6757260)
6. Chen, K.R., Sim, C.Y.D., Row, J.S.: A compact monopole antenna for super wideband applications. *IEEE Antennas Wirel. Propag. Lett.* **10**, 488–491 (2011)
7. Balanis, C.A.: *Antenna Theory Analysis and Design*, 2nd edn. Wiley, New York (1995)
8. Garg, R., Bhartia, P., Bahl, I., Ittipiboon, A.: *Microstrip Antenna Design Handbook*. Artech house, London (2001)

Investigation of MultiSlot and Stacked Layer on Dual Band Printed Dipole Antenna

Mohamad Hafize Ramli, Mohamad Zoinol Abidin Abd. Aziz,
Mohd Azlishah Othman, Badrul Hisham Ahmad,
Mohd Kadim Suaidi and Abdul Halim Dahalan

Abstract In this paper, the investigation of multislot and stacked layer on dual band dipole antenna is presented. The effect of the stack on dipole and a slot dipole with a stacked antenna was looked into for different types of slots. Three slots were focused in this paper, which were H-slot, T-slot, and U-slot. All the designs were designed and were simulated using Computer Simulation Technology (CST) software. The investigation was done on the return loss and the radiation patterns of the dipole antennas based on the effect of different types of slots. The simulation results showed that the multislot and stacked layers improved the efficiency and the bandwidth of the basic dipole antenna at 5.8 GHz.

1 Introduction

Recently, both in urban and indoor environments, the wireless communication system has been developed exponentially worldwide. The increasing demands of the usage of wireless communication devices have made the broadband and multi-band antenna designs vital in the system. Hence, in order to enhance the performance

M.H. Ramli · M.Z.A.A. Aziz (✉) · M.A. Othman · B.H. Ahmad · M.K. Suaidi
Center for Telecommunication Research and Innovation (CeTRI), Faculty of Electronics
and Computer Engineering, Universiti Teknikal Malaysia Melaka (UTeM), Hang Tuah Jaya,
76100 Durian Tunggal, Melaka, Malaysia
e-mail: mohamadzoinol@utem.edu.my

M.H. Ramli
e-mail: hafize_ramli@rocketmail.com

M.A. Othman
e-mail: azlishah@utem.edu.my

A.H. Dahalan
Faculty of Engineering Technology, Universiti Teknikal Malaysia Melaka (UTeM),
Hang Tuah Jaya, 76100 Durian Tunggal, Melaka, Malaysia
e-mail: abdulhalim@utem.edu.my

of the antenna, researchers have applied several methods to overcome a number of identified problems. The microstrip antennas have advantages, such as compact, low in cost, and ease of fabrication [1], whereas the printed dipole with integrated balun [2–5] has omnidirectional features, and it can be used as an element on antenna array architecture. On the other hand, printed dipole with U-slotted arms [6] generate new resonant frequencies at 5.2 GHz, while the features of dual band printed dipole antenna with parasitic elements have been described by [7, 8], and the U-slot stacked patch antenna [1] observes the effect of stacked elements. Besides, the experimental results showed that the stacked or parasitic elements operated with dipole antennas to realize the additional resonance modes.

In this study, the properties of stacked elements of the dipole with various types of slots are discussed based on the performance of antennas. A basic dipole antenna (Design A) that operated at 2.45 GHz frequency band was designed. The dual band frequencies were achieved by adding a slot on the similar conductor plane (top layer) and the stacked layer above the conductor. The additional stacked layer and slot produced two resonant modes. The designed antenna was targeted to operate for WLAN applications based on the IEEE standard, which has the operating frequencies of 2.4–2.4835 GHz (IEEE 802.11b/g), and 5.725–5.825 GHz (IEEE 802.11a).

2 Antenna Design

Figure 1 shows the design structure for dipole antenna. The antenna was modified from the previous work by [2, 3]. The antenna was designed on a FR-4 substrate with a thickness, h , of 1.6 mm and permittivity, ϵ_r , of 4.4, and a tangent loss, $\tan\delta$, of 0.019. The dimension of the structure was 75.85×50 ($W_{sub} \times L_{sub}$) mm. The microstrip via-hole balun acted as unbalance to balance transformer between the two printed dipole strips and the coaxial feed line. The length of the dipole arms, L_d , was used to determine the first resonant modes, which were 2.45 GHz. The optimized antenna parameters for WLAN operation are given (in millimetres, mm) as follows: Dipole arms: $L_d = 20.4$, $W_d = 6$, $g_1 = 3$; microstrip balun feed: $L_f = 31$,

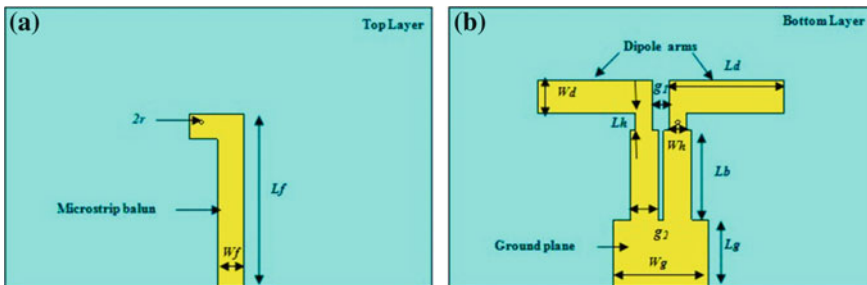


Fig. 1 The geometry of basic dipole antenna Design A: **a** Top layer. **b** Bottom layer

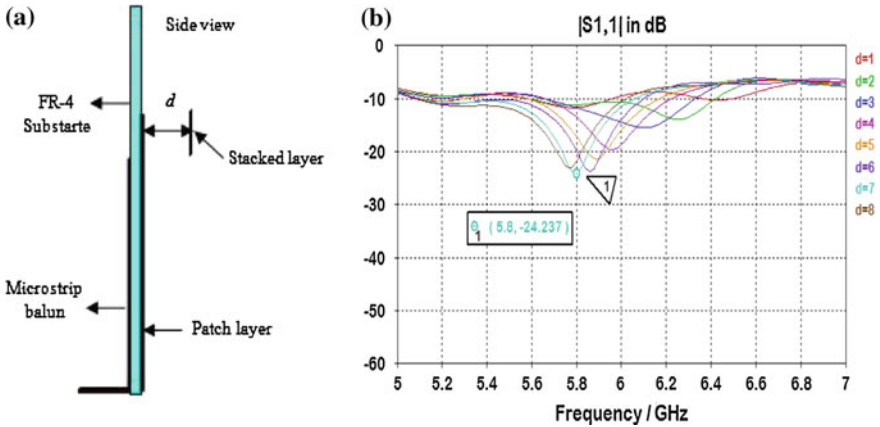


Fig. 2 The structure of stacked layers antenna. **a** Design structure of the stacked layer antenna Designs B, C, and D. **b** The effect of distance, *d*, on return loss

$L_b = 16$, $L_h = 3$, $W_f = 4.5$, $W_b = 5$, $W_h = 3$, $g_2 = 1$; Via hole radius: $r = 0.375$; and Ground plane: $L_g = 12$, $W_g = 17$. Four designs were simulated and compared in this paper, which were a basic dipole antenna (Design A), a radiator dipole arm with stacked layers (Design B), a slot radiator dipole arm with stacked layers (Design C), and a slot radiator and ground with stacked layers (Design D). Figure 2 shows the structure of stacked layer antenna and the effect of distance, *d* on return loss.

The simulation process had been carried out to investigate the effect of the various slot structures on the performance of the antennas, which was present in Design C. The slot that was investigated had been H-slot, T-slot, and U-slot, which were applied to the dipole arms. The stacked layer was also added to Design C with a *d* of 7 mm. Figures 3a, b, and c show the design structure of Design C with parameters of H-slot, T-slot, and U-slot using a width slot of 1 mm.

Figures 4a, b, and c show the additional slot on the ground element of dipole arm Design D. This structure was produced to investigate if the additional slot on ground element could affect the performance of the antenna. The parameter of the

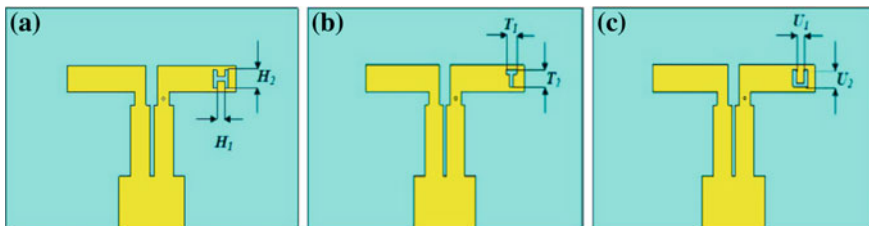


Fig. 3 The parameter of slot on dipole arms (driven): **a** H-slot ($H_1 = 2$ mm, $H_2 = 4$ mm and slot width, $w = 1$ mm), **b** T-slot ($T_1 = 3$ mm, $T_2 = 4$ mm, slot width, $w = 1$ mm), and **c** U-slot ($U_1 = 2$ mm, $U_2 = 4$ mm, slot width, $w = 1$ mm)

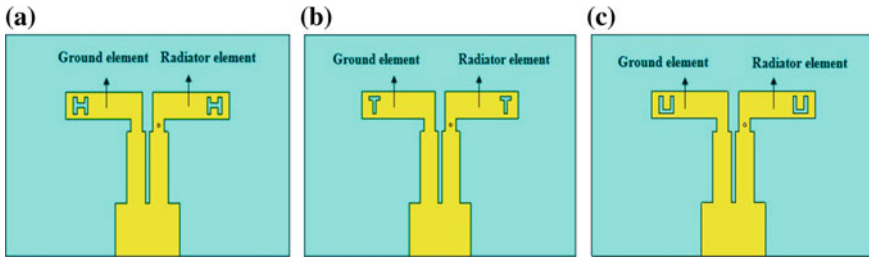


Fig. 4 The parameter structure of slots on dipole arm for radiator and ground elements: **a** H-slot, **b** T-slot, and **c** U-slot

additional slot used on the ground dipole arm had been similar to Design C. The proposed antenna also included stacked layer at radiator and ground elements, is presented. This additional structure was used to increase the efficiency and the directivity of the antenna.

3 Results and Discussion

This section discusses the parametric analysis results for the different slots with additional stacked layer on the printed basic dipole antenna. The parameters of the antenna that had been investigated were return loss, gain, directivity, and radiation pattern. Figures 5, 6, and 7 show the comparison of return loss for various types of designs. The designs that were investigated in this paper were the basic dipole antenna Design A, basic dipole with additional stacked layer Design B, H-slot stacked layer on radiator elements Design C, and H-slot stacked layer at both dipole radiator and ground elements Design D. The results showed that Designs B, C, and D did not affect too much on resonant frequency of 2.45 GHz. However, the significant effect was observed at resonant frequency of 5.8 GHz. Table 1 shows the

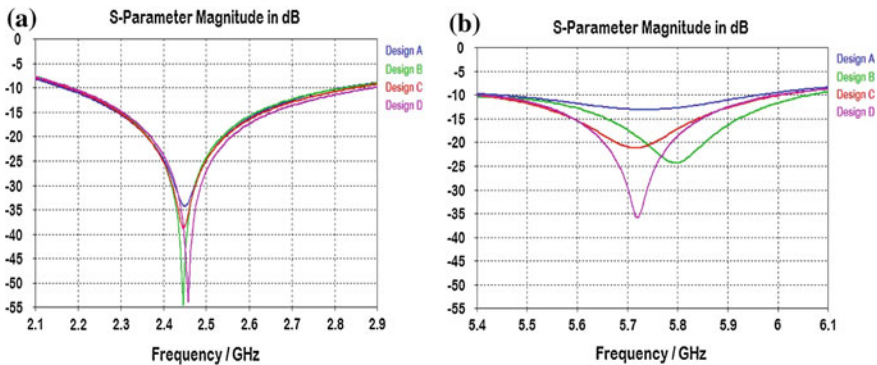


Fig. 5 Return loss for Designs A, B, C, and D, with additional H-slot: **a** 2.45 GHz. **b** 5.8 GHz

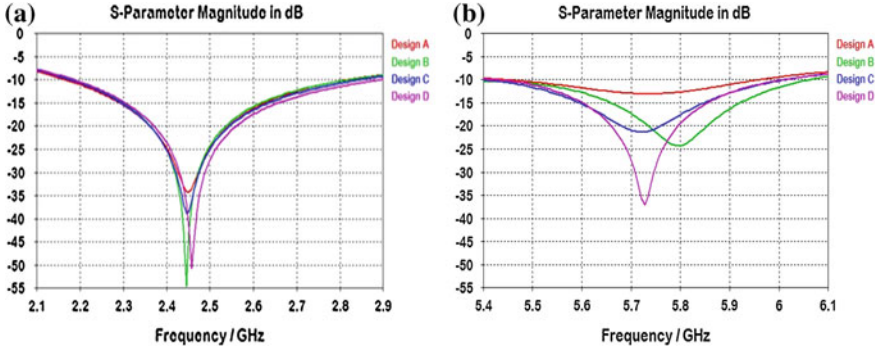


Fig. 6 Return loss for Designs A, B, C, and D, with additional T-slot. a 2.45 GHz. b 5.8 GHz

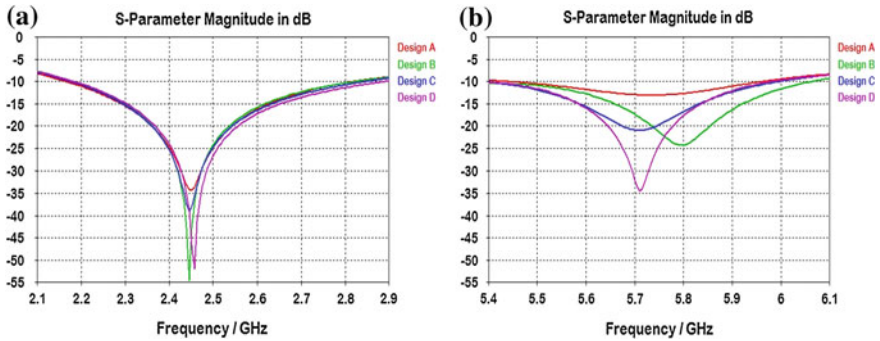


Fig. 7 Return loss for Designs A, B, C, and D, with additional U-slot. a 2.45 GHz. b 5.8 GHz

Table 1 The return loss and bandwidth for Designs A, B, C, and D at frequencies 2.45 and 5.8 GHz

| Parameter | Frequency (GHz) | A | B | C (H-Slot) | D (H-Slot) | C (T-Slot) | D (T-Slot) | C (U-Slot) | D (U-Slot) |
|------------------|-----------------|--------|--------|------------|------------|------------|------------|------------|------------|
| Return loss (dB) | 2.45 | -34.28 | -54.68 | -34.90 | 41.62 | -38.92 | -40.00 | -34.92 | 41.50 |
| | 5.8 | -12.68 | -24.28 | -17.14 | -18.63 | -17.20 | -19.48 | -16.69 | -17.66 |
| Bandwidth (GHz) | 2.45 | 0.66 | 0.65 | 0.66 | 0.72 | 0.68 | 0.72 | 0.67 | 0.71 |
| | 5.8 | 0.52 | 0.65 | 0.62 | 0.62 | 0.62 | 0.62 | 0.63 | 0.63 |

Table 2 The gain and directivity for Designs A, B, C, and D at frequencies 2.45 and 5.8 GHz

| Parameter | Frequency (GHz) | A | B | C (H-Slot) | D (H-Slot) | C (T-Slot) | D (T-Slot) | C (U-Slot) | D (U-Slot) |
|-------------------|-----------------|-------|-------|------------|------------|------------|------------|------------|------------|
| Gain (dB) | 2.45 | 2.642 | 2.660 | 2.682 | 2.772 | 2.682 | 2.772 | 2.783 | 2.773 |
| | 5.8 | 3.678 | 4.501 | 4.2 | 4.442 | 4.241 | 4.562 | 4.241 | 4.357 |
| Directivity (dBi) | 2.45 | 3.632 | 3.624 | 3.651 | 3.724 | 3.650 | 3.722 | 3.650 | 3.772 |
| | 5.8 | 4.941 | 5.656 | 5.471 | 5.552 | 5.508 | 5.623 | 5.432 | 5.485 |

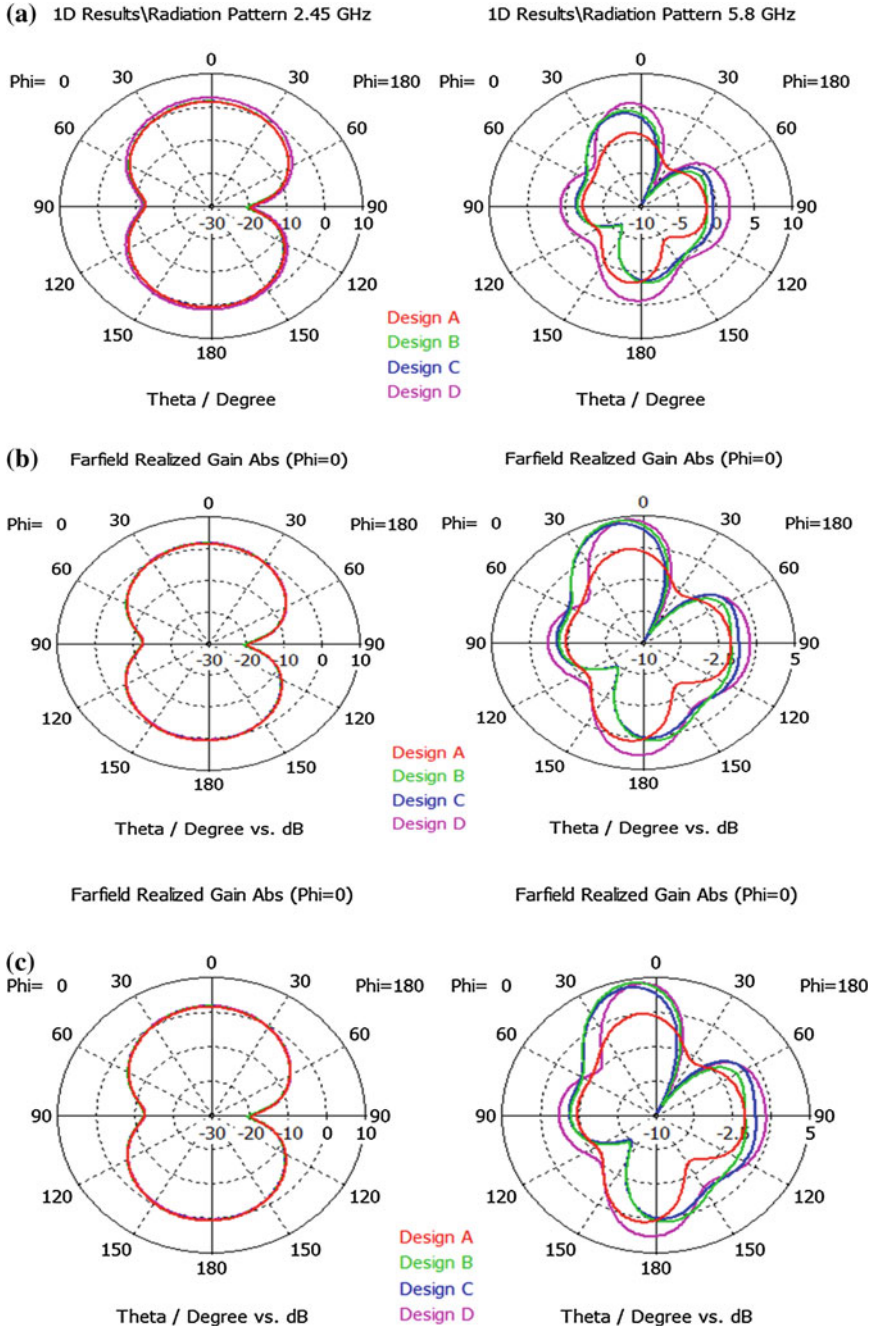


Fig. 8 The simulated radiation pattern of Design A, B, C and D at frequency of 2.45 and 5.8 GHz
a H-slot, b T-slot, c U-slot

return loss and bandwidth for Designs A, B, C, and D at frequencies 2.45 and 5.8 GHz, and the return loss for H-slot, T-slot, and U-slot. From the results, the additional slot with stacked had slightly increased the efficiency and the bandwidth of the antenna.

Table 2 shows the gain and directivity of the antennas for Designs A, B, C, and D at frequencies 2.45 and 5.8 GHz. Designs C and D illustrated the gain and the directivity of the antennas with additional H-slot, T-slot, and U-slot. The results showed that when the additional slot with stacked was applied to the basic dipole antenna, the gain and directivity increased to 2.45 GHz. However, different characteristics had been noted at frequency 5.8 GHz. This was because the return loss of the designed antenna had shifted due to the additional slot stacked.

Figure 8 shows the comparison of radiation patterns between Designs A, B, C, and D at frequencies of 2.45 and 5.8 GHz. There was not much difference in the radiation pattern for all the designs at 2.45 GHz. Probably; this had been due to the main radiation that was contributed by the main radiator of the basic dipole. However, there were significant changes or effects of the additional slot and stacked layers on the dipole antenna at the frequency of 5.8 GHz. The radiation pattern of the basic dipole with slot and stacked layer revealed the big half power beam width and the first null beam width.

4 Conclusion

In this paper, a printed dipole with integrated balun and additional H-slot, T-slot, and U-slot was designed. The simulation results showed that the addition of stacked layer produced the dual band frequencies at 2.45 and 5.8 GHz. Hence, this antenna is suitable for the WLAN application. Meanwhile, the slots on the dipole arm increased the bandwidth. Bigger coverage was obtained by using slots on both dipole arms. In future, the fabrication of antenna prototype can be used to validate the presented simulated data and analysis.

Acknowledgments The authors would like to thank Universiti Teknikal Malaysia Melaka (UTeM) for their support in obtaining the information and materials for the development of our work, and we also thank the anonymous referees, whose comments led to an improved presentation of our work. Lastly, we would like to thank the Ministry of Higher Education for the PJP/2013/FTK (7C) /S01244 research grant.

References

1. Surmeli, K., Turetken, B.: U-slot stacked patch antenna using high and low dielectric constants material combinations in S-band. In: 2011 XXXth URSI General Assembly and Scientific Symposium, pp. 1–4 (2011)
2. Kung, L., Yang, C., Tang, T., Chang, H., Shie, W.: A Dual-band Printed Dipole Antenna With Integrated Balun Covering UMTS and WiMAX Bands, pp. 2679–2682 (2009)

3. Chuang, H., Kuo, L., Member, S.: 3-FDTD Design Analysis of a 2.4 GHz Polarization-Diversity Printed Dipole Antenna with Integrated Balun and Polarization-Switching Circuit for WLAN and Wireless, pp. 374–381 (2003)
4. Jaisson, D.: Fast design of a printed dipole with an integrated balun, August 2006. In: IEEE Proceedings on Microwave Antenna Propagation, pp. 389–394 (2006)
5. Theodore, G.V., Vaitopoulos, E.G., Sergiadis, G.D.: A Wideband Printed Dipole Antenna with Optimized Tapered Feeding Balun for ISM and FWA Bands, pp. 7–8 (2006)
6. Su, C., Chen, H., Wong, K.: Printed Dual-band Antenna with U-slotted Arms 2.4/5.2 GHz WLAN Operations, pp. 1308–1309 (2002)
7. Chang, M., Weng, W.: A Dual-Band Printed Dipole Slot Antenna, pp. 274–277 (2011)
8. Floc, H.J.M., Ahmad, A.E.S.: Dual-band printed dipole antenna with parasitic element for compensation of frequency space attenuation. *Int. J. Electromagnet Appl.* 2(5), 120–128 (2012)

A Numerical Study on MM-NEMO Scheme: Impact of Rising Number of Mobile Routers and Cell Residence Time

Shayla Islam, Aisha Hasan A. Hashim, Mohamed Hadi Habaebi, Wan H. Hassan, Suhaimi A. Latif, Mohammad Kamrul Hasan and H.A.M. Ramli

Abstract Signaling overhead is a significant issue for mobile network due to increase traffic load with packet loss and delay during frequent movement of Mobile Router (MR) from one subnet to another in Network Mobility Basic Support protocol (NEMO BSP). Accordingly, advance preparation mechanism (i.e. Fast Hierarchical Mobile IPv6) works very well as a node mobility solution in order to solve these matters. Yet, combining this host-based protocol for macro mobility handoff in NEMO environment is a challenging issue as both MR and its Mobile Network Nodes (MNNs) must be taken into consideration. In this paper, a numerical framework is developed to study the total handoff cost of Macro Mobility scheme in NEMO (MM-NEMO). The numerical results confirms that MM-NEMO

S. Islam (✉) · A.H.A. Hashim · M.H. Habaebi · S.A. Latif · M.K. Hasan · H.A.M. Ramli
Department of Electrical and Computer Engineering, International Islamic University
Malaysia (IIUM), Kuala Lumpur, Malaysia
e-mail: iium19612@hotmail.com

A.H.A. Hashim
e-mail: aisha@iium.edu.my

M.H. Habaebi
e-mail: habaebi@iium.edu.my

S.A. Latif
e-mail: suhaimie@iium.edu.my

M.K. Hasan
e-mail: hasankamrul@ieee.org

H.A.M. Ramli
e-mail: hadibahmr@iium.edu.my

W.H. Hassan · H.A.M. Ramli
Department of Electrical and Computer Engineering, Malaysia-Japan International Institute
of Technology, University Technology Malaysia (UTM), Kuala Lumpur, Malaysia
e-mail: whh2@hotmail.com

scheme outperforms the standard NEMO BSP related to total handoff delay cost (51 % less than that of NEMO-BSP) regardless of increasing the number of MRs as well as cell residence time.

Keywords NEMO BSP · MM-NEMO · MR · MNN · Total handoff delay cost

1 Introduction

Mobility management is a major issue that supports Mobile Nodes (MNs) or Mobile Routers (MRs) during roaming to ensure continuous Internet connectivity in wireless networks. The most recognized mobility management protocols are categorized into Network Mobility (NEMO) and host mobility [1]. The host mobility protocols (e.g. Mobile IPv6) allow only a single node to be linked with the internet whereas the NEMO protocols (e.g. NEMO BSP) allow the entire network to be linked with the internet through Mobile Router (MR) [2]. Authors have characterized the fundamental approach to concentrate NEMO termed as NEMO BSP which is regarded the greatest outspread mobility protocol for the time being [1]. NEMO BSP works at Layer 3 (L3) and gets the advantages of Mobile IPv6 being a coherent continuation of the MIPv6. MRs with its Mobile Network Nodes (MNNs) are two main entities in NEMO. Providing continuous Internet connectivity of the entire NEMO is the main focus of NEMO BSP [2]. However, in NEMO network, providing an uninterrupted communication (seamless handoff) is still an open issue for the current researchers regarding higher handoff cost which include Location Update Cost (LUC) as well as Total Packet Delivery Cost (TPDC) issues as these issues are not considered in NEMO BSP [1–6]. Keeping in mind the drawbacks of NEMO BSP, the authors in [7–9] have studied on the cost of each entity in NEMO BSP in terms of signaling cost, mobility rate, traffic rate and network size. It is obvious from analytical model that, the cost on Home Agent (HA) keeps on increasing with the increase of MNNs as increased MNNs results in much more data traffic that are being routed via HA in NEMO. This scenario is not same like the case for Central Location Manager (CLM) in SINEMO. Precisely, mobility signaling costs is dominated by tunneling cost. In MM-NEMO scheme [4], the Fast Binding Update (FBU) message is wrapped up with the improved Router Solicitation Proxy (RtSolPr) message earlier to the Layer 2 (L2) handoff. Thus, it is potential to diminish the LUC for macro mobility handoff. Nevertheless, total handoff cost is not considered by this study.

The main aim of this paper is to study the Total Handoff Cost (THC) of Macro Mobility scheme in NEMO (MM-NEMO) and resolve how these costs are changed by increasing a number of MR as well as cell residence time. The involvement of this paper includes: (i) developing mathematical models to estimate THC which includes TPDC of MM-NEMO scheme as well. (ii) Investigate the influence of increasing number of MR, cell residence time and packet arrival rate on THC and ratio.

The remaining part of the paper is organized as follows: Sect. 2 concisely illustrates MM-NEMO scheme. Then, to evaluate handoff cost of MM-NEMO, the numerical framework is offered in Sect. 3. Relative numerical outcomes between MM-NEMO and NEMO BSP is analyzed in Sect. 4 followed by conclusion in Sect. 5.

2 Overview of the MM-NEMO Scheme

An essential component to support mobility management is the handoff management. A handoff technique must be when the serving MR moves between different domain [10]. The MM-NEMO scheme is similar to Fast Hierarchical Mobile IPv6 (FHMIPv6) [3, 4, 10] (as shown in Fig. 1). In MM-NEMO scheme, MR is capable to perform macro mobility handoff with predictive mode only. The serving MR is the gateway in between access Router (MR6 and MR8 act as access router in Fig. 1) and Local Fixed Node (LFN). It is assumed that the serving MR is capable to encapsulate Fast Binding Update (FBU) message to the Router Solicitation Proxy (RtSolPr) message. Moreover, it is also presumed that all nodes are Local Fixed Node (LFN) beneath the serving MR and signaling message for LFN is totally

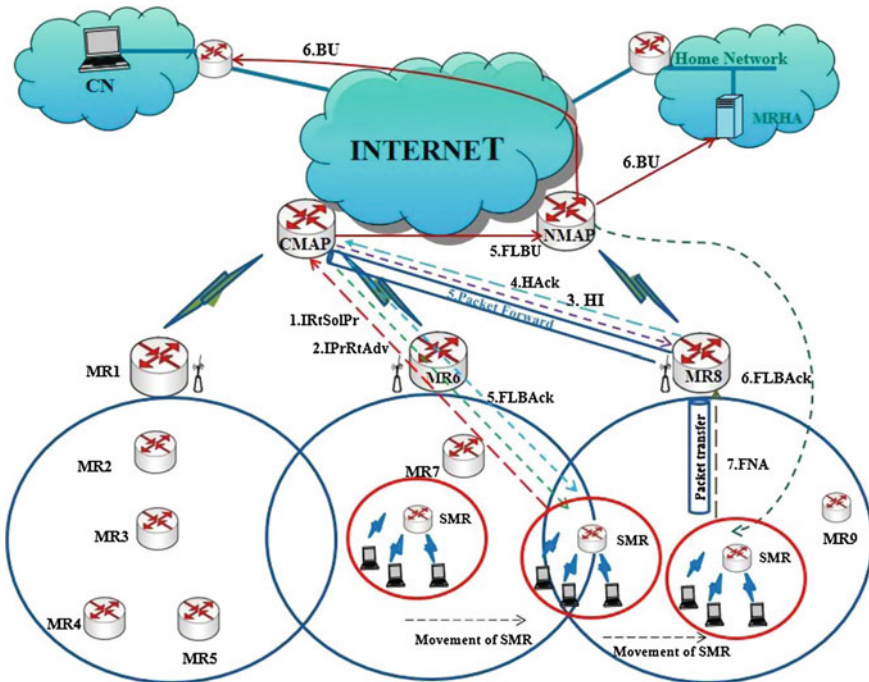


Fig. 1 Handoff scenario of the MM-NEMO architecture [5]

controlled through the serving MR during macro mobility handoff. Otherwise, the MR performs a NEMO BSP handoff. According to the MM-NEMO scheme, the Fast Binding Update (FBU) message is wrapped up with the improved RtSolPr message earlier to the Layer 2 (L2) handoff. Hence, the Current Mobility Anchor Point (CMAP) is capable to receive all correlated information together with RtSolPr message to form both New Link CoA (NLCoA) as well as New Regional CoA (NRCoA) in place of the serving MR. Thus, it is possible to reduce total handoff cost for macro mobility handoff. Handover scenario of MM-NEMO scheme with location update cost and simulation results has discussed details in [4, 5].

3 Numerical Approach

The Performance evaluation of the MM-NEMO scheme is carried out mainly based on significant metrics like Total Packet Delivery Cost (TPDC) as well as Location Update Cost (LUC) to notify the present location for the period of macro/micro mobility handoff to its HA. The LUC to inform the current location via transmitting signaling message along with the TPDC that transmit data packets from Correspondent Node (CN) to serving MR via the MAP is referred to as Total Handoff Cost (THC) [10]. So, the THC of the MM-NEMO scheme is expressed as:

$$THC_{MM-NEMO}^{PRE} = (LUC_{MM-NEMO}^{PRE} + TPDC_{MM-NEMO}^{PRE}) \quad (1)$$

where, $LUC_{MM-NEMO}^{PRE}$ and $TPDC_{MM-NEMO}^{PRE}$ denote the LUC as well as TPDC with predictive mode for the MM-NEMO scheme respectively.

3.1 Total Location Update Cost

According to MM-NEMO scheme, there are two types of movements are performed mainly: mobility inside Same MAP domain (SMAP) as well as mobility among Different MAP domain (DMAP). The earlier one is a sort of movement inside a MAP domain whereas the later one is a movement between two MAPs. Therefore, two location update procedures are included in the signaling cost. When the MR with LFN enters into a MAP domain in NEMO with predictive mode, the LUC of MM-NEMO scheme can be calculated as [4, 10]:

$$LUC_{MM-NEMO}^{PRE} = N_{SMR} \times \frac{P_M \times DMAP_{MM-NEMO} + (1 - P_M) \times SMAP_{MM-NEMO}}{T_{SMR}} \quad (2)$$

$$SMAP_{MM-NEMO} = D_{CMR-CMAP} + D_{CMAP-NMAP} \quad (3)$$

Table 1 Parameters for numerical evaluation

| Parameters | Value |
|---|------------|
| Number of the serving MR (N_{SMR}) | 20 |
| Number of correspondents node (N_{CN}) | 1 |
| The average cell residence time for the serving MR (T_{SMR}) | 120 s. |
| Number of message via wireless in intra mobility (x) | 7 |
| Number of message via wired in intra mobility (y) | 11 |
| $d_{SMR-CMR}$, $d_{CMR-CMAP}$, $d_{NMR-NMAP}$, $d_{SMR-NMR}$, | 1 hop |
| $d_{HAMR-CN}$, $d_{HAMR-CMAP}$, $d_{HAMR-NMAP}$, $d_{CMAP-NMAP}$, $d_{NMAP-CN}$ | 6 hops |
| $d_{CMR-NMR}$ | 2 |
| Processing cost at MAP ($C_{Tunnel-MAP}$) | 12 |
| Lookup cost at home agent of the serving MR (C_{lookup_HAMR}) | 25 |
| Number of message via wireless in inter mobility (X) | 2 |
| Number of message via Wired in intra mobility (Y) | 2 |
| Signaling cost of each message via wireless link (β) | 2 |
| Signaling cost of each message via wired link (γ) | 1 |
| Packet arrival rate (λ_p) | 10 pact./s |

$$D_{MAP_{MM-NEMO}} = S_{MAP} + D_{NMAP-HAMR} \quad (4)$$

From Eq. 1, P_M indicates the probability of performing the mobility among different domain to notify movement of the serving MR and T_{SMR} indicates average cell residence time for the serving MR. From Eqs. 3 to 4, D_{x-y} represents the hop distance among different regions where as S_{MAP} and D_{MAP} refers to signaling message exchanged in between same and different MAP for MM-NEMO scheme respectively. System parameters with the values are listed in Table 1 [4, 10].

3.2 Total Packet Delivery Cost

As MM-NEMO scheme integrates the improved FHMIPv6 in NEMO environment, hence not only the HA of the serving MR maintains the binding cache table as in NEMO BSP but also MAP maintains binding cache table in order to translate the RCoA and LCoA of the serving MR. When CN sends packets to the current location of serving MR, MAP intercepts the packets at first. Then, it is tunneled to the current location of the serving MR. Hence, the cost at MAP includes both the look up cost and routing cost [4, 10]. The PDC of MM-NEMO can be calculated as:

$$PDC_{MM-NEMO}^{PRE} = N_{SMR} \times N_{CN} \times \lambda_p \times (C_{Tunnel_MAP} \times C_{Lookup}) \quad (5)$$

where, total number of the serving MR and Correspondent Nodes (CN) are denoted as N_{SMR} , N_{CN} respectively. In case of any unsuccessful transmission, some packets

might be lost [10]. Consequently, Total Packet Delivery Cost (TPDC) in the MM-NEMO scheme can be computed as the totaling of PDC and packet loss cost which is as follows:

$$TPDC_{MM-NEMO}^{PRE} = P_{SUCCESS} \times PDC_{MM-NEMO}^{PRE} + P_{FAIL} \times \tau \times C_{LOSS} \quad (6)$$

In Eq. 6, $P_{SUCCESS}$ and P_{FAIL} denotes the success as well as failure probability to execute fast handoff effectively with predictive mode for the serving MR respectively. In addition, τ represents the growing rate when the CN transfers the packets again to the serving MR. The packet delivery cost during successful and unsuccessful handoff is specified as $PDC_{MM-NEMO}^{PRE}$ and C_{LOSS} respectively.

4 Result Discussion

4.1 LUC for Number of the Serving MR

The LUC of the MM-NEMO scheme is compared with the standard NEMO BSP from Eqs. (2), (3) and (4) as depicts in Fig. 2. Mostly, handoff happens recurrently as soon as cell residence time decreases. As a result, it becomes obligatory for the serving MR to inform it's HA for the recurrent movement from one region to another region. Accordingly, increases the LUC in NEMO BSP. Instead, it becomes avoidable for the serving MR to notify it's HA for macro mobility because of including the MAP theory with fast handoff method in the MM-NEMO scheme. This considerably decreases the TPDC and THC. Hence, it is summarized by analyzing the Fig. 2, as the cell residence time is increased; it is required less location update for MM-NEMO compared to NEMO BSP.

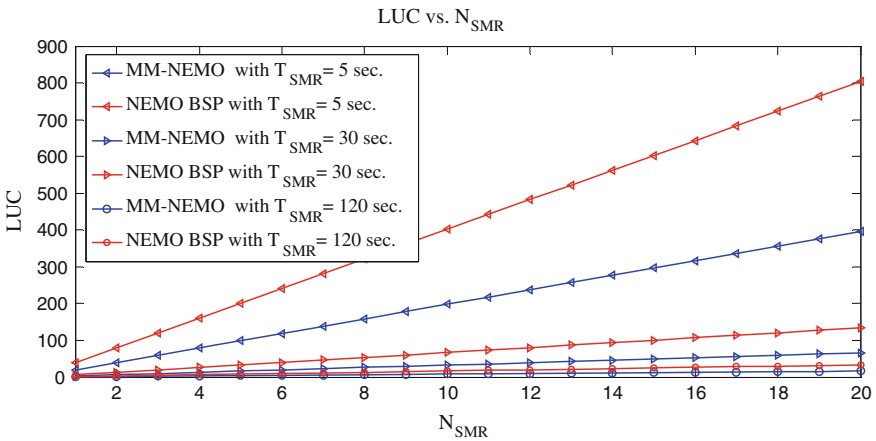


Fig. 2 LUC versus N_{SMR}

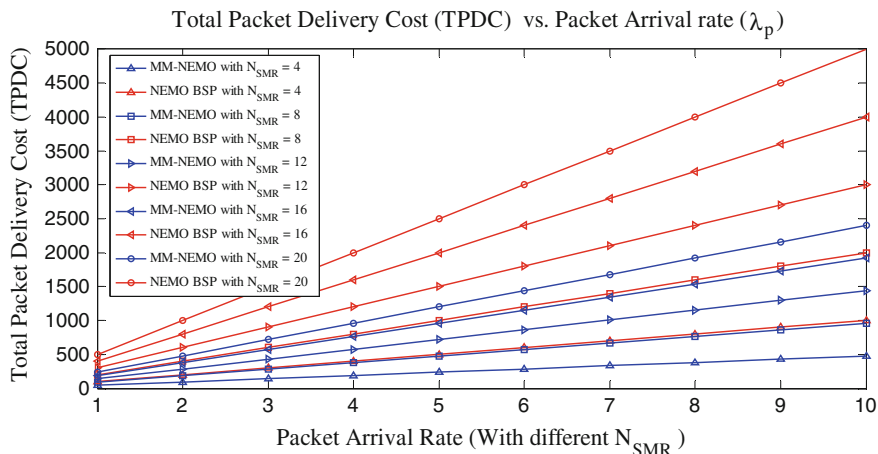


Fig. 3 Total packet delivery cost versus packet arrival rate

4.2 TPDC for Different Packet Arrival Rate

The TPDC is illustrated from Eqs. (5) to (6) for different number of the serving MR in Fig. 3. With the increase of serving MR numbers, the packet processing and routing cost increases at MAP accordingly. Hence, it resulted in increased packet delivery cost for both MM-NEMO scheme and NEMO BSP. Yet, the MM-NEMO performs better when λ_p increase. Moreover, it is observed from the Fig. 3 that the TPDC of MM-NEMO is not much higher like NEMO BSP since multiple tunneled packets need to be routed from CN to the serving MR via HA of the serving MR in NEMO BSP. Thus, the MM-NEMO scheme is better suited for real time application as all packets are sent periodically along with higher rate.

4.3 Total Handoff Cost

The variation of total handoff cost for MM-NEMO and NEMO BSP is illustrated in Fig. 4 as a function of the different number of serving MR along with average subnet residence time. Raised number of serving MR send greater number of LUs along with much more processing cost at HA and MAP. With the aim of establishing the characteristics of the THC, TPDC leads the LU cost. As depicted in Fig. 4, the THC is much higher than that of MM-NEMO scheme since multiple tunnels need to establish in NEMO BSP. For both the proposed scheme and NEMO BSP, if the number of the serving MR is static then no need to inform its HA and CN frequently which effects directly on the total handoff cost for both MM-NEMO and NEMO BSP. Moreover, cell residence time decrement has led the location update cost to rise abruptly for NEMO BSP which in turn increases the total handoff

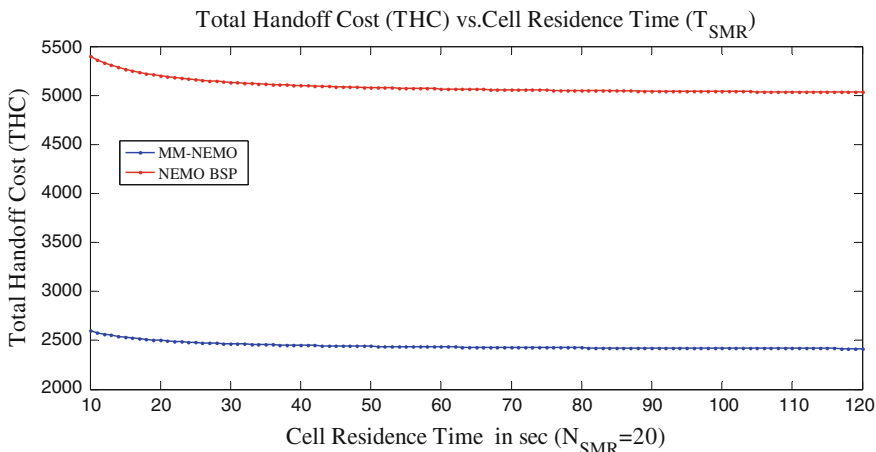


Fig. 4 Comparison of THC (with different cell residence time)

cost significantly. Furthermore, from the achieved results, it is evident that the MM-NEMO scheme is cost effective than that of NEMO BSP. When the cell residence time < 10 s, NEMO-BSP provides higher handoff cost compared to the MM-NEMO scheme as observed in Fig. 4. As there is a relation between LU cost and PD cost, Fig. 5 shows the THC ratio of the MM-NEMO scheme as well as NEMO BSP. The ratio of cost changes when the range of cell residence time is between 20 and 80 s with different number of the serving MR as it is noticed from Fig. 5. While the cost ratio is wrapping into the value 0.48; it can be considered that the MM-NEMO has saved the cost by 52 %.

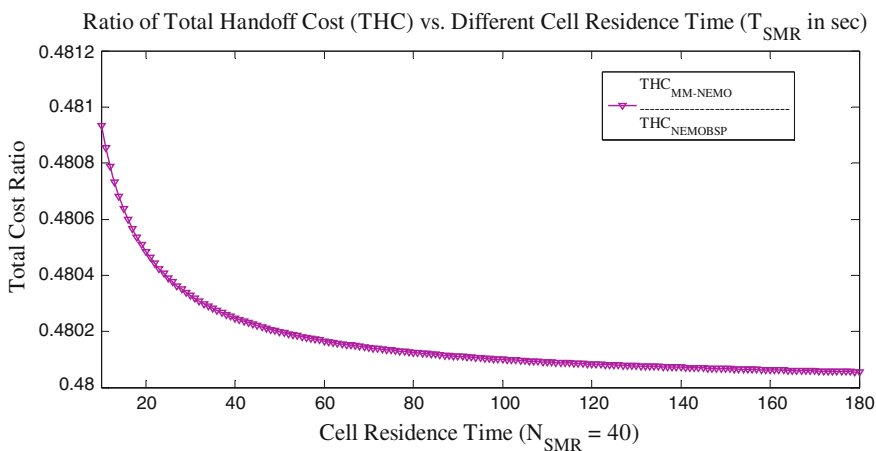


Fig. 5 Cost ratio of MM-NEMO scheme against NEMO-BSP

5 Conclusion

In this paper, a numerical framework is developed to study the total handoff cost of Macro Mobility scheme in NEMO (MM-NEMO). The major contribution of this paper is to reduce total handoff cost by including fast handoff with NEMO network. The MM-NEMO scheme eradicates the necessity to notify the current movement of the serving MR before leaving to the current network to its HA. According to the proposed scheme, one Round Trip Time (RTT) among the serving MR as well as the MAP can be diminished in order to reduce the signaling messages exchanging period during fast handoff operation. This mitigated time whether increasing the number of mobile routers and cell residence time or not. This is a significant issue in NEMO network and can result in a huge improvement of the total handoff cost (52 % reduced than NEMO BSP). Also the possibility of receiving FLBack message by serving MR on the previous link is considerably enhanced.

Acknowledgments A special thanks to the Government of Malaysia, through Ministry of Education for the education sponsorship.

References

1. Zhu, Z., Wakikawa, R., Zhang, L.: A survey of mobility support in the internet, RFC 6301 (2011)
2. Devarapalli, V., Wakikawa, R., Petrescu, A., Thubert, P.: Network mobility (NEMO) basic support protocol, RFC 3963 (2005)
3. Yoo, S., Choi, S., Su, D.: Analysis of fast handover mechanisms for hierarchical mobile IPv6 network mobility. *Wireless Pers. Commun.* **48**(2), 215–238 (2009). doi:[10.1007/s11277-008-9518-x](https://doi.org/10.1007/s11277-008-9518-x)
4. Shayla, I., Aisha Hassan, H., Hasan, M.K., Khalifa, O.O., Saeed, R.A.: Macro mobility scheme in NEMO to support seamless handoff. In: *IEEE International Conference on Computer and Communication Engineering (ICCCE2012)* (2012). doi:[10.1109/ICCCE.2012.6271186](https://doi.org/10.1109/ICCCE.2012.6271186)
5. Aisha Hassan, H., Wan, H.H., Shayla, I., Saeed, R.A., Jamal, D., Khalifa Othman, O.: An enhanced macro mobility management scheme in NEMO environment to achieve seamless handoff. *World Appl. Sci. J.* **21**, 35–39 (2013). doi:[10.5829/idosi.wasj.2013.21.mae.99910](https://doi.org/10.5829/idosi.wasj.2013.21.mae.99910)
6. Li, L.S., Tsai, Y., Lin, P.: An efficient fast handoff scheme in hierarchical MIPv6 for NEMO. In: *IEEE International Symposium on Computer, Communication, Control and Automation*, pp. 90–94 (2010). doi:[10.1109/3CA.2010.5533787](https://doi.org/10.1109/3CA.2010.5533787)
7. Pack, S., Kwon, T., Choi, Y., Park, E.: An adaptive network mobility support protocol in hierarchical mobile Ipv6 networks. In: *IEEE Transactions on Vehicular Technology*, pp. 1–1 (2009). doi:[10.1109/TVT.2009.2015328](https://doi.org/10.1109/TVT.2009.2015328)
8. Lee, J., Chilamkurti, N., Ernst, T.: Performance analysis of PMIPv6-based network mobility for intelligent transportation systems. *IEEE Trans. Veh. Technol.* **61**(1), 74–85 (2012). doi:[10.1109/TVT.2011.2157949](https://doi.org/10.1109/TVT.2011.2157949)
9. Shohrab, H.S., Atiquzzaman, M.: Cost analysis of mobility management entities of SINEMO. In: *IEEE International Conference on Communications (ICC)* (2011). doi:[10.1109/icc.2011.5962982](https://doi.org/10.1109/icc.2011.5962982)
10. Zhang, L., Pierre, S.: Evaluating the performance of fast handover for hierarchical MIPv6 in cellular networks. *J. Network* **3**(6), 36–43 (2008)

Design Strategy for Optimum Planar Square Loop FSS with Different Dielectric Substrates

F.C. Seman and N.K. Khalid

Abstract This paper proposes a systematic design strategy that can be used as a proper guideline in order to design a square loop Frequency Selective Surface (FSS) with a band-stop characteristic at the specified target resonant frequency. This approach is applicable to all types of the substrate with pre-defined dielectric permittivity. In order to demonstrate the proposed design strategy, the FSS is designed to attenuate signal operating at 900 MHz where the square loop element is etched on paper, FR-4 and Rogers substrates. The simulated results are in good agreement with the calculated results.

1 Introduction

Frequency Selective Surfaces (FSSs) have been extensively used for decades in various applications such as dichroic reflectors [1], antenna radomes [2] and spatial filters [3]. A large and growing body of literatures has proposed various techniques to reduce the size of the unit cell by miniaturizing the FSS element [4–6]. As suggested in [4], the reduction of the element size can improve the angular stability of the FSS. However, the problem arises as the element miniaturization can deteriorate the bandwidth performance of the FSS [7]. Thus, an approach known as the interweaving technique is proposed to design a wideband FSS with miniaturized unit cell [8]. In order to do a parameter adjustment when designing the FSS, many researchers used a full-wave solution and an equivalent circuit method. For instance, Hosseinipناه et al. in [9], modeled the proposed FSS with an equivalent

F.C. Seman (✉) · N.K. Khalid
Wireless and Radio Science Centre (WARAS), Faculty of Electrical and Electronic
Engineering, Universiti Tun Hussein Onn Malaysia, 86400 Batu Pahat, Johor, Malaysia
e-mail: fauziahs@uthm.edu.my

N.K. Khalid
e-mail: nur.khalida.khalid@gmail.com

circuit in which, the relationship between the resonant frequency and the values of the inductance, L and capacitance, C is expressed by the equation

$$fr = 1 / 2\pi\sqrt{LC} \quad (1)$$

In addition, by adjusting the values of L and C , the bandwidth of the designed FSS can be further optimized as the bandwidth is directly proportional to the value of the inductance and inversely proportional to the capacitance value as expressed by the equation [9]

$$BW \propto \sqrt{L/C} \quad (2)$$

Nonetheless, to date far little attention has been paid to a proper guideline in understanding the electrical principles behind the optimization of the physical dimensions of the FSS. Thus, in this paper, a detailed explanation regarding the steps to design the FSS that is capable to provide a band-stop characteristic at the specified target resonant frequency on different types of the substrate will be further discussed. The effects of the properties of the dielectric substrate on the frequency response of the FSS will be further investigated by using three different types of the dielectric substrate which are paper ($\epsilon_r = 2.31$), FR-4 ($\epsilon_r = 4.3$) and Rogers ($\epsilon_r = 6.15$). The geometry of the FSS element together with the equivalent circuit model of the proposed FSS is presented in Sect. 2. In general, the proposed design strategy involves few optimization stages which include element length parameter, periodicity and combination of element length and element width parameters. First and foremost, in Sect. 3, the optimized value of the element length for each substrate is calculated. In order to tune the frequency closer to the target resonant frequency, the periodicity of the FSS is optimized as shown in Sect. 4. At the last stage, the optimization of the element length and element width is done simultaneously to tune the resonant frequency exactly at 900 MHz as demonstrated in Sect. 5.

2 FSS Design

Previous studies showed that the square loop FSS offers a stable frequency response under various angles of incidence for both TE and TM polarizations [4]. This type of element is proven to have a great performance in terms of the bandwidth as compared to other types of conventional element such as circular loop and cross-dipole [10].

Thus, in this paper, a square loop FSS which resonates at single frequency band, 900 MHz is designed as shown in Fig. 1a, where p is the periodicity, a is the length of the element, w is the width of the element and g is the gap between the substrate and the element. This paper focuses on single frequency band only since

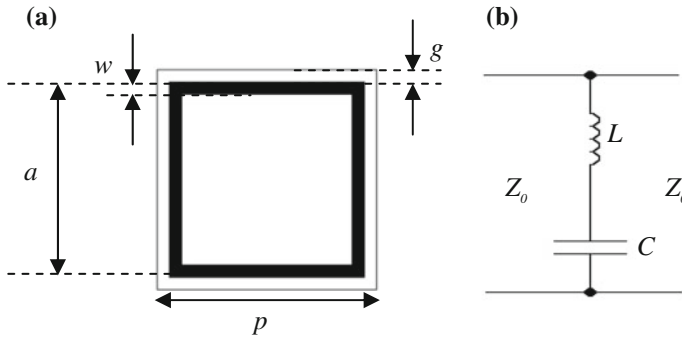


Fig. 1 **a** Unit cell of square loop FSS. **b** An equivalent-circuit model of square loop FSS

the multi-band FSS has to take into account the effect of the mutual coupling between the elements. Previously, in [11, 12], this technique has been used as a fundamental guideline to design the proposed FSS. Based on the simulated and measured results obtained, it is proven that this design strategy is applicable to design a square loop FSS with a band-stop characteristic.

In general, the total length of the loop is equal to one wavelength. According to Tachikawa et al. in [13], the resonant frequency of a single square loop FSS is expressed by the equation

$$fr = \frac{c}{\lambda\sqrt{\epsilon_r}} = \frac{c}{4(a-w)\sqrt{\epsilon_r}} \tag{3}$$

where c is the speed of light, a is the side length of the element, w is the width of the element and ϵ_r is the dielectric permittivity of the substrate. As illustrated in Fig. 1b, the proposed square loop FSS can be represented by an equivalent circuit in which an inductive element, L is in series with a capacitive element, C . In order to ensure that the proposed FSS is capable to tune the resonant frequency exactly at the specified frequency, the design strategy is divided into three optimization stages which will be explained in more details below.

3 Optimization of Element Length

First and foremost, in the first stage of optimization, the length of element, a is calculated using Eq. 3 to tune the resonant frequency at 900 MHz. At this stage, the periodicity, p and width of the element, w are fixed to 60 and 1 mm, respectively. Since the dielectric permittivity of the substrate, ϵ_r varies depending on the material, the calculated value of a is different for all three types of the substrate as presented in Table 1.

Table 1 The calculated element length of all three types of the substrate when $p = 60$ mm

| ϵ_r | Calculated ($a - w$) | Periodicity, p (mm) | Gap between the substrate and the element, g (mm) |
|--------------|--------------------------------------|-----------------------|---|
| 2.31 | 54.8 mm $a = 55.8$ mm, $w = 1$ mm | 60 | 2.1 |
| 4.3 | 40.2 mm $a = 41.2$ mm, $w = 1$ mm | 60 | 9.4 |
| 6.15 | 33.6 mm $a = 34.6$ mm, $w = 1$ mm | 60 | 12.7 |

Equation 1 shows that the resonant frequency is inversely proportional to the values of inductance and capacitance. The inductive impedance in the equivalent circuit is contributed by the vertical side of the element whereas the horizontal side of the element contributes to the conductive impedance [3]. Consequently, a longer side length, a is required in order to tune a lower resonant frequency.

Figure 2 shows the simulated transmission frequency response that is obtained for all three types of the substrate when the same periodicity, p is used. As expected, the simulated resonant frequencies that are obtained for all three types of the substrates are not similar to 900 MHz. The simulated resonant frequencies that are obtained for paper, FR-4 and Rogers are equal to 1060, 1960 and 2400 MHz, respectively. This is due to the fact that Eq. 3 that is used to calculate the element length, a does not take into account the periodicity, p of the FSS. The variation of the periodicity indirectly can enlarge or decrease the gap between the substrate and the element, g which will then affect the value of the capacitance. Thus, further optimization is done in the following section in order to ensure that the simulated

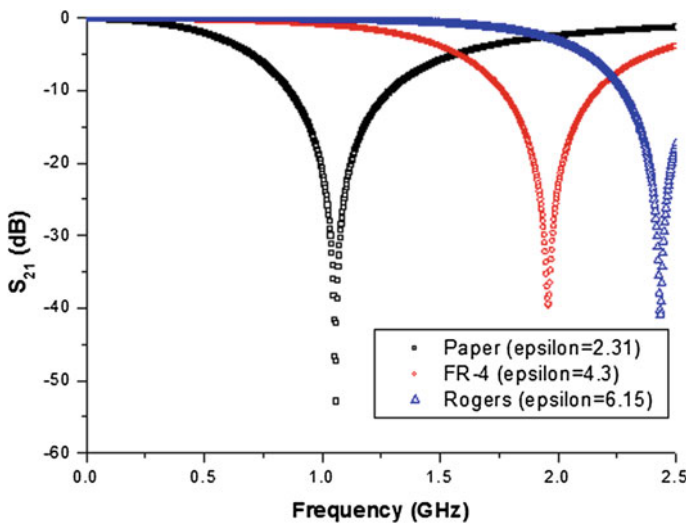


Fig. 2 Simulated transmission frequency response of all three types of the substrate when $p = 60$ mm

Table 2 The optimized values of periodicity, p of all three types of the substrate

| ϵ_r | Calculated ($a - w$) | Periodicity, p (mm) | Gap between the substrate and the element, g (mm) |
|--------------|--|-----------------------|---|
| 2.31 | 54.8 mm $a = 55.8 \text{ mm}, w = 1 \text{ mm}$ | 59 | 1.6 |
| 4.3 | 40.2 mm $a = 41.2 \text{ mm}, w = 1 \text{ mm}$ | 43 | 0.9 |
| 6.15 | 33.6 mm $a = 34.6 \text{ mm}, w = 1 \text{ mm}$ | 36 | 0.7 |

resonant frequency is closed to the target resonant frequency by taking into consideration the periodicity of the FSS.

4 Optimization of Periodicity

For the second stage of optimization, the periodicity of the FSS needs to be optimized to tune the resonant frequency closer to 900 MHz. As previously discussed, the resonant frequency can be reduced by increasing the value of the capacitance. The capacitance value can be adjusted according to the equation

$$C = \epsilon r A / g \quad (4)$$

where A is the effective area of two horizontal element and g is the distance between them, which is equal to $(p-a)$ [9]. In order to increase the value of the capacitance, the periodicity as well as the gap between the substrate and the element, g is further decreased as tabulated in Table 2.

Figure 3 shows the simulated transmission frequency response that is obtained for all three types of the substrate when the periodicity, p is optimized. It can be seen that for the first substrate, paper, the resonant frequency shifts left by 40 MHz when the periodicity decreases from 60 to 59 mm. Similarly, for FR-4, the resonant frequency reduces to 1100 MHz when p equals 43 mm. Besides, as the periodicity of the Rogers substrate decreases up to 36 mm, the resonant frequency shifts left to 1160 from 2400 MHz.

5 Optimization of Element Length and Element Width

In order to tune the resonant frequency exactly at 900 MHz, both design parameters, length of the element, a and width of the element, w are varied simultaneously for all three types of the substrate.

From Fig. 4, it can be seen that by increasing the values of a and w , the resonant frequency can be further reduced to 900 MHz. This is due to the fact that these two

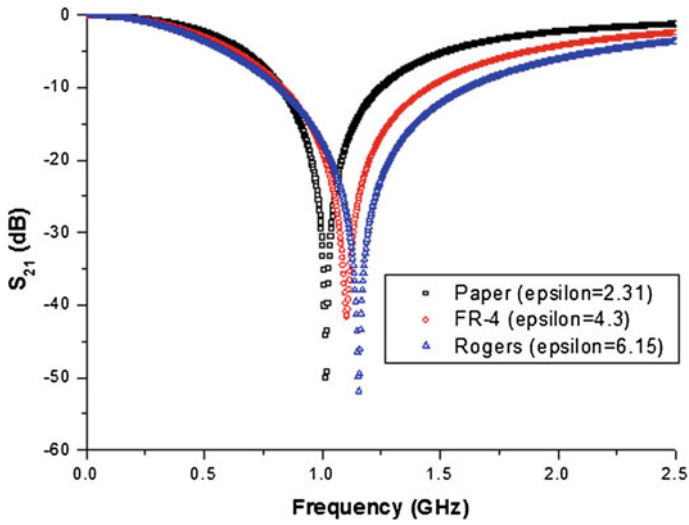


Fig. 3 Simulated transmission frequency response of all three types of the substrate when the periodicity, p is optimized

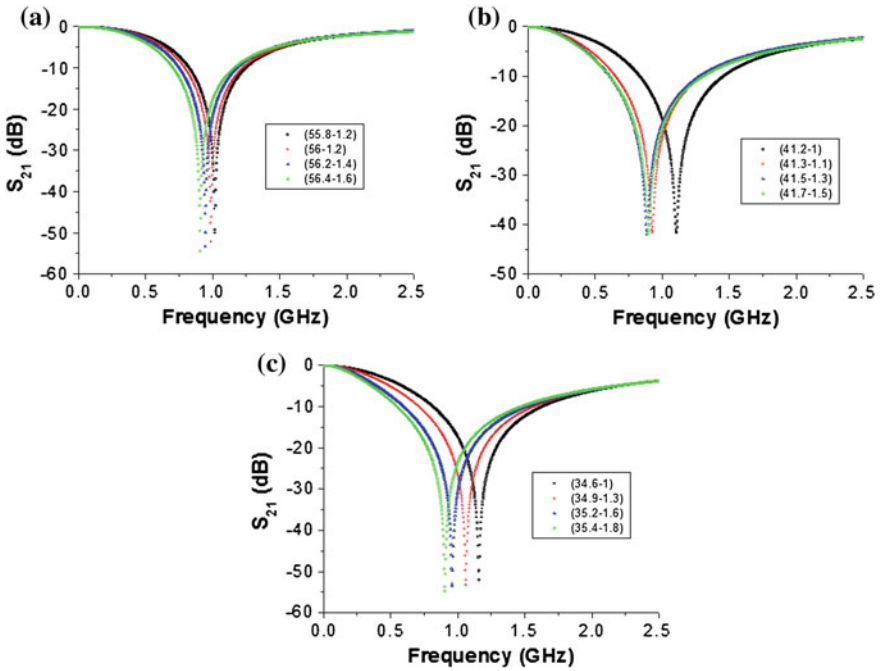


Fig. 4 Simulated transmission frequency response of a paper b FR-4 and c Rogers substrates with different combinations of $(a - w)$

Table 3 Simulated resonant frequency and bandwidth of all three types of the substrate at the first and third stages of optimization

| ϵ_r | Resonant frequency, f_r (MHz) | | -10 dB bandwidth (%) | |
|--------------|---------------------------------|---------|----------------------|---------|
| | Stage 1 | Stage 3 | Stage 1 | Stage 3 |
| 2.31 | 1060 | 900 | 38 | 50 |
| 4.3 | 1960 | 900 | 16.8 | 77.8 |
| 6.15 | 2400 | 900 | 11.9 | 102.2 |

parameters corresponding to the value of inductance which is inversely proportional to the resonant frequency. Table 3 compares the simulated resonant frequency and bandwidth that are obtained at the first and third stages of optimization. The -10 dB bandwidth at the third stage of optimization is much higher as compared to before. This can be explained using the Eq. 2. At the last stage of optimization, the sum of the inductance value is relatively higher than the capacitance value which indirectly leads to the bandwidth improvement.

At this final stage, the designed FSS is expected to tune the resonant frequency exactly at the specified frequency since all the FSS design parameters have been taken into consideration.

6 Conclusions

The strategy of designing the square loop FSS with single frequency band is demonstrated. By considering the relationship between the design parameters such as element length, periodicity and element width with the values of inductance and capacitance, the target resonant frequency can be achieved although the square loop element is etched on different types of the substrate. In this paper, the target resonant frequency of 900 MHz is achieved for paper, FR-4 and Rogers substrates. The simulated results are in very good agreement with the calculated results. To abbreviate the contents of the paper, the measured results are not shown in this paper. However, the experimental verification has been performed in [11, 12], with good agreement obtained between the simulated and measured results.

Acknowledgments The authors would like to thank the Ministry of Education Malaysia for supporting this study under the Exploratory Research Grant Scheme (ERGS/1/2012/TK06/UTHM/02/1/E005).

References

1. Pasian, M., et al.: Accurate modeling of dichroic mirrors in beam-waveguide antennas. *IEEE Trans. Antennas Propag.* **61**(4), 1931–1938 (2013)
2. Zhao, J., Xu, X.: Study of the effect of a finite FSS radome on a horn antenna. In: *IEEE International Conference on Microwave Technology and Computational Electromagnetics (ICMTCE)*, pp. 74–76 (2011)

3. Sung, G.H.H., et al.: A frequency-selective wall for interference reduction in wireless indoor environments. *IEEE Antennas Propag. Mag.* **48**(5), 29–37 (2006)
4. AlKayali, H., Qasem, N.: Convoluted frequency selective surface wallpaper to block industrial, scientific, and medical radio bands inside buildings. In: *American Academic and Scholarly Research Journal*, vol. 5, No. 3 Special issue, April 2013
5. Natarajan, R., et al.: A compact frequency selective surface with stable response for WLAN applications. *IEEE Antennas Wireless Propag. Lett.* **12**, 718–720 (2013)
6. Parker, E.A., et al.: Frequency selectively screened office incorporating convoluted FSS window. *Electron. Lett.* **46**(5), 317–318 (2010)
7. Vallecchi, A., Schuchinsky, A.G.: Entwined spirals for ultra compact wideband frequency selective surfaces. In: *Proceedings of the Fourth European Conference on Antennas and Propagation (EuCAP)*, pp. 1–3, April 2010
8. Huang, F., et al.: Interwoven convoluted element frequency selective surfaces with wide bandwidths. *Electron. Lett.* **42**(14), 788–790 (2006)
9. Hosseinpanah, M., et al.: Design of square-loop frequency selective surfaces utilize C-band radar stations. In: *International Conference on Microwave and Millimeter Wave Technology (ICMMT)*, vol. 1, pp. 66–68, April 2008
10. Wu, T.K.: *Frequency Selective Surface and Grid Array*. Wiley, New York (1995)
11. Khalid, N.K., Seman, F.C.: Double square loop frequency selective surface (FSS) for GSM shielding. In: *International Conference on Communication and Computer Engineering (ICOCOE)* (2014)
12. Seman, F.C., Khalid, N.K.: Investigations on fractal square loop FSS at oblique incidence for GSM applications. In: *7th Electrical Power, Electronics, Communications, Controls and Informatics International Seminar in Conjunction with 1st Joint Conference UB-UTHM (EECCIS)* 2014
13. Tachikawa, K., et al.: Transmission properties of dual-band loop slot frequency selective surfaces on plastic board. In: *15th International Symposium on Antenna Technology and Applied Electromagnetics (ANTEM)*, pp. 1–4, 25–28 June 2012

Estimations of Fade Margin for the New Malaysian MEASAT-3B Ku-Band Link

**Khairayu Badron, Ahmad Fadzil Ismail, Ani Liza Asnawi,
Norun Fariahah Abdul Malek, Suriza Zainal Abidin
and Md. Rafiqul Islam**

Abstract Satellite services in Malaysia open the doors to contemporary telephone and data transmission facilities whilst at the same time foster and strengthen the union between its peninsula and the Borneo continent. Satellite communications also contribute significantly to the quick growth of computer networking in Malaysia, as well as providing the new high definition (HD) direct-to-home (DTH) satellite television services. Satellite systems with operating frequencies of Ku-band and higher have been extensively used for Earth-space communications in the temperate climate countries for decades. The same cannot be said for tropical region. One of the likely limiting factors is the absence of accurate rain fade information. Satellite engineers and designers have to establish the required fade margin to overcome rain attenuation; which need to be incorporated into the system in the effort to accomplish the preferred link performance. This is also applied in the case of the recently launched the Malaysian MEASAT-3B satellite. With this in mind, a comprehensive set of previously acquired signal measurements can certainly shed lights on the propagation characteristics to be endured. In this paper, the probable fade margins are proposed. They are based on deductions and estimations of 1 year (2009) local radar-derived rainfall rate data and the latest ITU-R rain attenuation prediction model.

K. Badron (✉) · A.F. Ismail · A.L. Asnawi · N.F.A. Malek · S.Z. Abidin · Md. Rafiqul Islam
Faculty of Engineering, International Islamic University Malaysia, 50310 Jln Gombak,
Kuala Lumpur, Malaysia
e-mail: khairayu@iium.edu.my

A.F. Ismail
e-mail: af_ismail@iium.edu.my

A.L. Asnawi
e-mail: aniliza@iium.edu.my

N.F.A. Malek
e-mail: norun@iium.edu.my

S.Z. Abidin
e-mail: suriza@iium.edu.my

Md. Rafiqul Islam
e-mail: rafiq@iium.edu.my

1 Introduction

Communications satellites allow live transmissions of radio, television, and telephone to be sent anywhere in the world. The way humans connect with each other have been revolutionize by communication satellites. Direct-broadcast satellite (DBS) or Direct to Home (DTH) is a term used referring for satellite television broadcasts intended for home reception. Using this technique we can easily access to live television channel from other country [1]. This is an alternative to the traditional cable television that have been serving home viewers for decades. Figure 1 shows the typical broadcasting satellite set-up.

MEASAT Satellite System Sdn. Bhd. (MEASAT) is the operator of Malaysian Ku-band satellite pioneering the Information and Communication Technology Industry and one of the Asia’s biggest broadcast distributors offering DTH in the neighborhoods of Asian market. MEASAT-3B has been launched on 12 September 2014. MEASAT-3B will be used to expand video and data services across Malaysia, India, Indonesia and Australia. The system is anticipated to increase data connectivity level up by between 10 and 20 %, bridging the digital breach in Malaysia [2]. MEASAT-3B operates as many as 48 Ku-band transponders simultaneously from the 91.5°E orbital location, where it will be co-located with MEASAT-3 and MEASAT-3A. The ground station of the MEASAT-3B is located at the current MEASAT facility (2.937°N and 101.658°E) [3]. Given bearing is 254° 08’ 45” and elevation angle towards the satellite is 77.4°. It will be a very commanding satellite where there will be more than double the current MEASAT-3A Ku-Band capacity. The satellite will allow the Malaysian operator to meet the increasing requirements and demands of DTH and telecommunications services in the region. MEASAT-3B broadcasting services would be the preferred means over cable TV due to its lower cost, reduced complexity of the set up, high definition, portability and increased number of channels [4]. Unfortunately, the most severe setback of such DTH service is signal disruptions due to heavy rainfall. The signal

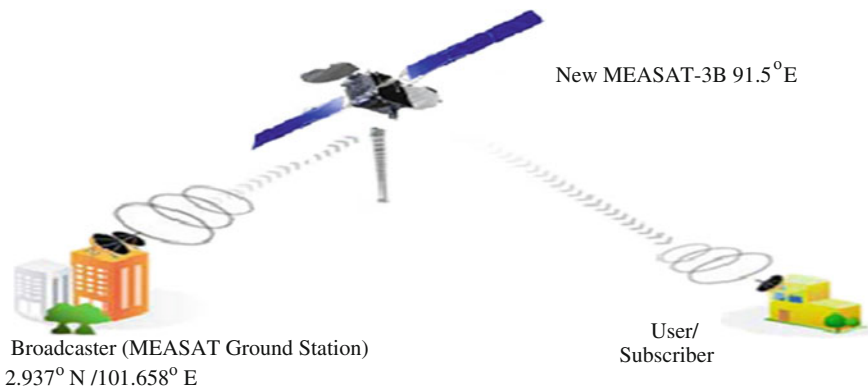


Fig. 1 Typical MEASAT satellite broadcast configuration

discontinuation is the result of microwave radio frequency (RF) signal absorption by atmospheric hydrometeors namely rain. The losses are prevalent at frequencies above 10 GHz [5].

2 Rain Fade Estimations

2.1 ITU-R Prediction Methods

At present, the method implemented in all ITU-R prediction technique is based on the estimation of the attenuation exceeded at 0.01 % of the time, which is originated from the rainfall rate exceeded at the same time exceedance. From a theoretical point of view, the impression of equiprobable analysis is not reliable with meteorological information and not entirely agreeable. Nevertheless, the accurateness obtained in select cases using the prediction method is consistent with the quality and variability of available rain intensity data [6]. The schematic presentation of an Earth-space path involving the said parameters in the attenuation prediction process is given in Fig. 2 as shown:

The specific attenuation γ_R can be determined for a given value of rainfall rate at time exceedance 0.01 %, $R_{0.01}$. Determination of the k and α values using the frequency-dependent coefficients, k_H , k_V , α_H , and α_V from Table 1 of the ITU-R P. 838-3 [7] is given by:

$$\gamma_R = k(R_{0.01})^\alpha = 7.2 \text{ dB km}^{-1} \tag{1}$$

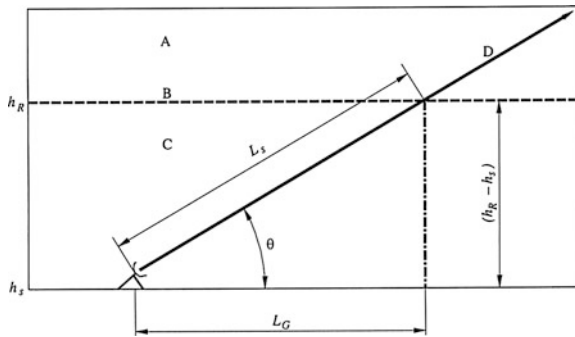


Fig. 2 Graphic presentation: **a** frozen precipitation, **b** rain height, **c** liquid precipitation, **d** Earth-space path, h_R rain height, h_s station height, θ elevation angle, L_G horizontal projection, L_S slant-path length [6]

Table 1 Site characteristics

| Site name | MMD radar station | Satellite ground station | MEASAT-3B |
|-----------|-----------------------|--------------------------|-----------|
| Location | 2° 51' N/101° 39'60"E | 2.937°N/101.658°E | 91.5°E |

When multiplied with the effective path length L_E , the corresponding attenuation value at 0.01 % time exceedance $A_{0.01}$ can be calculated as:

$$A_{0.01} = \gamma_R L_E = 15.92 \text{ dB} \quad (2)$$

The estimated attenuation, A to be exceeded for other percentages, p of an average year, in the range 0.001 to 5 %, is determined from the attenuation to be exceeded for 0.01 % for an average year using (2):

$$A_p = A_{0.01} \left(\frac{p}{0.01} \right)^{-(0.655+0.033 \ln(p)-0.045 \ln(A_{0.01})-\beta(1-p) \sin \theta)} \text{ dB} \quad (3)$$

where in the case of the MEASAT-3B, θ will be the elevation angle equivalent to 77.4° and β will be equal to 0.1646. Several previous investigations pointed out that the rain attenuation prediction models proposed by ITU-R somehow severely underestimate the signal attenuation due to rain in tropical region [8–10]. An example of the generated annual statistics is shown in Fig. 6.

2.2 Radar-Derived Rain Attenuation Prediction

Weather radars have been cleverly exploited for investigating propagation phenomena which affect satellite communication links [11, 12]. Weather radar returns can be used to estimate both attenuation and depolarization produced by hydrometeors. This study emulated comparable techniques as proposed by previous investigators [13–22] in the attempt to estimate the to-be-experienced rain attenuation. It was proposed that an equivalent rain rate or signal attenuation can be deduced from reflectivity values using particular assumptions. An S-band radar operated by Malaysian Meteorological Department (MMD) is located at approximately 8 km south of the MEASAT ground station. It operates at frequency of 2.85 GHz. The weather radar, satellite and ground station location impression is illustrated in Fig. 3. Table 1 lists both site coordinates.

In today's radar technology, there are two types of radar product that can assist the derivation of the rain attenuation prediction. The constant altitude plan position (CAPPI) view portrays the affected rainy area of the ground station and the neighboring rain cells. The range height indicator (RHI) view depict vertical landscape of the affected rainy area; from the ground station to the satellite. Figures 4 and 5 show the examples of CAPPI and RHI views respectively. In Fig. 4,

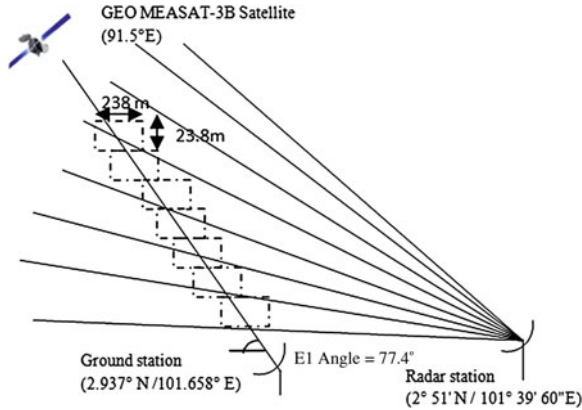


Fig. 3 Geometry illustration of radar, satellite and ground station location

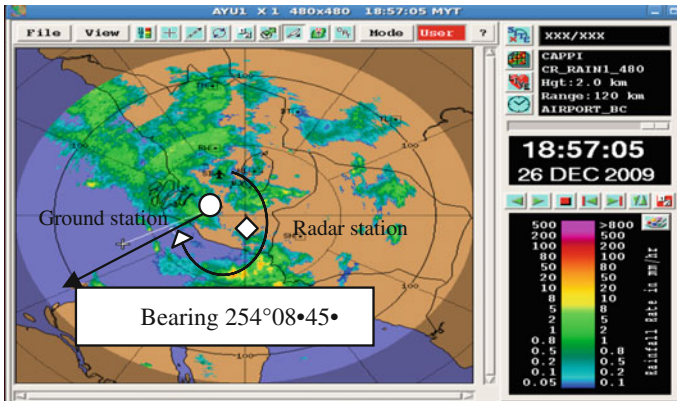


Fig. 4 CAPPI views shows the ground station affected by rain

the black line plotted is the satellite path link from the ground station. In Fig. 5, the red squares show the illustration of the bins/gates' resolution. Bin is the radar range resolution in horizontal and vertical position. For the analysis involved, the bin size is 238 m × 23.8 m. The values in raw data (dBZ) format can be converted into rainfall rate readings. From the rainfall rate values along the propagation path, estimation of rain attenuation can be derived.

The rainfall rate, R deduced from the radar reflectivity, Z by exploiting local radar data acquired from the MMD:

$$R_i = \sqrt[3]{\frac{Z}{a}} \tag{4}$$

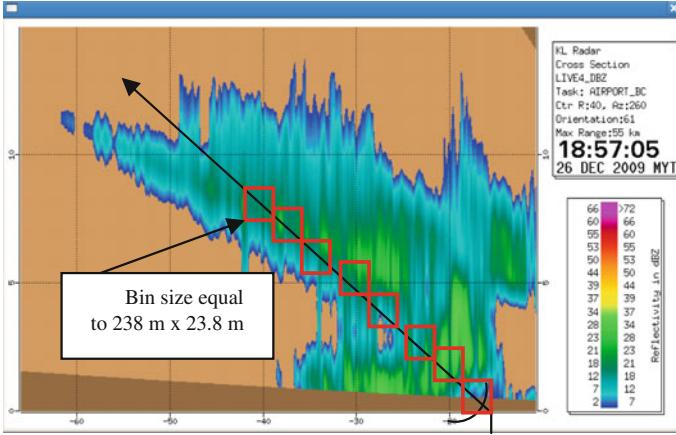


Fig. 5 RHI views shows the link affected by rain

with a set of general parameters of $a = 220$ $A = 200$ and $b = 1.6$ proposed by Marshal and Palmer in [13]. In (4), R_i is the rainfall rate value derived from the radar. The rain attenuation values can now be estimated using the derived rainfall rate data according to the power law equation [14] as in (5):

$$A_i = kR_i^a L_{ei}^b \quad (5)$$

where A_i is the attenuation per bin, L_{ei} is the effective length affected by rain within the bin, and k and α are the coefficients adopted from the ITU-R P838-3 recommendation [7]. The color bar in Figs. 4 and 5 indicates only 16 levels of the reflectivity group values (dBZ) for ease of display. A software identified as ‘productx’ is capable of providing the actual reflectivity values for each bin. Once the productx along the satellite path is generated, the actual Z values in each bin for the range height indicator (RHI) is now ready to be converted to rainfall rate, R . The rain attenuation is calculated along the entire propagation path according to the range resolution of the bin/gate as illustrated in Fig. 5. The amount of the slant path fading was then calculated through the numerical summation of:

$$\sum_{i=0}^n A_i = kR_i^a \cdot \Delta L_{ei} \quad (6)$$

ΔL_{ei} is the path length at each i th bin along the slant path between the Earth station and the satellite affected by rain. Table 2 list an example of the radar-derived attenuation calculated values.

Table 2 Radar derived attenuation for each bin for 77.4° elevation angle for the stated event

| Bin No. | Reflectivity (Z) | Rainfall rate (mm/hr) | Path length (km), ΔL_i | Rain attenuation, A (dB) |
|--------------------------------------|------------------|-----------------------|--------------------------------|--------------------------|
| 1 | 18 | 0.49 | 0.283999 | 0.00414 |
| 2 | 23 | 1.00 | 0.283999 | 0.01134 |
| ... | ... | ... | ... | ... |
| ... | ... | ... | ... | ... |
| 600 | 23 | 1.00 | 0.283999 | 0.01696 |
| Total attenuation, ΣA_i (dB) | | | | 3.27 |

3 Results and Discussion

An exact fade margins are very critical in ensuring the reliability of the system in order to layout a new satellite link. These predicted values of signal loss and fading are commonly utilized in the process of establishing the satellite design parameters. The estimated annual rain fade statistics using ITU-R recommendation and radar derived rain attenuation prediction can be viewed in Fig. 6. It can be observed that the deduced rain attenuation statistics values estimated using radar data are higher than the ITU-R predicted values at all times exceedance. Table 3 catalogues selected fade margin at specific time exceedances for the new MEASAT-3B Ku-band satellite-Earth link in Malaysia. These initial outcomes suggested that due to the severity of the rain induced attenuation that will be confronted, the Ku-band

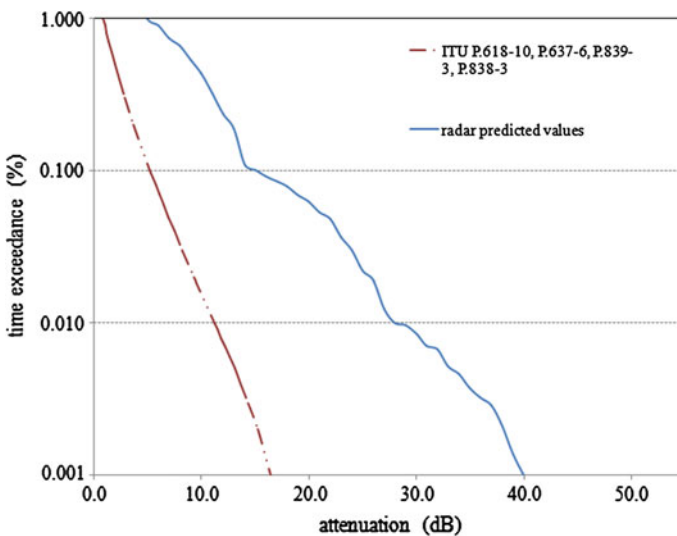


Fig. 6 Plot of ITU-R predicted attenuation statistics, ITU-R predicted statistics using local values and radar derived attenuation

Table 3 Estimated fade margins at selected time percentages

| Time exceedance | Radar-derived attenuation (dB) | ITU-R P618-11 (dB) | RMSE |
|-----------------|--------------------------------|--------------------|------|
| 1.000 | 3.27 | 1.26 | 2.02 |
| 0.300 | 10.4 | 4.7 | 1.42 |
| 0.100 | 13 | 8 | 1.25 |
| 0.010 | 25 | 13 | 3.00 |
| 0.001 | 35 | 28 | 1.75 |

satellite broadcasting operation in Malaysia and others in tropical region may not be easily achievable to operate at 99.7 % availability (equivalent to 0.3 % time exceedance) to concur with the strict broadcasting QoS requirement [22].

It is very crucial to be capable of accurately estimate the to-be-encountered impairments of the given link in order to devise the services efficiently.

4 Conclusion

Initial study results have identified that propagation impairment can be indeed quite severe for Malaysian environment i.e. tropical climates. The standard performances are expected to be taxing in order to achieve the expected QoS in these regions. Possible ways to overcome the effects of rain fade are uplink power control, site diversity, variable rate encoding, larger receiving antennas (i.e. higher gain) than the required size for normal weather conditions. Production of predicted impairment statistics has been highlighted in this paper and is therefore may be central and need to be taken into serious consideration in the design and deployment of the new home receiver system.

References

1. Gomez, J.M.: *Satellite Broadcast Systems Engineering*, 1st edn. Artech House, Boston (2002)
2. <http://www.measat.com/3b/overview/mission.html>. Accessed 2 March 2014
3. <http://www.astrium.eads.net/en/programme/-measat-3b.html>. Accessed 2 March 2014
4. Itagaki, T., Cosmas, J., Haque, M.: An interactive digital television system designed for synchronised and scalable multi-media content over DVB and IP networks, multimedia and expo, 2004. ICME '04. In: 2004 IEEE International Conference on, vol. 3, pp. 2155, 2158, 27–30 June 2004
5. Allnutt, J.E., Peregrinus, P.: *Satellite-to-ground radiowave propagation: theory, practice, and system impact at frequencies above 1 GHz* (1989)
6. Recommendation ITU-R P. 618–11: Propagation data and prediction methods required for the design of Earth-space telecommunication systems (2013)
7. ITU-R: Specific attenuation model for rain for use in prediction methods. Recommendation ITU-R P. 838-3, Geneva (2005)

8. Zabidi, S.A., Md. Rafiqul, I., Wajdi, A.K.: Rain attenuation prediction of optical wireless system in tropical region. In: 2013 IEEE International Conference on Smart Instrumentation, Measurement and Applications (ICSIMA), pp. 1, 5, 25–27 Nov 2013
9. Badron, K., Ismail, A.F., Din, J., Tharek, A.R.: Rain induced attenuation studies for V-band frequency in tropical regions. In: Antennas and Propagation Conference, 2009. LAPC 2009. Loughborough, pp. 689, 692, 16–17 Nov 2009
10. Singh, M.S.J., Hassan, S.I.S., Ain, M.F., Igarashi, K., Tanaka, K., Iida, M.: Proposed rain attenuation model revised from ITU used for prediction in tropical climates. In: 2005 Fifth International Conference on Information, Communications and Signal Processing, pp. 994, 996
11. Badron, K., Ismail, A.F., Ramli, H.A.M., Ismail, M., Ooi, S.T., Jamil, S.F.: Evaluation of RazakSAT's S-band link signal measurement with the radar derived rain attenuation. In: 2013 IEEE International Conference on Space Science and Communication (IconSpace), pp. 380, 384, 1–3 July 2013
12. Schnabl, G.: Polarimetric radar measurements of rain and radar derived attenuation and depolarization in rain at 20/30 GHz. In: 18th European Microwave Conference, 1988, pp. 436, 441, 12–15 Sept 1988
13. Marshall, J.S., Palmer, W.K.: The distribution of raindrops with size. *J. Atmos. Sci.* **5**(4), 165–166 (1948)
14. Olsen, R.L., Rogers, D.V., Hodge, D.B.: The aRb relation in the calculation of rain attenuation. *IEEE Trans. Antennas Propag.* **AP-26**, 318–329 (1978)
15. Baldini, L., Gorgucci, E., Romaniello, V.: An integrated procedure for rainfall estimation using C-band dual-polarization weather radars. In: Radar Conference, 2008. RADAR '08. IEEE, pp. 1–4, 26–30 May 2008
16. Eastment, J.D., Thurai, M., Ladd, D.N., Moore, I.N.: Radiowave propagation research in the tropics using a transportable multiparameter radar system. *J. Electron. Commun. Eng.* **10**, 4–16 (1998)
17. Dissanayake, A., Lin, K.T.: Ka-band rain attenuation estimation using weather radar. *J. Space Commun.* **18**(1, 2), 53–58 (2002)
18. Yeo, J.X., Lee, Y.H., Kumar, L.S., Ong, J.T.: Comparison of S-band radar attenuation prediction with beacon measurements. *IEEE Trans. Antennas Propag.* **60**(10), 4892–4900 (2012)
19. Maekawa, Y., Miyamoto, S., Sawai, K., Shibagaki, Y., Sato, T., Yamamoto, M., Hashiguchi, H., Fukao, S.: Estimation of rain attenuation characteristics of satellite communication links using x-band meteorological radars. In: ICCAS-SICE, 2009, pp. 1320, 1323, 18–21 Aug 2009
20. Elbert, B.R.: *Introduction to Satellite Communication*, Artech House, Boston (2008)
21. Ismail, A.F., Badron, K., Yaccop, A.A.H., Yao, Y.D.: Determination of Ku-band specific attenuation parameters based on measurements in the tropics. In: 2013 IEEE Antennas and Propagation Society International Symposium (APSURSI), pp. 2008, 2009, 7–13 July 2013
22. <http://www.skmm.gov.my/skmmgovmy/files/attachments/QoS%20MS2003-FINAL.pdf>

Improve the Performance of Cooperative Spectrum Sensing Using Hopping Sequence Scheme

Ammar Abdul-Hamed Khader, Mainuddin Mainuddin
and Mirza Tariq Beg

Abstract A significant impact on the spectrum efficiency and quality of service (QoS) of a secondary user (SU) is the ability to capture a frequency slot for transmission in an idle channel. Hence, the SU needs to sense the related spectrum in order to classify a licensed frequency band as occupied or vacant. Spectrum sensing can be a demanding task for a single user due to the random nature of the wireless channel and networks. Cooperative sensing by eight SU nodes have been proposed in this paper to mitigate the effects of channel fading and try to detect the presence/absence of two primary users (PUs). A sensing policy for coordinating the cooperative process is proposed based on two levels hierarchical-fuzzy logic system (H-FLS) by adding a Hopping Sequence (HS) module to the detectors. Two hopping methods are proposed, Random Hopping (RA-H) and Sequential Hopping (SE-H). The simulation results shows enhancement in probability of detection over conventional cooperative sensing.

1 Introduction

A novel technology aimed at more efficiently utilizing the spectrum is Cognitive Radio (CR), which has attracted the attention of many researchers across the globe. While current radio systems employ inflexible spectrum allocation strategies, resulting in inefficient spectrum utilization. CR technology enables a secondary user

A.A.-H. Khader (✉)

Department of Computer Engineering, University of Mosul, Mosul, Iraq
e-mail: ammar_hameed_eng@yahoo.com

A.A.-H. Khader · M. Mainuddin · M.T. Beg

Department of Electronics and Communication Engineering, Jamia Millia Islamia,
New Delhi, India
e-mail: moin_sl@rediffmail.com

M.T. Beg

e-mail: mtbeg@jmi.ac.in

(SU) with cognitive access ability to use the idle channel resources of the primary radio systems. This idle channel resource, can be used by the SU to exchange information, which is temporarily unoccupied by the primary user (PU), provided it does not interfere with the smooth communication of the primary system [1, 2]. Therefore, spectrum sensing is needed by a CR system to identify such spectrum opportunities and to characterize the possible interference levels to the primary system. The goal of spectrum sensing is to determine the status of the spectrum and the activity of the licensed users by periodically sensing the target frequency band. A definition of spectrum opportunity is “a situation where there is such free spectrum that a secondary transmitter–receiver pair could use for their communication so that interference from the secondary transmitter to the primary receiver will be below an allowed level, and the interference from the primary transmitter to the secondary receiver will also be at an acceptable level needed for reliable communication” [3–5]. The challenging is in using Fuzzy Logic Control System (FLCS) in CR systems, but it has been scantily investigated so far. Fuzzy Logic (FL) is suitable for the uncertainty information process involved in CR network [6]. One of an attractive technique of FLS is particularly in case where target problem are difficult to model with traditional mathematical methods but at the same time easier for human being to understand. The rule based decision making achievable by FL enables efficient inclusion of incomplete information and it provides saving in computational complexity [7].

FL provides a simple way to get definite conclusion and solution based on Fuzzy input information. The steps of a FL can be summarized as: (1) The measurements of the parameters to be analyzed is received as an input values. (2) Subjecting the input value to if-then fuzzy rules. (3) One single output decision obtained from averaging and weighting the results from all individual rules. (4) Defuzzification of output to get a value between 0 and 1. Two major components are required to develop a fuzzy logic controller: (1) Definition of a membership function for each output/input parameter. (2) Designing the fuzzy rules. The membership function is a graphical representation of the magnitude of participation of each input. The input membership values is used by the FL rules as weighting factors to determine their influence on the output set [8].

The fuzzy rule for a single layer has the form:

$$\mathbf{If} (x_1 \text{ is } A_{11}) \mathbf{and} (x_2 \text{ is } A_{21}) \mathbf{and} (x_3 \text{ is } A_{31}) \mathbf{and} (x_4 \text{ is } A_{41}) \mathbf{Then} (u \text{ is } B_1) \dots \quad (1)$$

Assuming there are (n) input variables and there are (m) fuzzy sets defined for each input variable, the number of fuzzy rules is given by $N = m^n$. The common problem in all complex systems is that, the number of rules increases exponentially with increasing input variables. This complexity of the system growing exponentially with the number of variables describing the system, and is not unique to fuzzy systems (FS). Obviously there is only one possible topology for the single layer FS with all variables as input into a single layer FS. Given a fuzzy rule base with M

rules and n antecedent variables, a fuzzy controller as given in (2) and (3) uses a singleton fuzzifier, Mamdani product or minimum inference engine and centre average defuzzifier to determine output variables [9].

$$u = \frac{\sum_{l=1}^M \bar{u}^l \left(\prod_{i=1}^n \mu_{A_i}^l(x_i) \right)}{\sum_{l=1}^M \left(\prod_{i=1}^n \mu_{A_i}^l(x_i) \right)} \quad (2)$$

$$u = \frac{\sum_{l=1}^M \bar{u}^l \left(\min_{i=1}^n \mu_{A_i}^l(x_i) \right)}{\sum_{l=1}^M \left(\min_{i=1}^n \mu_{A_i}^l(x_i) \right)} \quad (3)$$

Hierarchical Fuzzy System (HFS) is solving the curse of dimensionality. The number of fuzzy rules could be a linear or nearly-linear function of the number of inputs by arranging the inputs in hierarchical ways and allowing the consequent part of a rule to be an antecedent to another rule [10].

In this paper a collaborative method for simultaneously sensing two bands is proposed. Where a proposed Hopping Sequence (HS) module is added to the two levels H-FL designed system to increase the probability of detection when the PU(s) and/or SU(s) are in mobility state. The two hopping methods proposed here are Random Hopping (RA-H) and Sequential Hopping (SE-H).

2 Related Work

Spectrum sensing is a crucial step in CR networks and unreliable detection of spectrum is strongly related to the issues of hidden node problem, channel fading/shadowing, poor performance of energy detectors at low signal to noise ratio (SNR), all of these suggest that the PU-SU distance is crucial in deciding the spectrum sensing accuracy. For large distances, interference of SUs will be minimized no doubt, but the sensing accuracy will not be good and this will not give optimized scheduling [8, 11]. Many techniques such as auction mechanisms [12] and local bargaining [13] have been developed in the literature on assignment the spectrum in CR. In [14], based on the probabilities of available channel obtained from spectrum sensing, a method is proposed which optimizes power allocation and channel in a multi-channel environment. A novel distributed collusion mechanism in [15] is unveiled that allocates channels in the spectrum pool by using bidding theory and graph colouring. Adaptive resource management by fuzzy reasoning has been studied on several varied issues related to dynamic spectrum sharing strategies and models and spectrum sensing [16, 17] but relatively few works are found in open literature for SU scheduling using fuzzy inference procedure. The assignment problem has been addressed using the graph colouring algorithm without considering the mobility of secondary users in [18].

For the case of HS module that proposed here and added before the H-FLS, it is the first time happened in the literature as the knowledge of the authors.

3 System Description

Assuming that the network consists of eight CU or (SU) nodes working in collaborative manner and try to detect the presence of two PUs. Where four CUs start sensing whether one of these two frequency bands are occupied or vacant in a sequential manner.

The general combining rule for cooperative spectrum sensing is “m out of N rule” that can be presented as [6]:

$$D = \sum_{n=1}^N D_n \begin{array}{l} \geq m : \text{ signal present} \\ < m : \text{ signal absent} \end{array} \quad (4)$$

where N is the total number of the cooperative nodes, D_n is the decision of the nth cooperative cognitive radio node, and m is the number of users that is set as the threshold. By setting $m = 1$, $m = N$, or $m = N/2$, OR, AND and majority combining rules are obtained from (4) corresponding to the cases that PU is declared present if one node, all nodes, or most of the nodes detect the PU.

A simple fuzzy decision making algorithm for decision fusion for the case of four cooperative SUs nodes was designed to test the feasibility of FL in cooperative spectrum sensing combining schemes given in (1). This scheme takes divided into two branch with two hierarchical levels in each, where 1st level in 1st branch consists of three inputs (antecedents) to FLS1 fed from three CUs detectors. While 2nd level in 1st branch FLS2 consists of two inputs, one fed from the fourth CU detector and the other input from the output of FLS1. The 2nd output of FLS2 in 1st branch gives the final decision for four cooperative CU nodes and produces as an output the combined sensing result, i.e., PU1 present or absent. The same things happened in 2nd branch but for other four CUs to detect PU2. Using two levels H-FLS reducing the number of fuzzy rules. Where in 1st FLS the number of rules are ($3^3 = 27$) and in 2nd FLS are ($3^2 = 9$), while they become ($3^4 = 81$) if we used only one level FLS.

The developed fuzzy system included three antecedents, each with three membership functions (MBFs) in 1st FLS, two antecedents with three MBFs in 2nd FLS and one output for each FLS with three MBFs also. The names of the input MBFs describing the strength of the individual sensing nodes' decisions are; Low, Medium and High. The names of the output MBFs describing the strength of the combined sensing result are Low, Medium, and High indicating the combined likelihood of the presence of PU signal. Mamdani rule is used here because this type of fuzzy rule based system (FRBS) provides a natural framework to include expert knowledge in the form of linguistic rules and also provide a highly flexible means to formulate knowledge, while at the same they remain interpretable. Based on combination of the sensing results from different CU nodes, the fusion centre makes the final decision regarding the presence or absence of the PUs.

If $T_n[k]$ for $n = 1, 2, \dots, N$ represents the received signal power of n th SU at time instant k and hypotheses H_0 and H_1 denote the absence and presence of a primary signal respectively, then the signal power received by n th SU is given by:

$$T_n[k] = \sum_N (Y[n])^2 \quad (5)$$

Then

$$H_0 : Y [n] = W[n] \text{ signal absent} \quad (6)$$

$$H_1 : Y [n] = X[n] H[n] + W[n] \text{ signal present} \quad (7)$$

where $X[n]$ is the primary signal, $H[n]$ denotes the channel gain between the PU and the n th SU and $W[n]$ is the additive white Gaussian noise (AWGN). The number of rules in 1st level HFS is 27 and 9 in 2nd level for both branches. Tables 1 and 2 represents all combinations of the rules.

4 Simulation Model and Hopping Patterns

A simulated transmitted signals passing through Rayleigh Fading channels. The noisy signals are fed to eight spatially diverged SU nodes to determine their power. These SU nodes try to arrange their works using HS module, where four of them serially combined together and focus on one PU at a time and take the decision cooperatively to overcome the hidden node problem and send their information to the fusion centre as in Fig. 1. The benefit of adding this proposed HS module before FLS become clear when the PU(s) and/or SU(s) are in mobility state. So using the eight detectors to sequentially detect the presence of two mobile PU in steps.

4.1 Random Hopping (RA-H)

In this scheme an individual hopping number is randomly selected among 1 to K , where K is the number of SUs nodes. This will done sequentially where two groups of four numbers are chosen randomly to control the SUs nodes in each step and to sense two PUs. Table 3 illustrate an example of (RA-H). There are no same four number of SUs repeated in these steps i.e. unique groups. The benefit of this hopping sequence appears when the SU nodes are randomly spaced around the two PUs and also some or all of SUs are in randomly movement like SU7, SU2 and SU8 where PU1 moving from point (P1) to (P2) and PU2 moving from (P3) to (P4) as in Fig. 2.

Table 1 Rule base to determine Pro. of PU Pres. from 1st level

| Rule no. | CU _n | CU _{n+1} | CU _{n+2} | PRO. of PU PRS. at FLS1 |
|----------|-----------------|-------------------|-------------------|-------------------------|
| 1 | Low | Low | Low | Low |
| 2 | Low | Low | Medium | Low |
| 3 | Low | Low | High | Low |
| 4 | Low | Medium | Low | Low |
| 5 | Low | Medium | Medium | Low |
| 6 | Low | Medium | High | Medium |
| 7 | Low | High | Low | Low |
| 8 | Low | High | Medium | Medium |
| 9 | Low | High | High | Medium |
| 10 | Medium | Low | Low | Low |
| 11 | Medium | Low | Medium | Low |
| 12 | Medium | Low | High | Medium |
| 13 | Medium | Medium | Low | Low |
| 14 | Medium | Medium | Medium | Medium |
| 15 | Medium | Medium | High | High |
| 16 | Medium | High | Low | Medium |
| 17 | Medium | High | Medium | High |
| 18 | Medium | High | High | High |
| 19 | High | Low | Low | Low |
| 20 | High | Low | Medium | Medium |
| 21 | High | Low | High | Medium |
| 22 | High | Medium | Low | Medium |
| 23 | High | Medium | Medium | High |
| 24 | High | Medium | High | High |
| 25 | High | High | Low | Medium |
| 26 | High | High | Medium | High |
| 27 | High | High | High | High |

Table 2 Rule base to determine Pro. of PU Pres. from 2nd level

| Rule no. | Prob. of PU Pres. at FLS1 | CU _{n+3} | Combination of results at FLS2 |
|----------|---------------------------|-------------------|--------------------------------|
| 1 | Low | Low | Low |
| 2 | Low | Medium | Low |
| 3 | Low | High | Medium |
| 4 | Medium | Low | Low |
| 5 | Medium | Medium | Medium |
| 6 | Medium | High | High |
| 7 | High | Low | Medium |
| 8 | High | Medium | High |
| 9 | High | High | High |

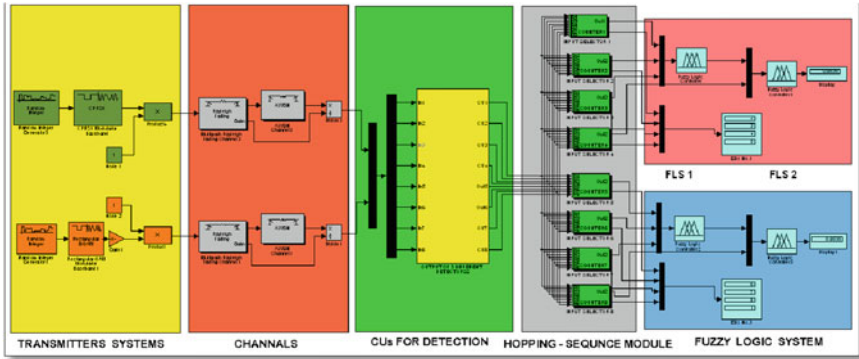


Fig. 1 Simulation block for two PU and eight SU detectors with HS module

Table 3 Example of (RA-H) and (SE-H) sequences

| | Mode | Step number | | | | | | | | |
|------|--|-------------|---|---|---|---|---|---|---|---|
| | | 1 | 2 | 3 | 4 | 5 | 6 | 7 | 8 | 9 |
| RA-H | Four different SUs chosen to Sense PU1 | 2 | 1 | 7 | 3 | 2 | 5 | 1 | 1 | 8 |
| | | 4 | 8 | 2 | 2 | 8 | 4 | 5 | 2 | 3 |
| | | 3 | 7 | 8 | 4 | 4 | 6 | 6 | 3 | 6 |
| | | 5 | 5 | 1 | 1 | 3 | 2 | 4 | 8 | 2 |
| | Four different SUs chosen to Sense PU2 | 7 | 4 | 3 | 6 | 7 | 3 | 8 | 4 | 1 |
| | | 8 | 2 | 4 | 7 | 5 | 8 | 7 | 5 | 5 |
| | | 6 | 3 | 5 | 8 | 1 | 1 | 3 | 7 | 4 |
| | | 1 | 6 | 6 | 5 | 6 | 7 | 2 | 6 | 7 |
| SE-H | Four different SUs chosen to Sense PU1 | 1 | 2 | 3 | 4 | 5 | 6 | 7 | 8 | 1 |
| | | 2 | 3 | 4 | 5 | 6 | 7 | 8 | 1 | 2 |
| | | 3 | 4 | 5 | 6 | 7 | 8 | 1 | 2 | 3 |
| | | 4 | 5 | 6 | 7 | 8 | 1 | 2 | 3 | 4 |
| | Four different SUs chosen to Sense PU2 | 5 | 6 | 7 | 8 | 1 | 2 | 3 | 4 | 5 |
| | | 6 | 7 | 8 | 1 | 2 | 3 | 4 | 5 | 6 |
| | | 7 | 8 | 1 | 2 | 3 | 4 | 5 | 6 | 7 |
| | | 8 | 1 | 2 | 3 | 4 | 5 | 6 | 7 | 8 |

4.2 Sequential Hopping (SE-H)

Any four SUs (as organized in the hopping sequence) in 1st step collect a different information about PU1 and the rest four SUs collect a different information about PU2, then they send their information to the fusion centre (FC) to estimate the probability of the two PUs presents or not. In 2nd step three of those SUs that already contribute in 1st step will remain in sensing process of same PU and only

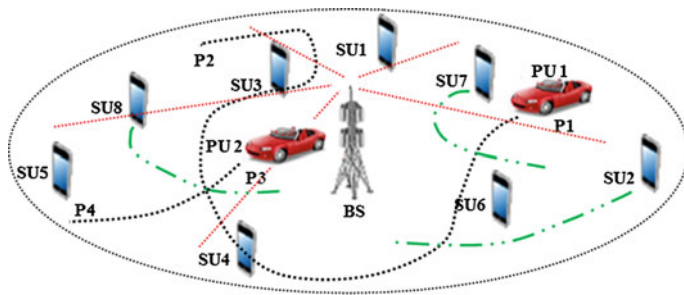


Fig. 2 Wireless network structure for 8 SUs randomly spaced where three mobile SUs (7, 2, 8) and two mobile PUs

one new SU will assist them in this new step and so on as in Table 3. So in every step, four SUs will cooperate to verify *cooperative spectrum sensing* (CSS).

For more reliability we can wait till the 8th step complete its checking i.e. all the eight SUs go through checking these two PUs. But if there is any problem in time delay and the decision making must be taken fast, we can stop the hopping sequence and getting the results in any step.

Figure 3 illustrate the benefit of (SE-H) module where PU1 start moving from point (P1) to point (P2) so it become close to SU3, SU4, SU5 and SU6 but far from SU1 and SU2. From this example we can visualise how much the detection error will become if using stationary SU detectors and depends only on the decision of SU1, SU2, SU3 and SU4. At the beginning and before PU start moving, the probability of detection (P_d) is high because the four SU detectors above can detect the presence of PU1. But after PU1 reaching (P2), the P_d will be less because SU1 and SU2 couldn't be able to detect the presence of PU. So design a stationary detectors while there are mobile PU(s) will give less P_d . If anyone thinking to increase the number of stationary detectors to achieve better P_d without using HS module, this will cause an expense of design complexity and more costly.

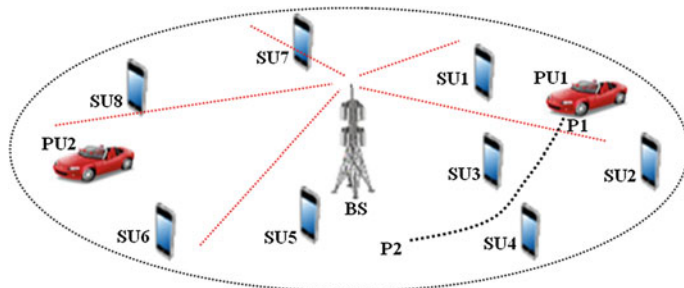


Fig. 3 Wireless network structure for 8 stationary SUs randomly spaced, one mobile PU1 and one stationary PU

5 Results and Discussion

The decision surface (D.S.) for FLS1 and FLS2 is shown in Figs. 4 and 5 respectively. Where the Pro. of PU Pre. become high when the power of two CUs exceed the threshold value of 50 % in FLS1.

Table 4 illustrate the probability of PU1 presents of FLS1 for many states of input power values that determined by CU detectors after applying (8) and (9) where three SUs are used to determine the Pro. of PU Pre. in FLS1. This determined power compared with a threshold level to convert it to a probability of absent/present from 0 to 1. As in Fig. 1 this value of probability will be fed with another input (CU_{n+3}) to 2nd FLS as in Table 5. Where at the end, four CUs are used to determine the overall Pro. of PU Pre.. The results obtained here after applying Eqs. (8, 9) but with less variable i.e. L = 1, 2, ..., 9 and i = 1, 2 because of only two inputs (x1, x2).

$$C_{avg3}^l = \frac{\sum_{i=1}^3 w_i^l C_i^l}{\sum_{i=1}^3 w_i^l} \tag{8}$$

There are 27 rules applied in FLS1. Where L = 1, 2, ... 27 and C_{avg3}^l is defined as in (7) in which w_i^l is the number of experts choosing linguistic label (i) for the consequence of rule l and Cⁱ is the centroid of the ith consequence set (i = 1, 2, 3; L = 1, 2, ... 27). For every input (x1, x2, x3) the output y_{FLS}(x1, x2, x3) of the designed system is computed as [17]:

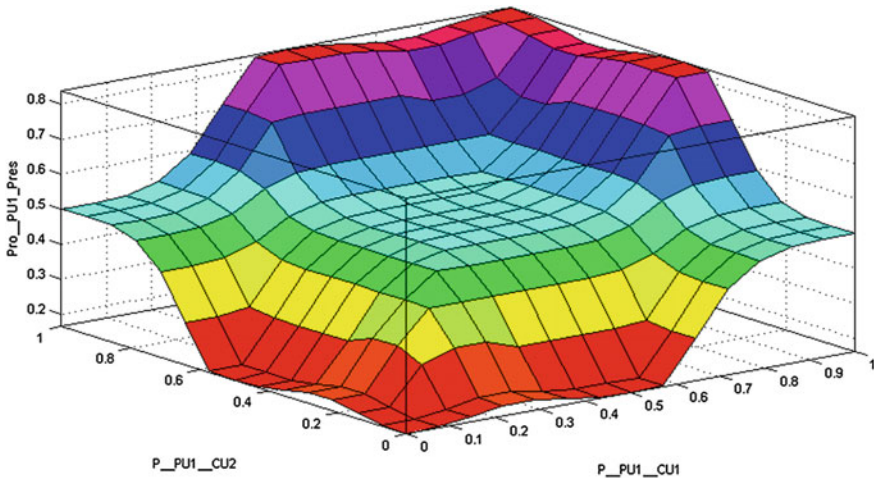


Fig. 4 D.S. for Pro. D.S. for FLS1: Pro. PU Pre. with power values for two CUs

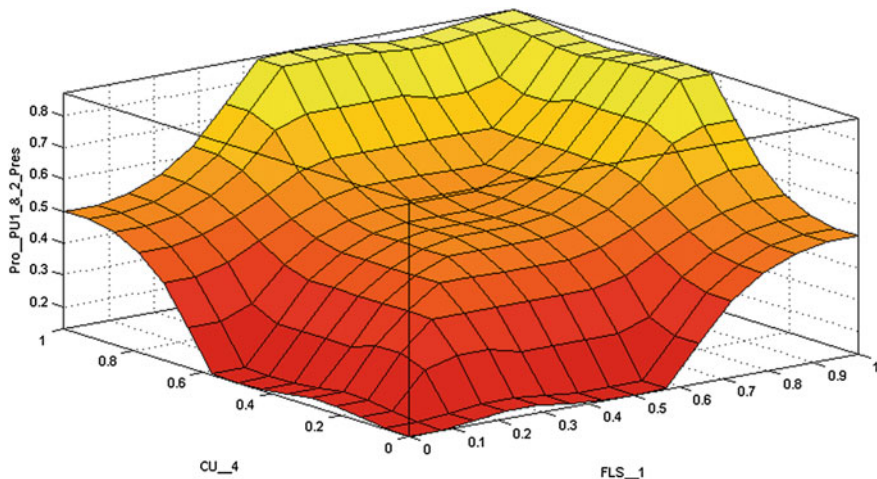


Fig. 5 D.S. for Pro. PU1 Pre. versus FLS1 & CU 4

Table 4 The percentage probability of FLS1 for different power values determined in CUs

| Value of (n) | Pro. of PU Pres. at CU _n | Pro. PU Pres. at CU _{n+1} IF = 9 THEN take CU _{n-7} | Pro. PU Pres. at CU _{n+2} IF > = 9 THEN take CU _{n-6} | Pro.PU1 Pres.at FLS1 |
|--------------|-------------------------------------|--|--|----------------------|
| 1 | 0.114 | 0.50 | 0.898 | 0.50 |
| 2 | 0.50 | 0.898 | 0.994 | 0.827 |
| 3 | 0.898 | 0.994 | 0.886 | 0.825 |
| 4 | 0.994 | 0.886 | 0.427 | 0.825 |
| 5 | 0.886 | 0.427 | 0.129 | 0.501 |
| 6 | 0.427 | 0.129 | 0.669 | 0.340 |
| 7 | 0.129 | 0.669 | 0.114 | 0.262 |
| 8 | 0.669 | 0.114 | 0.500 | 0.338 |

$$y_{FLS1}(x1; x2; x3) = \frac{\sum_{l=1}^{27} \mu F_1^l(x1)\mu F_2^l(x2)\mu F_3^l(x3)C_{avg3}^l}{\sum_{l=1}^{27} \mu F_1^l(x1)\mu F_2^l(x2)\mu F_3^l(x3)} \tag{9}$$

Figure 6 shows P_d of three states vs. different values of SNR in dB: (1) With HS module and mobile SUs (green colour (upper curve)), (2) With HS module and stationary SUs (red colour (middle curve)) and (3) without HS module (blue colour (lower curve)).

Where P_d increases with increasing SNR and using HS module. Figure 7 illustrates increasing the value of P_d with number of iteration steps, it starts with 48 % at 1st step or without using HS module, to reach 100 % at iteration step number 8. From Table 5 we can know that PU is present and no any CU can

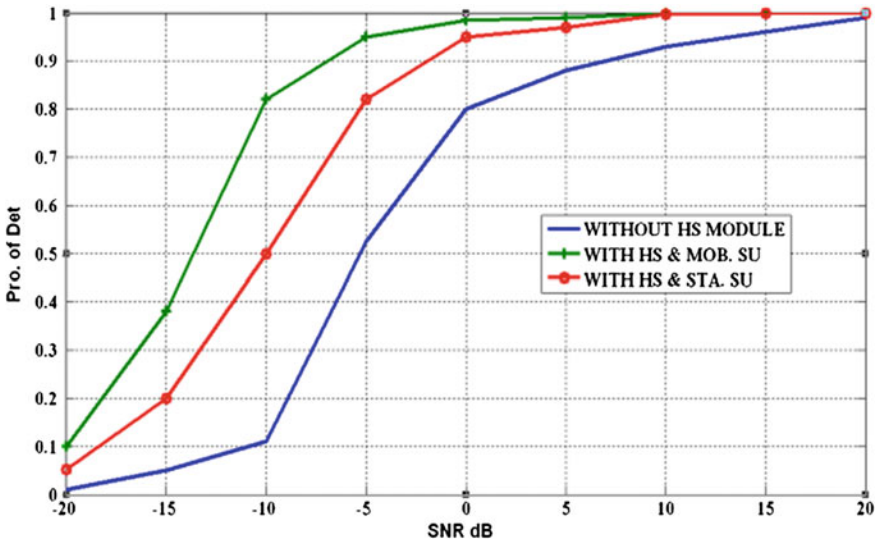


Fig. 6 P_d with SNR for three state: without HS module, with HS & mobile SUs and with HS and stationary SUs (up to down)

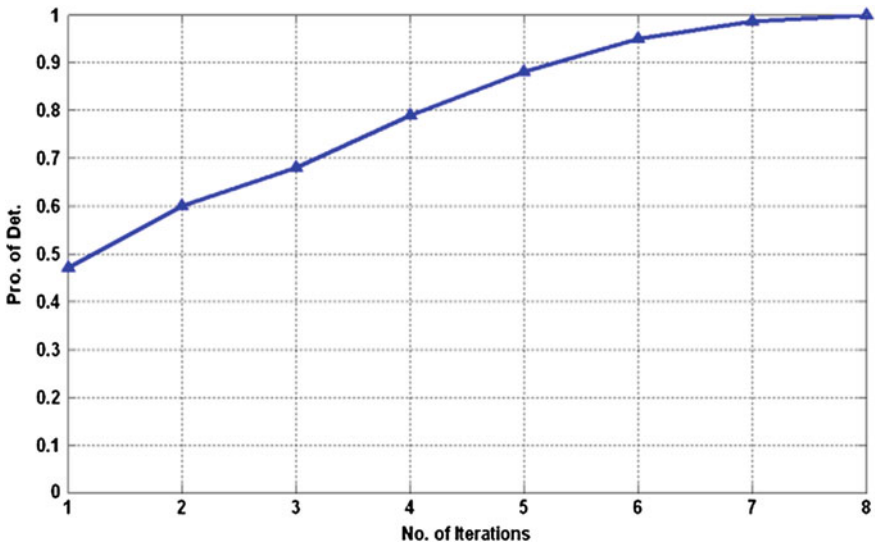


Fig. 7 The value of Pro. of Det. (P_d) with number of iteration steps

occupy its channel at this time because after eight steps five values out from eight are greater than 50 % i.e. (87.0, 80.1, 67.9, 52.9 and 71.4) and only three values are less. The worst value in this table is (19.4) which indicates that the channel is idle

Table 5 The overall percentage probability of FLS2 for different power values determined in CU_{n+3} and the output of FLS1

| Value of (n) | Pro. PU Pres. at CU_{n+3} IF ≥ 9 THEN take CU_{n-8} | % Pro. PU1 Pres. at FLS1 | Overall % Pro. of PU1 Pres. at FLS2 |
|--------------|---|--------------------------|-------------------------------------|
| 1 | 0.994 | 0.50 | 87.0 |
| 2 | 0.886 | 0.827 | 80.1 |
| 3 | 0.427 | 0.825 | 67.9 |
| 4 | 0.129 | 0.825 | 47.9 |
| 5 | 0.669 | 0.501 | 52.9 |
| 6 | 0.114 | 0.340 | 19.4 |
| 7 | 0.5 | 0.262 | 42.7 |
| 8 | 0.898 | 0.338 | 71.4 |

and PU1 is absent when CU_6 (0.427), CU_7 (0.129), CU_8 (0.669), and CU_1 (0.144) cooperatively sensing PU1. So waiting till the eighth step of sequence to complete then determining the Pro. of PU Pers. is better than taken the decision before that.

6 Conclusion

A decision making system by obtaining cooperative knowledge about spectrum availability for two PU has been presented here. A two layer hierarchical fuzzy logic system has been designed to coordinate the cooperative spectrum sensing at the detectors. To mitigate the effects of channel fading, eight SU nodes cooperatively detect the presence of two PUs by adding a proposed Hopping Sequence (HS) module before the fuzzy system modules. Where four SUs cooperatively detect one PU at a time. Two hopping methods are proposed, Random Hopping (RA-H) & Sequential Hopping (SE-H). The simulation results shows enhancement in probability of detection over conventional cooperative sensing.

Acknowledgments The authors sincerely thank the Ministry of Higher Education and Scientific Research in Iraq and Jamia Millia Islamia in India, who provide the financial support and advice. The product of this research paper would not be possible without them.

References

1. Yuan, G., Grammenos, R.C.Y., Wenbo, W.: Performance analysis of selective opportunistic spectrum access with traffic prediction. *IEEE Trans. Veh. Technol.* **59**(4), 1949–1959 (2010)
2. Yücek, T., Arslan, H.: A survey of spectrum sensing algorithms for cognitive radio applications. *IEEE Commun. Surv. Tutor.* **11**(1), 116–130 (2009) (First Quarter)
3. Hossain, E., Dusit, N., Zhu, H.: *Dynamic Spectrum Access and Management in Cognitive Radio Networks*. Cambridge University Press, Cambridge (2009)

4. Marinho, J., Monteiro, E.: Cognitive radio: survey on communication protocols, spectrum decision issues, and future research directions. Springer Science Business Media, LLC, New Jersey (2011)
5. Khader, A.A., Mainuddin, M., Beg, M.T.: Bouncy detector to differentiate between GSM and WIMAX signals. *Adv. Intell. Syst. Comput.* **264**, 379-390 (2014) (Springer)
6. Xi-yun, Z., Ju-hu, L.L., Peng, C., Wei-ling, W.: A fuzzy logic based handoff technique in cognitive radio network. *Adv. Inf. Sci. Serv. Sci. (AISS)* **4**(7) (2012)
7. Matinmikko, M., Rauma, T., Mustonen, M.: Application of fuzzy logic to cognitive radio system. *IEICE Trans. Commun.* **E92-B**(12), 3572–3580 (2009)
8. Moeen Taghavi, E., Abolhassani, B.: A fuzzy secure spectrum sensing (F3S) scheme for cognitive radios in adversarial environment. In: Proceedings of CSIT, International Conference on Computer Communication and Management, vol. 5, IACSIT Press, Singapore (2011)
9. Zajackowski, J.: Analysis of the hierarchical fuzzy control using evolutionary algorithms. Ph. D. thesis, CQ University (2010)
10. Salgado, P.: Rule generation for hierarchical collaborative fuzzy system. *Appl. Math. Model.* **32**, 1159–1178 (2008)
11. Mitra, D., Mahapatra, R.D.: FIS based cognitive radio scheduling. *IEEE Inter. Conf. Fuzzy Syst.* (2013)
12. Huang, J., Berry, R., Honig, M.: Auction-based spectrum sharing. *ACM Mob. Netw. Appl. (MONET)* **119**(3), 405–418 (2006)
13. Kloeck, C., Jaekel, H., Jondral, F.: Dynamic and local combined pricing, allocation and billing system with cognitive radios. In: *IEEE DySPAN*, pp. 73-81 (2005)
14. Zheng, H., Peng, C.: Collaboration and fairness in opportunistic spectrum access. In: 40th Annual IEEE International Conference on Communications (ICC), pp. 3132–3136 (2005)
15. Wang, J., Huang, Y., Jiang, H.: Improved algorithm of spectrum allocation based on graph coloring model in cognitive radio. In: International Conference on Communications and Mobile Computing, pp. 353–357 (2009)
16. Baldo, N., Zorzi, M.: Cognitive network access using fuzzy decision making. *IEEE Trans. Wireless Commun.* **8**, 3523–3535 (2009)
17. Yang, S.-F., Wu, J.-S.: A spectrum sharing method based on fuzzy logic in IEEE 802.22 WRAN. In: Proceedings IEEE International Conference Wireless Communication and Signal Processing (WCSP), pp. 1–5 (2010)
18. Le, T., Hong-Sam, D.L., Hung, L.Q.: Opportunistic spectrum access using fuzzy logic for cognitive radio networks. *Int. J. Wireless Inf. Networks* **18**(3), 171–178 (2011)

Investigation of Rice Husk/CNTs Composites Performance in Microwave Properties

Yeng Seng Lee, Fareq Malek, Ee Meng Cheng, Wei Wen Liu, Fwen Hoon Wee, Muhammad Nadeem Iqbal, Liyana Zahid, Been Seok Yew, Ahmad Zaidi Abdullah, Nur Sabrina Noorpi, Nurhakimah Mohd Mokhtar and Mohd Asri Jusoh

Abstract This paper is to study the performance of rice husk and carbon-nanotubes nanotubes (RH-CNTs) composite material as a microwave absorber. The rice husk (RH) is a lossy material that contains dielectric properties which suitable used as microwave absorber. The dielectric properties are playing a main role in microwave absorption of any material. The dielectric properties of materials were measured using an Agilent dielectric probe. The microwave absorption performance of rice husk and CNTs composites was investigated by using rectangular waveguide transmission line in simulation. The microwave absorbers were designed and simulated using the Computer Simulation Technology Microwave studio software (CST-MWS). The ability of microwave absorption between rice husk and RH-CNTs was compared in

Y.S. Lee (✉) · F.H. Wee · M.N. Iqbal · L. Zahid
School of Computer and Communication Engineering, Universiti Malaysia Perlis (UniMAP),
Pauh Putra Campus, 02600 Arau, Perlis, Malaysia
e-mail: leeyengseng@gmail.com

F.H. Wee
e-mail: weefwenhoon@gmail.com

M.N. Iqbal
e-mail: mr.nadeemiqbal@gmail.com

L. Zahid
e-mail: liyanazahid@gmail.com

F. Malek · A.Z. Abdullah · N.S. Noorpi · N.M. Mokhtar · M.A. Jusoh
School of Electrical Systems Engineering, Universiti Malaysia Perlis (UniMAP),
Pauh Putra Campus, 02600 Arau, Perlis, Malaysia
e-mail: mfareq@unimap.edu.my

A.Z. Abdullah
e-mail: zaidiabdullah@unimap.edu.my

N.S. Noorpi
e-mail: nursabrina@unimap.edu.my

N.M. Mokhtar
e-mail: nurhakimah@unimap.edu.my

8.2–12.4 GHz. The microwave absorption with different thickness of RH-CNTs samples was investigated. The results show that the RH-CNTs composites have a better ability of microwave absorption compared than pure rice husk.

1 Introduction

Recent years, carbon nanotubes (CNTs) are useful in many of fields, including the material, chemical and electrical application. Single-walled carbon nanotubes (SWCNTs) and multi-walled carbon nanotubes (MWCNTs) are most common types of CNTs [1, 2]. RH-CNTs can absorb the energy from electromagnetic waves and convert it to heat due to its characteristic properties of these composite materials [3]. Furthermore, carbon is an important component in microwave absorbing material and CNTs have high content of carbon. Besides, rice husk material also contain of 33–37 % carbon which is suitable to use as microwave absorber [4]. Rice is one of the popular foods in the world and also the major agricultural waste in the rice husk form. The agricultural waste of rice husk will be burnt which cause air pollution and unfriendly to our environment [5]. In this paper is to reuse the agricultural waste of rice husk and composite with CNTs. By adding CNTs into RH for composites is to enhance the dielectric properties and microwave absorption of the pure rice husk. The performance of RH-CNT in microwave absorption as microwave absorber is investigated.

Dielectric material can define as a material that has ability store energy when an external electric field passes through the material [6]. The microwave lossy materials have been characterized in terms of the electrical permittivity with complex permittivity, $\epsilon_r = \epsilon_r' - j\epsilon_r''$ [7]. Where the real part, ϵ_r' , is the dielectric constant, and the imaginary part, ϵ_r'' , is the dielectric loss factor. The dielectric constant, ϵ_r' defines the ability of a dielectric material to store electromagnetic signal, whereas

M.A. Jusoh
e-mail: asrijusoh@unimap.edu.my

E.M. Cheng
School of Mechatronic Engineering, Universiti Malaysia Perlis (UniMAP), Pauh Putra
Campus, 02600 Arau, Perlis, Malaysia
e-mail: emcheng@unimap.edu.my

W.W. Liu
Institute of Nano Electronic Engineering (INEE), Universiti Malaysia Perlis (UniMAP),
01000 Kangar, Perlis, Malaysia
e-mail: wwliu@unimap.edu.my

B.S. Yew
Faculty of Innovative Design and Technology, Universiti Sultan Zainal Abidin (UniSZA),
Kampus Gong Badak, 21300 Kuala Terengganu, Terengganu, Malaysia
e-mail: bseokyew@unisza.edu.my

the dielectric loss factor ϵ_r'' represents its ability to dissipate the electromagnetic signal [8, 9]. Dielectric constant is equivalent to relative permittivity, ϵ_r , or the absolute permittivity, ϵ relative to the permittivity of free space, ϵ_0 . Equation (1) shows the permittivity of free space.

$$\epsilon = \epsilon_r \epsilon_0 \quad (1)$$

When an electromagnetic field propagates within a lossy material, the electromagnetic signals will be reflected, absorbed, and transmitted.

2 Materials Measurement

The multi-wall carbon nanotubes were used to composite with rice husk. The dielectric properties of both RH and RH-CNTs materials were measured over the frequency range of 8.2–12.4 GHz using a commercial dielectric probe with an Agilent E8362B P-series Network Analyzer (PNA) [10]. The dielectric properties result of the samples were generated by using the commercialize Agilent Technologies 85070E software. The dielectric probe must be calibrated with air (open), short (metal), and water before conduct any measurement [11]. The calibration is important to avoid from error and incorrect data. Figure 1a, b shows the Agilent dielectric probe and measured sample.

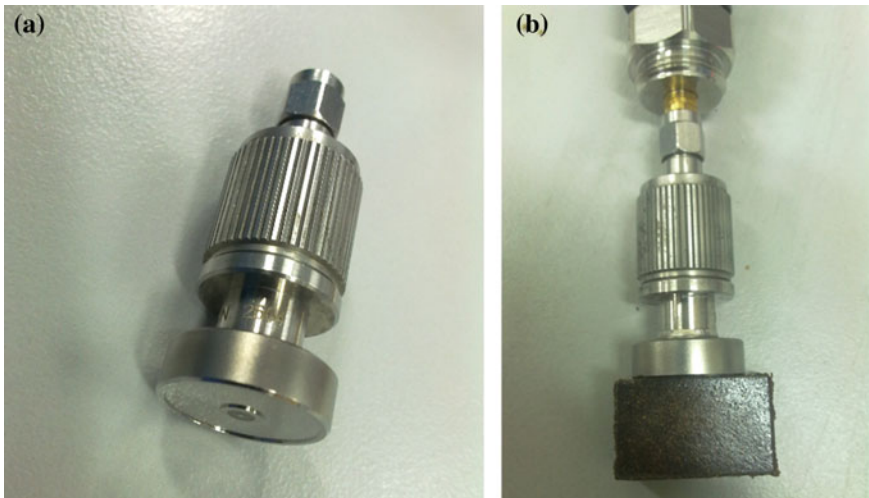


Fig. 1 a Dielectric probe and b measure sample using dielectric probe

3 Simulation

3.1 Rectangular Waveguide

Rectangular waveguide is a rectangular solid which completely fills a rectangular wave guide operating in the TE₁₀ mode. In general, the term waveguide refers to constructs that only support non-TEM mode propagation [12]. The rectangular waveguide is unable to support wave propagation below a certain frequency (cutoff frequency). The length, a and width, b of WR-90 rectangular waveguide are 22.860 and 10.160 mm were shown in Fig. 2.

For air $\epsilon = 1$, $\mu = 1$, $c = 3 \times 10^8 \text{ ms}^{-1}$. The cutoff frequency is given by Eq. (2);

$$f_{c_{mn}} = \frac{c}{2} \sqrt{\left(\frac{m}{a}\right)^2 + \left(\frac{n}{b}\right)^2} \quad (2)$$

In simulation, the dimension of the waveguide port important to determine the cutoff frequency of the rectangular waveguide. The length and width of the rectangular waveguide are playing important role in determining which frequency the rectangular waveguide to operate [13]. Hence, the cutoff frequency of the rectangular waveguide X-band from the data sheet and simulation are compared. In general, a particular mode is only supported above its cutoff frequency. For cutoff frequency of X-band (WR-90) rectangular waveguide is 6.56 GHz from calculation. In simulation, the cutoff frequency is 6.56 GHz.

The microwave absorbers of RH and RH-CNTs were designed using the Computer Simulation Technology Microwave studio software (CST-MWS). The dimension of microwave absorber sample in CST simulation was shown in Fig. 3. The microwave absorber sample insert into the rectangular waveguide, WR-90 for simulation. The simulation result can check the ability absorption of the material. Figure 4 shows the sample placed inside the rectangular waveguide.

Before simulate the result, the dielectric constant and loss factor of the sample must be defined in the CST-MWS over 8.2–12.4 GHz frequency range. In this simulation, two port method was use to simulate the result. The result of port 1 (S_{11})

Fig. 2 Dimension of rectangular waveguide

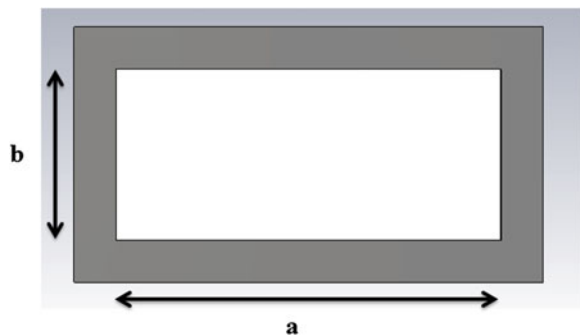


Fig. 3 Dimension of microwave absorber sample

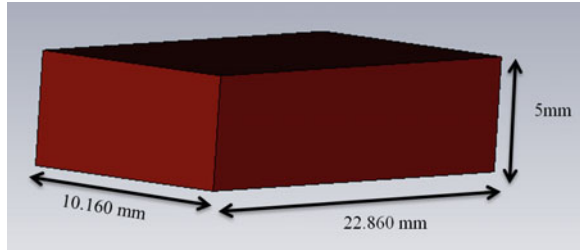
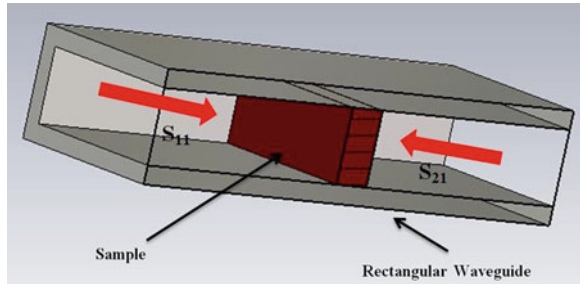


Fig. 4 Sample placed inside rectangular waveguide holder



was the reflected energy where port 2 (S_{21}) was the transmitted energy. The formula used to calculate the absorption is shown in Eq. (3):

$$A = [1 - (s_{11})^2 - (s_{21})^2] \cdot 100\% \quad (3)$$

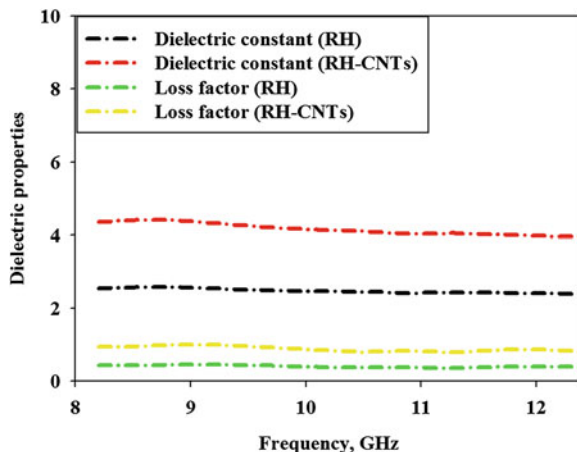
where A , S_{11} , and S_{21} are the percentage of absorption energy, reflection loss, and transmission loss respectively.

4 Results and Discussion

4.1 Dielectric Properties

The dielectric properties of rice husk and RH-CNTs measured by using dielectric probe is shown in Fig. 5. The dielectric constant and loss factor of RH material shows clearly difference after composite with CNTs. The RH-CNTs has higher dielectric constant and loss factor compare to RH material. The difference average loss factor values between RH and RH-CNTs are 0.48. For dielectric constant, the average value of the RH is 2.48 where the RH-CNTs is 4.16. The values of dielectric properties of RH increases due to the increment of carbon content after composites with CNTs. CNTs are nanomaterial which has high carbon content.

Fig. 5 Dielectric properties of RH and RH-CNTs samples



4.2 Reflection Loss and Microwave Absorption

Figure 6 shows the percentage absorption of RH and RH-CNTs samples over 8.2–12.4 GHz frequency range. The percentage absorption of RH sample is from 18 to 24 %. For RH-CNTs sample, it able to absorb 20–48 % of electromagnetic signal over 8.2–12.4 GHz. From the Fig. 6, the graph shows the RH-CNTs microwave absorber sample has higher absorption than pure rice husk microwave absorber. Therefore, the carbon nanotubes not only increase the dielectric properties of rice husk, it also enhances the absorption ability of pure rice husk.

The sample of RH-CNTs also been design and simulate in various thickness (5, 10, 15, and 20 mm) over frequency range 8.2–12.4 GHz. The absorption (%) of RH-CNTs with different thickness is shown in Fig. 7. The microwave absorption of RH-CNTs obviously shows increasing when the thickness of RH-CNTs samples increased. The RH-CNTs sample with thickness 20 mm has highest values of microwave absorption 62–80 % compare to 5, 10 and 15 mm over 8.2–12.4 GHz.

Fig. 6 Microwave absorption of RH and RH-CNTs samples

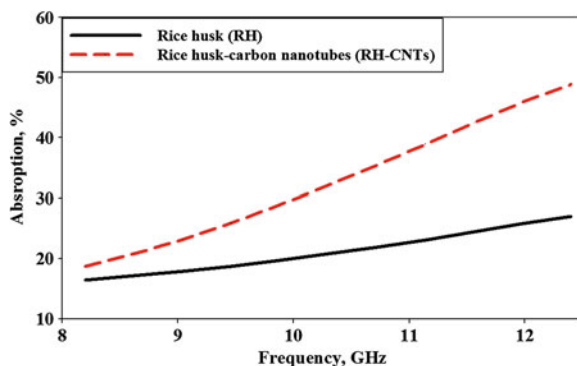


Fig. 7 RH-CNTs samples with different thickness

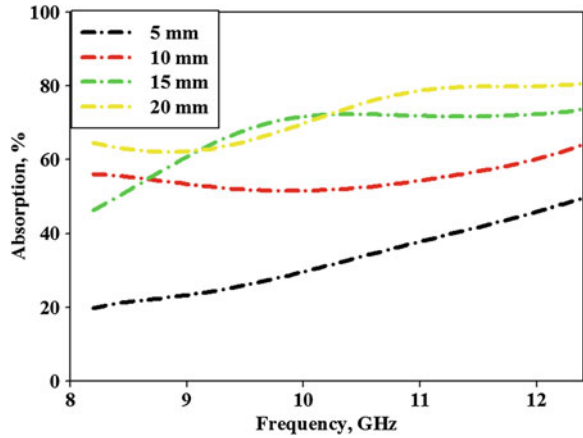


Table 1 Average values absorption, % of the different samples over 8.2–12.4 GHz

| Samples | Thickness (mm) | Absorption (%) |
|-----------|----------------|----------------|
| Rice Husk | 5 | 21.10 |
| RH-CNTs | 5 | 32.96 |
| RH-CNTs | 10 | 54.99 |
| RH-CNTs | 15 | 67.34 |
| RH-CNTs | 20 | 71.94 |

All of the samples show the lowest microwave absorption at 8.2 GHz and highest microwave absorption at 12.4 GHz. The thicker the samples, the harder the electromagnetic wave radiate through the samples and more easily trap inside the samples. Then, the dielectric properties will take part to store and dissipate the electromagnetic waves which trap inside the sample. Table 1 shows the average values of microwave absorption (%) of the different samples and thicknesses.

5 Conclusions

This paper discussed the comparison of RH and RH-CNTs performance in dielectric properties and microwave absorption. The result shows the RH-CNTs has higher ability to absorb microwave signal compare with pure rice husk. The CNT has enhanced the dielectric Properties performance of pure RH. The difference of microwave absorption between RH and RH-CNTs are 2–24 %. The different thickness of RH-CNTs samples was investigated. The thicker the sample has the higher ability to absorb microwave signal. Hence, the rice husk performance in microwave absorption can be improved by composite with CNTs. For microwave absorber, carbon is the important element in microwave absorption. By adding some extra carbon into rice husk materials, the amount of carbon content in rice

husk increases. Due to the increasing of carbon in RH-CNTs composites, the dielectric properties were increases as well. Therefore, the RH-CNTs composite has higher microwave absorption compare to pure rice husk. RH-CNTs has potential use as microwave absorber in X-band.

References

1. Liu, W.-W., Aziz, A., Chai, S.-P., et al.: The effect of carbon precursors (methane, benzene and camphor) on the quality of carbon nanotubes synthesised by the chemical vapour decomposition. *Physica E Low-Dimens Syst. Nanostruct.* **43**(8), 535–1542 (2011)
2. Liu, W.-W., Aziz, A., Chai, S.-P., et al.: Preparation of iron oxide nanoparticles supported on magnesium oxide for producing high-quality single-walled carbon nanotubes. *Carbon* **50**(1), 342 (2012)
3. Liu, Q., Li, X.: Study on the microwave permeability of the CNT complex in 2–18 GHz. *Appl. Phys. Res.* **2**(2), 185 (2010)
4. Iqbal, M.N., Malek, M.F.B.A., Ronald, S.H., Bin Mezan, M.S., Juni, K.M., Chat, R.: A study of the EMC performance of a graded-impedance, microwave, rice-husk absorber. *Prog. Electromagnet. Res.* **131**, 19–44 (2012)
5. Malek, F., Nornikman, H., Nadiyah, O.: Pyramidal microwave absorber design from waste material using rice husk and rubber tire dust. *J. Telecommun. Electron. Comput. Eng.* **4**, 1 (2012)
6. Awang, Z., Zaki, F.A.M., Baba, N.H., Zoolfakar, A.S., Bakar, R.A.: A free-space method for complex permittivity measurement of bulk and thin film dielectrics at microwave frequencies. *Prog. Electromagnet. Res. B* **51**, 307–328 (2013)
7. Liu, Y., Luo, F., Zhou, W., et al.: Dielectric and microwave absorption properties of Ti₃SiC₂ powders. *J. Alloy. Compd.* **576**, 43–47 (2013)
8. Sabouroux, P., Ba, D.: Epsimu, a tool for dielectric properties measurement of porous media: application in wet granular materials characterization. *Prog. Electromagnet. Res. B* **29**, 191–207 (2011)
9. Zhu, H., Zhang, L., Zhang, L., et al.: Electromagnetic absorption properties of Sn-filled multi-walled carbon nanotubes synthesized by pyrolyzing. *Mater. Lett.* **64**(3), 227–230 (2010)
10. Zahid, L., Malek, M.F.B.A., Normikman, H., Mohd Affendi, N.A., Ali, A., Hussin, N., Ahmad, B.H., Abdul Aziz M.Z.A.: Development of pyramidal microwave absorber using sugar cane bagasse (SCB). *Prog. Electromagnet. Res.* **137**, 687–702 (2013)
11. Lee, Y.S., Malek, M.F.B.A., Cheng, E.M., Liu, W.W., You, K.Y., Iqbal, M.N., Wee, F.H., Khor, S.F., Zahid, L., Haji Abd Malek, M.F.B.: Experimental determination of the performance of rice husk-carbon nanotube composites for absorbing microwave signals in the frequency range of 12.4–18 GHz. *Prog. Electromagnet. Res.* **140**, 795–812 (2013)
12. Al-Moayed, N.N., Afsar, M.N., Khan, U.A., et al.: Nano ferrites microwave complex permeability and permittivity measurements by *t/r* technique in waveguide. *IEEE Trans. Magn.* **44**(7), 1768–1772 (2008)
13. Afsar, Y., Wang, M.N.: Measurement of complex permittivity of liquids using waveguide techniques. *Prog. Electromagnet. Res.* **42**, 131–142 (2003)

Development of Spectrum Management Tool for Malaysia Using Open-Source GIS Software

**Mohamad Afif Saman, Ahmad Fadzil Ismail,
Khairayu Badron, Huda Adibah Mohd Ramli,
Wahidah Hashim and Ahmad Nasruddin 'Atiqullah Fakrullah**

Abstract The mobile communication technology growth in Malaysia, particularly in cellular network has led to higher demand of spectrum access. However, with limited number of radio spectrum availability, an effective spectrum management tool is needed. The commercial software will be an expensive solution for a long run in the rapidly changing environment of mobile technologies. Hence the development of open-source spectrum management tool that not only efficient but also cost effective is needed. The tool must be able to manage existing spectrum and assist in spectrum planning for new base station (BS). It also must be able to identify possible interference that could happen between BS. This paper will highlight the development of spectrum management tool using open-source resources for Malaysian authority. The simple cost effective tool is able to do proper spectrum management and planning for 2G, Global System for Mobile Communications (GSM), and 3G, Universal Mobile Telecommunications System (UMTS) networks.

M.A. Saman (✉) · A.F. Ismail · K. Badron · H.A.M. Ramli
Faculty of Engineering, International Islamic University Malaysia, Kuala Lumpur, Malaysia
e-mail: mafifsaman@gmail.com

A.F. Ismail
e-mail: af_ismail@iium.edu.my

K. Badron
e-mail: khairayu@iium.edu.my

H.A.M. Ramli
e-mail: hadibahmr@iium.edu.my

W. Hashim
College of Information Technology, Universiti Tenaga Nasional, Jalan IKRAM-UNITEN,
43000 Kajang, Selangor, Malaysia
e-mail: wahidah@uniten.edu.my

A.N. Fakrullah
Malaysian Communications and Multimedia Commission, Off Persiaran Multimedia, 63000
Cyberjaya, Selangor Darul Ehsan, Malaysia
e-mail: ahmad.nasruddin@cmc.gov.my

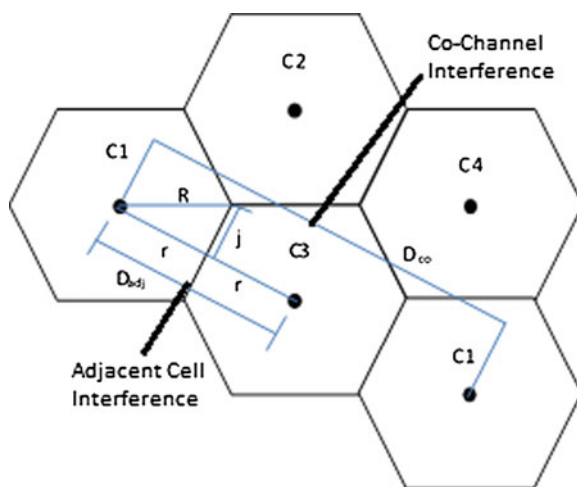
1 Introduction

Mobile communication has been a part of basic necessity of today's society. Almost everybody owns a mobile phone today. Initially, the mobile phone is used to make a phone call and short messaging service (SMS). However, nowadays its functions have been expanded and evolved into a smartphone. Today's people are not only making a phone call or SMS with their phones, but also accessing the internet, streaming media, downloading and uploading files and doing businesses online from the phones. These activities required a lot of radio spectrum bandwidth which is a very limited resource [1]. There are few solutions developed to increase the efficiency and availability of spectrum bandwidth. One of the simplest solutions is to build a new base station (BS) to cater the increasing number of users. Adding new BS is not a simple task. It required proper planning. Without proper planning, the radio frequency (RF) signal from the BS can cause interference with other BS RF signal. Eventually, this can lead to signal corruption, degrading the service quality of the BS.

There are two types of common BS interference, adjacent channel interference and co-channel interference as shown in Fig. 1 [2].

In Malaysia, Malaysian Communications and Multimedia Commission (MCMC) carries the task of managing radio spectrum. MCMC regulates and coordinates the availability according to their own spectrum planning and assignment plan [3]. MCMC performs the spectrum management activities using commercial spectrum management software [4]. The software are robust and stable. They can efficiently perform spectrum management processes. However, mobile communication technologies are evolving rapidly. Using commercial software will prove to be not cost effective in a long term. The basic software for spectrum management are expensive and cost around hundred thousand of Euros. They are

Fig. 1 Adjacent cell and co-channel cell interference



also inflexible and need update to accommodate the new mobile technologies. These require additional cost which will run for years. This paper proposes using open-source software to develop a low-cost spectrum management tool as solution. Nowadays, many applications software are built using open-source resources as its technologies evolved quicker than commercial resources [5]. In recent years, there are a lot of open-source geographical information system (GIS) software emerging in the market. Within years, their capabilities to perform numerous tasks have expanded. Using GIS software as the development platform, an advance spectrum management tool can be possibly achieved. Since the proposed tool is an open-source software, the organization only need to its own employee to enhance the spectrum management tool in the future.

This paper is organized as follows. Section 2 provides the research scope and methodology. Section 3 identifies the algorithm and modelling for spectrum monitoring tool. Section 4 highlights the software overview and overall design of the proposed tool. Section 5 discusses the preliminary results and findings of the research. Section 6 summarizes and concludes this paper. Section 7 gives recommendation for future research.

2 Research Scope and Methodology

2.1 Research Scope

The aim of the proposed spectrum management tool is to assist MCMC in spectrum management activities. Some of the activities involve are spectrum occupancy management, spectrum planning, interference identification and spectrum monitoring [4]. The current development stage of the proposed tool concerns only with spectrum management and planning. BS coverage cell will be shown with the aid of GIS software. A simple interference identification algorithm is implemented to help in spectrum management and planning activities. Moreover, the tool is built using only open-source resources. Cellular networks in Malaysia, namely Global System for Mobile Communications (GSM) and Universal Mobile Telecommunications System (UMTS) networks will be the focus of proposed tool.

2.2 Methodology

First, review on existing spectrum management tool and existing open-source GIS software are done. Then, the chosen model is implemented in the development of spectrum management tool. Data for spectrum management and planning are analyzed. The result from proposed tool is evaluated with existing spectrum management tool for benchmarking.

3 Path Loss Models and Implementation

Cell coverage range can be determined by using the RF propagation path loss model. There are few existing standard empirical path loss models available to calculate the path loss. The proposed tool has considered Hata model for GSM900 while Cost-231 Hata model for GSM1800 and UMTS2100 [6]. The Hata model is calculated using the following equation:

$$L_p(dB) = 69.55 + 26.16 \log_{10}(f_{MHz}) - 13.82 \log_{10}(h_t) - a(h_r) + (44.9 - 6.55 \log_{10}(h_t)) \log_{10}(d_{km}) - K \quad (1)$$

where:

d_{km} distance between base station and mobile station in km

f_{MHz} carrier frequency in MHz

h_t Base antenna height in meter

h_r Mobile antenna height in meter

$$a(h_r) = \begin{cases} (1.1 \log_{10}(f_{MHz}) - 0.7)h_r - (1.56 \log_{10}(f_{MHz}) - 0.8), & \text{open, suburban and small city area} \\ 3.2(\log_{10} 11.75(h_r))^2 - 4.97, & \text{large city}(f_{MHz} > 400) \end{cases} \quad (2)$$

$$k = \begin{cases} 4.78(\log_{10}(f_{MHz}))^2 - 18.33.78(\log_{10}(f_{MHz})) + 40.94, & \text{open area} \\ 2 \left[\log_{10} \left(\frac{f_{MHz}}{28} \right) \right]^2 - 5.4, & \text{suburban area} \\ 0, & \text{medium - small City and large city}(f_{MHz} > 400) \end{cases} \quad (3)$$

The extension of Hata model, COST-231 Hata is calculated using the equation below:

$$L_p(dB) = 46.3 + 33.9 \log_{10}(f_{MHz}) - 13.82 \log_{10}(h_t) - a(h_r) + (44.9 - 6.55 \log_{10}(h_t)) \log_{10}(d_{km}) + C \quad (4)$$

Where:

d_{km} distance between base station and mobile station in km

f_{MHz} carrier frequency in MHz

h_t Base antenna height in meter

h_r Mobile antenna height in meter

$a(h_r)$ Equation (3)

$C = 0$ medium city and suburban areas or

$C = 3$ metropolitan areas

The maximum distance is then determined by rearranging terms (1) into (5) and (4) into (6)

$$d_{km} = \text{antilog}_{10} \left(\frac{Lp(\text{dB}) - 69.55 - 26.16 \text{Log}_{10}(f_{\text{MHz}}) + 13.82 \text{Log}_{10}(h_t) + a(h_r) + K}{44.9 - 6.55 \text{Log}_{10}(h_t)} \right) \quad (5)$$

$$d_{km} = \text{antilog}_{10} \left(\frac{Lp(\text{dB}) - 46.3 - 33.9 \text{Log}_{10}(f_{\text{MHz}}) + 13.82 \text{Log}_{10}(h_t) + a(h_r) - C}{44.9 - 6.55 \text{Log}_{10}(h_t)} \right) \quad (6)$$

The external factor in RF propagation such as environments and weather conditions need to be considered in calculating the path loss. In reality, the environments around BS do not always consist of only flat surfaces. The terrain around BS could consist of many hills and man-made structures or buildings. These factors are considered as obstructions and introduce additional propagation effects such as reflection, scattering and diffraction. In general, reflection happens when the signal size is smaller than the obstacle's size. The signal will lost some of its power and bounce back from the obstacle into weaker signal. Scattering occurs when the obstacle's size and signal size are similar to each other and the signal scattered into smaller signals. Diffraction on the other hand happened around the edge of the obstacles and the signal got deflected into various directions. While the chosen path loss models do include the losses according to the area type around BS, additional losses due to effects of the terrain should be added to the loss calculated using Eqs. (1) or (4) for total loss [7].

At the current stage of development, single knife-diffraction effect modelling has been considered to calculate the diffraction loss due to terrain. Receiver would not be able to retrieve the signal when the path loss value exceeds the threshold value. The threshold value for the path loss can be determined using the equation

$$Lp_{\text{max}} = P_{Tx} + G_{Tot} - R_s. \quad (9)$$

Where

| | |
|-------------------|-----------------------------|
| Lp_{max} | Losses in dB |
| P_{Tx} | Transmitted Power in dBm |
| G_{Tot} | Total gains in dB |
| R_s | Receiver sensitivity in dBm |

In the proposed tool, the frequency blocks assigned by MCMC have been adopted for the spectrum management. MCMC has assigned specific blocks of channels to cellular service providers in Malaysia.

4 Software Overview and Design

The paper intention is to highlight the development of spectrum management tool using open-source software. The proposed model and algorithm has been implemented using Quantum GIS (QGIS) 2.2.0, codename Valmiera. The tool is written using PyQt programming language, a language that using QT C++ GUI programming with Python binding. QGIS is an open-source geographical information system (GIS) software which is used to visualize geographical pattern of data on computer [8]. The rapid development of open-source GIS software has led to its usage in communication technology research such as by [9, 10, 11]. The proposed tool will require users to determine the type of operation desired through its graphical user interface (GUI). Then, all necessary data for the operation will be loaded by QGIS from the database. At this stage, PostgreSQL with PostGIS extension has been chosen as the database management system (DBMS) for the propose tool. It is an open-source DBMS.

The tool's developing process is modeled from Boehm spiral software process model. By cyclically iterating the four basic quadrant of spiral model. A prototype for proposed spectrum management tool has been developed at current stage of development. At this stage, the proposed tool can display the coverage area of BS according to the antenna pattern type for spectrum planning. By taking all the requirement data, the tool can visualize the coverage area of BS using the path loss values. The maximum distance of the coverage will first be calculated. Then, the threshold value for the BS signal propagation will be determined. Next, path loss will be calculated. Users will be given an option to include the diffraction loss in the calculation. If included, the diffraction loss will be added to the total path loss. The total loss together with the threshold value will be used to display the BS coverage area on the map.

5 Preliminary Results and Discussion

A plugin named **Malaysia Spectrum Management Tool** "Malspectrum" has been developed as in Fig. 2. The plugin is accessed by clicking the plugin name under the 'Plugin' menu or by clicking on the plugin's icon. Before the plugin can process any spectrum management activity, some basics layers have to be loaded into Qgis first. Firstly, a terrain layer will be loaded. Next, a layer called 'Area' is loaded. The Area layer is created from Qgis using polygon vector data containing information about the type of area around BS. The areas type are open area, suburban, small city and medium-large city. Then, the map layer is loaded. Qgis has external plugin called 'OpenLayers' plugin which can be downloaded from Qgis plugins repository. It can load map layer from OpenStreetMap, Google, Yahoo, and Bing map online. By using this plugin, users will save the time from georeferencing the earth map. Furthermore, the map will be more accurate for spectrum management

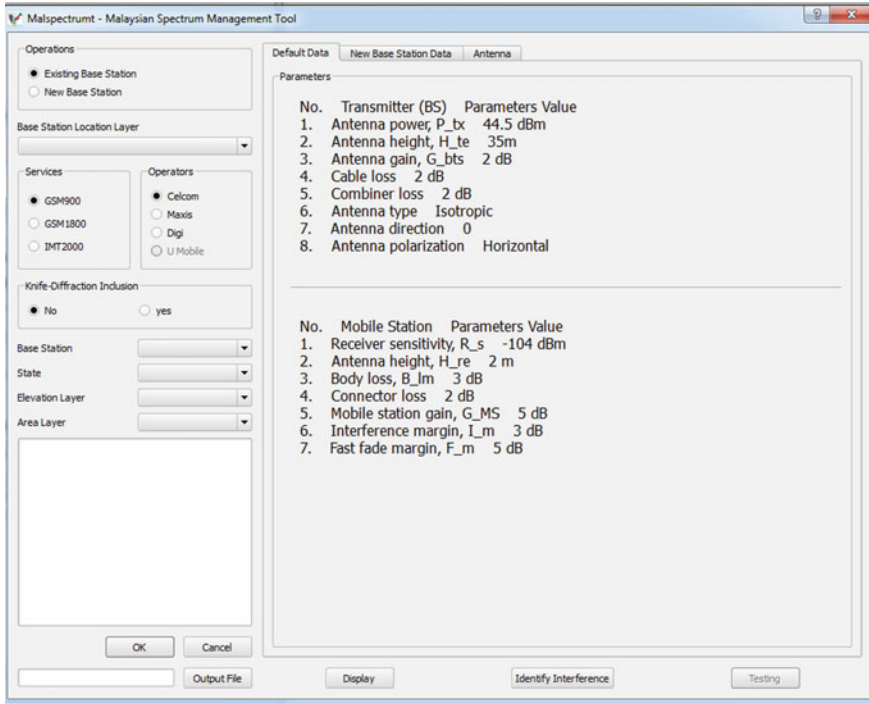


Fig. 2 Spectrum display GUI

process. Finally, the BS location layer will be added by retrieving the data from database. The location is represented using point type vector data.

In the current development stage, users can select to perform spectrum management of existing BS or spectrum planning of new BS. In the spectrum management process, users can display the cell coverage area of existing BS by selecting the appropriate data such as service provider, network and BS site. The output for will be a polygon raster format image with embedded path loss values data. In the early stage of development, the output image was written using vector polygon data format. However, the continuous nature of path loss data, led to poor result and data manipulation of vector format output. The raster format enables the proposed tool to produce output with meaningful data using colour codes. The colour codes is used to represent the different path loss value ranges on the map. Figure 3 demonstrates cell coverage with knife-diffraction loss effect. With the irregular terrain shape environment, it provides better and accurate result. This result can assist MCMC in managing the current spectrum for initial decision. If cellular provider received complained about ‘no signal transmission’, MCMC can use the result to provide initial answer whether or not signal should be available in the area. As for new BS planning, the tool will test for simple adjacent channel or co-channel interference. If there is no possible interference, user can proceed with

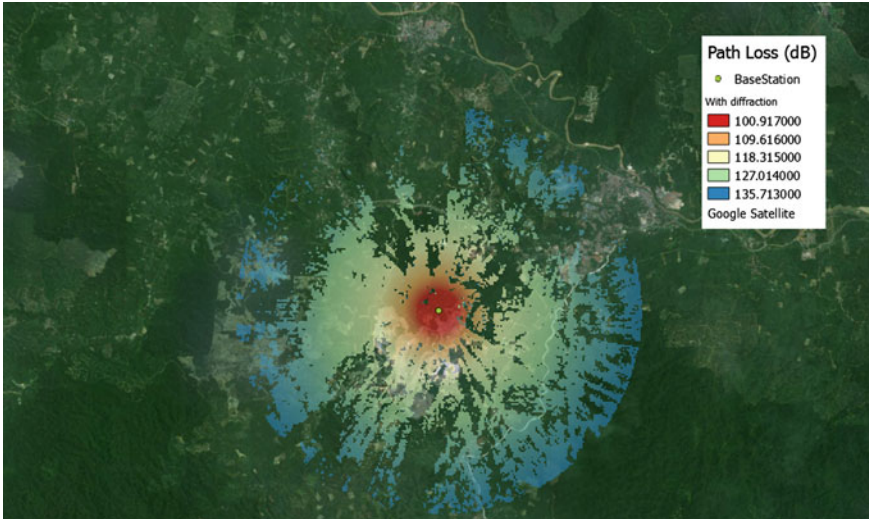


Fig. 3 Cell coverage with diffraction loss

BS cell coverage display and will be prompted an option to proceed with the request. Users can choose any type of antenna as long as the radiation pattern file is available. A log file will be produced.

6 Conclusion

The prototype of the proposed tool and its results are presented in this paper. The proposed tool is developed using open-source resources. Qgis has been chosen as the GIS platform while PostgreSQL has been chosen as the DBMS in the proposed tool development. The tool is intended for spectrum management and spectrum planning of GSM and IMT cellular networks. The cell coverage area can be visualized on the map and simple interference algorithm has been implemented. The research will continue to develop better prototype model and finally lead to the working product.

7 Future Work

Currently, the prototype model only accounting the effect of diffraction loss. In reality, there are several other effects. The next prototype model should include several other propagation models such as Walfisch-Ikegami model, or Longley-Rice model, the effect of multi-path as well as adding another unit to measure the output such as received power.

References

1. Chandra, A.: Spectrum management for future generation wireless based technology. In: European Wireless Technology Conference, (EuWIT), Rome, pp. 201–205 (2009)
2. Schiller, J.: *Mobile Communication*, 2nd edn, pp. 43–44. Great Britain, Pearson Education (2003)
3. Latef, A.S.A., Hassan, R.: Spectrum management system: a study. In: International Conference on Electrical Engineering and Informatics (ICEEI), Bandung, pp. 1–6 (2011)
4. SKMM: *MyCoverage*, Malaysia, vol. 1, issue 1, pp. 36–41 (2007)
5. Acuna, S.T., Castro, J.W., Dieste, O., Juristo, N.: A systematic mapping study on the open source software development process. In: 16th International Conference on Evaluation and Assessment in Software Engineering (EASE 2012), Ciudad Real, pp. 42–46 (2012)
6. Blaunstein, N., Christodoulou, C.: *Radio Propagation and Adaptive Antennas for Wireless Communication Links*. Wiley, New Jersey (2007)
7. Seybold, J.S.: *Introduction To RF Propagation*, pp. 175–180. Wiley, United States of America (2005)
8. Quantum GIS: Index. <http://www.qgis.org/> (2013)
9. Shu, Z., Li, H., Liu, G., Xie, Q.: Application of GIS in telecommunication information resources management system. In: International Conference on Information Management, Innovation Management and Industrial Engineering (ICIII), Shenzhen, pp. 401–404 (2011)
10. Alexandris, G., Giannikos, I.: A new model for maximal coverage exploiting GIS capabilities. *Eur. J. Oper. Res.* **202**, 328–338 (2010)
11. Umar, R., Abidin, Z.Z., Ibrahim, Z.A.: Implementing the GIS technique for RFI mapping for radio astronomy in Malaysia. In: IEEE International Conference on Space Science and Communication (IconSpace), pp. 25–27 (2011)

Monopole Ellipse Antenna for Ultra-Wideband Applications

M.C. Lim, S.K.A. Rahim, M.I. Sabran and A.A. Eteng

Abstract In this paper, an Ultra wideband (UWB) ellipse monopole antenna is presented. The proposed antenna consists of an ellipse patch fed by a coplanar waveguide (CPW) transmission line. The antenna provides coverage for the UWB spectrum, achieving reflection coefficients ≤ -10 dB from 2.83 to 10.66 GHz, thereby yielding a 7.77 GHz impedance bandwidth. The impedance bandwidth is achieved through a variation of the minor axis of the ellipse patch. The antenna gain is slightly enhanced by a center cut at the top ground plane. Simulations show quasi omnidirectional radiation patterns for the proposed antenna at three resonance frequencies of 4.8, 6.7 and 9.35 GHz within the UWB spectrum.

Keywords Ultra wideband (UWB) · Coplanar waveguide (CPW)

1 Introduction

The Federal Communication Commission (FCC), in February 2002, allocated an unlicensed ultra wideband spectrum spanning 3.1–10.6 GHz, leading to a rapid increase in UWB antenna research [1]. The demands of most modern wireless communication systems require miniaturized and multi-functional antennas. UWB antennas provide wide frequency coverage, eliminating the need for multiple

M.C. Lim (✉) · S.K.A. Rahim · M.I. Sabran · A.A. Eteng
Wireless Communication Center, Universiti Teknologi Malaysia,
81310 Skudai Johor, Malaysia
e-mail: archuan@gmail.com

S.K.A. Rahim
e-mail: sharulkamal@fke.utm.my

M.I. Sabran
e-mail: mursyid@fkegraduate.utm.my

A.A. Eteng
e-mail: aeakaa2@live.utm.my

antennas in a system. Besides, the immense bandwidth of UWB signaling allows for high-speed data transmission from 100 Mbps to 1 Gbps [2].

A common realization of UWB antennas is the microstrip antenna. Microstrip antennas have received broad attention owing to their light weight, ease of fabrication, low profile, and ease of integration with other electronic circuits. Currently, two types of microstrip UWB antenna in use are microstrip line transmission [3] and the co-planar waveguide (CPW)-fed antenna [4]. The CPW-fed antenna has several advantages compared with microstrip line transmission antenna such as lower dispersion, wider bandwidth, and lower radiation loss [5]. Various shapes and polarizations of monopole UWB antennas have been presented such as rectangular patch [6], U-patch [2], circular disc patch [7], elliptical [8], circular polarized (CP) [9], and dielectric resonator antenna (DRA) [10].

In this paper, an ellipse monopole UWB CPW-fed antenna is presented with minor gain improvement. The proper ground plane design improves the gain of the antenna. The proposed antenna complies with the FCC UWB spectrum (3.1–10.6 GHz), achieving a reflection coefficient lower than -10 dB from 2.83 to 10.66 GHz.

2 Antenna Design

The antenna design and optimization are achieved using CST Microwave Studio 2013. The geometry and fabrication of the proposed antenna design are shown in Figs. 1 and 2, respectively. The radiator patch of the antenna is an ellipse shape with a CPW as a transmission line. The overall size of the antenna is $35 \text{ mm} \times 30 \text{ mm} \times 1.6 \text{ mm}$. The width of transmission line is 3 mm and the inset gap is 0.8 in order to archive a 50Ω characteristic impedance. The antenna is fabricated on an FR-4 substrate, with 1.6 mm thickness, permittivity of 4.7 and a loss tangent of 0.019. Table 1 lists the design parameters of the proposed UWB monopole antenna.

Fig. 1 Geometry of proposed antenna

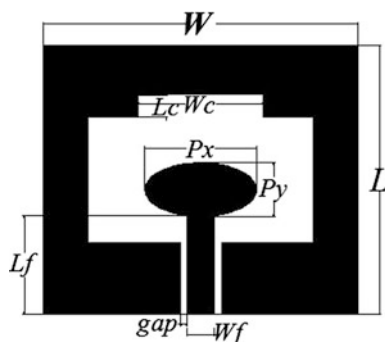


Fig. 2 Fabricated proposed antenna

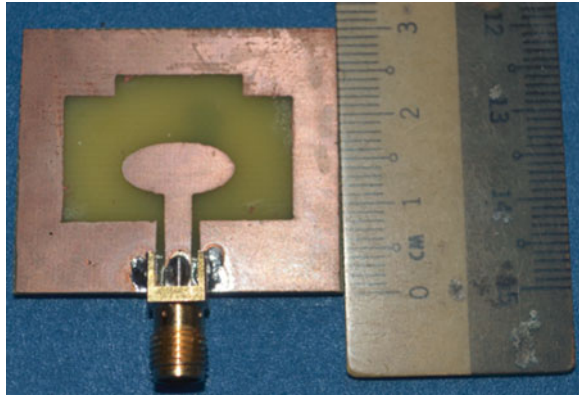


Table 1 Parameter of ellipse monopole antenna

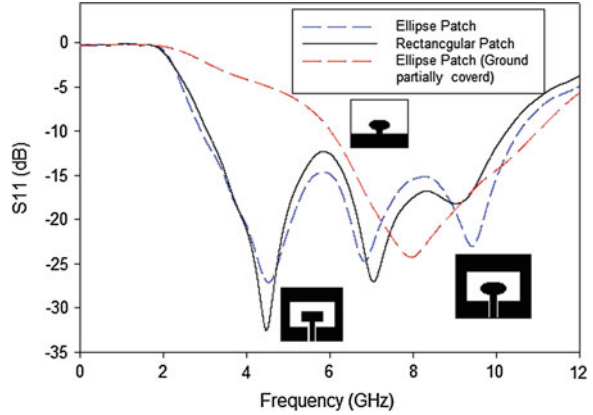
| Parameter | Dimension (mm) |
|-----------------------------|----------------|
| Width of substrate, W | 35 |
| Length of substrate, L | 30 |
| Width of patch, P_x | 12.4 |
| Length of Patch, P_y | 6 |
| Width of center cut, W_c | 14 |
| Length of center cut, L_c | 2.5 |
| Fed line width, W_f | 3 |
| Fed line length, L_f | 11 |
| Inset gap, gap | 0.8 |

3 Parametric Studied

The CPW-fed antenna generates the UWB spectrum with a combination and overlapping of a few resonance frequencies instead of one resonance frequency [11]. The proposed antenna has three resonance frequencies to achieve broad bandwidth, namely: 4.8, 6.7 and 9.35 GHz. The radiator of proposed antenna is ellipse shape with dimensions $P_x \times P_y$.

In this paper, the first resonance is contributed by the partial ground plane with the ellipse patch. The second and third resonances are generated by the fully surrounded the ground plane as shown in Fig. 3. A parametric study has been carried out with various shape designs such as rectangular patch, ellipse patch with partial and fully surrounded ground.. The simulation results show that the ellipse shaped radiator with partially ground has a bandwidth from 6 to 11 GHz, and is unable to cover the entire UWB spectrum. The rectangular patch with fully surrounded ground plane is able to generate 3 resonances, but its bandwidth of 3.05–10.25 GHz is not broad enough to cover the whole UWB spectrum. Finally, the ellipse shape with a fully surrounded ground plane is able to improve the upper

Fig. 3 Comparison of return loss for ellipse patch, rectangular patch and ellipse patch (ground partially covered)

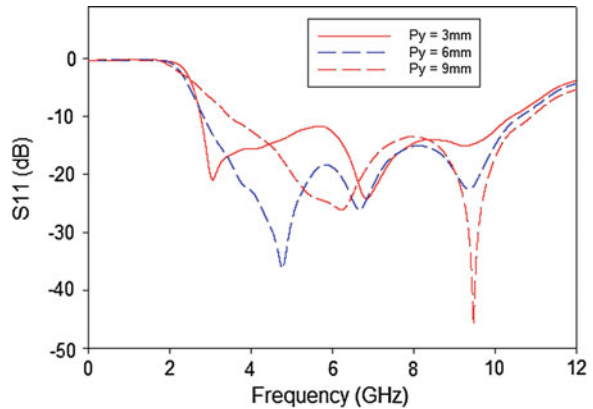


reflection coefficient to achieve a wider bandwidth from 2.83 to 10.66 GHz, thus meeting the UWB spectrum requirement (3.1–10.6 GHz, reflection coefficient ≤ -10 dB).

Figure 4 is a comparison of the reflection coefficient of an ellipse patch, a rectangular patch, and an ellipse patch with a partially covered ground. Investigations for different P_y patch dimensions have also been carried out. With $P_y = 3$ mm, the impedance bandwidth is 2.76–10.4 GHz. Further, with $P_y = 9$ mm parameter, the impedance bandwidth is 3.48–10.88 GHz. Lastly with P_y optimized, the suitable parameter is 6 mm and able to covered the UWB spectrum frequency which is 2.83 to 10.66 GHz.

Figure 5 depicts the return loss of proposed antenna with top ground center cut and without a center cut. The proposed antenna has a center cut with dimension $W_c = 14$ mm and $L_c = 2.5$ mm. The top ground plane with center cut has a lower

Fig. 4 Comparison of return loss for different P_y



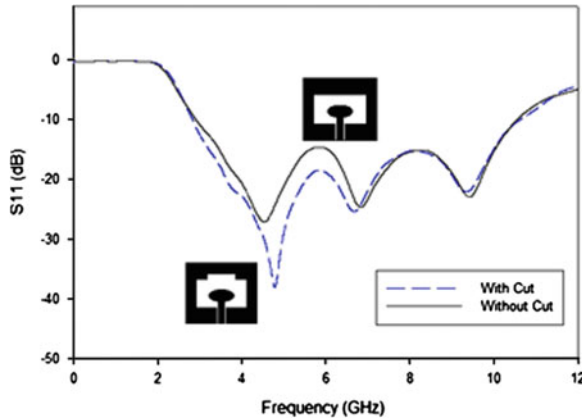


Fig. 5 Comparison of return loss center ground plane with center cut and without center cut

resonance at 4.5–6.2 GHz as compared to without the cut. After 6.2 GHz onwards, the reflection coefficient results were quite similar to each other.

To archive higher gain for ellipse patch antennas, the cutting at the center of ground was performed. Figure 6 illustrates a comparison between without center cut and various center cut (W_c) lengths, from 10 to 14 mm. The proposed antenna is able to achieve 3.47 dB compared with 2.89 dB at 8.1 GHz. After optimizing, the best result is achieved with $W_c = 14$ mm. Figure 7a shows an equal current

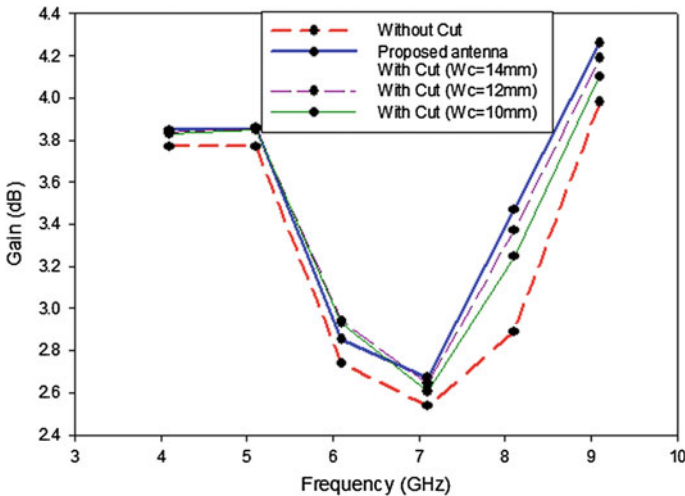


Fig. 6 Comparison of gain without center cut and various W_c length

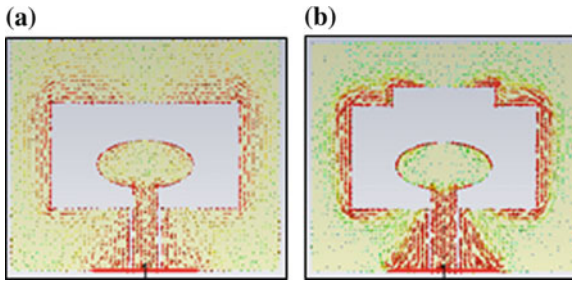


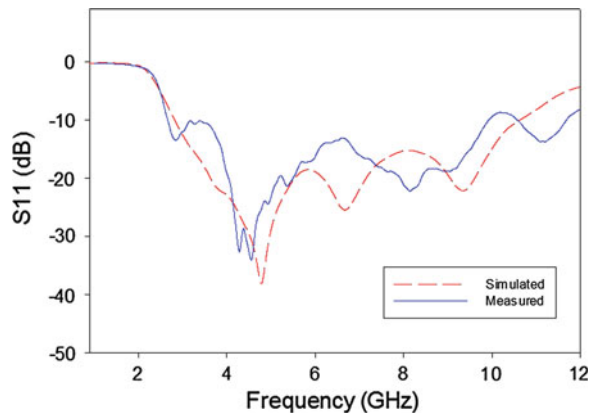
Fig. 7 Electric current distribution at 8.1 GHz: **a** top of ground center without cut **b** top of ground center with cut

distribution around the inner portion of the ground plane. Based on the Fig. 7b the current is stronger than Fig. 7a and contributes higher gain for proposed antenna.

4 Results and Discussions

The simulated and measured results for the reflection coefficient presented in Fig. 8. The simulated and measurement results have some discrepancies, especially in higher frequency. It maybe due to minor fabrication error. Figure 9 illustrates the radiation pattern for E-plane and H-plane polarization. Three resonances from the proposed antenna, which are 4.8, 6.7 and 9.35 GHz, have been simulated, respectively. The simulated radiation patterns at these three resonances are quasi omnidirectional. Apart from that, the gain of proposed antenna has minor improved with top of ground plane cut modification.

Fig. 8 Comparison of return loss simulated with measured result



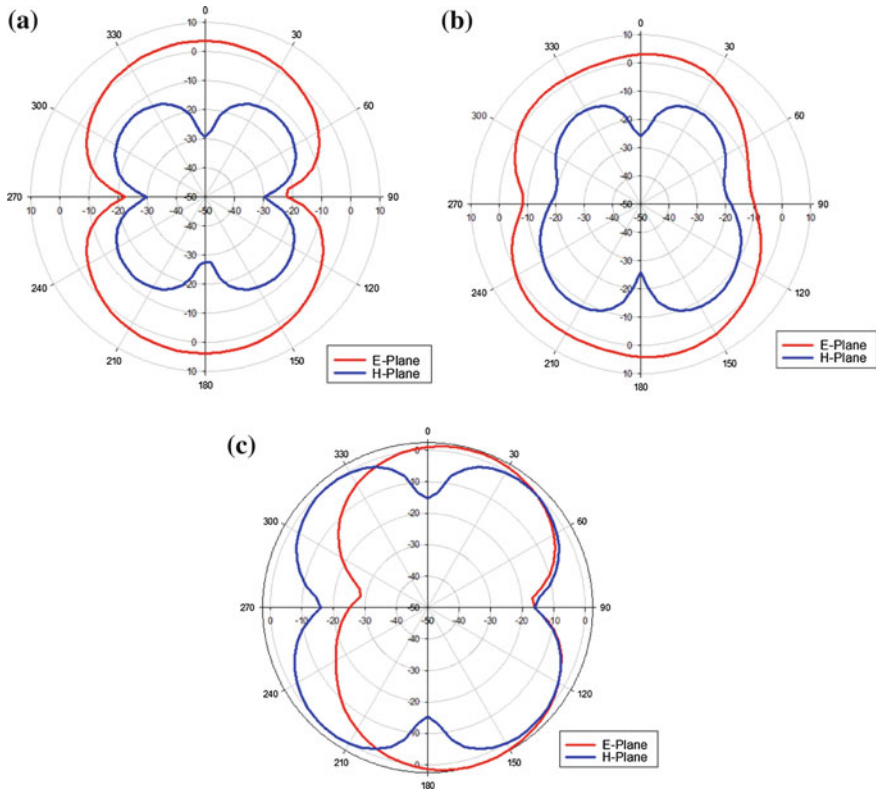


Fig. 9 Radiation pattern of various resonance frequencies for proposed antenna: **a** 4.8 GHz **b** 6.7 GHz, and **c** 9.35 GHz

5 Conclusion

An ellipse monopole UWB antenna with minor gain improvement has been proposed. The achieved bandwidth covers from 2.83 to 10.66 GHz and 3.77:1 bandwidth ratio. Proposed antenna shows an average 6.48 % gain improvement compared with an ellipse antenna without a top ground plane cut.

Acknowledgments The authors wish to acknowledge the Ministry of Higher Education (MOHE) for the sponsorship of this work. The authors would also like to thank the Wireless Communication Centre (WCC), Faculty of Electrical Engineering and Universiti Teknologi Malaysia (UTM) for their support.

References

1. Federal Communications Commission, Washington, DC, USA: Revision of part 15 of the commission's rules regarding ultra-wide-band transmission systems first report and order FCC 02.V48. Technical report (2002)
2. Koohestani, M., Golpour, M.: U-shaped microstrip patch antenna with novel parasitic tuning stubs for ultra wideband applications. *IET Microwaves Antennas Propag.* **4**, 938 (2010)
3. Adnan, R.A.A.-A.S., Hraga, H.I., Zainal Abidan, Z., Usman, M., Jones, S.M.R.: Design studies of ultra-wideband microstrip antenna for ultra-wideband communication. In: *Loughborough Antennas and Propagation Conference*, vol. 2009, p. 365, 16–17 Nov 2009
4. Kim, H., Jung, C.W.: Ultra-wideband endfire directional tapered slot antenna using CPW to wide-slot transition. *Electron. Lett.* **46**, 1183 (2010)
5. Naser-Moghadasi, M., Danideh, A., Sadeghifakhr, R., Reza-Azadi, M.: CPW-fed ultra wideband slot antenna with arc-shaped stub. *IET Microwaves Antennas Propag.* **3**, 681 (2009)
6. Hadinegoro, R., Surjati, I., Ningsih, Y.K.: Ultra wideband microstrip antenna using T-shaped stub fed by coplanar waveguide. In: *Quality in Research Conference 2013*, pp. 208–211 (2013)
7. Liang, J., Guo, L., Chiau, C.C., Chen, X., Parini, C.G.: Study of CPW-fed circular disc monopole antenna for ultra wideband applications. *IEE Proc. Microwaves Antennas Propag.* **152**, 520 (2005)
8. Adam, A.A., Rahim, S.K.A., Tan, K.G., Reza, A.W.: Design of 3.1–12 GHz printed elliptical disc monopole antenna with half circular modified ground plane for UWB application. *Wireless Pers. Commun.* **69**, 535–549 (2013)
9. Danesh, Sh., Rahim, S.K.A., Khalily, M., Okonkwo, U.A.K.C., Sabran, M.: UWB monopole antenna with circular polarization. *Microw. Opt. Technol. Lett.* **54**(4), 949–953 (2012)
10. Abedian, M., Rahim, S.K.A., Danesh, S.H., Khalily, M., Noghabaei, S.M.: Ultrawideband dielectric resonator antenna with WLAN band rejection at 5.8 GHz. *IEEE Antennas Wireless Propag. Lett.* **12**, 1523–1526(2013)
11. Gautam, A.K., Yadav, S., Kanaujia, B.K.: A CPW-fed compact UWB microstrip antenna. *IEEE Antennas Wireless Propag. Lett.* **12**, 151–154 (2013)

Synthesis of a Biasing Circuit for a Reconfigurable WiMAX Antenna (RWA) at 2.3 GHz

Muzammil Jusoh, Mohammad Ramlee Kamarudin,
Mohamad Rubel Basar, Soh Ping Jack, Thennarasan Sabapathy
and Ku Nurul Fazira Ku Azir

Abstract This research focuses on identifying the values of capacitors and inductors of a PIN diode biasing circuit to generate an optimum performance for a 2.35 GHz WiMAX antenna. The optimization involves the testing of a new range of capacitors between 47 and 330 pF and inductors from 18 to 56 nH on a fabricated reconfigurable WIMAX antenna (RWA). Advanced Design System (ADS) software is deployed to obtain simulation results using the touchstone block implementation technique. Four sets of the capacitor—inductor values are proposed based on the reflection coefficient (S_{11}) and transmission coefficient (S_{21}) to possibly achieve the best performance of the RWA. The four sets are; set 1: $C = 47$ pF, $L = 56$ nH, set 2: $C = 100$ pF, $L = 56$ nH, set 3: $C = 150$ pF, $L = 56$ nH and set 4: $C = 330$ pF, $L = 56$ nH. It is discovered that by simulation, set 2 produces the optimal S_{11} and S_{21} compared to the other combination sets. The resulting S_{11} and S_{21} is -26.61 and -0.046 dB, respectively. To further verify this, a complete set of biasing circuit consisting of a PIN diode, two 56 nH inductors and two 100 pF

M. Jusoh (✉) · M.R. Basar · S.P. Jack · T. Sabapathy · K.N.F.K. Azir
Embedded, Network and Advanced Computing (ENAC), School of Computer
and Communication Engineering, Universiti Malaysia Perlis, Arau, Malaysia
e-mail: muzammil@unimap.edu.my

M.R. Basar
e-mail: rubel24434@yahoo.com

S.P. Jack
e-mail: pjsoh@unimap.edu.my

T. Sabapathy
e-mail: thenna84@gmail.com

K.N.F.K. Azir
e-mail: fazira@unimap.edu.my

M.R. Kamarudin
Wireless Communication Centre (WCC), Faculty of Electrical Engineering,
Universiti Teknologi Malaysia, Johor Bahru, Malaysia
e-mail: ramlee@fke.utm.my

capacitors are integrated on the fabricated RWA. It is found that the combination of these components a PIN diode, produced a maximum gain of 6.28 dBi and a reflection coefficient of -15.08 dB at 2.35 GHz. Moreover, the these lumped component values also enabled the RWA to channel WiMAX signals directionally at the broadside, depending on the user locations.

1 Introduction

During the past decade, reconfigurable antennas have attracted huge attention among researchers due to its multi-band operation, multi-radiation pattern (directional or divisive or omnidirectional) and multi-polarization (circular or linear or elliptical) capabilities [1, 2]. These antennas are suited for commercial and military communication, where multiple functions can be enabled only through the use of a single antenna. Relative to conventional antennas, this will then result in a compact-sized antenna and consequently cost reduction.

Theoretically, the electronically reconfigurable antenna can be achieved using radio frequency (RF) switches, such as PIN diodes, varactor diodes, micro-electromechanical system (MEMS) and gallium arsenide MOSFETS (GaAs FETs). These devices can either be used for beam-, polarization- or frequency-alteration by switching between 'ON' and 'OFF' states [3, 4]. However, the inclusion of lump elements in the antenna and microwave devices is challenging. It can cause signal and efficiency deterioration between measurements and simulations. Therefore, it is important to reduce switching loss in biasing circuits of these reconfigurable antennas by choosing the appropriate lump element values. Such circuit's development using 100 pF capacitor and 22 nH inductor values has already been verified to be functioning well in [5, 6].

Nevertheless, to the authors' best knowledge, no further research has been carried out towards determining other suitable capacitors and inductor values. In this work, the analyzed circuit model considers commercial capacitance values (C) of 47, 100, 150 and 330 pF and inductance values (L) of 18, 27, 39 and 56 nH at 2.35 GHz. This is aimed for the WiMAX band (between 2.30 and 2.39 GHz). All RF PIN diode circuits are simulated and analyzed using the Advanced Design System (ADS) software. The investigated PIN diode model, BAR50-02 V from Infineon Technologies is imported into the ADS software. In the PIN diode OFF state (0 V DC supply), the S_{11} is approximately -0.74 dB (86 % RF power reflection) with its S_{21} close to 8 dB isolation. When the PIN diode is ON (5 V DC supply) $S_{11} = -20$ dB (1 % RF power reflection) while $S_{21} = 0$ dB isolation.

This research analyzed and verified the performance of a compact design reconfigurable WiMAX antenna (RWA) via simulations and measurements. Such RWA is designed to be integrated with the *proposed* biasing circuit. An optimized biasing circuit using $L = 56$ nH and $C = 100$ pF are positioned at the specific locations on the RWA's spiral feed line to enable directional beams at 320 or 35°

and divisive broadside beams at 43° and 330° , respectively. Besides offering more flexibility, a non-contacting aperture-coupled feed is utilized to separate the radiating element and feed structure.

2 Synthesis of Biasing Circuit

Biasing circuit is significant in predetermining the voltages or currents at various points of an electronic circuit. The bias point refers to the steady-state operating condition of an active device with no input signal applied. Therefore, a bias voltage is applied to the PIN diode in electronic switches to allow its operation in a particular region with minimum resistance.

Each of the switches is built using two capacitors acting as DC blocks, two RF chokes in the form of inductors and a PIN diode with a DC supply [3, 5, 8]. The DC source supplied to the inductor eventually shorts the circuit, whereas the capacitor functions as a DC choke to ensure current flow in the other direction, switching the PIN diode into its ON state. Figure 1 shows the fabricated RF switches on the antenna feed lines. The DC is supplied through the white wire and shorted to the ground via black wire.

The BAR50-02 V PIN diode from Infineon Technologies is capable of controlling the RF current for switching and attenuation. It is especially useful as an antenna switch for mobile communication between the ranges of 10 MHz to 6 GHz. From the datasheet, a minimum voltage of 0.95 V is required to operate the PIN diode at low forward resistance.

This research investigates other inductor and capacitor values from [6–8] in the biasing circuit for the proposed reconfigurable WiMAX antenna. This lead to the proposed four sets of PIN diode switches tabulated in Table 1. The commercial capacitor (C) values; 47, 100, 150, and 330 pF and inductor (L) values; 18, 27, 39 and 56 nH are considered. By minimizing the S_{11} and maximizing the S_{21} in the PIN diode’s ON and OFF states, this research will propose four sets of PIN diode switches based on the best pair of C and L. The modelling of this circuit is

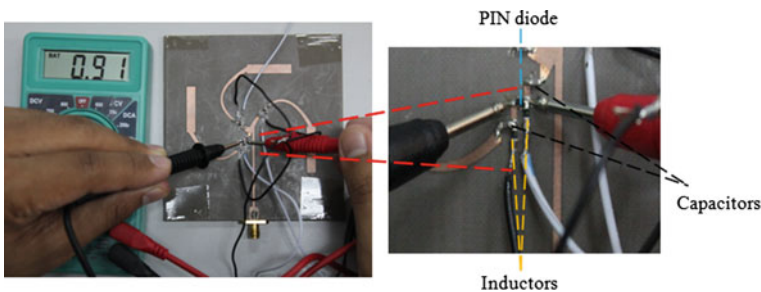


Fig. 1 Circuit verification of PIN diode performance

Table 1 Result analysis of various capacitor and inductor values

| pF | nH | V = 0 V (Diode OFF) | | V = 5 V (Diode ON) | |
|---------|--------|--------------------------------------|-----------------------------------|-----------------------------------|-----------------------------------|
| | | S ₁₁ (f = 2.35 GHz) dB | S ₂₁ (f = 2.35 GHz) | S ₁₁ (f = 2.35 GHz) | S ₂₁ (f = 2.35 GHz) |
| C = 47 | L = 18 | -0.756 | -8.004 | -16.125 | -0.145 |
| | L = 27 | -0.745 | -8.048 | -20.39 | -0.076 |
| | L = 39 | -0.733 | -8.124 | -24.78 | -0.051 |
| | L = 56 | -0.721 | -8.189 | -29.98 | -0.041 |
| C = 100 | L = 18 | -0.763 | -7.699 | -15.32 | -0.046 |
| | L = 27 | -0.751 | -8.029 | -19.144 | -0.090 |
| | L = 39 | -0.738 | -8.097 | -22.78 | -0.059 |
| | L = 56 | -0.727 | -8.155 | -26.61 | -0.046 |
| C = 150 | L = 18 | -0.755 | -7.965 | -15.109 | -0.172 |
| | L = 27 | -0.746 | -8.023 | -18.77 | -0.094 |
| | L = 39 | -0.734 | -8.088 | -22.23 | -0.062 |
| | L = 56 | -0.723 | -8.145 | -25.79 | -0.048 |
| C = 330 | L = 18 | -0.757 | -7.93 | -14.88 | -0.179 |
| | L = 27 | -0.753 | -8.072 | -18.45 | -0.099 |
| | L = 39 | -0.741 | -8.11 | -21.74 | -0.066 |
| | L = 56 | -0.731 | -8.17 | -25.04 | -0.050 |

performed based on the scattering matrix theory, explained by the analogy of a single section, quarter-wave impedance transformer. An electrical network may be described by an unlimited number of S-parameters ports, but in this work, our analysis is limited to a two-port circuit switch.

3 PIN Diode Switch Configuration Proposed

Based on the equivalent biasing circuit model shown in Fig. 2, a series of circuit simulations are performed using Agilent's ADS software. The lines depict the electrical path, whereas the V_{DC} and the V_{in} are the DC switch control voltage and the RF signal, respectively. The 0 V/5 V V_{DC} source is supplied to the circuit to switch the inductor (L1) and PIN Diode into its ON or OFF states accordingly. In addition to that, two 50 Ω loads are used to terminate port 1 and port 2 to determine the reflection and transmission parameter; S₁₁, S₂₂ and S₂₁, S₁₂ respectively, one after another.

The proposed set of the PIN diode switch is based on the circuit analysis done on commercial inductor values. It considered for ON and OFF state conditions. The first set; C = 47 pF with varying L of; 18, 27, 39 and 56 nH. The second set; C = 100 pF with varying L of; 18, 27, 39 and 56 nH. The third set; C = 150 pF with varying L of; 18, 27, 39 and 56 nH. The fourth set; C = 47 pF with varying L of; 18, 27, 39 and 56 nH.

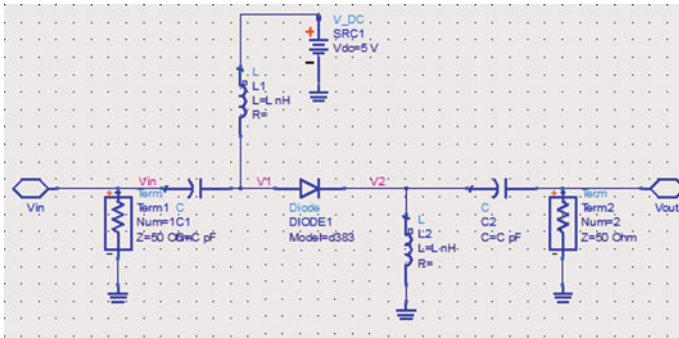


Fig. 2 Schematic of the circuit model from the ADS software

The first analysis is performed for a capacitor value of 47 pF integrated with inductor values of L ; 18, 27, 39 and 56 nH. Analysis of is based on its S_{11} and S_{21} at each of the PIN diode's *OFF* and *ON* conditions. As in Fig. 3, the combination of $C = 47$ nH and $L = 56$ nH (highlighted in black) indicates the maximum S_{11} and the highest S_{21} isolation. Even as the PIN diode is in the ON state, the S_{11} resulted in a value close to -30 dB and high transmission, with S_{21} close to 0 dB, indicating V_{in} is approximately equivalent to V_{out} as depicted in Fig. 4.

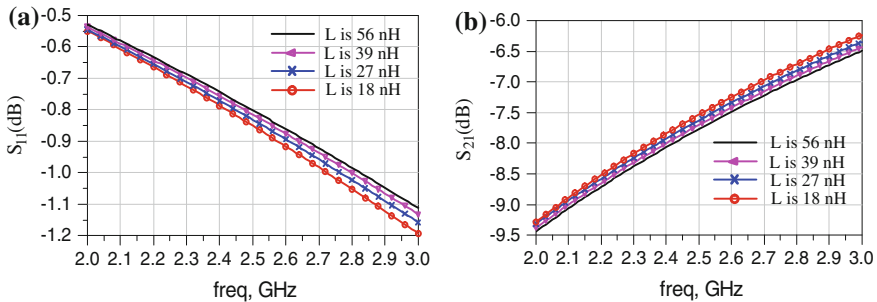


Fig. 3 Circuit analysis of $C = 47$ pF with various L in OFF state. a S_{11} . b S_{21}

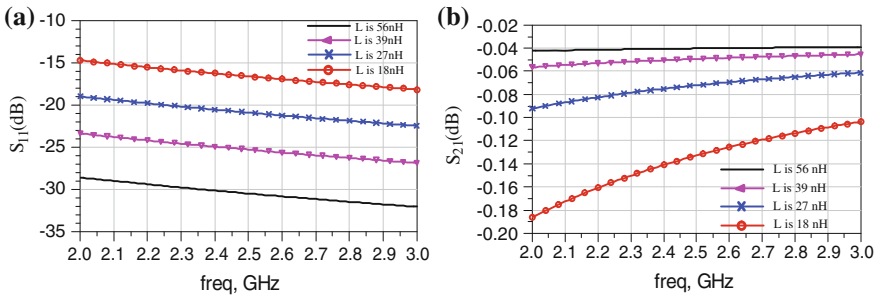


Fig. 4 Circuit analysis of $C = 47$ pF with various L in ON state. a S_{11} . b S_{21}

4 Analysis and Measurement

The circuit verification results for the reconfigurable WiMAX antenna are shown in Table 1. In order to get better isolation and transmission of RF power during OFF and ON states, we use four optimum inductor values of 18, 27, 39 and 56 nH and capacitors of 47, 100, 150, and 330 pF for the circuit shown in Fig. 2. All these values are commercial devices and available in the market. Their selection is based on the literature review and varied with some tolerance.

For each ON and OFF PIN diode stage (0 and 5 V DC supply), its S_{21} and S_{11} are shown in Table 1. During the circuit deactivation/OFF state, the PIN diode is an open circuit and no RF current is able to pass-through. Ideally, S_{21} indicates high isolation with zero transmission, whereas $S_{11} = 0$ dB depicts 100 % power reflection. In the circuit activation/ON condition, the PIN diode is in a short circuit and maximum RF current is transferable. Ideally, the S_{11} should be minimized to achieve better impedance matching while S_{21} will have 100 % power transmission.

It is clear from Table 1 that during the 0 V DC supply (PIN diode is OFF), the S_{11} is around -0.74 dB (almost 86 % reflection of RF power) while its S_{21} represent nearly 8 dB isolation. On the other hand, during the 5 V DC supply (PIN diode is ON) S_{11} is around -20 dB (nearly 1 % reflection of RF power) and S_{21} shows nearly 0 dB isolation. However, the transmission and isolation of RF power during the circuit switch ON and OFF improved with the increasing value of inductor for all capacitor values. Based on the circuit analysis summarized in Table 1, this research proposed four sets of PIN diode switch configuration; set 1: $C = 47$ pF, $L = 56$ nH, set 2: $C = 100$ pF, $L = 56$ nH, set 3: $C = 150$ pF, $L = 56$ nH.

5 Reconfigurable WiMAX Antenna (RWA)

To proof the concept of the circuit biasing technique, the proposed set of PIN diode switches with L is 100 pF and C is 56 nH are implemented into the reconfigurable antenna. The antenna is fabricated on a Taconic substrate with relative permittivity of 2.2, substrate thickness of 1.5748 mm, copper thickness of 35 μm and loss tangent of 0.0009. Minimum loss tangent value avoids the attenuation of the signal through the substrate.

Figure 5 shows the proposed antenna fed using an aperture coupled feed technique. It is separated by the top and bottom substrates denoted as radiators and feed line respectively. The PIN diode switches integrated in the feed network avoids spurious radiation which eventually increases antenna efficiency [6–8]. The proposed antenna resonates at 2.39 GHz and operates between 2.38 and 2.41 GHz with a S_{11} of less than -10 dB. Moreover, this novel antenna successfully generated directional beams at 320° or 35° and divisive broadside beams at 43° and 330° .

The proposed switching circuit is then developed in CST using two methods, namely; (1) copper strip line representation; and (2) touchstone block

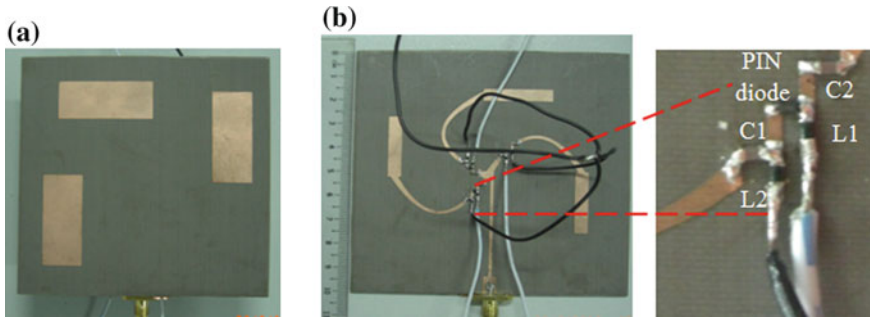


Fig. 5 Geometry of the fabricated antenna structure. **a** Radiating element surface. **b** Spiral feed network integrates with RF switches

implementation [1, 2]. The presence of the copper strip line indicates the ON state (as the current is allowed to flow), whereas its absence indicates the OFF state (with the gap existing between the two points). Touchstone blocks (TSB) denoted as SnP file characterizes the n -port network parameters of an n -port active device or a passive network [9].

Figure 6a, b show the simulated and measured reflection coefficients of the proposed antenna. Regardless of the switch configurations, the simulated reflection coefficient achieved resonant at 2.39 GHz with a high impedance matching of nearly -30 dB. Meanwhile, the measured reflection coefficient is slightly shifted by 10 MHz to the left. Besides, it produced a better return loss of approximately 15 dB compared to the simulated. It is worth noting that a proper alignment between the proposed antenna spiral feed line (bottom substrate) and its radiating elements (top substrate) must be ensured to enable good agreements between simulations and measurements. However, these losses are acceptable since the WiMAX operating frequency is less than $S_{11} < -10$ dB.

Figure 7 depict the measured radiation patterns using different PIN diode configurations. It is observed that the main pattern is radiated on the y - z axis at the

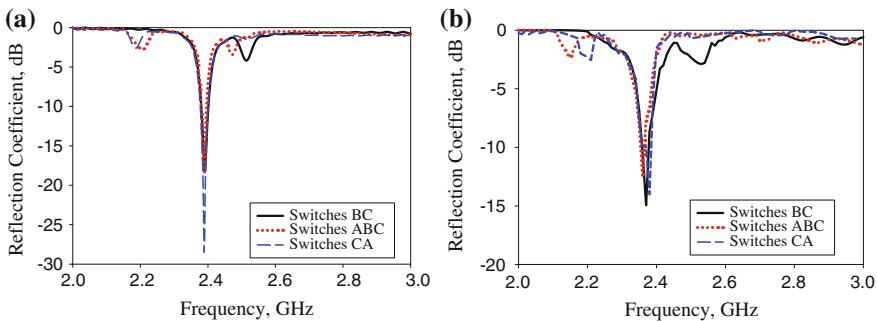


Fig. 6 Reflection coefficient of the proposed antenna. **a** Simulated. **b** Measured

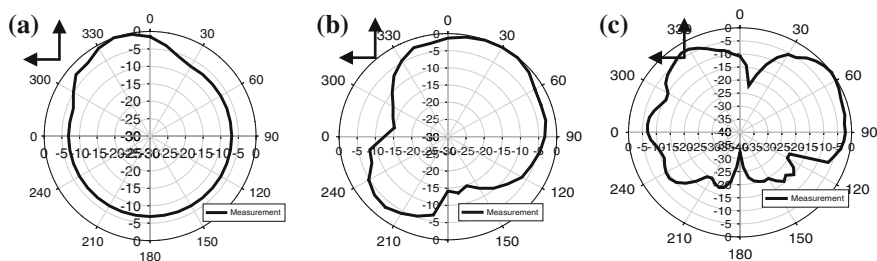


Fig. 7 Measured radiation patterns. **a** Switches B and C are ON. **b** Switches A, B and C are ON. **c** Switches A and C are ON. Switches not mentioned are OFF

resonance frequency of 2.39 GHz. By controlling the PIN diode switches and the implementation of the spiral feed arm design, the proposed antenna is capable of the reconfigurable beam feature. The rectangular radiating element and spiraling feed at 0, 90 and 180° contributed to the phase shift. Therefore, the main lobe radiation can be tuned to the desired direction with specific PIN diode switch configuration at the specific location. This resulted in either a directional beam at 320 or 35°, or divisive broadside beams at 43 and 330°. As PIN switches B and C are ON, the antenna steers the radiation pattern towards 320° with a gain of 3.35 dBi. By turning ON all switches, the measurement shows that the proposed antenna directs the beam to 35° with optimum major lobe of 2.8 dBi as shown in Fig. 7b. When the switch C and A are ON, the antenna achieved divisive broadside beam at 43 and 330° with a gain of 3.21 and 2.95 dBi respectively. The highly directional peaks have been enabled by a proper feed line to radiating surface matching and coupling using an appropriate size, position and shape of aperture slots. Measurements also indicate a very good agreement with simulations, as the directional and divisive broadside beam radiation patterns are successfully formed.

6 Conclusion

Four novel sets of PIN diode switch are proposed and analyzed; set 1: $C = 47$ pF, $L = 56$ nH, set 2: $C = 100$ pF, $L = 56$ nH, set 3: $C = 150$ pF, $L = 56$ nH. The performance of each configuration is validated via ADS software. During the 0 V DC supply (PIN diode OFF), the S_{11} has 86 % of power reflection and S_{21} indicates 8 dB of power isolation. When 5 V DC is insert (PIN diode ON), the resulting S_{11} indicates only 1 % of power reflection and S_{21} of close to 0 dB isolation, showing that the V_{in} is approximately equivalent to V_{out} . It is discovered that the transmission and isolation of RF power during PIN diode in the ON and OFF state is improved by incrementing the inductor values towards the capacitor values. Nonetheless, the proposed reconfigurable antenna works well with the integration of the proposed

PIN diode switch values of C of 100 pF and L of 56 nH. Besides being compact, the control of the PIN diode in the proposed antenna enabled beam configurability, either with a directional beam at 320 or 35° and with divisive beams at 43, 330°.

Acknowledgments The authors would like to thank Research University Grant UTM (Vote 05H34 and 00M22), Ministry of Higher Education, Universiti Teknologi Malaysia (UTM) and Universiti Malaysia Perlis (UniMAP) for their support and encouragement.

References

1. Jusoh, M., Sabapathy, T., Jamlos, M.F., Kamarudin, M.R.: Reconfigurable four-parasitic-elements patch antenna for high-gain beam switching application. *IEEE Antenna Wirel. Propag. Lett.* **13**(1), 79–82 (2014)
2. Jusoh, M., Aboufoul, T., Sabapathy, T., Alomainy, A., Kamarudin, M.R.: Reconfigurable multi-directional beam of microstrip patch antenna using PIN diode switch for WiMAX application. *IEEE Antenna Wirel. Propag. Lett.* **13**, 1–4 (2014)
3. Row, J.-S., Shih, C.-J.: Polarisation-diversity ring slot antenna with frequency agility. *IEEE Trans. Antenna Propag.* **60**(8), 271–277 (2012)
4. Chen, R.-H., Row, J.-S.: Single-fed microstrip patch antenna with switchable polarization. *IEEE Trans. Antenna Propag.* **56**(4), 66–68 (2008)
5. Ali, M.T., Tan, M.N.M., Rahman, T.A., Kamarudin, M.R., Jamlos, M.F., Sauleau, R.: A novel reconfigurable planar antenna array (RPAA) with beam steering control. *Prog. Electromagn. Res. B* **20**, 125–146 (2010)
6. Hamid, M.R., Gardner, P., Hall, P.S., Ghanem, F.: Switchable wideband-narrowband tapered slot antenna. In: *Loughborough Antennas and Propagation Conference*, pp. 241–244. Loughborough, UK, 16–17 November 2009
7. Jusoh, M., Jamlos, M.F., Kamarudin, M.R., Malek, M.F., Romli, M.A., Ahmad, Z.A., Mat, M.H., Zulkefli, M.S.: A reconfigurable ultra-wideband (UWB) compact tree-design antenna system. *Prog. Electromagn. Res. C* **30**, 131–145 (2012)
8. www.agilent.com

Design of Bandpass Filter Based on Metamaterial Concepts

Ahmed Hameed Reja, Syed Naseem Ahmad and Asaad A.M. Al-Salih

Abstract A design of an ultra-wideband (UWB) bandpass filter (BPF) is presented depending on the composite right/left handed-transmission line (CRLH-TL) basis. The interdigital (ID) coupled lines and complementary split ring resonators (CSRRs) are the tools used to realize an UWB microwave filter with an appreciable size reduction and better performance. The bandwidth resulted from this filter is 5.6 GHz operating at 3.2 GHz center frequency. The interdigital elements are connected to the input and output ports through square closed rings in the upper side of the microstrip line, whereas the CSRRs are etched in the ground of the microstrip line. All components contribute together to get metamaterial (MTM) media containing negative permittivity and negative permeability. The simulated results show that the filter has a flat insertion loss of less than 1 dB with an acceptable return loss performance in the frequency range (0.4–6) GHz. The achieved quality factor is equal to 0.57 and the fractional bandwidth is over 100 %.

Keywords Bandpass · Filter · Interdigital · Metamaterial · Resonator · Ultra-wideband

A.H. Reja (✉)

Electromechanical Engineering Department, University of Technology, Baghdad, Iraq
e-mail: ahmad8171@yahoo.com

A.H. Reja · S.N. Ahmad

Electronics and Communication Engineering Department, Jamia Millia Islamia,
New Delhi, India
e-mail: snahmad@jmi.ac.in

A.A.M. Al-Salih

Electrical Engineering Department, University of Baghdad, Baghdad, Iraq
e-mail: alsalih1996@yahoo.co.in

1 Introduction

The design of UWB devices such as filters is required in the UWB systems used in microwave and other similar applications. To miniaturize a system, the devices inside the system must also be miniaturized. Metamaterials (MTMs) concept was involved as the key to solve this problem. The basic properties of MTMs were proposed theoretically by V.G. Veselago at the end of 1967, representing the first MTM with negative media properties of permittivity (ϵ_r) and permeability (μ_r) [1]. The design of the UWB planar filters and some other relevant devices using CSRRs [2] has actually taken a great advantage of the new compact designs [3]. The MTM components have thus become powerful elements in microwave technology due to their sub-wavelength dimensions [4]. The CSRRs are thereby etched in the lower plane of the microstrip to remove the undesired frequency spurious band [5].

In the last decades, several techniques for the design of UWB filters based on MTM components have been witnessed [6]. Whereby, a microstrip of UWB-BPF centered at 3.4 GHz with 4.8 GHz bandwidth has been introduced. The insertion loss (S_{21}) of this filter was less than 0.9 dB and the return losses (S_{11}) were better than 10 dB [7]. Furthermore, the design analysis of an UWB filter based on CRLH-TL concept has been delineated in Refs. [8–10]. From a different perspective, Gil et al. in [11] presented the design of CRLH-TL based on CSRRs and interdigital capacitors (IDCs) with transmission bandwidth of 7.5 GHz for UWB applications in the interval (3.1–10.6) GHz. The device has had a relatively small size and reasonable performance. Further presented, fabricated, and measured was a four-cell CRLH-UWB filter based on defected ground structure (DGS) and microstrip IDC. In addition, an UWB filter with passband range (3.2–7.5) GHz and insertion loss of less than 0.5 dB has also been achieved [12]. Within a different approach, an UWB filter combining a conventional bandpass characteristic, and negative permittivity (ϵ_r) MTM made of CSRRs was presented. Hereby, a new technique to improve the matching between the host TL and the CSRRs was proposed. The filter has had bandwidth of 8.4 GHz, an insertion loss of less than 1 dB and a 22 dB rejection at 5.4 GHz [13]. Moreover, a simplified left-handed transmission line (LH-TL) structure-based UWB-BPF has been proposed. The filter has thereby had a return loss of higher than 12 dB, and the group delay was approximately 0.25 ns at the pertinent bandpass interval [14].

From another corner, an UWB filter using fractal shape or CSRRs structures etched in the ground plane as a DGS and series capacitive gap in the upper conductor was fabricated and tested. The insertion loss was better than 1.5 dB except at high frequencies and the bandwidth of the 10 dB return loss was 128 % [15]. Besides, a compact UWB-BPF based on open circuited lines planted in a DGS was proposed. The equivalent circuit model of this filter with notch implementation was also presented. In this filter the insertion loss was whereby less than 1 dB throughout the passband range of (3.1–10.6) GHz with 7.5 GHz bandwidth and the group delay in the passband interval was less than 0.2 ns except for the notched band [16]. On the other hand, the process of adding capacitive cross coupling to the

conventional CRLH structure has led to control the phase shift in the right-handed passband. A compact UWB-BPF with good selectivity, low insertion loss of less than 1.35 dB, rejection level of higher than 20 dB at the stopband range of (11.95–16) GHz, and flat group delay across the passband was thereby obtained [17]. Another attempt in the field exhibited the design procedure of a compact BPF in UHF CRLH-TL. The CRLH-TL was utilized to miniaturize the overall size up to 80 % at 0.61 GHz and reject higher ordered harmonics up to 4th order [18]. From a different corner, a compact UWB-BPF using single unit cell CRLH-TL was designed. It operated from (4–9.5) GHz with $S_{21} < -1.5$ dB, and reduced total size up to 7 % [19]. Ahmed Reja et al. in March 2014 was manifested a study about the effect of adding MTM components on the conventional microstrip in the LPF design [20]. They have further upgraded their efforts in the same year through developing new UWB-BPFs based on tuning forks (TFs) shape and CSRRs [21].

This paper presents an UWB-BPF based on CRLH-TL. The ID-TLs and CSRRs are both used to miniaturize the filter size and for appreciable performance in microwave filters design. In addition, to improve the performance more and more, the closed rectangular rings have been connected to input and output ports of the filter. All those components contribute together in order to get MTM media that has negative index of refraction (n) by which the device has been miniaturized. This paper complements the work of the last-mentioned two other earlier works in the field [20, 21].

2 Microwave Frequency Description

The microwave frequency band description is listed in Table 1. The concentration in this work on a range of microwave frequencies has been restricted to cover U to C bands of frequencies for pragmatic technical reasons. Some of its applications are illustrated in Table 2.

3 CRLH-TL Circuit Model

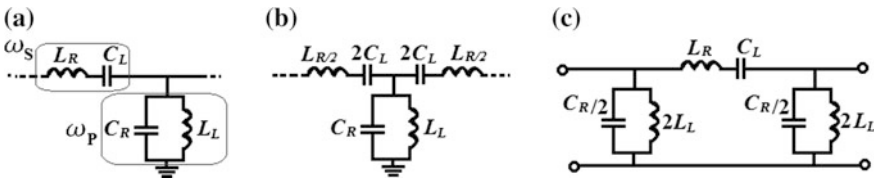
In this work, an UWB-BPF is designed based on CRLH-TLs concept. CSRRs etched in the ground plane and ID-TLs printed on the upper side of microstrip line are introduced to satisfy the necessity of the filter design. The equivalent circuits of the CRLH-TL are shown in Fig. 1a [8], b [4], and c [22]. The filter takes on bandpass property under the balanced case and illustrates the series resonance (ω_s)- and the shunt resonance (ω_p)-angular frequencies as

Table 1 Description of microwave frequency band

| Description of microwave frequency band | | |
|---|-----------------|----------------------------------|
| Frequency (GHz) | Wavelength (mm) | Photon energy (μeV) |
| 0.3–300 | 1000–1 | 1.24–1240 |

Table 2 Part of microwave frequencies and some of its applications

| Microwave frequencies with its applications | | | |
|---|-----------------------|-----------------|---|
| Band | Frequency range (GHz) | Wavelength (mm) | Applications |
| U | 0.3–1 | 1000–300 | TV broadcasts, FRS and GMRS radios, microwave devices, radio astronomy |
| L | 1–2 | 300–150 | GPS, GSM, military telemetry |
| S | 2–4 | 150–75 | Surface ship and weather radars, GPS, mobile phones, wireless communications, satellites, microwave devices and ovens |
| C | 4–8 | 75–37.5 | Telecommunications, long-distance radio |

**Fig. 1** CRLH-TL equivalent circuits. **a** Unit cell. **b** T-circuit model. **c** Pi-circuit model

$$\omega_s = \frac{1}{\sqrt{C_L L_R}} \text{ rad/s}, \quad \omega_p = \frac{1}{\sqrt{C_R L_L}} \text{ rad/s} \quad (1)$$

The center frequency (f_o) of the passband is expressed as [8] as

$$f_o = \sqrt{f_{cL} \cdot f_{cR}} = \frac{1}{2\pi \cdot \sqrt{4L_R C_R L_L C_L}} \quad (2)$$

where, f_{cL} , f_{cR} are the high- and low-cutoff frequencies of pure left hand (LH)-TL and pure right hand (RH)-TL, respectively. L_R , C_R , L_L and C_L are the RH and LH inductances and capacitances respectively. To get UWB filter, L_L , C_L must be as large as possible while L_R , C_R as small as possible in case of CRLH-TL.

4 Components of the Proposed UWB Filter Design

4.1 CSRRs Structure

CSRRs are interesting particles introduced by Falcone et al. in [23] and J. D. Baena et al. in 2005 [24]. The topology of the CSRR unit cell coupled with TL and its equivalent circuit are illustrated in Fig. 2. The CSRRs components were presented to produce a negative effective permittivity (ϵ_r) at resonance frequency depending

Fig. 2 CSRR unit cell, **a** topology, **b** equivalent circuit model

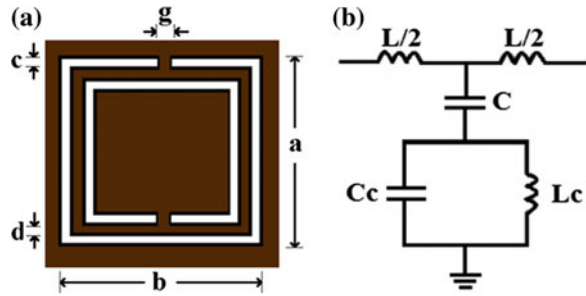


Table 3 Characteristics of CSRRS

| a (mm) | b (mm) | c (mm) | d (mm) | g (mm) | f_c (GHz) | f_o (GHz) | BW (GHz) |
|--------|--------|--------|--------|--------|-------------|-------------|----------|
| 3.5 | 3.5 | 0.2 | 0.1 | 0.1 | 6.0 | 3.2 | 5.6 |

on its dimensions. CSRRs elements are etching in the ground plane of the microstrip line as a defected ground structure (DGS) without any extra space added, and hence, it is effective for miniaturizing microwave devices. The equivalent circuit model of CSRRs loaded TLs and their equivalent values of the pertinent intrinsic inductances and capacitances can be calculated using methods which are delineated in [24]. It is essential that both the insertion loss and return loss ought to be improved if this structure were to be integrated into the UWB filter design.

The calculations were performed to obtain the relative effective permittivity (ϵ_r) from the scattering parameters (S_{21} and S_{11}) of the proposed CSRR MTMs [25, 26]. The simulation results of the structure can be obtained using high frequency structure simulator (HFSS). Three cells of CSRRs with 0.1 mm gap between them were used. The optimized dimensions of CSRRs structure have been set to overcome the tail in the upper side of response curve and to get reduction in size of the design. The parameters in Table 3 manifest that the rings achieved sharp cutoff beyond 6.0 GHz to limit the width of band into 5.6 GHz, with center frequency (f_o) of 3.2 GHz.

4.2 Interdigital (ID) Coupled Lines Structure

The generalized model of the single ID coupled lines structure and its equivalent circuit are illustrated in Fig. 3. The geometry of an n-number of fingers of interdigital line (n_{ID}) described with finger width (W), finger length (l) and the spacing between two adjacent fingers (S). The space (S) in ID coupled lines taken as small as possible (practically ≥ 0.1 mm) to get high matching and coupling. The dimensions of this structure are chosen with respect to the required frequency (f_o).

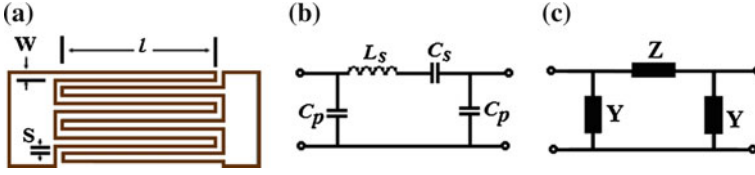


Fig. 3 Proposed ID coupled lines, **a** topology of generalized model, **b** equivalent circuit model, **c** auxiliary equivalent circuit model

To calculate the circuit parameters shown in Fig. 3b; L_s (very small and can be neglected), C_s , and C_p , firstly, the S-parameters of the ID coupled lines are determined using computer aided design (CAD). After that, S-parameters are converted into admittance parameters (Y) and impedance parameters (Z), using standard conversion formulae as shown in the equivalent circuit in Fig. 3c. Finally, the parameters of ID coupled lines equivalent circuit are obtained [8].

The capacitance of ID line shape is given as follows [27].

$$C_{ID}(pF) = \frac{\epsilon_{eff} \cdot (n_{ID} - 1) \cdot l \cdot K(k)}{18\pi \cdot 10^{-3} \cdot K'(k)} \quad (3)$$

The value of effective permittivity (ϵ_{eff}) in case of $W/h < 1$ is expressed in (4) while the approximated value is the first part of (5) and mainly it depends on dielectric constant (ϵ_r).

$$\epsilon_{eff} = \frac{\epsilon_r + 1}{2} + \frac{\epsilon_r - 1}{2} \left[\frac{1}{\sqrt{1 + \frac{12h}{W}}} + 0.04 \left(1 - \frac{W}{h}\right)^2 \right] \quad (4)$$

$$k = \tan^2 \left(\frac{W \cdot \pi}{4(W + S)} \right), \quad k' = \sqrt{1 - k^2} \quad (5)$$

$$\frac{K(k)}{K'(k)} = \frac{\pi}{\ln \left[2 \frac{1 + \sqrt{k'}}{1 - \sqrt{k'}} \right]} \quad (6)$$

$K(k)$ and $K'(k)$ are the complete elliptic integral of the first kind and its complement. l is the length of each finger. The approximate formula (7) is commonly used to quickly approach the inductance (with presence of the ground stub) in case of the interdigital line (L_{ID}). The substrate height (h) and thickness metallization (t) are the requested value for this calculation.

$$L_{ID}(nH) = 2l \times 10^{-4} \left[\ln \left(\frac{l}{W + t} \right) + 1.193 + \frac{0.224(W + t)}{l} \right] \cdot K_g \quad (7)$$

$$K_g = 0.57 - 0.145 \ln\left(\frac{W}{h}\right) \quad (8)$$

The design dimensions are $W = 0.2$ mm, $S = 0.035$ mm, and $l = 9.5$ mm, which are smaller than quarter wavelength account for strong capacitive coupling to achieve the UWB filtering. Whereas, the input and output ports formed as rectangular closed rings with 0.2 mm width.

5 Simulation Results of UWB-BPF

In this work, the design is applied on the Rogers RT-duroid 5880 substrate that has ϵ_r of 2.2, substrate height (h) of 0.5 mm. The HFSS has been used as assistant tool for simulation, and the important detailed results were the transmission (S_{21})- and reflection (S_{11})-coefficients. From scattering parameters details, the group delay (τ_d), voltage standing wave ratios (VSWRs), and quality factor (Q) have been calculated using the formulae below. The group delay (τ_d) is hereby given as in [20].

$$\tau_d = \frac{d\angle_{21}}{d\omega} \quad \text{s} \quad (9)$$

$$VSWR_1 = \frac{1 + |S_{11}|}{1 - |S_{11}|}, \quad VSWR_2 = \frac{1 + |S_{22}|}{1 - |S_{22}|} \quad (10)$$

$$Q = \frac{f_o}{BW} \quad (11)$$

where \angle_{21} is the phase angle of S_{21} in radians, ω is the angular frequency in radians per second and BW is the bandwidth in GHz.

The possibility of designing UWB filters operating in microwave frequencies region is available. The UWB-BPF design presented is shown in Fig. 4; having four fingers in each side in opposite direction in the upper plane of a microstrip line. These fingers are connected to the closed rectangular rings terminated with the

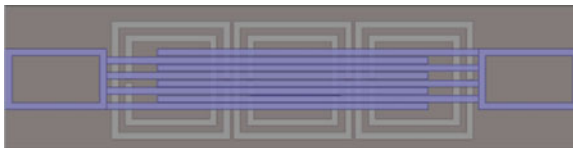


Fig. 4 Geometric design of UWB-BPF

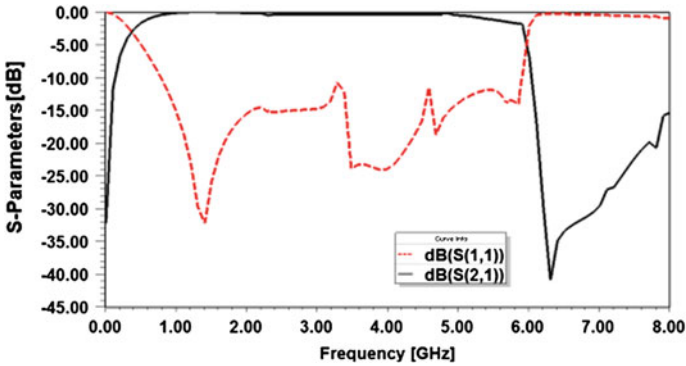


Fig. 5 Frequency response of UWB filter

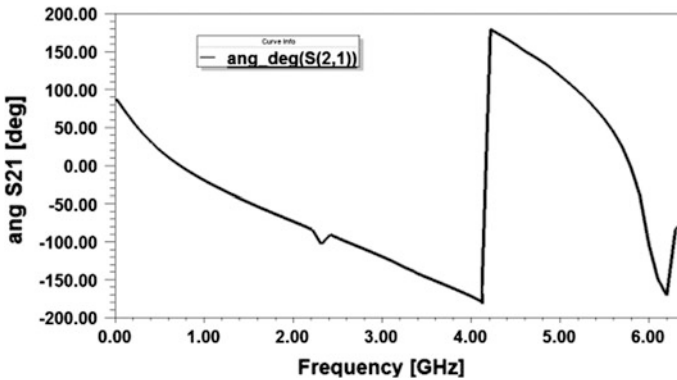


Fig. 6 The phase of UWB filter

input and output ports. Every ring has external dimensions of $1.8 \text{ mm} \times 3 \text{ mm}$ and strip width equal to 0.2 mm .

The process of etching three unit cells of CSRRs in the ground plane of the microstrip line is essentially useful to overcome the tail of transmission response. The overall external dimensions of the design is $17 \text{ mm} \times 4.3 \text{ mm}$. The variations of S-parameters and phase response for this filter are shown in Figs. 5 and 6, respectively. The maximum attenuation of $|S_{11}|$ is approximately 33 dB at 1.4 GHz. The bandwidth of bandpass is equal to 5.6 GHz starting from 0.4 to 6 GHz. The group delay and VSWRs are shown in Figs. 7 and 8, respectively. The group delay variation is nearly constant and equal to 0.15 ns in passband interval except at 2.1 GHz, while the VSWRs are smaller than 2 in passband interval.

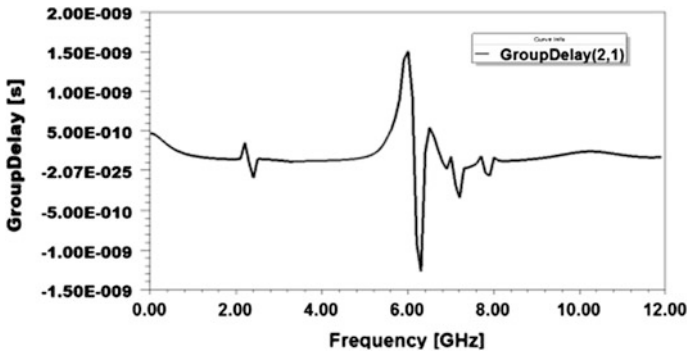


Fig. 7 Group delay of UWB filter

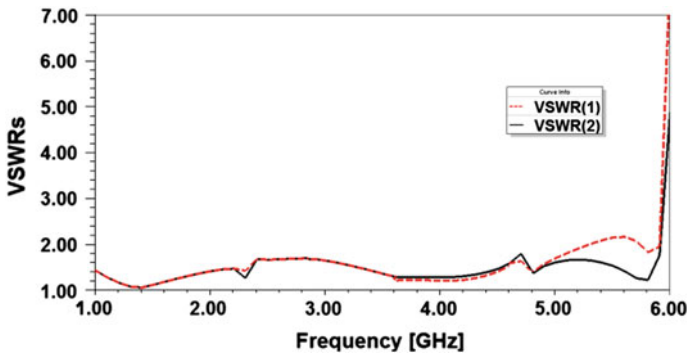


Fig. 8 VSWRs of UWB filter

6 Comparison with Other Works

A comparison between this work with some other works in [21, 28, 29] of UWB filters related to resonance frequency (f_o), bandwidth (BW), length of device (l), insertion loss (S_{21}), return loss (S_{11}), and quality factor (Q) are listed in Table 4. The approximate miniaturization in the presented design is 53 % compared to the design in [28]. The roll-off has sharp cutoff in this design better than other designs.

Table 4 Comparison between different UWB filters design

| Design | f_o (GHz) | BW (GHz) | Length l (mm) | IL _{max.} S_{21} (-dB) | RL _{min.} S_{11} (-dB) | Q |
|-----------------|-------------|----------|-----------------|-----------------------------------|-----------------------------------|-------|
| [21] | 5.4 | 10 | 17 | 0.05 | 32 | 0.5 |
| [28] | 6.85 | 8 | 17.3 | 1 | 12 | 0.856 |
| [29] | 5.8 | 2 | 17 | 0.1 | 20 | 2.9 |
| Proposed design | 3.2 | 5.6 | 17 | 0.05 | 12 | 0.57 |

7 Conclusion

A new idea for designing an UWB microwave MTM filter using ID couple lines and CSRRs components is presented. This design has been achieved and improved into wideband width equal to 5.6 GHz at 3.2 GHz resonance frequency. The design achieved flat insertion loss of lesser than 1 dB and return loss better than 12 dB. The stopband roll-off has very sharp slope in the upper cutoff frequency. The miniaturization of the filter with controllable bandwidth has been achieved depending on CSRRs dimensions. The BPF performance has been simulated and optimized depending on finite element method (FEM).

Acknowledgments The authors express their gratitude to the Ministry of Higher Education and Scientific Research in Baghdad—Iraq and Jamia Millia Islamia in New Delhi—India for supporting this work.

References

1. Veselago, V.G.: The electrodynamics of substances with simultaneously negative values of ϵ and μ . *Usp. Fiziol. Nauk* **92**, 517–526 (1967)
2. Falcone, F., Lopetegi, T., Laso, M.A.G., Baena, J.D., Bonache, J., Beruete, M., Marqués, R., Martín, F., Sorolla, M.: Babinet principle applied to metasurface and metamaterial design. *Phys. Rev. Lett.* **93**(12), 197401(1–4) (2004)
3. Solymar, L., Shamoniina, E.: *Waves in Metamaterials*. Oxford University Press, New York (2009)
4. Marqués, R., Martín, F., Sorolla, M.: *Metamaterials with Negative Parameters: Theory, Design, and Microwave Applications*. Wiley, New York (2008)
5. Navarro-Cía, M., Carrasco, J.M., Beruete, M., Falcon, F.: Ultra-wideband metamaterial filter based on electroinductive-wave coupling between microstrips. *Prog. Electromagn. Res. Lett.* **12**, 141–150 (2009)
6. Hao, Z.-C., Hong, J.-S.: Ultrawideband filter technologies. *IEEE Microw. Mag.* **11**(4), 56–68 (2010)
7. García-García, J., Bonache, J., Martín, F.: Application of electromagnetic bandgaps to the design of ultra-wide bandpass filters with good out-of-band performance. *IEEE Trans. Theory Tech.* **54**(12), 4136–4140 (2006)
8. Caloz, C., Itoh, T.: *Electromagnetic Metamaterials: Transmission Line Theory and Microwave Applications*. Wiley, New Jersey (2006)
9. Kahng, S., Ju, J.: Left-handedness based bandpass filter design for RFID UHFB and applications. *Proc. KJMW* **1**, 165–168 (2007)
10. Ju, J., Kahng, S.: Design of the miniaturized UHF bandpass filter with the wide stopband using the inductive-coupling inverters and metamaterials. In: *Proceedings Korea Electromagnetic Engineering Society Conference 2007*, vol. 1, pp. 5–8 (2007)
11. Gil, M., Bonache, J., Martín, F.: Metamaterial filters with attenuation poles in the pass band for ultra wide band applications. *Microw. Opt. Technol. Lett.* **49**(12), 2909–2913 (2007)
12. Li, B., Dai, X.-W., Wu, B., Liang, C.-H.: Ultra wideband filter design based on composite right-/left-handed transmission line. *Microw. Opt. Technol. Lett.* **49**(10), 2379–2381 (2007)
13. Ali, A., Hu, Z.: Metamaterial resonator based wave propagation notch for ultrawideband filter applications. *IEEE Antennas Wirel. Propag. Lett.* **7**, 210–212 (2008)

14. Han, W., Feng, Y.: Ultra-wideband bandpass filter using simplified left-handed transmission line structure. *Microw. Opt. Technol. Lett.* **50**(11), 2758–2762 (2008)
15. An, J., Wang, G.-M., Zeng, W.-D., Ma, L.-X.: UWB filter using defected ground structure of von koch fractal shape slot. *Prog. Electromagn. Res. Lett.* **6**, 61–66 (2009)
16. Lin, W.-J., Houg, M.-P., Lin, D.-B., Tang, I.-T.: Investigation in open circuited metal lines embedded in defected ground structure and its applications to UWB filters. *Wireless and microwave technology conference (WAMICON)*, pp. 1–4 (2010)
17. Huang, J.-Q., Chu, Q.-X.: Compact UWB band-pass filter utilizing modified composite right/left-handed structure with cross coupling. *Prog. Electromagn. Res.* **107**, 179–186 (2010)
18. Ghahremani, B., Kamyabi, M.: The design of a novel compact CRLH band pass filter with harmonics suppression. *Prog. Electromagn. Res. C* **16**, 99–110 (2011)
19. Zulkifli, F.Y., Atmaja, A., Rahadjo, E.T.: Implementation of single cell composite right—left handed transmission line for ultra wideband bandpass filter. *Int. J. Technol.* **2**, 121–128 (2012)
20. Reja, A.H., Ahmad, S.N., Mahmoud, D.A.: Study the effect of adding new components on conventional microstrip LPF design. In: 2014 International Conference on INDIACom, pp. 42–47, 5–7 Mar 2014
21. Reja, A.H., Ahmed, S.N., Al-Salih, A.A.M.: New ultra-wideband filters based on tuning forks shape and CSRRs. In: IEEE International Conference on Aerospace Electronics and Remotesensing Technology (ICARES 2014), Yogyakarta, Indonesia, pp. 173–180, 13–14 Nov 2014 (Under Publication)
22. Kahng, S.: Ultrawideband bandpass filter using composite right- and left-handedness line metamaterial unit-cell. In: Mukherjee, M. (ed.) *Advanced Microwave and Millimeter Wave Technologies: Semiconductor Devices, Circuits and Systems*, ISBN 978-953-307-031-5, pp. 395–402, 1 Mar 2010
23. Falcone, F., Lopetegi, T., Baena, J.D., Marques, R., Martin, F., Sorolla, M.: Effective negative stop-band microstrip lines based on complementary split-ring resonators. *IEEE Microw. Wirel. Compon. Lett.* **14**(6), 280–282 (2004)
24. Baena, J.D., Bonache, J., Martin, F., Marques, R., Falcone, F., Lopetegi, T., Laso, M.A.G., Garcia, J., Gill, I., Sorolla, M.: Equivalent-circuit models for split ring resonators coupled to planar transmission lines. *IEEE Trans. Microw. Theory Tech.* **53**(4), 1451–1461 (2005)
25. Chen, X., Grzegorzczak, T.M., Wu, B.I., Pacheco, J., Kong, J.A.: Robust method to retrieve the constitutive effective parameters of metamaterials. *Phys. Rev. E* **70**(1), 016608 (2004)
26. Smith, D.R., Vier, D.C., Koschny, Th., Soukoulis, C.M.: Electromagnetic parameter retrieval from inhomogeneous metamaterials. *Phys. Rev. E* **71**, 036617 (2005)
27. Bahl, I.J.: *Lumped Elements for RF and Microwave Circuits*. Artech House, Inc., Boston (2003)
28. Zayniyev, D., Budimir, D., Zouganelis, G.: Microstrip filters and diplexers for WiMAX applications. In: *International Symposium on Antennas and Propagation Society*, pp. 1561–1564, 14–15 June 2007
29. Baik, J.-W., Han, S.-M., Jeong, C., Jeong, J., Kim, Y.-S.: Compact ultra-wideband bandpass filter with EBG structure. *IEEE Microw. Wirel. Compon. Lett.* **18**(10), 671–673 (2008)

A Comparative Study of Electromagnetic Absorption of PIFA and Helical Antenna in the Human Head

M.I. Hossain, M.R.I. Faruque and M.T. Islam

Abstract In this paper, a comparative analysis of electromagnetic (EM) absorption in the human head is presented using planar inverted-F antenna (PIFA) and helical antenna. Both antennas are designed for operating in global system for mobile (GSM) 900 MHz. The EM absorption is evaluated by using two parameters-the peak specific absorption rate (SAR) in the human head tissue and total absorbed power from the mobile phone user. Three different distance configurations are considered to take effects of distance of mobile phone from human head on EM absorption for both antennas. The investigation is based on the finite-difference time-domain (FDTD) method of CST Microwave Studio. The results show that the PIFA provides a significantly lower value of peak SAR in the human head than that of helical antenna. In case of PIFA, total absorbed power is more than 34 % than that of helical antenna.

1 Introduction

The wearable Technology i.e. a combination of wireless technology with human body is a growing trend in the field of mobile communication. The mobile phones emit electromagnetic radiation, which disrupts the biological system of the human body [1]. The effects of EM radiation on human tissues can be classified into two categories comprising thermal effects and non-thermal effects. The absorbed EM energy of the biological organism is converted into heat inside the human body. When this heat exceeds the normal heat range of organism, the temperature rise will occur, which is called thermal effect [2]. Thermal effect from EM radiation has the

M.I. Hossain (✉) · M.R.I. Faruque
Space Science Center (ANGKASA), Universiti Kebangsaan Malaysia,
UKM, Bangi, Selangor, Malaysia
e-mail: ipk_eee@yahoo.com

M.T. Islam
Department of Electrical, Electronic and Systems Engineering,
Universiti Kebangsaan Malaysia, UKM, Bangi, Selangor, Malaysia

ability to cause disruption of tissue cell function and development. Besides this, thermal effects may cause headaches, earaches, blurring of vision, and bad sleep. On the other hand, the non-thermal effects might cause the cells to activate the third messenger systems and gene expression mechanisms. The use of a mobile phone for a long period of time may lead to the Deoxyribonucleic Acid (DNA) damage, brain tumor, cancer and other diseases [3].

The defined parameter for power absorption in the human body is SAR which is directly related to the electric and magnetic field distribution in the human body tissues [4]. International authoritative bodies have defined SAR limit for the EM devices used in the vicinity of human body considering user health. American National Standards Institute (ANSI) and Federal Communication Commission (FCC) has define the SAR limit to 1.6 W/kg per 1 g of tissue [5]. International Commission on Non-Ionizing Radiation Protection (ICNIRP) and IEEE has impose the limit of 2 W/kg absorbed per 10 g of tissue.

The PIFA and helical antenna are two mostly used antennas for mobile phone. In [6], a comparison has been presented among a monopole and PIFA antenna. The size of presented handset antennas and casings are noticeably greater than modern handsets. In [7], SAR analysis has been reported for helical antenna with metallic box at 900 MHz. This investigation provides a comparative study on EM absorption in the human head phantom of PIFA and helical antenna operating at GSM 900 MHz.

2 Models and Methods

Figure 1 shows the helical antenna geometry with conducting box which operates at GSM frequency 900 MHz. The helical antenna is fed by a 50 Ω coaxial line. The E-shaped PIFA structure with FR-4 substrate (0.8 mm thickness) is shown in Fig. 2.

Fig. 1 Geometry of helical antenna with metallic box

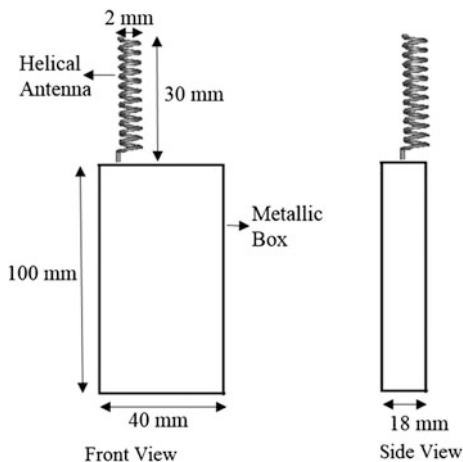


Fig. 2 Geometry of PIFA with FR-4 substrate

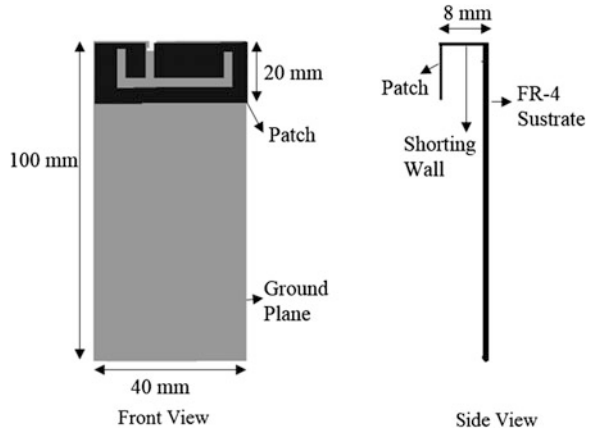
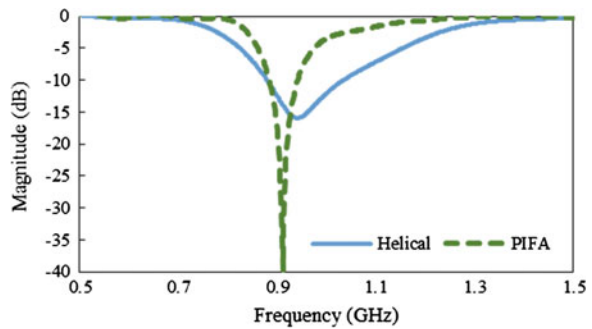


Fig. 3 Reflection coefficients (S_{11}) of PIFA and helical antenna



The PIFA consists of patch, ground, feed and shortening point. The distance between antenna patch and ground plane is 8 mm. Figure 3 indicates the reflection coefficient (S_{11}) of PIFA and helical antenna.

Three-dimensional anatomical models were used for head and hand phantom. The head model provided by the whole brain atlas website consists of six types of tissues: bone, brain, skin, muscle, fat, and eye. The electrical properties of head and hand model are listed in Table 1.

The EM radiation effects on human health is often evaluated by the parameter SAR, which is a defined figure to evaluate the power absorption in the human body. According to the definition of IEEE, SAR is defined as the time derivative of incremental energy absorption by an incremental mass contained in a volume element of a certain density, as shown in (1) [8]:

$$SAR = \frac{d}{dt} \left(\frac{dW}{dm} \right) = \frac{d}{dt} \left(\frac{dW}{\rho dV} \right) \tag{1}$$

Table 1 The electrical properties of the head and hand phantoms tissues

| Tissues | Conductivity (S/m) | Relative permittivity |
|---------|--------------------|-----------------------|
| Muscle | 1.50 | 55.95 |
| Skin | 1.48 | 49.60 |
| Brain | 1.11 | 41.7 |
| Bone | 0.12 | 4.83 |
| Fat | 0.13 | 5.10 |
| Eye | 2.03 | 68.6 |
| Hand | 1 | 20 |

where, the symbols dW and dm represent incremental energy, incremental mass respectively. ρ and V stand for density and volume respectively.

The total absorbed power by the user’s head can be calculated by formula (2) [9]:

$$P_{abs} = \frac{1}{2} \int_V \sigma |E|^2 dv \tag{2}$$

The numerical simulation of SAR values and total absorbed power were evaluated adopting the FDTD method on the Computer Simulation Technology (CST) Microwave Studio. The Fig. 4 shows the simulation setup indicating the relative positions of the mobile handset and human head model. In lossy-Drude simulation model, $128 \times 128 \times 128$ cells domain was used with cell size of $\Delta x = \Delta y = \Delta z = 3$ mm. The SAR values were evaluated adopting IEEE standard algorithm using 1 and 10 g body tissues averaging [10]. The stimulated power 600 mW was used in experimental set-up and the SAR calculation was performed in the post processing phase of the simulation.

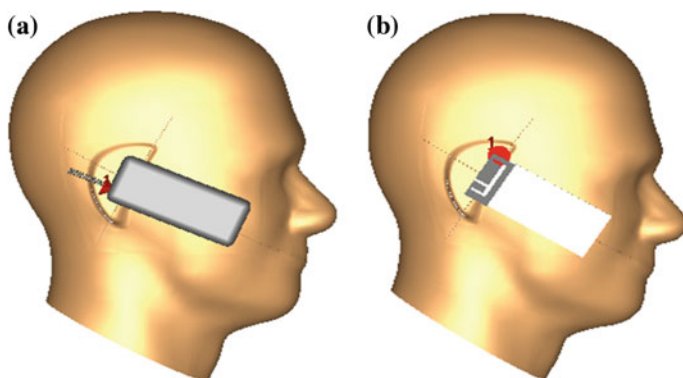


Fig. 4 Talk position configuration **a** with helical antenna **b** with PIFA

3 Results and Discussions

In this investigation, a comparison of EM absorption in the human head between helical antenna and PIFA is presented. Tables 2 and 3 represent the 3D distribution of SAR for helical antenna and PIFA with three different distance (0, 5, and 10 mm)

Table 2 1 g SAR values for PIFA and helical antenna

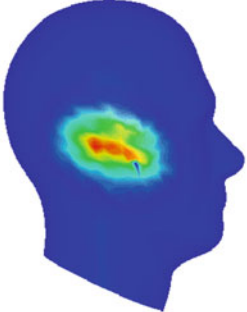
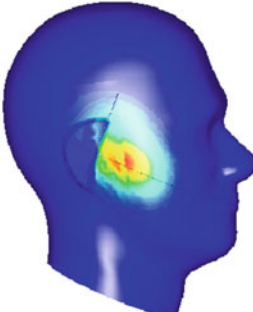
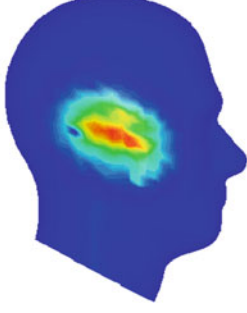
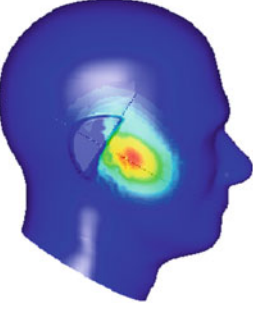
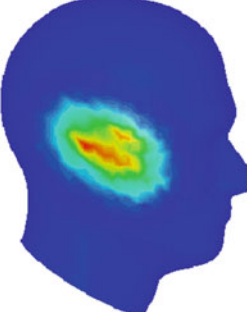
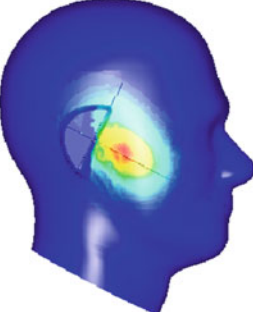
| Dis. | Helical Antenna | PIFA |
|-------|--|--|
| 0 mm |  <p>4.29 W/Kg</p> |  <p>3 W/Kg</p> |
| 5 mm |  <p>3.19 W/Kg</p> |  <p>2.45 W/Kg</p> |
| 10 mm |  <p>2.42 W/Kg</p> |  <p>1.95 W/Kg</p> |

Table 3 10 g SAR values for PIFA and helical antenna

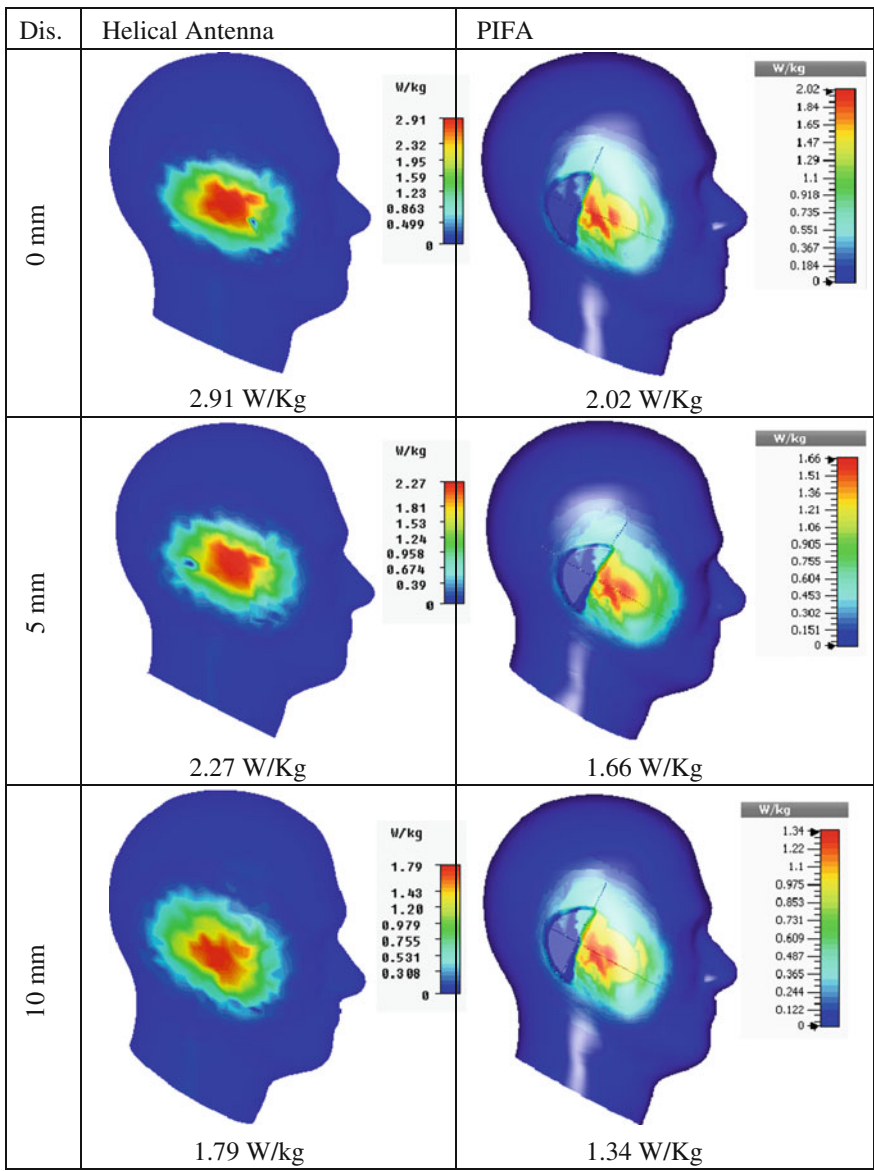
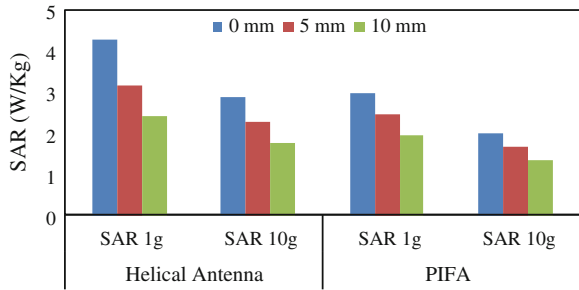


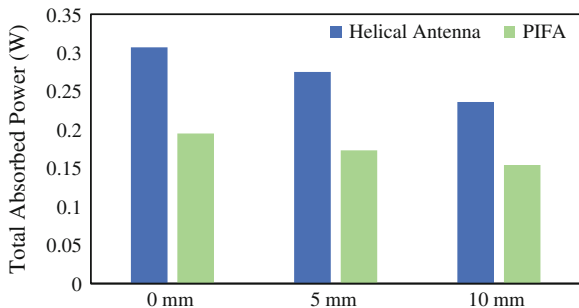
Fig. 5 SAR values for PIFA and helical antenna



configurations considering 1 and 10 g of tissue averaging respectively. Moreover, Fig. 5 shows the peak SAR values for helical and PIFA at 900 MHz with different distances. From the obtained results, it is clear that the SAR values from helical antenna are always higher than that of PIFA. For 0 mm distance configuration, helical antenna produces 30.1 % higher 1 g SAR in the human head than PIFA. Similarly, 23.2 and 19.4 % higher 1 g SAR is observed for helical antenna in case of 5 and 10 mm distance configurations respectively. In addition, PIFA provides 30.6, 26.9, and 25.1 % lower 10 g SAR than that of the helical antenna for 0, 5, and 10 mm distance configurations respectively. Increasing the distance between cell phone antenna and human head phantom results significantly lower SAR as the strength of the induced electric field is inversely proportional to the distance. For helical antenna, 5 and 10 mm distance configurations provide 25.6 and 43.6 % reduction in 1 g SAR respectively than that of 0 mm distance configuration. Similarly, 22 and 38.5 % 10 g SAR reduction can be obtained with 5 and 10 mm separation between helical antenna and head model respectively. On the other hand, PIFA shows 18.33 and 35 % 1 g SAR reduction for 5 and 10 mm spacing increment respectively. For 10 g SAR value, 5 and 10 mm configurations provide 17.8 and 33.7 % decrement respectively in case of PIFA compared with 0 mm distance configuration. The results indicate that the SAR values decrease more quickly for helical antenna with increasing distance of the antenna from the human head model.

Figure 6 illustrates the values of total absorbed power by the user’s head for both PIFA and helical antenna. The values of total absorbed power also exhibit similar tendency as like as SAR values. Comparing with helical antenna, PIFA provides

Fig. 6 Total absorbed power by user’s head for PIFA and helical antenna



significantly lower power absorption in the user's head. For 0, 5, and 10 mm distance configurations, helical antenna provides 36.5, 37.1, and 34.7 % higher absorbed power in the human head than that of PIFA.

4 Conclusion

In this paper, a comparison of EM absorption in the human head has been presented between PIFA and helical antenna at GSM 900 MHz. The SAR and total absorbed power have been computed in the human head phantom to assess which cell phone antenna has less health hazards. The obtained results indicate that the SAR from helical antenna are always higher than that of PIFA for all cases. Helical antenna produces 20 % higher 1 g SAR and 25 % 10 g SAR than that of PIFA. Increasing the separation between antenna and human head phantom results significantly lower SAR as the strength of the induced electric field is inversely proportional to the separation. The results indicate that the SAR values decrease more quickly for helical antenna with increasing distance of antenna from the human head model. In case of total absorbed power by the user's head, PIFA absorbs less than 30 % power than helical antenna.

References

1. Islam, M.T., Faruque, M.R.I., Misran, N.: SAR reduction in a muscle cube with metamaterial attachment. *Appl. Phys. A Mater. Sci. Process.* **103**(2), 367–372 (2011)
2. Wainwright, P.: Thermal effects of radiation from cellular telephones. *Phys. Med. Biol.* **45**(8), 2363 (2000)
3. Khurana, V.G., Teo, C., Kundi, M., Hardell, L., Carlberg, M.: Cell phones and brain tumors: a review including the long-term epidemiologic data. *Surg. Neurol.* **72**(3), 205–214 (2009)
4. Hossain, M.I., Mohammad, R.I.F., Islam, M.T., Hanafi, N.H.M.: Application of auxiliary antenna elements for SAR reduction in the human head. *Adv. Mater. Res.* **974**, 288–292 (2014)
5. Faruque, M.R.I., Islam, M.T., Misran, N.: Effects of dielectric values and substrate materials on electromagnetic (EM) absorption in human head. *Frequenz* **66**(3–4), 79–83 (2012)
6. Jensen, M.A., Rahamat-Samii, Y.: EM interaction of handset antennas and a human in personal communication. *Proc. IEEE* **83**(1), 7–17 (1995)
7. Kouveliatis, N.K., Panagiotou, S.C., Varlamos, P.K., Capsalis, C.N.: Theoretical approach of the interaction between a human head model and a mobile handset helical antenna using numerical methods. *Prog. Electromagnet. Res.* **65**, 309–327 (2006)
8. Faruque, M.R.I., Islam, M.T., Misran, N.: Analysis of electromagnetic absorption in mobile phones using metamaterials. *Electromagnetics* **31**(3), 215–232 (2011)
9. Hwang, J.-N., Chen, F.-C.: Reduction of the peak SAR in the human head with metamaterials. *IEEE Trans. Antennas Propag.* **54**(12), 3763–3770 (2006)
10. Faruque, M.R.I., Husni, N.A., Hossain, M.I., Islam, M.T., Misran, N.: Effects of mobile phone radiation onto human head with variation of holding cheek and tilt positions. *J. Appl. Res. Technol.* **12**(5), 871–876 (2014)

Assessment of Conversion Methods to Acquire 1-Minute Integration Time Rain Intensity Statistic

Muhamad Haziq Khairolanuar, Ahmad Fadzil Ismail,
Ahmad Zamani Jusoh, Nuurul Huda Mohd Sobli
and Khairayu Badron

Abstract This paper presents some preliminary findings of assessments carried out pertaining to the applicability of rain intensity conversion methods. Five conversion methods were identified in this study namely the ITU-R, Segal, Burgeuno, Chebil-Rahman and Khairolanuar et al. 1 year of rain intensity data were acquired from the Malaysian Meteorological Department (MMD) and utilized in the investigation. The research methodology involves productions of annual rain intensity cumulative distributions at 1-minute integration time using mentioned conversion methods. Predicted values established by ITU-R are used as benchmark. The values are then compared with values acquired using other conversion methods; in order to validate the applicability and effectiveness of each method. Based on the evaluation, it can be observed that the Khairolanuar *et al.* method seems to be a befitting conversion method and capable of generating values with smallest percentage difference.

M.H. Khairolanuar (✉) · A.F. Ismail · A.Z. Jusoh · N.H.M. Sobli · K. Badron
Department of Electrical and Computer Engineering, Kulliyyah of Engineering, International
Islamic University Malaysia (IIUM), Jln. Gombak, Kuala Lumpur, Selangor, Malaysia
e-mail: haziq.khairolanuar@yahoo.com

A.F. Ismail
e-mail: af_ismail@iium.edu.my

A.Z. Jusoh
e-mail: azamani@iium.edu.my

N.H.M. Sobli
e-mail: hudaah@iium.edu.my

K. Badron
e-mail: khairayu@iium.edu.my

1 Introduction

In the design of Earth-to-space communication links, rain attenuation information has to be identified. This is due to the fact that rain can severely attenuate links with operating frequencies above 10 GHz. Raindrops absorb and scatter energy from the incident radio wave, resulting in rain attenuation which can degrade the reliability and performance of the communications link. In order to devise the services efficiently, it is important to accurately estimate the to-be-encountered impairments of the given link. Researchers have put extensive efforts in measuring and modeling the rain attenuation along the desired propagation path. Predictions are engaged in order to assess whether an acceptable service can be delivered at the involved receiver's area. Among established prediction models are the ones recommended by the radio communications sector of the International Telecommunication Union (ITU-R) [1], the Dissanayake, Allnut and Haidara (DAH) rain induced attenuation model [2] and the Crane models [3, 4]. One of the advantages of the prediction models is the ability to exploit the information to be used in other area. Most of the established prediction methods employ rain intensity information at 0.01 % time exceedance of the annual statistics ($R_{0.01}$) at 1-minute integration time. Several tools such as impact disdrometer and rain gauges are the common tools used in collecting the data. However, this information is not readily available as most of the data are collected in longer integration time especially data obtained from meteorological department. Several methods [5–10] have been proposed by researchers to convert statistics acquired at longer integration time into statistics at 1-minute integration of time. Unfortunately, the validity of these conversion methods are questioned by researchers particularly in the heavy rainfall regime of tropical countries as most methods depend almost entirely on measurements in temperate climate countries [7]. Malaysia is located in a tropical region where the rainfall intensity is significantly higher compared to the other parts of the world. High rainfall intensity has caused severe degradation in the reliability and performance Earth-to-space communication link in Malaysia. It is important to accurately predict the fading outage due to rain in Malaysia as it will help system designer to realistically determine link availability, establish the link margin and provide means to combat rain effects. This paper outlines the production of annual cumulative distributions of rainfall intensity using Segal, Burgueno, Chebil-Rahman, Khairolanuar et al. and ITU-R conversion methods. The results are then correlated with each other to find the likelihood. The synopsis of the employed conversion methods to convert statistics acquired at longer integration time into statistics at 1-minute integration of time is outlined in the next section.

2 Excerpts of Rainfall Intensity Conversion Methods

In 1986, Segal proposed an empirical conversion method using rainfall intensity data from 47 stations in Canada. Approximately 10 years of data were used in developing the technique. The 1-minute integration time of rainfall intensity statistics, $R_1(P)$ can be obtained by using the following relationship:

$$R_1(P) = aP^b R_\tau(P). \quad (1)$$

where a and b are empirical constant, $R_\tau(P)$ is the input rainfall intensity data for τ integration of time and P is time exceedance value for the exact rainfall intensity input value.

In 1988, another empirical conversion method was proposed by Burgueno using rainfall intensity data for period of 49 years. The 1-minute integration time of rainfall intensity statistics, $R_1(P)$ can be obtained by using the suggested expression (2):

$$R_1(P) = aR_\tau(P)^b. \quad (2)$$

where a and b are empirical constant and $R_\tau(P)$ is the input rainfall intensity data for τ integration of time.

In 1999, Chebil-Rahman proposed another conversion method based on the 1 min and hourly rainfall data. The 1 min data were collected at 3 sites for almost 3 years and hourly data were obtained from Malaysian Meteorological Services (MMS), former name of MMD, involving 35 sites at various locations around Malaysia. The 1-minute integration time of rainfall intensity statistics, $R_1(P)$ can be obtained by using the proposed relationship (3):

$$R_1(P) = (aP^b + c \exp(dp))R_\tau(P). \quad (3)$$

where a , b , c and d are empirical constant, $R_\tau(P)$ is the input rainfall intensity data for τ integration of time and P is time exceedance value for the exact rainfall intensity input value.

In 2012, the ITU-R has proposed a new recommendation that claims capable of enabling users to generate statistics known as P(R) of the local rainfall intensity, R (mm/h) at 1-minute integration time. The recommendation allow users to choose inputs either from global digital maps of rainfall parameters derived from numerical weather prediction data or local measurements statistic of rainfall intensity at integration times up to 60 min. The statistics compiled using locally measured rainfall intensity combined with an integrated conversion model are of great interest as it is anticipated that they can offer the best approximation as outlined in [8]. Figure 1 shows the full workflow of the proposed conversion method.

In 2014, Khairolanuar et al. proposed another empirical conversion utilizing polynomial relationship exploiting rainfall intensity data acquired in Malaysia.

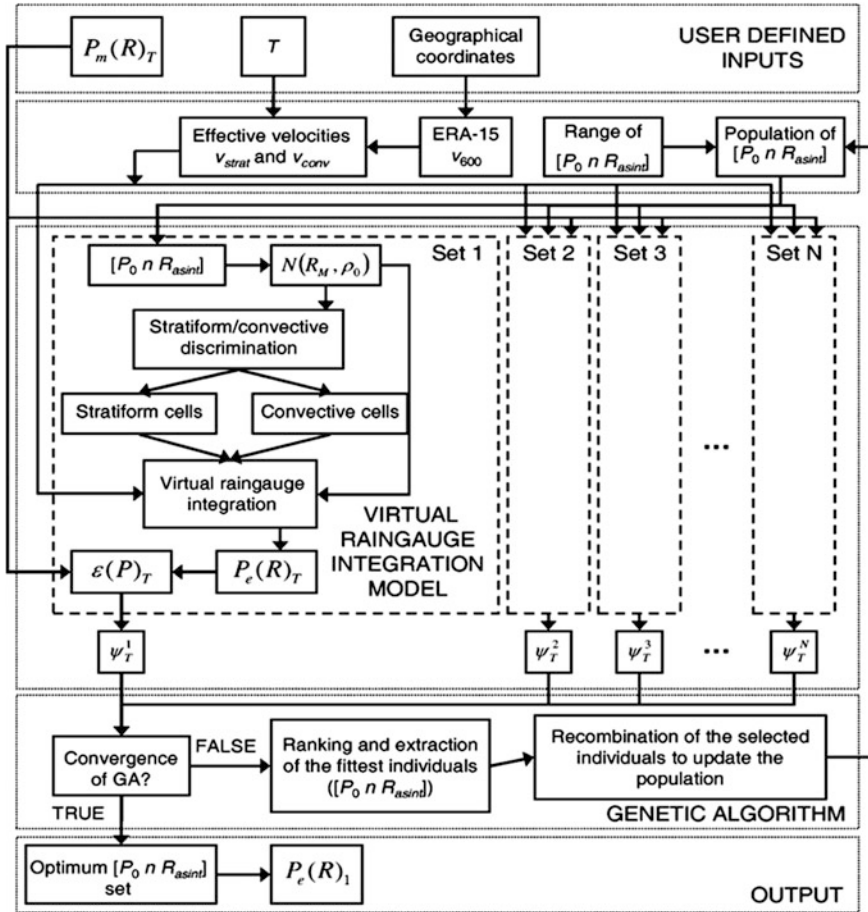


Fig. 1 ITU-R conversion method workflow [8]

The duration of collected data is for almost 2 years period. The data were acquired using optical rain gauge. The 1-minute integration time of rainfall intensity statistics, $R_1(P)$ can be obtained by using the presented formulation (4):

$$R_1(P) = aR_\tau(P)^4 + bR_\tau(P)^3 + cR_\tau(P)^2 + dR_\tau(P) + e. \tag{4}$$

where a, b, c, d and e are empirical constant, $R_\tau(P)$ is the input rainfall intensity data for τ integration of time.

Table 1 lists the empirical constant values for Segal’s, Burgueno’s and Khairolanuar et al. methods.

Table 1 Empirical constant values for 60 min

| Empirical constant | Segal | Burgueno | Chebil- Rahman | Khairolanuar et al. |
|--------------------|--------|----------|----------------|---------------------|
| a | 1.759 | 0.92 | 0.772 | 0 |
| b | -0.054 | 1.24 | -0.041 | 1.2659E-3 |
| c | - | - | 1.141 | -0.084193 |
| d | - | - | -2.570 | 2.1584 |
| e | - | - | - | 2.0883 |

3 Data Collection and Measurement

Figure 2 shows the tipping bucket used. The measurement system is located at 2° 44' N latitude and 101° 42' E, within the vicinity of Kuala Lumpur International Airport (KLIA) Sepang. The acquired data are for a period of 1 year from 1st January 2009 until 31st December 2009. The rain intensity data were collected every 60 min using standard tipping bucket type rain gauge. Table 2 lists the specification of the rain gauge.

Annual cumulative distribution was generated from the collected rain intensity data. Figure 3 shows the plotted statistic. From the collected data, the highest rainfall intensity recorded is at 71.83 mm/h.

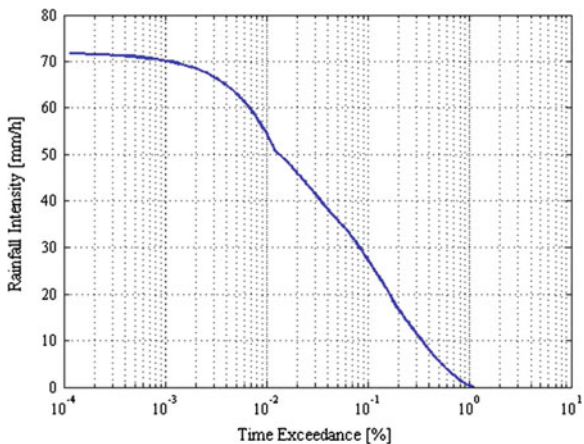
Fig. 2 MMD standard tipping bucket



Table 2 Tipping bucket specifications

| | Specifications |
|---------------------|------------------------|
| (Lat, Lon) | (2° 44' N, 101° 42' E) |
| Receiving collector | 203 ± 0.2 mm |
| Accuracy | ±1 % to 200 mm/h |
| Bucket capacity | 0.2 mm |
| Dimension | Height: 300 mm |
| | Body diameter: 230 mm |
| | Base diameter: 280 mm |
| Net weight | 5.5 kg |

Fig. 3 Annual statistic of rain intensity at 60-minute integration time



4 Results and Analyses

The plotted 60 min rain intensity statistic was converted to 1 min rain intensity statistic using 5 conversion methods, namely Segal’s, Burgueno’s, ITU-R’s, Chebil-Rahman and Khairolanuar et al’s methods. Figure 4 shows the converted 1 min rain intensity statistic using the mentioned conversion methods including the propose value from ITU-R Rain Maps [12]. From the result, it can be observed that the highest rain intensity value at 0.01 % time exceedance is generated by Burgueno’s conversion method with 130.6 mm/h follow by Segal’s method with 122.7 mm/h, Chebil-Rahman’s method with 111.2 mm/h, ITU-R Rain Map’s with 91.75 mm/h, ITU-R physical’s method with 90.77 mm/h and last but not least Khairolanuar *et al*’s method with 74.14 mm/h. Table 3 shows summary of rainfall intensity values at 0.01 % time exceedance for all converted statistics.

Fig. 4 Converted 1 min statistics

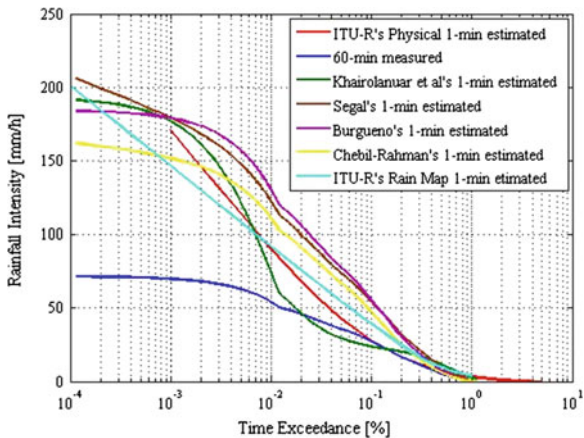


Table 3 Rain intensity values at 0.01 % time exceedance ($R_{0.01}$)

| ITU-R physical (mm/h) | ITU-R rain map (mm/h) | Segal (mm/h) | Burgueno (mm/h) | Khairolanuar et al. (mm/h) | Chebil-Rahman (mm/h) |
|-----------------------|-----------------------|--------------|-----------------|----------------------------|----------------------|
| 90.77 | 91.75 | 122.7 | 130.6 | 74.14 | 111.2 |

The plotted models were then compared with the ITU-R rain intensity conversion method. The ITU-R rain intensity conversion method was chosen as subject of reference due to its applicability to the local climate [11]. The assessments of each method applicability were further investigated by determination of the root mean square error (RMSE) and percentage error of rain intensity value at 0.01 % time exceedance. The relevant RMSE in this study can be defined as follow:

$$RMSE = \sqrt{\frac{1}{n} \sum_{i=1}^n (ECD_i - ITUD_i)^2} \tag{5}$$

where n is the number of data, ECD is the empirical conversion data and ITUD is the ITU data. Table 4 lists the RMSE and percentage difference for each conversion method as compared to ITU-R conversion method with value 90.77 mm/h. From the table, it can be noticed that ITU-R’s rain maps method has the lowest percentage difference value with 1.080 % follow by Khairolanuar et al’s method, 18.321 %, Chebil-Rahman’s method, 22.507 %, Segal’s, 35.177 % and lastly, Burgueno’s method at 43.880 %.

Table 5 lists the RMSE and percentage error for each conversion method as compare with ITU-R rain map with value of 91.75 mm/h. From the table, it can be noticed that ITU-R’s rain maps method has the lowest percentage difference value

Table 4 Root mean square error and percentage error at 0.01 % time exceedance as compare with ITU-R conversion method

| | Segal | Burgueno | Khairolanuar et al. | Chebil-Rahman | ITU-R rain maps |
|---------------------------|--------|----------|---------------------|---------------|-----------------|
| RMSE (%) | 23.972 | 28.425 | 12.283 | 16.015 | 10.958 |
| Percentage difference (%) | 35.177 | 43.880 | 18.321 | 22.507 | 1.080 |

Table 5 Root mean square error and percentage error at 0.01 % time exceedance as compared to ITU-R rain map

| | Segal | Burgueno | Khairolanuar et al. | Chebil-Rahman | ITU-R physical |
|---------------------------|--------|----------|---------------------|---------------|----------------|
| RMSE (%) | 24.625 | 28.091 | 18.388 | 15.220 | 10.958 |
| Percentage difference (%) | 33.733 | 42.343 | 19.193 | 21.199 | 1.068 |

with 1.068 % follow by Khairolanuar et al. method, 19.193 %, Chebil-Rahman's method, 21.199 %, Segal's, 33.733 % and lastly, Burgueno's method at 42.343 %.

5 Conclusion

In this paper it can be concluded that based on comparison between the values of available conversion methods with the ITU-R conversion method and ITU-R rain map at 0.01 % time exceedance, the value of Khairolanuar et al's has the lowest percentage difference value of below 20 % follow by Chebil-Rahman's, Segal's and Burgueno's methods. Khairolanuar et al's and Chebil-Rahman's methods have reasonably low RMSE value of below 19 % as compared to the rest of conversion methods. It appears that low differences have been identified between converted values by ITU-R conversion method and ITU-R rain map proposed values. Evaluations are currently carried out using data collected at other locations and findings will be shared in future publication.

Acknowledgments The authors acknowledge the Research Management Centre of the International Islamic University Malaysia (IIUM) and Malaysian Ministry of Education for the financial support. The reported research findings are part of the deliverables for the research funded under IIUM's Research University Initiatives. This research is being sponsored under Research Acculturation Grant Scheme (RAGS) Research Project RAGS12-048-0048 by Malaysian Ministry of Education.

References

1. Recommendation ITU-R P.618-11: Propagation data and prediction methods required for the design of earth-space telecommunication systems (2013)
2. Dissanayake, A., Allnut, J., Haidara, F.: A prediction model that combines rain attenuation and other propagation impairments along earth-satellite paths. *IEEE Trans. Antennas Propag.* **45**, 1546-1558 (1997)
3. Crane, R.K.: Prediction of attenuation by rain. *IEEE Trans. Commun.* **28**, 1717-1733 (1980)
4. Crane, R.K., Shieh, H.-C.: A two-component rain model for the prediction of site diversity performance. *Radio Sci.* **24**, 641-655 (1989)
5. Segal, B.: The influence of rain gauge integration time on measured rainfall-intensity distribution functions. *J Atmos. Oceanic Technol.* **3**, 662-671 (1986)
6. Burgueno, A., Puigcerver, M., Vilar, E.: Influence of rain gauge integration time on rain rate statistics used in microwave communications. *Ann. Telecommun.* **43**, 522-527 (1988)
7. Ismail, A.F., Hashim, W., Abdullah, K., Malek, N.A.: Empirical conversion of rainfall rate distribution for various integration times in Malaysia. In: 2011 IEEE International on RF and Microwave Conference (RFM), 270-273 (2011)
8. Capsoni, C., Luini, L.: A physically based method for the conversion of rainfall statistics from long to short integration time. *IEEE Trans. Antennas Propag.* **57**, 3692-3696 (2009)
9. Chebil, J., Rahman, T.A.: Rain rate statistical conversion for the prediction of rain attenuation in Malaysia. *Electron. Lett.* **35**, 1019-1021 (1999)

10. Khairolanuar, M.H., Ismail, A.F., Jusoh, A.Z., Sobli, N.H.M., Malek, N.F.A., Zabidi, S.A.: New empirical conversion technique for 1-minute integration time of precipitation intensity in Malaysia. *Aust. J. Basic Appl. Sci.* **8**, 290–295 (2014)
11. Khairolanuar, M.H., Ismail, A.F., Jusoh, A.Z., Khan, S., Alam, Z.: Assessment of ITU-R conversion method for 1-minute integration time of precipitation intensity in Malaysia. *Wireless Technology and Applications (ISWTA)*, 2014 IEEE Symposium on. 141–145 (2014)
12. Recommendation ITU-R P.837–6: Characteristics of precipitation for propagation modelling (2012)

Analysis of Permanent Magnet Brushless AC Motor Using Two Dimensional Fourier Transform-Parseval's Theorem

Ankita Dwivedi, S.K. Singh and R.K. Srivastava

Abstract The performance analysis of electrical machines using field solution is necessary for obtaining a closed form analytical solution in terms of machine's physical parameters. A closed form of solution provides an easy useful tool for the design analysis and optimization of an electromagnetic device. The paper presents a simple numerical-analytical solution for determining the performance characteristics of Surface Mounted Permanent Magnet (SMPM) Brushless AC motor on pole-by-pole basis. The Fourier transform applicable to Linear Induction Motor (LIM) is modified and adapted for PMBLAC motor. The performance is obtained in Fourier Space using Parseval's entity. A good correlation between computed results, experimental and published results validates the approximation used in the analysis.

Abbreviations

| | |
|--------|---|
| A | Magnetic Vector Potential (A/m) |
| D | Diameter of stator bore of original machine (m) |
| H_c | Coercivity of magnets (A/m) |
| I_S | Stator current (A) |
| J_S | Peak stator equivalent linear current density (A/m) |
| J_R | Peak rotor equivalent linear current density (A/m) |
| N | Number of turns per coil |
| T | Torque (Nm) |
| τ | Pole pitch of original motor (m) |
| f | Frequency of stator supply (Hz) |
| g_c | Corrected air clearance using Carter's coefficient |

A. Dwivedi (✉) · S.K. Singh · R.K. Srivastava
Department of Electrical Engineering, Indian Institute of Technology (BHU),
221005 Varanasi, India
e-mail: ankitadwd1808@gmail.com

S.K. Singh
e-mail: rksrivastava.eee@itbhu.ac.in

R.K. Srivastava
e-mail: sksingh.eee@itbhu.ac.in

| | |
|-------------------------|---|
| h_C | Thickness of Magnets (m) |
| k_{w1} | Winding factor |
| l | Subscript layer number |
| n | Even number > 100 |
| p | Number of Poles |
| v | Peripheral Linear velocity of rotor (m/s) |
| w_t, w_{tr}, w_o, w_s | widths of slot-teeth, tooth-tip, slot-openings and conductor respectively |
| w_c | |
| μ_i | Permeability of iron (H/m) |
| μ_l | Permeability of respective layer (H/m) |
| σ_l | Conductivity of respective layer (S/m) |
| φ | Phase difference between the two current densities |
| β | Fourier index of any layer |
| ω | Angular frequency (rad/s) |

1 Introduction

PMBL motors are well acknowledged for their use in domestic and industrial applications owing to their high efficiency, high torque density and high power density. The availability of higher power low cost permanent magnets has enabled the manufacturing and operation of these energy efficient motors. The design analysis and optimization of these motors requires a closed form solution of field equations in terms of machine physical dimensions. Although Finite Element Method (FEM) and Boundary Element Method (BEM) software are commercially available for design analysis of electrical machines, but their use require sizable costs of software and hardware, large computation time and dedicated expertise. In the literature, methods present for design analysis of Permanent Magnet (PM) machines are Equivalent Magnetic Circuit Method [1], dq0 model [2], Bessel's function [3], FEM [4, 5], BEM [6], Fourier Series [7–9] and Conformal Mapping [10, 11]. Although Fourier Transform Method for solution of Maxwell's equations [12–14] is a powerful technique, but its use in the analysis of Permanent Magnet Brushless Machines has not yet been reported.

In this present paper, a numerical-analytical Fourier transform model applicable for analyzing Linear Induction motor (LIM) has been modified and adapted for obtaining torque speed characteristics of PMBLAC motor. The advantages of proposed method can be observed as: the total magnetic field produced by armature reaction .i.e., stator winding currents and by PMs can be obtained simultaneously rather than by using superposition principle [7, 8]. Permanent magnets are represented using a continuous linear current sheet. The performance characteristics of the PMBLAC motors using proposed analysis can be directly calculated from the physical dimensions of the motor. In contrast with Fourier series method, the computational time for Fourier Transform is independent of speed.

2 Layer Model of PMBLAC Motor

The Fourier Transform model applicable to composite secondary LIM was used for estimating the total thrust in presence of entry and exit end effects [13]. The deterioration in the thrust has been found to be negligible for the case, when the number of poles is more 100 or more. On these lines, the Fourier transform model has been adapted for estimating the thrust of PMBLAC motor on pole-by-pole basis with an assumption that the numerical model of machine has large number of poles. This assumption is essential when the performance is determined in Fourier space utilizing Parseval’s entity, because in this method the components of different forces cannot be separated. Such an assumption is not required, when the performance is determined in Real space using Residue theorem.

The layer model of electrical machines has been used for analyzing linear as well as rotary machines. A rotary PMBLAC motor is presented in Fig. 1. The layer model for this motor is shown in Fig. 2a, b with stator and permanent magnets on rotor being replaced by their respective homogenized layers. The model is divided into four regions: Region-I is the back iron beneath PM’s layer; Region-II is the PM layer on rotor active surface—the infinitesimal thin linear current sheet is assumed to be pasted on the layer representing the magnet $j_R(x) = J_R \exp(\omega t - kx \pm \phi)$ A/m, here the peak rotor current density J_R is a function of thickness of magnet and its coercivity (H_c) and is given by $J_R = H_c h_m / \tau$ [8]; Region-III is the air clearance between stator and PM rotor which is corrected using Carter’s coefficient. For isotropic model shown in Fig. 2a, where the saturation in the stator core is neglected, Region-IV is smooth stator with infinite relative permeability. The isotropic model is particularly true for machines having larger clearance between stator and rotor. On the active surface of Region-IV infinitesimal thin linear current sheet

Fig. 1 A typical 12-slot surface mounted PM motor (not to the scale)

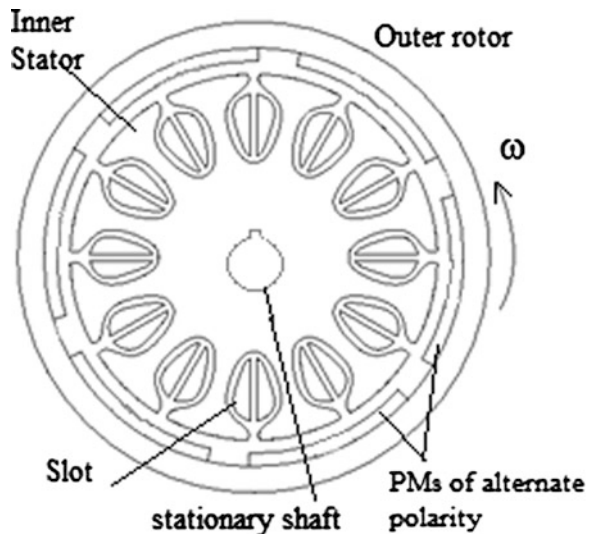
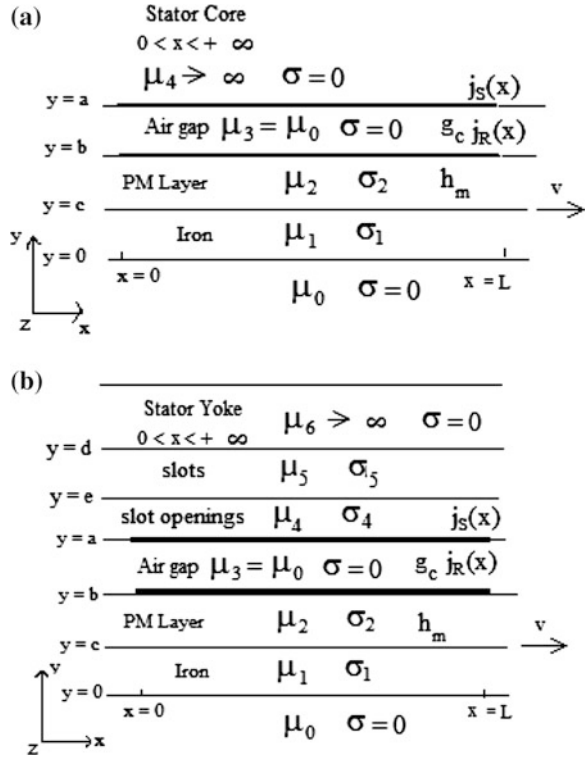


Fig. 2 A typical linear model of PMBL motor. **a** Isotropic Layer Model of PMBLAC motor—stator winding replaced by linear current density $j_s(x)$ and PM layer are replaced by linear current density $j_p(x)$ (not to the scale). **b** Anisotropic layer model of PMBLAC motor taking slots and slot openings into account. (Current sheets are assumed to be infinitesimally thin)



$j_s(x) = J_S \exp j(\omega t - kx)$ A/m representing the winding is assumed to be present for both the isotropic and anisotropic models, where peak linear current density is $J_S = \sqrt{2}N k_{w1}I_1/\tau_p$ [13]. When air clearance is less, machine is subjected to magnetic saturation. In case of anisotropic model shown in Fig. 2b, the stator region is divided into slot-wedge or slot-openings and actual slots having conductor and slot-teeth, which are represented by Region-IV and Region-V respectively. The stator yoke having infinite permeability is represented by Region-VI.

For anisotropic model, the slotted regions of stator are replaced by homogenized material properties. When a layer consists of two materials in slot, the equivalent material property i.e., permeability and conductivity takes care of the variation or change in the magnetic flux and electric currents respectively. The anisotropic magnetic permeability in the region of slot wedge and main slot having conductors are calculated as [15],

$$\mu_{w,x} = \frac{\mu_0 \mu_i (w_o + w_t)}{\mu_i w_o + \mu_0 w_t}; \quad \mu_{w,y} = \frac{\mu_i w_t - \mu_0 w_o}{w_o + w_t}$$

$$\mu_{s,x} = \frac{\mu_0 \mu_i (w_c + w_t)}{\mu_i w_c + \mu_0 w_t}; \quad \mu_{s,y} = \frac{\mu_i w_t - \mu_0 w_c}{w_c + w_t}$$

For adapting the Fourier transform model applicable to dual current sheet PMBLAC motor, it is assumed that the effective length of machine is from $x = 0$ to $x = L$, where $L = 2n\tau$. Here is ' τ ' the pole pitch of stator winding and even number ' n ' can be taken as more than 100 (say). In dual current sheet model of PMBLAC motor, the rotor current sheet under steady state conditions runs at exact synchronous peripheral speed as decided by number of poles and applied stator supply frequency. It has been shown that when rotor peripheral speed is equal to synchronous speed or $v = v_s = 2\tau f$, the angle is $\phi = \pm 90^\circ$ [13], or in other words the phase difference between two current sheets is $\phi = \pm 0.5 k\tau$.

The general governing field equation for different layers is,

$$\nabla^2 \mathbf{A} = \mu \{ \mathbf{J} + \nabla \times \mathbf{M} + j\omega\sigma\mathbf{A} + v\omega\sigma(\partial\mathbf{A}/\partial x) \} \quad (1)$$

The Magnetic Vector Potential (MVP) \mathbf{A} gives $\mathbf{B} = \nabla \times \mathbf{A}$ and $\nabla \cdot \mathbf{A} = 0$. As has been mentioned earlier, the active winding is replaced by $j_s(x)$ linear current sheet and in the layer of alternate permanent magnets, $\nabla \times \mathbf{M}$ is replaced by an equivalent linear current sheet $j_R(x)$ representing the permanent magnets. The recoil permeability of magnet is closer to that of free space, so permanent magnet layer is assumed to have average magnetic and conducting properties. Though the material ferrite has zero conductivity, the material like NdFeB has a finite conductivity. The field equation for conducting moving media having linear peripheral speed ' v ' is given by,

$$\nabla^2 \mathbf{A} = j\omega\mu\sigma\mathbf{A} + \mu\sigma v(\partial\mathbf{A}/\partial x) \quad (2)$$

Here by definition, the x quantities are Fourier transformed to ξ . A set of equations need to be solved using separation of variables. In Fourier space, the solution of magnetic fields takes the form,

$$A_l(\xi, y) = M_l(\xi)e^{\beta y} + N_l(\xi)e^{-\beta y} \quad (3)$$

where, subscript ' l ' is the layer number and ' β ' is the Fourier index of the respective layer. The Fourier indices for iron can be derived as $\chi = \sqrt{\xi^2 + j\sigma_1\mu_1\omega + j\xi\sigma_1\mu_1v}$ and for PM layer $\gamma = \sqrt{\xi^2 + j\sigma_2\mu_2\omega + j\xi\sigma_2\mu_2v}$. For 0th layer, one can assume,

$$A_0(\xi, y) = M_0(\xi)e^{\xi y} \quad (4)$$

The general Boundary conditions for isotropic model is,

$$H_l - H_{l-1} = J(\xi) \quad (5)$$

Here $J(\xi)$ is the Fourier transform of the current sheet between the two layers. The MVP in air clearance can be determined by separation of variables and hence the thrust or torque in Fourier Space using Maxwell's Stress Tensor [13].

The MVP in air clearance for both the isotropic and anisotropic model can be easily determined. The typical expression for the MVP in air clearance may take a form,

$$A_3(\xi, y) = \frac{\mu_3}{\xi} \left[\frac{W(\xi, a)}{K(\xi)} \right] J_s(\xi) \quad (6)$$

The total torque produced by PMBLAC motor can be computed for proposed model by Parseval's Theorem is given by,

$$T = \frac{Dp}{4\pi n} \text{Re} \int_{-\infty}^{+\infty} J_s^*(\xi) B_{3y}(\xi, a) d\xi \quad (7)$$

Here $J_s^*(\xi)$ is the Complex conjugate of Fourier transform of stator linear current density. Upon solving we get,

$$T = Dp \frac{\mu_3 J_s^2}{2\pi n} \int_{-\infty}^{+\infty} \frac{1 - \cos(\xi + k)L}{\xi(\xi + k)^2} \text{imag} \left[\frac{W(\xi, a)}{K(\xi)} \right] d\xi \quad (8)$$

The torque is calculated numerically using above equation. The general distribution of thrust force integrand in Fourier Space at standstill, 400 and 800 rpm for experimental PMBLAC motor whose details are given in [16] is depicted in Fig. 3. The force distribution is more pronounced at $\xi = -\pi\tau$ in real axis. As such, the range of ' ξ ' and step length ' $d\xi$ ' both have been obtained using trial and error method, so as to cover the relevant distribution of integrands in Fourier space. The numerical integration has been performed using MATLAB software for real value of $\xi = -250$ to $+50$ at a step length of $d\xi = 0.1081$.

3 Results and Validation of Proposed Motor

3.1 Experimental Validation

For verification of proposed Fourier transform–Parseval's entity based theoretical analysis, a prototype of PMBL motor working with sinusoidal excitation was developed [16]. The expected results obtained with constant current analysis are shown in Fig. 4, while results obtained from constant voltage is depicted in Fig. 5. The effect of saturation due to presence of stator slotting is also included.

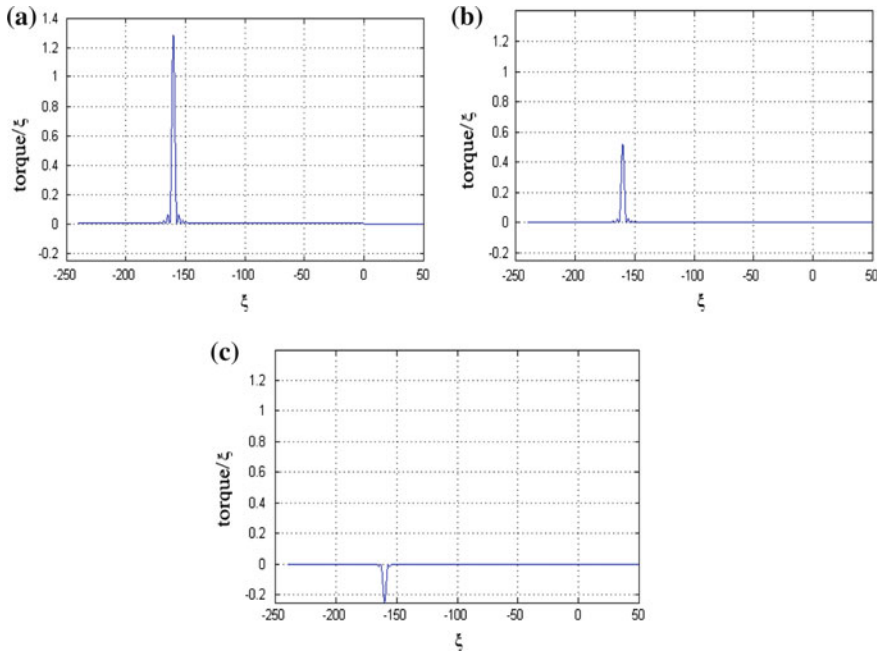


Fig. 3 Typical variation of torque integrands of PMLAC motor at **a** standstill **b** 400 RPM **c** 800 RPM

Fig. 4 Expected constant current torque-speed characteristics of PMBL motor

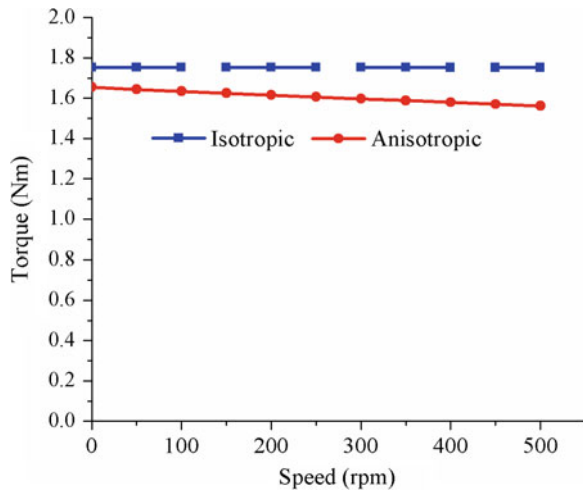
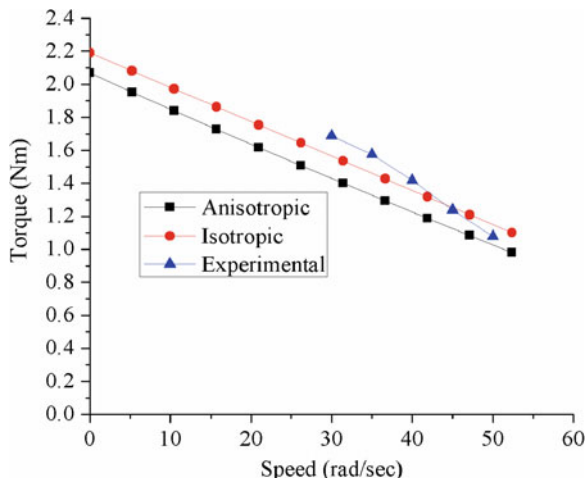


Fig. 5 Validation of constant voltage torque-speed characteristics of PMBL motor



For constant voltage analysis, current is calculated as,

$$V = RI_s + E$$

where, E is the speed induced EMF/phase induced in the stator windings calculated as,

$$E = k_e \omega$$

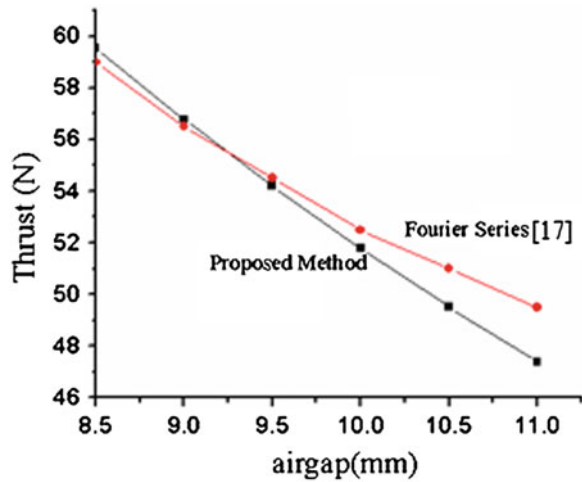
In the present case, the air gap was fairly large and magnetic saturation is unlikely to be present. The experimental data were obtained using frictional loading and torque was indirectly calculated by using first principle.

As expected, the measured torque closely agrees with the analytical torque calculated as shown in Fig. 5, verifying the effectiveness of proposed FT method for PMBL motors. Due to the presence of large air gap, the effect of saturation is not dominant.

3.2 Analytical Validation

The method has been applied to the motor used in [17] and the results obtained from proposed model are compared to the results obtained Fourier analysis. The variation of thrust force with air gap obtained from the two methods is shown in Fig. 6 and the graph shows a good agreement between the results obtained from the two methods.

Fig. 6 Comparison of effect of variation of air gap on thrust of PMBL motor using Fourier Analysis [17] and proposed Fourier transform- Parseval's method



4 Conclusions

An analytical method based on Fourier Transform for evaluation of performance of Surface Mounted PM motor with dual current sheet is introduced in the paper using Parseval's Theorem. Both isotropic and anisotropic models are considered and the effect of stator slotting on the performance of PMBLAC motor is shown. The developed model has been validated using experimental and published results. The proposed model is found to be effective in determining the characteristics of PMBLAC motors. It provides a closed form solution for the design analysis and parametric studies of SMPM Brushless AC motor.

The analysis assumes that the phase current is perfectly sinusoidal, which is not the case in case of actual PMBLAC motor. However the model can be easily extended to calculate the characteristics of multi-phase SMPM/IPM BLAC motors and cogging torque in these motors.

Appendix

The detailed analysis, derivations of layer indices ξ , χ , γ and derivations of expressions valid for present model of PMBL motor for $K(\xi)$ and $W(\xi)$ can be easily derived. Typical method is reported at length in Ref. [13]. The expression for $W(\xi)$ for double current sheet SMPM motor is given below,

$$\begin{aligned}
W(\xi, a) = & [me^{\pm j0.5k\tau} \sinh \xi(a-b)K(\xi)] \\
& - [1 + me^{\pm j0.5k\tau} \cosh \xi(a-b)] \left[\frac{\mu_2 \gamma}{\mu_1 \gamma} \sinh \gamma c \cdot \sinh \gamma(b-c) \cdot \cosh \xi(a-b) \right. \\
& + \frac{\mu_3 \mu_1 \gamma}{\mu_0 \mu_2 \gamma} \sinh \gamma c \cdot \sinh \gamma(b-c) \cdot \sinh \xi(a-b) + \frac{\mu_1 \xi}{\mu_0 \gamma} \sinh \gamma c \cdot \cosh \gamma(b-c) \cdot \cosh \xi(a-b) \\
& + \frac{\mu_3 \gamma}{\mu_1 \xi} \sinh \gamma c \cdot \cosh \gamma(b-c) \cdot \sinh \xi(a-b) + \cosh \gamma c \cdot \cosh \gamma(b-c) \cdot \cosh \xi(a-b) \\
& + \frac{\mu_3}{\mu_0} \cosh \gamma c \cdot \cosh \gamma(b-c) \cdot \sinh \xi(a-b) + \frac{\mu_2 \xi}{\mu_0 \gamma} \cosh \gamma c \cdot \sinh \gamma(b-c) \cdot \cosh \xi(a-b) \\
& \left. + \frac{\mu_3 \gamma}{\mu_2 \xi} \cosh \gamma c \cdot \sinh \gamma(b-c) \cdot \sinh \xi(a-b) \right]
\end{aligned}$$

Similarly the quantity $K(\xi)$ can also be determined. The derivation of these quantities for anisotropic model can be similarly done taking care of anisotropic permeability.

References

1. Jin, H., Yoon, S., Hwang, D., Hyun, D.: Analysis of PMLSM using three dimensional equivalent magnetic circuit network method. *IEEE TMAG* **33**(5–2), 4143–4145 (1997)
2. Pillay, P., Krishnan, R.: Modeling, simulation and analysis of permanent-magnet motor drives-part I: the permanent-magnet synchronous motor drive. *IEEE Trans. Ind. Appl.* **25**(2), 265–273 (1989)
3. Zhu, Z.Q., Ng, K., Schofield, N., Howe, D.: Improved analytical modelling of rotor eddy current loss in brushless machines equipped with surface mounted permanent magnets. *IEEE Proc. Elect. Power Appl.* **151**(6), 685–693 (2006)
4. Bianchi, N., Canova, A.: FEM analysis and optimization design of an IPM synchronous motor. In: *International Conference on Power Electronics, Machines and Drives*, pp. 49–54 (2002)
5. Demerdash, N.A.O., Alhamadi, M.A.: Three-dimensional finite element analysis of permanent magnet brushless DC motor drives-status of the state of the art. *IEEE Trans. Ind. Appl.* **43**(2), 268–275 (2008)
6. Qaseer, L., Marzouk, R.: Hybrid Finite-Element–Boundary Element Analysis of a Single-Sided Sheet Rotor Linear Induction Motor. *IEEE Trans. Energ. Conv.* **29**(1), 188–195 (2014)
7. Gysen, B.L.J., Meessen, K.J., Paulides, J.J.H., Lomonova, E.A.: General formulation of the electromagnetic field distribution in machines and devices using fourier analysis. *IEEE Trans. Magn.* **46**(1), 39–52 (2010)
8. Deng, Z., Boldea, I., Nasar, S.A.: Fields in permanent magnet linear synchronous machines. *IEEE TMAG* **22**(2), 107–112 1986
9. Faiz, J., Salari, M.E., Shahgholian, Gh.: Reduction of cogging force in linear permanent magnet generators. *IEEE TMAG* **46**(1), 135–140 (2010)
10. Boughrara, K., Ibtouen, R., Zarko, D., Touhami, O., Rezzoug, A.: Magnetic field analysis of external rotor permanent-magnet synchronous motors using conformal mapping. *IEEE TMAG* **46**(9), 3684–3693 (2010)
11. Zarko, D., Ban, D., Lipo, T.A.: Analytical solution for electromagnetic torque in surface permanent-magnet motors using conformal mapping. *IEEE TMAG* **45**(9), 2943–2954 (2009)
12. Sudan, R.N.: Interaction of a conducting fluid stream with a travelling wave of magnetic field of finite extension. *J. Appl. Phys.* **34**, 641–650 (1963)

13. Yamamura, S., Ito, H., Ishulawa, Y.: Theories of linear, induction motor and compensated linear induction motor. *IEEE Trans. Power Apparatus Syst.* **PAS-91**(4), 1700–1710 (1972)
14. Srivastava, R.K., Kumar, S.: An alternative approach for calculation of braking force of an eddy-current brake. *IEEE TMAG.* **45**(1), 150–154 (2009)
15. Sprangers, R., Motoasca, E.T., Lomonova, E.: Extended anisotropic layer theory for electrical machines. *IEEE TMAG* **49**(05), 2217–2220 (2013)
16. Srivastava, R.K., Singh, S.K., Dwivedi, A., Gollapudi, S.: PM enhanced sensing—a tool to study PMBLDC/AC motors. *Int. J. Smart Sens. Intell. Syst.* **6**(4), 1456–1478 (2013)
17. Zadeh, V.S., Isfahani, A.H.: Multiobjective design optimization of air-core linear permanent-magnet synchronous motors for improved thrust and low magnet consumption. *IEEE Trans. Mag.* **42**(3), 446–452 (2006)

Dual Band Stacked Artificial Magnetic Conductor with Dipole Antenna

R. Dewan, M.K.A. Rahim, M.R. Hamid, N.A. Samsuri,
M.F.M. Yusoff, B.D. Bala and M.E. Jalil

Abstract This paper proposed a design of dual substrate layer Artificial Magnetic Conductor (AMC) which operates at operating frequency of 2.45 and 5.8 GHz. The top circular ring and the bottom rectangular AMC patch correspond to higher and lower frequency respectively. The offset effect due to distance and angular variations on the reflection phase has also been studied. The study further extended to the effect of double and quadruple circular ring AMC on the top substrate layer of stacked AMC. The dual band stacked AMC is then integrated onto two dipole antennas operating at 2.45 and 5.8 GHz band. The performance of antenna with and without AMC is observed in terms of reflection coefficient, directivity and radiation patterns.

R. Dewan (✉) · M.K.A. Rahim · M.R. Hamid · N.A. Samsuri · M.F.M. Yusoff
B.D. Bala · M.E. Jalil
Department of Communication Engineering, Faculty of Electrical Engineering,
Universiti Teknologi Malaysia, 81310, Johor Bahru, Johor, Malaysia
e-mail: raimidewan@gmail.com

M.K.A. Rahim
e-mail: mkamal@fke.utm.my

M.R. Hamid
e-mail: rijal@fke.utm.my

N.A. Samsuri
e-mail: asmawati@fke.utm.my

M.F.M. Yusoff
e-mail: fairus@fke.utm.my

B.D. Bala
e-mail: bashirbala@yahoo.com

M.E. Jalil
e-mail: ezwanjalil@gmail.com

1 Introduction

Artificial Magnetic Conductor (AMC) is a sub class of metamaterials. Metamaterial is a composite resonant structure that exhibit unique characteristic of materials that are not naturally existed in nature [1]. By designing metamaterial, the unique characteristics of non-naturally occurring material can be realized. AMC is a metamaterial which mimics the behavior of Perfect Magnetic Conductor (PMC) [2].

PMC is capable of inducing zero reflection phase of image current with respect to the source current. The zero reflection characteristic by PMC is not existed in nature. Conventional Perfect Electric Conductor (PEC) is used at the antennas ground plane. Unlike PMC, it introduces image current which is out of phase (180°) with respect to the source current. The out of phase reflected current by PEC creates a destructive interference with source current, decreasing radiation efficiency and gain. To compensate the aforementioned issue, the PEC layer should be separated from radiating antenna by a distance of $\lambda/4$. However, the penalty is that, the antenna is no longer low profile which is undesirable for most antenna design. In contrast, reflected current by PMC which is in phase with source current, constructive interference with it, subsequently increasing the radiation efficiency and gain [3].

AMC which mimics the behavior of PMC can be used to replace the conventional PEC layer as backed ground plane of an antenna. In practical design, PEC is represented by copper conductive layer [4, 5]. In this paper, a dual band stacked AMC is proposed. The AMC is then integrated with dual band dipole antenna.

2 Design

The AMC and antenna are designed on FR-4 substrate with permittivity, loss tangent and thickness of 4.5, 0.019 and 1.6 mm respectively. The AMC and antenna design is simulated using computer simulation technology (CST) 2012 microwave studio software. The design section is divided to 3 sub sections as follows:

2.1 AMC Design

The AMC with rectangular patch shape on single substrate layer backed by a ground plane is a conventional design. The related equation to approximate the initial dimension of patch is as reported in [6]. Each unit cell in periodic array of AMC on substrate of permittivity ϵ and thickness h mm, separated with each other by distance of s mm, with slot capacitance of C_s . The effective equivalence of discontinuity of microstrip-gap and odd field distribution is C_{eq}^o . K is the wave number.

$$C_s = \frac{\epsilon_0}{2} [1 - 0.636 \ln(k_0 h)] \tag{1}$$

$$C_{eq}^o = \frac{\epsilon}{2\pi} \left[\ln 2 + \ln \left(\frac{A}{A-1} + \sqrt{\frac{A+1}{A-1}} \right) \right] \tag{2}$$

$$A = \cosh \left(\frac{s\pi}{2h} \right) \tag{3}$$

The proposed AMC unit cell consists of two AMC patch interleaved by two substrate layers with bottom substrate layer backed by ground plane as shown in Fig. 1a, d. Figure 1b shows the design of circular ring AMC while Fig. 1c shows the

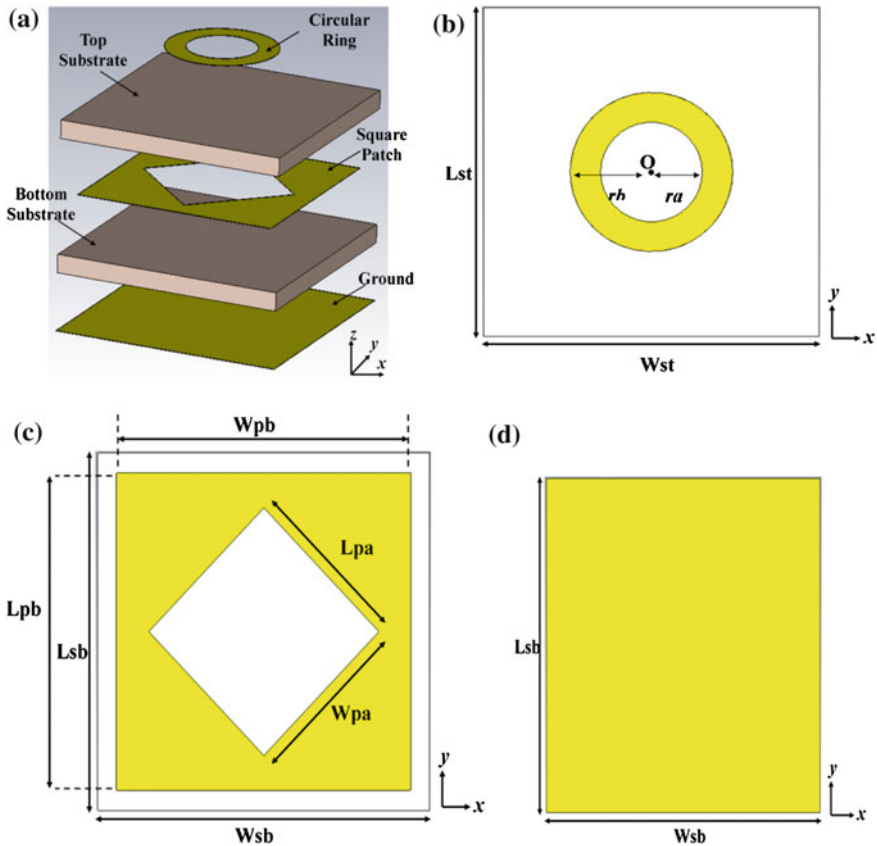


Fig. 1 a Exploded 3 Dimensional (3D) diagram of double stacked AMC unit cell. b The geometrical design of circular ring AMC (at front side) of top substrate layer, c slotted rectangular AMC patch (at front side) of bottom substrate layer and d ground layer (at back side) of bottom substrate layer

Table 1 AMC Dimensions

| Parameter | Length (mm) | Parameter | Length (mm) |
|-----------|-------------|-----------|-------------|
| Lst | 20.83 | rb | 5.03 |
| Lpb | 18.45 | Wst | 20.83 |
| Lsb | 20.83 | Wpa | 10.20 |
| Lpa | 10.20 | Wpb | 18.45 |
| Ra | 3.15 | Wsb | 20.83 |

rectangular patch AMC. The dimension of the double stacked AMC is tabulated in Table 1. The rectangular patch and circular ring operates at 2.45 and 5.8 GHz which gives the dual band characteristics of the proposed stacked AMC.

The design of circular ring patch is a modified form of initial design of circular patch. It is shown in Fig. 2 that by introducing circular ring instead of circular patch of similar radius of r_b , the reflection phase is further shifter to the lower frequency. Thus, it allows further size miniaturization of the circular structure itself.

The study is also extended on the effect of offsetting AMC circular ring on the reflection phase. The offset studies is divided into two, first study involving the offset of circular ring by distance only while the second study involves the offset of AMC circular ring by distance and angle. The centre of circular AMC denoted by O is taken as the origin of coordinate (0,0). A 1 unit in coordinate value is equivalent to 1 mm of translation of the structure. Figure 3 shows the offset representation study that will be carried out. θ is the angle by offset of AMC circular ring with respect to x axis.

The final study of AMC design is on the effect of number of AMC circular ring to the reflection phase. The study involves the effect of single, double and quadruples of AMC circular ring as shown in Fig. 4.

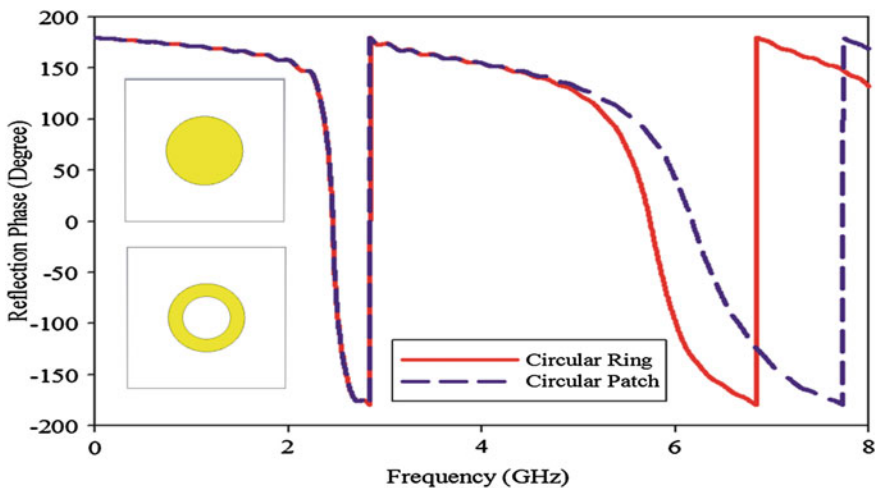


Fig. 2 The reflection phase diagram correspond to circular ring and circular patch

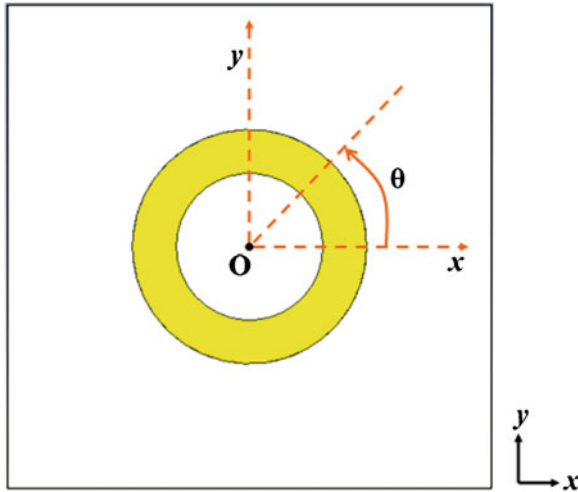


Fig. 3 The offset diagram of circular ring

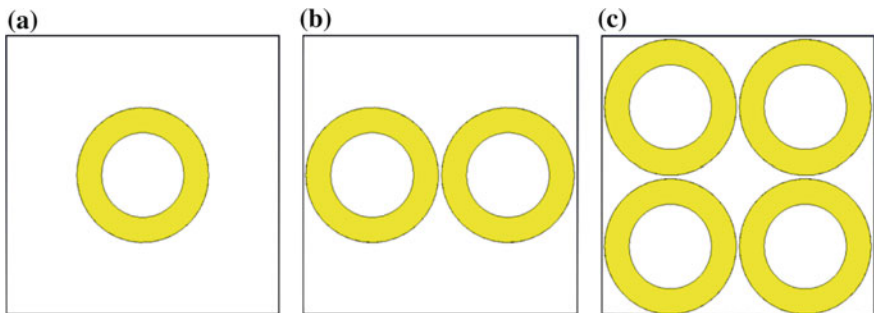


Fig. 4 a Single circular ring, b double circular ring, and c quadruple circular ring AMC (at front side) of top substrate layer

2.2 Dual Band Dipole Antennas Design

Two dipole antennas which operate at 2.45 and 5.8 GHz is designed as shown in Fig. 5. The shorter dipole, each with length of d_2 mm operates at higher frequency, while the longer dipole, each with length of d_3 mm operates at lower frequency. d_2 and d_3 is proximately equal to $\lambda/2$ for 5.8 and 2.45 GHz respectively, with similar widths of 3 mm. The dipole pairs are separated by distance of d_1 which corresponding to $\lambda/4$ of the lower frequency. Dimensions are shown in Table 2.

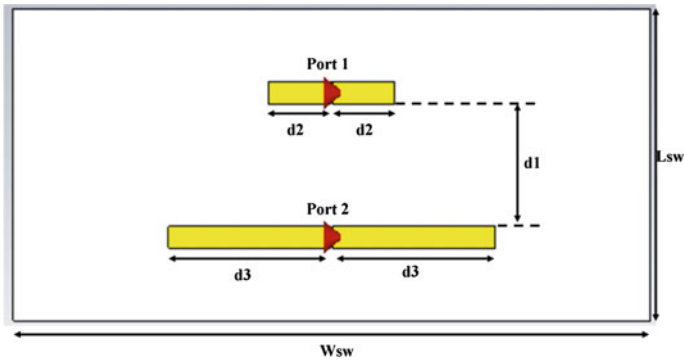


Fig. 5 Dual band dipole antenna design

Table 2 Dual Band Dipole Antenna Dimensions

| Parameter | Length (mm) | Parameter | Length (mm) |
|------------------|-------------|-----------|-------------|
| $d1 = \lambda/4$ | 16.58 | Lsw | 42.36 |
| d2 | 8.50 | Wsw | 86.57 |
| d3 | 22.09 | | |

2.3 AMC Integrated Dipole Antenna Design

The final design involves the integration of the stacked AMC with the two dipole antennas. Figure 6 shows the integrated structure with an air gap of $g = 8$ mm which is 0.12λ . The air gap is exceptionally lower than the required distance required by PEC layer ($\lambda/4 = 0.25\lambda$) as backed ground plane with improved antenna performance.

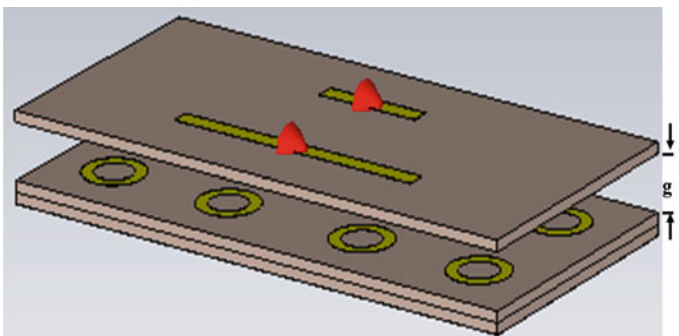


Fig. 6 AMC integrated dipole antenna with air gap g mm

3 Result and Discussions

Several parametric studies have been carried out on the AMC circular rings which are shown in Figs. 7 and 8. In Fig. 7a, it can be observed that offsetting the circular ring by distances have negligible effects on reflection phase. In contrast, the translation of circular ring together with angle variations affects the reflection phase curve for the upper frequency as shown in Fig. 7b.

As seen from Fig. 8a, the additional number of circular ring significantly distorted the dual band reflection phase band characteristics as opposed with initial single ring. This inferred that, single AMC circular ring is the best number of rings that can be collocated with each of the proposed rectangular AMC patch in bottom AMC substrate layer. From Fig. 8b, the reflection coefficients of S11 and S22 at 5.8 and 2.45 GHz are improved with the inclusion of AMC.

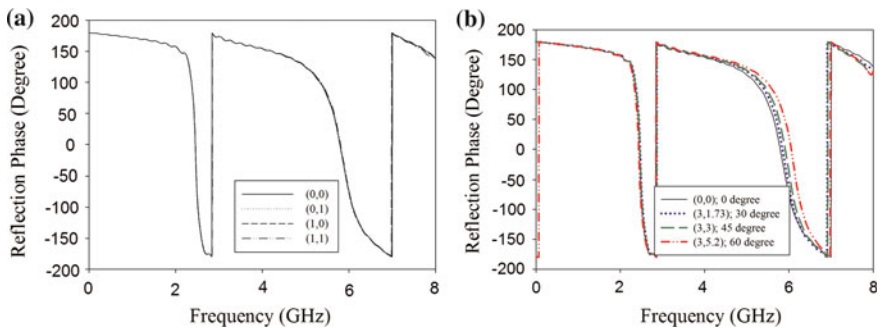


Fig. 7 a Reflection phase variations with respect to offset of circular ring by distance and b Reflection phase variations with respect to offset of circular ring by distance and angle

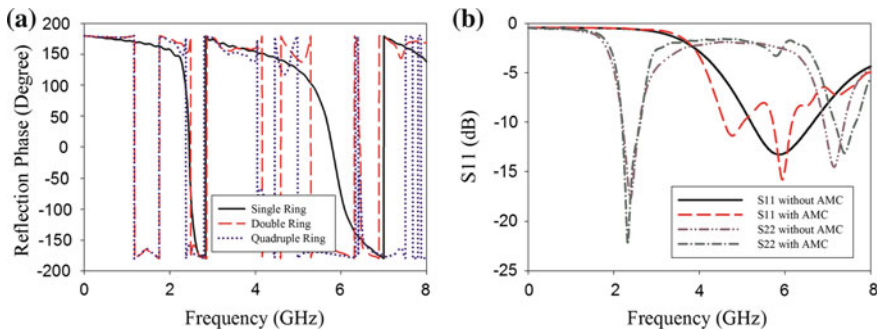


Fig. 8 a Reflection phase variations with addition of circular ring and b simulated reflection coefficients

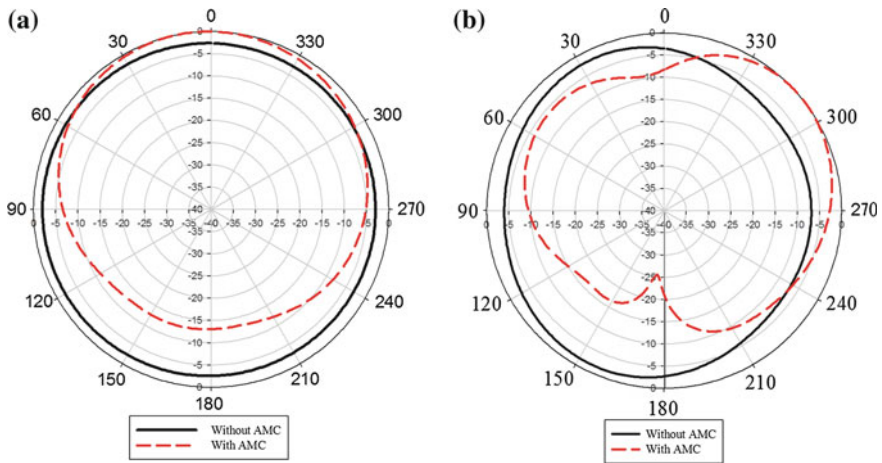


Fig. 9 Simulated E-field radiation patterns at **a** 2.45 GHz and **b** 5.8 GHz

Figure 9a, b show the simulated results of E-field radiation patterns at 2.45 and 5.8 GHz respectively. At 2.45 GHz, the low directivity of dipole antenna is improved from 2.624 to 6.121 dBi with the inclusion of stacked AMC. Similarly, the directivity is improved from 3.533 to 5.778 dBi at 5.8 GHz.

4 Conclusion

The dual band stacked AMC unit cell operates at 2.45 and 5.8 GHz has been designed and simulated. Several parametric studies such as the offset of circular rings by distance, angles and additional circular rings have been conducted. The AMC is integrated with dual band dipole antenna with similar operating frequencies. With the inclusion of AMC, the reflection coefficients and directivity of the dipole antenna is significantly improved.

Acknowledgments The authors thank the Ministry of Higher Education (MOHE) for supporting the research work; Research Management Centre (RMC), School of Postgraduate (SPS), Communication Engineering Department and Universiti Teknologi Malaysia (UTM-JB) Johor Bahru for the support of the research under grant no R.J130000.7923.4L811, 4F360 and 04H38.

References

1. Al-Naib, I., Jansen, C., Singh, R., Walther, M., Koch, M.: Novel THz Metamaterial designs: from near- and far-field coupling to high-Q resonances. *IEEE Trans. Terahertz Sci. Technol.* **3**, 772–782 (2013)
2. Abbasi, N.A., Langley, R.J.: Multiband-integrated antenna/artificial magnetic conductor. *IET Microwaves Antennas Propag.* **5**, 711–717 (2011)

3. Dewan, R., Rahim, S.K.B.A., Ausordin, S.F., Purnamirza, T.: The improvement of array antenna performance with the implementation of an artificial magnetic conductor (AMC) ground plane and in-phase superstrate. *Prog. Electromagnet. Res.* **140**, 147–167 (2013)
4. Abu, M., Rahim, M.K.A.: Single-band and dual-band artificial magnetic conductor ground planes for multi-band dipole antenna. *Radioengineering* **21**, 999–1006 (2012)
5. Akhoondzadeh-Asl, L., Nourinia, J., Ghobadi, C., Hall, P.S.: Influence of element shape on the bandwidth of artificial magnetic conductors. *J Electromagnet. Waves Appl.* **21**, 929–946 (2007)
6. Zhang, Y., Von Hagen, J., Younis, M., Fischer, C., Wiesbeck, W.: Planar artificial magnetic conductors and patch antennas. *IEEE Trans. Antennas Propag.* **51**, 2704–2712 (2003)

Performance of Sugarcane Bagasse and Rubber Tire Dust Microwave Absorber in Ku Band Frequency

**Liyana Zahid, Mohd Fareq Abd Malek, Cheng Ee Meng,
Liu Wei Wen, Lee Yeng Seng, Ahmad Zaidi Abdullah,
Nur Sabrina Md Noorpi, Nurhakimah Mohd Mokhtar
and Mohd Asri Jusoh**

Abstract The electromagnetic interference (EMI) absorbing materials in various microwave frequency were required most now due to increasing demand of electromagnetic compatibility (EMC) for electronic devices with various electromagnetic environments. So, absorber materials are needed in RF/Microwave to eliminate and absorb electromagnetic energy. Absorbers can be used to create a free space environment in anechoic chamber. This work describes the performances which are the reflection loss and absorption for composite of sugarcane bagasse mixed with rubber tire dust microwave absorber in Ku Band frequency (12.4–18 GHz). The parameters such as dielectric properties, reflection coefficient (S_{11}) and transmission coefficient (S_{21}) were investigated. The main objectives of this research are to design and develop a microwave absorber with new green materials which are sugarcane

L. Zahid (✉) · L.Y. Seng
School of Computer and Communication Engineering, University Malaysia Perlis
(UniMAP), Pauh Putra Campus, 02600 Arau, Perlis, Malaysia
e-mail: liyanazahid@gmail.com

L.Y. Seng
e-mail: leeyengseng@gmail.com

M.F.A. Malek · A.Z. Abdullah · N.S.M. Noorpi · N.M. Mokhtar · M.A. Jusoh
School of Electrical System Engineering, University Malaysia Perlis (UniMAP), Pauh Putra
Campus, 02600, Arau, Perlis, Malaysia
e-mail: mfareq@unimap.edu.my

A.Z. Abdullah
e-mail: zaidiabdullah@unimap.edu.my

N.S.M. Noorpi
e-mail: nursabrina@unimap.edu.my

N.M. Mokhtar
e-mail: nurhakimah@unimap.edu.my

M.A. Jusoh
e-mail: asrijusoh@unimap.edu.my

bagasse and other waste material such as rubber tire dust. These agricultural wastes can help save the nature and the fabrication cost of microwave absorber can be reduced. Based on the result, it proved that the sugarcane bagasse-rubber tire dust can be a good alternative material to be used as microwave absorber and can operate in frequency range between 12.4 and 18 GHz.

Keywords Microwave absorber · Reflection coefficient (S_{11}) · Transmission coefficient (S_{21}) · Ku Band · Absorption

1 Introduction

Agricultural waste from the agricultural industries is usually abundant in Malaysia. The agricultural waste is considered as not useful. Agricultural waste is waste produced at agricultural premises as a result of agricultural activity. The examples of the agricultural waste are sugarcane bagasse, rice husk, rice straw, banana leaves and others. Agriculture waste has potential to be used as an alternative material for the microwave absorber used in the anechoic chamber [1]. A microwave absorber is used to attenuate the energy in electromagnetic wave [2, 3]. It has been used in most microwave application to eliminate stray or unwanted radiation. All these energy could interfere and disturb the system's operation. [4–6]. This RF/microwave absorber will be installed in anechoic chamber to recreate a free space environment [7]. In most absorbers, there is consisting of a filler material inside a matrix to do most of the absorbing. In this work, the material such as sugarcane bagasse has been used. Then the rubber tire dust was added with sugarcane bagasse (SCB) and turned them into composite. Elemental analysis of raw sugarcane bagasse using scanning electron microscope (SEM) showed that the content of carbon in sugarcane bagasse is 17.89 % [8]. Carbon is an element that can provide good reflection loss performance. The pore structure and surface area are the parameters for the carbon material. The pore structure which is the volume of the pores can determine and limit the sizes of the molecules that can be adsorbed. When microwave passed through the absorber, an electrical energy will be produced. Then, the electrical energy is transformed into thermal energy. That is why carbon is important because

C.E. Meng

School of Mechatronic Engineering, University Malaysia Perlis (UniMAP), Pauh Putra Campus, 02600, Arau, Perlis, Malaysia
e-mail: emcheng@unimap.edu.my

L.W. Wen

Institute of Nano Electronic Engineering (INEE), University Malaysia Perlis (UniMAP), Pauh Putra Campus, 02600, Arau, Perlis, Malaysia
e-mail: wwliu@unimap.edu.my

carbon can help transforming microwave energy to thermal energy [9]. The usage of ferrite tiles was one of the recent innovations that could enhance the performance of anechoic chamber [10]. So, in this work, the composite of sugarcane bagasse with rubber tire dust has been fabricated and this is one of the innovations to improve the performance of microwave absorber. Rubber tire dust is tire wear and it has a difficulty in disposing and storing it. By mass, tire treads composed of 40–60 % of natural and/or synthetic rubbers, approximately 30 % of carbon black, and 10–20 % of extender oil sand [11]. The performance of the samples will be measured in the range frequency of 12.4–18 GHz.

2 Methodology

In this project, the work include of fabricating the sample which is the composite of sugarcane bagasse with rubber tire dust. To test its feasibility, the resins have been mixed to the materials. Then, the dielectric properties consist of dielectric constant and loss factor were defined. In this work, the dielectric properties needed to be determined at first. So, the Agilent 85071E Software was being used [12]. The measured reflection and transmission coefficients, S_{11} and S_{21} of samples were obtained from this transmission line technique measurement. The samples that are being tested were samples of pure sugarcane bagasse, pure rubber tire dust, and composite of sugarcane bagasse with rubber tire dust in frequency ranges between 12.4 and 18.0 GHz. Figure 1 shows the materials used which are sugarcane bagasse and rubber tire dust.

The dimension of the sample is thickness, $t = 5$ mm, width, $w = 7.9$ mm and length, $l = 15.8$ mm Fig. 2.

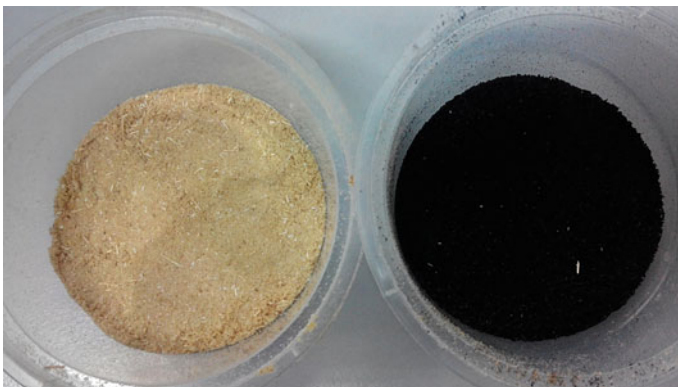


Fig. 1 The materials used in fabricating the sample, sugarcane bagasse and rubber tire dust

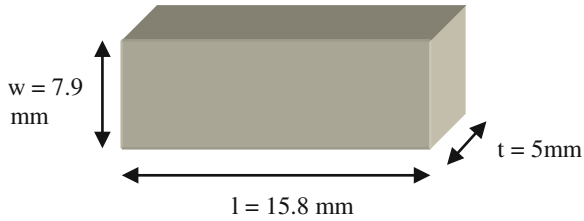


Fig. 2 The dimension of the sample

The thickness of the sample has been calculated using the thickness of sample formula,

$$t = \frac{m}{d \times l \times w} \quad (1)$$

- t = thickness of sample
- m = mass of the sample
- d = density of the sample
- l = length of the sample
- w = width of the sample

2.1 Transmission Line Measurement

Many techniques have been used for dielectric constant measurement such as free space measurement technique [13] and transmission line technique [14–16]. In this work, this transmission line technique has been used where the reflection coefficient and transmission coefficient are measured. A sample with adequate thickness is filled in the section of waveguide which means the sample is placed between two waveguide. Generally, electromagnetic absorbers are being categorized by (a) absorbers that absorb propagated microwave signal in empty space or vacuum and (b) those that absorb standing wave that is inside waveguide [17].

3 Result and Discussion

3.1 Dielectric Properties

Dielectric can be classified as when a material has the ability to store energy when an external electric field is applied. It consists of real part which represents the storage which is dielectric constant and the imaginary part which represents of loss [18].

3.1.1 Dielectric Constant

Dielectric constant can vary significantly with frequency. Figure 3 showed the complex permittivity for pure sugarcane bagasse. Table 1 below shows the dielectric constant and loss factor of the two materials which are pure sugarcane bagasse and pure rubber tire dust in the range frequency of 12.4–18 GHz.

The tire dust indicates the higher value of dielectric constant which is 3.38. Due to the large refractive index of the medium, the signal propagated at slow movement thus resulting in higher value of the dielectric constant [19]. Loss factor is the dissipation of energy in material which is related to the imaginary part (ϵ'') [20]. The quantity ϵ'' is a measure of the attenuation of the electric field cause by the material. This loss factor is in consideration of microwave absorption.

Measurement of the Samples Using Transmission Line Technique

S_{11} is the reflected signal and how much the power reflected from the antenna and S_{21} is the transmission signal from port 2 to port 1 which means the power received at Port 2. Figures 4 and 5 shows the S_{11} and S_{21} for pure sugarcane bagasse and composite of sugarcane bagasse and rubber tire dust in range frequency of 12.4–18 GHz. Table 2 showed the average reflection loss and percentage of the microwave signal absorption.

In this work, the average reflection loss of sugarcane bagasse sample is 14.04 dB and the absorption is about 38 %. Then, the next sample is fabricated in composite of sugarcane bagasse and rubber tire dust. The composition of sugarcane bagasse-rubber tire dust is 50:50 respectively. The average reflection loss for composite of

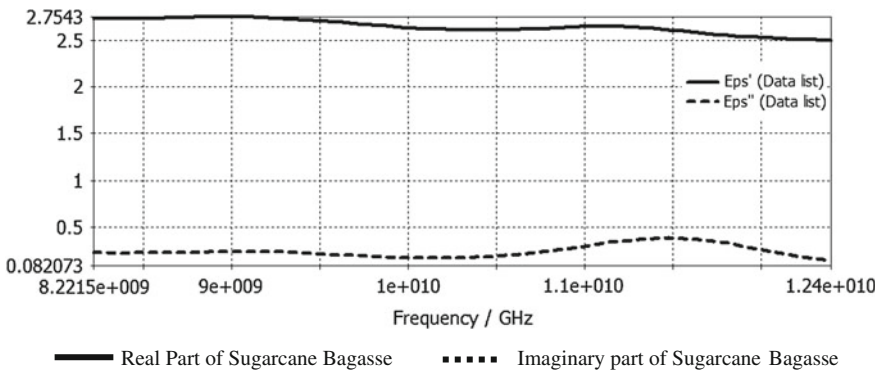


Fig. 3 Frequency spectrum of the complex permittivity of sugarcane bagasse sample

Table 1 Dielectric constant and loss factor of pure sugarcane bagasse and pure rubber tire dust

| Material | Dielectric constant, ϵ' | Loss factor |
|-------------------------|----------------------------------|-------------|
| | 12.4–18 GHz | |
| Sugarcane bagasse (SCB) | 2.88 | 0.25 |
| Rubber tire dust | 3.38 | 0.14 |

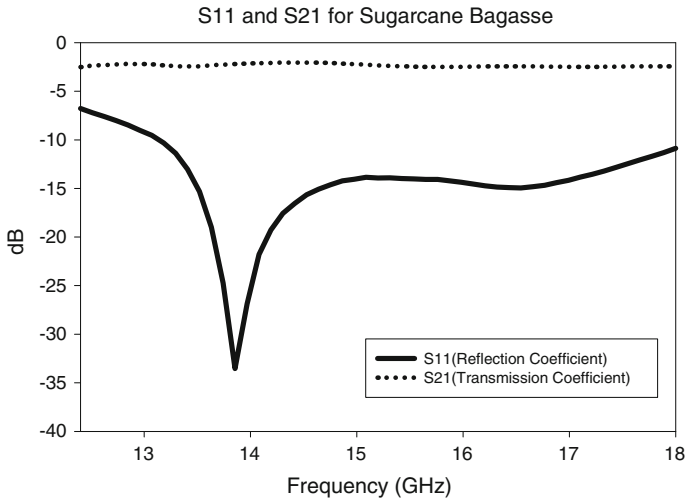


Fig. 4 S11 and S21 for sample of sugarcane bagasse

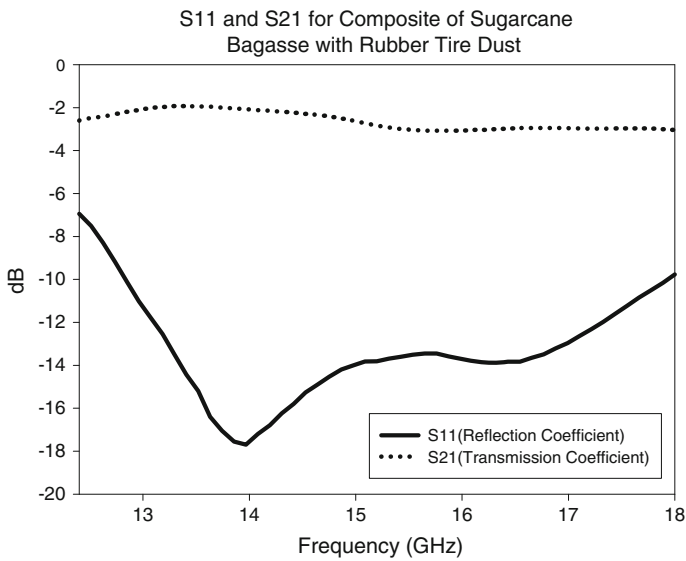


Fig. 5 S₁₁ and S₂₁ for composite of sugarcane bagasse with rubber tire dust

SCB and RTD is 13.22 dB. From the result, it shows that when sugarcane bagasse was added with rubber tire dust, it enhances the performance of the absorber which is 40.44 % of absorption compare to pure sugarcane bagasse which is 38 %. So, rubber tire dust can be a potential material to be added to sugarcane bagasse in fabricating the microwave absorber in range frequency 12.4–18 GHz.

Table 2 Average reflection loss and absorption of sugarcane bagasse and composite of sugarcane bagasse with rubber tire dust

| Frequencies (GHz) | Pure sugarcane bagasse spectrum of the complex permittivity of sugarcane (SCB) | | Composite of sugarcane bagasse with rubber tire dust | |
|-------------------|--|----------------|--|----------------|
| | Average reflection coefficient (dB) | Absorption (%) | Average reflection coefficient (dB) | Absorption (%) |
| 12.4–15.0 | -14.981 | 36.95 | -13.672 | 35.49 |
| 15.0–18.0 | -13.712 | 38.81 | -12.823 | 44.46 |
| 12.4–18.0 | -14.039 | 38 | -13.222 | 40.44 |

4 Conclusion

Based on the performances which are reflection loss, transmission coefficient and percentage of absorption from the measurement using the transmission line technique, the sugarcane bagasse-rubber tire dust has the potential to be used as the alternative material in fabricating the microwave absorber. The main objectives of this research are to design, develop, fabricate and measure an efficient, environmental friendly and low cost microwave absorber using agricultural waste such as sugarcane bagasse and mixed with other waste which is rubber tire dust. By using the sugarcane bagasse, it can help reduce the abundant of agricultural waste and reduce the cost of production of the microwave absorber compared to use the existing expensive material such as polyurethane and polystyrene. The fabricated microwave absorber can operate successfully in the microwave range frequency 12.4–18 GHz (Ku Band).

References

1. Nornikman, H., Soh, P.J., Azremi, A.A.H., Wee, F.H., Malek, M.F.: Investigation of agricultural waste as an alternative material for microwave absorber. In: Progress in Electromagnetics Research Symposium, PIERS Moscow, Russia, pp. 1287–1291 2009
2. Wilkerson, J., Skeen, M.M., Patrick, D.F., Hodges, R.D., Schimizzi, R.D., Vora, S.R., Feng, Z., Gard, K.G., Steer, M.B.: Acoustic-RF anechoic chamber construction and evaluation Glenwood Garner III, NC State University, Raleigh
3. Chung, B.K., Chuah, H.T.: Modeling of RF absorber for application in design of anechoic chamber. Prog. Electromagn. Res. (PIER) **43**, 273–285 (2003)
4. Emerson, W.H.: Electromagnetic wave absorbers and anechoic chambers through the years. IEEE Trans. Antennas Propag. **AP 21**(4), 484–490 (1973)
5. Paul, D.: Emerson and cuming, microwave products, “Tech Notes of Theory and Application of RF/Microwave Absorbers”, (2012)
6. Iqbal, M.N., Malek, F., Ronald, S.H., Shafiq, M., Juni, K.M., Chat, R.: A study of the EMC performance of a graded-impedance microwave, rice- husk absorber. Prog. Electromagn. Res. **131**, 19–44 (2012)

7. Hemming, L.H.: *Electromagnetic Anechoic Chamber—A Fundamental Design and Specification Guide*. IEEE Press and Wiley Interscience, Canada (2002)
8. Devnarain, P.B., Arnold, D.R., Davis, S.B.: Production of activated carbon from South African sugarcane bagasse. In: *Proceedings Congress of the South African Sugar Technologists Association*, vol. 76, pp. 477–489 (2002)
9. Lam, S.S., Chase, H.A.: A review on waste to energy processes using microwave pyrolysis. *Energies* **5**, 4209–4232 (2012)
10. Dash, G., Ampyx L.L.C.: How RF anechoic work (1999). <https://alum.mit.edu>
11. Kumata, H.: Evaluation of hydrogenated resin acids as molecular markers for tire-wear debris in urban environments. *Environ. Sci. Technol.* **45**, 9990–9997 (2011)
12. Agilent, Technologies Inc: *Agilent 85071E Materials Measurement Software Technique Overview* (2012)
13. Wee, F.H., Soh, P.J., Suhaizal, A.H.M., Nornikman, H., Ezanuddin, A.A.M.: Free space measurement technique on dielectric properties of agricultural residues at microwave frequencies. In: *International Microwave and Optoelectronics Conference (IMOC) 2009*
14. Chung, B.-K.: Dielectric constant measurement for thin material at microwave frequencies. *Prog. Electromagn. Res. (PIER)* **75**, 239–252 (2007)
15. Challa, R.K., Kajfez, D., Gladden, J.R., Elsherbeni, A.Z., Demir, V.: Permittivity measurement with a non-standard waveguide by using TRL calibration and fractional linear data fitting. *Prog. Electromagn. Res. B* **2**, 1–13 (2008)
16. Chung, B.K.: A convenient method for complex permittivity measurement of thin materials at microwave frequencies. *J. Phys. D Appl. Phys.* **39**, 1926–1931 (2006)
17. Taylor and Francis Group, LLC: *Absorber Materials* (2009)
18. Agilent Technologies: *Basic of Measuring the Dielectric Properties Materials—Application Notes*, 26 June 2006
19. Lesurf, J.: Warp factor $\epsilon!$ University of St. Andrews (2006). http://www.st-andrews.ac.uk/~www_pa/Scots_Guide/info/comp/passive/capacity/dielec/di_const/dicon.html
20. Iqbal, M.N., Malek, M.F., Lee, Y.S., Zahid, L., Mezan, M.S.: A study of the anechoic performance of rice husk based, geometrically tapered, hollow absorbers. *Int. J. Antennas Propag.* **2014**, 9 (2014)

Multi-resonator Using Complementary Split Ring Resonator for Chip-Less RFID Application

Mohd Ezwan Bin Jalil, Mohammad Kamal A. Rahim,
Noor Asmawati Samsuri and Raimi Dewan

Abstract A novel multi-resonator using slotted complementary split ring resonator (CSRR) on planar transmission line is proposed for the design of chip-less RFID tag. The 4 bit multi resonator is operates from 4 to 5 GHz. The tag consists of a micro strip open stub resonators and two UWB monopole antennas. The 65 mm × 50 mm chip-less RFID tag is designed on a Taconic substrate with permittivity of 2.75. In the end, the chip-less tag has a 8-bit—data capacity are designed in the range of 4–5.8 GHz.

1 Introduction

Radio Frequency Identification (RFID) system has been implemented in various applications such as toll road payment, equipment tagging, logistic tracking and security devices [1]. The RFID system element consists of a reader which transmits encoded signal to interrogate the tag, transponder (tags), and subsequently store the ID information in an integrated circuit. The integrated circuit stores and process the radio-frequency signal. The RFID system is able to transfer data information within short range of distance via wireless communication for tracking and identification purpose.

M.E.B. Jalil (✉) · M.K.A. Rahim · N.A. Samsuri · R. Dewan
Faculty of Electrical Engineering, UTM-MIMOS CoE in Telecommunication
Communication Engineering Department, University Technology Malaysia,
81310 Johor Bahru, Johor, Malaysia
e-mail: ezwanjalil@gmail.com

M.K.A. Rahim
e-mail: mkamal@fke.utm.my

N.A. Samsuri
e-mail: asmawati@fke.utm.my

R. Dewan
e-mail: raimidewan@gmail.com

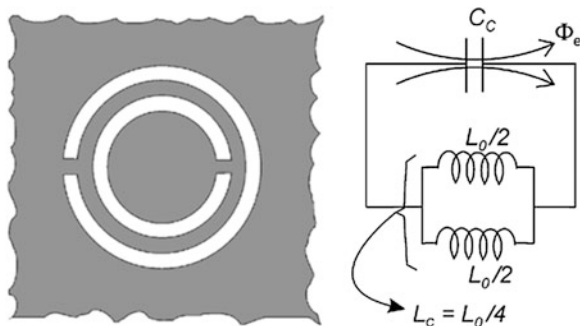
Compact and low cost chip-less RFID are the criterias for the design of future RFID system. Currently, the conventional RFID tag consist of integrated component such as microchip and antenna element, whereby the information is encoded and stored in microchip while the antenna act as a signal receiver and transmitter. In this paper, chip-less RFID without microchip has been introduced. The information bits are the encoded bit with other passive element structure.

The chip-less RFID types are classified into two main groups; time-domain by analyzing the reflected echoes generated by inductive and capacitive discontinuities while frequency domain by method of spectral signature encoding. Based on the method of spectral signature encoding, a near field chip-less RFID tag with an array of two half-wavelength resonator on transmission line is presented in [2]. A compact 8-bit complementary rectangular split ring resonator are designed which operates from 7.5 to 11 GHz [3].

The chips-less RFID tags based on the LC resonator has been proposed by using spit-wheel, microstrip open stub and spur line techniques [4–6]. One of the LC resonant methods to design chip-less RFID based on spectral signature encoding is using split ring resonator structure. The split ring resonator (SRR) has high Q value which is suitable for filter application. The SRR structure has been placed in the back side of the substrate and under the slots to achieve high magnetic coupling between line and rings at resonance frequency. The similar concepts are applied for the design of chip-less RFID antenna by encoding the bits from the combined two SRR elements. The CSRR structure which is the negative image SRR consists of two half wavelength of different length rings which are coupled with each other to resonate at single frequency. In contrast, the CSRR requires electric coupling and thus, the structure oriented in such a way it is perpendicular to the electric field.

Small electrical dimension of CSRR with planar transmission line can be described by lumped-equivalent circuit. The equivalent CSRR circuit proposed by Baena [7] which shown in Fig. 1 whereby the C and R is the equivalent capacitance and resistive elements respectively. L_c is the equivalent inductance of two mutual inductance between slit and inductance of the split. Each inductance of the single SRR unit, $L_o/2$ where $L_o = 2\pi r_o L_{pu1}$ and L_{pu1} is per unit length inductance which connects the disk to the ground plane.

Fig. 1 Equivalent circuit of CSRR element



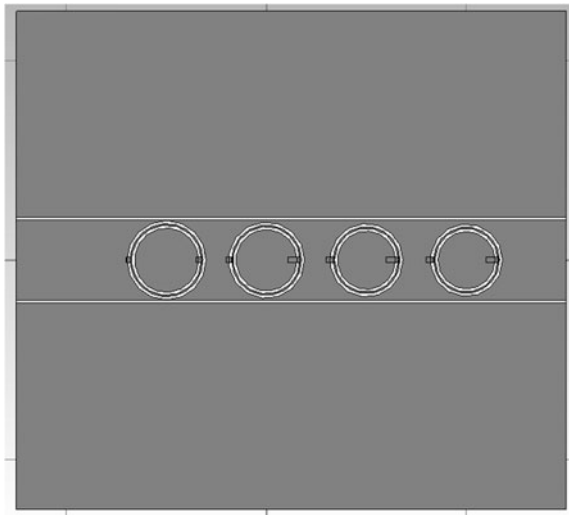
In this paper, a 4 bit complementary split ring resonator (CSRR) using coplanar waveguide (CPW) feed line transmission has been investigated. The multi-resonator as chip-less RFID tags are presented in this paper. The multi-resonator is combined with transmitting and receiving CPW feed Ultra Wide Band antenna with different orientation. The chip less RFID system is designed on Taconic substrate with thickness of 1 mm, permittivity of 2.75 and loss tangent 0.0003.

2 Tag Design

The 4-bit chip-less tag is designed using (CSRR) on CPW feed transmission line as shown in Fig. 2 and the proposed design is simulated with Computer Simulation Technology (CST) Microwave Studio 2013. The slotted strip line is introduced in the SRR to create stop-bands filter. The CSRR has two circular rings which the separation of the two rings is located at two opposite side of the resonator. The inner ring of CSSR is used as loading element for the outer ring to generate a single stop band. Each combination of the ring resonator represent one bit of information. The condition of inner and outer ring resonator represent “0” bit for no-split or “1” bit for split as shown in Fig. 3. The slot continuity within the CSRR structure (no-split) has cause the corresponding frequency of CRRS to resonate at a higher frequency outside the required frequency range. The chip-less tag is encoded in the range of 4–6 GHz.

The stub length is determined to be 8 mm to obtain a transmission line with an impedance of 50 Ω . The design parameters of chip-less RFID tag are shown in Table 1. The different diameters of split ring resonator structure correspond to different frequency signature of the chip-less tag. The symmetrical structure of the

Fig. 2 4 bit complementary split ring resonator (CSRR) chip-less RFID



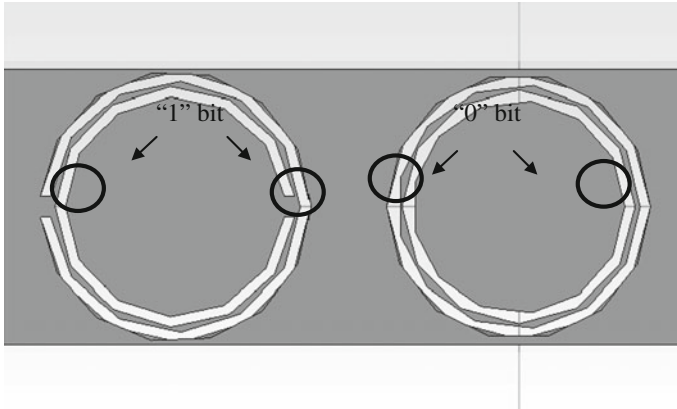


Fig. 3 Two state condition of split ring (“1” bit) and non-split ring (“0” bit)

split ring resonator structure allows the chip-less tag to retain the frequency signature regardless of the tag orientations. The gap between CSRR has improved the transmission characteristic. By increasing the gap, the inductance effect between CSRR can be minimized. The width of ring resonator determines the bandwidth of the corresponding frequency. The electric field distribution in coplanar waveguide (CPW) is concentrated between the ground plane and micro strip line. Thus, the CPW structure exhibit good performance by the minimization of metal loss and losses in using thin substrate. The existence of losses might increase the insertion losses. The CPW structure requires only single side conducting layer; thus, the structure has is easy to be fabricated.

From the simulated transmission characteristic result in Fig. 4, four stop bands is observed. The stop band is produced due to the resonance of inner and outer split ring resonator. First, second, third and fourth frequency signature is at 4.20, 4.38, 4.57 and 4.7 GHz, respectively. For the circuit with ID = 1111, four non-overlapping stop bands are produced as shown in Fig. 4. When the ID = 0101 are determined, the second and fourth resonance resonate at the fixed frequency signature as well as the

Table 1 Chip-less RFID dimension

| Parameter | Dimension (mm) |
|----------------------------------|----------------|
| Radius of first CSRR | 3.20 |
| Radius of second CSRR | 3.05 |
| Radius of third CSRR | 2.90 |
| Radius of forth CSRR | 2.85 |
| Gap between inner and outer ring | 0.15 |
| Gap between CSRR | 2.25 |
| Width the inner and outer ring | 0.30 |
| Width of substrate | 55.00 |
| Length of substrate | 50.00 |

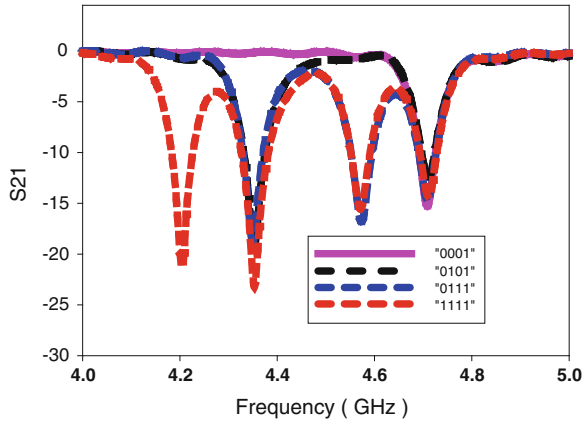


Fig. 4 Transmission characteristic of 4 bit CSRR resonators

second and fourth resonance of CSRR with ID = 1111. Consistent results obtained from all four types of CRRS conditions/state can be used for the encoding of information bit for chip-less RFID application.

The proposed chip-less RFID system operates from 3 to 6 GHz which requires the antenna to operating within similar frequency range to ensure transmission and reception of the interrogated signal. In this research, a compact and simple CPW fed UWB monopole antenna with wide bandwidth is designed to operate from 3 to 12 GHz. The antenna has a high average gain from 3 to 4.5 dBi in the range of 2.5–6 GHz to ensure the increase reading range of the tag as shown in Fig. 5a. The radiation pattern is near omni-directional which produces good transmission and

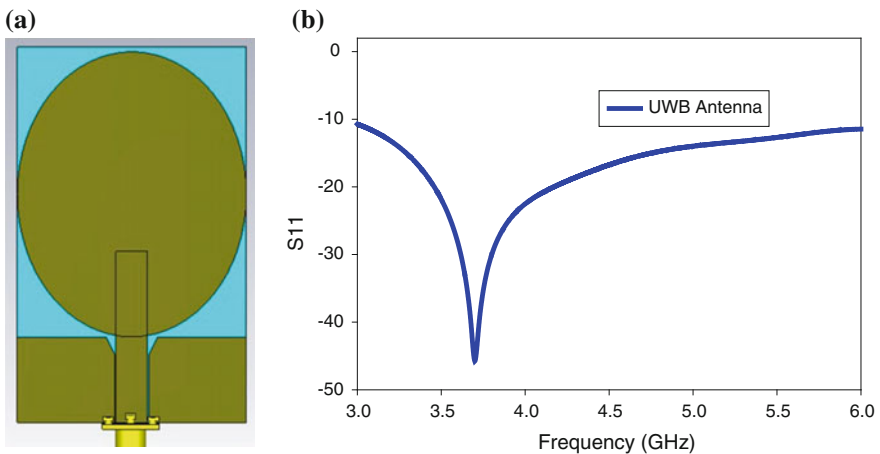


Fig. 5 a CPW fed UWB antenna with overall dimension of 66 mm x 40 mm b Simulated reflection coefficient of CPW fed UWB antenna

reception of signal in all direction. The simulated reflection coefficient of antenna is well performed from 2.5 to 6.0 GHz as shown in Fig. 5b. The same antenna structure is used as the reader antenna.

3 Result and Discussion

The consistent transmission characteristic result of the 4 bit chip-less tag have motivated for a design of 8 bit chip-less tag to operate from 4 to 6 GHz. From the Fig. 6, the eight bit is represented by eight resonant null. The SRR with “11111111” information code resonate at distinguished frequency of 4.15, 4.32, 4.67, 4.76, 4.88, 5.03, 5.16 and 5.49 GHz as shown in Fig. 7. The dimension of the 8 bit prototype is 10.5 cm × 5 cm × 0.1 cm.

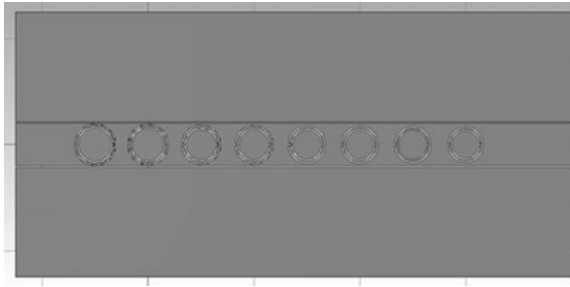
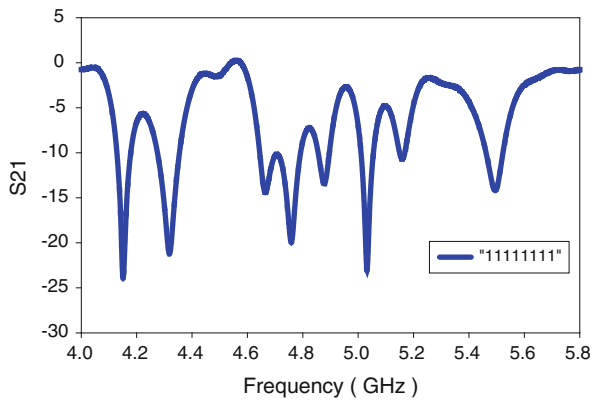


Fig. 6 Transmission characteristic of 8 bit CSRR resonators with length = 105 mm and width = 50 mm

Fig. 7 Transmission characteristic of 4 bit CSRR resonator with information “11111111”



4 Conclusion

The chip-less antenna using circular SRR on CPW transmission line which operate from 4 to 5.6 GHz with 8 bits of data have been designed and analyzed. The concept of circular SRR is proposed to maximize and stabilize the bit amount for chip-less RFID application. The integration between UWB antenna, microstrip stub line and transmission line to form a prototype of chip-less RFID is realized and will be discussed in the future work. The compact chip-less RFID based on CSRR with single sided conducting layer has the potential to be produced on flexible material such paper and plastic for wearable application.

Acknowledgments This work was supported by Ministry of Higher education (MOHE), Research Management Centre (RMC), Universiti Teknologi Malaysia (UTM JB) Johor Bahru, under research grant no. 05H35, 04H38, 4F360 and 4L811.

References

1. Ahsan, K., Shah, H., Kingston, P.: RFID applications: an introductory and exploratory study. *IJCSI: Int. J. Comput. Sci. Issues* **7**(1) 3 (2010)
2. Lee, W.-S., Jang, H.-S., Lee, W.-S., Oh, K.-S., Yu, J.-W.: Design of near-field chipless RFID tags and reader based on transmission line. In: *Microwave Conference Proceedings (APMC), Asia-Pacific* (2013)
3. Bhuiyan, M.S., Azad, A., Karmakar, N.: Dual-band modified complementary split ring resonator (MCSRR) based multi-resonator circuit for chipless RFID tag .In: *2013 IEEE Eighth International Conference on Intelligent Sensors, Sensor Networks and Information Processing* (2013)
4. Bhuiyan, M.S.; Karmakar, N.: Chipless RFID tag based on split-wheel resonators. In: *7th European Conference on Antennas and Propagation (EuCAP)* (2013)
5. Jalil, M.E., Kamal, M., Rahim, A., Samsuri, N.A., Dewan, R.: Chipless RFID Tag based on meandered line resonator. In: *IEEE Asia-Pacific Conference on Applied Electromagnetics (APACE)* (2014)
6. Sum, M., Dinesh, R., Nijas, C.M., Mridula, S., Mohanan P.: Frequency coded chipless RFID tag using spurline resonator. *Radioengineering* **23**, 203 (2014)
7. Baena, J.D., Bonache, J., Martín, F., Sillero, R.M., Falcone, F., Lopetegui, T., Laso, M.A.G., García-García, J., Gil, I., Portillo, M.F., Sorolla, M.: Senior, equivalent-circuit models for splitting resonators and complementary split-ring resonators coupled to planar transmission lines. *IEEE Trans. Microw. Theory Tech.* **53**(4), 1451 (2005)

Energy Detection Spectrum Sensing Measurement Using GNU Radio and USRP B200 at Wi-Fi Frequency

K.H. Yusof, M.K.A. Rahim, K.M. Yusof and M.E. Jalil

Abstract Spectrum sensing is one of the main tasks of cognitive radio, it decides whether the spectrum band is occupied by the primary or not. One of the techniques of spectrum sensing is energy detection (ED). Theory and simulation of ED are well established, however the real measurement of ED performance is not many, especially using Universal Software Radio Peripheral (USRP) B200 at Wi-Fi frequency. So, real measurement of ED performance using USRP B200 is collected and compared with theory. The result shows, that the ED performance measured using USRP B200 follows the theory.

1 Introduction

As the technology of wireless communication growing, the demands in frequency spectrum also rise. The old way of static allocation frequency spectrum leads to inefficient utilization of the spectrum, such as, TV band, FM band, mobile communication band and etc. Several analysis and studies had been carried out by spectrum regulators to investigate this issue [1]. The studies show that most of the spectrum frequency is underutilized.

K.H. Yusof (✉) · M.K.A. Rahim · K.M. Yusof · M.E. Jalil
Communication Engineering Department, Faculty of Electrical Engineering, Universiti
Teknologi Malaysia, Utm Johor Bahru, 81310 Johor, Malaysia
e-mail: khilmi89@gmail.com

M.K.A. Rahim
e-mail: mkamal@fke.utm.my

K.M. Yusof
e-mail: kamalmy@fke.utm.my

M.E. Jalil
e-mail: ezwanjalil@gmail.com

Cognitive radio (CR) technology can be a solution to allocate the spectrum resource properly, this is because cognitive radio is able to learn the environment and to dynamically adapt its operating parameters to make best use of the available spectrum. One of the primary tasks of CR is spectrum sensing. The function of spectrum sensing is to detect presence of primary user utilizing the channel, in order to access the channel without causing interference to primary user [2].

There are several techniques of spectrum sensing, some of it are matched filter, cyclostationary, and energy detection [3]. These techniques are well established in theoretical and simulation. There are some measurement done using the USRP version 2 (USRP2) in [4, 5]. So in this paper measurement using GNU Radio with USRP B200 at Wi-Fi frequency is collected to find performance of energy detection. Then the measured result is analyzed and compared with theory.

This paper is organized as follows. Section 2 introduced the technical background, the theory of energy detection spectrum sensing and related equations. The measurement setup for data collection is presented in Sect. 3. Section 4 is the results and discussion of the measured energy detection performance. Lastly, Sect. 5 concludes the paper.

2 Technical Background

2.1 Energy Detection Spectrum Sensing

Energy detection (ED) is one common way of spectrum sensing because of its low complexities, computation and implementation. In energy detection technique, the primary user signal is detected by comparing the output of the energy detector with a threshold, λ_E which depends on the noise floor.

Figure 1 shows the schematic representation of conventional energy detection spectrum sensing. The energy detection work by sampling the received signal in time domain first, then it is passed to Fast Fourier Transform (FFT) to represent the signal in frequency domain, after that, the output of the FFT is converted to energy by finding its magnitude squared. Then, the energy samples collected are averaged by its number of samples, N and finally compared to a threshold value to decide whether the primary user signal is occupying the frequency band or not.

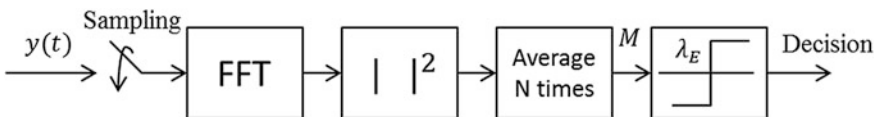


Fig. 1 Schematic representation of energy detection spectrum sensing

2.2 The Performance Measures of Energy Detection

The performance of the energy detection algorithm can be measured using two probabilities, probability of detection P_d and probability of false alarm P_f [3, 6].

P_f is the probability that the incorrect decision that considered the frequency decision is occupied when it is actually not, it can be formulated as in Eq. (1). The value of P_f should be kept as low as possible to prevent underutilization of transmission opportunities.

P_d can also be described as the probability of detecting a signal on the selected frequency when it is truly present. So, a large detection probability is desired. P_d can be written as in Eq. (2). Both Eqs. (1) and (2) are taken from [7], where λ_E is threshold, σ_w^2 is noise variance, N is number of samples, SNR is signal to noise ratio, and $Q(\cdot)$ is the complementary distribution function of standard Gaussian.

According to IEEE802.22 Standard [8], desired P_f value is below than 0.1 (10 %) and P_d should be greater than 0.9 (90 %).

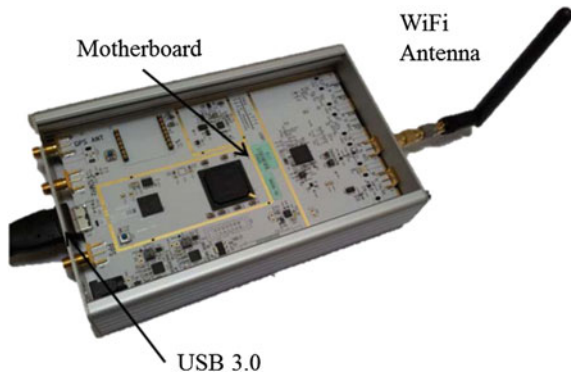
$$P_f = Q\left(\left(\frac{\lambda_E}{\sigma_w^2} - 1\right)\sqrt{N}\right) \quad (1)$$

$$P_d = Q\left(\left(\frac{\lambda_E}{\sigma_w^2} - SNR - 1\right)\sqrt{\frac{N}{2SNR + 1}}\right) \quad (2)$$

3 Measurement Setup

The hardware used for measurement is USRP B200 from Ettus Research, and two laptops. The USRP B200 (Fig. 2) provides a fully integrated, single board, Universal Software Radio Peripheral platform with continuous frequency coverage from 70–6 GHz. Designed for low-cost experimentation, it combines a fully integrated direct conversion transceiver providing up to 56 MHz of real-time bandwidth, an

Fig. 2 USRP B200 by Ettus Research



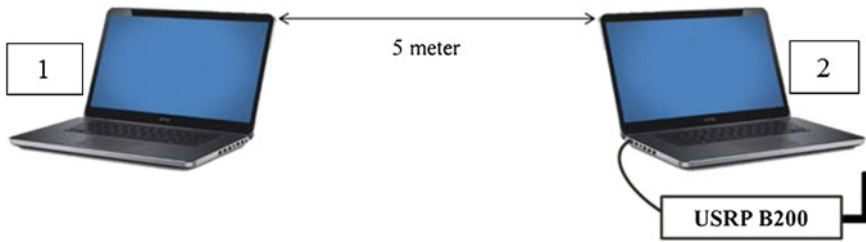


Fig. 3 Measurement Setup

open and reprogrammable Spartan6 FPGA, and fast and convenient bus-powered super speed USB 3.0 connectivity.

The software used is GNU Radio and MATLAB. GNU radio is an open source software that provides various kinds of blocks and module that can be used with USRP B200 to implement simple applications as well as record or measured real time data. Data processing, calculation, and plotting graph are done using MATLAB.

The measurement setup is shown in Fig. 3. Two laptops were placed at a distance of 5 m from each other. Both laptops are connected using Wi-Fi ad hoc (point to point) connection, and one of the laptop is connected with the USRP B200 for data collection.

The data is captured at center frequency 2.437 GHz (Wi-Fi channel 6) by executing the GNU Radio flow graph (Fig. 4) on laptop 2. There were two types of data captured, first was noise level, and the second was received signal level. The parameters and value used for measurement is shown in Table 1. 40 numbers of samples were taken, with sample number 1 consist of 1024 FFT data, sample number 2 have $2 \times 1024 = 2048$ FFT data, and so on until sample number 40. The data is then processed using MATLAB. The measurement was taken at the P18 AMAL Lab, UTM.

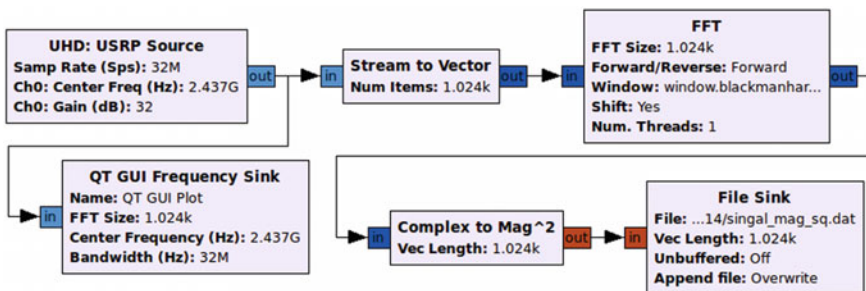


Fig. 4 One of the GNU Radio Companion flow graph used for capturing data

Table 1 Parameters for USRP B200 measurement

| Parameter | Value/range |
|------------------|-------------|
| Sample rate | 32 Msps |
| Center frequency | 2.437 GHz |
| FFT size | 1024 |
| No. of sample | 1–40 |

4 Results and Discussion

This section is divided into three, selection of threshold value, comparison between measurements and theory for probability of false alarm, and lastly comparison between measurements and theory for probability of detection.

4.1 Threshold Value Selection

Figure 5 shows the measured result for probability of false alarm, P_f against number of samples, N with three threshold values. Threshold value λ_E is selected based on the noise variance σ_w^2 . The measured noise variance is around -110 dB, therefore threshold value of -109 , -108 and -107 dB are selected to find which value gives the best performance for ED spectrum sensing in terms of P_f . It is desirable to achieve P_f less than 0.1 at small N .

From Fig. 5 it can be seen that at $N = 10$, threshold value of -107 dB ($P_f = 0.0532$) performs better compared to -108 ($P_f = 0.1368$) and -109 dB ($P_f = 0.2637$). Therefore, threshold value -107 dB is selected for probability of false alarm P_f and probability of detection P_d measurement.

Fig. 5 Graph of probability of false alarm P_f , against number of samples N with three threshold variation, -109 , -108 , and -107 dB

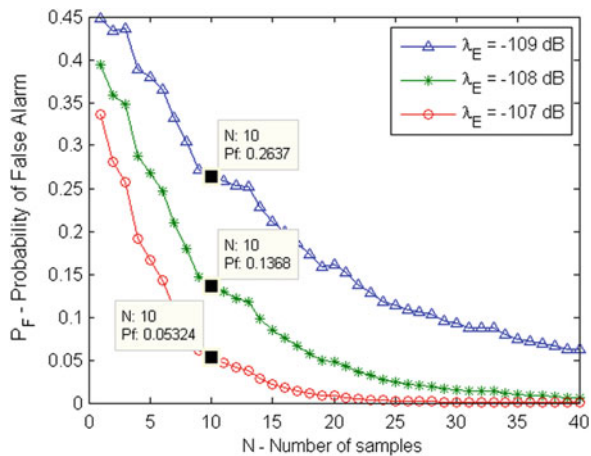
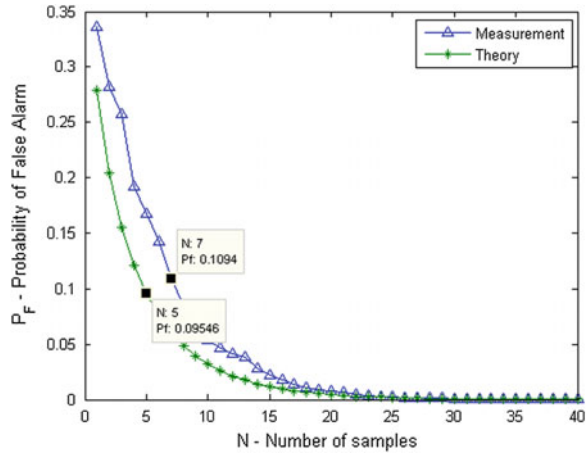


Fig. 6 Graph of probability of false alarm P_f , against number of samples N for measurement and theory with threshold selected at -107 dB



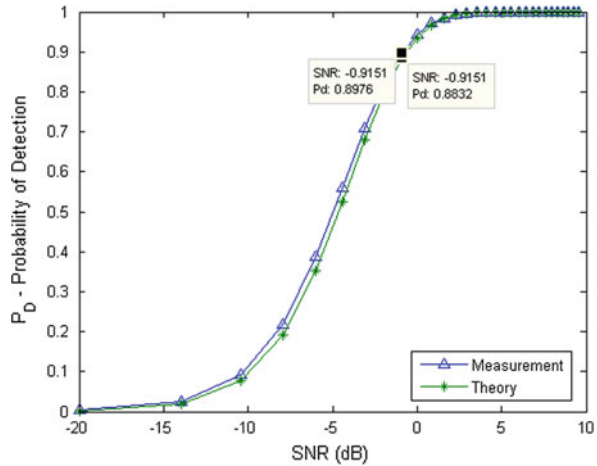
4.2 Comparison Between Measurement and Theory for Probability of False Alarm, P_f

Figure 6 shows P_f versus N for measurement and theory with threshold set to -107 dB. It can be seen that the measurement plot for P_f almost follow the theoretical P_f plot with 7 % maximum difference in P_f value compared to theory. The theoretical P_f plot falls below the desired P_f value ($P_f < 0.1$) at least number of samples ($N = 5$) compared to measurement plot ($N = 7$).

4.3 Comparison Between Measurement and Theory for Probability of Detection, P_d

In Fig. 7 the values of probability of detection, P_d are plotted for measurement and theory. The threshold is set to -107 dB and the signal to noise ratio, SNR varies from -20 to 10 dB, keeping the number of samples to 40 samples. It can be seen that the measurement plot for P_d performs slightly better compared to theory at SNR lower than -1 dB. At SNR equals to -0.9 dB, both measurements ($P_d = 0.8976$) and theoretical ($P_d = 0.8832$) reached the desired P_d value ($P_d > 0.9$). The measurement plot for P_d conforms to the theoretical plot. The measurement plot seems to be slightly better compared to the theoretical, this can be explained by referring to Eq. (2), as the SNR is varied, and threshold λ_E is fixed, P_d now depends only on noise variance σ_w^2 , so if the measured σ_w^2 is lower than theory, the resulting P_d will be higher than theoretical plot.

Fig. 7 Graph of probability of detection P_d , against signal to noise ratio SNR for measurement and theory with threshold selected at -107 dB



5 Conclusion

Threshold value -107 dB is selected because it gives the best performance in terms of P_f . From the result, it can be concluded that, measurement plot using the USRP B200 for probability of false alarm P_f and probability of detection P_d almost follows the theory. As measured performance using USRP B200 conforms to the theory of conventional energy detection, hence future experiment can be done using different type of energy detection or even different spectrum sensing technique.

Acknowledgments The authors thank the Ministry of Higher Education (MOHE) for supporting the research work; Research Management Centre (RMC), School of Postgraduate (SPS), Communication Engineering Department and Universiti Teknologi Malaysia (UTM-JB) Johor Bahru for the support of the research under grant no R.J130000.7923.4L811, 4F360 and 04H38.

References

1. Bacchus, R.B., Fertner, A.J., Hood, C.S., Roberson, D.A.: Long-term, wide-band spectral monitoring in support of dynamic spectrum access networks at the IIT spectrum observatory. In: Proceedings of the 3rd IEEE International Symposium on New Frontiers in Dynamic Spectrum Access Networks (DySPAN 2008) (2008)
2. Mitola, J., Maguire G.Q.Jr.: Cognitive radio: making software radios more personal. *IEEE Pers. Commun.* **6**, 13–18 (1999)
3. Yucek, T., Arslan, H.: A survey of spectrum sensing algorithms for cognitive radio applications. *IEEE Commun. Surv. Tutor.* **11**, 116–130 (2009)
4. Weber, C., Hildebrandt, G.: Evaluation of blind sensing algorithms in the 2.4 GHz ISM-band on GNU radio and USRP2. In: 2012 International Symposium on Wireless Communication Systems (ISWCS) pp. 551–555 (2012)

5. Khandakar, A., Mohammed, A., El Sherif, A.: Experimental threshold determination for secondary users using USRP and Gnu radio. In: *Digital Information and Communication Technology and its Applications (DICTAP)*, pp. 62–68 (2014)
6. Ma, J., Li, G.Y., Juang, B.-H.: Signal Processing in cognitive radio. *Proc. IEEE* **97**, 805–823 (2009)
7. Liang, Y.-C., Zeng, Y., Peh, E.C.Y., Hoang, A.T.: Sensing-throughput tradeoff for cognitive radio networks. *IEEE Trans. Wirel. Commun.* **7**, 1326–1337 (2008)
8. IEEE Standard for Information technology—Local and metropolitan area networks—Specific requirements—Part 22: Cognitive Wireless RAN Medium Access Control (MAC) and Physical Layer (PHY) specifications: Policies and procedures for operation in the TV. *IEEE Std 802.22-2011*, pp. 1–680 (2011)

Double Layer Polarization Insensitive Metamaterial Absorber with Dual Resonances

Osman Ayop, Mohamad Kamal A. Rahim, Noor Asniza Murad
and Noor Asmawati Samsuri

Abstract This paper presents the design of double layer polarization insensitive metamaterial absorber with dual resonant frequencies at 9 and 10 GHz. A unit cell of the metamaterial consists of four circular rings with copper lines printed on 0.8 mm thick FR4 substrate. The simulated result shows that the dual band metamaterial absorber achieves 89.25 and 95.97 % for normal incident electromagnetic waves at 9 and 10 GHz respectively. The corresponding full width half maximum (FWHM) are 2.99 and 3.32 %. The simulation result verified that the absorber is perform well at any polarization of incident electromagnetic waves and operate at wide operating angles which are 63° and 62° for TE mode and TM mode respectively.

1 Introduction

Metamaterial, since many years has attracted a lot of attention in the research field of science and technology due to their unique properties that is not exist in nature but can be physically realizable [1]. A lot of advanced material design can be obtained by using structural physic. Some of them are negative refraction [2], acoustic cloaking metamaterial [3], the perfect lens [4], artificial magnetic conductor [5], and perfect absorbers [6]. One of the interest sub-topic of metamaterial is

O. Ayop (✉) · M.K.A. Rahim · N.A. Murad · N.A. Samsuri
Faculty of Electrical Engineering, Universiti Teknologi Malaysia,
81301 Johor Bahru, Malaysia
e-mail: osman@fke.utm.my

M.K.A. Rahim
e-mail: mkamal@fke.utm.my

N.A. Murad
e-mail: asniza@fke.utm.my

N.A. Samsuri
e-mail: asmawati@fke.utm.my

perfect absorbers. It have been reported by many researches that by engineering the metamaterial structure, perfect absorber can be obtained. The concept of perfectly match layer is used to design perfect metamaterial absorbers. The concept is to match the surface impedance of the metamaterial structure with the free space impedance to maximize the absorption of electromagnetic waves [7]. Many absorber design can absorb electromagnetic waves very efficient for normal incident waves but if the incident angle is increased, the absorbance is decreased. Several works have been done to extend the high absorbance for large excitation angle of incident wave [8]. Other than incident angle, polarization is also critical in metamaterial design [9]. Good absorber can maintain the absorbance properties for any polarization of incident waves. Therefore, this paper proposes a metamaterial absorber that can work at dual band, large operating angle and not sensitive to polarization state.

2 Metamaterial Design

The schematic of the proposed unit cell metamaterial absorber is shown in Fig. 1. The structure consists of double layer dielectric substrate with dielectric constant of 4.6 and loss tangent of 0.019. Both dielectric substrates are separated by a full metal plane. At the top and bottom surfaces, there are four resonant elements printed at each surface. The resonant elements are constructed by four circular rings structure with copper lines in different arrangement for each circular ring. The original circular ring structure resonates at 10 GHz. The copper lines are added to the circular ring to obtain resonant frequency of 9 GHz. The dimension of the structure

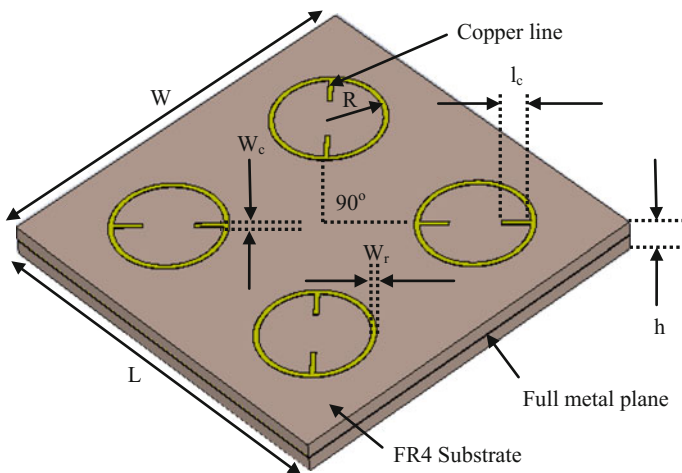


Fig. 1 The unit cell of the proposed metamaterial absorber. Each unit cell consists of four identical resonant elements but with 90° angle different

is optimized using full wave simulation. The size of substrate for the unit cell is $18 \text{ mm} \times 18 \text{ mm} \times 1.67 \text{ mm}$ ($W \times L \times h$). The average radius of the circular ring structures, R is 2.70 mm. The width of the rings, W_r is 0.24 mm. The length, l_c and width, W_c of the copper lines are 1.23 and 0.24 mm respectively. A full metal plane with significant thickness (0.07 mm) is placed in between the dielectric layers to simplify the analysis where the transmittance can be reduced to zero for all frequency investigated in this study. So that, the absorbance value can be determined by using only the reflectance value.

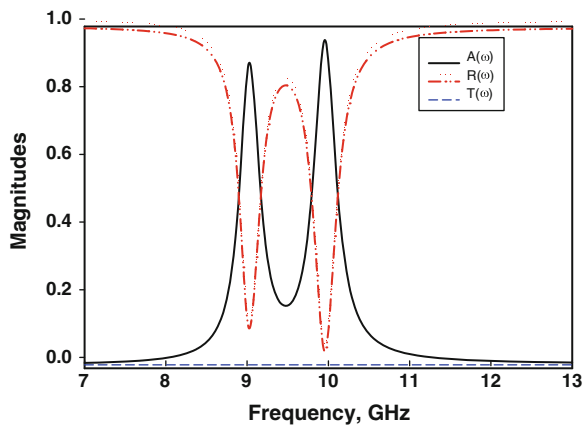
3 Simulation Result and Discussion

The simulation results are divided into five sections. The first section is the characteristics of metamaterial absorber for normal incident waves. The second section is the characteristic of absorbance for different polarization state. The third section is the operating angle of metamaterial absorber for TE mode and TM mode. The fourth section is the characteristic of electric field distribution and the fifth section discusses the characteristic of surface current distribution for the proposed metamaterial absorber.

3.1 Transmittance, Reflectance, and Absorbance

For any absorber design, the magnitude of absorbance, $A(\omega)$ is determined by the magnitudes of transmittance, $T(\omega)$ and reflectance, $R(\omega)$. The relation for all parameters are given by $A(\omega) = 1 - T(\omega) - R(\omega)$. Since $T(\omega)$ is 0 for all frequencies, the absorbance can be simplified by $A(\omega) = 1 - R(\omega)$. The result for $A(\omega)$, $R(\omega)$, and $T(\omega)$ are illustrated in Fig. 2. Figure 2 clearly indicates that the transmittance is 0 for

Fig. 2 The magnitude of transmittance, reflectance, and absorbance for normal incident wave



all frequencies. This is due to the present of full metal plane that is sandwiched by two dielectric substrates. The simulated result shows that two resonant frequencies achieved at 9 and 10 GHz. The reflectance at the resonant frequencies are 10.75 and 4.03 % with absorbance of 88.25 and 95.97 % respectively. The corresponding full width half maximum (FWHM), which the metamaterial absorber can maintain 50 % of absorbance magnitude are 3.00 and 3.30 %.

3.2 Absorbance Magnitude for Different Polarization State

For any metamaterial design, the polarization sensitivity is being a main concern. Polarization sensitive type of metamaterial absorber cannot operate at all polarization state. They can only operate at specific polarization of incident wave thus can limit the capability of the structure for any application where polarization independency is important. In this design, the additional of copper lines will introduce a second resonant frequency at lower frequency, which is 9 GHz. This is due to the increment of electrical length within the resonant element. The copper lines are placed in such a way that the overall structure can obtain dual resonant frequencies which is 9 GHz due to the copper lines and 10 GHz due to the original circular ring structure. Each unit cell consists of four resonant elements which different arrangement (90° angle different with the neighboring elements) to maintain the response for different polarization state. In this section, the metamaterial absorber is simulated for different polarization angle which are 0° , 20° , 45° , 60° , and 90° and the result is presented in Fig. 3. From Fig. 3, it can be seen that the absorbance magnitude and resonant frequencies are almost the same for all polarization angle. This prove that the metamaterial absorber do not sensitive to any polarization state of incident electromagnetic waves for normal incident wave.

Fig. 3 The characteristic of absorbance for different for different polarization angle

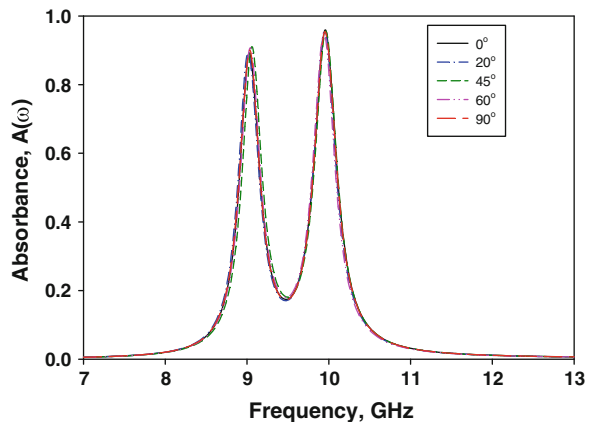
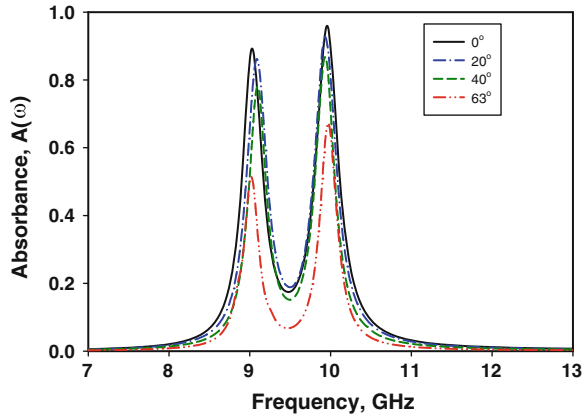


Fig. 4 The Absorbance for TE polarization incident wave (TE mode)



3.3 Operating Angle

Other than polarization independency, the operating angle of the proposed metamaterial is also considered in this paper. The operating angle is determined by 50 % of absorbance magnitude at specific incident angle. In practical, metamaterial absorber can absorb almost all incident EM waves. But, if incident angle is increased, the absorbance will normally decrease because the magnetic flux, which drive the counter circulating current in the substrate will be less effective.

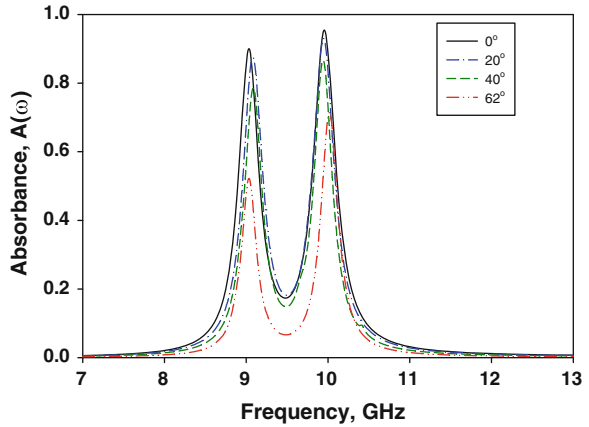
To determine the operating angle, simulation work is carried out for variation of TE and TM polarization incident waves. For TE polarization incident waves (TE mode), the electrical component of excitation EM waves is always tangential to the surface of absorber for any incident angles. For TM polarization incident waves (TM mode), the magnetic component of excitation EM waves should be tangential to the surface of absorber for all incident angles of excitation waves.

The simulated TE mode for the proposed metamaterial absorber is presented in Fig. 4. From the figure, dual resonant frequencies are achieved for all incident angle but with different absorbance magnitudes. The incident angle is simulated for 0°, 20°, 40° and 63°. The absorbance is only simulated up to 63° because beyond that, the metamaterial absorber can no longer maintain the absorbance magnitude above 50 %. The same case goes for simulated TM mode as presented in Fig. 5. The incident angle is simulated for 0°, 20°, 40° and 62°. The operating angle is observed at 62°.

3.4 Electric Field Distribution

The characteristic of electric field distribution can be used to explain the physical behavior of the proposed metamaterial absorber. For the proposed metamaterial absorber, the electric field distribution is simulated at the peak absorption

Fig. 5 The Absorbance for TM polarization incident wave (TM mode)



frequencies, which are 9 and 10 GHz as shown in Fig. 6. Figure 6a shows the electric field distribution for the first resonant, 9 GHz. It can be seen that stronger power loss concentrated on the copper lines and also on the copper ring part adjacent to the copper lines. This may be due to the increase in electrical length of the structure as the presence of additional copper lines. Consequently, lower resonant frequency is achieved compared to the original circular ring structure. On the other hand, Fig. 6b shows that the strong power loss are focused on the circular ring part only which is located 90° away from copper lines. This will contribute to the second resonant at 10 GHz.

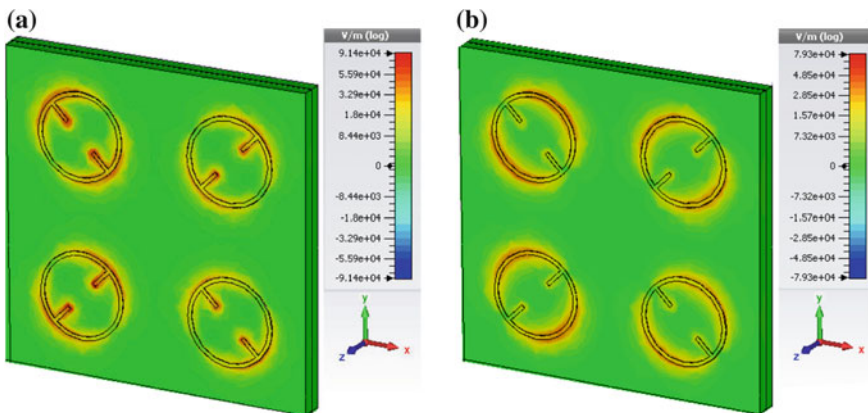


Fig. 6 The simulated electric field distribution of the metamaterial absorber for **a** 9 GHz and **b** 10 GHz

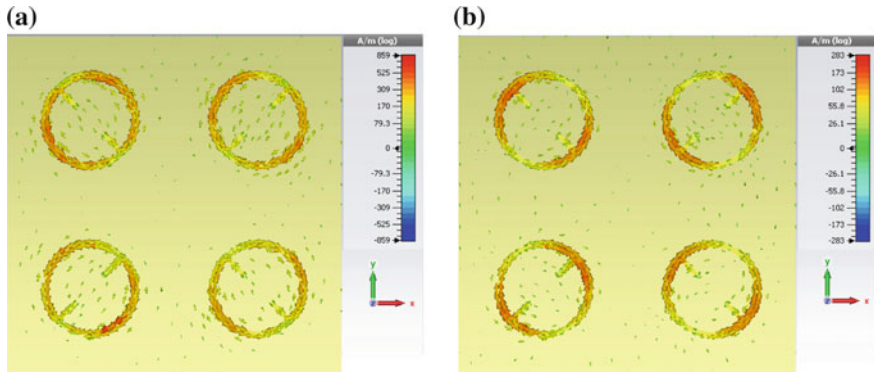


Fig. 7 The simulated surface current distribution of the metamaterial absorber for **a** 9 GHz and **b** 10 GHz

3.5 Surface Current Distribution

Surface current distribution is then investigated to observe the behavior of the current flow. The simulated surface current distribution is presented in Fig. 7. It is observed that upon interaction with incident electromagnetic waves, the flow of current is seen as dipolar response. The current is flowing upward and downward alternately. For 9 GHz, the current is flowing inside and outside the copper lines as shown in Fig. 7a. For 10 GHz, the currents is flowing upward and downward circulating the circular rings, but no current flow is observed inside the copper lines as shown in Fig. 7b.

4 Conclusion

In summary, a double layer polarization insensitive metamaterial absorber with dual resonant has been designed and simulated. The performance of this metamaterial absorber is observed in term of absorbance magnitude for different polarization angle and different incident angle of electromagnetic waves. The simulated result shows that this kind of absorber do not sensitive to any polarization state and also operating at wide angle of incident wave. To understand the physical behavior of the proposed metamaterial absorber, the surface current and electric field distribution are plotted and studied. From the characteristic of surface current and electric field distribution, the origin of resonance can be significantly observed.

Acknowledgments The authors thank the Ministry of Higher Education (MOHE) for supporting the research work, Research Management Centre (RMC), School of Postgraduate (SPS), Communication Engineering Department (COMM) Universiti Teknologi Malaysia (UTM) and all members of Advanced Microwave Lab P18 FKE-UTM for giving motivation, knowledge sharing and support of the research under grant no R.J130000.7923.4S007/04H38/4L811/04H23/4F277.

References

1. Veselago, V.G.: The electrodynamics of substances with simultaneously negative electrical and magnetic permeabilities. *Sov. Phys. Usp.* **10**, 509–517 (1968)
2. Shalaev, V.M., Cai, W., Chettiar, U.K., Yuan, H.-K., Sarychev, A.K., Drachev, V.P., Kildishev, A.V.: Negative index of refraction in optical. *Opt. Lett.* **30**, 3356–3358 (2005)
3. Chena, H., Chan, C.T.: Acoustic cloaking in three dimensions using acoustic metamaterials. *Appl. Phys. Lett.* **91**, 183518 (2007)
4. Wang, W., Lin, L., Yang, X., Cui, J., Du, C., Luo, X.: Design of oblate cylindrical perfect lens using coordinate transformation. *Opt. Express* **16**(11), 8094–8105 (2008)
5. Abu, M., Rahim, M.K.A., Suidi, M.K., Ibrahim, I.M., Nor, N.M.: Dual band artificial magnetic conductor. In: 2009 IEEE International Conference on Antenna, Propagation and System (INAS 2009), Johor Bahru, Malaysia (2009)
6. Landy, N.I., Sajuyigbe, S., Mock, J.J., Smith, D.R., Padilla, W.J.: Perfect metamaterial absorber. *Phys. Rev. Lett.* **100**, 207402 (2008)
7. Ye, D., Wang, Z., Wang, Z., Xu, K., Zhang, B., Huangfu, J., Li, C., Ran, L.: Towards experimental perfectly-matched layers with ultra-thin metamaterial surfaces. *IEEE Trans. Antennas Propag.* **60**(11), 5056–5062 (2012)
8. Tao, H., Bingham, C.M., Strikwerda, A.C., Pilon, D., Shrekehamer, D., Landy, N.I., Fan, K., Zhang, X., Padilla, W.J., Averitt, R.D.: Highly flexible wide angle incident terahertz metamaterial absorber: design, fabrication and characterization. *Phys. Rev. B* **78**(7), 241103 (2008)
9. Yoo, M., Lim, S.: Polarization-independent and ultrawideband metamaterial absorber using a hexagonal artificial impedance surface and a resistor-capacitor layer. *IEEE Trans. Antenna Propag.* **62**(5), 2652–2658 (2014)

A Low Profile Dual-Mode Reconfigurable Antenna Design

Thennarasan Sabapathy, Muzammil Jusoh, R. Badlishah Ahmad and Muhammad Ramlee Kamarudin

Abstract A low profile dual-mode reconfigurable antenna design is introduced in this work. Two properties, namely frequency and radiation pattern are reconfigured using the proposed antenna. Parasitic patch array helps to produce the radiation pattern reconfiguration. Meanwhile, frequency reconfigurability is achieved with a resizable slot located at the back of the antenna. At frequency around 5.8 GHz, the antenna able to reconfigure the radiation pattern to three different directions with average peak gain of approximately 7dBi. Frequency reconfiguration is achieved at four different frequencies from 4.6 to 5.75 GHz.

1 Introduction

A reconfigurable antenna is known as the antenna that has the capability to modify the antenna's properties such as radiation pattern, polarization, or frequency/bandwidth in some desirable fashion. Depends on the systems requirement the antenna is designed to alter any of the properties. Mainly, these types of antennas

T. Sabapathy (✉) · M. Jusoh · R.B. Ahmad
Embedded, Network and Advanced Computing (ENAC), School of Computer and Communication Engineering, Universiti Malaysia Perlis, Arau, Malaysia
e-mail: thenna84@gmail.com

M. Jusoh
e-mail: muzammil@unimap.edu.my

R.B. Ahmad
e-mail: badli@unimap.edu.my

M.R. Kamarudin
Faculty of Electrical Engineering, Wireless Communication Centre (WCC),
Universiti Teknologi Malaysia, Johor, Malaysia
e-mail: ramlee@fke.utm.my

are reconfigured using the aid of RF switches. When an antenna is designed to change its frequency it is known as frequency reconfigurable antenna. Such antenna is capable of modifying the antenna's frequency to certain operating bands which suit multiple applications in a single system. Such antenna can be useful for various applications such as Cognitive Radio (CR) or multi radio platforms [1]. Frequency reconfigurable antennas are also designed for UWB application [2] where the antenna is able to select the desired operating frequency within the UWB band based on the RF switches configuration. On the other hand, polarization reconfigurable antennas [3, 4] change their polarization to support wireless systems such Global Positioning System (GPS), Compass Navigation Satellite System (CNSS) and Wireless Fidelity (WiFi). Meanwhile, radiation pattern reconfigurable antenna is able to change its radiation pattern of the antenna where the direction of the peak antenna gain and/or the antenna beam-width could be changed according to the desired manner.

In recent findings, two or more properties of the antenna were performed with reconfiguration. In work [5] a reconfigurable antenna known as multifunctional reconfigurable array (MRA) is proposed and this antenna can reconfigure all three properties (frequency, radiation pattern and polarization). Similar approach also used by work [6] to obtain multi-functions. However, the number switches and number of arrays required to design the antenna is the trade-off to obtain the multiple functions. Obviously, not many systems require all three types of reconfiguration in a single antenna. Reducing the reconfiguring capability of the antenna reduces the complexity and the size of the antenna. This work presents a reconfigurable antenna which has the conformal profile that can reconfigure two properties of the antenna, namely frequency and the radiation pattern. Frequency reconfiguration by this antenna is capable of increasing spectral density while the pattern reconfiguration able to improve the signal reception of the antenna at high operating frequency. The antenna consists of an active microstrip patch and two parasitic elements. Underneath the driven element, a slot is positioned on the ground plane. The variation of the slot size with the RF switches provides frequency reconfigurable functionality. The antenna is capable to reconfigure four different frequencies from 4.6 to 5.75 GHz using five switches (RF p-i-n diodes) placed in the slot. Meanwhile the parasitic elements which are adjacent to the driven element help to reconfigure the radiation pattern of the antenna at certain higher frequencies (5.6–5.8 GHz). The design of this work closely related to works [7, 8], where the principle of Yagi-Uda patch array antenna is adopted for pattern reconfiguration while slotted ground technique is deployed for frequency reconfiguration. The combination of these two methods in a single antenna design successfully performs the multi-mode reconfiguration. The size of the antenna is relatively small with a dimension of 32×76 mm. In what follows, Sect. 1 describes the details of the proposed antenna. Then, the results are presented, and the performances of the antenna are investigated.

2 Antenna Design

Figure 1 illustrates the physical structure of the proposed antenna. The antenna consists of three parallel patches on a full grounded Taconic dielectric substrate with a thickness of 1.6 mm and a dielectric constant (ϵ_r) of 2.2. The center rectangular patch has a width of $W = 19$ mm and length of $L = 15.7$ mm. This is the driven element (DE) of microstrip array where it is fed through a subminiature (SMA) probe from the back of the antenna. At the DE, the feed location, a is optimized to achieve a desired input impedance of 50Ω . The size of the antenna is given by substrate width, $W_s = 76$ mm and substrate length, $L_s = 32$ mm. The parasitic elements (PEs) are named as PE1 and PE2 as shown in Fig. 1. The PEs are smaller than the DE where the width and length are denoted as W' and L' . The optimized parasitic elements' physical dimension is as follows: $W' = 0.9 \times W$ mm, $L' = 0.998 \times L$ mm. The gap between all elements is 2 mm. As shown in Fig. 1b

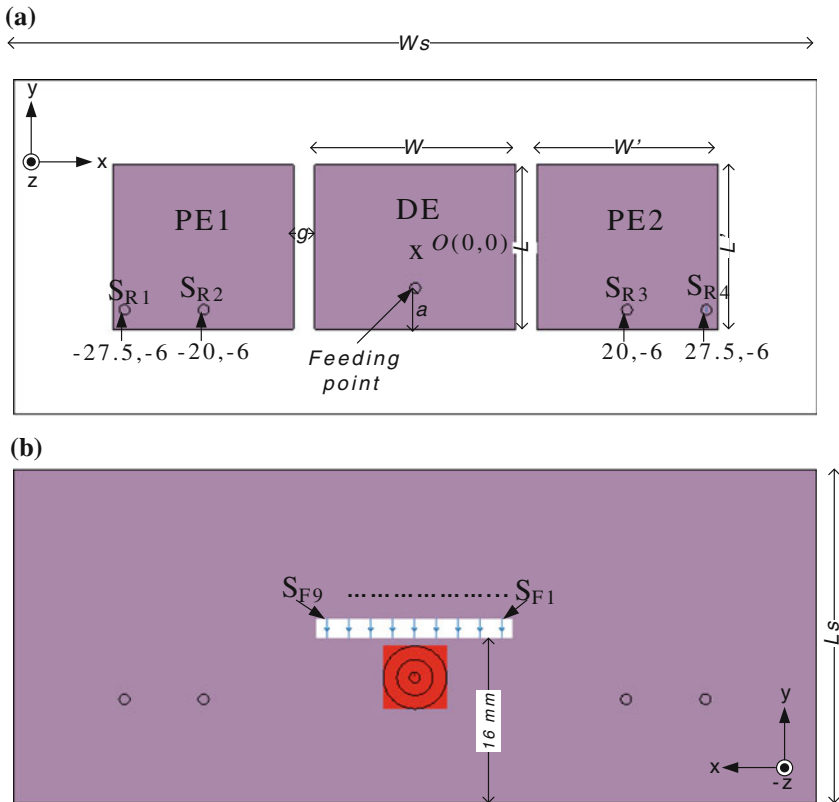


Fig. 1 Antenna structure. a Front and b Back

a slot with $18 \times 1.5 \text{ mm}^2$ is created for the purpose of frequency reconfiguration. In what follows, the deployment of the switches for reconfigurable properties of the antenna is described.

2.1 Reconfiguration Mechanism

Radiation pattern and frequency can be reconfigured in a single antenna with the help of RF switches. The antenna consists of thirteen RF switches. Lumped element networks of the RF switch at ON state and OFF state are used to represent the switches in simulation. HPND-4005 PIN diode is adopted as the RF switches to control the reconfigurable mechanism of the antenna. According to the technical data sheet provided by the manufacturer [9], the HPND-4005 PIN diodes are simulated as $4.6\text{-}\Omega$ resistor and 0.017-pF capacitor in the ON and OFF states respectively. The positioning of the diodes and radiation mechanism of each property are described in the following subsection.

Radiation Pattern Four RF switches are required to perform the radiation pattern reconfiguration. As illustrated in Fig. 1a, S_{R1} to S_{R4} are placed at the parasitic elements. These switches mainly contribute the radiation pattern reconfiguration of the antenna. They connect the parasitic element to the ground plane underneath of the antenna. Switching ON the PIN diode connects the element to the ground plane while switching OFF the PIN diode disconnects the element from the ground plane. Switching the PIN diode ON directs the parasitic element to act as a reflector which will push the beam towards an opposite direction. On the other hand, switching the PIN diode OFF will make the parasitic element to act as director that will pull the beam. Overall, three sets of directive beam patterns can be obtained. The switching configuration and the direction for each pattern is tabulated in Table 1. Note that S_{F1} to S_{F9} are all ON when pattern reconfiguration is applied.

Frequency At the back of the antenna, a slot is created on the ground plane. Resizing the effective length of the slot, reconfigure the resonant frequency of the antenna. S_{F1} to S_{F9} are placed across the slots to reconfigure the frequency of the antenna. When the switches are ON, the effective size of the slot is reduced, hence it reconfigure the frequency to higher resonant. The respective switching configuration for each resonant frequency is tabulated in Table 2. Note that only S_{R2} and S_{R3} are ON when frequency reconfiguration is applied.

Table 1 Details of switches configuration for pattern reconfiguration

| Configuration | S_{R1} | S_{R2} | S_{R3} | S_{R4} | Direction |
|---------------|----------|----------|----------|----------|---------------|
| P1 | ON | OFF | OFF | OFF | +x |
| P2 | OFF | ON | ON | OFF | $x = 0^\circ$ |
| F5 | OFF | OFF | OFF | ON | -x |

Table 2 Details of switches configuration for frequency reconfiguration

| Configuration | S _{F1} | S _{F2} | S _{F3} | S _{F4} | S _{F5} | S _{F6} | S _{F7} | S _{F8} | S _{F9} |
|---------------|-----------------|-----------------|-----------------|-----------------|-----------------|-----------------|-----------------|-----------------|-----------------|
| F1 | OFF | OFF | OFF | OFF | ON | OFF | OFF | OFF | OFF |
| F2 | OFF | OFF | OFF | ON | ON | ON | OFF | OFF | OFF |
| F3 | OFF | OFF | ON | ON | ON | ON | ON | OFF | OFF |
| F4 | OFF | ON | ON | ON | ON | ON | ON | ON | OFF |
| F5 | ON | ON | ON | ON | ON | ON | ON | ON | ON |

3 Results and Analysis

The proposed antenna designed and the results are analyzed. It can be seen from Fig. 2 that for pattern reconfiguration, the antenna is capable of directing its beam to three directions. An average peak gain of ~8 dBi can be obtained for all three sets of beampatterns. For P1 and P3, a maximum tilt angle of 27° can be obtained. Meanwhile, the antenna also operates at a common frequency bandwidth from 5.678–5.949 GHz as can be noticed in Fig. 3. As one could expect, the resonant frequencies of P1 and P3 are similar.

Meanwhile, for frequency reconfiguration, the antenna is able to achieve five sets of resonant frequencies. This result is presented in Fig. 4. The corresponding beam patterns results are presented in Fig. 5. Table 3 summarizes the results by frequency reconfiguration. The S₁₁ improves as the resonant frequency increases. It can be noticed that F4 and F5 are close thus it can be considered as single band.

Fig. 2 Beam patterns by pattern reconfiguration at 5.8 GHz frequency

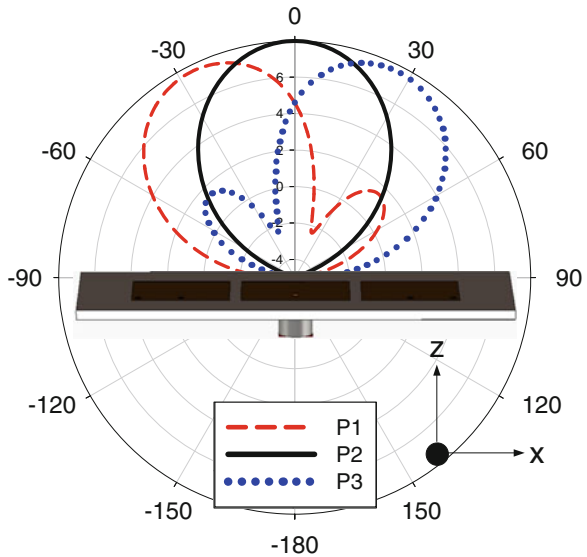


Fig. 3 Reflection coefficient by pattern reconfiguration

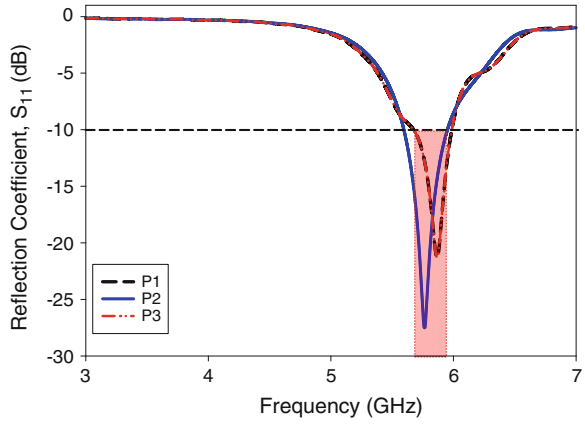


Fig. 4 Resonant frequencies by frequency reconfiguration

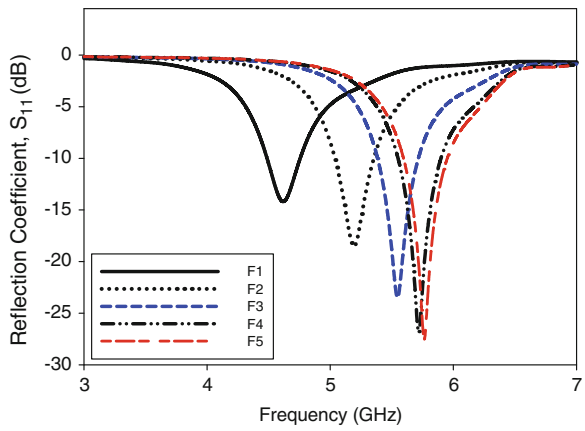


Fig. 5 Beam patterns by frequency reconfiguration

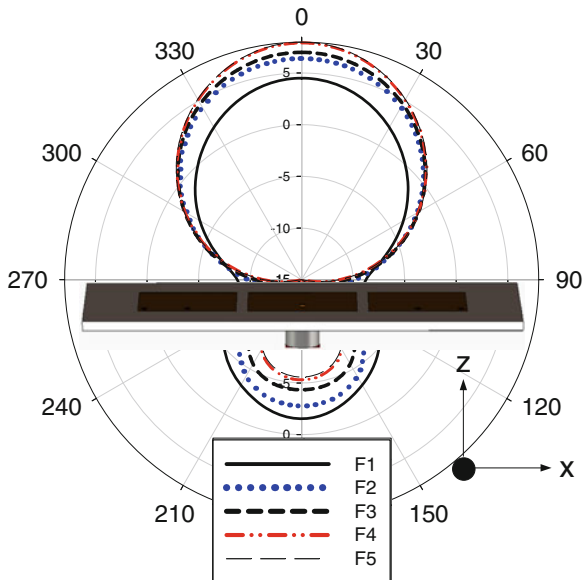


Table 3 Resonant frequencies, bandwidth and the associated antenna gain for by frequency reconfiguration

| Frequency | Resonant frequency (GHz) | Bandwidth (%) | Peak gain (dBi) |
|-----------|--------------------------|---------------|-----------------|
| F1 | 4.624 | 5.7 | 4.5 |
| F2 | 5.208 | 6.0 | 6.2 |
| F3 | 5.544 | 5.9 | 7.0 |
| F4 | 5.721 | 6.0 | 7.8 |
| F5 | 5.764 | 6.1 | 8.0 |

Thus effectively the frequency reconfiguration produces four frequency bands. The beam pattern results show that the peak gain of the antenna increases as the resonant frequency increases while the back lobe level decreases.

4 Conclusion

A dual-mode reconfigurable microstrip patch antenna is developed for pattern reconfiguration and frequency reconfiguration application. Parasitic arrays are adopted for pattern reconfiguration while slot underneath of the antenna is used for frequency reconfiguration. The proposed antenna is able to steer the beam to three directions (-27° , 0° , $+27^\circ$) with an average peak gain of ~ 8 dBi. On the other hand, it can reconfigure up to four effective frequency bands from 4.624 to 5.764 GHz. The reconfigurability is obtained by switching the PIN diodes. The results show that the proposed antenna is potentially suitable for multiple applications such as frequency scanning and direction finding using a single platform.

Acknowledgments The authors would like to thank Research University Grant UTM (Vote 05H34 and 00M21), Ministry of Higher Education, Universiti Teknologi Malaysia (UTM) and Universiti Malaysia Perlis (UniMAP) for their support and encouragement.

References

1. Songnan, Y., Chunna, Z., Pan, H.K., Fathy, A.E., Nair, V.K.: Frequency-reconfigurable antennas for multiradio wireless platforms. *IEEE Microwave Mag.* **10**, 66–83 (2009)
2. Boudaghi, H., Azarmanesh, M., Mehranpour, M.: A frequency-reconfigurable monopole antenna using switchable slotted ground structure. *IEEE Antennas Wirel. Propag. Lett.* **11**, 655–658 (2012)
3. Liao, W.-J., Yeh, J.-T., Chang, S.-H.: Circularly polarized chip antenna design for GPS reception on handsets. *IEEE Trans. Antenna Propag.* **67**, 1–1 (2014)
4. Pei-Yuan, Q., Guo, Y.J., Can, D.: A dual-band polarization reconfigurable antenna for WLAN Systems. *IEEE Trans. Antenna Propag.* **61**, 5706–5713 (2013)

5. Yuan, X., Li, Z., Rodrigo, D., Mopidevi, H.S., Kaynar, O., Jofre, L., Cetiner, B.A.: A parasitic layer-based reconfigurable antenna design by multi-objective optimization. *IEEE Trans. Antenna Propag.* **60**, 2690–2701 (2012)
6. Rodrigo, D., Cetiner, B.A., Jofre, L.: Frequency, radiation pattern and polarization reconfigurable antenna using a parasitic pixel layer. *IEEE Trans. Antenna Propag.* 1–1 (2014)
7. Sabapathy, T., Jamlos, M.F.B., Ahmad, R.B., Jusoh, M., Jais, M.I., Kamarudin, M.R.: Electronically reconfigurable beam steering antenna using embedded RF pin based parasitic arrays (Erppa). *Prog. Electromagn. Res.* **140**, 241–261 (2013)
8. Majid, H.A., Abdul Rahim, M.K., Hamid, M.R., Murad, N.A., Ismail, M.F.: Frequency-reconfigurable microstrip patch-slot antenna. *IEEE Antenna Wirel. Propag. Lett.* **12**, 218–220 (2013)
9. HPND-4005 beam lead PIN diode, Datasheet, edited. Avago Technologies, San Jose, CA (2006)

Fade Margin Estimation Technique Using Radar Data for Satellite Link

Khairayu Badron, Ahmad Fadzil Ismail, Mimi Aminah Wan Nordin, Farah Nadia Mohd Isa and Aniliza Asnawi

Abstract The fade margin is an important parameter used by the operator to measure the link availability for a given time. Fade margin is a parameter that is used in the design of satellite links to ensure optimal performance of the link. A new technique is proposed where the fade margin of a satellite link can be estimated using attenuation statistics of radar data. Data set acquired from Malaysian meteorological radar for the year 2009 is used in the study. Radar return or reflectivity is used in the process of generating the attenuation values. The reflectivity is first converted into rainfall rate value and the specific attenuation is then calculated. The rain attenuation values can be derived by the multiplication of the specific attenuation and the path length affected. The rainfall rate derived from radar information is used in calculating the slant path attenuation of the satellite link. The databases of rain attenuation is then compiled with the time duration to acquire the cumulative distribution function (CDF) for the specified link. The satellite link investigated are based on the RazakSAT link in relation to its ground station located at Sg Lang, Banting, Selangor, Malaysia for X-band and MEASAT-3 satellite in relation to its ground station at Cyberjaya, Selangor, Malaysia for Ku-band.

K. Badron (✉) · A.F. Ismail · M.A.W. Nordin · F.N.M. Isa · A. Asnawi
Faculty of Engineering, International Islamic University Malaysia,
Jln Gombak, 50310 Kuala Lumpur, Malaysia
e-mail: khairayu@iium.edu.my

A.F. Ismail
e-mail: af_ismail@iium.edu.my

M.A.W. Nordin
e-mail: mimie@iium.edu.my

F.N.M. Isa
e-mail: farahn@iium.edu.my

A. Asnawi
e-mail: aniliza@iium.edu.my

1 Introduction

In designing a new satellite link, the performance prediction of the satellite are vital step to ensure the reliability of the systems. It is very critical to be capable to predict accurately the impairment of the given link in order to devise the services efficiently. The predicted value of signal loss and fading are commonly used in the process of establishing the satellite design parameters [1]. Good performance of the link is usually expressed as the expected quality of the channel for a very high percentage of time (at least a month and usually a year). For satellite systems, the desired performance is commonly known as “clear sky”. The performance can be specified for instance, at availability of 99.99 % of time at a given receiving locality or at a specified percentage of locations within a reception area [2]. Availability is the percentage of total time a service is enabled or being used, or is available to be utilized. In satellite communication terminologies, the link availability is defined as percentage of time in a year when the link will perform as per the link’s requirement. For example, military communication satellite requires 99.99 % availability for a year, which translates to link accessibility of 8759.1 h and an unavailability of 0.876 h ($8760 - 8759.1 \text{ h} / 8760 \text{ h} \times 100$). Predictions are employed in order to know whether a satisfactory service can be provided at the reception point or area. Furthermore, these parameters are also used for spectrum allocation to avoid mutual interference with other systems occupying the same frequency band. In this paper, the cumulative distribution function (CDF) for a satellite link will be derived using radar data. These data can be used for the calculation of the fade margin for the system’s best performance.

2 System Configuration and Measurement

The satellite links that is being investigated is between the satellite ground station located at Pusat Angkasa Negara, Banting, Selangor ($N2^{\circ}47'16.9973''$ and $E101^{\circ}30'58.612''$) and the RazakSAT satellite orbiting at Near Equatorial Orbit (NEqO) at altitude of 685 km. The second satellite link that is being investigated is between MEASAT ground station and the MEASAT-3 satellite at $91.5^{\circ}E$. The Malaysian Meteorological Department (MMD) weather radar that is used to derive the CDF is located in the vicinity of KLIA at ($N2^{\circ}51'48.5722''$ and $E101^{\circ}40'37.5366''$). The distance between the KLIA radar station and the RazakSAT ground station is about 19.4 km whilst the distance from the MEASAT-3 ground station to the KLIA radar station is about 8 km. The radar system is programmed to operate in two scanning approaches; Airport and Aerial mode. Each mode consists of three different volumes (Vol) scan called task; (i) Vol-A for long range observation at low elevation; (ii) Vol-B for medium range observation and (iii) Vol-C for short range observation at high elevation. Each mode includes sweeps of the surrounding area at a predetermined elevation angles. The radar automatically shifts from Aerial mode to

Table 1 Radar specification

| Tasks | Aerial scan | Airport scan |
|--------------------|--|--|
| Elevation angle(s) | 0.7, 1.5, 2.0, 3.0, 5.0, 7.5, 10.0, 15.0, 20.0, 25.0, 30.0, 40 | 0.7, 1.0, 1.5, 5.0, 10.0, 05.0, 20.0, 30.0, 40.0 |
| PRF (Hz) | 300 (Vol A)/1000 (Vol B & C) | 300 (Vol A)/1000 (Vol B & C) |
| Pulse width (s) | 3μ (Vol A)/1μ (Vol B & C) | 3μ (Vol A)/1μ (Vol B & C) |
| RPM | 2 (Vol A)/4 (Vol B & C) | 2 (Vol A)/4 (Vol B & C) |
| Max range (km) | 480 (Vol A)/128 (Vol B & C) | 480 (Vol A)/240 (Vol B & C) |
| Reflector dia (m) | 8.5 | 8.5 |
| Freq (MHz) | 2874.5 | 2874.5 |
| μ (cm) | 10.43 | 10.43 |
| Polar | Vertical | Vertical |
| Radom | 12 m | 12 m |

Airport mode when its sensor detects rain of more than 0.1 mm/h within the 20 km² vicinity from KLIA. The airport mode provides coverage up to 480 km in contrast to only 128 km during aerial mode coverage. Approximately 300 volume raster scans were acquired per day in which each scan was generated in duration of about less than 5 min. The radar antenna rotates at the speed of 2 revolution per minute (RPM) with pulse repetition frequency (PRF) equals to 300 Hz for scanning elevation angles of less than 5°. The radar will rotate at faster speed of 4 revolution per minute (RPM) with PRF equals to 1000 Hz for angles of elevation between 5° to 40°. Table 1 lists the radar characteristics. An IRIS software system by Vaisala is installed to generate and display MMD radar products. The radar automatically computes a range-corrected and equipment-calibrated measurement of reflectivity identified by the symbol Z. Reflectivity, Z can vary from extremely large values for heavy rain, to very small values for mist. To make this wide range of Z viewable on computer screens, the software converts the reflectivity values into a logarithmic scale which is expressed in units of decibels (dBZ). The reflectivity, Z in unit dBZ is calculated from (1):

$$dBz = 10 \log Z \tag{1}$$

Figure 1 shows the setup of the system. Table 1 shows the radar specification.

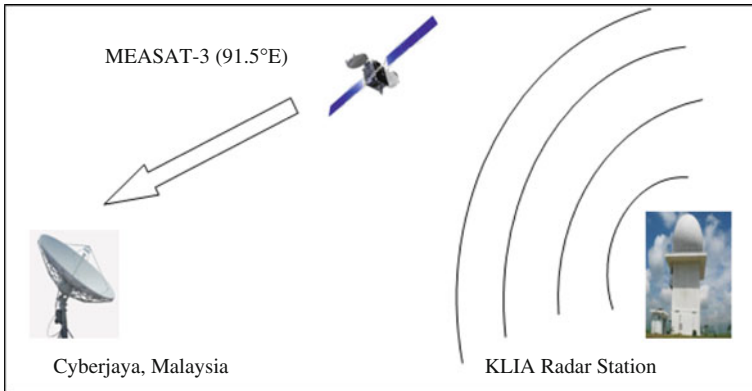


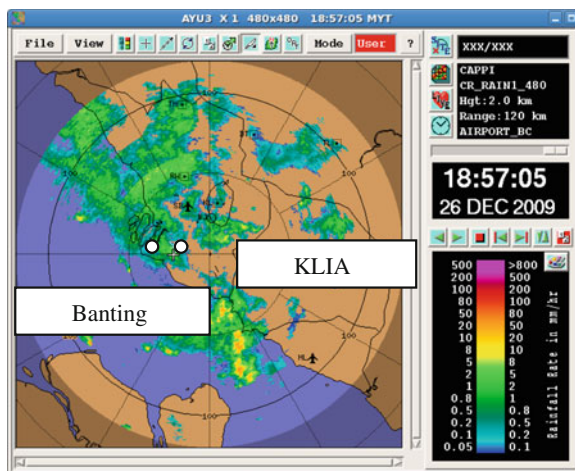
Fig. 1 System setup and configuration for MEASAT-3 link

3 Cumulative Distribution Function Calculation Technique

The technique to calculate the CDF is described in this section. CDF describes the attenuation level for a given percentage of time. The steps used to derive the CDF are as given in Step 5 below:

Step 1: The location to be analyzed must be identified using a horizontal view. The horizontal view of the location is important to make sure that the observed area experiences rain. Figure 2 shows the constant altitude plan position indicator (CAPPI) view of the location.

Fig. 2 CAPPI view of the location



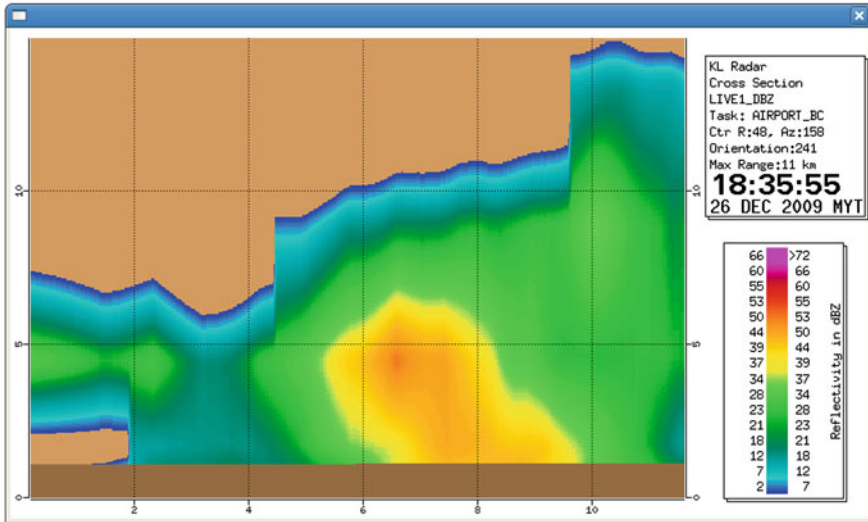


Fig. 3 RHI views of the location

The location of the ground station at SgLang, Banting, Selangor is being identified. The vertical cross section at the point of the ground station is being plotted. Figure 3 shows an example of the cross section of the location known as Range Height Indicator (RHI) in the radar data product.

Step 2: The radar data reflectivity value of the cross section is then extracted from the RHI plot. These values are known as the ‘productx’. The rain attenuation is compiled based on 5 min integration time available where 5 min is the shortest or can be more than 1 h; depends on the cumulated 5 min integration times. For example, on 12/05/2009 the total rain time is based on 5 min data set time multiple by 6 data sets which means the rain time is 30 min. Rain attenuation data set values for each cross section of the event available were composed for that particular year in monthly order. Figure 4 shows an example of the real values from the image in Fig. 3.

Step 3: Once the reflectivity reading in dBz is available, the link affected is traced and the rain attenuation is calculated. The rainfall rate, R is then calculated from the radar reflectivity, Z by exploiting local radar data acquired from the MMD.

$$R_i = \sqrt[b]{\frac{Z}{a}} \tag{4}$$

where, R_i is the rainfall rate value derived from the radar, and $a = 220$, $b = 1.6$ as proposed by Marshal and Palmer in [3]. Next, the rain attenuation values can be estimated using R_i data according to the power law equation [4] as in (5);

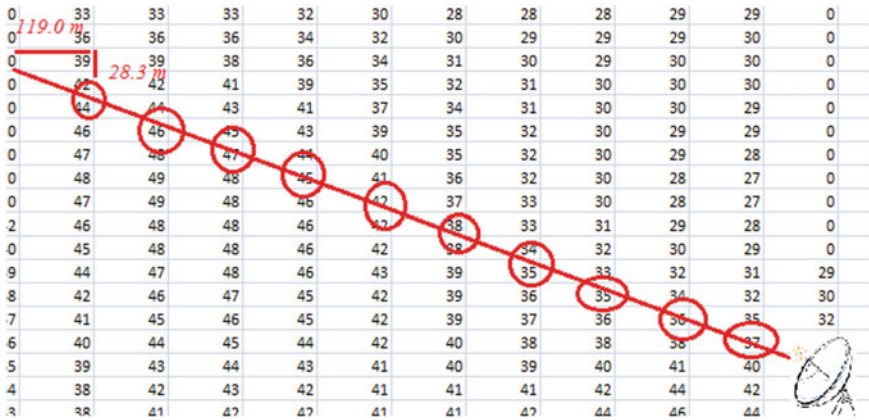


Fig. 4 Real values of reflectivity data

$$A = k R^\alpha \cdot L_e \tag{5}$$

where A is the attenuation per bin, L_e is the effective length affected by rain within the bin, and k and α are the coefficients adopted from the ITU-R P838-3 recommendation [5].

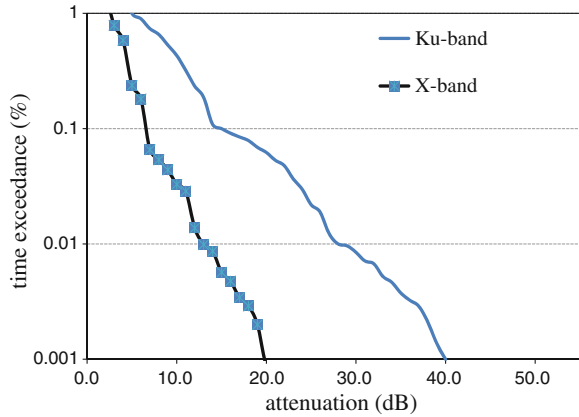
Step 4: After the rain attenuation, A for each cross section from the radar data for the year 2009 is calculated, the cumulative distribution function (CDF) can now be derived. The generated dataset comprises of the rain attenuation values with the 5 min integration time.

Step 5: The period for a given attenuation level is listed. These period is then converted to a percentage time over a year The lowest rain attenuation values will be added to the next level of rain attenuation values in a cumulative form so as to create the CDF. The CDF of the satellite link, $F(X)$ can be expressed as the integral of its probability of each rain attenuation level exist, f_x over time, t as follow:

$$F(X) = \int_0^0 f_x(t) \tag{4}$$

where b is the time exceedance value. An example of the Malaysian RazakSAT satellite (X-band frequency)and MEASAT-2 Broadcasting Satellite (Ku-Band frequency) CDF from radar derived is shown in Fig. 5.

Fig. 5 CDF of the RazakSAT link(X band) and Measat-3B link (Ku band) using radar derived rain attenuation



4 Conclusion

The S-band single polarization radar reflectivity are able to estimate the rain attenuation for Earth-satellite link. The per event basis comparison with the satellite link measurements has proved that the radar reflectivity values can be used as a good estimator for rain attenuation prediction. The advantage of the radar return value is that it is capable of providing areal precipitation where it is almost impossible using rain gauges. The values of the rainfall rate from the radar reflectivity are known at any instantaneous point along the slant path. With the assimilation of the radar reflectivity and the appropriate Z-R relation, we can predict the actual attenuation during convective rain or stratiform rain events at any location and time. This is significant since such rain events are frequent in tropical regions like Malaysia. This is very important for the satellite engineers and researchers as an alternative means to plan link budget estimation and set-up.

References

1. Ismail, A.F., Watson, P.A.: Characteristics of fading and fade countermeasures on a satellite-Earth link operating in an equatorial climate, with reference to broadcast applications. In: *Microwaves, Antennas and Propagation, IEEE Proceedings*, vol. 147, no. 5, pp. 369, 373 (2000)
2. Badron, K., Ismail, A.F., Islam, M.R., Abdullah, K., Din, J., Tharek, A.R.: Rain fade characteristics analyses for V-band link in tropical region. In: *Microwave and Millimeter Wave Technology (ICMMT), 2010 International Conference on*, pp. 121,124 (2010)
3. Marshal, J.S., Palmer, W. McK.: The distribution of raindrops with size. *J. Meteorol.* **5**, 165–166 (1948)
4. Olsen, R.L., Rogers, D.V., Hodge, D.B.: The aRb Relation in the calculation of rain attenuation. In: *IEEE Transactions on Antennas and Propagation, AP-26*, pp. 318–329 (1978)
5. ITU-R: Specific attenuation model for rain for use in prediction methods, recommendation ITU-R P. 838-3, Geneva (2005)

Circular Polarization Textile Antenna for GPS Application

Shakhirul Mat Salleh, Muzammil Jusoh, Abdul Hafizh Ismail, Mohd Najib Mohd Yasin, Muhammad Ramlee Kamarudin and Roshayati Yahya

Abstract A right-handed circular polarization (RHCP) textile antenna for Global Positioning System (GPS) application is proposed. The circular polarization (CP) is achieved by truncated two opposite edged of the 84 mm square patch. The proposed antenna design use a shieldit super as the radiator and felt fabric as substrates. Such presented antenna attains a good bandwidth of 90 MHz from 1.53–1.62 GHz. Besides, the antenna is capable to perform an axial ratio of less than <3 between 1.56 and 1.62 GHz which covered the GPS operating frequency of 1.575 GHz. Moreover, this paper discussed the parametric study of the truncated patch in order to achieve CP. The simulated result shows that the presented antenna is potential for point-to-point wireless communication system.

S. Mat Salleh (✉) · A.H. Ismail
Faculty of Engineering Technoogy, Universiti Malaysia Perlis (UniMAP),
Kampus Pauh Putra, 02600 Arau, Perlis, Malaysia
e-mail: shakhirul@yahoo.com

A.H. Ismail
e-mail: abdulhafizh@unimap.edu.my

M. Jusoh
Embedded, Network and Advanced Computing (ENAC), School of Computer
and Communication Engineering, Universiti Malaysia Perlis (UniMAP),
Kampus Pauh Putra, 02600 Arau, Perlis, Malaysia
e-mail: muzammil@unimap.edu.my

M.N. Mohd Yasin
School of Electrical System Engineering, Universiti Malaysia Perlis (UniMAP),
Kampus Pauh Putra, 02600 Arau, Perlis, Malaysia
e-mail: najibyasin@unimap.edu.my

M.R. Kamarudin · R. Yahya
Wireless Communication Centre (WCC), Faculty of Electrical Engineering,
Universiti Teknoogi Malaysia (UTM), 81310 Skudai, Johor, Malaysia
e-mail: ramlee@fke.utm.my

R. Yahya
e-mail: rhayati@uthm.edu.my

1 Introduction

Recently, the investigation on wearable monitoring system which focusing on body-worn communication is rapidly growing. The wireless monitoring application such as GPS, has been widely used in various transportation operations and planning [1]. The interest in implementing textile technology as a wearable antenna for on body communication has gained huge attention since the fabric material does not force the wearer to abandon the comfort zone [2]. Moreover, the advantages of textile antenna are light weight, easy to integrate with clothes, and low implementation cost as compared to the conventional microstrip antenna [3].

The conductive textile has been broadly used for wearable antenna for instance Zelt, Pure Copper Taffeta Fabric, Copper Conducting sheet, Silver Plated Nylon Thread, and Nora dell [1, 2, 4]. The conductivity and thickness are importantly required to design the wearable antenna since it gives influence to the antenna physical dimension and performance. The conductive textile characteristic used in this research is summarized in Table 1. In this paper, the Shieldit super is chosen as conductive element since it's provide advantages of excellent conductivity, low corrosion, easily attached to the substrate by using iron (fabrication proses), and more hydrophobic, which reduces proneness to moisture absorption [5].

The textile materials (substrates) usually have a very low relative permittivity that affords reducing the surface wave losses and improving the impedance bandwidth of the antennas [6]. In this work, felt fabric is used as substrates and the real permittivity has been measured and discussed more in the following section. The other available fabric for wearable antenna is foam, flannel fabric, denim jeans, and cotton [1–4].

Circular polarization (CP) antenna can obtain using various techniques for example by design the L shape microstrip-line to get an orthogonal phase magnitude in order to excite 90^0 time-phase difference between them [7]. Another technique to achieve CP is using either single, or two, or more feeds by adjusting the physical dimension of the patch and this technique has been reported in [8]. Instead of rectangular patch, circular patch also can produce CP by making slot and stub [9, 10] or by adding tabs [11]. This paper focuses on rectangular patch by analyzing the dimensions of the truncated edge square patch in order to get CP [11].

Table 1 Characteristics of conductive textile

| Material | Thickness (mm) | Conductivity (S/m) |
|----------------------------|----------------|---------------------|
| Zelt | 0.0635 | 1.749×10^5 |
| Pure Copper Taffeta | 0.08 | 2.5×10^5 |
| Copper Conducting sheet | 0.03 | NA |
| Silver Plated Nylon Thread | 0.105 | 1.538×10^6 |
| Nora dell | 0.105 | NA |

NA The value is not available

2 Antenna Description

2.1 Materials and Methods

The radiating element (patch and ground) of the antenna is made of the Shieldit super with the thickness of 0.17 mm and conductivity of 6.67×10^5 S/m [5]. It is a polyester base material coated using nickel and copper. Meanwhile, felt is chosen as the substrate due to the thickness of 1.7 mm which respectively larger than other wearable textile such as denim jean (0.7 mm) [3], cotton fabric (0.5 mm) [4], and flannel fabric (1 mm) [2]. Theoretically, the larger substrate fabric thickness provides a wide bandwidth for the antenna design. The real part of the permittivity, ϵ' for felt has been measured in Radar Laboratory of Faculty of Electrical Engineering at Universiti Teknologi Malaysia Skudai, Johor. The measured ϵ' indicates 1.22 at 1.575 GHz using solid probe and Vector Network Analyzer. For measurement purposes, the felt fabric is cut into ten similar pieces of 10 mm \times 10 mm each, and then stacked into ten layers with the thickness of up to 17 mm. Such probe can only measure for materials thickness of more than 3 mm. The measurements have been done for four times using a commercial open-ended coaxial probe and the average value has been taken as a final result.

2.2 Antenna Design

As referred to the previous work, one of the technique to get CP is by designing the square patch radiator ($L = W$) with both opposite edge is truncated. The antenna can easily achieve a Right Hand Circular Polarization (RHCP) and Left Hand Circular Polarization (LHCP) by determine the feed line location. By changing the feed line

Fig. 1 Trimmed square ($L = W$) [11]

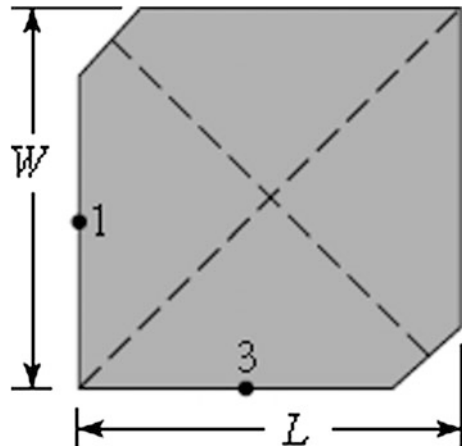
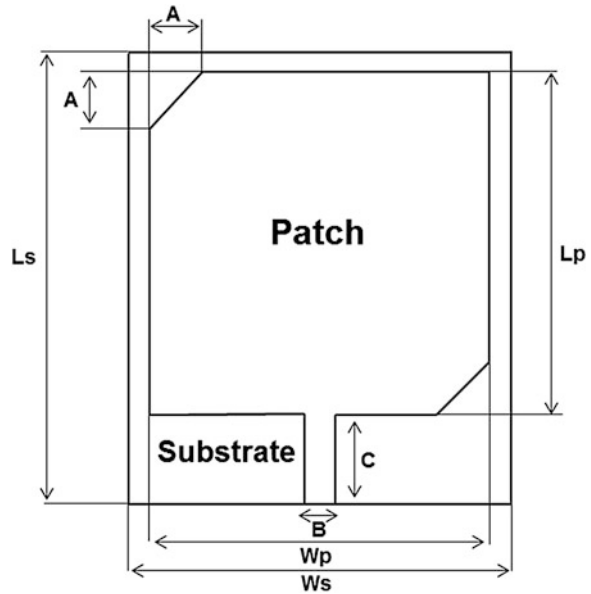


Fig. 2 The proposed antenna structure



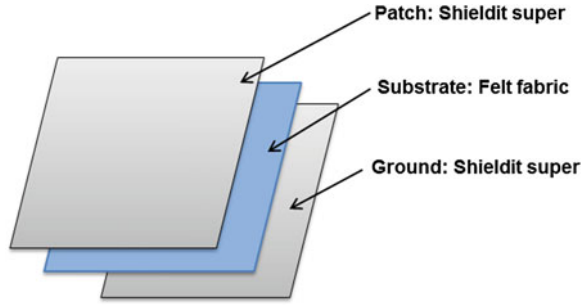
to point 3, the antenna is capable to attain RHCP and by placing the feed line to point 1, the LHCP is obtain as shown in Fig. 1 [11].

The proposed geometrical antenna is illustrated in Fig. 2 with the radiator square size of 84 mm × 84 mm and it has been truncated as much as A = 14 mm in order to get the CP. The optimized parameters of the circular polarization antenna are shown in Table 2. The parametric study had been done by adjusting the truncated (A) size at 8, 10, 12, 14, 16, and 18 mm. All simulated results are discussed in Sect. 3. The scheme of the textile antenna layers is shown in Fig. 3.

Table 2 Parameters of the circular polarization antenna

| | | |
|---|---------------------------|------------------------|
| Optimized parameters | Patch length, L_p | 84 mm |
| | Patch width, W_p | 84 mm |
| | Truncated length, A | 14 mm |
| | Substrate length, L_s | 111 mm |
| | Substrate width, W_s | 94 mm |
| | Feed length, C | 22 mm |
| | Feed width, B | 7.5 mm |
| Patch and ground plane (shieldit super) | Thickness, h_s | 0.17 mm |
| | Conductivity | 6.67×10^5 S/m |
| Substrate (felt fabric) | Thickness, h_s | 1.7 mm |
| | Permittivity, ϵ' | 1.22 |

Fig. 3 Scheme of the textile antenna layer



3 Results and Discussions

3.1 Reflection Coefficient

Figure 4 shows the comparisons of six difference truncated length towards the S11 performance and the data is organized for easy analysis in the Table 3. From Table 3, the truncated patch for 10, 12, and 14 mm only achieved the operating frequency of 1.575 GHz. The best reflection coefficient is -18.77 dB by truncated of 12 mm, with bandwidth from 1.54 to 1.60 GHz. While the truncated 10 and 14 mm achieved a significant reflection coefficient of -11.28 and -16.25 dB respectively. However, the analysis need to consider the axial ratio as well, whether the truncated patch 10, 12, and 14 mm is acquire the circular polarized.

3.2 Axial Ratio

AR is the main parameter to determine the antenna functionality and quality of CP. According to the previous work, any antenna is considered CP when it has AR

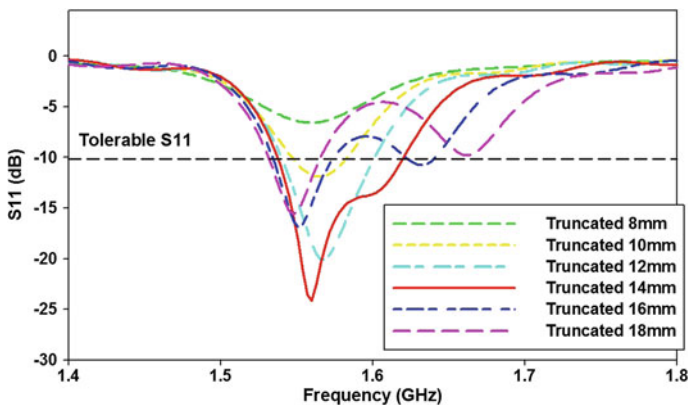


Fig. 4 The simulated result of reflection coefficient

Table 3 Analysis result of simulated reflection coefficient

| Truncated X and Y (mm) | Bandwidth (GHz) | S11 (dB) at 1.575 GHz |
|------------------------|-----------------|-----------------------|
| 8 | NA | -6.10 |
| 10 | 1.54-1.58 | -11.28 |
| 12 | 1.54-1.60 | -18.77 |
| 14 | 1.53-1.62 | -16.25 |
| 16 | 1.53-1.57 | -9.88 |
| 18 | 1.53-1.56 | -7.57 |

NA The value is not available

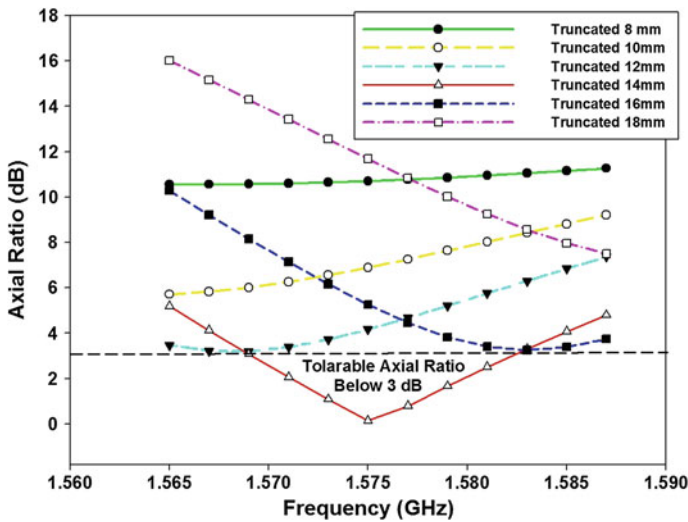


Fig. 5 The simulated result of axial ratio

bandwidth of less than 3. Figure 5 shows the simulated axial ratio result for square patch antenna truncated at $A = 8, 10, 12, 14, 16,$ and 18 mm. The graph indicates that the truncated square length of 14 mm obtains the tolerable axial ratio below than 3 hence achieve circular polarization. Table 4 shows the details of axial ratio at several truncated lengths.

Table 4 Analysis result of simulated axial ratio

| Truncated X and Y (mm) | Bandwidth (GHz) below 3 dB | S11 (dB) at 1.575 GHz |
|------------------------|----------------------------|-----------------------|
| 8 | NA | 10.70 |
| 10 | NA | 6.89 |
| 12 | NA | 4.16 |
| 14 | 1.56-1.62 | 0.13 |
| 16 | NA | 5.26 |
| 18 | NA | 11.68 |

NA The value is not available

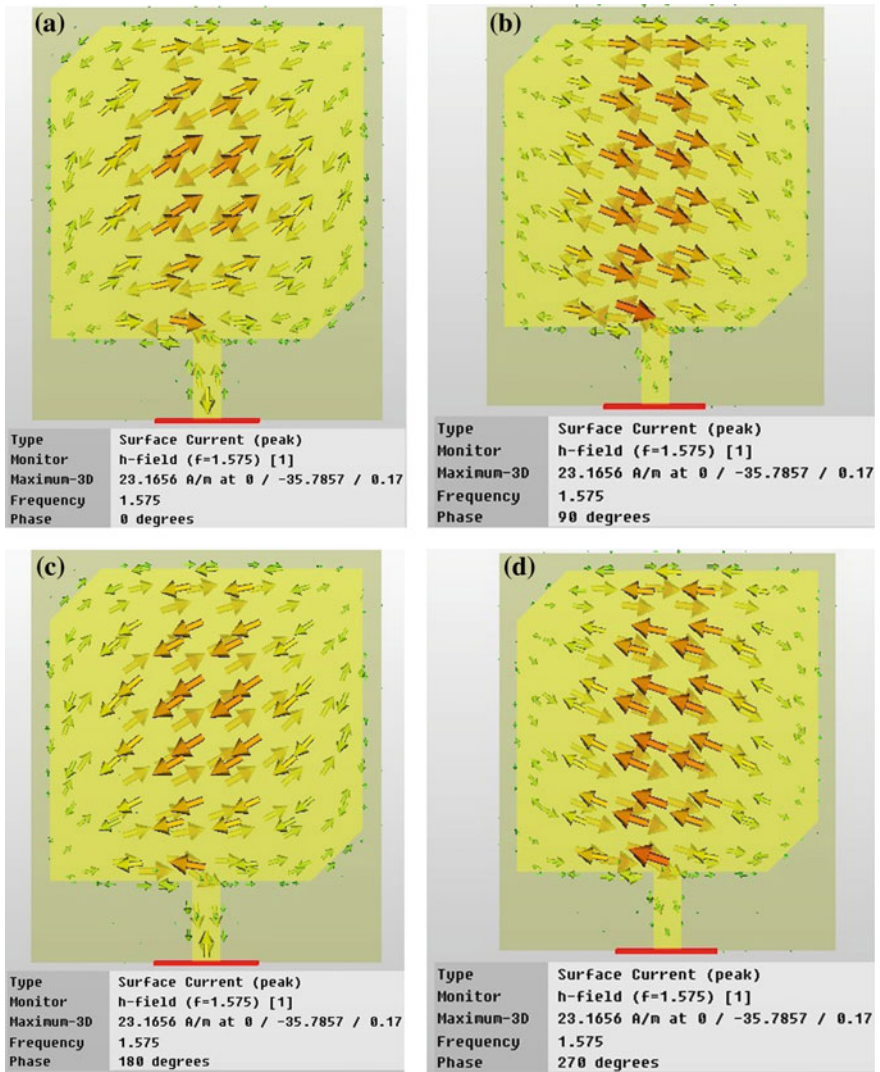


Fig. 6 Simulated surface current distribution of the square patch antenna truncated at 14 mm. **a** 0° phase, **b** 90° phase, **c** 180° phase, **d** 270° phase

The truncated square patch for 14 mm achieved a 0.13 dB axial ratio at 1.575 GHz with covering AR bandwidth from a frequency of 1.56–1.62 GHz. While the truncated at 12 and 16 mm, the axial ratio is 4.16 and 5.26 dB with approximately near tolerable axial ratio.

3.3 Radiation Pattern

CP can be proven from the surface current ability to circulate from 0° to 360° . The magnetic current behavior for the truncated square patch at 14 mm is analyzed in Fig. 4. It demonstrates the surface current at phase 0° , 90° , 180° and 270° is rotating clock-wise. This kind of current rotation generated the right-hand circular polarization (RHCP) (Fig. 6).

4 Conclusion

An analysis of circular polarization square patch textile antenna is proposed in this paper. The parametric study is focusing on the truncated part which author believes give significant influence to the CP achievement. Such truncation at the edge of a square patch is done at six different lengths of 8, 10, 12, 14, 16, and 18 mm. The simulated reflection coefficient shows the truncated patch at 10, 12, and 14 mm have achieved tolerable S11 of less than <-10 dB at GPS frequencies of 1.575 GHz. However, the truncated antenna with a length of 14 mm can obtain good circular polarization with the axial ratio below 3 dB between frequencies 1.56–1.62 GHz. Furthermore, the antenna generated RHCP at 1.575 GHz respectively.

Acknowledgments Authors would like to thank the members of the Wireless Communication Center (WCC), UTM and Dr Nor Hisham Bin Haji Kamis from Radar Laboratory of Faculty of Electrical Engineering, UTM for helping and providing the equipment facilities to enable this work to be completed. Authors also would like to thank the Faculty of Engineering Technology, UniMAP a MOHE for providing the sponsorship.

References

1. Jais, M.I., Jamlos, M.F., Malek, M.F.: Conductive E-textile analysis of 1.575 GHz rectangular antenna with H-slot for GPS application. In: Antenna and Propagation Conference, Loughborough (2012)
2. Bruce, K.B., Cardelli, L., Pierce, B.C.: Textile UWB antenna bending and wet performances. *Int. J. Antennas Propag.* **61**, 4411–4418 (2012)
3. Yahya, R., Kamarudin, M.R.: Effect of rainwater and seawater on the permittivity of denim jean substrate and performance of UWB eye-shaped antenna. *IEEE Antenna Wirel. Propag. Lett.* **13**, 806–809 (2014)
4. Shakhirul, M.S., Jusoh, M., Sahadah, A., Nor, C.M., Rahim, H.A.: Embroidered wearable textile antenna on bending and wet performances for UWB reception. *Microwave Opt. Technol. Lett.* **56**, 2158–2163 (2014)
5. Mohd Iman, J., Mohd Faizal, J., Muzammil, J., Sabapathy, T., Muhammad Ramlee, K., Ahmad, R.B., Azremi, A.A.-H., Emi Izhanizam, A., Soh, P.J., Vandenbosch, G.A.E., Nur Laila Khamariah, I.: A novel 2.45 GHz switchable beam textile antenna (SBTA) for outdoor wireless body area network (WBAN) applications. *Prog. Electromagnet. Res.* **138**, 613–627 (2013)

6. Ahmad, S., Saidin, N.S., Isa, C.M.C.: Development of embroidered sierpinski carpet antenna. In: Asia-Pacific Conference on Applied Electromagnetics (APACE) (2012)
7. Rudy Yuwono, R.S.: 2.4 GHz circular polarized mirostriap antenna for RFID application. In: International Conference on Communication and Computer Engineering (2014)
8. Ismail, M.F., Rahim, M.K.A., Hamid, M.R., Majid, H.A., Yusof, M.F.M.: Compact dual-fed slotted circular polarization antenna with reflector for RF energy harvesting. In: 7th European Conference on Antenna and Propagation (EuCAP) (2013)
9. Joseph, R., Fukusako, T.: Circular polarized broadband antenna with circular slot on circular ground-plane. *Prog. Electromagnet. Res. C* **26**, 205–217 (2012)
10. Ismail, M.F., Rahim, M.K.A., Hamid, M.R., Majid, H.A.: Circularly polarized textile antenna with bending analysis. In: International RF and Microwave Conference (2013)
11. Balanis, C.A.: *Antenna Theory Analysis and Design*. Wiley, USA (2005)

Power Management in LTE Femtocell Networks

Jing Huey Lim, R. Badlishah Ahmad, Muzammil Jusoh
and Thennarasan Sabapathy

Abstract With the introduction of LTE and LTE-Advance, small cell technology is gradually highlighted. Femtocell as one of the economical small cell technology that attracts attention by improving coverage and capacity. Nevertheless, the deployment of Femtocell stirs up the issue of cross-tier interference. The hybrid infrastructure which built up of Macrocell and small cell layers interferences each other especially in co-channel scenario. Many discussions are initiated to resolve the issue such as Femtocell base station transmit power control scheme, radio resource allocation scheme. In this paper, the framework of Long Term Evolution-Advanced (LTE-A) has been simulated. The resulting contour plots do not miss out every single point in the network. In addition, a user friendly Graphical User Interface (GUI) is developed to ease the configuration process of the simulation.

1 Introduction

Traditionally, wireless service is achieved through simple Macrocell signaling. Although the Macrocell is upgradable, generally coverage areas cannot be expanded. Due to network capacity and data throughput depends on signal quality, it is useless even if one may suggest to have Macrocell to allocate more resources for

J.H. Lim (✉) · R. Badlishah Ahmad · M. Jusoh · T. Sabapathy
Embedded, Network and Advanced Computing (ENAC), School of Computer
and Communication Engineering, Universiti Malaysia Perlis, Arau, Malaysia
e-mail: jing-huey_lim@keysight.com

R. Badlishah Ahmad
e-mail: badli@unimap.edu.my

M. Jusoh
e-mail: muzammil@unimap.edu.my

T. Sabapathy
e-mail: thenna84@gmail.com

indoor usage. Furthermore, in conjunction with the high investment in Macrocell, the increment of indoor cellular demand as reported in [1] shows that 60–80 % of traffic is generated indoor. This urges the cellular operator to seek for more efficient and more cost effective solution. Among the alternatives, small cell technology is highly considered. The coexistence of Macrocell network with DAS and other small cells are known as “Heterogeneous network” or “HetNet”.

Femtocell, the technology invented over centuries was then being revisited again. With the cell size reduced (indirectly indicates number of cells increased), growing traffic and complex network highlights the need for Femtocell revolution in autonomic system and cost reduction. Research in [2] explains the reason of financial pressures that drive the wireless communication network future towards auto-configuration. LTE that is using OFDMA and IP-based provides a brand new platform to accommodate Femtocell (Femtocell backhaul is intrinsically IP). Mobile Experts [3] claimed that 70 million small cells will be shipped in year 2017 (including Femtocell and Picocells). Moreover, that LTE small cell will occupy the major part of forecast growth in the next 5 years with more than two-thirds of small cells will be deployed in 2017.

2 Background

A few related published works are done to analyze the interference issue related to hybrid network. Saquib et al. [4] presented a survey on different methods of interference and resource management in orthogonal frequency-division multiple access (OFDMA)-based Femtocell networks. The Authors compared different approaches such as Femto-aware spectrum management, power control, etc. Interference mitigation technique which is introduced in [5] contains a variety of combinations between inner and outer cell frequency allocation. This method evolves and becomes demand based dynamic dedicated resource in this paper. Constant Femtocell radius power control is introduced in [6] highlights the necessity to control output power of Femtocell base station to reduce unnecessary impact to Macrocell users. A well-known power control algorithm introduced by Foschini and Miljanic [7] and Mitra [8] have deep investigation on distributed iterative power algorithm which has proven to asynchronously converge. This algorithm solely relies on locally available information. Its objective is to get the minimum power which satisfy the target Signal to Interference and Noise Ratio (SINR) constraint. Xiao et al. [9] further enhanced [7, 8] and introduced a Distributed power control algorithm using utility-based power control (UBPC) which has soften the target SINR requirement.

The above studies provide a solid groundwork for this research to work on a user-friendly graphical simulator which helps in investigating interference mitigation in hybrid environment. This paper includes the Femtocell base station power management schemes in conjunction with adaptive radio spectrum allocation.

The resulting performance is presented in attractive 2-D plane. Furthermore, a customization GUI allows flexibility in customizing the environment.

The paper is organized as follows. Section 3 introduces the power control scheme modeling. Section 4 describes GUI with the critical configurations used in the simulation. The performance of the system and result is shown in Sect. 5. Section 6 draws conclusion of the overall research.

3 Modeling Power Control Schemes

The performance of the system is evaluated through SINR and capacity two dimension plot. There are three Femto base station power control schemes being evaluated. To further improve the system, the best performance scheme of the three is selected to integrate with dynamic radio allocation scheme and adaptive bit per symbol (bps) allocation scheme. The power control schemes are listed as below:

1. Constant Femto base station power control
2. Constant Femtocell radius base station power control
3. Constant Femtocell SINR base station power control

Constant Femto base station power control is the simplest way among all. Femto base stations transmit at a fix value. In second power control method, Femto base stations adjust the output power to ensure balance power of power received from serving Femto base station and Macro base station at its radius r . In short, Eq. (1) describes this fix radius power control is:

$$P_f = \min(P_m + G_\theta - PL_m(d) + PL_f(r), P_{\max}) \quad (1)$$

where

| | |
|------------|--|
| P_f | Femto base station power received at radius r |
| P_m | Macro base station power |
| G_θ | Macro base station antenna gain |
| $PL_m(d)$ | Path loss with d as distance between Macrocell and measurement point |
| $PL_f(r)$ | Path loss of Femtocell at radius r |
| P_{\max} | Femtocell maximum transmit power |

The algorithm in last technique involves Femto base station power adjustment to ensure intended SINR achieved by Femto user within a specific area. The algorithm can be summarized in Eq. (2). In any scenario, the Femto base station output power is bounded by its maximum transmit power.

$$P(k+1) = \frac{SINR_t}{SINR_c} P(k) \quad (2)$$

where

$P(k+1)$ Femto base station next iteration's output power

$P(k)$ Femto base station at kth iteration

$SINR_t$ Target SINR

$SINR_c$ Current SINR

In this paper, the best performance power control method will be selected and incorporate with dynamic radio allocation scheme. When any Macro user experiences high co-channel interference (which indirectly affects SINR), the dynamic radio allocation scheme will be initiated. The network spectrum will be divided into two with the smaller unused portion is assigned to this group of user. In order to make full use of this high SINR environment, variable bps is introduced. At good condition SINR, the higher bps is used, while with low SINR, lesser bps is used.

4 Graphical User Interface (GUI)

The plug and play nature of Femtocell demands a simulation tool that has high flexibility. A simulator is developed in MATLAB. In order to configure the environment, no coding skill is required. User just has to input some parameters through user friendly interface and simulation starts with just a button hit. Figure 1 shows the software interface before simulation starts. Most of the parameters used in the simulation has exposed to GUI for handy configuration.

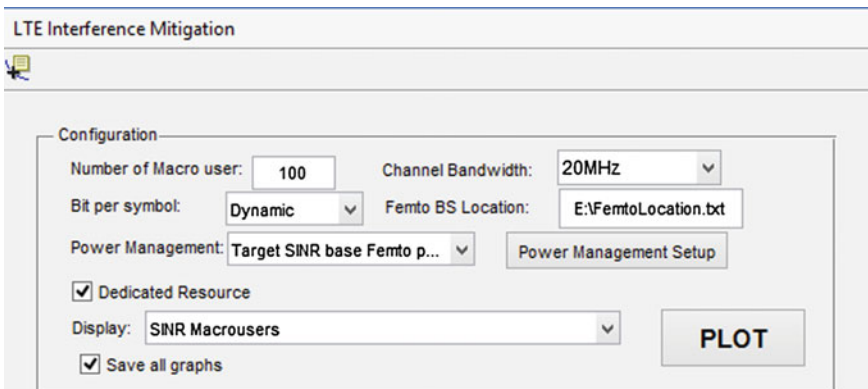


Fig. 1 GUI of the simulation software

5 Simulation Results and Discussion

There are 5 Femtocells being placed in the network. Low Macro user’s SINR surrounds near Femtocells’ region as shown in Fig. 2. The co-channel signal transmitted from the Femtocell causes high interference to Macro users. The color bar on the right shows the SINR level in decibel (dB). When the Femtocell is located away from Macrocell (Macrocell base station is represented by a “Star”), the bigger blue color region is formed. In other words, this causes more interference to bigger region. Figure 3 shows Femtocell radius based power control. The Macro user SINR plot shows significant reduction of the weak SINR regions. Nevertheless, in special scenario when the Femtocell is located very near to Macrocell, the transmit power of Femto base station is saturated to maximum Femtocell power, which is 21 dBm in our example. The power control scheme which shows the least low SINR level region is SINR based method as shown in Fig. 4. The scheme tries to hit target SINR of 4 dB within the radius 10 m of Femtocell territory. Same as radius base scheme, the power is saturated at maximum Femto base station power.

In Capacity plot the capacity level in the unit of bit per second is plotted. At the same time, the Femtocells are numbered to ease the discussion. Similar to SINR plot, Femtocell which is located further from Macrocell contains larger area of low capacity e.g. Femtocell #2 has bigger low capacity area than Femtocell #4. Figure 5 shows the capacity plot of fixed Femto base station transmit power. Compare Figs. 5 and 6, Femtocell #2 has smaller low capacity region. This shows that in fixed radius scheme, output power of Femto base station has been reduced to maintain constant Femtocell radius coverage. When observing Femtocell #3 and #4, the radius of low capacity region has been enlarged in radius based scheme. Radius based scheme has discovered that Femtocell base station #3 and #4 have the potential to transmit at higher power into achieve power equilibrium at targeted

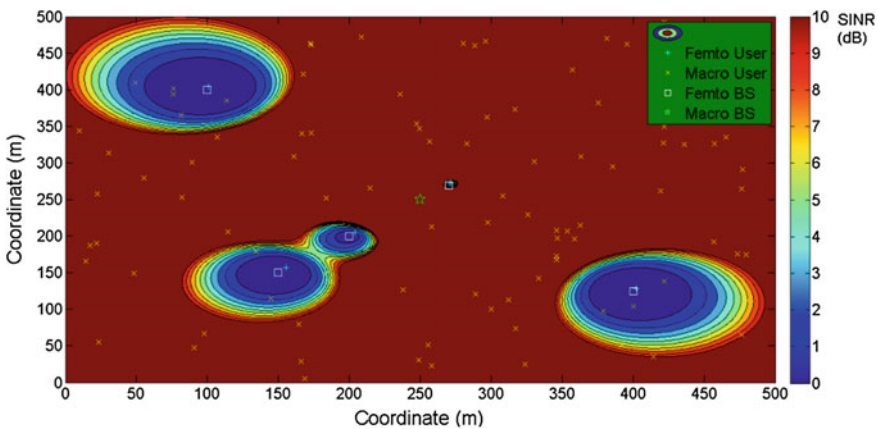


Fig. 2 SINR of Macro user using fixed power control scheme

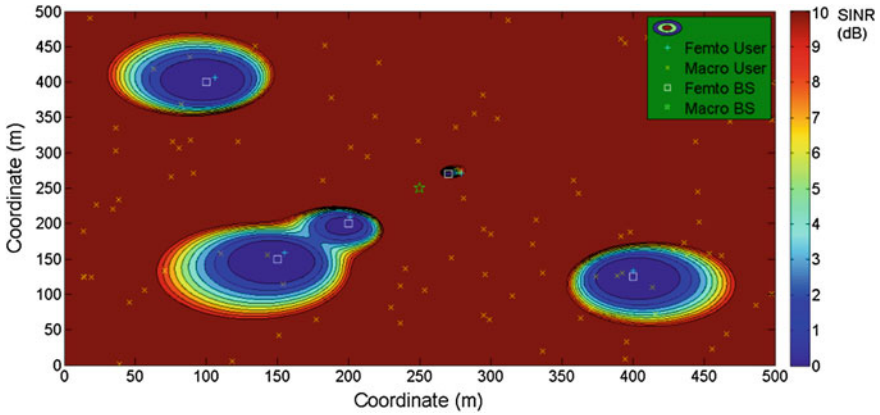


Fig. 3 SINR of Macro user using radius based power control scheme

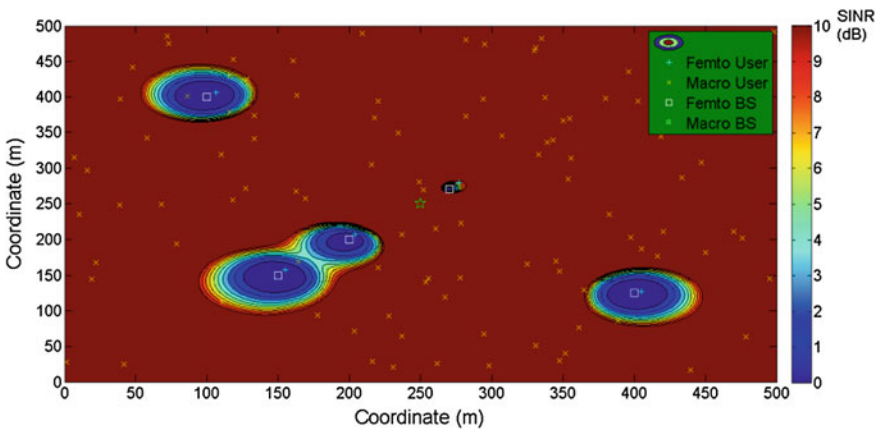


Fig. 4 SINR of Macro user using SINR based power control scheme

Femtocell radius. With the excellent result in SINR, it is expected that capacity plot of SINR based power control scheme has the best performance among all. Figure 7 shows the smallest low capacity region of all the Femtocells.

SINR based is selected as the outstanding performance power control scheme. Low SINR spots are further enhanced by dynamically assigned dedicated radio resource. In this way, they are no longer sharing the same channel like every other do. The overall spectrum is divided into two parts with the smaller spectrum is assigned to the weak SINR regions. By observing Fig. 8, the weak SINR area (especially at the center zone of Femtocell) has been strengthened with stronger signal which is using specific spectrum. Figure 8 is showing the capacity plot with

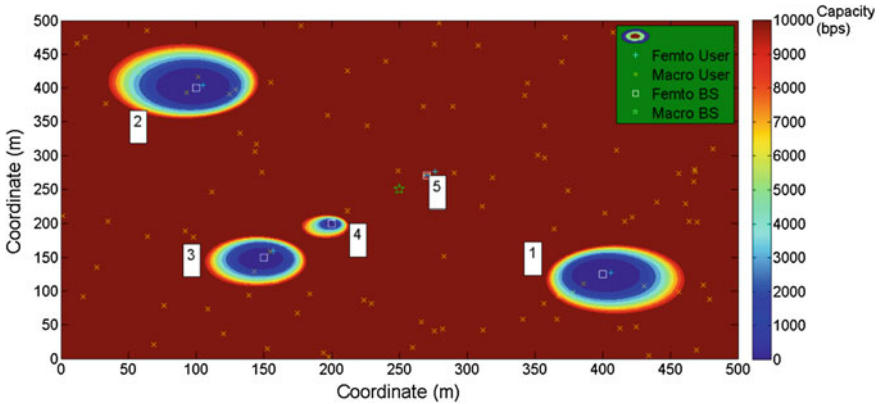


Fig. 5 Capacity of Macro user using fixed power control scheme

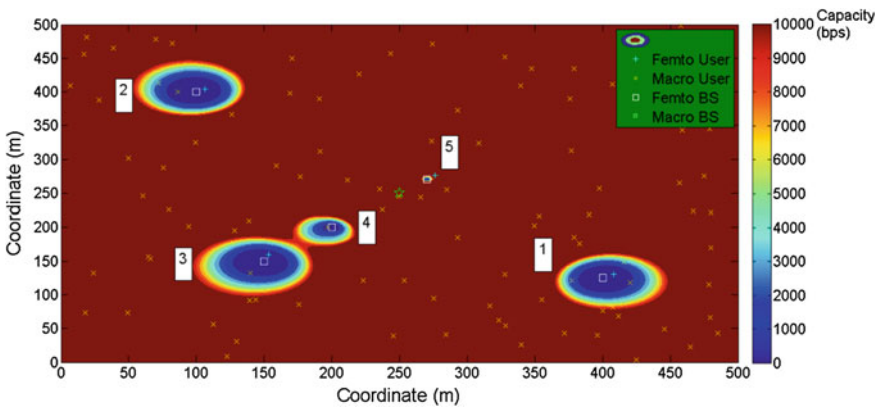


Fig. 6 Capacity of Macro user using radius based power control scheme

corresponds to this SINR plot. The color bar scale has to be adjusted to 10 times higher than Fig. 7 (without dedicated spectrum) in order to show the result clearly. The improved performance of the system is compromised by having drop of capacity at high SINR regions. This is proven in Fig. 7 where the capacity of 86,955 bps at point [321, 373] is shown; while in Fig. 8 the capacity at the same point shows 82,139 bps.

By using adaptive bps technique, the capacity of the overall network grows healthier. Most of the regions has turned into red, which indicates that the capacity is 100 kbps and above. Figure 9 shows the evident of outstanding capacity plot after enhancing the system with dedicated resource and adaptive bps implementations.

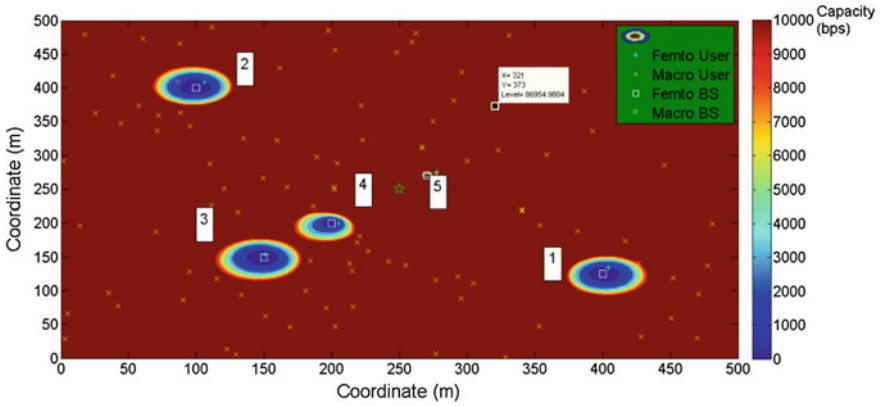


Fig. 7 Capacity of Macro user using SINR based power control scheme

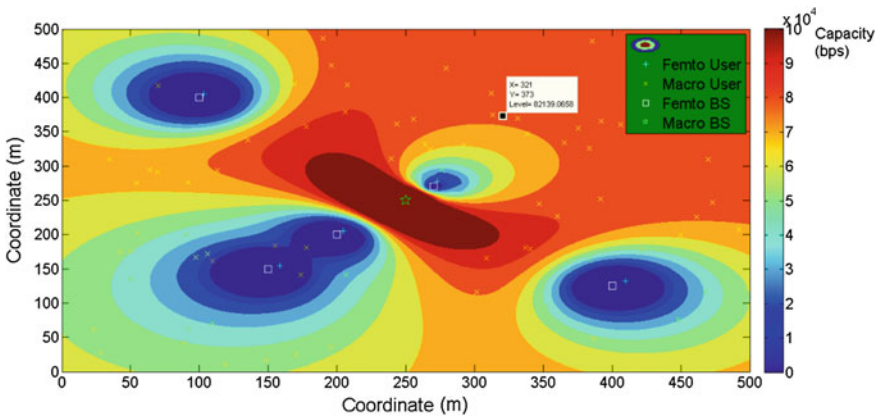


Fig. 8 Capacity using SINR based power control with dedicated resource

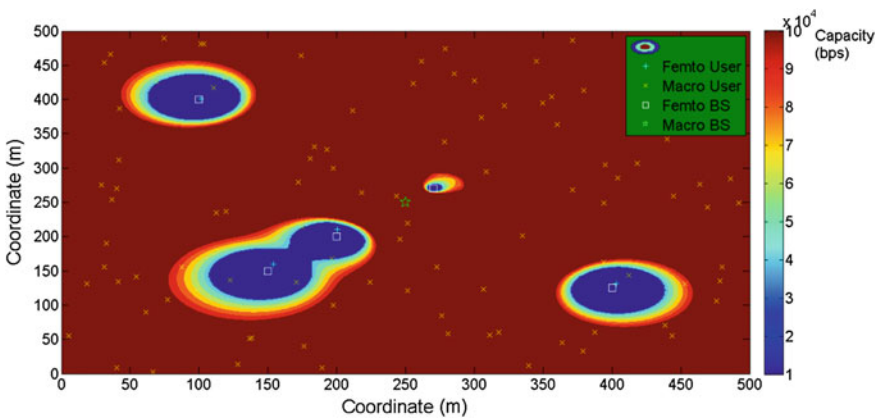


Fig. 9 Capacity using SINR based power control with dedicated resource and dynamic bps

6 Conclusion and Future Work

In this paper, the three power control schemes have simulated and further improved by introducing dynamic radio allocation scheme and adaptive bps allocation. The SINR based power control has outstanding result among all. The capacity of SINR based power control scheme that works with dynamic radio allocation and adaptive bps allocation has approximately improved 10 times the performance of the system the other two schemes. A possible future work is to simulate the indoor environment which considers penetration loss. In addition, co-tier interference mitigation which is not discussed in this paper can be further researched.

References

1. Mobile network operator challenges. <http://www.iet.ntnu.no/workshop/SNOW2012/presentations/lehne.pdf>
2. Claussen, H., Ho, L., Karimi, H., Mullany, F., Samuel, L.: I, base station: cognisant robots and future wireless access networks. In: Proceedings IEEE Consumer Communications and Networking Conference, vol. 1, pp. 595–599 (2006)
3. Mobile Experts. <http://www.pnnewsire.com/news-releases/new-forecast-predicts-shipment-of-70-million-small-cells-by-2017-139208144.html>
4. Saquib, N., Hossain, E., Le, L.B., Kim, D.I.: Interference management in OFDMA femtocell networks: issues and approaches. In: Wireless Communications, IEEE, pp. 86–95 (2012)
5. Bouras, C.: Interference management in LTE femtocell systems using an adaptive frequency reuse scheme. In: Wireless Telecommunication Symposium (WTS), pp. 1–7 (2012)
6. Claussen, H.: Performance of macro- and co-channel femtocells in a hierarchical cell structure. In: IEEE 18th International Symposium on Personal, Indoor and Mobile Radio Communications 2007 (PIMRC'07) (2007)
7. Foschini, G.J., Miljanic, Z.: A simple distributed autonomous power control algorithm and its convergence. *IEEE Trans. Veh. Technol.* **42**, 641–646 (1993)
8. Mitra, D.: An asynchronous distributed algorithm for power control in cellular radio systems. In: Proceedings 4th Winlab Workshop Third Generation Wireless Information Network, Rutgers University, pp. 249–257 (1993)
9. Xiao, M., Shroff, N., Chong, E.: Utility-based power control in cellular wireless systems. In: 12th IEEE Annual Joint Conference of the IEEE Computer and Communications Societies 2001, (INFOCOM'01.), vol. 1, pp. 412–421 (2001)

Design and Analysis of a Circular Ring Patch Antenna Array for UHF Applications

Usama Ahmed Adem, Ajmal Hussain Shah,
Chandrasekharan Nataraj, Sathish Kumar and Sheroz Khan

Abstract In this paper a compact Circular Patch Ring Antenna Array (CPRAA) for UHF TV reception is presented. The proposed antenna consists of ring patches arranged in a 2×2 array and sits on the FR4 dielectric substrate. The patches are jointed with the Wilkinson power divider and fed by a BALUN. The results show that the antenna achieves a significantly high gain of 11.21 dB. The antenna resonates at the frequency of 638 MHz under UHF band with an operating bandwidth of 200 MHz. The proposed antenna is compact and cost effective and thus suitable for receiving TV broadcast channels and other applications under UHF frequency band.

Keywords Circular patch ring antenna array · 2×2 ring patch array solar Wilkinson power divider · BALUN · UHF TV reception

U.A. Adem (✉) · A.H. Shah · C. Nataraj · S. Kumar
School of Engineering, Asia Pacific University of Technology and Innovation,
Kuala Lumpur, Malaysia
e-mail: engtele.usamaahmed@gmail.com

A.H. Shah
e-mail: ajmal@apu.edu.my

C. Nataraj
e-mail: chander@apu.edu.my

S. Kumar
e-mail: dr.satish@apu.edu.my

A.H. Shah · C. Nataraj · S. Khan
International Islamic University Malaysia (IIUM), Selangor, Malaysia
e-mail: cnar32.sheroz@gmail.com

1 Introduction

Television broadcasting has seen an incredible growth since mid of the last century. Initially only 12 channels under Very High Frequency (VHF) band were introduced for TV broadcasting. Later, the FCC allocated 70 additional channels above this band and called them “Ultra High Frequency” or the UHF band. UHF signals are inherently less efficient and prone to more losses in the conversion of radio waves to the electrical signals used by the TV receivers.

Good UHF reception therefore requires considerable attention to the antenna design and installation than VHF reception. Extensive research has been carried out in designing antennas to improve the UHF TV reception. The antenna plays an important role in TV broadcasting applications. An antenna converts radio frequency (RF) currents into electromagnetic waves and vice versa. Outdoor and indoor TV reception antennas are available in different shapes and sizes. However most of the outdoor antennas are large in size and need extra care during installation. On the other hand indoor antennas are handy but still require considerable space.

A Micro strip ring patch antenna often used MIC components for the measurement of dispersion characteristics of Micro strip lines. The resonance condition for the Micro strip ring antenna can be obtained from the EM fields existing in an annular cavity surrounded by magnetic walls [1].

In this paper, a compact Micro strip ring patch antenna for UHF TV reception and other applications is presented.

2 Antenna Design and Geometry

In this section the antenna design steps are described.

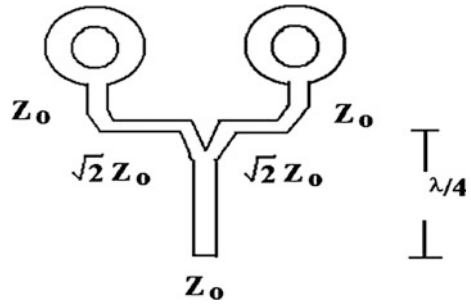
2.1 Wilkinson Power Divider

When the elements in an array antenna combined, all the powers are summed up at a point. The sum of the powers is guided by a device called Wilkinson power divider or power combiner. The Wilkinson power combiner offers broad bandwidth and equal phase characteristics at each of its output ports.

Figure 1 shows the schematic diagram of the Wilkinson power combiner which is used here to feed two elements of the proposed antenna.

The output port isolation is obtained by series termination. Each of the quarter wavelength line has a characteristic impedance of $\sqrt{2}Z_0$ and the output is terminated by a resistor of $2Z_0$ impedance while Z_0 is the system characteristic impedance.

Fig. 1 Single section of Wilkinson power combiner [2]



The Wilkinson power combiner offers an adequately flat response over more than one octave band. However, the isolation is affected by the load impedance at the band edges. The performance can be further improved by adding a $\lambda/4$ transformer in front of the power divider step or power combiner step. The input VSWR of the uncompensated power combiner is higher than the compensated.

2.2 Balun Design

BALUN stands for balance to unbalance. It is a device mainly to provide impedance matching and helps in increase the broadband operation of the antenna.

The Balun acts as a matching circuit between a balance and an unbalance device. A Balun is used between an antenna and a receiver circuit to ensure maximum power transfer to the receiver thus minimizing return loss. The Micro strip Balun is available in many shapes and designs. The design varies from one application to another. Figure 2 shows a few examples of Micro strip Balun circular ring patch antenna array operate at VHF and UHF frequency bands.

2.3 The Antenna Geometry

First step is to calculate the resonant frequency of the proposed ring antenna at UHF band (470–806 MHz), we get:

$$\begin{aligned}
 f_c &= \frac{f_2 + f_1}{2} \\
 f_c &= \frac{470 \times 10^6 + 806 \times 10^6}{2} \\
 f_c &= f_{m0} = 638 \text{ MHz} \\
 \lambda &= \frac{c}{f}
 \end{aligned}
 \tag{1}$$

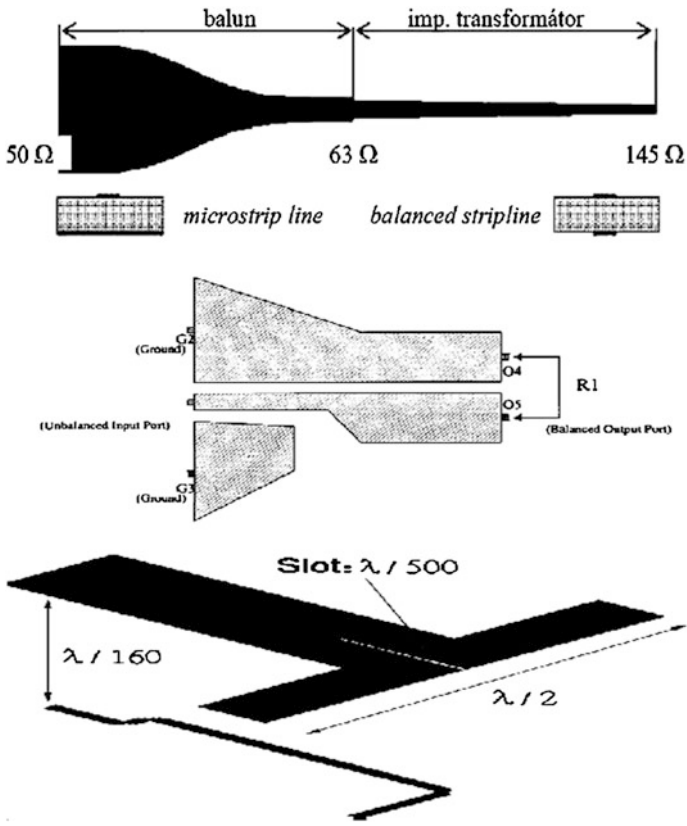


Fig. 2 Typical example of Balun [3]

where λ is a wavelength in measured in meter, f is an operating frequency and c is a speed of light, 3×10^8 m/s.

$$\lambda = \frac{3 \times 10^8}{638 \times 10^6} = 47 \text{ cm}$$

Since the optimizing factor is in range of 0.4–0.5 then let it be

$$0.4 \times 47 \text{ cm} = 18.8 \text{ cm} \tag{2}$$

Refers to Eq. 2 and calculation of λ , it shows that the length of the antenna is about 18.8 cm long. The substrate chosen is FR4 with a thickness of 1 mm and a dielectric constant of 3.45.

The second step is to calculate the width of the ring (t) [4].

$$f_{mn0} = \frac{ck_{mn0}}{2\pi\sqrt{\epsilon_e}} \quad (3)$$

$$a_e = a \left[1 + \frac{2h}{\pi a \epsilon_r} \left(\ln \frac{\pi a}{2h} + 1.7726 \right) \right]^{1/2} \quad (4)$$

$$b_e = b \left[1 + \frac{2h}{\pi b \epsilon_r} \left(\ln \frac{\pi b}{2h} + 1.7726 \right) \right]^{1/2} \quad (5)$$

The dominant wave number for the circular ring patch found to be where a_e and b_e are the effective radii of the ring, h is the thickness and ϵ_r is the relative dielectric constant for the substrate material. Thus, the width (t) of the ring patch can be determined by taking the difference of b_e and a_e . In mathematics, it can be expressed as:

$$t = b_e - a_e \quad (6)$$

The dominant wave number for the circular ring patch found to be

$$k_{mn0} = \frac{4\pi}{3(b_e - a_e)} \quad (7)$$

Substitute Eq. 3 into Eq. 6 and simplify, we get

$$f_{mn0} = \frac{2\pi c}{3\pi\sqrt{\epsilon_e}(w)} \quad (8)$$

In general, the resonance frequency of a single circular patch ring antenna is determined by the width of the ring.

$$\begin{aligned} f_{mn0} &= \frac{2\pi c}{3\pi\sqrt{\epsilon_e}(t)} \\ 638 \times 10^6 &= \frac{2\pi \times 3 \times 10^8}{3\pi\sqrt{3.45}(t)} \\ t &= 1.68 \text{ cm} \\ t &= b_e - a_e = 1.68 \text{ cm} \end{aligned}$$

Let's select the radius $a_e = 18.8/4 \text{ cm} = 3.02 \text{ cm}$

$$\begin{aligned} 1.68 &= b_e - 3.02 \\ b_e &= 4.7 \text{ cm} \end{aligned}$$

The third step is to calculate the width of strip line. The design of the strip line which connect the all the antennas into one point should follow the Wilkinson power combiner rules. Let the “*w*” is the width of the strip line, based on Wilkinson Power Combiner, the combined power factor is given by:

$$k = 0.57 - 0.145 \ln \frac{w}{h} \tag{9}$$

Using -3 dB half power combiner, the factor of *k* is 0.5 ($10\log_{10}0.5 = -3$ dB), thus:

$$\begin{aligned} 0.5 &= 0.57 - 0.145 \ln \frac{w}{h} \\ 0.487 &= \ln(w/h) \\ w/h &= e^{0.487} \\ w &= 1.62 \times 0.001 \\ w &= 0.163 \text{ cm} \end{aligned}$$

All the lengths jointed from ring to the centre of combined point are using standard Micro strip length which is $\lambda/4$. Thus, the total length will be:

$$\begin{aligned} \ell &= \frac{18.8}{4} \\ &= 4.7 \text{ cm} \end{aligned}$$

The complete diagram of the proposed antenna geometry is shown in Fig. 3. The fourth step is to design a Balun for the antenna. Five sections of impedance

Fig. 3 Antenna design geometry

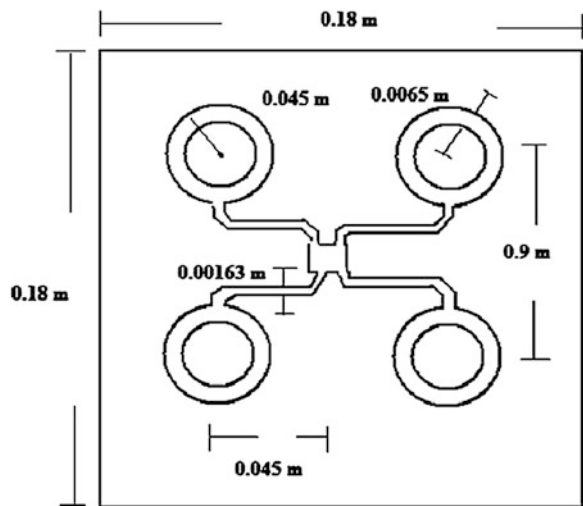
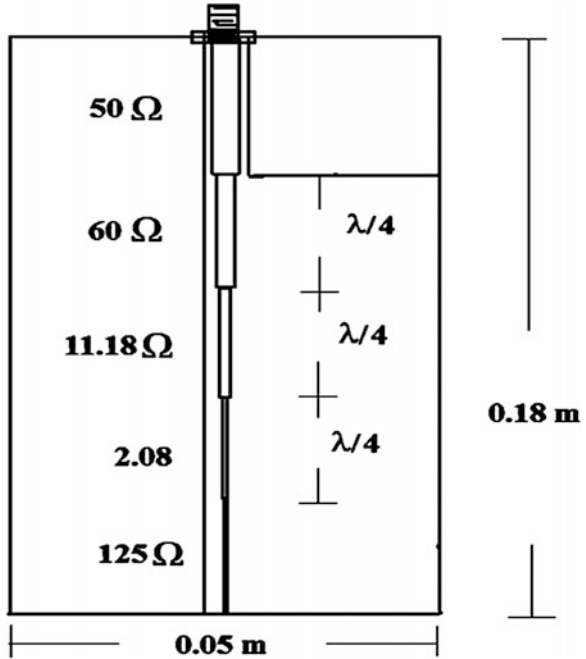


Fig. 4 Balun design geometry



transformers are required to design the Balun. Each section has a length of $\lambda/4$. The complete diagram of the Balun with its dimension is shown in Fig. 4.

The Balun helps in matching the impedance of ring antenna and the feed point. The impedance of the five sections of transformers represented by Z_0 , Z_F , Z_1 , Z_2 and Z_3 are calculated below.

$$\begin{aligned}
 Z_0 &= 50 \Omega \\
 Z_1 &= 1.2 \text{ (choose 100\% bandwidth)} \\
 Z_F &= 2.5 \times 50 \Omega \\
 &= 125 \Omega \text{ (actual impedance)} \\
 Z_1 &= 1.2 \times 50 \Omega \\
 &= 60 \Omega \text{ (actual impedance)} \\
 Z_2 &= \sqrt{Z_F} = \sqrt{125} = 11.18 \Omega \\
 Z_3 &= Z_F/Z_1 = 125/60 = 2.08
 \end{aligned}$$

3 Results and Discussions

The antenna is simulated and the performance is evaluated by the following parameters.

1. Return Loss
2. Gain
3. Directivity
4. Antenna Efficiency
5. VSWR
6. Radiation Pattern

The 3D design view of the proposed antenna using simulation software is shown in Fig. 5.

The S_{11} result for the circular ring patch antenna is shown in Fig. 6.

As can be seen in Fig. 6, the return loss of approximate -32.511 dB at 623.4 MHz is evident. Figure 7 shows the antenna gain of 11.214 dB which is a significantly high gain for the UHF TV reception and other applications. Figure 8 illustrates the directivity of the antenna. A directivity of 11.214 dB is evident in the figure.

Figure 9 shows the radiated power gain of the antenna. In the figure the radiated power gain of the antenna of 21.231 dBm is evident. Figure 10 shows the 3D radiation pattern of the antenna.

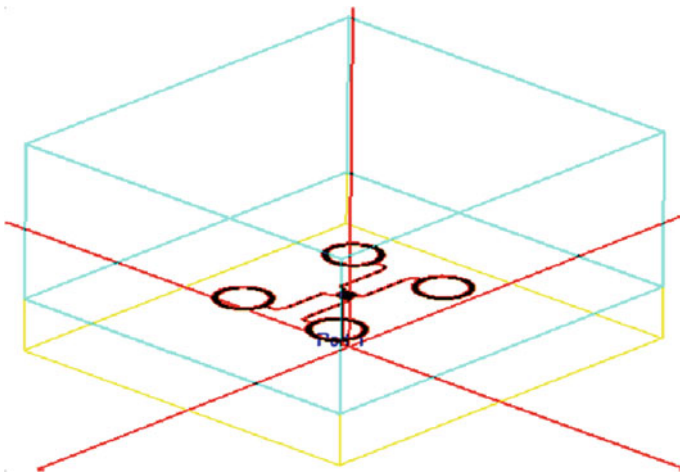


Fig. 5 3D design view of the proposed antenna

Fig. 6 Simulation result for the circular ring patch antenna

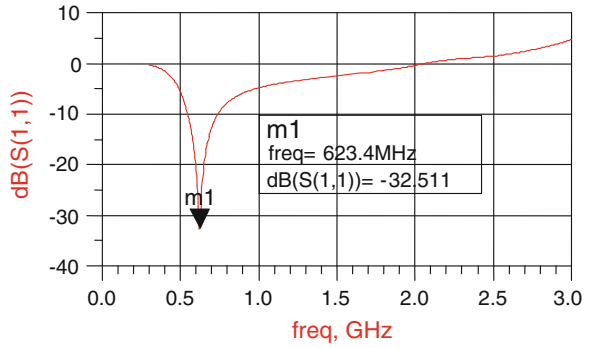


Fig. 7 The antenna gain

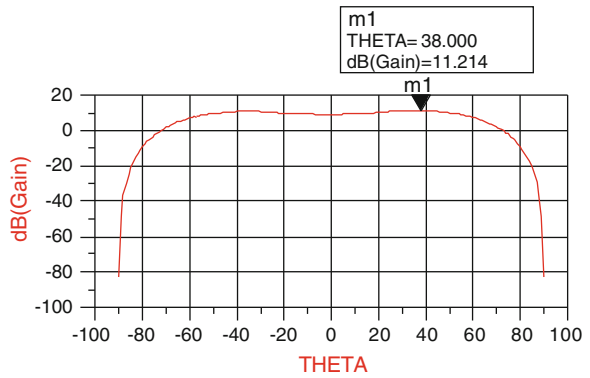


Fig. 8 The antenna directivity

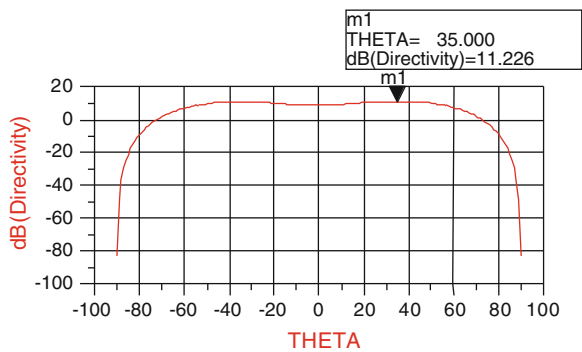


Fig. 9 The antenna radiated power gain

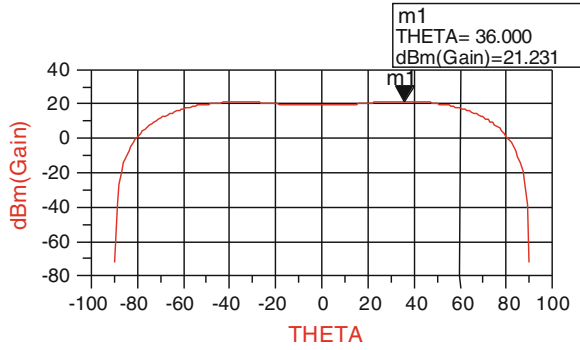


Fig. 10 3D radiation pattern of the proposed antenna

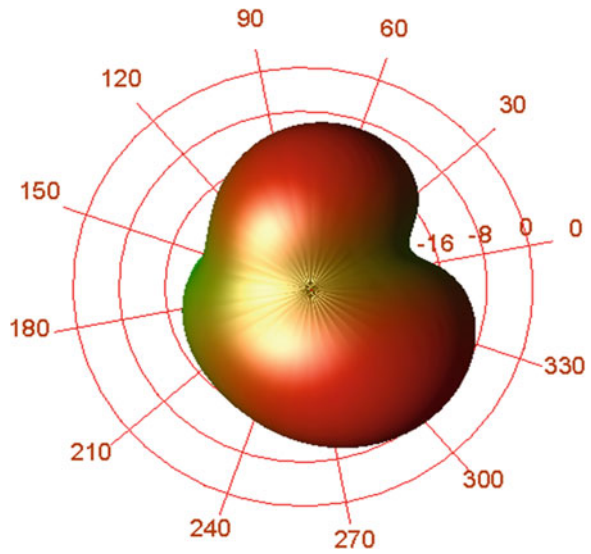


Table 1 Performance evaluation of the proposed antenna

| Parameters | Value |
|----------------|------------------------|
| Gain | 11.21 dB |
| Directivity | 11.22 dB |
| Radiated power | 21.231 dBm |
| Effective area | 1.448×10^{-5} |
| S_{11} | -32.51 |
| Frequency | 623.4 MHz |
| VSWR | 1.005 |
| Impedance | 50 Ω |
| Bandwidth | 200 MHz |
| Height (h) | 18 cm |
| Width (w) | 18 cm |

4 Conclusion

Good UHF reception requires a compact and a high gain indoor antenna. In this paper a compact cost effective, high gain indoor antenna is presented. The antenna size is reduced by 60 % of a commercially available UHF antenna. The antenna is resonated at 638 MHz and has an operating bandwidth of 200 MHz. The antenna radiates a power of 21.231 dBm. It achieved a gain of 11.21 dB and a directivity of 11.22 dB. A minimum return loss of -32.51 dB and a VSWR of 1.005 at the resonant frequency of 623.4 MHz. Hence the proposed antenna is recommended for UHF TV reception and other applications in the same band.

References

1. Barrett, R.M., Sanders, A.: Antenna Handbook. Longman, New York (2008)
2. Bailey, A.E.: Microstrip Antenna Designs. Prentice-Hall, New York (2009)
3. Helszajn, J., Ng, F.L.: Microwave Engineering. McGraw-Hill, New York (2009)
4. Chi, C.Y., Rebeiz, G.M.: Radio Frequency and Application. Prentice-Hall, New York (2011)

Broadband Triangle Shape Printed Antenna for Mobile Wireless Communication

T. Alam, M.R.I. Faruque and M.T. Islam

Abstract In this paper, a broadband antenna for mobile wireless communication is presented and experimentally investigated. The proposed antenna is incorporated with triangle shape radiator and defected ground. The main radiator is connected with $50\ \Omega$ microstrip feed line. The antenna has achieved measured VSWR ≤ 2 impedance bandwidth of 1.05 GHz (1.66–2.71 GHz) and 1.42 GHz (3.28–4.7 GHz), which cover GSM 1800, 1900, 2100, UMTS, Bluetooth (2.40–2.80 GHz), WLAN (2.40–2.485 GHz), WiMAX (2.50–2.69 GHz), and WiMAX (3.40–3.60 GHz). Moreover, the antenna has shown good antenna performances with stable radiation pattern and appreciable gain.

1 Introduction

Recently, along with rapid advancement of wireless technology wideband compact antenna for lower frequency bands become a challenging issues to the antenna researchers. Microstrip feed printed antennas has become most studied structure due to its some interesting features, like low cost, compact, lightweight, easy fabrication and installation.

Many low-cost small antennas have been investigated over the last decade [1, 2]. However, the appeal of wideband antenna is becoming robust as today mobile

T. Alam (✉) · M.R.I. Faruque
Space Science Centre (ANGKASA), Universiti Kebangsaan Malaysia,
43600 UKM Bangi, Selangor, Malaysia
e-mail: touhid13@yahoo.com

M.R.I. Faruque
e-mail: rashed@ukm.edu.my

M.T. Islam
Department of Electrical, Electronic & System Engineering, Universiti Kebangsaan Malaysia,
43600 UKM Bangi, Selangor, Malaysia
e-mail: tariqul@ukm.edu.my

wireless devices are needed to have the function of multi-standard operations. Li et al. proposed a broadband planar antenna which achieved 40 % impedance bandwidth (VSWR < 2) with antenna size of $18 \times 69 \text{ mm}^2$ [3]. Alam et al. proposed parasitic element loaded antenna for mobile wireless antenna which can cover GSM 1800, GSM 1900, GSM 2100, UMTS, Bluetooth (2.40–2.80 GHz), WLAN (2.40–2.485 GHz), WiMAX (2.50–2.69 GHz), and WiMAX (3.40–3.60 GHz). However, the antenna dimension was $50 \times 62.9 \text{ mm}^2$ [4]. Montero et al. proposed a coplanar hybrid antenna having size of $56 \times 24 \times 6 \text{ mm}^3$ for GSM 1800, PCS 1900, UMTS 2100, WLAN 2450/5200 applications [5]. Spline-shaped ultra wideband antenna for mobile application is presented in [6], which can operate at DCS 1800, the PCS 1900, the UMTS (1920–2170 MHz), and the ISM (2400–2485 MHz) bands. Though, the antenna was $51.2 \times 60 \text{ mm}^2$. Dual arm structure antenna is illustrated for DCS, PCS, UMTS and WLAN application in [7] with physical size of $119 \times 50 \text{ mm}^2$.

In this communication, a new broadband triangle shape antenna is illustrated for handheld devices, which can operate at GSM 1800, GSM 1900, GSM 2100, UMTS, Bluetooth (2.40–2.80 GHz), WLAN (2.40–2.485 GHz), WiMAX (2.50–2.69 GHz), and WiMAX (3.40–3.60 GHz). The physical dimension of the presented antenna is $37 \times 47 \times 1.6 \text{ mm}^3$, which is compact than reported antennas. The antenna performances has been analyzed and experimentally validated. Additionally, the electromagnetic absorption rate of the proposed antenna has been investigated.

2 Antenna Design

The geometric layout of the suggested antenna is depicted in Fig. 1, which is printed on low cost FR4 substrate material of $37 \times 47 \times 1.6 \text{ mm}^3$. The proposed antenna assimilated with inverted C-shaped ground plane and a triangular shape radiator. A 50Ω microstrip feeding line is connected with prime radiator. The presented antenna parameters are: $L = 47 \text{ mm}$, $W = 37 \text{ mm}$, $Wf = 1 \text{ mm}$, $Lf = 20 \text{ mm}$, $L1 = 22 \text{ mm}$, $L2 = 15.55 \text{ mm}$, $L3 = 15.55 \text{ mm}$, $L4 = 25.75 \text{ mm}$, $L5 = 24.5 \text{ mm}$, $L6 = 12 \text{ mm}$, $L7 = 15.5 \text{ mm}$ and $h = 1.6 \text{ mm}$.

3 Result and Discussions

The proposed antenna prototype has been fabricated and experimentally validate with measured one. The design and simulation of the proposed antenna have been performed by using the commercially available CST microwave studio and Ansoft high-frequency structure simulator (HFSS) software. The VSWR measurement has been performed using an Agilent TE8362C network analyzer. The surface current distribution of the presented antenna is presented in Fig. 2. It is shown from Fig. 2

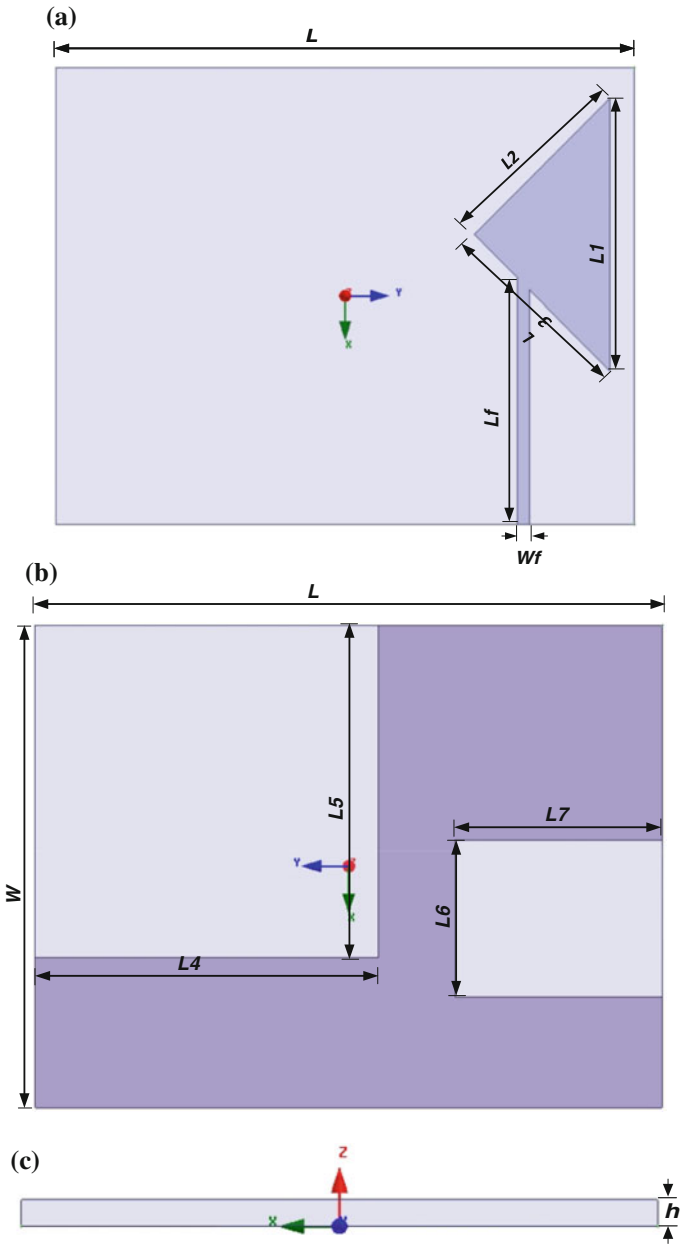


Fig. 1 Geometric layout of the presented antenna. **a** Top view, **b** bottom view, **c** side view

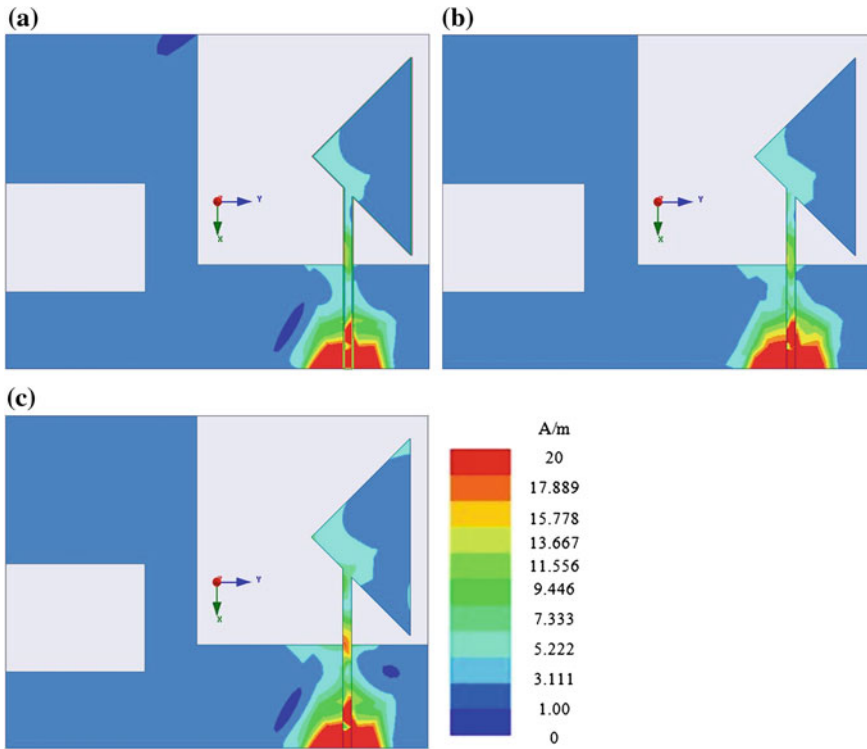


Fig. 2 Surface Current distribution of the presented antenna **a** At 1.8 GHz **b** At 2.4 GHz **c** At 3.6 GHz

that the maximum current flows in feed line towards triangle shape radiator. There are some leakage current near feeding port.

Moreover, the smith chart of the presented antenna is also illustrated in Fig. 3. The simulated and measured VSWR is presented in Fig. 4. It is seen that the antenna has achieved measured VSWR ≤ 2 impedance bandwidth of 1.05 GHz (1.66–2.71 GHz) and 1.42 GHz (3.28–4.7 GHz), which cover GSM 1800, 1900, 2100, UMTS, Bluetooth (2.40–2.80 GHz), WLAN (2.40–2.485 GHz), WiMAX (2.50–2.69 GHz), and WiMAX (3.40–3.60 GHz). From Fig. 4, it is observed that the measured and simulated VSWR are identical. The radiation pattern of the presented antenna has been demonstrated in Fig. 5. It is shown from Fig. 5 that the antenna shows nearly omnidirectional radiation pattern at E-plane. Moreover, the researchers have been analyzed specific absorption rate [8–10]. To comply with the requirement of IEEE and ICNIRP guideline, the SAR value of the presented antenna has been analyzed and presented in Fig. 6. It is observed from Fig. 6 that, the electromagnetic absorption rate fulfill the requirements of IEEE and ICNIRP guideline for the electromagnetic absorption rate.

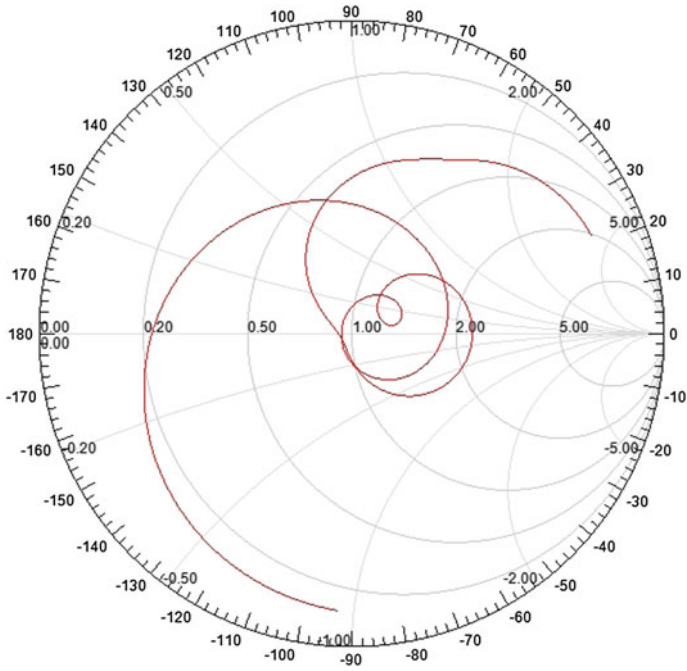
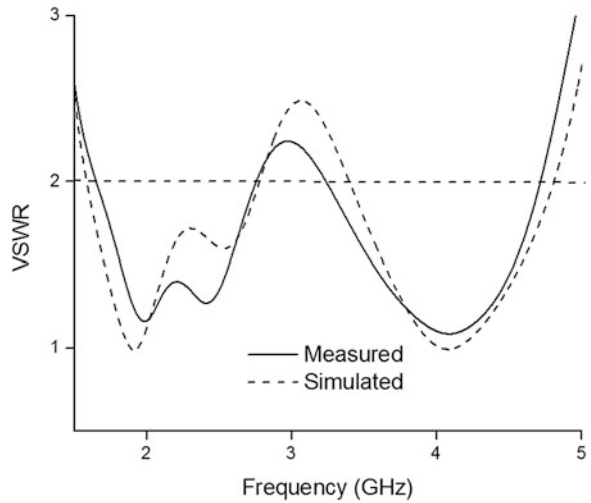


Fig. 3 Smith chart of the presented antenna

Fig. 4 Measured and simulated VSWR of the presented antenna



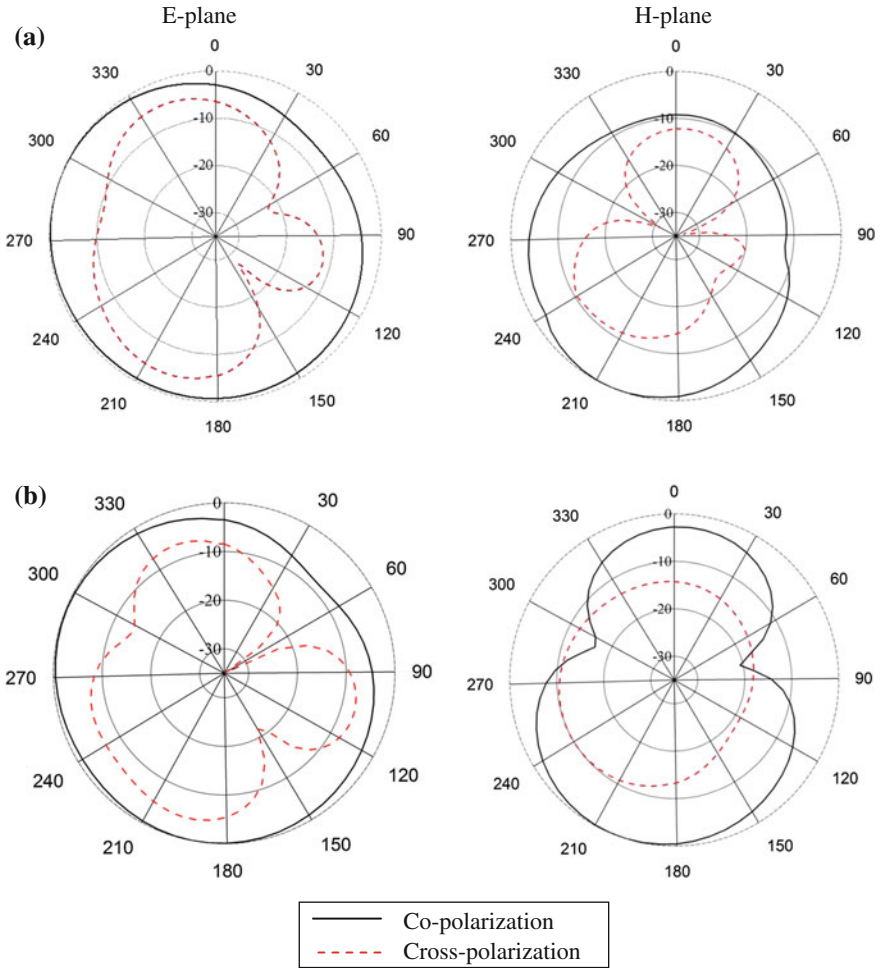


Fig. 5 Radiation pattern of the presented antenna at a 1.8 GHz and b 2.4 GHz

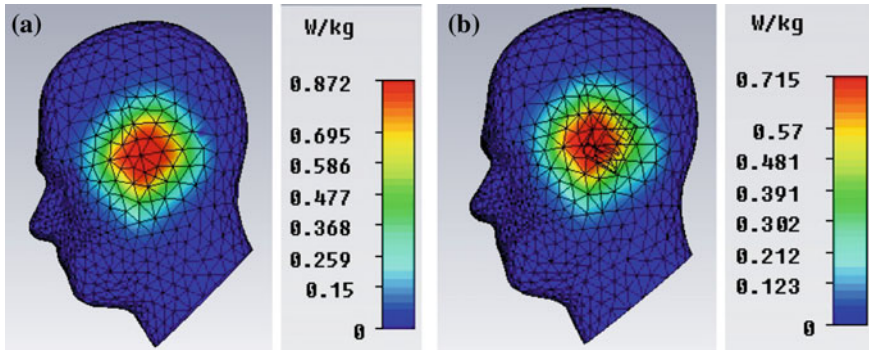


Fig. 6 a 10 g SAR at 1.8 GHz, b 10 g SAR at 2.4 GHz

4 Conclusion

A new compact triangle shape radiator with inverted C-shape ground plane is presented for mobile wireless communication. Experimental result shows that the obtained $VSWR \leq 2$ impedance bandwidth of 1.05 GHz (1.66–2.71 GHz) and 1.42 GHz (3.28–4.7 GHz) with compact size of $37 \times 47 \times 1.6 \text{ mm}^3$. So, the proposed antenna can play significant role in mobile wireless communication.

References

1. Samsuzzaman, M., Islam, M.: Wideband hook-shaped circularly polarised antenna. *Electron. Lett.* **50**, 1043–1045 (2014)
2. Alam, T., Faruque, M.R.I., Islam, M.T.: Wideband linearly polarized printed monopole antenna for C-band. *Adv. Comput. Commun. Eng. Technol.* pp. 205
3. Li, R.L., Pan, B., Papapolymerou, J., Laskar, J., Tentzeris, M.M.: Broadband low-profile antennas for wireless applications. *IET Microwaves Antennas Propag.* **1**, 396–400 (2007)
4. Alam, T., Faruque, M.R.I., Islam, M.T.: Printed circular patch wideband antenna for wireless communication. *Informacije MIDEM* **44**, 212–217 (2014)
5. Sanchez-Montero, R., Langley, R.J., Salcedo-Sanz, S., Portilla-Figueras, J.A.: Coplanar hybrid antenna for mobile and wireless applications. *IET Microwaves Antennas Propag.* **5**, 192–199 (2011)
6. Lizzi, L., Azaro, R., Oliveri, G., Massa, A.: Printed UWB antenna operating over multiple mobile wireless standards. *IEEE Antennas Wirel. Propag. Lett.* **10**, 1429–1432 (2011)
7. Zhou, D., Abd-Alhameed, R.A., See, C.H., Alhaddad, A.G., Excell, P.S.: Compact wideband balanced antenna for mobile handsets. *Microwav. Antennas Propag. IET* **4**, 600–608 (2010)
8. Faruque, M.R., Islam, M.T.: Novel triangular metamaterial design for electromagnetic absorption reduction in human head. *Prog. Electromagnet. Res.* **141**, 463–478 2013

9. Faruque, M.R.I., Islam, M.T., Misran, N.: The study of specific absorption rate (SAR) reduction in mobile phones using materials and metamaterials. *Int. J. Phys. Sci.* **6**, 7212–7221 (2011)
10. Islam, M.T., Faruque, M.R.I., Misran, N.: Specific absorption rate analysis using metal attachment. *Informacije MIDEM* **40**, 238–240 (2010)

Parametric Analysis of a Low Profile UWB Trapezoidal Antenna for Ultra Wireless Communication System

Noor Z.A. Naharuddin and Nurul H. Noordin

Abstract This paper presents the analysis of CPW—fed trapezoidal monopole antenna with return loss lower than -10 dB and VSWR lower than 2. The proposed antenna operates from 2.2 to 11.5 GHz and is suitable for ultra wideband applications. This antenna consists of a ground plane, a feed line and a trapezoidal radiating structure. The trapezoidal shaped patch is chosen because of its simple structure, which reduces the complexity of its geometrical optimization process. Initially the proposed antenna is designed with a single trapezoidal shaped patch and later additional structures were loaded at the bottom of the patch. With a total size $38\text{ mm} \times 51\text{ mm} \times 1.6\text{ mm}$ and designed on a substrate with dielectric constant 4.4, the antenna satisfies the licensed frequency band of S band (2–4) GHz, C band (4–8) GHz and X band (8–12) GHz application.

1 Introduction

Ultra-wideband (UWB) technology has been around for so many years and in the past 20 years, UWB was used for radar, sensing, military communications and niche applications. UWB systems offered a lot of advantages to consumer such as low complexity, low cost, noise-like signal, resistant to severe multipath and jamming, very good time domain resolution allowing for location and tracking applications. All these advantages and variety of applications is strong evidence of

N.Z.A. Naharuddin (✉) · N.H. Noordin
Faculty of Electrical and Electronics Engineering, University Malaysia Pahang, Pekan,
Pahang, Malaysia
e-mail: zirwatu01@gmail.com

N.H. Noordin
e-mail: hazlina@ump.edu.my

the viability and flexibility of the technology [1]. The UWB systems are usually applied for WLAN and IEEE 802.11 protocols set the frequency ranges 2.4, 3.6, 4.9, 5 and 5.9 GHz bands for WLAN channels. While C band (4–8) GHz and X band (8–12) GHz are normally used for short range tracking, missile guidance, mapping, marine radar and airborne intercept [2, 3]. Antennas that display the characteristic like a high pass filter is becoming popular in a UWB system as these kinds of antennas could differentiate different kind of pulse signals [1]. However, designing a UWB antenna is challenging process as these antennas requires proper impedance matching, accurate type of feed and excitation, compact in size, and typically these antenna are limited to short range transmission. Coplanar waveguide (CPW)—fed antennas are frequently used in UWB system based on their advantages in salient features. There are many previous work investigated CPW—fed antenna in different kinds of shapes like octagon, circular, linear, semi-circle, and flower shaped [3–7], etc. In this paper, a reconfigurable CPW—fed antenna is proposed. The reconfiguration of the antenna will be achieved electronically by using PIN diode as its RF switches. All the experiment in this paper is to investigate the effects of geometrical altering to the operating frequency of the proposed antenna. Simulation of the antenna is carried. At this stage the model has been simulated using the time domain solver, Computer Simulation Technology (CST) Microwave Studio and discussed here.

2 Antenna Structure and Design

The geometrical configurations of the proposed antenna are shown in Fig. 1. The dimensions of the antenna are as follows in Table 1.

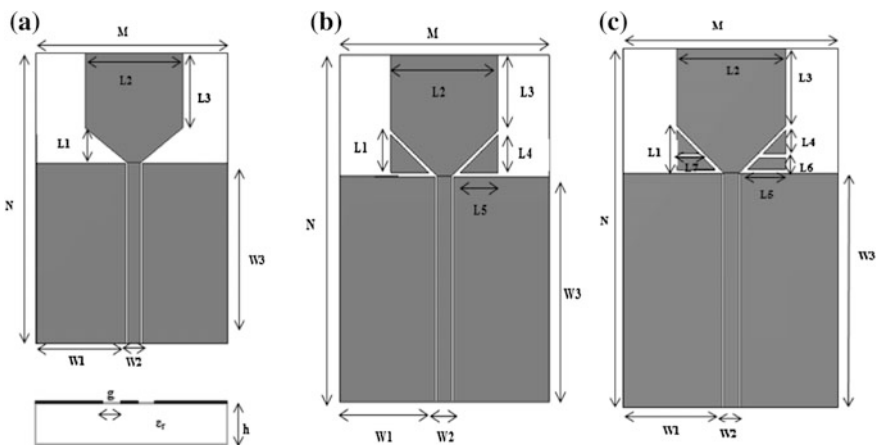


Fig. 1 Proposed antenna with different radiating elements **a** Basic *trapezoidal* patch. **b** Added with *triangular* patches. **c** Added with *triangular* and *trapezium* patches

Table 1 Antenna's dimensions

| Parameter | Value (mm) |
|-----------|------------|
| M | 38 |
| N | 51 |
| W1 | 17.5 |
| W2 | 2.6 |
| W3 | 32 |
| L1 | 7.8 |
| L2 | 19 |
| L3 | 11.2 |
| g | 0.2 |
| h | 1.6 |

From Fig. 1a, the CPW—fed trapezoidal antenna is designed on a FR4 substrate with dielectric constant $\epsilon_r = 4.4$ and the substrate thickness is 1.6 mm. This antenna structure is symmetrical along the y-axis. The simulation of this antenna has been done and the geometrical structure will be adjusted by experimental test.

Figure 1b shows the addition of triangular structures at the bottom of the trapezoidal patch. The dimensions of the triangular patches are $L4 = 6.8$ mm, $L5 = 8.6$ mm and all others dimension is same with Fig. 1a. There is a 0.5 mm gap between the additional structures and the main radiating trapezoidal patch. The gap between the trapezoidal patch to the ground plane is also fixed at 0.5 mm.

Figure 1c shows the geometry of the antenna with the addition of radiating elements. The triangular patches have been notched to be the smaller triangular and trapezium patches. Only three dimensions had changed from the basic structure which are $L4 = 3$ mm, $L6 = 1.5$ mm and $L7 = 4$ mm. There is a 0.5 mm gap between all the radiating elements. The effects of adding the new structure to the return loss of the antenna will be evaluated and discussed in the next section.

From the design of antenna in Fig. 1c, the adjustment has been made by adding connectors between all elements in radiating structure. Figure 2 shows the labels and location of the connectors in the antenna. The total length and width of the connector structure are 0.5 and 0.5 mm respectively. The width and the placement of the connectors on the antenna will be adjusted experimentally to investigate the effects of current path to the antenna's performance. The experiment has been done based on Table 2.

Fig. 2 Antenna geometry added with connector between all patches

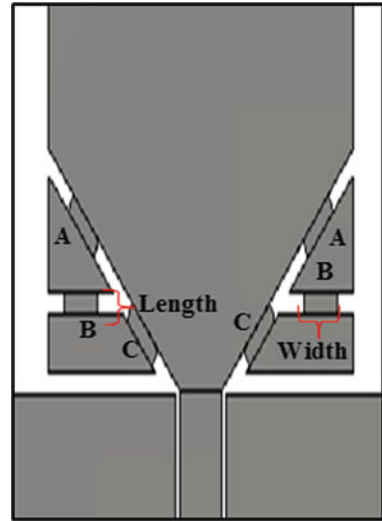


Table 2 The variation of the proposed antenna

| Width of connector (mm) | Connector | | |
|-------------------------|-----------|---------|---------|
| | A | B | C |
| 0.5 | Present | Present | Present |
| | Present | Present | Absent |
| | Present | Absent | Present |
| | Absent | Present | Present |
| 1.0 | Present | Present | Present |
| | Present | Present | Absent |
| | Present | Absent | Present |
| | Absent | Present | Present |
| 2.0 | Present | Present | Present |
| | Present | Present | Absent |
| | Present | Absent | Present |
| | Absent | Present | Present |

3 Simulation and Results

Three proposed figures of CPW-fed antenna have been simulated and the results showed on Fig. 3. Results in term of return loss have been obtained for Fig. 1a–c designed structures. Simulation results from Fig. 3 were simplified in Table 3.

Figure 1a covered the widest bandwidth compared with other two figures. Wide of bandwidth observed from the frequency range which return loss is lower than -10 dB Maximum return loss for Fig. 1b is the highest among all those three figures and it shown that Fig. 1b structures had a best impedance matching. Figure 1c had more resonant frequencies than others referred to the curve of simulation results in Fig. 3. All figures had their own maximum return loss and the values are -17 , -33 , -21 dB which observed at 3.6, 6.4 and 6.8 GHz respectively.

The structure shown in Fig. 2 has been simulated with variations in the dimensions of the connector based on Table 2. All the results of return loss shown in Fig. 4.

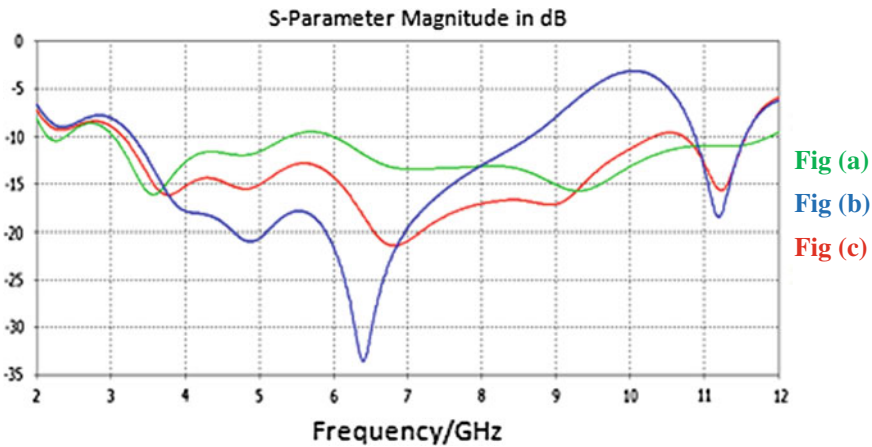


Fig. 3 Simulated return loss with different structures

Table 3 Results obtained from Fig. 3

| Figure 1 | (Frequency range) < -10 dB | Maximum return loss (dB) | Resonant frequencies (GHz) |
|----------|------------------------------|--------------------------|----------------------------|
| (a) | 2.2–11.8 GHz | -17 | 2.4, 3.6, 4.9, 9.4 |
| (b) | 3.4–11.5 GHz | -33 | 4.0, 4.9, 6.4, 11.2 |
| (c) | 3.2–11.5 GHz | -21 | 3.8, 4.8, 6.8, 9.0, 11.2 |

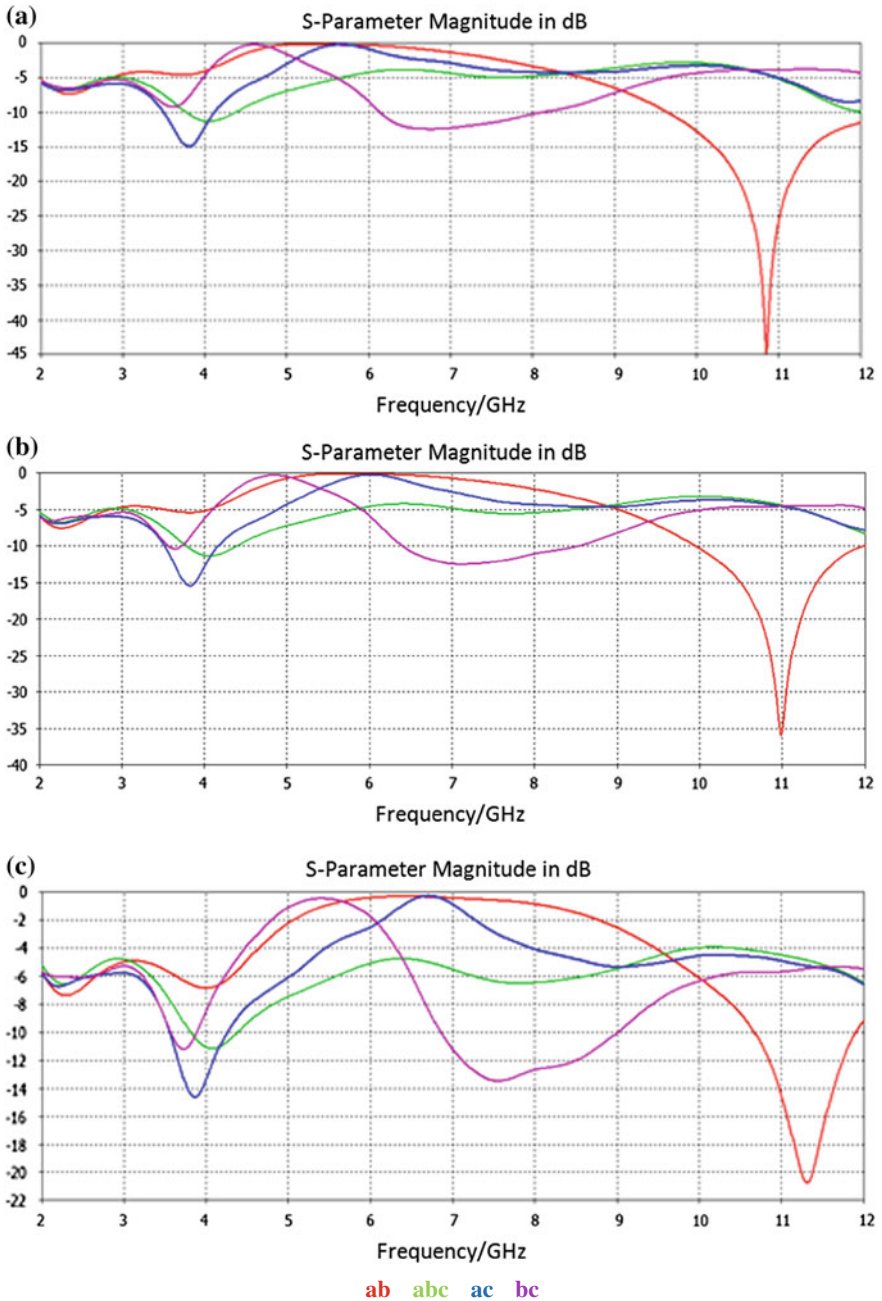


Fig. 4 Return loss against frequency of proposed antenna from simulation with different width a 0.5 mm, b 1 mm, c 2 mm and 4 different position of connector

Table 4 Results obtained from Fig. 4

| Connector | (Frequency range) < -10 dB (GHz) | Maximum Return loss (dB) | Resonant frequencies (GHz) |
|------------------------|----------------------------------|--------------------------|----------------------------|
| Connector width 0.5 mm | | | |
| ab | 9.6–12 | -45 | 10.8 |
| abc | 3.8–4.4 | -12 | 4.0 |
| ac | 3.5–4.2 | -15 | 3.8 |
| bc | 6.2–8.0 | -13 | 6.5 |
| Connector width 1 mm | | | |
| ab | 10–12 | -36 | 11 |
| abc | 3.6–4.4 | -12 | 4.2 |
| ac | 3.5–4.2 | -15 | 3.8 |
| bc | 6.4–8.5 | -13 | 7.0 |
| Connector width 2 mm | | | |
| ab | 10.6–11.8 | -21 | 11.3 |
| abc | 3.8–4.4 | -11 | 4.2 |
| ac | 3.5–4.3 | -14.5 | 3.8 |
| bc | 3.5–9.0 | -13.8 | 3.6, 7.5 |

Simulation results from Fig. 4 were simplified in Table 4 to make comparison between all those structure with different connector width and position. Table 4 summarizes the results obtained from Fig. 4.

From Table 4, the highest lowest return loss in every connector width obtained at the present of ab connector. Compared between all widths, 0.5 mm gets the best impedance matching observed at frequency 10.8 GHz. The bandwidth all structures become narrow and only one resonant frequency obtained from simulation except the present of connector bc with 2 mm width.

4 Directivity and Gain

Directivity and gain of antenna from Fig. 2 with connector width 0.5 mm were obtained because they had the most suitable structure to represents the reconfigurable antenna by using PIN diode for UWB communication system (Fig. 5).

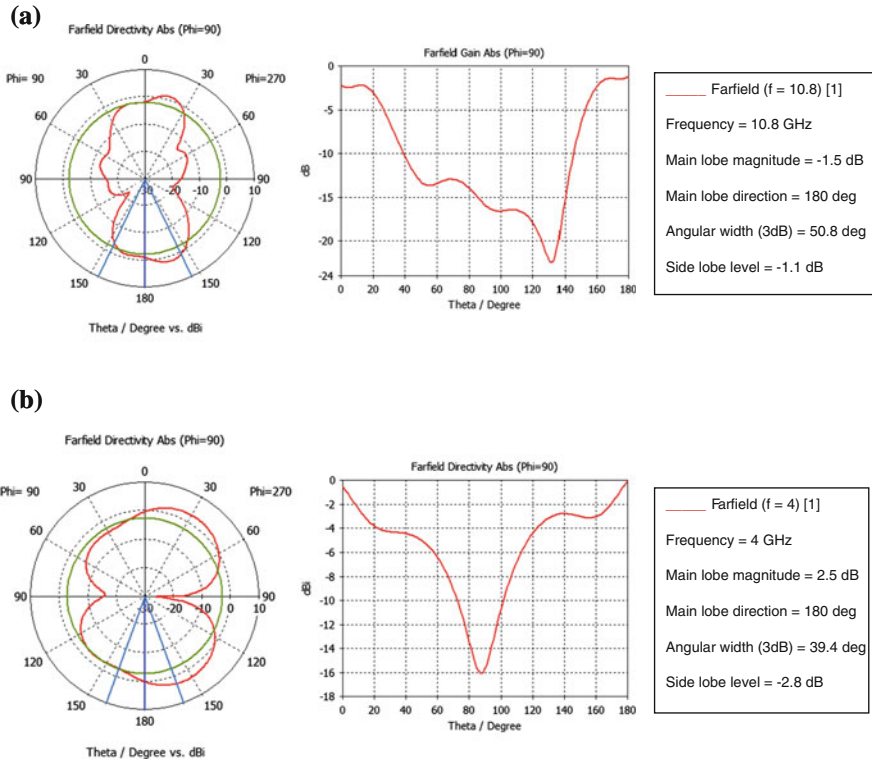


Fig. 5 Farfield directivity and gain of antenna with present of **a** *ab* connectors at frequency 10.8 GHz, **b** *abc* connectors at frequency 4 GHz, **c** *ac* connectors at frequency 3.8 GHz and **d** *bc* connectors at frequency 6.5 GHz

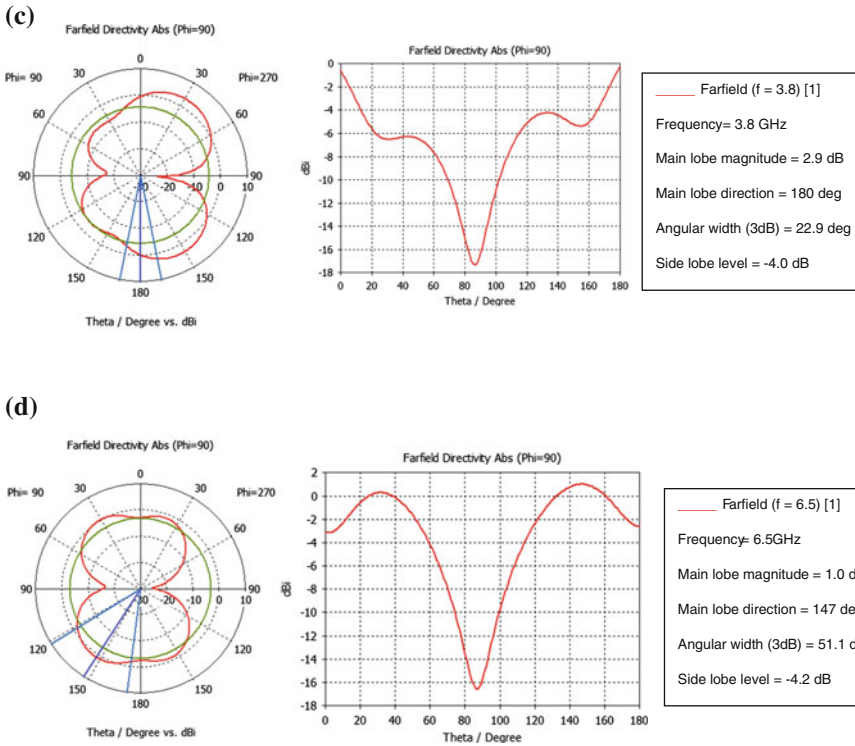


Fig. 5 (continued)

5 Conclusion

This paper presents the effects of geometrical alteration to the bandwidth and impedance matching of antenna. The geometry of trapezoidal radiator was varied in order to yield maximum bandwidth and return loss. Optimization structure at the bottom area of radiator will strongly affects the impedance bandwidth. This condition related with current distribution from feeding line to radiating element. The Ultra Wide Bandwidth (UWB) operation will achieved when there are a number of resonant parts due to different radiating elements on antenna.

Acknowledgments The authors have special thanks to Institute of Postgraduate Studies and Faculty of Electrical and Electronics Engineering for their supports.

References

1. Oppermann, I.: UWB: Theory and Applications. Wiley, New York (2004)
2. Balakrishna, I., Malmathanraj, R., Raghavan, S.: Compact CPW-fed antenna for wideband application. In: IEEE Students' Technology Symposium (TechSym) (2011)
3. Balakrishna, I., Suresh Kumar, M., Sriram Kumar, D.: CPW-fed antenna for 2.4 GHz WLAN application. In: IEEE International 2010 Conference on Communication Control and Computing Technologies (ICCCCT), 2010
4. Gunavathi, N., Pandeewari, R., Raghavan, S.: A CPW-fed octagon-shaped aperture antenna for lower band UWB applications. In: India Conference (INDICON), 2009 Annual IEEE, 2009
5. Boroomandisorkhabi, B., et al.: A novel UWB circular CPW antenna with triple notch band characteristics. In: Antennas and Propagation Conference (LAPC), Loughborough 2013
6. Gunavathi, N., Pandeewari, R., Raghavan, S.: A CPW-fed flower shaped band-notched monopole aperture antenna for UWB applications. In: Computing Communication and Networking Technologies (ICCCNT), International Conference (I2010)
7. Augustin, G., Denidni, T.A.: Coplanar waveguide-fed uniplanar trapezoidal antenna with linear and circular polarization. *IEEE Trans. Antennas Propag.* **60**(5), 2522–2526 (2012)

Investigation of Inverted Suspended Rectangular Patch Circular Polarized Antenna

K.S. Phoo, M.Z.A. Abd. Aziz, B.H. Ahmad, M.A. Othman,
M.K. Suaidi and F. Abd. Malek

Abstract In this paper, broadband circular polarized antenna with different slot configuration are designed and investigated. The proposed antennas are designed at 2.4 GHz for Wireless Local Area Network (WLAN) application. The antennas are designed by using L-probe amendment with inverted rectangular patch. This technique is used to improve the bandwidth and gain of antenna. The effects on the antenna performance are investigated for the configuration of rectangular and triangular slot that embedded on the inverted rectangular patch. The inverted rectangular patch is embedded with two circular slots which are parallel with each other. The position of the circular slots is altered to determine the orientation of circular polarization. The simulation is done by using Computer Simulation Technology (CST) software. Each inverted suspended circular polarized antenna is achieved bandwidth more than 200 MHz and meet broadband application. The axial ratio for each circular polarized antenna is below 3 dB.

1 Introduction

Nowadays, circular polarized (CP) antenna is widely used in modern wireless communication system, especially in satellite, radar, navigation system and others. CP antenna transmit and receive signals in all planes, meanwhile the linear

K.S. Phoo · M.Z.A. Abd. Aziz (✉) · B.H. Ahmad · M.A. Othman · M.K. Suaidi
CeTRI, Faculty of Electronics and Computer Engineering, Universiti Teknikal Malaysia
Melaka (UTeM), Durian Tunggal, Melaka, Malaysia
e-mail: mohamadzoinol@utem.edu.my

K.S. Phoo
e-mail: khoshin_89@hotmail.com

F. Abd. Malek
School of Computer and Communication Engineering, Universiti Malaysia Perlis, Arau,
Perlis, Malaysia
e-mail: mfareq@unimap.edu.my

polarized antenna only transmit and receive signals in one plane [1]. Hence, CP antenna can provide better performance, reduce signal degradation and combat multipath effect when compare with linear polarized antenna [2–8].

The electric field at a point for CP is traces a circle as a function of time and it can only be achieved when the magnitude of both components are similar [1]. CP is classified into Right-Handed Circular Polarization (RHCP) when the electric field is rotated in clockwise and Left-Handed Circular Polarization (LHCP) when the electric field is rotated in counter-clockwise. There are few techniques can be used to design CP antenna, which included perturbation [3, 6], slot [3, 6, 8], nearly square patch [1, 6], altered the position or number of feed [1, 7] and so on.

2 Antenna Design

The configurations for inverted suspended rectangular patch with rectangular and triangular slot for RHCP and LHCP are illustrated in Fig. 1. The proposed antennas are designed by using FR4 board with thickness of substrate, $h = 1.6$ mm. The dielectric constant of the FR4 substrate, $\epsilon_r = 4.4$ and tangent loss, $\tan \delta = 0.019$. The thickness of copper, t is 0.035 mm.

Each proposed antenna is connected with coaxial probe feed to the strip line in order to present as L-probe feed. In this paper, the CP antennas are designed with combination of copper ground plane and inverted suspended rectangular patch which separated with 10 mm air gap. The dimension of copper ground plane for each proposed antenna is similar with the size of FR4 substrate. The length and width of each inverted rectangular patch for the proposed circular polarized antenna are designed with similar dimension and represented as L and W respectively. At the same time, the strip line which printed at the opposite side of the inverted rectangular patch for each proposed circular polarized antenna also designed with similar dimension, where the length and width of the strip line are represented as L_f and W_f respectively. The dimensions for the proposed antennas are tabulated in Table 1.

3 Result and Discussion

This session is investigated and presented the comparison simulation result of resonant frequency (f_r), return loss (RL), bandwidth (BW), gain, directivity, total efficiency, axial ratio, and radiation pattern for each proposed antenna. The effects on the CP antenna performance are analyzed with the variation of different configurations of slot which embedded on the inverted suspended rectangular patch.

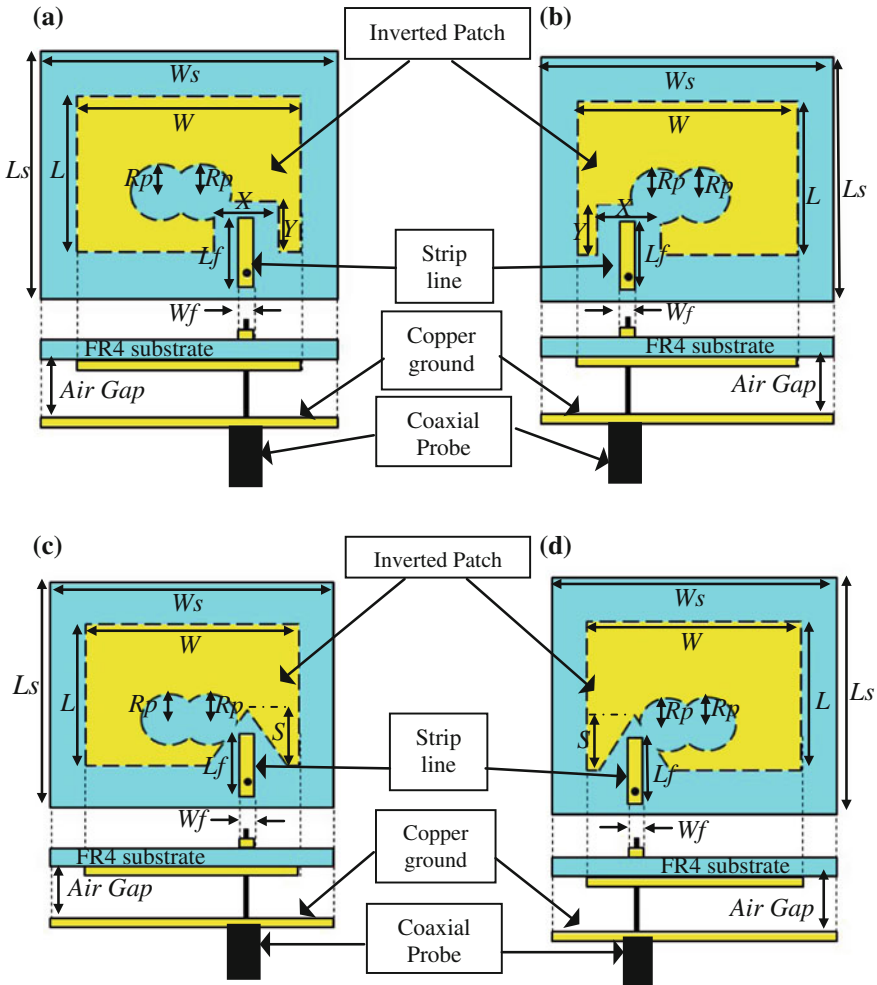


Fig. 1 Geometry of broadband inverted suspended rectangular patch circular polarized antenna. **a** Rectangular slot for LHCP. **b** Rectangular slot for RHCP. **c** Triangular slot for LHCP. **d** Triangular slot for RHCP

3.1 Resonant Frequency (F_r), Bandwidth (BW) and Return Loss (RL)

The simulated S-parameter result for each broadband circular polarized with different configuration of slot are compared and presented in Fig. 2. Based on the simulation result, proposed antenna with rectangular slot configuration for RHCP and LHCP achieved similar S-parameter result. At the same time, this phenomenon is happened on the RHCP and LHCP antenna with triangular slot. Each proposed

Table 1 Dimensions for broadband inverted suspended rectangular patch circular polarized antenna

| Description | Design parameter | Dimension (mm) |
|----------------------------|------------------|----------------|
| Width of substrate | W_s | 90 |
| Length of substrate | L_s | 80 |
| Width of patch | W | 60 |
| Length of patch | L | 42 |
| Width of strip line | W_f | 3 |
| Length of strip line | L_f | 15 |
| Radius of circular slot | R_p | 6.5 |
| Width of rectangular slot | X | 15 |
| Length of rectangular slot | Y | 11 |
| Height of triangular slot | S | 13 |
| Air gap | gap | 10 |

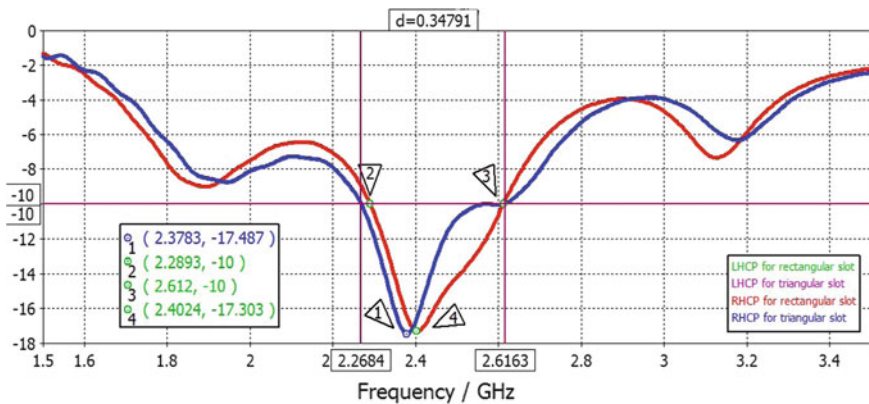


Fig. 2 Comparison of simulation S-parameter result for broadband CP antenna with different shape of slots

antennas are covered frequency at 2.4 GHz. CP antenna with rectangular slot achieved resonant frequency at 2.4024 GHz with return loss -17.3 dB. The CP antenna with rectangular slot covered frequency from 2.2893 GHz until 2.612 GHz and this means that the bandwidth for the CP antenna with rectangular slot configuration is 322.7 MHz.

Then, CP antenna with triangular slot achieved resonant frequency at 2.3783 GHz with return loss -17.49 dB. CP antenna with triangular slot covered frequency from 2.2684 GHz until 2.6163 GHz. Hence, the bandwidth for CP antennas with triangular slot achieved 347.91 MHz which are better than the CP antennas with rectangular slot. Generally, CP antennas which designed with the rectangular and triangular slot are achieved bandwidth more than 200 MHz and meet broadband specification.

3.2 Gain, Directivity and Total Efficiency

The proposed antennas are designed by using inverted suspended rectangular patch with separation of air gap. This technique is applied to improve the gain and bandwidth of the antenna. The gain of the antenna will be improved as the separation of air gap increase. Optimum results are obtained as the air gap is stacked to 10 mm. The comparison of simulated gain for CP antenna with rectangular and triangular slot is shown in Fig. 3a. The gain for CP antenna with rectangular slot achieved 7.87 dB and this is slightly better than the CP antenna with triangular slot which achieved gain at 7.70 dB. Overall, the gain for each antenna achieved above 6 dB from frequency 2 GHz until 2.7 GHz.

Based on the simulation result as shown in Fig. 3b, the directivity for the LHCP and RHCP antenna with rectangular slot achieved 8.28 dBi and both are slightly better than the LHCP and RHCP antenna with triangular slot which achieved 8.14 dBi. The directivity for the proposed antennas is above 6 dBi from frequency 2 GHz until 3 GHz. As illustrated in Fig. 3c, the simulated total efficiency for the CP antennas with rectangular slot achieved -0.4 dB which is almost similar with the CP antenna with triangular slot that achieved -0.44 dB.

3.3 Axial Ratio

The performance of the CP antenna can be determined and analyzed from the axial ratio of the antenna. When the axial ratio of the antenna is below 3 dB, the antenna will be known as CP. However, the antenna will be known as linear polarized when the axial ratio of the antenna is above 3 dB. The comparison of axial ratio for broadband CP antenna with different shape of slot is shown in Fig. 4.

The axial ratio for the CP antenna with rectangular slot obtained 0.23 dB, meanwhile the CP antenna with triangular slot obtained 0.85 dB. This also means that CP antenna with rectangular slot is better than the axial ratio of CP antenna with triangular slot. The 3 dB axial ratio bandwidth of the CP antenna with rectangular slot achieved 659.8 MHz, which is from 2.0199 GHz until 2.6797 GHz. However, the 3 dB axial ratio bandwidth for the CP antenna with triangular slot is wider than the 3 dB axial ratio bandwidth for the CP antenna with rectangular slot.

3.4 Radiation Pattern

Comparison of radiation pattern for LHCP and RHCP antenna with rectangular slot and triangular slot when $\Phi = 0^\circ$ and $\Phi = 90^\circ$ are illustrated in Figs. 5 and 6 respectively. Based on the Fig. 5, the radiation pattern for LHCP antenna with rectangular slot and triangular slot are similar when $\Phi = 0^\circ$. However, the orientation of main lobe for RHCP antenna with rectangular slot and triangular slot are

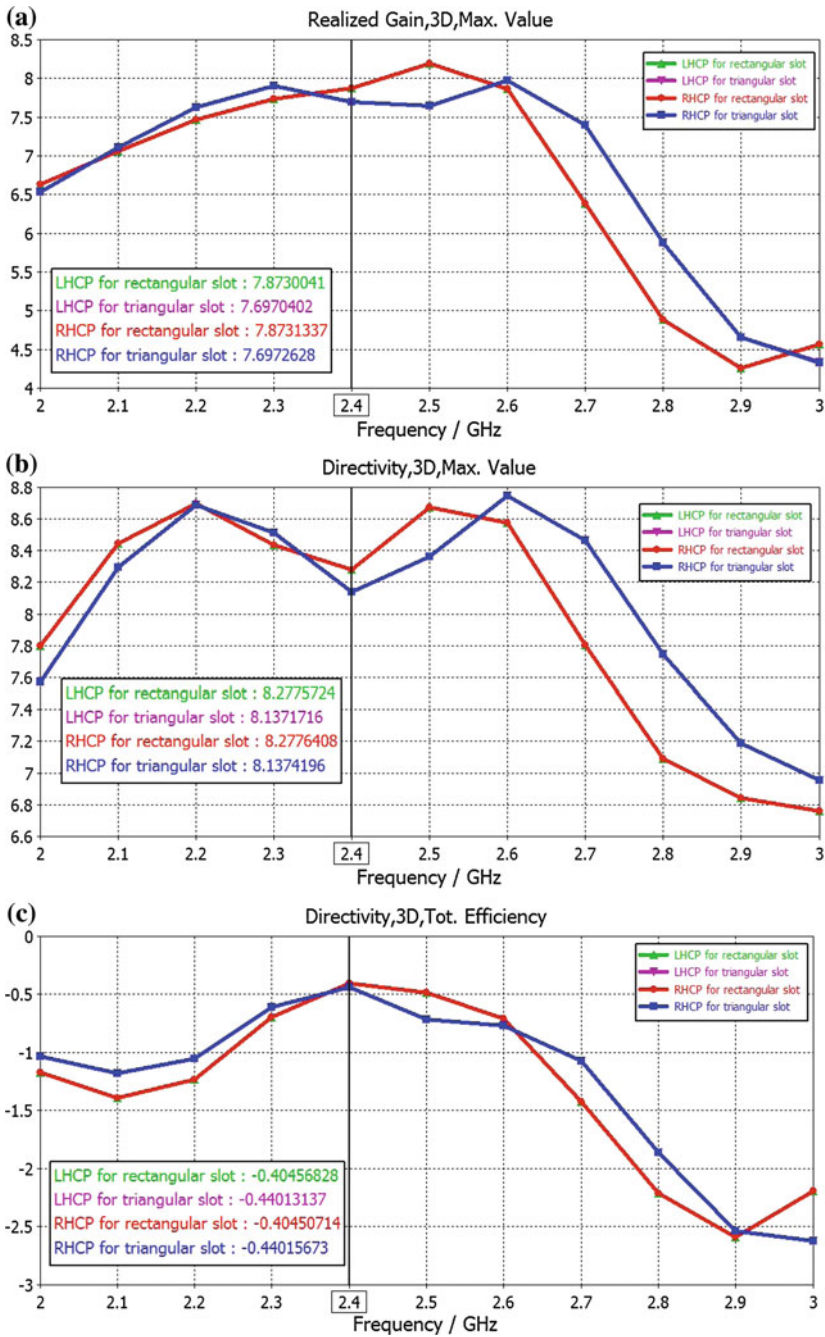


Fig. 3 Comparison of simulation result for broadband CP antenna with different shape of slots. **a** Gain. **b** Directivity. **c** Total efficiency

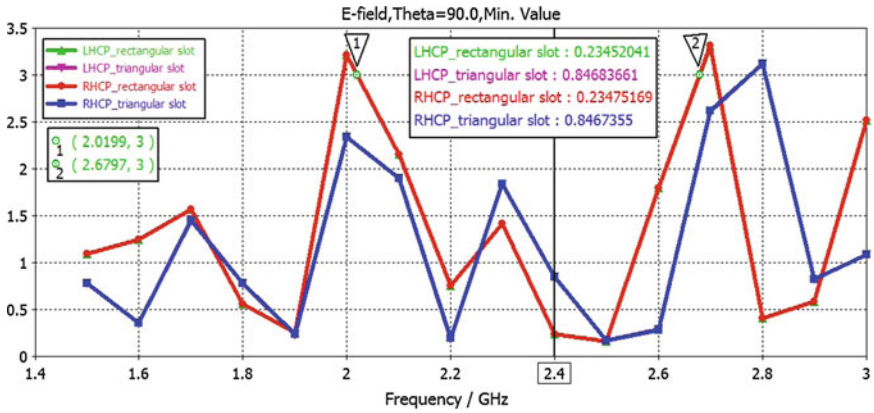


Fig. 4 Comparison of axial ratio for broadband CP antenna with different shape of slots

Fig. 5 Comparison of radiation pattern for broadband CP antenna with different shape of slots when $\Phi = 0^\circ$

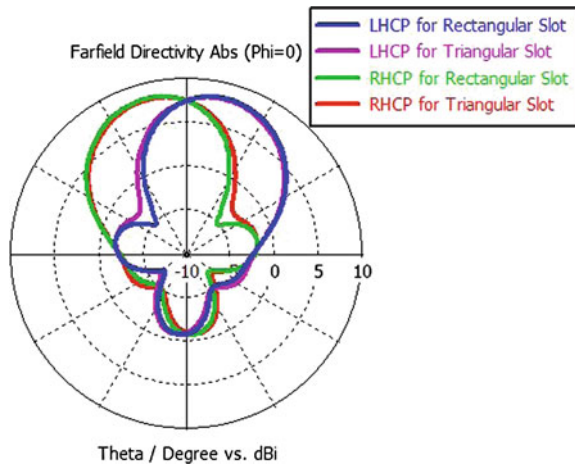
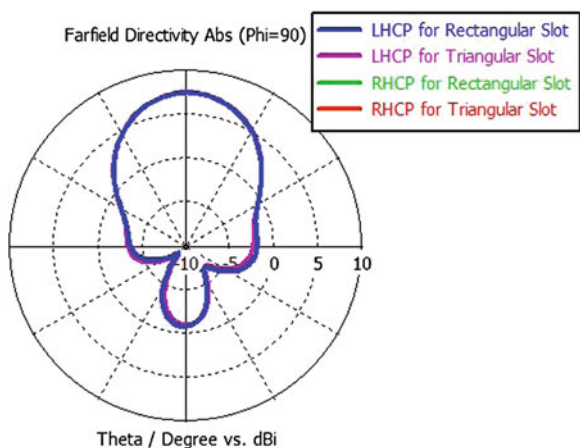


Fig. 6 Comparison of radiation pattern for broadband CP antenna with different shape of slots when $\Phi = 90^\circ$



different with the LHCP antenna. The main lobe direction for both RHCP antennas with rectangular slot and triangular slot are at 15° . Then, the main lobe direction for LHCP antennas with rectangular slot and triangular slot are at 0° .

4 Conclusion

In this paper, broadband inverted suspended circular polarized antenna with rectangular slot and triangular slot are designed and investigated. The proposed antennas are designed by using inverted suspended rectangular patch with separation of 10 mm air gap. This technique is verified to enhance the gain and bandwidth of the microstrip patch antenna. Based on the simulation result, each antenna is achieved frequency at 2.4 GHz for WLAN application. The bandwidth for CP antenna with rectangular slot is 322.7 MHz and the bandwidth for CP antenna with triangular slot is 347.91 MHz. This also indicated that, the bandwidth of the CP with rectangular slot and triangular slot are more than 200 MHz and meet broadband application. Besides, the gain, directivity and total efficiency are almost similar for each proposed antenna. The simulated axial ratio for CP with rectangular slot and triangular slot are slightly different. The axial ratio for each configuration of CP antennas is below 3 dB and this is also means that the proposed antennas are performed as circular polarization. However, the 3 dB axial ratio bandwidth of CP antenna with triangular slot is wider than the CP antenna with rectangular slot.

Acknowledgments The authors would like to thank Universiti Teknikal Malaysia Melaka (UTeM) for supporting in obtained the information and material in the development for our work. We also want to thank anonymous referees whose comments led to an improved presentation of our work. Lastly, we also thank the Ministry of Education Malaysia (MOE) for PJP/2013/FKEKK (1C) /S01129 research grant.

References

1. Balanis, C.A.: *Antenna Theory Analysis and Design*, 3rd Edn. Wiley, New Jersey (2005)
2. Cai, Y.M., Li, K., Yin, Y.Z., Hu, W.: Broadband circularly polarized printed antenna with branched microstrip feed. *IEEE Antennas Wirel. Propag. Lett.* **13**, 674–677 (2014)
3. Mousavi, P., Miners, B., Basir, O.: Wideband L-shaped circular polarized monopole slot antenna. *IEEE Antennas Wirel. Propag. Lett.* **9**, 822–825 (2010)
4. Guo, Y.X., Bian, L., Shi, X.Q.: Broadband circularly polarized annular-ring microstrip antenna. *IEEE Trans. Antennas Propag.* **57**(8), 2474–2477 (2009)
5. Wong, K.L.: *Compact and Broadband Microstrip Antennas*, vol. 168. Wiley, New York (2004)
6. Wu, J.J., Ren, X.S., Li, Z.X., Yin, Y.Z.: Modified square slot antennas for broadband circular polarization. *Prog. Electromagnet. Res. C* **38**, 1–14 (2013)
7. Zhang, X.Y., Lin, S., Wang, Y.D., Liu, S.Y., Zhang, X.Y.: Broadband circularly polarized antenna with a T-type fractal boundary wide-slot and a L-shape strip. In: *Microwave Conference Proceedings (CJMW)*, China-Japan Joint, pp. 1–3 (2011)
8. Yang, S.L.S., Lee, K.F., Kishk, A.A., Luk, K.M.: Design and study of wideband single feed circularly polarized microstrip antennas. *Prog. Electromagnet. Res.* **80**, 45–61 (2008)

Dual-Band Copper Rod Monopole Antenna for Wireless Communication System

**Abdul Halim Dahalan, Mohamad Hafize Ramli,
Mohamad Zoinol Abidin Abd. Aziz, Mohd Azlishah Othman,
Badrul Hisham Ahmad and Mohd Kadim Suaidi**

Abstract In this paper, a dual-band copper rod monopole antenna for a wireless communication system is initiated. The antenna has been designed based on meander line technique using the monopole rod elements and rectangular ground structure. Each element of meander lines was designed with a half wavelength to radiate at a frequency of 2.4 and 5.8 GHz for Wireless Local Area Network (WLAN) application. The proposed antenna was designed and simulated by using Computer Simulation Technology (CST) software. The bandwidth of reflection coefficient of less than -10 dB could be observed at (f_1-f_2) 331 MHz and (f_1-f_2) 358 MHz for Design A. Then, the additional cone and inverse-cone shape reflector shifted the frequency to the left from the 2.4 GHz band and to the right at 5.8 GHz band. The desired frequency could be obtained by adjusting the size of the copper reflector.

A.H. Dahalan

Faculty of Engineering Technology, Universiti Teknikal Malaysia Melaka (UTeM),
Hang Tuah Jaya, 76100, Durian Tunggal, Melaka, Malaysia
e-mail: abdulhalim@utem.edu.my

M.H. Ramli · M.Z.A.A. Aziz (✉) · M.A. Othman · B.H. Ahmad · M.K. Suaidi
Faculty of Electronics and Computer Engineering, Center for Telecommunication Research
and Innovation (CeTRI), Universiti Teknikal Malaysia Melaka (UTeM), Hang Tuah Jaya,
76100, Durian Tunggal, Melaka, Malaysia
e-mail: mohamadzoinol@utem.edu.my

M.H. Ramli
e-mail: hafize_ramli@rocketmail.com

M.A. Othman
e-mail: azlishah@utem.edu.my

1 Introduction

In the revolution of the development of wireless communication system, researchers had discovered wideband and multi-band frequency of a single antenna structure that has been proposed in order to meet the needs of multiple applications [1, 2]. For the WLAN applications, it can be operated at two frequency ranges, which are 2.4 GHz for low band frequencies to 5.8 GHz for high band frequencies. The antenna with WLAN must work in these frequencies, which can transmit and receive the signal simultaneously in these two bands. There are several methods used to design such antennas such as Minkowski patch antenna [3], bow tie antenna [4], fork-shaped monopole [5, 6] and many more. The meander branch style technique, which is widely used in the lower frequency, is able to reduce the original antenna physical size up to 40 % [7, 8].

In this paper, a dual-band copper rod monopole antenna for wireless communication system, which is a WLAN system, has been proposed. The dual-band characterizations were achieved by using two meander branch lines. These two branches have been designed in order for each line to be able to control its desired frequency. The antenna design is described in Sect. 2, followed by the performance results that have been simulated and investigated for the proposed antenna in Sect. 3.

2 Antenna Design

The proposed antenna was designed by using a copper rod with a diameter of 0.65 mm. Three antenna structures were proposed in this paper. The first antenna was the dual band monopole antenna (Design A). Then, a cone-shaped copper reflector was above the rectangular ground for about 2 mm (Design B). Lastly, an inverse cone-shaped copper reflector was added above the rectangular ground for about 2 mm (Design C). Figure 1 shows the geometry and the design structure of the proposed antenna. The antenna has been designed to mount on the rectangular ground of 10×10 ($Lg \times Sg$) mm. The ground structure was made of rectangular copper with a dimension of $W \times L \times T$. Then, 50 ohm SMA coaxial probe feed was used to feed the antenna through printed line, L_{B2} . Meanwhile, Fig. 2 shows the dimension of the additional cone and inverse cone-shaped copper reflector on the proposed antenna.

The rod elements were designed by using a meander line technique to reduce the size of the antenna. The dual-band frequencies were generated by two different radiators of the proposed antenna, which are L_{A1} and L_{B1} . Each radiator's length was referred from the edge of point X until the end of the respective radiator for $\lambda/2$ (half-wavelength). Further optimization process was carried out to obtain the resonant frequency at 2.4 and 5.8 GHz. The optimized parameter values for each element were given in millimetres (mm) as follows: First radiator: $L_{A1} = 8$, $L_{A2} = 5$,

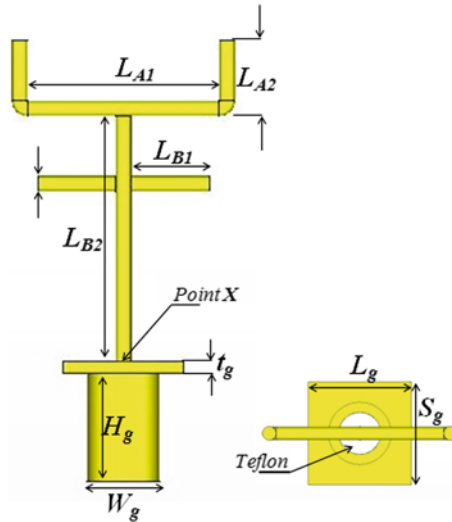


Fig. 1 The geometry and overview structure of the proposed antenna (Design A)

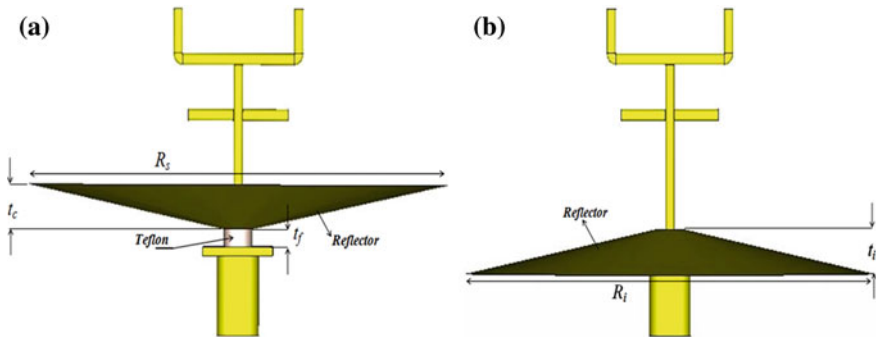


Fig. 2 The geometry and structure of the additional shaped copper reflector **a** cone (Design B), and **b** inverse cone (Design C)

second radiator: $L_{B1} = 6.5$, $L_{B2} = 20.5$, and ground structure: $L_g = 10$, $S_g = 10$, $H_g = 10$, $W_g = 6.1$, $t_g = 1$, cone-shaped copper reflector: $R_s = 30$ mm, $t_c = 5$ mm, $t_f = 2$ mm, inverse cone-shaped copper reflector: $R_i = 30$ mm, $t_i = 2$ mm.

3 Results and Discussion

This section presents the performance results of the proposed antenna with additional cone and inverse cone-shaped copper reflector. The performance results such as return loss, gain, directivity, surface current and radiation pattern on the desired

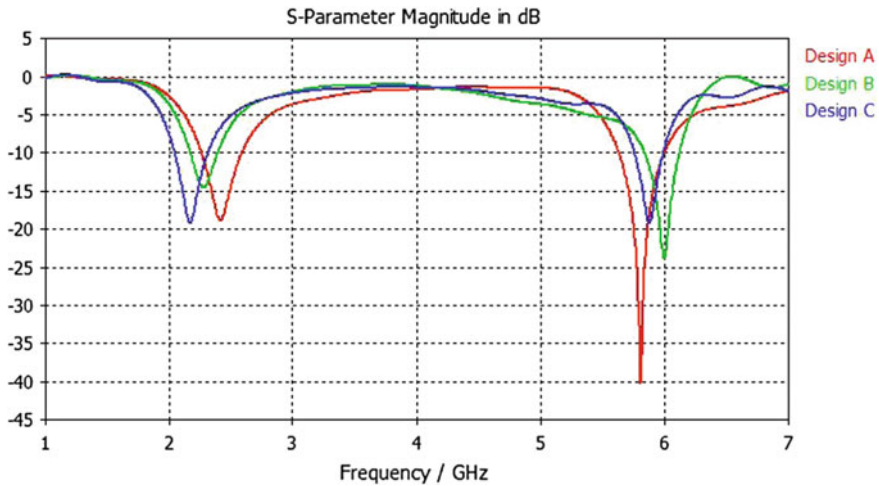


Fig. 3 Reflection coefficient versus frequency of Design A, B and C

frequency were analyzed. Figure 3 shows the return loss of the proposed antenna for two operating frequency bands. From the result, the reflection coefficient (S_{11}) for Design A at 2.4 GHz was -18.769 dB and the bandwidth was about 331 MHz (f_1-f_2). The second radiator could be found at the frequency of 5.8 GHz with a reflection coefficient (S_{11}) of -40.229 dB with simulated bandwidth about 358 MHz (f_1-f_2). Meanwhile, the performance result for the reflection coefficient (S_{11}) for Design B and C was shifted to the left from 2.4 to 2.284 GHz with a reflection coefficient of -14.518 dB and 2.17 GHz with a reflection coefficient of -19.113 dB. Then, the second radiator showed that the frequency was shifted to the right from 5.8 to 6.004 GHz with a reflection coefficient of -23.786 dB and 5.884 GHz with -19.196 dB for Design B and C respectively when the additional cone and inverse cone were added to the proposed antenna, Design A.

Table 1 shows the simulated gain and directivity of the proposed antenna at 2.4 and 5.8 GHz. When the cone-shaped copper reflector was added to the proposed antenna, the gain and directivity decreased. Meanwhile, when the inverse cone was added to the proposed antenna, the gain decreased. There was an increment of directivity that could be seen when the inverse cone was added. The maximum gain and directivity of 4.075 dB and 4.936 dBi were found on a 5.8 GHz frequency for Design C.

Table 1 The gain and directivity for Design A, B, and C at frequencies 2.4 and 5.8 GHz

| Frequency (GHz) | Gain (dB) | | | Directivity (dBi) | | |
|-----------------|-----------|-------|--------|-------------------|-------|-------|
| | A | B | C | A | B | C |
| 2.4 | 1.724 | 1.268 | 0.7424 | 1.997 | 1.815 | 1.618 |
| 5.8 | 3.299 | 2.314 | 4.075 | 3.518 | 2.697 | 4.936 |

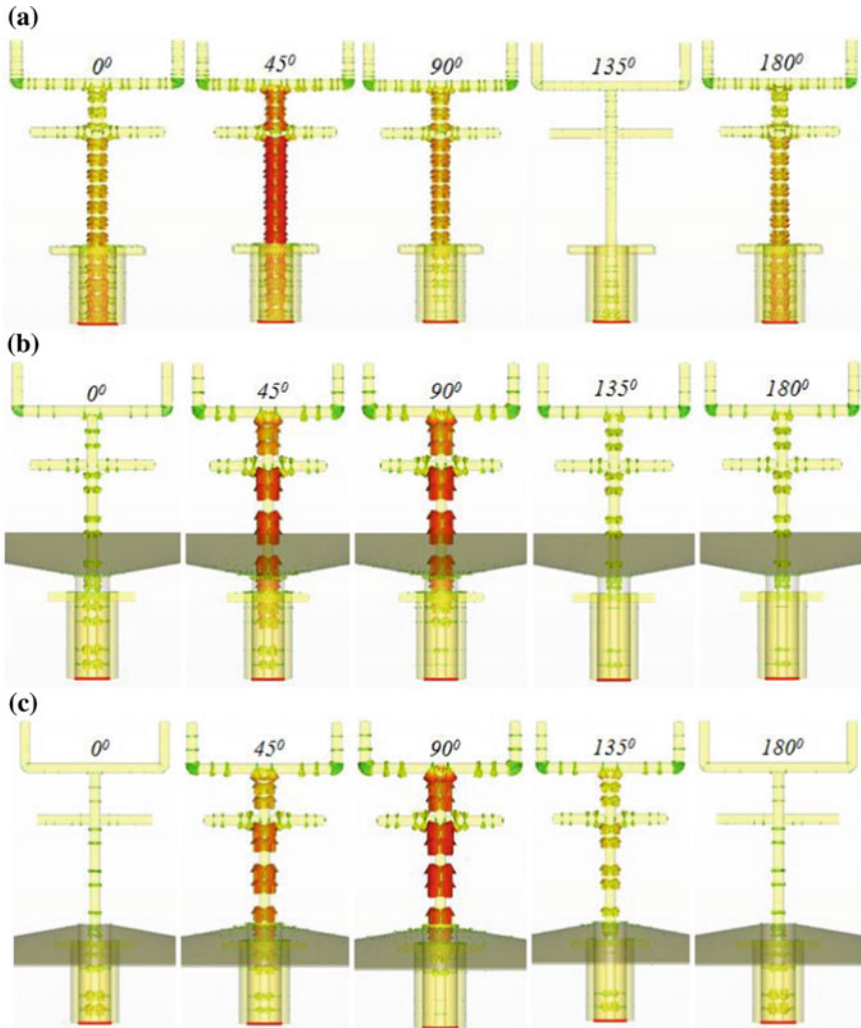


Fig. 4 Surface current distribution at 0° , 45° , 90° , 135° and 180° at 2.4 GHz. **a** Design A, **b** Design B, and **c** Design C

Figures 4 and 5 show the surface of current distribution at phase angles of 0° , 45° , 90° , 135° and 180° at frequencies of 2.4 and 5.8 GHz. The current was concentrated along the feed line for 2.4 GHz at phase angles of 45° and 90° for Design A, B and C. For the second frequency of 5.8 GHz, the surface current was concentrated between the first and second lines at phase angles of 90° and 135° for Design A and C and 45° and 90° for Design B of the proposed antenna to create the resonance frequency of 5.8 GHz.

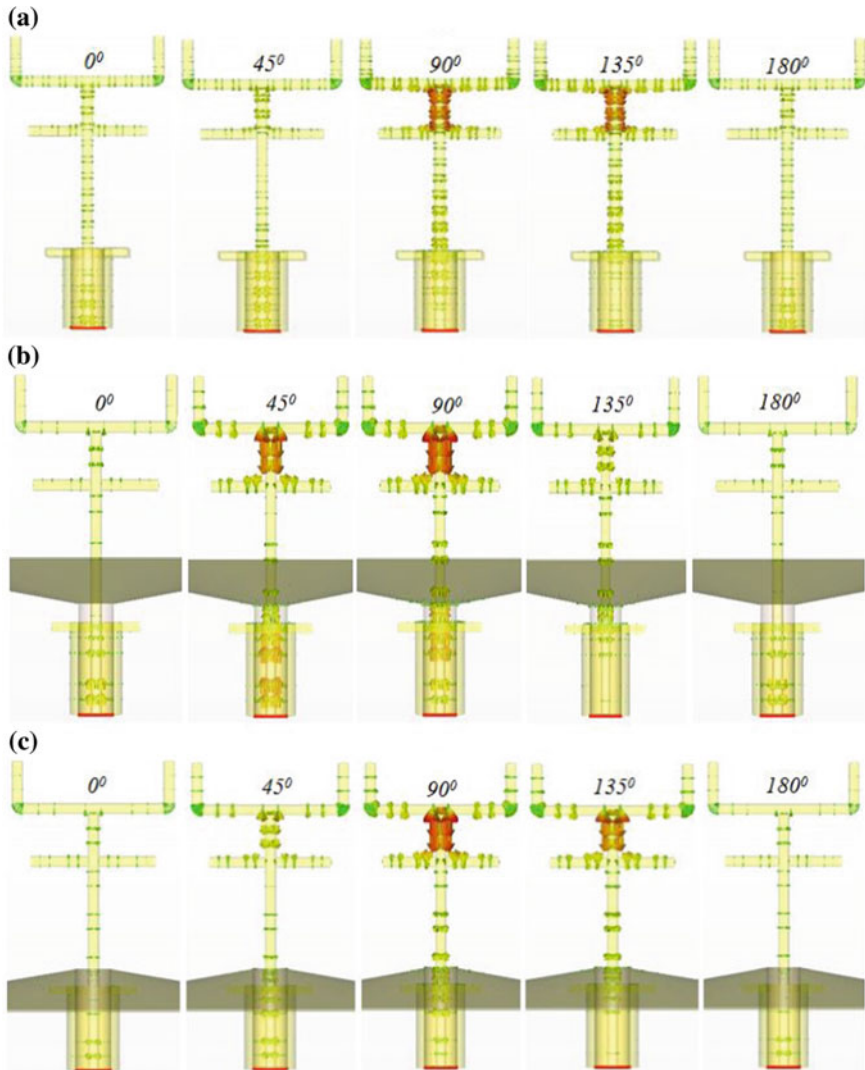


Fig. 5 Surface current distribution at 0°, 45°, 90°, 135° and 180° at 5.8 GHz. **a** Design A, **b** Design B, and **c** Design C

Figure 6 shows the radiation pattern of the proposed antenna at 2.4 and 5.8 GHz. The radiation patterns seem similar to number 8 at a frequency of 2.4 GHz for $\phi = 0^\circ$ and $\phi = 90^\circ$. Meanwhile, the radiation pattern for $\phi = 0^\circ$ and $\phi = 90^\circ$ at 5.8 GHz seems similar to a butterfly shape at an elevation angle of $+50^\circ$, -50° , $+140^\circ$ and -140° . The half power beam width (HPBW) for radiation pattern at 2.4 GHz is wider compared to the radiation pattern at 5.8 GHz. This is due to the directivity at 5.8 GHz, which shows more directivity than at 2.4 GHz.

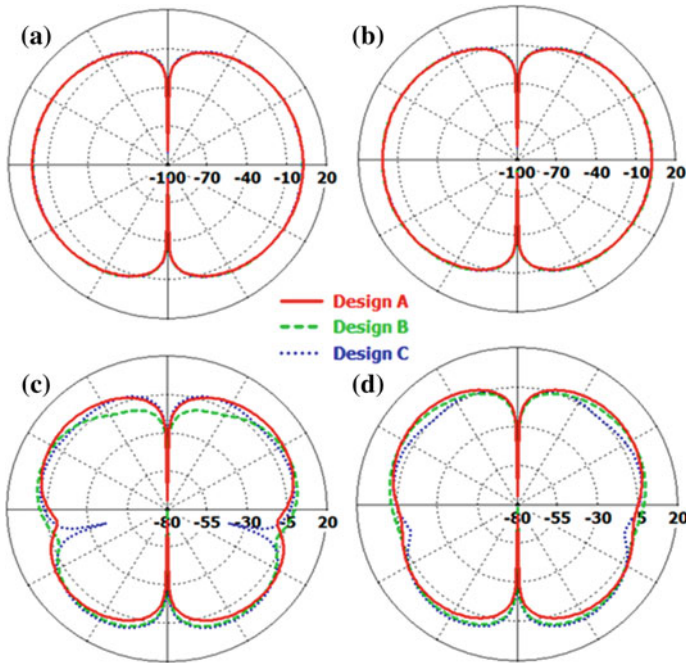


Fig. 6 Radiation pattern of the proposed antenna for $\phi = 0^\circ$ **a, c** and for $\phi = 90^\circ$ **b, d** at 2.4 and 5.8 GHz

4 Conclusion

In this paper, a multi-band monopole antenna was designed and analyzed to support the IEEE 802.11a and IEEE 802.11b (2.4–2.484 GHz and 5.725–5.825 GHz). The first radiator's line branch was designed to resonate at 2.4 GHz. Meanwhile, the second radiator's line was designed to operate at the frequency of 5.8 GHz. The desired return loss could be obtained by adjusting the size of the reflector. It shows that the additional cone and inverse cone decrease the gain and directivity at 2.4 GHz, but increase the gain and directivity at 5.8 GHz. The results of simulated return loss, bandwidth, gain, directivity, surface current and radiation pattern are shown by the antenna.

Acknowledgments The authors would like to thank Universiti Teknikal Malaysia Melaka (UTeM) for their support in obtaining the information and materials for the development of this paper, and we would also like to thank anonymous referees, whose comments led to an improved presentation of this paper. Lastly, we would like to thank the Ministry of Higher Education for the PJP/2013/FTK (7C) /S01244 research grant.

References

1. Yao, Y., Wang, X., Yu, Y.: Multiband planar monopole antenna for LTE MIMO systems. *Int. J. Antennas Propag.* (2012)
2. Yuan, Y., Junsheng, Y., Xiaodong, C.: Compact multi-band planar antenna design. In: *Proceeding of APMC 2012, Kaohsiung, Taiwan, 4–7 December* (2012)
3. Lee, E.C., Soh, P.J., Hashim, N.B.M., Vandenbosch, G.A.E., Volski, V., Adam, I., Mirza, H., Aziz, M.Z.A.A.: Design and fabrication of a flexible Minkowski fractal antenna for VHF applications. In: *Proceedings of the 5th European conference on antennas and propagation (EUCAP)*, pp. 521–524 (2011)
4. Taib, S.N., Othman, M.A., Makzhan, W.N.A., Arshad, T.S.M., Yaisn, N.Y.M., Ismail, M.M., Misran, M.H., Said, M.A., Sulaiman, H.A., Ramlee, R.A.: An analysis of low pass filter using bowtie Defected Ground Structure (DGS) at 10 GHz for radar application. In: *2013 3rd international conference on instrumentation, communications, information technology, and biomedical engineering (ICICI-BME)*, pp. 85–89 (2013)
5. Ojaroudi, M., Ojaroudi, N., Ghadimi, N.: Dual band-notched small monopole antenna with novel coupled inverted U-Ring strip and novel fork-shaped slit for UWB applications. *IEEE Antennas Wirel. Propag. Lett.* **12**, 182–185 (2013)
6. Xu, P., Yan, Z.H., Wang, C.: Multi-band modified fork-shaped monopole antenna with dual L-shaped parasitic plane. *Electron. Lett.* **47**(6), 364–365 (2011)
7. Wang, X., Chen, W., Feng, Z.: Multiband antenna with parasitic branches for laptop applications. *Electron. Lett.* **47**(6), 364–365 (2007)
8. George, G., Nagarajun, R., Tiripurasundari, D., Poonkuzhali, R., Alex, Z.C.: Design of meander line wearable antenna. In: *Proceeding of 2013 IEEE conferences on information and communication technologies (ICT)*, pp. 1190–1193 (2013)

Investigation of the Shape of SRR Slot and Hybrid Material on Wideband Monopole Antenna

T.K. Ong, B.H. Ahmad, M.Z.A. Abd. Aziz, M.A. Othman,
M.K. Suaidi and F. Abd. Malek

Abstract This paper investigates the characteristic of the shape of split ring resonator (SRR) slot and hybrid substrate on a monopole antenna at a wideband ranged from 4.61 to 10.23 GHz. All antenna designs involved in this investigation are simulated in Computer Simulation Technology (CST) Microwave Studio software in open space environment. The SRR-slotted designs are printed on FR4 epoxy board with dielectric constant of 4.4 and tangent loss of 0.019. Subsequently, the hybrid substrate is a multilayer constructed by FR4 substrate and glass substrate with dielectric constant of 6.9 and conductivity of 0.0005 S/m. Antenna parameters such as frequency, return loss, gain, directivity, and efficiency will also be studied and analyzed in this paper. The result shows that the adding of SRR slot contributes to a notch function creation whereas the adding of hybrid substrate will cause widen bandwidth of first frequency band, shorten bandwidth of second frequency band, and the shifting in notch-band.

1 Introduction

In the advancement of current wireless communication system, the increment in number of wireless applications has gain the attention of antenna designers. Some of these applications may also involve huge packets of data such as high definition videos and images as well as video conferencing where these may need a wider bandwidth to provide efficient transfer rate. In order to tackle the demand of

T.K. Ong · B.H. Ahmad · M.Z.A. Abd. Aziz (✉) · M.A. Othman · M.K. Suaidi
Univeriti Teknikal Malaysia Melaka (UTeM), Durian Tunggal, Melaka, Malaysia
e-mail: mohamadzoinol@utem.edu.my

F. Abd. Malek
School of Computer and Communication Engineering, Universiti Malaysia Perlis,
Arau, Perlis, Malaysia
e-mail: mfareq@unimap.edu.my

multi-functionality and high data transfer rate, the research have been done to improve the antenna functioning from a single band to multiband as well as to improve a narrow band to wideband and ultra-wideband (UWB) where each frequency representing for a single application [1–6]. This contribution has made the antenna to be compact in term of multi-function and also allowed high data transmission in shorter time. In order to design a wideband antenna, monopole antenna has been chosen because of its low weight, low cost, and simple structure.

However, there is another consideration come in when designing of antenna which operates in wideband or UWB system. Although the wideband and UWB provide wide platform for data transferring, they might be interfered with other allocated frequency bands such as Wireless Local Area Network (WLAN) (2.4–2.484 GHz), Worldwide Interoperability for Microwave Access (WiMAX) (3.3–3.6 GHz), WLAN (5.15–5.35 GHz), WLAN (5.725–5.825 GHz), as well as Earth Exploration Satellite Service (EESS) (8.025–8.4 GHz). A band-stop filter can be added into the wireless communication system, but this is not preferable as it will increase the system's complexity and increase the cost of production. Hence, altering the antenna structure is another option for designers to tackle the occurrence of these interferences. Slots, stubs, and slits are often found to be applied on antenna's patch, ground and also feed line to change the electromagnetic properties on an antenna [7]. Another way of doing this is to use one of the metamaterials, split ring resonator (SRR) onto an antenna [8–10]. Pendry et al. examined that split ring resonator can provide negative permeability over certain frequency region by varying the structure of metamaterial and this characteristic is very helpful on creating a band notch on the operating frequency band [11]. Thus, notch function can be created by applying SRR onto the antenna design. Besides that, previous antenna designs has also employed hybrid material substrate or multilayer substrate which consists of different material with different dielectric constant to provide frequency selectivity, enhance bandwidth, gain, and directivity, as well as to decrease fabrication complexity and the cost [12–15]. However, less research was done on the antenna design where both SRR slot and hybrid substrate applied on the same monopole design.

In this paper, an investigation is done on a monopole antenna by applying SRR slot with different shape of slot on the monopole and later compared with the SRR-slotted monopole placing on a hybrid substrate. By this way, we can show the characteristic of SRR structure and hybrid substrate to the monopole antenna. It is believed that a monopole antenna can be well-designed if the characteristic of both of these elements can be controlled properly.

2 Antenna Design

The basic design of this investigation is a coaxial-fed rectangular patch monopole antenna connected with a flattened ground plane as shown in Fig. 1. The ground plane in this design is used to obtain wider bandwidth. The optimum design parameters and dimension of the monopole antenna are listed in Table 1 by doing

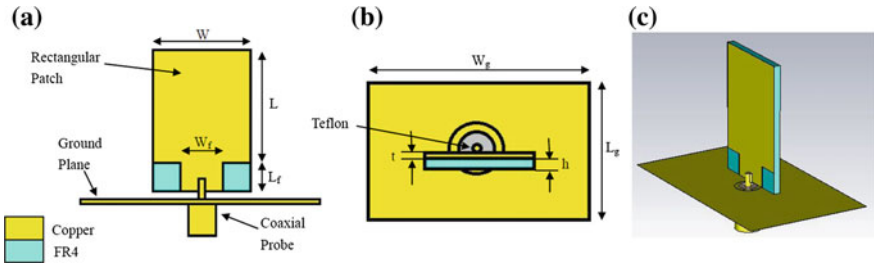


Fig. 1 Design structure and parameters of monopole antenna **a** front view **b** top view **c** 3D-view in CST microwave studio software

Table 1 Optimum design parameters and dimension of monopole antenna

| Description | Design parameters | Dimensions (mm) |
|--|-------------------|-----------------|
| Width of patch | W | 20 |
| Length of patch | L | 25 |
| Length of feed line | L_f | 5 |
| Width of feed line | W_f | 10 |
| Width of ground plane | W_g | 50 |
| Length of ground plane | L_g | 30 |
| Thickness of FR4 substrate | $h1$ | 1.6 |
| Thickness of copper layer | T | 0.035 |
| Distance from center patch to outer edge of inner ring | $r1$ | 3 |
| Distance from center patch to outer edge of outer ring | $r2$ | 5 |

parametric study on monopole antenna to obtain the widest bandwidth of the operating frequency band. The rectangular patch is printed on a FR4 substrate with dielectric constant, ϵ_{r1} of 4.4, tangent loss of 0.019, and thickness, $h1$ of 1.6 mm. All designs and parametric studies in this paper is simulated using CST Microwave Studio software in an open space environment.

The first investigation is done by applying various shape of SRR slot onto the center of the patch of monopole antenna while other design parameters' dimension and antenna structure remain the same. They are circular, triangular (point up), triangular (point down), square, and pentagonal SRR slots. The structure of SRR-slotted monopole antenna designs can be referred to Fig. 2. Next, the hybrid substrate will be applied on each SRR-slotted monopole antenna designs while other design parameters' dimension and antenna structure still remain the same. The hybrid substrate used in this stage is a multilayer substrate constructed by a FR4 substrate and glass with dielectric constant, ϵ_{r2} of 6.9, conductivity of 0.0005 S/m, and thickness, $h2$ of 1.6 mm. The structure of the hybrid substrate can be viewed in Fig. 2 as well.

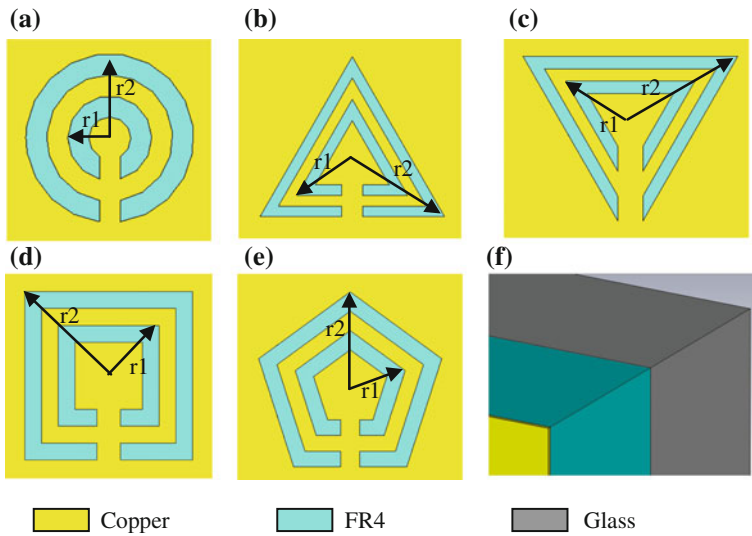


Fig. 2 Configurations of slot and hybrid substrate **a** circular slot **b** triangular slot (point up) **c** triangular slot (point down) **d** square slot **e** pentagonal slot **f** hybrid substrate (top right angle of monopole antenna)

3 Results and Discussions

The basic monopole antenna operates from 2.23–2.82 GHz and 4.61–10.23 GHz in at least 1 dB gain, 1.85 dB directivity, and 82 % total efficiency. In the investigation of different shape of SRR slot on monopole antenna, it has shown that the adding of the SRR slot onto the antenna patch will create a notch band at around 4 GHz but without affecting much on the first frequency band's bandwidth. The S11 graph in Fig. 3 shows the effect of every SRR slot's shape to the antenna. Tables 2 and 3 display where the notch located at the frequency band based on each antenna parameters studied. The result shows that the SRR slot can be used to create the notch, but different shapes of SRR slot will shift the notch in random order around 4 GHz. When the number of SRR slot's edges increases, it may also create more notch bands as shown by the result obtained from square and pentagonal SRR slot.

Next, the hybrid substrate is added to the SRR-slotted monopole antenna. The investigation is repeated for each shape of SRR slots. The simulated S11 graph in Fig. 4 shows that the adding of hybrid substrate has increased the first frequency band's bandwidth for at least 270 MHz and decrease the wideband bandwidth for almost 3 GHz. Besides that, by comparing the SRR-slotted monopole antenna design and SRR-slotted monopole antenna with hybrid, the adding of hybrid substrate will shift the notch band to lower frequency for nearly 150 MHz. The frequency notch and peak directivity for square and pentagonal SRR slot at second

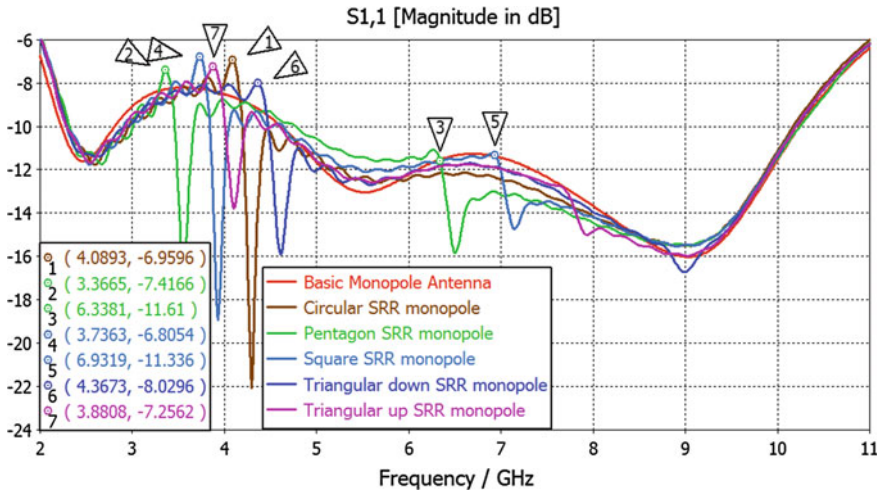


Fig. 3 Parametric study on shape of SRR slot on monopole antenna

Table 3 2nd notch frequency for each antenna parameter study on SRR-slotted monopole antenna

| Shapes of SRR slot | Frequency notch (GHz) | Gain notch (GHz) | Efficiency notch (GHz) | Peak directivity (GHz) |
|-------------------------|-----------------------|------------------|------------------------|------------------------|
| Circular | – | – | – | – |
| Triangular (point up) | – | – | – | – |
| Triangular (point down) | – | – | – | – |
| Square | 6.9319 | 7.0 | 7.0 | 6.6 |
| Pentagonal | 6.3381 | 6.4 | 6.4 | 6.4 |

Table 2 1st notch frequency for each antenna parameter study on SRR-slotted monopole antenna

| Shapes of SRR slot | Frequency notch (GHz) | Gain notch (GHz) | Efficiency notch (GHz) | Peak directivity (GHz) |
|-------------------------|-----------------------|------------------|------------------------|------------------------|
| Circular | 4.0893 | 4.2 | 4.2 | 4.2 |
| Triangular (point up) | 3.8808 | 4.0 | 4.0 | 4.0 |
| Triangular (point down) | 4.3673 | 4.4 | 4.6 | 4.6 |
| Square | 3.7363 | 3.8 | 3.8 | 3.8 |
| Pentagonal | 3.3665 | 3.6 | 3.4 | 3.4 |

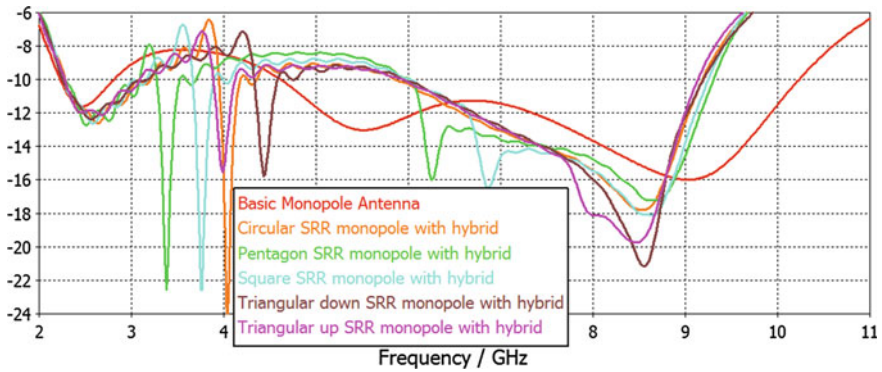


Fig. 4 Parametric study on shape of SRR slot on monopole antenna with hybrid substrate

Table 4 1st notch frequency for each antenna parameter study on SRR-slotted monopole antenna with hybrid substrate

| Shapes of SRR slot | Frequency notch (GHz) | Gain notch (GHz) | Efficiency notch (GHz) | Peak directivity (GHz) |
|-------------------------|-----------------------|------------------|------------------------|------------------------|
| Circular | 3.8391 | 4.0 | 4.0 | 4.0 |
| Triangular (point up) | 3.7696 | 3.8 | 4.0 | – |
| Triangular (point down) | 4.2144 | 4.4 | 4.4 | 4.4 |
| Square | 3.5611 | 3.6 | 3.6 | 3.6 |
| Pentagonal | 3.1997 | 3.4 | 3.4 | 3.2 |

Table 5 2nd notch frequency for each antenna parameter study on SRR-slotted monopole antenna with hybrid substrate

| Shapes of SRR slot | Frequency notch | Gain notch (GHz) | Efficiency notch (GHz) | Peak directivity (GHz) |
|-------------------------|-----------------|------------------|------------------------|------------------------|
| Circular | – | – | – | – |
| Triangular (point up) | – | – | – | – |
| Triangular (point down) | – | – | – | – |
| Square | – | 6.8 | 6.8 | – |
| Pentagonal | – | 6.2 | 6.2 | 6.0 |

notch band become not obvious after adding the hybrid substrate. This may be due to the increasing of the stop-band bandwidth and the notch’s gain, efficiency and directivity is in higher region (Tables 4 and 5).

4 Conclusion

In this paper, the investigation on a wideband monopole antenna by adding different shapes of SRR slot and hybrid material constructed by FR4 layer and glass layer was done. It was found that the adding of SRR slot can result in a notch function creation at around 4 GHz. However, the adding of SRR slot will not offer much difference to the first frequency band at 2.4 GHz and the reflection coefficient at 10.23 GHz of the second frequency band. On the other hand, the adding of hybrid material to the monopole antenna is not only able to affect the bandwidth of first frequency band and second frequency band as discussed in Sect. 3, it is also able to shift the notch to lower frequency. Thus, these characteristics of SRR slot and hybrid substrate can contribute to the smart antenna design in the future when involving tunable frequency notch and bandwidth alteration.

Acknowledgements The authors would like to send largest appreciation to Universiti Teknikal Malaysia Melaka (UTeM) for giving great platform in obtaining the information and materials for the entire research. We would also like to send our gratitude to anonymous referees whose comments led to an improved presentation of our works. Last but not least, we would like to thank the Ministry of Education Malaysia (MOE) for PJP/2013/FKEKK (12C)/S01183 research grant.

References

1. Majid, H.A., Rahim, M.K.A., Hamid, M.R., Ismail, M.F.: A compact frequency-reconfigurable narrowband microstrip slot antenna. *IEEE Antennas Wirel. Propag. Lett.* **11**, 616–619 (2012)
2. Chakraborty, U., Kundu, A., Chowdhury, S.K., Bhattacharjee, A.K.: Compact dual-band microstrip antenna for IEEE 802.11a WLAN application. *IEEE Antennas Wirel. Propag. Lett.* **13**, 407–410 (2014)
3. Ali Nezhad, S.M., Hassani, H.R.: A novel triband E-shape printed monopole antenna for mimo application. *IEEE Antennas Wirel. Propag. Lett.* **9**, 576–579 (2010)
4. Hsieh, H.W., Lee, Y.C., Tiong, K.K., Sun, J.S.: Design of a multiband antenna for mobile handset operations. *IEEE Antennas Wirel. Propag. Lett.* **8**, 200–203 (2009)
5. Krishna, D.D., Gopikrishna, M., Aanandan, C.K., Mohanan, P., Vasudevan, K.: Compact wideband koch fractal printed slot antenna. *IET Microwaves Antenna Propag.* **3**(5), 782–789 (2009)
6. Lee, J.M., Kim, K.B., Ryu, H.K., Woo, J.M.: A compact ultrawideband MIMO antenna with WLAN band-rejected operation for mobile devices. *IEEE Antennas Wirel. Propag. Lett.* **11**, 990–993 (2012)
7. Deegwal, J.K., Kumar, A., Yadav, S., Sharma, M.M., Govil, M.C.: Ultra-wideband truncated rectangular monopole antenna with band-notched characteristics. In: 2012 IEEE Symposium on Wireless Technology and Applications, ISWTA, pp 254–257 (2012)
8. Wang, N., Gao, P.: A novel printed UWB and bluetooth antenna with quad band-notched characteristics. In: 2013 International Workshop on Microwave and Millimeter Wave Circuits and System Technology, pp. 150–153 (2013)
9. Sarkar, D., Srivastava, K.V., Saurave, K.: A compact microstrip-fed triple band-notched UWB monopole antenna. *IEEE Antennas Wirel. Propag. Lett.* **13**, 396–399 (2014)

10. Sharma, M.M., Kumar, A., Yadav, S., Ranga, Y., Bhatnagar, D.: A compact ultra-wideband CPW-fed printed antenna with SRR for rejecting WLAN band. In: 2011 Indian Antenna Week (IAW), pp. 1–3 (2011)
11. Wu, B.I., Wang, W., Pacheco, J., Chen, X., Grzegorzczak, T.: A study of using metamaterials as antenna substrate to enhance gain. *Prog. Electromagnet. Res.* **51**, 295–328 (2005)
12. Eva, R.I., Oscar, Q.T., Luis, I.S.: Mutual coupling reduction in patch antenna arrays by using a planar EBG structure and a multilayer dielectric substrate. *IEEE Trans. Antennas Propag.* **56** (6), 1648–1655 (2008)
13. Kamogawa, K., Tokumitsu, T., Aikawa, M.: Multifrequency microstrip antennas using alumina-ceramic/polyimide multilayer dielectric substrate. *IEEE Trans. Microwave Theory Tech.* **44**(12), 2431–2437 (1996)
14. Chen, S.C., Liu, G.C., Chen, X.Y., Lin, T.F., Liu, X.G., Duan, Z.Q.: Compact dual-band GPS microstrip antenna using multilayer LTCC substrate. *IEEE Antennas Wirel. Propag. Lett.* **9**, 421–423 (2010)
15. Alix, R.A., Balanis, C.A.: Gain enhancement in microstrip patch antennas using hybrid substrates. *IEEE Antennas Wirel. Propag. Lett.* **12**, 476–479 (2013)

Analytical Study of Energy Absorption in Human Body Due to Bendable Behaviour of Textile Antenna

N.A. Elias, N.A. Samsuri and M.K.A. Rahim

Abstract Absorption of electromagnetic (EM) radiation by the human body has received tremendous attention due to rapid growth in Wireless Body Area Network (WBAN) applications. Specific Absorption Rate (SAR) is usually measured with the antenna in flat condition. However the emergences of flexible wearable textile antennas make it compulsory to analyse the SAR when the antenna is not in its normal flat condition. The absorption of EM radiation as well as the SAR distribution are analysed as a function of the antenna curvature sizes and different on-body locations and distances. The averaged SAR values demonstrate an increase of up to 92.3 % when the curved textile antenna is bent and placed 1 mm away from the body.

1 Introduction

In recent years, wearable textile antennas have received tremendous interest due to rapid growth in Wireless Body Area Network (WBAN) applications. WBANs can be utilized in various applications such as healthcare and medical monitoring, civil, military, education and personal electronics domains [1]. The body worn antennas have a basic requirement of being flexible; therefore textile antenna is a promising candidate since it can be fully integrated into intelligent garments, known as wearable electronic systems [2]. However, the flexibility nature of textile materials exposes the antenna to bending and crumpling conditions, or even the antenna may

N.A. Elias (✉) · N.A. Samsuri · M.K.A. Rahim
Communication Engineering Department, Universiti Teknologi Malaysia,
81310 Johor Bahru, Malaysia
e-mail: norfae89@gmail.com

N.A. Samsuri
e-mail: asmawati@fke.utm.my

M.K.A. Rahim
e-mail: mkamal@fke.utm.my

be twisted when being worn by a user. The bending and crumpling may deteriorate the antenna performance. It was reported in [3] that circularly polarized antennas lose their polarization property when bent. Besides, the resonant frequency, input impedance matching and bandwidth of the antenna fluctuated remarkably when the antenna is bent [4]. Furthermore, even in the normal flat condition, degradation of the wearable antennas performance is expected since the antenna is mounted in close proximity to the human body [5, 6]. But there is another major concern which is the potential adverse health effect from the backward radiation that goes towards the human body [7]. The health effect usually measured by SAR. SAR is the standard unit used to measure the rate of energy absorbed by the human body when exposed to the EM radiation. The mathematical equation for SAR is given by Eq. (1) below. It has been reported that the safety margin of the radiation standard set by Federal Communications Commission (FCC) [8] for adults are quite smaller than the exposure level that are known to cause harmful effect to animals. Therefore, the probability of children to absorb an amount of radiation greater than the maximum allowable limit is higher due to the fact that a child tissue will significantly absorb more radiation than adults. Generally, the effects of bending and crumpling of textile antennas have been widely studied by previous researches [9–12]. However, most of the studies only focused on the effect of antenna bending towards the antenna performance. Besides, most of previous researchers only used single layer or three layer body models in their simulation. Therefore, the main aim of this paper is to investigate the influence of bending on the SAR values of single band textile antenna using realistic voxel human body model. The bending effects at different body part and different distances between antenna and human body are also investigated. New finding are disclosed in this paper concerning to the energy absorption in layered body tissues under reactive near-fields exposure and the antenna being positioned not in normal flat orientation. The findings in this paper are also important as a guideline to ensure that the SAR levels is not be exceeded when the wearable antenna is being worn by the users.

$$SAR = \frac{(\sigma|E|^2)}{\rho}. \quad (1)$$

2 Antenna Bending

Dipole antenna is used as the radiating source in this study due to the fact that it can give a conservative estimation of the SAR induced by a monopole antenna, besides the smaller simulation space that it occupies. In this paper, a planar dipole antenna using denim fabric as the substrate is designed to operate at 2.4 GHz. The permittivity and loss tangent of the denim fabric is 1.7 and 0.025 respectively, measured by using open ended coaxial probe method.

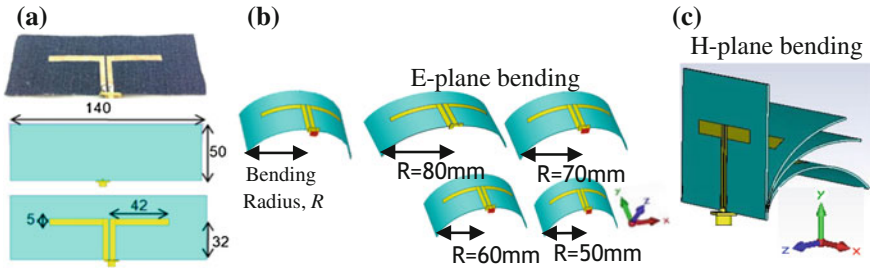


Fig. 1 **a** The fabricated antenna dimensions in millimeter (mm), **b** the antenna bent along xz -plane (E-plane) with varying bending radius, R **c** antenna bent along yz -plane (H-plane)

The antenna is bent over the cylinder in two principal planes xz (E-plane) and yz (H-plane) by varying the bending radius, R of the cylinder as illustrated in Fig. 1. The bending radii are varied in the range of 150–20 mm to mimic the actual bending scenario when it is placed on human arm, wrist and thigh. 20 mm represents the most bent antenna whilst the 150 mm indicating the least bending condition.

3 Simulated and Measured Antenna Resonant Performance

For the human body model, Gustav human body model (38 years old male with 176 cm height and 69 kg weight) made available by CST Microwave Studio software is used. The resolution is set to $2.08 \times 2.08 \times 2.0$ mm in the simulation, while the electrical properties of the human tissues and organs are the same as recommended by the IEEE and FCC [13]. In order to investigate the effect of antenna bending, 4 suitable antenna placements have been identified as illustrated in Fig. 2. The gap between the textile antenna and the voxel body model is varied to 1, 5, 10 and 20 mm respectively considering the thickness of the cloth and the air gap that exist in the realistic scenario of BANs.

In the measurement process, the antenna is bent towards Rohacell foam with permittivity close to air. Different thickness of Rohacell foam is placed in between the antenna and human body to vary the distance, d . The fabricated antenna's return loss performance is measured using Vector Network Analyzer (VNA). The simulated and measured results of the antenna bent in xz -plane in free space are illustrated in Fig. 3. A slight frequency detuning is observed when the antenna is bent but the return loss remains below -10 dB at the frequency investigated. The measurement results obtained are in good agreement with simulation results.

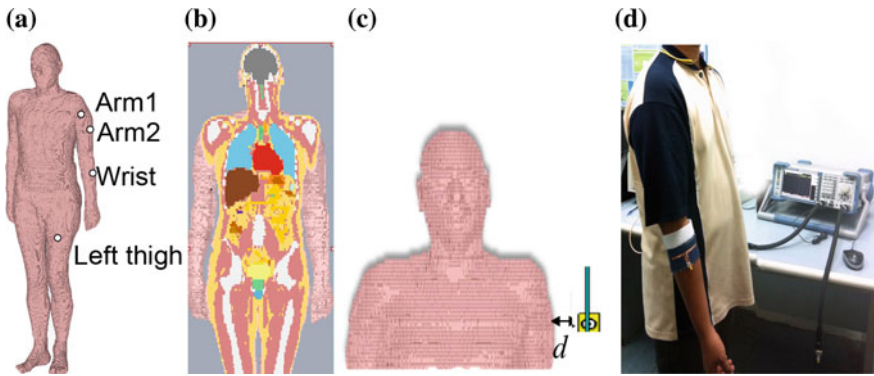


Fig. 2 a Four different antenna mounting positions, b The voxel body model which consists of detailed human organs and tissues, c depictions of the antenna-body separation distance, *d*, d the bent antenna resonance performance measured by using VNA

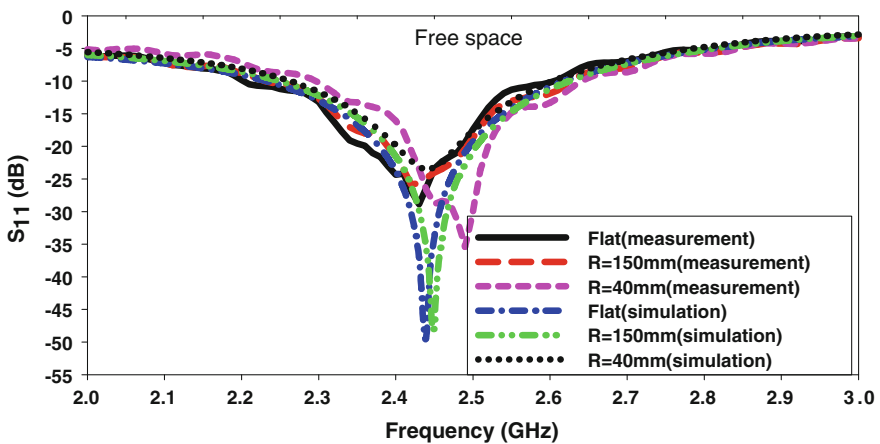


Fig. 3 The effects of different bending radii, *R* towards the antenna resonant frequency under *xz*-plane bending

Figure 4 depicts the variation of the antenna resonant frequencies for dipole textile antenna bent on *xz*-plane and placed 10 mm from the human arm1 and wrist. The measured results show that under E-plane bending conditions, the operating frequency detuned and shifted to higher frequency if compared to its actual operating frequency (in free space). As expected, in the vicinity of human body, the detuning effect of the resonant frequency is more prominent compared to when the antenna is bent in free space. It is observed that the more the antenna is bent, the more the resonant length is reduced and therefore the resonant frequency gets shifted up [9].

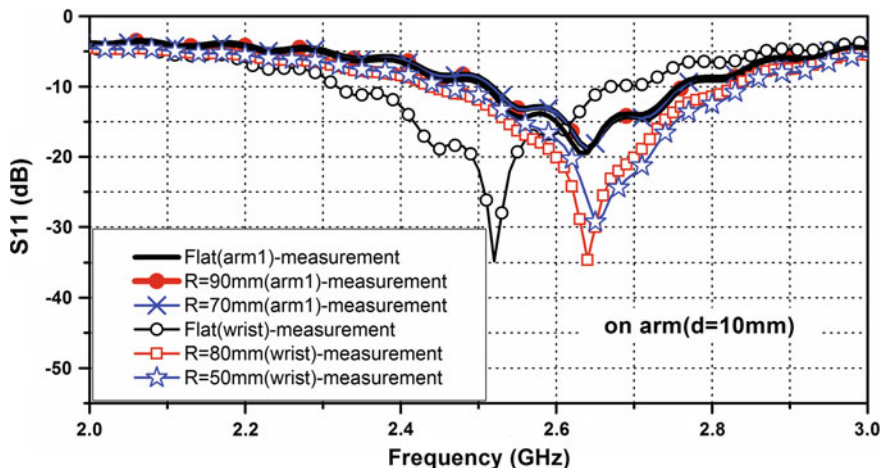


Fig. 4 The effects of bending radii, R and the variation of antenna position on human body towards the resonant frequency under xz -plane bending at $d = 10$ mm

4 Specific Absorption Rate (SAR)

This section will discuss on the SAR value when the antenna become bent when mounted on several positions on the human body. The electric field behavior of the bent antenna mounted close to the body will be presented to further discuss the variation of SAR for Arm2.

Figure 5 shows the peak 10 g SAR value for the arm tissue exposed to the radiation under xz -plane bending. The results include the effects of two different antenna positions (Arm1 and Arm2), different bending radius, R and the variation of the antenna-body distances, d on the SAR value. The input power is normalized to 1 W of accepted power. The results show that the bending has profound effect on SAR value and energy absorbed by the human body. The most severe bending; 50 mm bending radius gives the highest value of peak 10 g SAR. It can be observed that the smaller the bending radii, R , the higher the SAR value. All antenna-body separation distances considered in this paper possess the same trend of SAR increment under all bending conditions. In addition to that, the averaged SAR has notably decreased when the distance between the antenna and the human body is increased for all bending cases investigated regardless of their mounting position on the human body.

Figure 6 depicts the 10 g SAR value for different arm tissues when exposed to the antenna bent along the principal E-plane (xz -plane bending). It can be observed that the SAR value is highest on the surface of the body, that is, on the skin tissue. As the energy penetrates deeper into the fat tissue, a significant dropped can be seen at the skin-fat boundary. This is due to the larger relative dielectric property difference between the two media; skin and fat. Fat tissue is a poor conductor if compared to the skin and muscle tissues. And this study has shown good

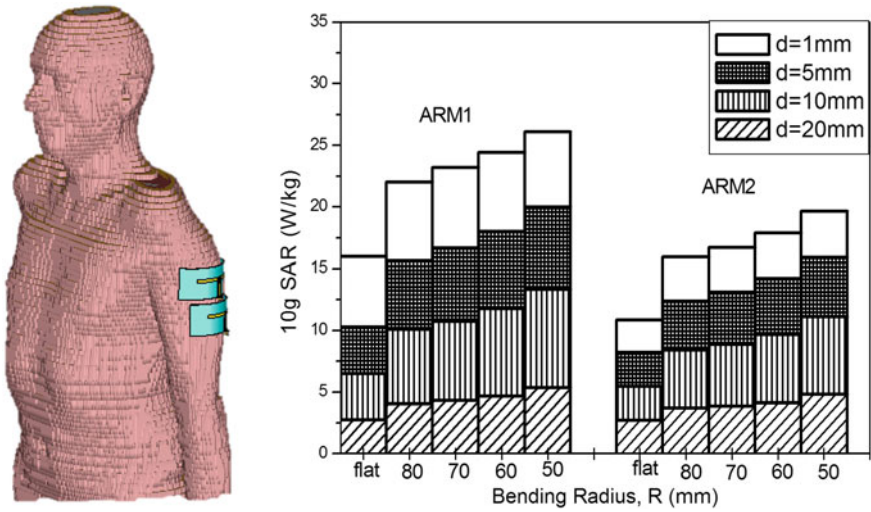


Fig. 5 Peak 10 g SAR value for the arm tissues exposed to the radiation under xz-plane bending with various antenna-body distances, d

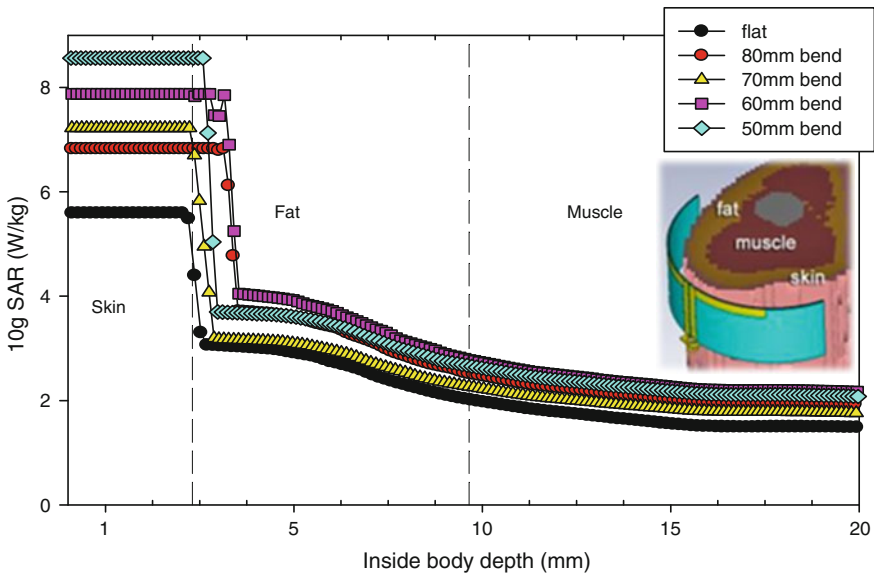


Fig. 6 SAR value inside different arm tissues for different curving radius at antenna-body distances, $d = 1$ mm (xz-plane bending)

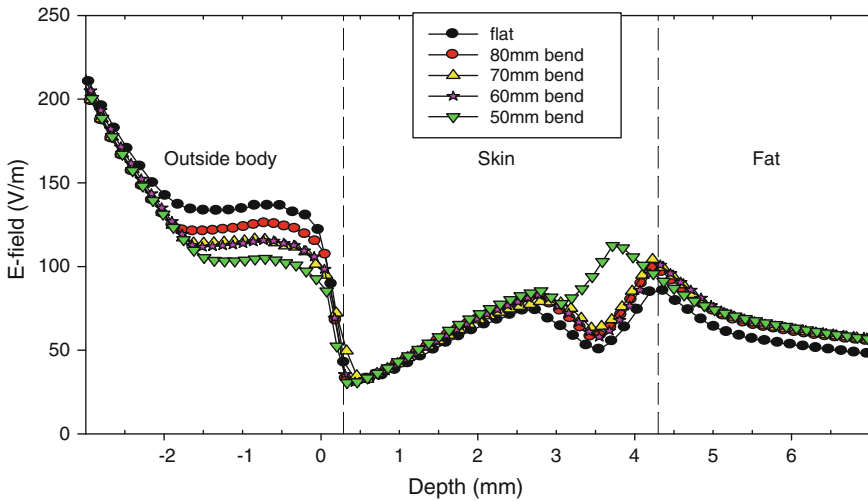


Fig. 7 E-field value outside body and inside different arm tissues for different curving radius at antenna-body distances, $d = 1$ mm (xz-plane bending)

agreement in which fat tissue as poor conductor, hence the SAR is significantly decreased in fat tissue. The energy continuously decays as it travels through the lossy tissue. Besides that, the results also ascertained that the bending has influenced the variations of the SAR value inside the tissue. This result is further verified by Fig. 7 since the electric field strength is directly related to the SAR value as shown in Eq. (1). Figure 7 shows that under extreme 50 mm bent, the antenna forward radiation degraded significantly compared to the other less extreme condition. However, the backward radiation field strength is greater than the flat and other bending condition when it traverse the human tissue.

Moreover, the behaviour of the E-field distribution under bending condition is of great interest when discussing SAR. Figure 8 illustrates the E-field distribution

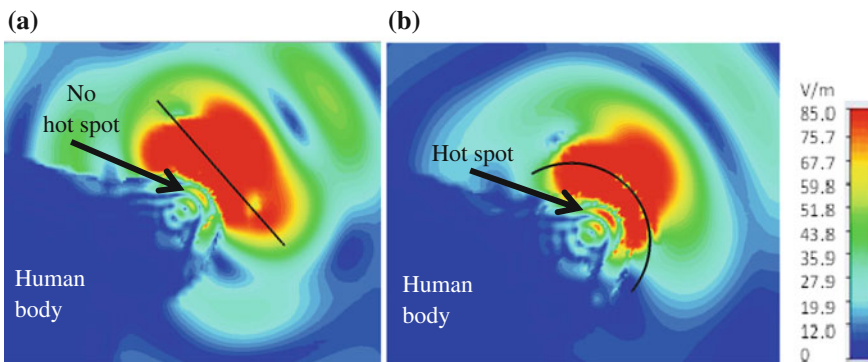


Fig. 8 Electric field distribution (V/m) in human arm exposed to the radiated power of 1 W under different curving radius with 1 mm antenna-body gap distance. **a** flat **b** $R = 50$ mm

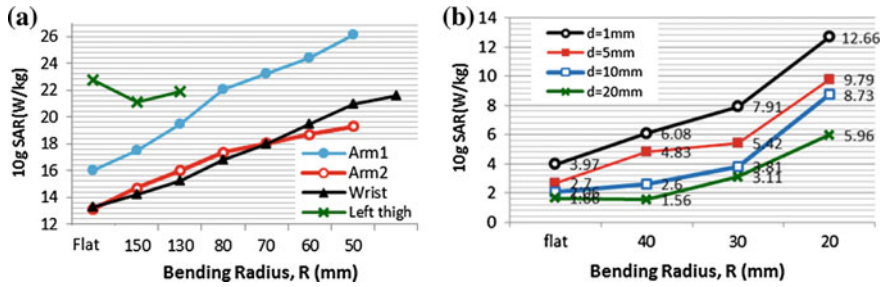


Fig. 9 a Peak 10 g SAR value for antenna mounted at four different positions at antenna-body distances, $d = 1$ mm under xz -plane bending. b Peak 10 g SAR value for the arm tissues exposed to the radiation under yz -plane bending with various antenna-body distances, d

indicating the backward radiation when the antenna is bent. It can be observed that the backward radiation is increased for the 50 mm bending radius if compared to the flat condition (as shown by the pointing arrow). The results for other bending radii are not presented in here because there is no significant variation is observed. The simulation is then repeated for four different antenna locations and the SAR result is presented in Fig. 9a. It is noticed that for all the mounting locations considered in this paper, the SAR value is increased with the decrement in the bending radii.

Figure 9b shows peak 10 g SAR value for the arm tissues exposed to the radiation under yz -plane bending with various antenna-body distances, d . It can be seen that the antenna under yz -bending also shows the same trend of increasing SAR as the antenna bending radii increases.

5 Conclusions

It is well known that the antenna mounted on different body part will give different SAR value. However this study has proved that the antenna bending will also influence the SAR value due to the increasing in antenna backward radiation. The averaged SAR value is increased for up to 92.3 % (xz -plane bending) and 218 % (yz -plane bending). However, the bent antenna along the xz -plane (E -plane) has higher SAR if compared to yz -plane. Therefore, choosing the right position for the antenna mounting, i.e. position which makes the antenna less exposed to bending is important in order to minimize the amount of bending.

Acknowledgments This work was supported by the Ministry of Education Malaysia (MOE), Research Management Centre (RMC), School of Postgraduate (SPS), Universiti Teknologi Malaysia (UTM) (grant Q.J130000.2523.04H23) and Universiti Teknikal Malaysia Melaka (UTeM).

References

1. Cordeiro, C., Fantacci, R., Gupta, S.K.S., Paradiso, J., Smailagic, A., Srivastava, M.: Guest editorial body area networking: technology and applications. *IEEE J. Sel. Areas Commun.* **27**, 1–4 (2009)
2. Boeykens, F., Vallozzi, L., Rogier, H.: Cylindrical bending of deformable textile rectangular patch antennas. *Int. J. Antennas Propag.* **2012**, 11 (2012)
3. Kellomaki, T.: Analysis of circular polarization of cylindrically bent microstrip antennas. *Int. J. Antennas Propag.* **2012**, 8 (2012)
4. Sankaralingam, S., Gupta, B.: Effects of bending on impedance and radiation characteristics of rectangular wearable antenna utilizing smart clothes. *Microwave Opt. Technol. Lett.* **54**, 1508–1511 (2012)
5. Bai, Q., Langley, R.: Crumpling of PIFA textile antenna. *IEEE Trans. Antennas Propag.* **60**, 63–70 (2012)
6. Elias, N.A., Samsuri, N.A., Rahim, M.K.A., Othman, N., Jalil, M.E.: Effects of human body and antenna orientation on dipole textile antenna performance and SAR. In: 2012 IEEE Asia-Pacific Conference on Applied Electromagnetics (APACE 2012), Melaka, Malaysia (2012)
7. Elias, N.A., Samsuri, N.A., Rahim, M.K.A., Othman, N.: The effects of human body and bending on dipole textile antenna performance and SAR. In *Proceedings of APMC 2012*, Kaohsiung, Taiwan, pp. 2A3–02 (2012)
8. FCC OET Bulletin 65: Revised Supplement C: Evaluating compliance with FCC guidelines for human exposure to radiofrequency electromagnetic fields (2001)
9. Sankaralingam, S., Gupta, B.: Development of textile antennas for body wearable applications and investigations on their performance under bent conditions. *Prog. Electromagn. Res. B* **22**, 53–71 (2010)
10. Han, W., Zhijun, Z., Yue, L., Zhenghe, F.: A dual-resonant shorted patch antenna for wearable application in 430 MHz band. *IEEE Trans. Antennas Propag.* **61**, 6195–6200 (2013)
11. Chahat, N., Zhadobov, M., Muhammad, S.A., Le Coq, L., Sauleau, R.: 60-GHz textile antenna array for body-centric communications. *IEEE Trans. Antennas Propag.* **61**, 1816–1824 (2013)
12. Subramaniam, S., Gupta, B.: Design and development of flexible fabric antenna for body-worn applications and its performance study under flat and bent positions. *Microwave Opt. Technol. Lett.* **53**, 2004–2011 (2011)
13. Federal Communications Commission: Body tissue dielectric parameter (2010)

A Comparative Study on Polarization Reconfigurable Circular Patch Antenna

Mohamed Nasrun Osman, Mohamad Kamal A. Rahim,
Mohd Fairus Mohd Yusoff, Mohamad Rijal Hamid,
Huda A. Majid, Mohd Ezwan Jalil and Khairul Hilmi Yusof

Abstract This paper presents a comparison between two approaches of designing polarization reconfigurable antennas. To achieve this special feature, it can be realized by introducing perturbation elements into the radiating components of the structure. Secondly, it also can be accomplished by altering the feeding networks, without any modification needed to the radiating elements. Both approaches are executed to the conventional circular patch microstrip antennas. For reconfigurability purposes, the switches are placed at the specific location. Consequently, by controlling the state of the switches (either ON or OFF), the polarization excites by the antenna can be reconfigured between three type of polarization modes, either left-hand circular polarization, right-hand circular polarization or linear polarization. For the proof of the concept, ideal case of switch (copper strips) is employed in the designs. Both of the structures are designed to operate in wireless local area

M.N. Osman (✉) · M.K.A. Rahim · M.F.M. Yusoff · M.R. Hamid · H.A. Majid
M.E. Jalil · K.H. Yusof
Communication Engineering Department, Faculty of Electrical Engineering,
UTM-MIMOS Center of Excellence, Universiti Teknologi Malaysia, 81310 UTM JB,
Johor, Malaysia
e-mail: nasrun_osman@yahoo.com

M.K.A. Rahim
e-mail: mkamal@fke.utm.my

M.F.M. Yusoff
e-mail: fairus@fke.utm.my

M.R. Hamid
e-mail: rijal@fke.utm.my

H.A. Majid
e-mail: huda_set@yahoo.com

M.E. Jalil
e-mail: ezwanjalil@gmail.com

K.H. Yusof
e-mail: khilmi89@gmail.com

network (WLAN) frequency band (2.4–2.48 GHz). The performances of both designs are presented and compared, and the advantages and disadvantages of the proposed design are discussed.

1 Introduction

Modern wireless telecommunication systems have rapidly grown and evolving, leads to the new conditions and requirements to have an integrated antenna with multi-functional and flexibility characteristics. Conventional antennas may face restrictions to adapt to the new adjustments due to its inflexible characteristics. Hence, the solution to tackle this issue is to use reconfigurable antennas. Reconfigurability has become an important and desired features of modern, agile, radio frequency (RF) systems for wireless and satellite communications, sensing and imaging [1]. To obtain this multi-functional feature, the antenna needs to have its characteristics; such as frequency, pattern of polarization, to be reconfigurable.

Recently, polarization reconfigurable antennas have gaining popularity and interest among researchers. In the wireless communication systems, such as wireless local area network (WLAN), these types of antennas are used to mitigate and reduce the multipath fading effect [2], especially in dealing with confined area and limited space systems. They are also used to realize frequency reuse for doubling the system capabilities. In addition, polarization reconfigurable antenna are also being utilized in the multiple-input-multiple-output (MIMO) systems to optimize and improve the channel capacity and overall performances of the systems [3, 4]. Polarization reconfigurable antennas means single antenna is capable to incorporate and offer multiple type of polarization senses, either between orthogonal linear polarization (LP), between LP to circular polarization (CP), or between left-hand circular polarization (LHCP) and right-hand circular polarization (RHCP).

Reconfigurability can be achieved in different ways, such as through modification of the antenna physical structure, radiating edge or feeding network. These modifications will alter the current distribution on the antenna structure, which accordingly change the antenna's polarization. In developing reconfigurability feature, microstrip patch antennas have been used widely in [5–7]. This is due to the fact that the microstrip patch antennas have simple fabrication, low profile, and most importantly easily can be integrated with switches, such as RF PIN diode [8] to form reconfigurable patch antenna.

Overall, this paper presents the comparison of different type of technique used in developing polarization reconfigurable antennas. Two types of techniques used are changing of radiating edge by incorporating of slits perturbation (Design A) and the alteration of feeding network (Design B). The paper begins with the explanations of geometry and configurations for both designs. Then, the simulated results obtained are analyzed. Finally, the performances of both designs are compared and discussed.

2 Antennas Geometry and Configuration

In this section, the approach and method used in both designs; slit perturbations and alterations of the feeding networks, are described. To ensure a fair comparison between these techniques, both are executed to the similar structure and substrate; circular-shaped microstrip patch antenna, Taconic RF-35, and operating in WLAN frequency band. Throughout the designs, the copper strips are utilized as switches for the proof of the concept. The presence of the copper strips indicates that the switches are in ON state, meanwhile, represents the OFF state when the copper strips are absence.

2.1 Design A: Slits Perturbation

Author in [9] has successfully developed the polarization reconfigurable patch antenna through slits perturbation method. The schematic geometry of the proposed antenna is illustrated in Fig. 1. The structure was implemented in a single layer of Taconic RF-4 substrate ($h = 1.52$ mm, $\epsilon_r = 3.54$), with the overall dimensions of the antenna is 55×55 mm. The proposed antenna consists of a circular patch with a radius of r , incorporated with four equal length slits on the top surface, and finite ground plane on the bottom surface. The slits, with a dimension of $L1 \times W1$, is located 90° apart from each other at the edge of the patch along the x -axis and y -axis. The switch is inserted across each slit at the distance $L2$ from the center of the circular patch, thus altering the slit length. The positioned of the switches is

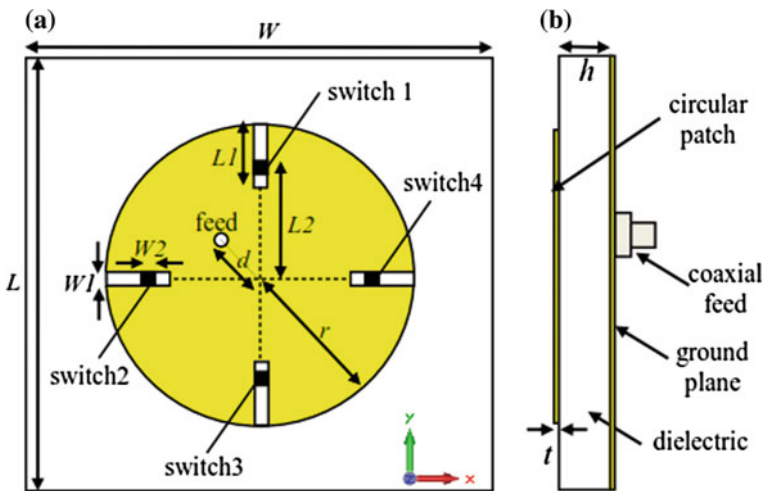


Fig. 1 Schematic of polarization reconfigurable with slits perturbation **a** front view **b** side view ($L = 55$, $W = 55$, $L1 = 5$, $L2 = 15.3$, $W1 = 1$, $W2 = 1$, $r = 17.9$, $d = 5.5$ (All are in mm) $\epsilon_r = 3.54$)

Table 1 Polarization states of the proposed polarization reconfigurable with slits perturbation

| Configuration | Switch state | | | | Polarization |
|---------------|--------------|-----|-----|-----|--------------|
| | S1 | S2 | S3 | S4 | |
| C1-LHCP | ON | OFF | ON | OFF | LHCP |
| C2-RHCP | OFF | ON | OFF | ON | RHCP |
| C3-LP | ON | ON | OFF | OFF | LP |

crucial as its determining the axial ratio response. The antenna is fed through the coaxial feed from the back of the structure, positioned diagonally at the distance of d from the center. Parameter d is optimized to obtain good impedance matching.

The approach and mechanism of the proposed antenna can be explained using the cavity model method [10]. Due to the diagonal feeding of the structure, two degenerated orthogonal resonant modes TM_{01} and TM_{10} are excited simultaneously. The existences of the slits perturbation drive the surface current from the perpendicular direction to move along it. However, the small width of the slits gives less effect to the current coming from parallel route. For example, when the pair of slits is cut on the x -axis of the patch, only TM_{01} mode will be affected without giving much effect on the TM_{10} mode, and vice versa.

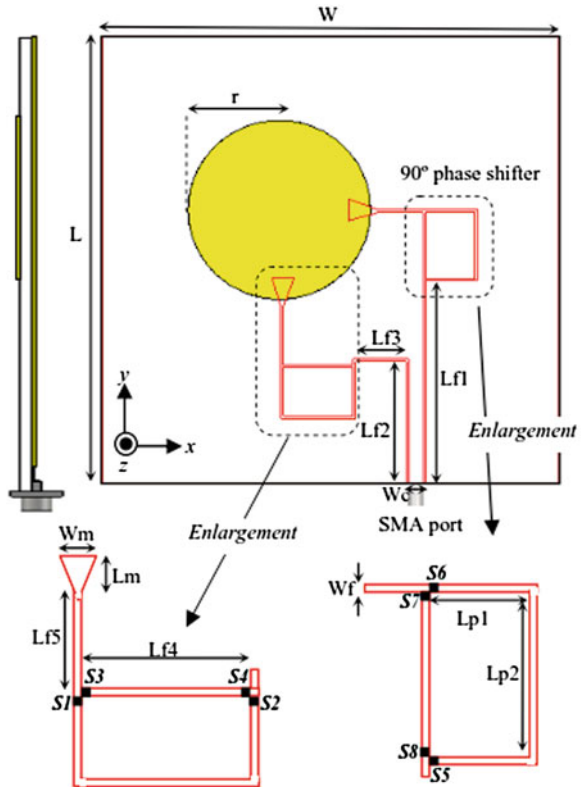
Due to the presence of the copper strips, the length's slit is altered, thus causing the effective surface current to flow through to the shortest distance instead of travelling around the slits. The length difference provides the phase delay between both modes. At the specific length difference, the antenna is excited by two orthogonal resonant modes that have the same amplitude and in phase quadrature, hence the CP is generated. Meanwhile, the LP is excited when the switches on the x -axis and y -axis are ON. The switching condition, with the respected polarization sense, is tabulated in Table 1.

2.2 Design B: Modification of Feeding Networks

The schematic geometry of the polarization reconfigurable patch antenna through modification of the feeding networks is illustrated in Fig. 2. The size of the whole structure is $L \times W$. A circular patch, having a radius of r is mounted on the top layer of the Taconic substrate (same properties as used in Design A). The antenna is excited with co-planar waveguide (CPW) feed-line (inner conductor: W_c , width of slots: W_p), and is positioned on the other sides of microwave substrate. The circular patch is coupled with two tapered impedance transformer (L_m , W_m) with triangular shaped, located on the x -axis and y -axis and these parameters were adjusted in order to obtain good impedance matching.

Two phase shifters are incorporated in the design, by prolonging the feed line slots about a distance of quarter wavelength, and later were optimized using parameter sweep technique to achieve good axial ratio response. This will provide a phase difference of 90° between two orthogonal modes; hence CP mode can be excited.

Fig. 2 Schematic of polarization reconfigurable with modification of feeding network ($L = 90$, $W = 90$, $r = 15$, $L_{f1} = 40.75$, $L_{f2} = 24.5$, $L_{f3} = 11$, $L_{f4} = 13.25$, $L_{f5} = 11.65$, $L_{p1} = 9.73$, $L_{p2} = 13.75$, $L_m = 6$, $W_c = 2.8$, $W_f = 0.5$, $W_m = 4.4$, $\epsilon_r = 3.54$ (All in mm)



On the other hand, LP is produced when the antenna is excited with the same length of the feed line (no phase difference). Therefore, for reconfigurability purposes, eight switches are utilized in the design. All switches are inserted on the junction of the phase shifters, thus enable of controlling the feed line; either activating (through the longer distance) or deactivating (through the shorter distance) the phase shifter. The switching configuration with the respected polarization is tabulated in Table 2.

Table 2 Polarization states of the proposed polarization reconfigurable through modification of feeding networks

| Configuration | Switch state | | | | | | | | Polarization |
|---------------|--------------|-----|-----|-----|-----|-----|-----|-----|--------------|
| | S1 | S2 | S3 | S4 | S5 | S6 | S7 | S8 | |
| C1-LHCP | OFF | OFF | ON | ON | ON | ON | OFF | OFF | LHCP |
| C2-RHCP | ON | ON | OFF | OFF | OFF | OFF | ON | ON | RHCP |
| C3-LP | OFF | OFF | ON | ON | OFF | OFF | ON | ON | LP |

3 Results and Discussion

The simulation was carried out using CST Microwave Studio commercial full wave software. The simulated result of the reflection coefficient between both designs is compared in Fig. 3a for CP configuration and Fig. 3b for LP configuration. It clearly can be seen that in Fig. 3a, the two orthogonal resonant modes (TM_{01} and TM_{10}) are excited. From Fig. 3a, the -10 dB bandwidths (BW) of reflection coefficient is 77 MHz (2.420–2.497 GHz), 79 MHz (2.420–2.499 GHz), 109 MHz (2.386–2.495 GHz) and 153 MHz (2.342–2.495), for LHCP (Design A), RHCP (Design A), LHCP (Design B) and RHCP (Design B), respectively. Meanwhile, for the case of LP, the -10 dB impedance matching is 40 MHz (2.439–2.479 GHz) and 58 MHz (2.420–2.478 GHz) for Design A and B, respectively. Good impedance matching was achieved for all switch configurations. It is also observed that Design B has a wider operating frequency compared to Design A due to different types of feeding method employed in both designs.

Figure 4 presents the comparison of the simulated axial ratio for LHCP and RHCP configurations between both designs. The simulated axial ratio, as referred to 3 dB axial ratio is 19 MHz (2.443–2.462 GHz), or about 0.77 % with respect to the center frequency of 2.452 GHz for both cases of CP in Design A. Meanwhile, for Design B, the 3 dB axial ratio BW is 23 MHz (2.443–2.466 GHz) and 26 MHz (2.445–2.471 GHz), for LHCP and RHCP configuration, respectively. From that, it is noted that the BW of CP is totally covered by the bandwidth of the LP. Since the proposed antenna performs a polarization reconfigurable antenna, the available BW will mainly depend on the BW of axial ratio. The comparison between Design A and B is summarized in Table 3.

Design A have uncomplicated feeding technique, less switches and smaller in dimension. It does not require extra structure or orthogonal feeding network to obtain phase delay between two orthogonal modes. CP is excited when there is a length difference between slits on the x -axis and y -axis. However, this design has

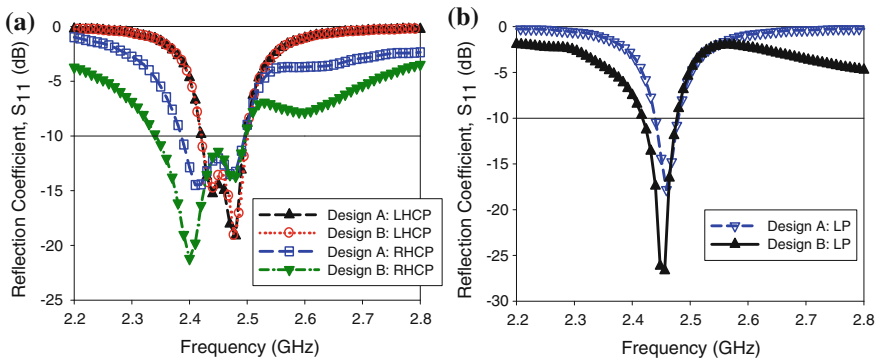


Fig. 3 Simulated reflection coefficient and axial ratio between both design **a** CP and **b** LP

Fig. 4 Comparison of simulated axial ratio between both designs

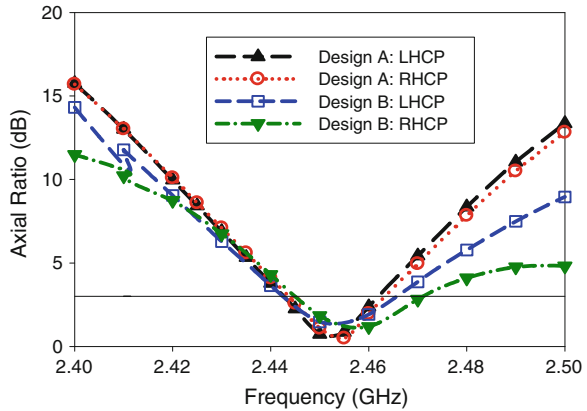


Table 3 Comparison between Design A (slit perturbations technique) and Design B (feeding networks technique)

| Details | -10 dB BW (MHz) | | | 3 dB AR BW (MHz) | | No of switch used | Dimension (mm) |
|----------|-----------------|------|------|------------------|------|-------------------|----------------|
| | LP | LHCP | RHCP | LHCP | RHCP | | |
| Design A | 40 | 77 | 79 | 19 | 19 | 4 | 55 × 55 |
| Design B | 58 | 109 | 153 | 23 | 26 | 8 | 90 × 90 |

few disadvantages, especially for the implementation of the real switches. Due to the importance of the switch position, the PIN diode shall be mounted appropriately on the structure. Moreover, as the slits are located on the radiating edge, the biasing network has to be properly considered, in order to give less effect on the performances of the antenna. Besides that, the probe feed technique used in the design provides smaller bandwidth of the reflection coefficient.

Meanwhile, Design B achieving circular polarization by feeding the antenna in two orthogonal locations with 90° phase shifter between them, thus was given a more complicated feeding network compared to Design A. To accommodate the phase shifter slot feed line, it required extra dimension. This design also necessitates more switches to obtain polarization reconfigurability. Conversely, the advantages of this method, it has much wider -10 dB reflection coefficient BW. Furthermore, Design B doesn't require any modification on the radiating element since the switches are inserted in the CPW feed line located on the ground plane. It will be much easier to mount the switches as it is placed at the junction. In addition, dual ports polarization reconfigurable with good isolations on the same structure can be developed by exploiting the odd and even mode of the CPW [11].

4 Conclusion

In this paper, polarization reconfigurable patch antenna that operates in WLAN frequency band is presented. The reconfigurability feature is executed using two techniques; loading of slits perturbation and modification of feeding network. Consequently, depending on the switching configurations, the polarization excited by both designs is capable to be reconfigured between LP, LHCP and RHCP. The simulated result of both designs are presented and compared. The advantages and disadvantages of both designs are explained. Since both techniques produce limited 3 dB axial ratio bandwidth for CP configuration, few techniques as discussed in [12] can be employed in the current design in order to have a wider axial ratio bandwidth. The implementation of real RF switches (PIN diode) is underway.

Acknowledgments The authors thank the Ministry of Higher Education for supporting the research work, Research Management Center (RMC), School of Postgraduate (SPS) and Communication Engineering Department, Universiti Teknologi Malaysia (UTM) for the support research under grant no RJ130000.7823.4F290.

References

1. Christodoulou, C.G., Tawk, Y., Lane, S.A., Erwin S.R.: Reconfigurable antennas for wireless and space applications. In: Proceedings of the IEEE, vol. 100, no. 7, July 2012
2. Ferrero, F., Luxey, C., Jacquemod, G., Staraj, R., Fusco, V.: Polarisation-reconfigurable patch antenna. In: International Workshop Antenna Technology: Small and Smart Antennas Metamaterials and Applications, vol. 1, pp. 73–76 (2007)
3. Piazza, D., Mookiah, P., D’Amico, M., Dandekar, K.R.: Experimental analysis of pattern and polarization reconfigurable circular patch antennas for MIMO systems. *IEEE Trans. Veh. Technol.* **59**(5), 2352–2362 (2010)
4. Cetiner, B.A., Akay, E., Sengul, E., Ayanoglu, E.: A MIMO system with multifunctional reconfigurable antennas. *IEEE Antennas Wirel. Propag. Lett.* **5**(1), 463–466 (2006)
5. Cao, W., Zhang, B., Liu, A., Yu, T., Guo, D., Pan, K.: A reconfigurable microstrip antenna with radiation pattern selectivity and polarization diversity. *IEEE Antennas Wirel. Propag. Lett.* **11**, 453–456 (2012)
6. Liu, W.-L., Chen, T.-R., Row, J.-S.: Reconfigurable microstrip antenna with pattern and polarization diversities. *Electron. Lett.* **43**(2), 77–78 (2007)
7. Sung, Y.J., Jang, T.U., Kim, Y.-S.: A reconfigurable microstrip antenna for switchable polarization. *IEEE Microwave Wirel. Compon. Lett.* **14**(11), 534–536 (2004)
8. Osman, M.N., Rahim, M.K.A., Yusoff, M.F.M., Hamid, M.R., Murad, N.A., Samsuri, N.A.: Polarization reconfigurable circular patch antenna with fixed operating frequency. In: 8th European Conference on Antenna and Propagation, pp. 2741–2743. Den Haag Holland (2014)
9. Nikolaou, S., Kim B., Vryonides, P.: Reconfiguring antenna characteristics using PIN diode. In: European Conference on Antennas and Propagation, pp. 3748–3752 (2009)
10. Chen, Y.B., Chen, T.B., Jiao, Y.C., Zhang, F.S.: A reconfigurable microstrip antenna for switchable polarization. *J. Electromagn. Waves Appl.* **20**(10), 1391–1398 (2006)

11. Li, Y., Zhang, Z., Chen, W., Feng, Z., Iskander, M.F.: A dual-polarization slot antenna using a compact CPW feeding structure. *IEEE Antennas Wirel. Propag. Lett.* **9**, 191–194 (2010)
12. Sainkar, S., Jeyakumar, A.: Design analysis of broadband circularly polarised compact microstrip antenna for wireless applications. *Int. J. Electron. Commun. Technol.* **2**(2), 135–139 (2011)

Design Annular Ring with Slots 4 GHz for Satellite Downlink Communication

**Saidatul Adawiyah Amiruddin, Mohd Azlishah Othman,
Muhammad Ramlee Kamarudin, Mohamad Harris Misran
and Mohamad Zoinol Abidin Abd. Aziz**

Abstract This project presents an overview of design of Annular Ring with Slots Microstrip Antenna for Satellite Downlink Communication. A satellite downlink communication needs the antenna that has low profiles, low cost and better efficiency. Annular ring with slots microstrip antenna can be one of the candidate for such application due to its low profiles and ease for fabrication. The antenna was designed by using CST Microwave Studio to obtain the S11, radiation pattern, gain, efficiency and bandwidth. The antenna was designed at 4 GHz and fabricated on the FR4 substrate with the dielectric constant of 4.4 and thickness of 1.6 mm. The gain and efficiency achieved at 4 GHz are 4.2 dBi respectively. Good agreement between measurement and simulation results was achieved. Therefore, the proposed antenna is suitable for the satellite downlink communication.

S.A. Amiruddin (✉) · M.A. Othman · M.H. Misran · M.Z.A. Abd. Aziz
Centre for Telecommunication Research and Innovation (CeTRI), Faculty of Electronic
and Computer Engineering, University Teknikal Malaysia Melaka, 76100 Durian Tunggal,
Melaka, Malaysia
e-mail: saidatul_adawiyah89@yahoo.com

M.A. Othman
e-mail: azlishah@utem.edu.my

M.H. Misran
e-mail: harris@utem.edu.my

M.Z.A. Abd. Aziz
e-mail: mohamadzoinol@utem.edu.my

M.R. Kamarudin
Wireless Communication Centre (WCC), Universiti Teknologi Malaysia, 81310 Skudai,
Johor, Malaysia
e-mail: ramlee@fke.utm.my

1 Introduction

Microstrip patch antenna is an antenna that can be installed or affixed on a flat surface e.g. FR4 board. Ground plane known as the patch is installed on the surface of the metals. It is usually used his deep simplicity of their fabrication and it too easy to change the custom or adapt to the type of antenna [1]. Basically the microstrip antenna is designed on a dielectric substrate using the same materials and lithographic processes used in making FR4 board [2]. The microstrip patch antenna usually used in GSM for mobile, wireless system (WLAN), satellite and WiMax. Typical single-frequency microstrip antenna design will be studied before and by submitting slot in the patch, required a compact, multi-band and broadband to achieve because of the efficient emit electromagnetic [3]. A good performance of antenna can be achieved with thick substrate whose dielectric constant in lower edge because, better efficiency, large bandwidth, loosely radiation into space, but an expense big element in size. The antenna of bandwidth and gain will affect when change the size of microstrip antenna [4]. In this project, the antenna theory is introduced to development of annular ring microstrip patch antenna. The antenna is designed for 4 GHz operating frequency and performed in order to improve the antenna gain the microstrip by using microstrip feed line method [5].

Nowadays, all antenna especially antenna for telecommunication systems require large bandwidth and compact dimensions size compared to basic antennas. Annular Ring is a one of way to solve this problem by using fabricates the antenna. Only a few people use annular Ring antenna on their design. The annular ring's application of the concept originally proposed from the circular patch geometry based on the basic shape by using the basic calculation of circular to get the radius of the outer [6].

The radius of inner based on the assumption at the beginning and parametric analysis to optimize suitable value for that annular ring antenna. Annular is not very complicated and does not need any angle; this will not improve the effective bandwidth and antenna radiation. Their ability filling the space can be put into long-term electricity small area in the annular ring antenna design.

2 Antenna Design

In designing an annular ring with slots 4 GHz for satellite downlink communication system, there have several dimension were used such as Inner of Radius (R_1), Outer of Radius (R_2) Width of Slot (W_s), Length of Slot (L_s), Length of microstrip feed line (L_f) and width of microstripline (W_f). Certain dimension should be calculate as a reference before optimization was been done (Fig. 1).

In design flow part, the process of an antenna design has been discussed. To make sure this antenna design of annular ring with slot antenna running smoothly, equation of calculation and theoretical of antenna should be understand.

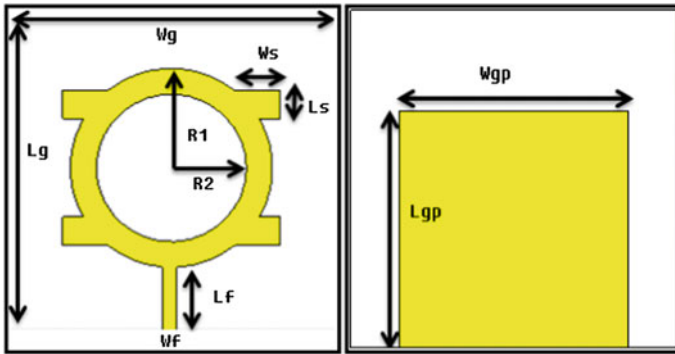


Fig. 1 Front (left) and back view (right) of an annular ring with slot antenna

$$a_e = \frac{1.841}{k_o \sqrt{\epsilon_r}}$$

$$a = \frac{a_e}{(1 + (2 \frac{h}{\pi} \epsilon_r a_e)) (\ln (\frac{\pi a_e h}{2}) + 1,7726)^{1/2}}$$

Fig. 2 Equation for calculating the outer radius of the ring

Before design the antenna, the important value is important that is used to calculate the radius of outer ring which is frequency resonant, substrate of height, substrate of dielectric constant, wavelength and permittivity.

First process is calculating all parameter by using formula given above, and then transfers the dimension value to the CST Software. For additional feed line on the patch, the assumption method will use for example the similar effect to ensure that the formula that has been used is correct. Then, dimension for every value was present. Besides that, the parameters value was also determined. Figure 2 shows that the equation has been used to calculated the outer radius of the ring, R2.

The antenna was simulated using CST Software. The proposed design has been optimized and the parameters are shown in Table 1. This antenna was fabricated on 1.6 mm FR4 substrate with dielectric constant of 4.4. The overall size of the antenna is 115, 115 and 1.6 mm for width, length and its thickness, respectively.

3 Parametric Study

This section is focusing on the performance of antenna by varying the parametric analysis such as width of slot, length of slot and radius of inner.

Table 1 Optimized parameters of the antenna

| Parameter | | Label | Gain Dimension (mm) |
|---------------|-----------------|----------|---------------------|
| Patch | Radius of outer | R1 | 35 |
| | Radius of inner | R2 | 26 |
| Feedline | Width | W_f | 5 |
| | Length | L_f | 22.5 |
| Slot | Width | W_s | 7 |
| | Length | L_s | 0.34 |
| Ground | Width | W_{gp} | 80 |
| | Length | L_{gp} | 80 |
| Substrate FR4 | Width | W_g | 114 |
| | Length | L_g | 114 |
| | Thickness | t | 0.035 |
| | Height | h | 1.6 |

Table 2 Effect of variation of width of slot

| Width of slot (mm) | Frequency resonant (GHz) | S11 (dB) | Gain (dBi) | Bandwidth (GHz) |
|--------------------|--------------------------|----------|------------|-----------------|
| 16.3 | 4.077 | -15.8274 | 2.825 | 0.1496 |
| 16.8 | 4.066 | -22.3012 | 4.878 | 0.21158 |
| 17.3 | 4.046 | -25.0536 | 5.595 | 0.24873 |
| 17.8 | 4.01 | -26.3538 | 6.309 | 0.11321 |
| 18.3 | 3.984 | -23.4935 | 6.529 | 0.10579 |
| 18.8 | 3.946 | -20.2350 | 6.981 | 0.10173 |
| 19.3 | 3.924 | -18.1549 | 7.266 | 0.099403 |

3.1 Effect of Variation of Width of Slot

Table 2 shows the results of variation of width of slots parametric study that the width of the slot parameters value of was changed from 16.3 until 19.3 mm. The table shows the width of slot affected so much in gain, S11 and bandwidth based on the overall changes. The increasing of width causes the frequency operation, S11 and bandwidth decrease except the gain of the antenna.

3.2 Effect of Variation of Length of Slot

Table 3 shows the result of the length of the slot value parameters are changed from 8.5 to 11.5 mm. The table shows that the length of slots affected so much in gain, frequency, S11 and bandwidth. When the length is increased, the bandwidth also increases but the frequency and gain decreased.

Table 3 Effect of variation of length of slot

| Length of slot (mm) | Frequency resonant (GHz) | S ₁₁ (dB) | Gain (dBi) | Bandwidth (GHz) |
|---------------------|--------------------------|----------------------|------------|-----------------|
| 8.5 | 4.028 | -13.6292 | 5.714 | 0.076524 |
| 9.0 | 4.018 | -16.8894 | 5.980 | 0.095495 |
| 9.5 | 4.028 | -29.7028 | 6.169 | 0.10349 |
| 10.0 | 4.01 | -26.3538 | 6.309 | 0.11321 |
| 10.5 | 4.008 | -34.1039 | 6.277 | 0.11747 |
| 11.0 | 4.004 | -46.6773 | 6.220 | 0.11894 |
| 11.5 | 3.998 | -32.8768 | 6.216 | 0.12041 |

Table 4 Effect of variation of radius of inner ring

| Radius of inner (mm) | Frequency resonant (GHz) | S ₁₁ (dB) | Gain (dBi) | Bandwidth (GHz) |
|----------------------|--------------------------|----------------------|------------|-----------------|
| 2.3 | 3.9682 | -18.4667 | 3.6857 | 0.0925 |
| 2.4 | 3.998 | -22.0306 | 2.5107 | 0.1019 |
| 2.5 | 4.004 | -23.8102 | 2.8952 | 0.1030 |
| 2.6 | 4.01 | -26.3538 | 2.7644 | 0.1125 |
| 2.7 | 4.006 | -18.3098 | 1.9302 | 0.2219 |
| 2.8 | 4.026 | -10.2610 | 0.2627 | 0.0351 |
| 2.9 | 3.934 | -6.5910 | 1.1189 | Out of range |

3.3 Effect of Variation of Radius of Inner Ring

The value parameters of the radius of inner are changed from 2.3 to 2.9 mm and the result was tabulated in Table 4. It can be seen that the increment in the radius has lowered down the gain and the reflection coefficient.

4 Result and Discussion

Figure 3 shows the prototype of the antenna and the result of the reflection coefficient and the radiation patterns are shown in Figs. 4, 5 and 6.

As shown in Fig. 4, it is clearly seen that there is a frequency shift between the simulated and measured result. The frequency from simulation at 4.01 GHz while from the measurement shows the frequency is at exactly 4 GHz. Due to inaccuracy in fabrication process, the size of the patch will differ from the actual size. This will definitely bring to the shifting in the operating frequency. The decrease in the length of the patches will increase the operating frequency and vice versa.

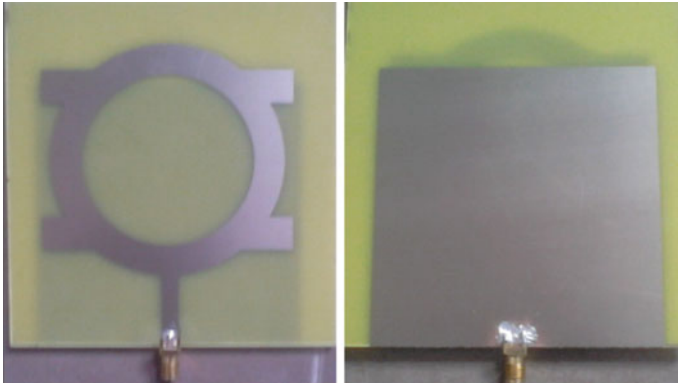


Fig. 3 Annular ring with slot after fabrication

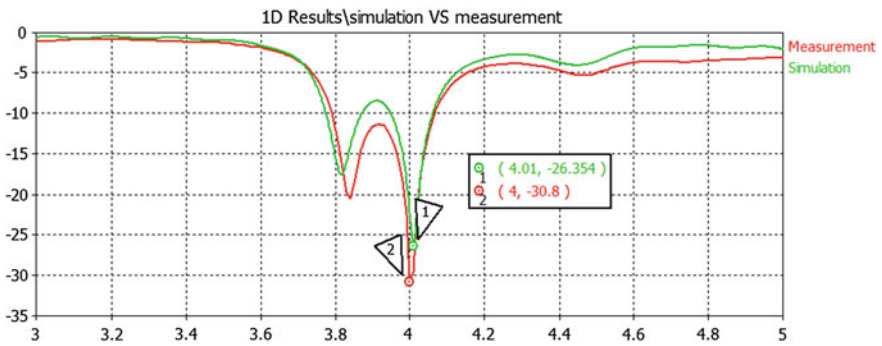


Fig. 4 Result of S11 between simulation and measurement

Figure 5 shows the value of the bandwidth between simulation and measurement result. Broadband of bandwidth can be considered as the frequency range, which the center frequency next to either, radiation efficiency of the beam and the acceptable value for those at the center frequency At the intersection of -10 dB S11 level to get the lower and upper frequency is 3.79 and 4.06 GHz respectively for measurement. Mean the bandwidth is 0.27 GHz. While the simulations at the intersection of -10 dB S11 level to get the lower and upper frequency are 3.94 and 4.06 GHz respectively which the bandwidth is 0.11 GHz. The comparison result between simulation and measurement much different because the other frequency shifting down below -10 dB. The different between simulation and measurement is 0.16 GHz.

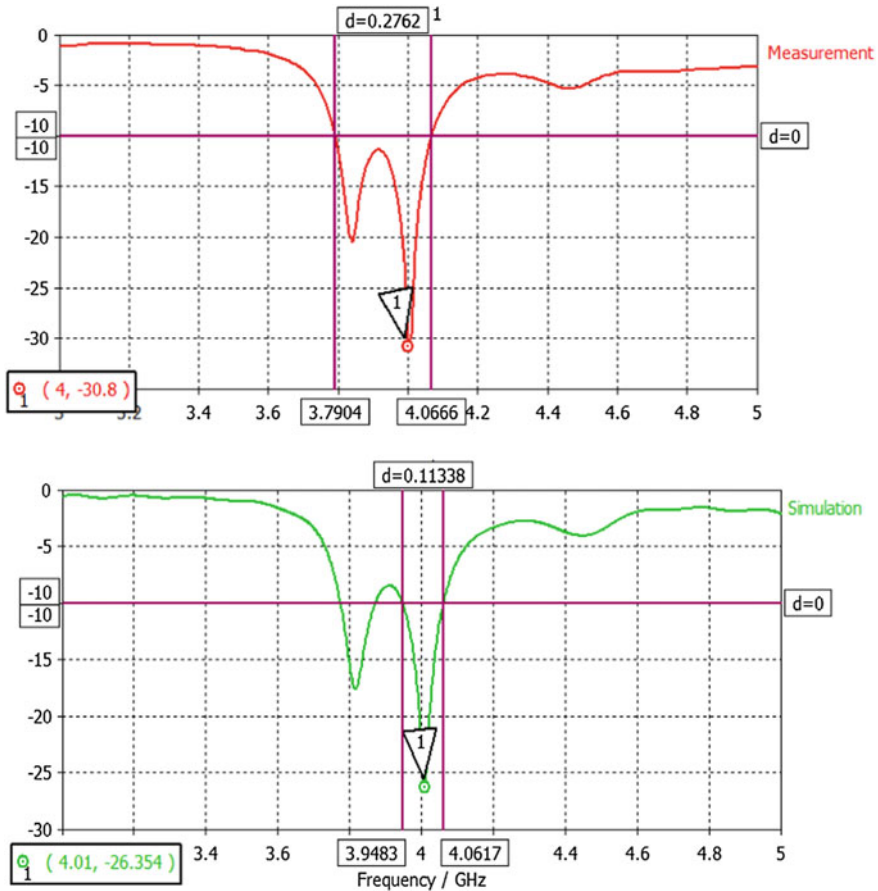


Fig. 5 Result of the bandwidth between simulation and measurement

Figure 6 shows that radiation pattern between simulation and measurement of fabrication in lab session. The radiation pattern of antenna is defined as a function of space coordinates for antenna which is mathematical function or a graphical representation of the radiation properties. Two basic causes of different result between simulation and measurement were determined. The first causes is calibrated setting is not perfect and loss of that are used in equation are not real. So, the measured gain is not accurate. The second causes is that the measured power level at the broadside angle is much more than the simulated one. It is obvious that more decrease at the broadside angle, the more increase on the gain of the antenna.

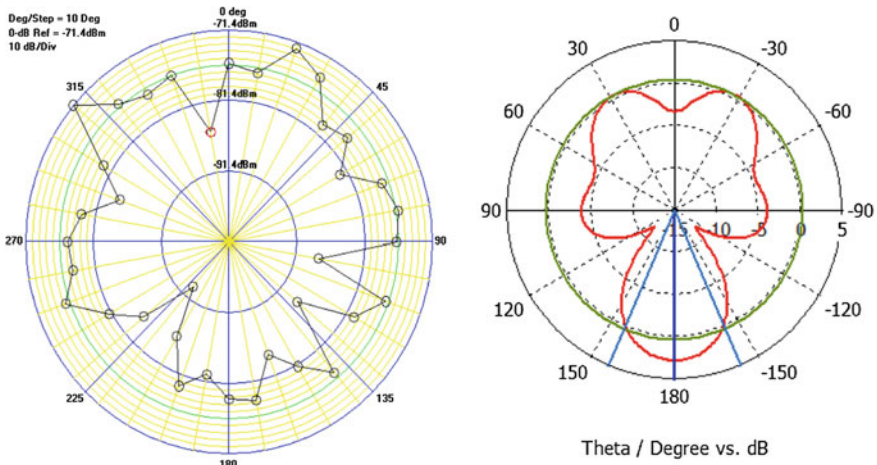


Fig. 6 Result of radiation pattern between simulation and measurement

5 Conclusion

This project is to design annular ring with slots patch antenna that operate at 4 GHz frequency by using FR4 substrate. This antenna design fabricated expected to get comparable or better performance to the basic antenna one. The basic microstrip antenna was design as a reference with a microstrip feed line as a feed. This project is divided into two main parts which is between simulation by using software and measurement of hardware after fabricate. The Annular Ring patch antenna can be used for future satellite downlink communication on frequency of the patch antenna. It may also be operate with other antenna based on the results of research. The size of Annular Ring with slots patch antenna turns out to be smaller than other patch antenna with the same frequency which to save the cost and space. As an overall conclusion, the planned has been done and the goals of this project also have been successfully and the performance of the antenna designed was achieved.

Acknowledgments First and foremost, the author would like to thank Universiti Teknikal Malaysia Melaka, Malaysia (UTeM) and Universiti Teknologi Malaysia for financial assistance under project grant FRGS(RACE)/2013/FKEKK/TK3/3 F00196 and Vot 00M22. Special dedication to kind-hearted project coordinating supervises lectures, student, parents, public and those involved directly and indirectly for their moral supports, contribution and cooperation in completing this paper.

References

1. Ibrahim, S.H.: Design and analysis considerations of 4 Ghz integrated antenna with negative resistance oscillator. **13**, 111–131 (2009)
2. Kumar, R., Dr. Dhukarya, D.C.: Design and analysis of circular ring microstrip antenna. **11**(1), Version 1.0 (2011)
3. Ganjehmarzy, R., Davoody, M.: Optimization of circular ring microstrip antenna using genetic algorithm (2008)
4. Chew, W.C.: A broad-band annular ring microstrip antenna. *IEEE Trans. Antennas Propag.* **AP-30**, 918–922 (1982)
5. Surekha, T.P., Ananthapadmanabha, T., Puttamadappa, C.: C-band VSAT data communication system and RF impairments. **270**, 64 (2007)
6. Bisht, N., Kumar, P.: A dual band fractal circular microstrip patch antenna for C-band applications. 12–16 Sept 2011

2 × 1 Circular Array Patch Antennas with Double Circular Slots for WLAN Application

Nik Muhammad Farid Nik Mohd Salleh, Mohd Fareq Abd Malek, Nornikman Hassan, Amier Hafizun Ab Rashid, Mohamad Zoinol Abidin Abd. Aziz, Mohd Khairulezmi Che Seman, Nornabila Md Nor, Saidatul Adawiyah Amiruddin, Badrul Hisham Ahmad, Ahmad Zaidi Abdullah and Nur Sabrina Md Noorpi

Abstract The purpose of this paper is to presents entire design of 2 × 1 circular array patch antenna for WLAN application of 2.4 GHz. Circular array with double circular slots microstrip antenna modeled due to the low profiles and easy to fabricate. The circuit was designed by using CST Microwave Studio for the entire dimension. The simulation results of the antenna are done to observe the return loss, radiation pattern, gain, directivity and bandwidth performance. This proposed

N.M.F.N.M. Salleh (✉) · N. Hassan · M.Z.A.A. Aziz · M.K.C. Seman · N. Md Nor
S.A. Amiruddin · B.H. Ahmad

Faculty of Electronics and Computer Engineering, Center for Telecommunication Research and Innovation, Universiti Teknikal Malaysia Melaka (UTeM), Melaka, Malaysia
e-mail: nikpayed@yahoo.com.my

N. Hassan
e-mail: nornikman84@yahoo.com

M.Z.A.A. Aziz
e-mail: mohamadzoinol@utem.edu.my

B.H. Ahmad
e-mail: badrullhisham@utem.edu.my

M.F.A. Malek · A.Z. Abdullah · N.S.M. Noorpi
School of Electrical Systems Engineering, Universiti Malaysia Perlis (UniMAP), Perlis, Malaysia
e-mail: mfareq@unimap.edu.my

A.Z. Abdullah
e-mail: zaidiabdullah@unimap.edu.my

N.S.M. Noorpi
e-mail: nursabriba@unimap.edu.my

A.H.A. Rashid
Jabatan Kejuruteraan Dan Kemahiran, Kolej Komuniti Segamat 2, Segamat, Johor, Malaysia
e-mail: amier.kk2@yahoo.com.my

circular array patch antenna has radiate -24.707 dB at resonant frequency of 2.40 GHz. The bandwidth of this antenna is 53 MHz while the gain is 8.521 dB. Two parametric studies on the effect of the two different circular radiuses (R_1 and R_2) are done in this work.

1 Introduction

Microstrip patch antenna is an antenna that can be installed or affixed on a flat surface printed circuit board (PCB). Basically the microstrip antenna is designed on a dielectric substrate using the same materials and lithographic processes used in making FR4 board. This microstrip patch antenna can be applied in many applications such as the wireless local area network (WLAN) [1–3], worldwide interoperability for microwave access (WiMAX) [4, 5] and other applications. Typical single-frequency microstrip antenna design will be studied before and by submitting slot in the patch, required a compact, multi-band and broadband to achieve. A good performance of antenna can be achieved with thick substrate which is better efficiency, large bandwidth, loosely radiation into space, but an expense big element in size. The antenna of bandwidth and gain will affect when change the size of microstrip antenna. Overall for this project, the antenna theory is introduced to design degree of freedom of the antenna which is radius. The antenna is designed for 2.4 GHz operating frequency and performed in order to improve the antenna gain the return loss by using quarter wave matching.

There are several works on the circular shaped patch antenna. In [6], the author designs the circular shaped patch antenna to create the circular polarized antenna at 2.4 GHz. The other works on circular shaped antenna is in these papers [7–11].

2 Antenna Design

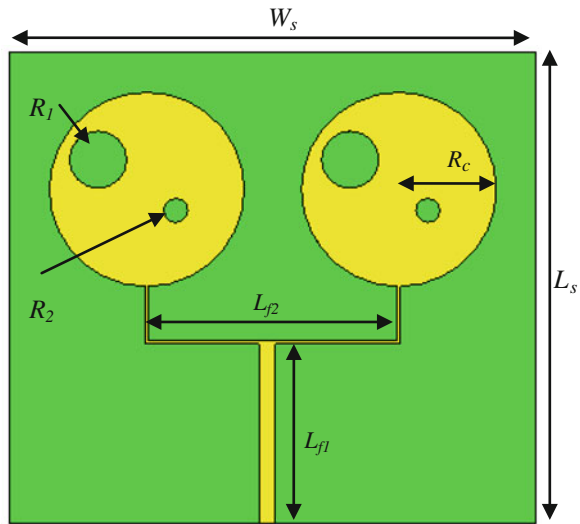
The work starting with designing the circular array patch antenna with double slots. Figure 1 shows the front view of the 2×1 circular patch antennas with double circular slots. This antenna is using FR-4 board with dielectric constant of 3.2 and thickness of 1.6 mm. The dimension of the substrate is 92 mm width \times 82.4 mm length. There is a large circle and a small slot with different sizes which is R_1 and R_2 with 50 ohm feeding line that connected with the SMA connector. Two slots with radius of 5.0 and 2.1 mm are designed for control the radiation characteristic. The main function of the slots is to increase the gain and also the return loss. In this array 2×1 antenna the fed is using a quarter-wavelength transmission line. Table 1 shows the dimension of the circular array patch antenna with double circular slots (Fig. 1).

Two different parametric studies are done in this work. The advantages of the circular patch shaped are only containing one degree of freedom. That mean, it

Table 1 2 × 1 circular array patch antenna with double circular slots

| Parameter | Label | Dimension (mm) |
|------------------------|----------|----------------|
| Substrate width | W_s | 92.0 |
| Substrate length | L_s | 82.4 |
| Circular radius | R_c | 29.8 |
| Feedline length 1 | L_{f1} | 31.4 |
| Feedline length 2 | L_{f2} | 43.4 |
| Circular slot radius 1 | R_1 | 5.2 |
| Circular slot radius 2 | R_2 | 3.1 |

Fig. 1 2 × 1 circular array patch antenna with double circular slots, **a** front view, **b** back view



doesn't have two dimension parameters can be adjust like rectangular or triangular patch shaped. So, for parametric study the parameter that we have adjusted only the radius compare to the rectangular has width and length of patch. Further enhanced by adjusting the Radius of slot R_1 and the Radius of slot R_2 are optimized value. For each parameter of the antenna, five values are chosen in order to observe the antenna simulation performance. After parametric study done on R_1 and R_2 , the optimize dimension is 5.2 and 3.1 mm, respectively.

3 Result

This section will analysis all the simulation results by CST Microwave Studio. The first parameter is the return loss, shown in Fig. 2. The resonant frequency for the proposed antenna is 2.4 GHz at -24.707 dB. The bandwidth for this proposed antenna is 52 MHz, in the frequency range between 2.375 and 2.427 GHz.

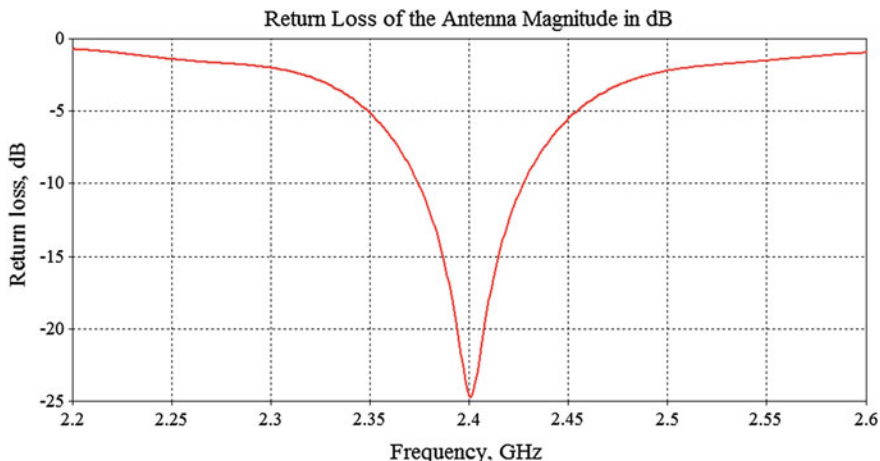


Fig. 2 Return loss performance of the 2×1 circular array patch antenna with double circular slots

Figure 3 shows the radiation pattern of the 2×1 circular array patch antenna with double circular slots at different phase. For $\phi = 0^\circ$, the radiation pattern shown the circular shaped at main lobe with smaller back lobe. For $\phi = 90^\circ$, the radiation pattern did not shows the sharp circular shaped.

Figure 4 shows the surface current at current of the 2×1 circular array patch antenna with double circular slots at different phase, covered from 0° to 180° . At 450 and 900, the current flows are concentrating at the both circular patch with a little current flow at feedline.qa

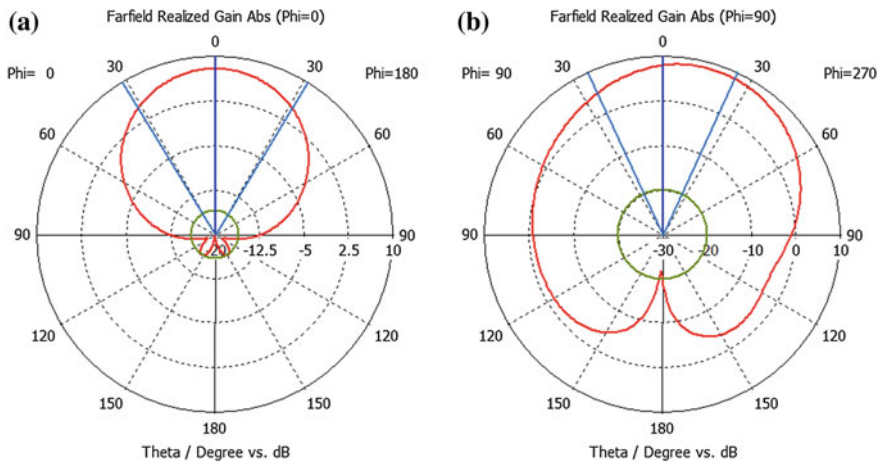


Fig. 3 Radiation pattern of the 2×1 circular array patch antenna with double circular slots at different phase, a 0° , b 90°

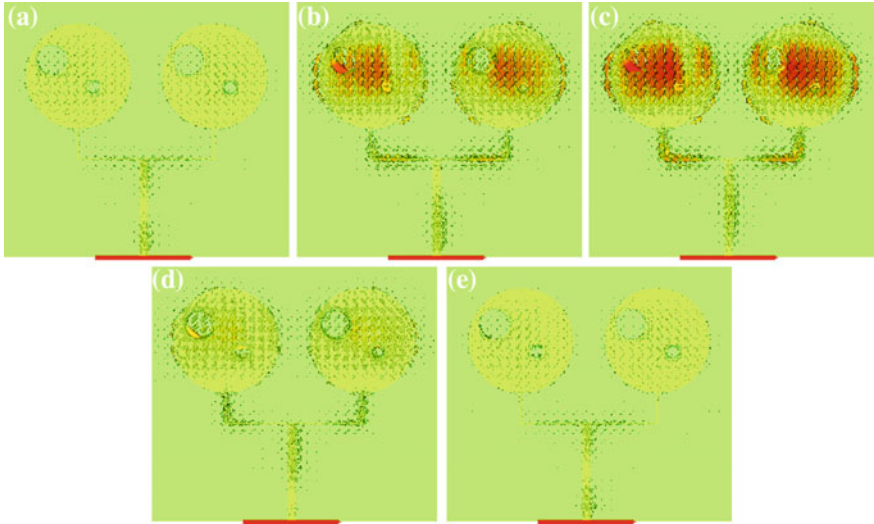


Fig. 4 Surface current of the 2 × 1 circular array patch antenna with double circular slots at different phase, **a** 0°, **b** 45°, **c** 90°, **d** 135°, **e** 180°

Figure 5 shows the parametric study on the different radius of R_l of the 2 × 1 circular array patch antenna with double circular slots. The best return loss occurs when $R_l = 6.2$ mm satisfy with 29.214 dB. The resonant frequency shifted to the left when varying the R_l dimension from 5.2 to 4.2 mm. The bandwidth are didn't change when varying the radius of R_l . Table 2 shows the several parameter of the

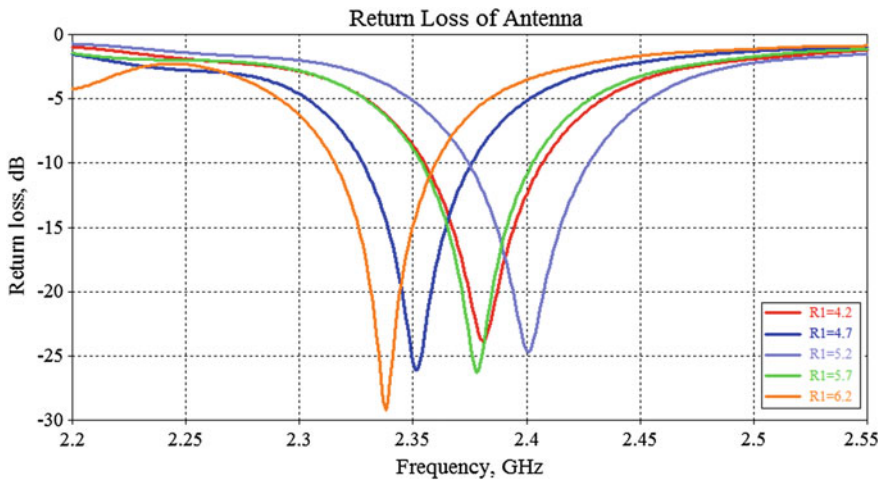


Fig. 5 Return loss performance of the 2 × 1 circular array patch antenna with double circular slots with different radius dimension of R_l

Table 2 Effect of R_1 changes dimension on 2×1 circular array patch antenna with double circular slots

| R_1 dimension (mm) | Resonant frequency (GHz) | Return loss (dB) | Bandwidth (MHz) |
|----------------------|--------------------------|------------------|-----------------|
| 4.2 | 2.381 | -23.803 | 49, 2.359–2.408 |
| 4.7 | 2.352 | -26.099 | 46, 2.328–2.374 |
| 5.2 | 2.400 | -24.707 | 52, 2.375–2.427 |
| 5.7 | 2.381 | -26.277 | 49, 2.354–2.403 |
| 6.2 | 2.378 | -29.214 | 44, 2.316–2.360 |

proposed antenna. The parameters are resonant frequency, return loss and bandwidth. All bandwidth are shown in the frequency range between 50 and 52 MHz.

Figure 6 shows the parametric study on the different radius of R_2 of the 2×1 circular array patch antenna with double circular slots. Based on the graph, the changes of the R_2 dimension can effect the resonant frequency and return loss, but didn't change the bandwidth value. Table 3 shows the varying value of the radius R_2 with it several parameters. When the R_2 dimension is 2.1 mm the resonant frequency shows at 2.367 GHz with return loss of -18.885 dB. This shows that the return loss and resonant frequency is decrease compare with the $R_2 = 3.1$ mm.

This proposed circular patch antenna capability to integrate with other communication devices such as amplifier, RF switch, RF filter or mixer [12–21]. The several devices potentially to use in complete RF communication system.

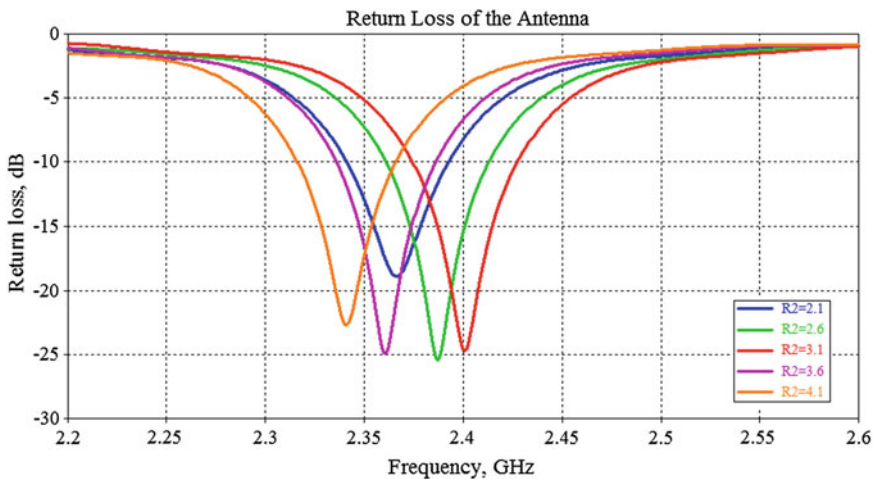


Fig. 6 Return loss performance of the 2×1 circular array patch antenna with double circular slots with different radius dimension of R_2

Table 3 Effect of R_2 changes dimension on 2 × 1 circular array patch antenna with double circular slots

| R_2 dimension (mm) | Resonant frequency (GHz) | Return loss (dB) | Bandwidth (MHz) |
|----------------------|--------------------------|------------------|-----------------|
| 2.1 | 2.367 | -18.885 | 51, 2.342–2.393 |
| 2.6 | 2.387 | -25.440 | 52, 2.361–2.413 |
| 3.1 | 2.400 | -24.707 | 52, 2.375–2.427 |
| 3.6 | 2.361 | -24.942 | 50, 2.336–2.386 |
| 4.1 | 2.341 | -22.716 | 50, 2.317–2.367 |

4 Conclusions

The proposed 2 × 1 circular array patch antenna with double circular slots are successfully presented in this paper. The circular array patch technique is effect to increase the gain of the antenna compare with the single circular patch antenna. The parametric study of the different dimension for R_1 and R_2 are also shown in this paper. The right dimension of these two radiuses can effect the location of the resonant frequency of the antenna. This antenna is successfully can be apply at 2.40 GHz for WLAN applications.

References

- Hui, L., Yin, Y.-Z., Fan, S.-T., Yang, Y.: A circular slot antenna with a pair of embedded L-strips for WLAN applications. In: 2011 IEEE 4th international symposium on microwave, antenna, propagation, and EMC technologies for wireless communications (MAPE), pp. 98–101 (2011)
- Sankaralingam, S., Gupta, B.: A circular disk microstrip WLAN antenna for wearable applications. In: 2009 annual IEEE India conference (INDICON), pp. 1–4 (2009)
- Pan, C.-Y., Tu, W.-L., Duan, J.-H., Jan, J.-Y.: Printed i-shaped monopole antenna with circular conductor-backed plane for WLAN operations. In: 2009 Asia Pacific microwave conference (APMC 2009), pp. 2475–2477 (2009)
- Jamlos, M.F., Rahim, R.A., Othman, H., Jusoh, M., Ahmad, Z.A., Romli, M.A., Salimi, M.N.: Dual-frequencies of co-polarization circular antenna for GPS and WiMAX application with corporate feeding technique. In: 2012 IEEE symposium on wireless technology and applications (ISWTA), pp. 134–137 (2012)
- Hazila, O., Aljunid, S.A., Malek, F., Sahadah, A.: Performance comparison between rectangular and circular patch antenna array. In: 2010 IEEE student conference on research and development (SCORED), pp. 47–51 (2010)
- Aziz, M.Z.A.A., Mufit, N.A.D.A., Suaidi, M.K., Salleh, A., Misran, M.H., Rahim, M.K.A.: 2012 6th European conference on antennas and propagation (EUCAP), pp. 907–911 (2012)
- Smida, A., Ghayoula, R., Troudi, A., Trabelsi, H., Gharsallah, A.: Beam synthesis of phased circular antenna arrays using Taguchi method. In: 2012 9th international conference on communications (COMM), pp. 155–158 (2012)
- Sharma, S., Savita, M.K.: Multi band circular antenna for ultrawideband wireless systems. In: 2012 Nirma University international conference on engineering (NUIcONE), pp. 1–3 (2012)

9. Zani, M.Z.M., Jusoh, M.H., Sulaiman, A.A., Baba, N.H., Awang, R.A., Ain, M.F.: Circular patch antenna on metamaterial. In: 2010 international conference on electronic devices, systems and applications (ICEDSA), pp. 313–316 (2010)
10. Islam, M.M., Islam, M.T., Faruque, M.R.I.: Bandwidth enhancement of a microstrip antenna for X-band applications. *ARPN J. Eng. Appl. Sci.* **8**(8) (2013)
11. Ezanuddin, A.A.M., Malek, M.F., Soh, P.J., Ahmad, R.B., Metamaterial entrenched circular microstrip antenna for Malaysia HAPS. In: 2010 Asia-Pacific symposium on electromagnetic compatibility (APEMC), pp. 102–105 (2010)
12. Othman, M.A., Bakar, S.A.A., Aziz, M.Z.A.A., Sinnappa, M., Ismail, M.M., Sulaiman, H.A., Misran, M.H., Meor Said, M.A., Ramlee, R.A.: An Analysis of UWB double sided circular disc bow-tie antenna. In: 2013 international conference on information communication and embedded systems (ICICES), pp. 584–587 (2013)
13. Zakaria, Z., Mutalib, M. A., Jusoff, K., Isa, M.S.M., Othman, M.A., Ahmad, B.H., Abd Aziz, M.Z.A.A, Suhaimi S.: Current developments of microwave filters for wideband applications. *World Appl. Sci. J.* **21**, 31-40 (2013)
14. Zakaria, Z., Yik, S.W., Aziz, M.Z.A.A., Mutalib, M.A.: A new class of dual-mode substrate integrated waveguide (SIW) filter with two metalized posts. *Aust. J. Basic Appl. Sci.* **7**(11), 170–177 (2013)
15. Shairi, N.A., Ahmad, B.H., Khang A.C.Z.: Design and analysis of broadband high isolation of discrete packaged PIN diode SPDT switch for wireless data communication. In: 2011 IEEE international RF and microwave conference (RFM), pp. 91–94 (2011)
16. Misran, M.H., Meor Said, M.A., Othman, M.A., Ismail, M.M., Sulaiman, H.A., Cheng, K.G.: Design of low noise amplifier using feedback and balanced technique for WLAN application. *Proc. Eng.* **53**, 323–331 (2013)
17. Md Shukor, M., Aziz, M.Z.A., Ahmad, B.H., Suaidi, M.K., Johar, M.F., Salleh, S.N., Azmin, F.A., Malek F.: Design and characteristic impedance modelling of dual band frequency selective surface (FSS) on hybrid material. In: 2014 8th European conference on antennas and propagation (EuCAP), pp. 1974–1978 (2014)
18. Abdul Hadi, M.H., Ahmad, B.H., Wong, P.W., Shairi N.A.: An overview of isolation improvement techniques in RF switch. *ARPN J. Eng. Appl. Sci.* **9**(3), 342–348 (2014)
19. Zakaria, Z., Sam, W.Y., D.M.A. Azam, Mutalib, M.A., Rahman, N.A., Yunus M.M.: Analysis of compact quadruple-mode antenna with wide bandwidth. In: 2014 8th European conference on antennas and propagation (EuCAP), pp. 2020–2024 (2014)
20. Othman, A.R., Ibrahim, I.M., Selamat, M., Samingan, M.S.A.S., Aziz, A., Halim H.C.: 5.75 GHz microstrip bandpass filter for ISM band. In: 2007 Asia-Pacific conference on applied electromagnetics (APACE 2007), pp. 1–5 (2007)
21. Zakaria, Z., Fadzil, M.F.M., Othman, A.R., Salleh, A., Isa, A.A.M., Haron, N.Z.: Development of wideband power amplifier for RF/microwave front-end subsystem. *J. Teknol.* **68**(3), 105–112 (2014)

Circular Polarized Patch Antenna for 1.8 and 2.4 GHz Applications

Muhammad Syafiq Noor Azizi, Mohd Fareq Abd Malek, Nornikman Hassan, Mohamad Zoinol Abidin Abd. Aziz, Mohd Khairy Ismail, Nur Azimah Basir, Muhamad Faisal Iswandi, Nurul Norhasmazuani, Badrul Hisham Ahmad, Nurhakimah Mohd Mukhtar and Mohd Asri Jusoh

Abstract This paper presented a patch circular polarized antenna for GSM technology at 1.8 GHz and WLAN technology at 2.4 GHz. A traveling wave microstrip array antenna consisting of square truncated patch operated as circular polarized has been designed, fabricated and measured. The inter element spacing; length and width of the square and circular patches of the array antenna were optimized by successive simulations using the CST software. This antenna had radiated at 1.8 and 2.4 GHz of resonant frequency with -38.563 and -24.967 dB of return loss respectively. The axial ratio for RHS circular polarized is $0.95 < 3$ dB at 2.4 GHz.

M.S.N. Azizi · N. Hassan · M.Z.A.A. Aziz (✉) · M.K. Ismail · N.A. Basir · M.F. Iswandi
N. Norhasmazuani · B.H. Ahmad
Faculty of Electronics and Computer Engineering, Center for Telecommunication Research
and Innovation, Universiti Teknikal Malaysia Melaka (UTeM), Melaka, Malaysia
e-mail: mohamadzoinol@utem.edu.my

M.S.N. Azizi
e-mail: syafiqnoorazizi@yahoo.com

N. Hassan
e-mail: nornikman84@yahoo.com

M.K. Ismail
e-mail: m021310033@student.edu.my

B.H. Ahmad
e-mail: badrulhisham@utem.edu.my

M.F.A. Malek · N.M. Mukhtar · M.A. Jusoh
School of Electrical Systems Engineering, Universiti Malaysia Perlis (UniMAP),
Perlis, Malaysia
e-mail: mfareq@unimap.edu.my

N.M. Mukhtar
e-mail: nurhakimah@unimap.edu.my

M.A. Jusoh
e-mail: asrijusoh@unimap.edu.my

1 Introduction

Microstrip patch antenna is an antenna that can be installed or affixed on a flat surface printed circuit board (PCB). Basically the microstrip antenna is designed on a dielectric substrate using the same materials and lithographic processes used in making FR-4 board. The microstrip patch antenna usually used in Global System for Mobile Communications (GSM) [1], wireless local area network (WLAN) [2, 3], satellite and Worldwide Interoperability for Microwave Access (WiMAX) [4]. Typical single-frequency microstrip antenna design will be studied before and by submitting slot in the patch, required a compact, multi-band and broadband to achieve. The antenna of bandwidth and gain will affect when change the size of microstrip antenna. The antenna is designed for 1.8 and 2.4 GHz operating frequency and performed in order to improve the antenna gain the return loss by using quarter wave matching. This project will design for lower cost and compact size.

The circular polarized microstrip antennas are one popular types of antenna. There are two variations, namely right hand polarized (RHP) and left hand polarized (LHP). In addition, circular polarization is important due to the regardless of the receiver orientation. It effects the antenna to receiving the signal at any direction. This also is because of the resulting wave that brought the angular variation. The circular polarization exists when there are two signals that have equal amplitude of 90° phase shifted. The axial ratio value of the antenna can be used to determine the best performance of the circular polarization. The axial ratio of the circular polarized must be less than 3 dB. The examples of the circular polarized are shown in this several papers [5–8]. The popular techniques to create the circular polarized is using truncated corner [9, 10].

For the present and future communications systems, one most important application is designing of microstrip antenna arrays which are attractive candidates for adaptive. The array antenna is capable to increase the gain performance of the antenna.

2 Antenna Design

The process of designing the antenna is majorly done by calculation and parametric study of the dimension. The substrate dimension is 147.25 mm length \times 147.25 mm width. The dielectric constant for the substrate is 4.4 and loss tangent is 0.0018. The targeting frequency for this proposed antenna is at 2.4 GHz. Figure 1 shows the of circular polarized patch antenna.

It has four truncated patch that connecting using the strip line with impedance matching calculation. The whole square along with truncated patch to act as right hand polarized (RHP). Table 1 shows the dimension of the proposed antenna.

Fig. 1 Plan view of circular polarized patch antenna with dimension and impedance matching

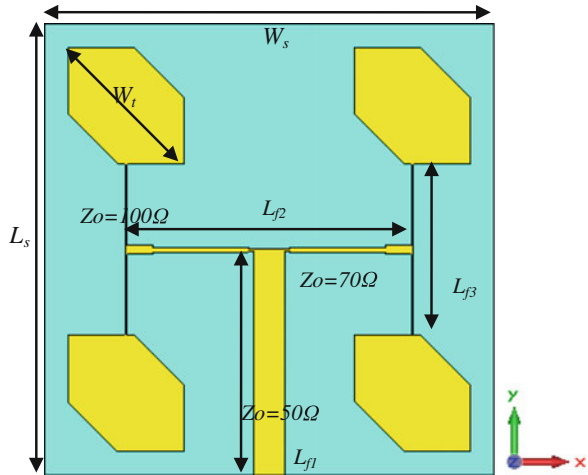


Table 1 2×1 circular array patch antenna with double circular slots

| Parameter | Label | Dimension (mm) |
|-----------------------|-------|----------------|
| Substrate width | W_s | 147.25 |
| Substrate length | L_s | 147.25 |
| Truncated patch width | R_c | 53.74 |
| Substrate thickness | T_s | 1.6 |
| Copper thickness | T_c | 0.035 |

Usually for quarter wave matching there have few values of resistance. The resistance depends on value of wavelength in matching such as $\lambda/4$ and $\lambda/8$. The width at $Z_0 = 50 \Omega$ is 3.06 mm, $Z_0 = 70 \Omega$ is 1.65 mm while $Z_0 = 100 \Omega$ is 0.71 mm.

3 Result

This section wills analysis all the results during simulation such as simulation by CST Microwave Studio. Figure 2 shows the return loss result for circular polarized patch antenna. From the graph, it radiate at two different resonant frequencies at 1.795 and 2.404 GHz with -38.563 and -24.967 dB, respectively. The bandwidth of this antenna is 52 MHz at first resonant frequency and 92 MHz ant second resonant frequency.

Figure 3 shows the surface current for circular polarized patch antenna at two different resonant frequencies of 1.795 and 2.404 GHz. Four different phases are considered to see the different of the surface current flow, consist from 0° , 45° , 90° , and 180° . It shows that the surface current are concentrate at the feedline for first resonant frequency while concentrate at truncated patch for the second resonant

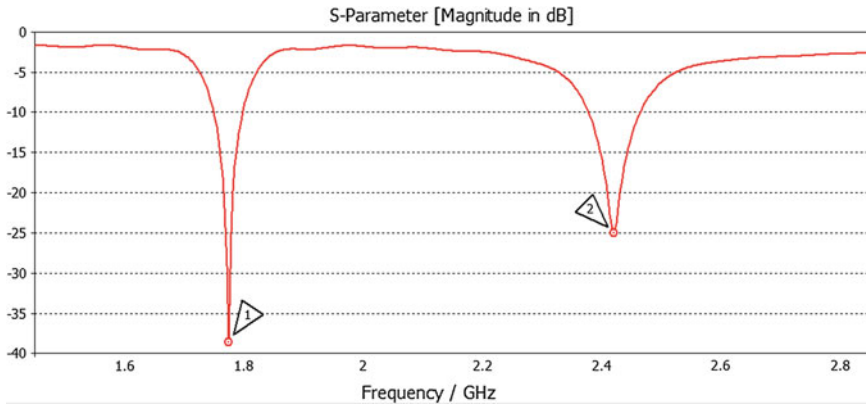


Fig. 2 Return loss performance of the circular polarized patch antenna

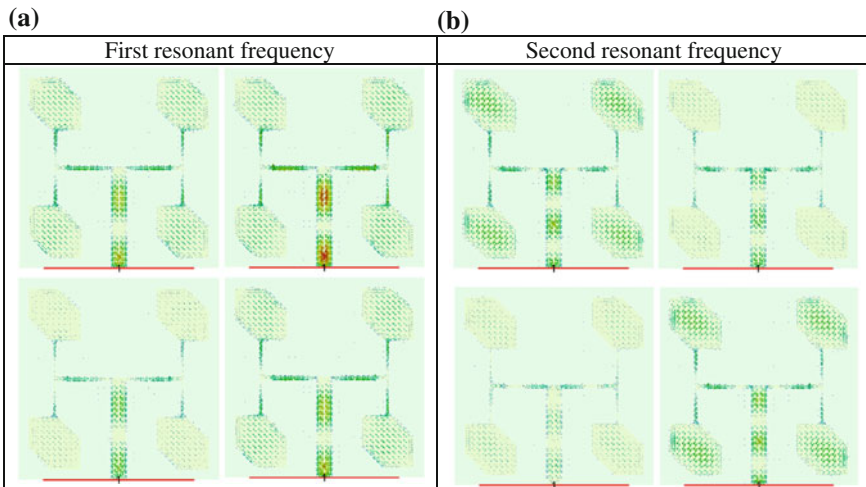


Fig. 3 Surface current of circular polarized patch antenna at different phase of 0° , 45° , 90° and 180° . **a** at the first resonant frequency of 1.795 GHz, **b** at the second resonant frequency of 2.404 GHz

frequency. Figure 4 shows the 3D radiation pattern of the proposed antenna. The main lobe shows that the signal radiate at the upper part of the patch.

Figure 5 shows the Radiation pattern of circular polarized patch antenna different phase of $\phi = 0^\circ$ and $\phi = 90^\circ$. For first resonant frequency at 1.795 GHz, the radiation pattern of this antenna is circle shaped while the second resonant frequency at 2.404 GHz is circular butterfly-liked shaped. Figure 6 shows the maximum gain performance over frequency for circular polarized patch antenna. The maximum gain at 1.8 and 2.4 GHz are 0.67 and 5.66 dB, respectively.

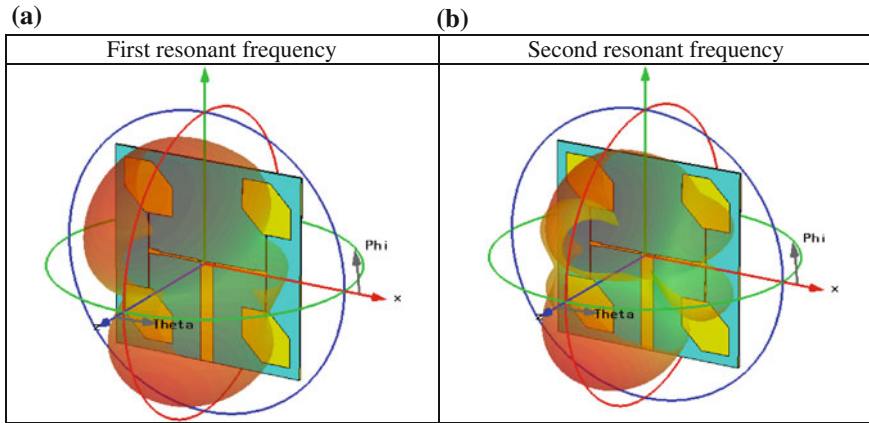


Fig. 4 3D radiation pattern of circular polarized patch antenna, **a** at the first resonant frequency of 1.795 GHz, **b** at the second resonant frequency of 2.404 GHz

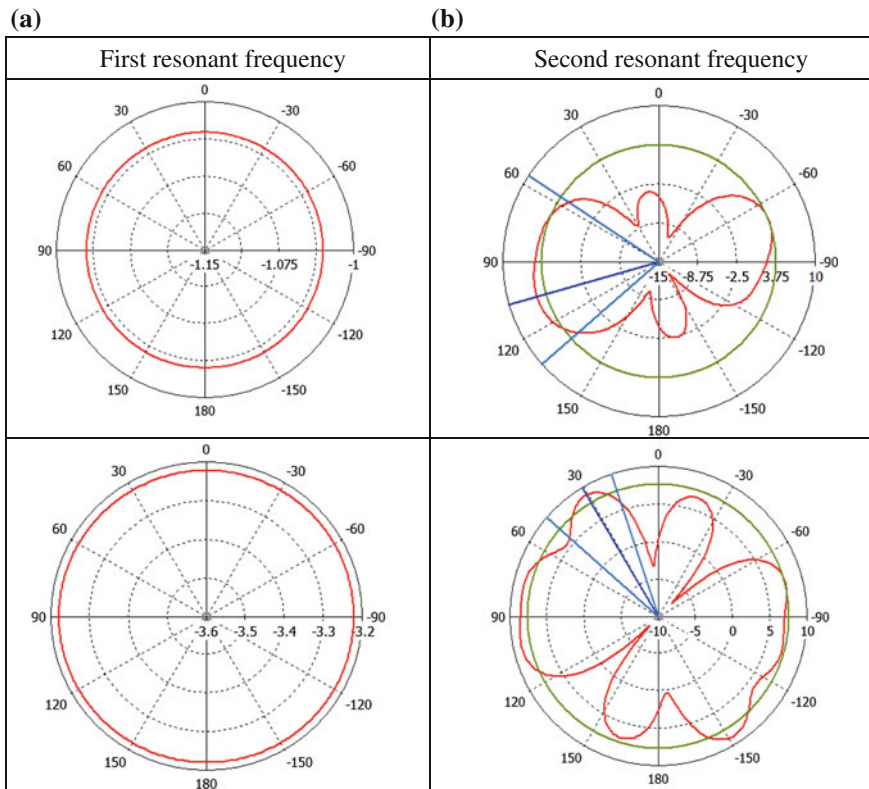


Fig. 5 Radiation pattern of circular polarized patch antenna different phase of $\phi = 0^\circ$ and $\phi = 90^\circ$, **a** at the first resonant frequency of 1.795 GHz, **b** at the second resonant frequency of 2.404 GHz

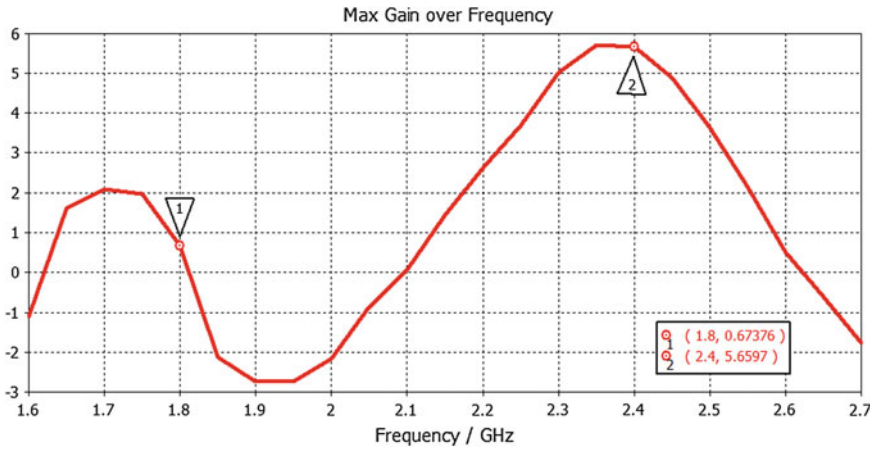


Fig. 6 The maximum gain performance over frequency for circular polarized patch antenna design

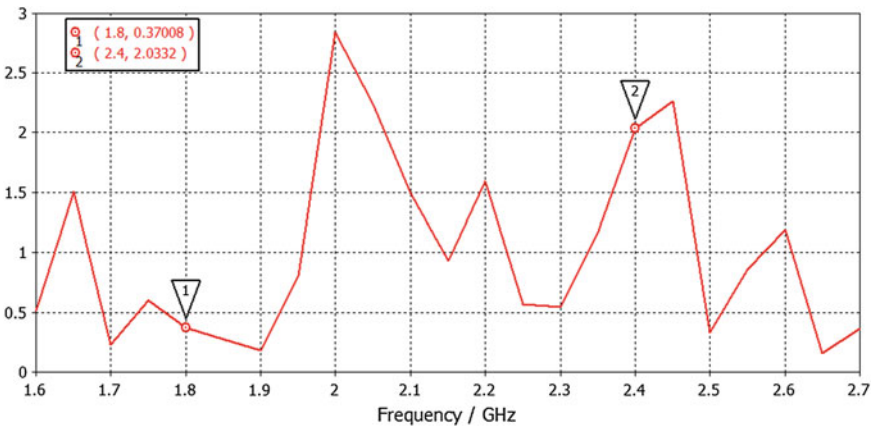


Fig. 7 The axial performance ratio performance over frequency for circular polarized patch antenna design

Figure 7 shows the axial ratio of circular polarized patch antenna design. It shows that the axial ratios at two different resonant frequencies are 0.37 and 2.03. It's also accepted the requirement when all frequency range from 1.6 to 2.7 GHz shows the axial ration less than 3.00.

This proposed circular polarized patch antenna design has potentially to combine several RF transmitter and RF receiver device to create the wireless local area network front-end system. The example potential RF devices are amplifier, switch, oscillator and filter [11–18].

4 Conclusions

The proposed circular polarized patch antennas that operate at dual frequencies are successfully presented in this paper. In this work, the truncated patch can effect the axial ratio value to the patch antenna. At resonant frequencies at 1.8 and 2.4 GHz, the result of return loss and gain of the antenna are accepted. This antenna potentially to use in two different applications of GSM and WLAN/WiFi applications.

References

1. Zakaria, Z., Zainuddin, N.A., Abd Aziz, M.Z.A., Husain, M.N., Mutalib, M.A.: Dual-band monopole antenna for energy harvesting system. In: 2013 IEEE symposium on wireless technology and applications (ISWTA), pp. 225–229
2. Zakaria, Z., Sam, W.Y., Azam, D.M.A., Mutalib, M.A., Rahman, N.A., Yunus, M.M.: Analysis of compact quadruple-mode antenna with wide bandwidth. In: 2014 8th European conference on antennas and propagation (EuCAP), pp. 2020–2024
3. Ramli, M.H., Abd Aziz, M.Z.A., Othman, M.A., Dahalan, A.H.: Dual band monopole antenna for wireless communication system. In: 2014 International symposium on technology management and emerging technologies (ISTMET), pp. 521–523
4. Jusoh, M., Jamlos, M.F., Kamarudin, M.R., Salimi, M.N., Malek, F., Jais, M.I.: A beam steering patch array antenna for WiMAX application. In: 2013 7th European conference on antennas and propagation (EuCAP), pp. 924–927
5. Aziz, M.Z.A.A., Mufit, N.A.D.A., Suaidi, M.K., Salleh, A., Misran, M.H., Rahim, M.K.A.: Study on microstrip X-linear polarized and X-circular polarized antenna. In: 2012 6th European conference on antennas and propagation (EUCAP), pp. 907–911
6. Aziz, M.Z.A.A., Mufit, N.A.A., Suaidi, M.K., Othman, M.A., Johar, M.F., Rahim, M.K.A.: Investigation of single and two notch on circular polarized patch antenna. In: 2012 International symposium on telecommunication technologies (ISTT), pp. 16–22
7. Prajapati, P.R., Murthy, G.G.K., Patnaik, A., Kartikeyan, M.V.: Design of compact circular disc circularly polarized antenna with koch curve fractal defected ground structure. In: 2014 XXXIth URSI general assembly and scientific symposium (URSI GASS), pp. 1–4
8. Khalily, M., Kamarudin, M.R., Mokayef, M., Jamaluddin, M.H.: Omnidirectional circularly polarized dielectric resonator antenna for 5.2-GHz WLAN applications. In: IEEE antennas and wireless propagation letters, pp. 443–446
9. Yahya, M., Awang, Z.: Cross polarization ratio analysis of circular polarized patch antenna. In: 2010 international conference on electromagnetics in advanced applications (ICEAA), pp. 442–445
10. Sabran, M.I., Rahim, S.K.A., Rani, M.S.A., Nor, M.Z.M.: A single band dual-fed circular polarization microstrip antenna for RFID application. In: 2011 IEEE international RF and microwave conference (RFM), pp. 137–140
11. Zakaria, Z., Mutalib, M.A., Jusoff, K., Isa, M.S.M., Othman, M.A., Ahmad, B.H., Abd Aziz, M.Z.A.A., Suhaimi, S.: Current developments of microwave filters for wideband applications. *World Appl. Sci. J.* **21**, 31–40 (2013)
12. Abdul Hadi, M.H., Ahmad, B.H., Wong, P.W., Shairi N.A.: An overview of isolation improvement techniques in RF switch. *ARPN J. Eng. Appl. Sci.* **9**(3), 342–348 (2014)

13. Misran, M.H., Meor Said, M.A., Othman, M.A., Ismail, M.M., Sulaiman, H.A., Cheng, K.G.: Design of low noise amplifier using feedback and balanced technique for WLAN application. *Proc. Eng.* **53**, 323–331 (2013)
14. Shairi, N.A., Ahmad, B.H., Khang A.C.Z.: Design and analysis of broadband high isolation of discrete packaged PIN diode SPDT switch for wireless data communication. In: 2011 IEEE international RF and microwave conference (RFM), pp. 91–94 (2011)
15. Zakaria, Z., Fadzil, M.F.M., Othman, A.R., Salleh, A., Isa, A.A.M., Haron, N.Z.: Development of wideband power amplifier for RF/microwave front-end subsystem. *J. Teknol.* **68**(3), 105–112 (2014)
16. Ja'afar, A.S., Hashim, N.M.Z., Isa, A.A.M., Ali, N.A., Darsono, A.M.: Analysis of indoor location and positioning via Wi-Fi signals at FKEKK, UTeM. *Int. J. Eng. Technol.* **5**(4), 3570–3579 (2013)
17. Ibrahim, A.B., Othman, A.R., Husain, M.N., Johal, M.S.: *Int. J. Comput. Theory Eng.* **4**(1), 93–97 (2012)
18. Hadi, M.H., Ahmad, B.H., Shairi, N.A., Wong, P.W.: Effect of a discrete PIN diode on defected ground structure. In: 2013 IEEE symposium on wireless technology and applications (ISWTA), pp. 333–337 (2013)

Short-Term Non-ionizing 2.45 GHz WBAN RF Exposure Does not Affect Human Physiological Measures and Cognitive Performance Exposed by Wearable Textile Monopole Antenna

Hasliza A. Rahim, Fareq Malek, Ping Jack Soh,
Fairul Afzal Ahmad Fuad, Che Muhammad Nor Che Isa,
Nurbaizatul Badrul Hisham, Noor Anida Abu Talib
and Farrah Salwani Abdullah

Abstract This paper presents a novel study of evaluating non-ionizing effect of 2.45 GHz Wireless Body Area Networks (WBAN) radiofrequency (RF) electromagnetic fields (EMF) exposure on human physiological parameters and cognitive performance. The study aims to test the hypothesis whether exposure of 2.45 GHz WBAN radio electromagnetic fields may affect physiological parameters and cognitive performance of human. Twenty healthy volunteers are involved in the test

H.A. Rahim (✉) · P.J. Soh · F.A.A. Fuad · C.M.N. Che Isa · N.B. Hisham
School of Computer and Communication Engineering, Universiti Malaysia Perlis, Pauh
Putra Campus, 02000 Arau, Perlis, Malaysia
e-mail: haslizarahim@unimap.edu.my

P.J. Soh
e-mail: pjsoh@unimap.edu.my

F.A.A. Fuad
e-mail: fairul@unimap.edu.my

C.M.N. Che Isa
e-mail: cmnor@unimap.edu.my

N.B. Hisham
e-mail: nurbaizatul@yahoo.com

F. Malek · N.A.A. Talib · F.S. Abdullah
School of Electrical System Engineering, Universiti Malaysia Perlis, Pauh Putra Campus,
Pauh Putra Campus, 02000 Arau, Perlis, Malaysia
e-mail: mfareq@unimap.edu.my

N.A.A. Talib
e-mail: anidatalib@unimap.edu.my

F.S. Abdullah
e-mail: farrahsalwani@unimap.edu.my

and exposed to 2.45 GHz WBAN RF radiation, emitted by a planar textile monopole antenna. Physiological measures of body temperature, systolic blood pressure, diastolic blood pressure and heart rate are obtained, along with cognitive performance outcomes. Results indicated that no significant difference is observed in any of the three sessions (pre, exposure and post) for all physiological parameters, $p > 0.05$. Insufficient evidence is found to indicate a difference in mean of all cognitive tests between WBAN RF and Sham exposure sessions, p 's > 0.05 .

1 Introduction

Textile antennas have received a lot of attention due to a growing interest in wearable systems. Since these antennas are purposely designed for on-body operation, at 2.45 GHz Industrial, Scientific and Medical (ISM) band, there is a concern on the effects of RF radiation emitted by these antennas. EMF radiations are able to produce thermal effects to body tissues when the exposure limit is exceeded. Thus, it is very important to conduct risk assessment on the RF radiation exposed by wearable textile antenna on human body so as to examine the possible physiological alteration caused by the RF radiation. In the open literature, numerous research has been reported to examine whether RF exposure emitted by mobile phone or base station may affect physiological parameters, cognitive performance and any other related human body parameters [1–6]. Nonetheless, no literature study has been carried out to determine the possible effect of non-ionizing 2.45 GHz WBAN RF radiating by wearable textile antenna on human physiological parameters including body temperature, blood pressure, and heart rate, and cognitive performances. To our knowledge, this study is the first to be reported in open literature to evaluate the effect of RF radiation by wearable textile antenna at 2.45 GHz on human physiological and cognitive performance. The study is conducted under high standard of experimental procedure, ensuring validity and important contribution to EMF effects on people's health.

2 Methods and Material

Twenty volunteers involve in the study (ten are female and ten are male; mean age is 25 years, with standard deviation (SD) = 2.4, minimum age = 23 years and maximum age = 31 year). All volunteers are randomly selected from Universiti Malaysia Perlis, Malaysia who currently study or work here. Before participating in the study, the volunteers are interviewed to determine whether they are physically fit and have no neurological or psychiatric history problems. Healthy volunteers are eligible to take part in the experiments. The study is approved by Ethical Committee, Universiti Malaysia Perlis (Perlis, Malaysia). The methods are carried

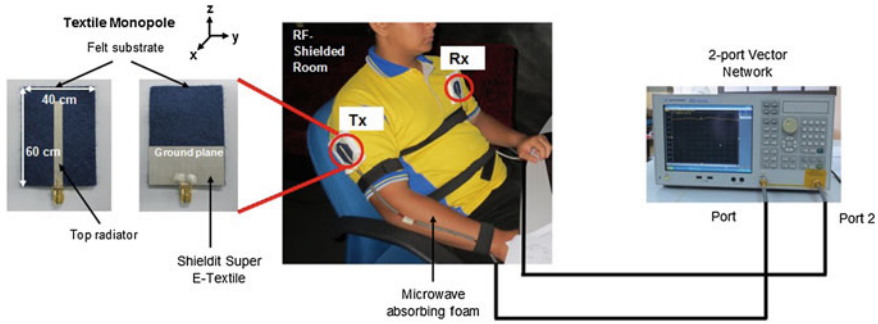


Fig. 1 On-body measurement setup in RF-shielded room, subject in sitting position

out in accordance with the approved guidelines. Written informed consent is obtained from all participants. At the end of experimental sessions, the participants receive small incentives for participation.

2.1 Design

The study is conducted in an RF shielded room, Electromagnetic Hyper Sensitivity (EHS) Laboratory, Jabatan Kejuruteraan Elektrik, Politeknik Tuanku Syed Sirajuddin, Arau, Perlis, Malaysia. The dimension of the RF-shielded room is $4 \times 3 \times 2.5 \text{ m}^3$. The room is furnished with one PC table with PC desktop, one sofa and a plastic armed chair. The presence of flat metallic sheets, covered behind the wall protects the room from the outside electromagnetics (EM) interferences. Subjects are seated on a comfortable armchair, with a distance of 0.5 m from the subject's head to the PC desktop, as shown in Fig. 1. The main objective of the study is to investigate the effects of 2.45 GHz WBAN exposure on physiological parameters and cognitive performance of human being. A counter-balanced randomized and cross-over single-blind condition is designed for the exposure session. Under single-blind condition, the subjects are unaware of the exposure types when they are exposed to WBAN RF radiation. Prior to the experiment sessions, the subjects are briefly described on the aims of the experiment and a short training of cognitive tasks is given to the subjects in the office room. The physiological parameters are assessed in three sessions; pre-exposure, exposure and post-exposure while cognitive performance is only assessed during the exposure session. The subjects attend a 1-h recording session, comprising 60-min of exposure recording. In the first 10-min interval recording, 5-min comprises of exposure-free (pre-exposure), 10-min of exposure and 5-min exposure-free (post-exposure), as shown in Fig. 2. Another 40-min is spent for cognitive tasks. The subject body receives a Radio Frequency (RF) exposure for 10-min. Constant ambient light and room temperature conditions (average: 28.26 ± 0.32) are ensured throughout the whole campaign.

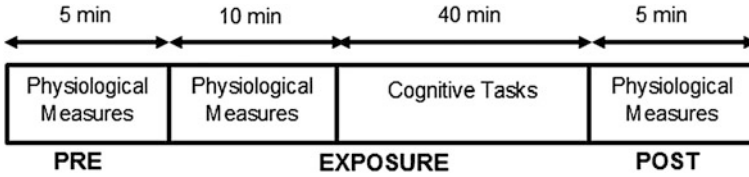


Fig. 2 Experimental time intervals. *Pre* Pre-exposure interval, *Post* post-exposure interval

2.2 Exposure

A pair of quarter-wave, omnidirectional planar textile monopole (TM) antenna operating at 2.45 GHz are utilized. The total dimension of TM is 40 mm × 60 mm with a substrate thickness of 1.7 mm, see Fig. 1. A patch length, $L_M = 0.25\lambda = 30.6$ mm. The quarter-wavelength monopole has an excellent impedance matching and radiation performance in narrowband frequency [7, 8]. To reduce the body coupling effect, TM is mounted 10 mm away from the body by using a thick foam with $\epsilon_r \approx 1$. TM exhibits a reflection coefficient, $S_{11} < -10$ dB over the entire 2.3–2.8 GHz band on the on-body. A 2-port Vector Network Analyzer (VNA) (Agilent model number 5071C ENA) is used to obtain the S_{21} parameter of transmitting (Tx)-receiving (Rx) antennas on on-body locations. RF input power supplied to TM is set to 0 dBm. Tx is fixed at the right side of upper arm while Rx is mounted on the left chest, mimicking the position of ECG sensor. The VNA is consistently calibrated. Two 4 m low-loss flexible Huber + Suhner coaxial cables (Multiflex-141) are utilized to connect Tx with port 1 and Rx with port 2 (see Fig. 1). The simulated Specific Absorption Rate (SAR) value using CST software for TM is 2.88 W/kg (right upper arm) which is well below the maximum permissible level of exposure, 4 W/kg in limbs, according to ICNIRP guideline [9].

2.3 Physiological Measures

The physiological measures consists of three key parameters, i.e., systolic blood pressure (SBP), diastolic blood pressure (DBP), heart rate (HR) and body temperature (BT). These parameters are taken in three sessions. 1. Before exposure (before mounting the body-worn antennas on the body), 2. During exposure (antennas are positioned on the body) and 3. After exposure (after antennas are removed). The blood pressure and heart rate of each subject are recorded using blood pressure wrist measurement device (Beurer, model BC58), complying to World Health Organization (WHO) classification.

2.4 Cognitive Performance

We investigate the effects of wearable TM antenna RF radiation on visual memory PAL and SSP tasks using CANTAB eclipse version 4.0 cognitive software, performed by each subject to assess the visual memory and working memory capacity during the exposure of on-body TM. Subjects are required to memorize specific pattern locations with random assignment in the allocated boxes. If the subject makes an error, the pattern is re-presented to remind the subject of their locations. Three trials are allowable if error is made. In the clinical mode of battery test, the number of patterns increases from 1 to 8. 14 outcome measures for PAL are split into 4 groups; errors, trials, memory scores, stage completed. In this paper, two outcome measures are presented in measuring PAL in the study which are PAL Total errors (adjusted), measuring the total number of errors across all assessed problem and all stages, with an adjustment for each stage not attempted due to previous failure) and PAL Mean errors to adjusted, measuring mean number of errors made before the stage is successfully completed.

Meanwhile, Spatial span (SSP) evaluates working memory capacity and the task is a visuospatial analogue of the Digit Span test. Nine white squares are shown in the task where some of the squares abruptly changes colour in random sequence. Subjects have to touch the white boxes on PC screen according to same order after the sequenced colour boxes disappear (clinical mode). The number of boxes varies from 2 to 9. Besides, in third task, Rapid Visual Processing (RVP) is executed by each subjects during the RF radiation to measure the performance of vigilance and attention where RVP A' corresponds to a signal detection measure of sensitivity to the target regardless of response tendency, scaling 0.00 (bad) to 1.00 (good).

3 Results and Discussions

As a reference, the comparison of measured S_{21} , averaging over 20 subjects, between without body and on-body link (right upper arm-to-left chest) are conducted to observe the electromagnetics (EM) wave propagation over the human body surface by utilizing TM antennas, see Fig. 3. The Tx and Rx are mounted on non-metallic tripods at 1 meter height from the ground, with vertical alignment in without body measurement setup. The very significant difference between S_{21} values without body (ca. -40 dB at 40 cm) and with body (ca. -64 dB at right upper arm-to-left chest link (distance of 37 cm)) are obvious. This indicates that the presence of human body attenuates EM wave as a portion of EM is absorbed by body tissue cells when EM wave propagates along the body surface. The EM absorption effect is further studied by evaluating two main parameters; physiological measures and cognitive performance of participants.

It is observed that the physiological data of three conditions; pre-exposure, exposure and post-exposure independent variables is normally distributed based on

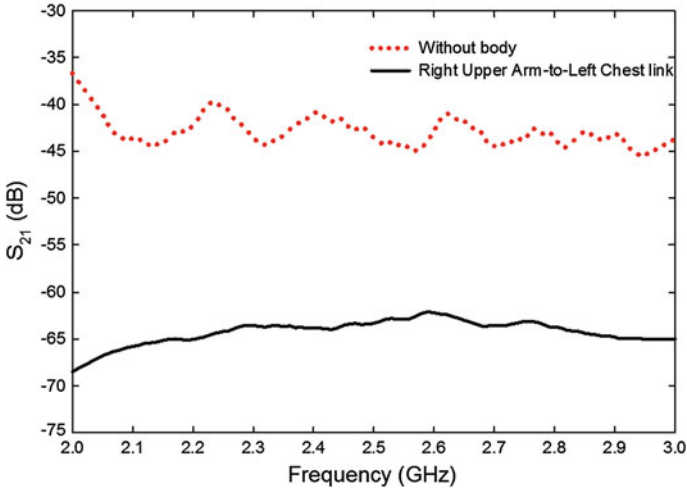


Fig. 3 S_{21} for without presence of body and right upper arm-to-left chest on-body link

Table 1 Statistical tests for physiological measures in pre, exposure and post-exposure sessions

| Physiological measures | 2.45 GHz WBAN | | | | |
|------------------------|---------------|---------------|---------------|----------|----------|
| | Pre | Exp | Post | <i>F</i> | <i>p</i> |
| | M (SD) | M (SD) | M (SD) | | |
| BT | 36.48 (0.10) | 36.32 (0.11) | 36.52 (0.08) | 2.25 | 0.12 |
| SBP | 117.65 (3.06) | 116.10 (3.26) | 116.20 (3.79) | 0.20 | 0.08 |
| DBP ¹ | 72.45 (2.11) | 72.95 (2.61) | 72.85 (2.48) | 0.004 | 0.994 |
| HR | 76.70 (2.30) | 75.65 (1.98) | 77.40 (1.99) | 0.76 | 0.47 |

M mean, *SD* standard deviation
 DBP¹ for original untransformed data

$p > 0.05$ by performing Shapiro-Wilk test, except for DBP. This confirms that the samples come from normal distributed population. A logarithmic transformation is performed to the DBP by transforming the data into normal distribution. The data is therefore analyzed using a one-way, within subjects analysis of variance (ANOVA) with repeated measures of 3 (sessions: pre-exposure, exposure and post-exposure) for each physiological measure. From Table 1, the ANOVA repeated measures of Greenhouse-Geisser *F*-test reveals that there is no significant difference among mean body temperature of subjects in all conditions on 2.45 GHz ISM band field exposures [$F(2, 19) = 2.25, p > 0.05$]. We also find no significant difference in any of the three sessions in mean systolic blood pressure, indicating that the systolic blood pressure is not affected when subjects are exposed to 2.45 GHz ISM band [$F(2, 19) = 0.20, p > 0.05$]. For mean DBP, no significant difference is observed across three sessions [$F(2, 19) = 0.004, p > 0.05$]. Mean heart rate is not affected by exposure as no significant difference is found in any of the three conditions [$F(2,$

Table 2 Results of cognitive performance

| Cognitive test | Sham | RF | Sham versus RF |
|-----------------------------|-------------|-------------|-----------------|
| | Mean (SE) | Mean (SE) | <i>p</i> -value |
| PAL total errors (adjusted) | 5.75 (1.50) | 6.40 (1.43) | 0.72 |
| PAL mean errors to success | 1.65 (0.44) | 0.38 | |
| SSP span length | 6.80 (0.47) | 6.65 (0.40) | 0.71 |
| RVP A' | 0.89 (0.03) | 0.90 (0.03) | 0.34 |

PAL Paired associated learning, *SSP* spatial span, *RVP* rapid visual processing, *SE* standard error

19) = 0.76, $p > 0.05$]. It can be seen from Table 1 that heart rate is reduced by 1.05 bpm during exposure and increased by 0.7 bpm in comparison between pre-exposure and post-exposure conditions.

We use paired sample *t*-test (software: SPSS version 18.0) to analyze the human cognitive performance in terms of visual memory, working memory capacity and attention (condition: RF and Sham). The paired sample *t*-test reveals that there is no significant difference between mean PAL total errors (adjusted) of subjects in both conditions on 2.45 GHz ISM band field exposures [$t(19) = 0.37$, $p > 0.05$]. In the PAL mean errors to success, error increases from Sham to RF exposure condition with no significant difference [$t(19) = 0.90$, $p > 0.05$]. In contrast, there is a decrease in SSP performance between Sham and RF exposure ($p = 0.353$; Table 2). Both conditions does not reach the maximum score 9 as the mean length, $M < 7$ in SSP. Furthermore, it is observed that RVP A' outcome slightly increases from Sham to RF radiation condition at a non-significant level [$t(19) = -0.98$, $p > 0.05$]. Thus, it can be concluded that data provides insufficient evident to indicate a difference in mean outcomes of PAL, SSP and RVP performances (Cognitive) which are assessed in both exposure sessions, WBAN RF and Sham.

4 Conclusion

This paper presents a novel study of risk assessment of non-ionizing 2.45 GHz WBAN RF radiation, emitted by wearable TM antenna on physiological parameters and behavioral (cognitive performance) of human, particularly on visual memory, working memory capacity, and attention. We demonstrate that RF exposure from wearable TM antennas at 2.45 GHz, operated on the body, does not affect physiological parameters (body temperature, blood pressure, and heart rate) and cognitive performance of human. This is the first stage of our study and this work can be considered as preliminary. Future work will be performed to confirm these preliminary results by using different types of textile antenna in a double-blinded condition.

Acknowledgments The authors would like to thank all volunteers who involve in this measurement campaign. The authors also would like to thank Jabatan Kejuruteraan Elektrik, Politeknik Tuanku Syed Sirajuddin, Arau, Perlis, Malaysia for their collaboration in this project. This work is

partially supported by the Knowledge Transfer Programme (KTP) grant by Ministry of Education (MOHE), Malaysia, under grant 9011-00016. The authors would like to express their highest gratitude to MOHE and Universiti Malaysia Perlis.

References

1. Hamblin, D.L., Wood, A.W., Croft, R.J., Stough, C.: Examining the effects of electromagnetic fields emitted by GSM mobile phones on human event-related potentials and performance during an auditory task. *Clin. Neurophys.* **115**, 171–178 (2004)
2. Regel, S.J., Negovetic, S., Roosli, M., Berdinas, V., Schudere, J., Huss, A., Lot, U., Kuster, N., Achermann, P.: UMTS base station-like exposure, well-being, and cognitive performance. *Environ. Health Persp.* **114**, 1270–1275 (2006)
3. Eltiti, S., Wallace, D., Ridgewell, A., Zougkou, K., Russo, R., Sepulveda, F., Mirshekar-Syahkal, D., Rasor, P., Deeble, R., Fox, E.: Does short-term exposure to mobile phone base station signals increase symptoms in individuals who report sensitivity to electromagnetic fields? A double-blind randomized provocation study. *Environ. Health Persp.* **115**, 1603–1608 (2007)
4. Cinel, C., Russo, R., Boldini, A., Fox, E.: Exposure to mobile phone electromagnetic fields and subjective symptoms: a double-blind study. *Psychomat. Med.* **70**, 345–348 (2008)
5. Eltiti, S., Wallace, D., Ridgewell, A., Zougkou, K., Russo, R., Sepulveda, F., Fox, E.: Short-term exposure to mobile phone base station signals does not affect cognitive functioning or physiological measures in individuals who report sensitivity to electromagnetic fields and controls. *Bioelectromagnetics* **30**, 556–563 (2009)
6. Trunk, A., Stefanics, G., Zentai, N., Kovac-Balint, Z., Thuroczy, G., Hernadi, I.: No effects of a single 3G UMTS Mobile phone exposure on spontaneous EEG activity. *ERP Correl. Automat. Deviance Detect. Bioelectromagnetics* **34**, 31–42 (2012)
7. Rahim, H.A., Malek, F., Adam, I., Ahmad, S., Hashim, N.B., Hall, P.S.: Design and simulation of a wearable textile monopole antenna for body-centric wireless communications. In: *PIERS Proceedings*, pp. 1377–1380 (2012)
8. Rahim, H.A., Malek, F., Hisham, N., Malek, M.F.A.: Statistical analysis of on-body radio propagation channel for body-centric wireless communications. In: *PIERS Proceedings*, pp. 374–378 (2013)
9. ICNIRP: Guidelines for limiting exposure to time-varying electric, magnetic, and electromagnetic fields (up to 300 GHz). *Health Phys.* **74**, 494–522 (1998)

Specifically Designed Tag Antenna Based on I-Loop Structure for UHF RFID Applications

Tajchai Pumpoung, Pitchanun Wongsiritorn,
Chuwong Phongcharoenpanich and Sompol Kosulvit

Abstract This paper presents the UHF RFID tag antenna designed for the operating frequency band of 920–925 MHz corresponding to the standard of UHF RFID in Thailand. The tag antenna was fabricated by using a thin FR4 substrate ($\epsilon_r = 4.3$) with the thickness of 0.25 mm. The pattern of the tag antenna is omnidirectional. The “KMITL” text bent dipole is the technique to reduce the physical size of the tag antenna. The I-loop structure is used to improve the impedances of the tag antenna to achieve the conjugate matching with the IC chip. The impedance of the IC chip at the frequency of 922.5 MHz is $21.29 - j191.7 \Omega$. The maximum read range is 4.5 m.

Keywords Impedance matching · Tag antenna design · T-match · UHF RFID tag antenna

1 Introduction

Nowadays, the RFID systems have been used in many applications such as logistics, supply chain, access control, product management in warehouse and many others [1, 2]. The main application of the ultra-high frequency (UHF) RFID is used in the processes of logistics and commercial managements because these

T. Pumpoung (✉) · P. Wongsiritorn · C. Phongcharoenpanich · S. Kosulvit
Faculty of Engineering, King Mongkut's Institute of Technology Ladkrabang, Bangkok
10520, Thailand
e-mail: o_onny1@hotmail.com

P. Wongsiritorn
e-mail: kacher_911@hotmail.com

C. Phongcharoenpanich
e-mail: kpchuwon@kmitl.ac.th

S. Kosulvit
e-mail: kpsompol@kmitl.ac.th

applications require the long-range communication [3, 4]. The standard of the UHF RFID in each country is different [5]. In Thailand, the allocated frequency of the UHF RFID is 920–925 MHz.

Generally, a UHF RFID tag is attached to a product package such as a parcel, a paper box and others. When a tag is used to identify an interested object, it is generally in the form of label with a logo of a product. Occasionally, the structure of the tag antenna can be clearly seen on the identified products.

Therefore, a logo of a product becomes a very important part that illustrates an identity of company brand or the brand of products. The tag antenna structure that can attract the users, while the characteristics of the tag antenna still have efficient performance for the interested applications becomes an urgent issue.

One of the importance for a logo tag design is the pattern of a desired logo which is become an important part for a tag antenna. These proposed logo is not only to identify the product brand but also become the radiating part of the tag antenna which can provide the desired characteristics of the tag antenna such as impedance matching of the tag antenna and the IC chip, appropriate read range, relatively small size with low cost for fabrication.

This paper presents the “KMITL” tag antenna with I-Loop structure. It is designed for UHF RFID applications with the impedance of the NXP G2XL IC chip [6] of the impedance $21.29 - j191.7 \Omega$ at the frequency of 922.5 MHz that is the center frequency of standard in Thailand.

2 The Tag Antenna Design

2.1 The Principle of the RFID System

The importance of the tag antenna design is the impedances of the tag antenna that has to conjugate match with the IC chip or the signal source because the conjugation of the both components that affect to the efficiency of the maximum read range between reader and tag antenna which is given by [7].

$$d_{\max}(\theta, \varphi) = \frac{c}{4\pi f} \sqrt{\frac{EIRP_R}{P_{IC}} \tau G_{\text{tag}}(\theta, \varphi)}, \quad (1)$$

where $G_{\text{tag}}(\theta, \varphi)$ is the tag gain.

$$\tau = \frac{4R_{IC}R_A}{|Z_{IC} + Z_A|^2} \leq 1 \quad (2)$$

τ is the power transmission coefficient which accounts for the impedance mismatch between the antenna ($Z_A = R_A + jZ_A$) and the IC chip ($Z_{\text{chip}} = R_{\text{chip}} + jZ_{\text{chip}}$).

Normally, from the matching technique for the UHF RFID tag antenna from the recently scientific literature, the structure will be often included the inductively

coupled loop [7, 8] or the T-matching structure [7, 9–12] to improve the matching impedance between the tag antenna and the IC chip. The I-loop structure which is similar to T-matching technique is presented to improve the matching condition.

2.2 Parametric Studies and Improvement of the Impedance

An initial design is to determine the sizes of the antenna to provide the compact size. W is the width of the tag antenna with 10 mm. L is the total length of the tag antenna with 40 mm or $\approx 0.5\lambda_d$ and λ_d is wavelength in the dielectric. The structure and equivalent circuit of the proposed tag antenna is presented in Fig. 1a. and Fig. 1b, respectively.

Then, the l_{sk} , l_{sm} , l_{si} , l_{st} and l_{sl} are defined as the widths of the each letter with 5 mm. The height of the letter is w_s with 8 mm. The spacing between each letter and the letters to the edge of the antenna are defined as g_k , g_{km} , g_{mi} , g_{il} , g_{tl} and g_l with 2.5 mm. The C_b , C_o , C_w are the parameters of the supporter, providing to attach the IC chip on the tag antennas with the sizes of 3, 5, 4 mm, respectively. The initial structure of “KMITL” tag antenna with I-loop structure is shown in the Fig. 2.

Next, the effect of the parameters is studied by a simulation. The logo is designed by starting with the first letter “I” until the last one is letter “L”. The impedance of the initial structure “KMITL” tag antenna with I-loop structure is illustrated in the Fig. 3. It is found that when each letter is added until it becomes completed “KMITL” letter at the center frequency of 922.5 MHz, the impedance of $1.23 + j91.78 \Omega$ is obtained.

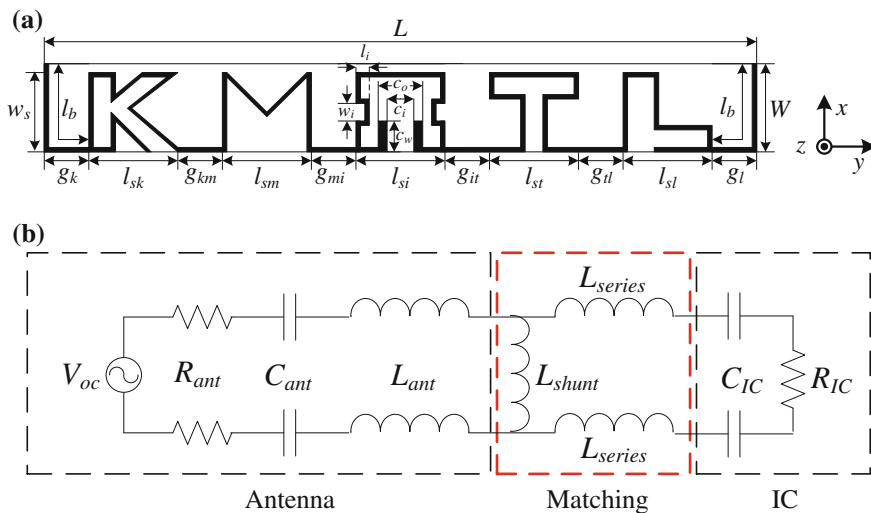


Fig. 1 The structure and the equivalent circuit of “KMITL” tag antenna with I-loop structure

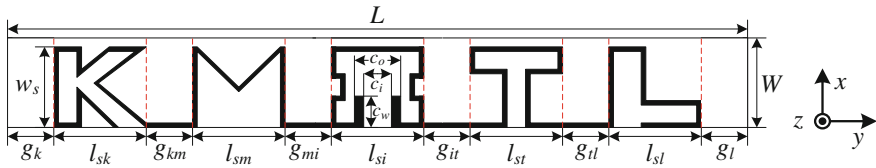


Fig. 2 The initial structure of “KMITL” tag antenna with I-loop structure

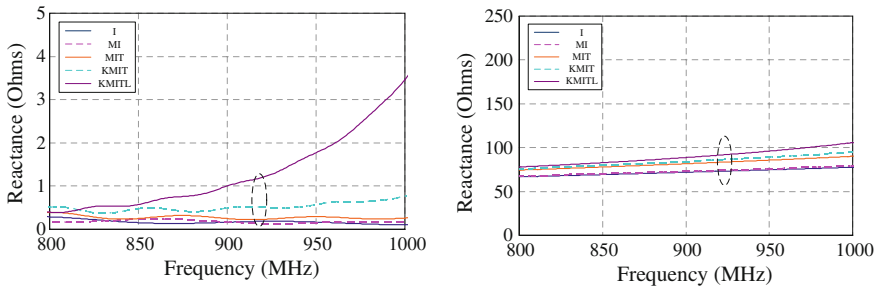


Fig. 3 The impedance of the initial structure “KMITL” tag antenna with I-loop structure

The second step is to improve the impedance of the antenna by extending the lengths of the bent dipoles on the both sides of the letter edges of K and L with 12.5 mm. These parameters are defined by l_b , as shown in Fig. 4.

Then, l_i is varied and w_i and l_{si} are fixed at 2.0 and 5.0 mm, respectively. It is obvious that when adding the bent dipole and various l_i parameter the resistance and reactance will be increased higher than the initial antenna. The appropriated matching impedance in this step is obtained when l_i is equal to 1.0 mm with $13.95 + j151.36 \Omega$ as shown in Fig. 5.

At the third step, parameter l_{si} is varied from 5.5 to 7.5 mm to improve the antenna impedance matching as shown in Fig. 6. It is obvious that the resistance and reactance is increased. At l_{si} of 6.5 mm, the closest impedance with the matching point is obtained with the impedance of $18.44 + j187.99 \Omega$ as shown in the Fig. 7.

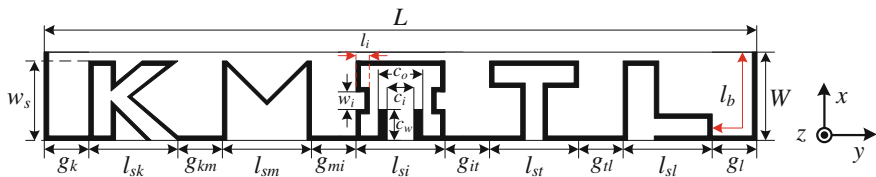


Fig. 4 The parameter and structure of “KMITL” tag antenna with I-loop structure with adding l_b and various l_i

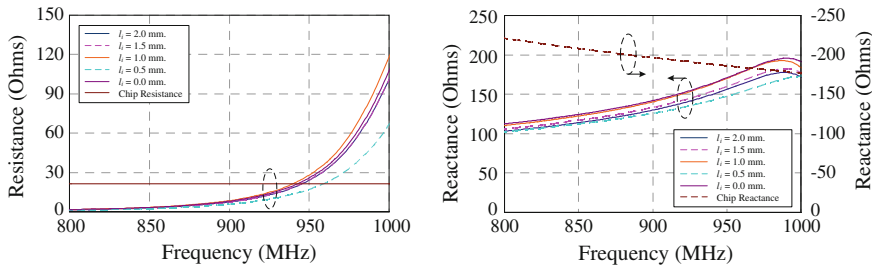


Fig. 5 The impedance of “KMITL” tag antenna with I-loop structure with adding l_b for various l_i

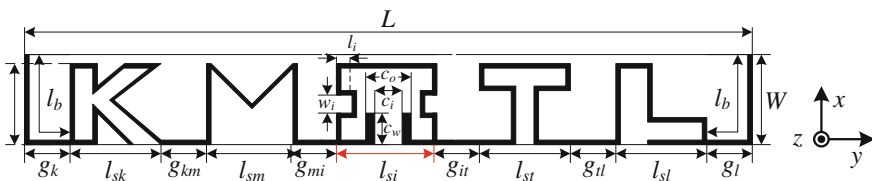


Fig. 6 The parameter and structure of “KMITL” tag antenna with I-loop structure

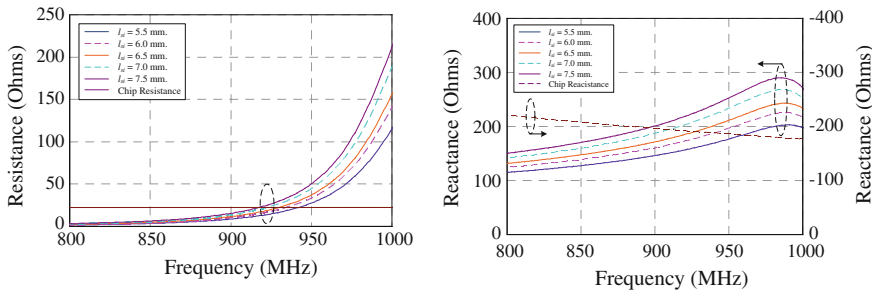


Fig. 7 The impedance of “KMITL” tag antenna with I-loop structure for various l_{si}

The final step is to adjust the l_i again to determine the desired impedance of the proposed tag antenna as shown in Fig. 8.

In Fig. 9, for the length of l_i from 0.5 to 2 mm, the impedances of the tag antenna are quite similar. However, at l_i of 2.5 mm, the impedance is rather different from other lengths. The best impedance of the proposed antenna is obtained when l_i is

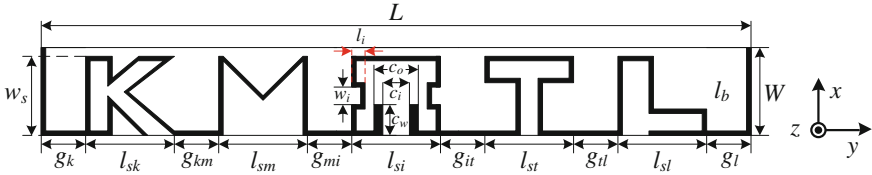


Fig. 8 The final structure of “KMITL” tag antenna with I-loop structure

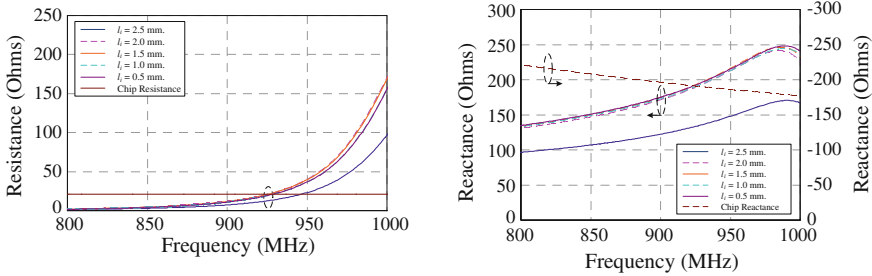
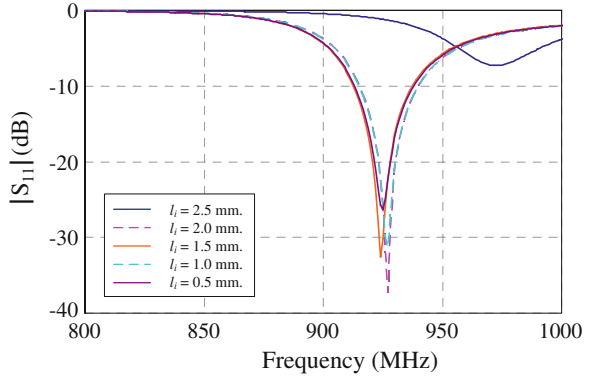


Fig. 9 The impedance of “KMITL” tag antenna with I-loop structure

Fig. 10 The $|S_{11}|$ (dB) of “KMITL” tag antenna with I-loop structure



equal to 1.5 mm with $19.63 + j190.35 \Omega$ at 922.5 MHz, and $|S_{11}|$ (dB) is -25.83 dB as shown in Fig. 10.

3 Characteristics

In this section, the simulated characteristics of the proposed antenna are illustrated which consist of $|S_{11}|$ (dB), the percentage transmission and radiation pattern.

3.1 The Characteristic Impedance and Transmission Coefficient

The simulated impedances of the designed tag antenna is illustrated in Fig. 11a with $19.63 + j190.35 \Omega$ at 922.5 MHz. Figure 11b shows $|S_{11}|$ (dB) and the percentage transmission of the tag antenna with -25.83 dB and 99.71 %, respectively.

3.2 The Radiation Pattern and Gain of the Antenna

The pattern of the proposed tag antenna is the omnidirectional beam as shown in Fig. 12a. In Fig. 12b the gain of the tag antenna is 1.87 dBi, considered at the center frequency of 920–922.5 MHz band.

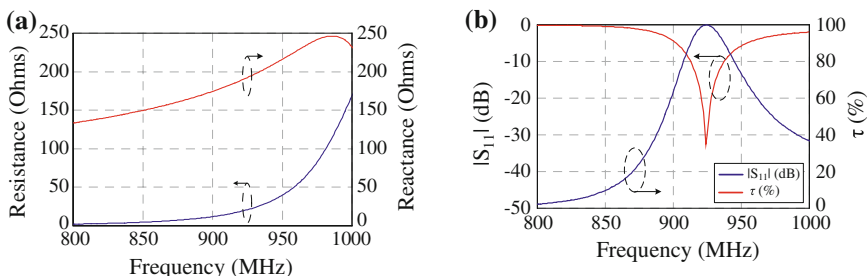


Fig. 11 a The impedance, and b the $|S_{11}|$ (dB) and percentage power transmission of “KMITL” tag antenna with I-loop structure

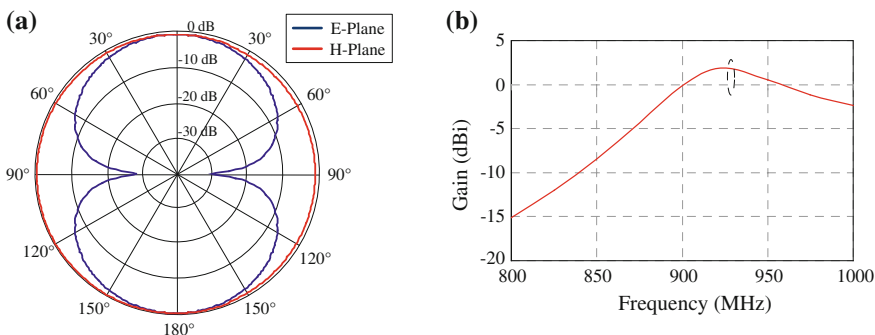


Fig. 12 a The radiation patterns, and b gain of the “KMITL” tag antenna

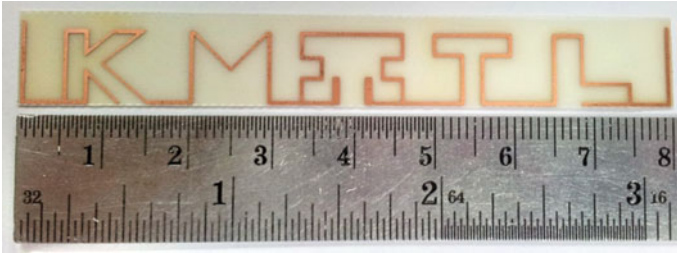


Fig. 13 The photograph of the prototype tag antenna

4 Fabrications and Measurement

The prototype antenna was fabricated by using the parameters in the final designed step. The proposed tag antenna has the size of $80 \times 10 \text{ mm}^2$. The photograph of the proposed antenna is depicted in Fig. 13. The maximum read range was measured by using Symbol Technology Reader (XR 480). The reader antenna radiates circular polarization, and its gain is 7.9 dBic. The obtained maximum read ranges are 4.5 m.

5 Conclusions

The tag antenna for the UHF-RFID system in Thailand is presented in this paper. From the design, it can operate for the UHF RFID of standard in Thailand. The dimension of the proposed antenna is $80 \times 10 \text{ mm}^2$ which can be achieved by using the I-loop structure and text bent technique to improve the matching condition. The I-loop structure is also added to improve the impedance matching and the noticeable structure of the tag antenna. The appropriate input impedance of the tag antenna for conjugate matching with the IC chip impedance is found to be $21.29 + j191.7 \Omega$. The input impedance of the proposed tag antenna is equal to $19.63 + j190.35 \Omega$, considered at the center frequency of 922.5 MHz. As a result, the percentage power transmission is approximately 99.71 % from the calculation. The radiation pattern is omnidirectional beam. From the measurement, the maximum read range of the proposed antenna is equal to 4.5 m. This tag antenna can be effectively employed in the national standard of the UHF RFID system in Thailand.

Acknowledgments Financial support from the Telecommunications Research and Industrial Development Institute, National Telecommunications Commission Fund (Grant No. PhD/009/2010) to Tajchai Pumpoung and Chuwong Phongcharoenpanich is acknowledged. This work is also supported by the Thailand Research Fund (TRF) under the Royal Golden Jubilee Ph.D. Program with Grant no. PHD/0073/2553.

References

1. Pumpoung, T., Phongcharoenpanich, C., Kosulvit, S.: Investigations of miniaturized meander line tag antenna for UHF RFID system. In: Proceedings of International Symposium on Antennas and Propagation 2010, pp. 587–590. ISAP Press, Macau (2010)
2. Ozguven, E.E., Ozbay, K.: An RFID-based inventory management framework for efficient emergency relief operations. In: IEEE International Conference on Intelligent Transportation Systems Anchorage 2012 (ITSC 2012), pp. 1274–1279. IEEE Press, Anchorage (2012)
3. Chawla, V., Ha, D.S.: An overview of passive RFID. *IEEE Commun. Mag.* **45**(9), 11–17 (2007)
4. Pumpoung, T., Phongcharoenpanich, C., Kosulvit, S.: UHF-RFID tag antenna with T-matching and two ended rectangular loops. In: Proceedings of Joint International Conference on Information & Communication Technology, Electronic and Electrical Engineering 2010, pp. 516–519. JICTEE Press, Luang Prabang (2010)
5. Seshagiri-R, K.V., Nikitin, P.V., Lam, S.F.: Antenna design for UHF RFID tags: a review and a practical application. *IEEE Trans. Antennas Propagat.* **53**(12), 3870–3876 (2005)
6. NXP Semiconductors: <http://www.nxp.com>
7. Marrocco, G.: The art of UHF RFID antenna design: impedance matching and size-reduction techniques. *IEEE Antennas Propagat. Mag.* **50**(1), 66–79 (2008)
8. Son, H.W., Tyo, C.S.: Design of RFID tag antennas using an inductively coupled feed. *IEEE Electron. Lett.* **41**(18), 994–996 (2005)
9. Balanis, C.A.: *Antenna Theory. Analysis and Design*, 3rd edn. Hoboken (2005)
10. Pozar, D.M.: *Microwave Engineering*, 3rd edn. USA (2008)
11. Pumpoung, T., Phongcharoenpanich, C., Kosulvit, S.: UHF-RFID tag antenna using diamond structure and rectangular loop. In: IEEE Proceedings of Electrical Engineering/Electronics, Computer, Telecommunications and Information Technology conference 2011, pp. 220–223. IEEE Press, Khon Kaen (2011)
12. Dobkin, D.M.: *The RF in RFID passive UHF in practice*. Burlington (2008)